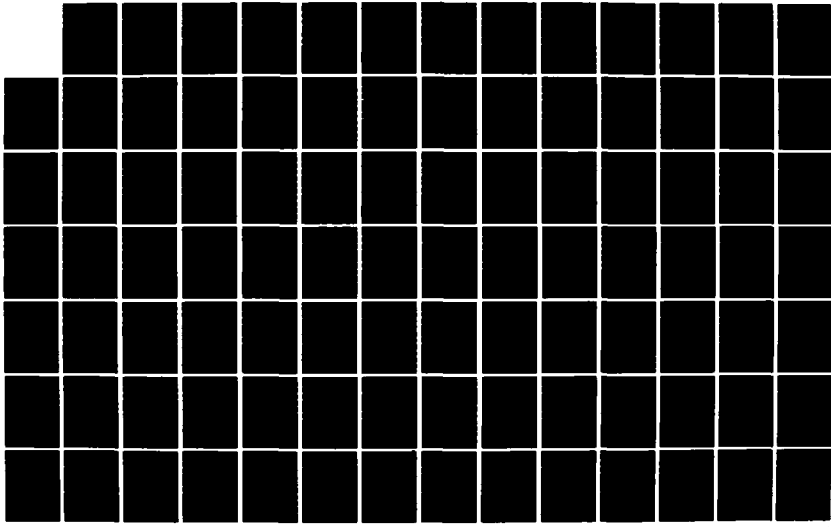


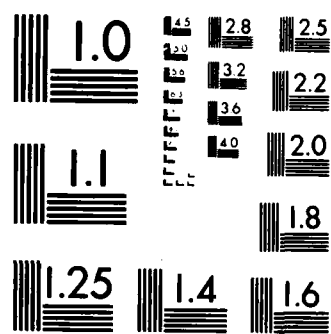
✓ AD-A150 028 SEMICONDUCTOR MATERIALS FOR HIGH FREQUENCY SOLID STATE 1/4  
SOURCES(U) SCIENTIFIC RESEARCH ASSOCIATES INC  
GLASTONBURY CT H L GRUBIN ET AL. 18 JAN 85

UNCLASSIFIED

SRA-R85-920016-F N00014-82-C-0697

F/G 20/12 NL





MICROCOPY RESOLUTION TEST CHART  
NATIONAL BUREAU OF STANDARDS-1963 A

(12)

AD-A150 020

DMC FILE COPY

SEMICONDUCTOR MATERIALS FOR HIGH  
FREQUENCY SOLID STATE SOURCES

FINAL REPORT: R85-920016-F

H.L. Grubin, J.P. Kreskovsky, M. Meyyappan and B.J. Morrison

Prepared for the Defense Advanced Research Project Agency

January 1985

Scientific Research Associates, Inc.  
P.O. Box 498  
Glastonbury, CT 06033



85 01 25 065

Unclassified

SECURITY CLASSIFICATION OF THIS PAGE

REPORT DOCUMENTATION PAGE

1. REPORT SECURITY CLASSIFICATION Unclassified		1b. RESTRICTIVE MARKINGS	
2a. SECURITY CLASSIFICATION AUTHORITY		3. DISTRIBUTION/AVAILABILITY OF REPORT Approved for Public Release Distribution Unlimited	
2b. DECLASSIFICATION/DOWNGRADING SCHEDULE			
4. PERFORMING ORGANIZATION REPORT NUMBER(S) R85-920016-F		5. MONITORING ORGANIZATION REPORT NUMBER(S)	
6a. NAME OF PERFORMING ORGANIZATION Scientific Research Associates Inc.	6b. OFFICE SYMBOL (If applicable)	7a. NAME OF MONITORING ORGANIZATION Office of Naval Research	
6c. ADDRESS (City, State and ZIP Code) P.O. Box 498 Glastonbury, CT 06033	7b. ADDRESS (City, State and ZIP Code) 800 North Quincy Street Arlington, VA 22217		
8a. NAME OF FUNDING/SPONSORING ORGANIZATION Defense Advanced Research Projects Agency	8b. OFFICE SYMBOL (If applicable)	9. PROCUREMENT INSTRUMENT IDENTIFICATION NUMBER N00014-82-C-0697	
8c. ADDRESS (City, State and ZIP Code) 1400 Wilson Boulevard Arlington, VA 22209	10. SOURCE OF FUNDING NOS.		
11. TITLE (Include Security Classification) Semiconducting Materials (unclassified)	PROGRAM ELEMENT NO.	PROJECT NO.	TASK NO.
12. PERSONAL AUTHOR(S) H.L. Grubin, J.P. Kreskovsky, M. Meyyappan, B.J. Morrison	WORK UNIT NO.		
13a. TYPE OF REPORT Final Report	13b. TIME COVERED FROM 82/6 TO 84/8	14. DATE OF REPORT (Yr., Mo., Day) 1985 January 18	15. PAGE COUNT 339
16. SUPPLEMENTARY NOTATION None			
17. COSATI CODES		18. SUBJECT TERMS (Continue on reverse if necessary and identify by block number) submicron devices, high speed transport, velocity overshoot, gallium arsenide, indium phosphide, gallium indium arsenide, band structure, scaling, velocity saturation	
19. ABSTRACT (Continue on reverse if necessary and identify by block number) This report summarizes the results of a study undertaken to examine the role of band structure, material characteristics, device feature size, and donor density on the electrical properties of two and three terminal submicron scale semiconductor devices. The study is based on the introduction of scaling to the space and time dependent moments of the Boltzmann transport equation. The study broadly concludes that while gallium arsenide is likely to remain the material of choice for present high speed-high frequency applications, materials with scattering rates higher than that of gallium arsenide, while retaining negative differential mobility, are to be sought after for two terminal active device operation. Materials with scattering rates below that of gallium arsenide are to be sought after for three terminal operation. It is demonstrated that the significant figures of merit for FET operation should be based on the $\Gamma$ valley mobility, rather than the high field saturated drift velocity. A hierarchy of materials choices is suggested in this study.			
20. DISTRIBUTION/AVAILABILITY OF ABSTRACT <input checked="" type="checkbox"/> UNCLASSIFIED/UNLIMITED <input type="checkbox"/> SAME AS RPT. <input type="checkbox"/> DTIC USERS <input type="checkbox"/>		21. ABSTRACT SECURITY CLASSIFICATION	
22a. NAME OF RESPONSIBLE INDIVIDUAL Dr. Larry R. Cooper		22b. TELEPHONE NUMBER (Include Area Code) (202) 696-4214	22c. OFFICE SYMBOL Code 427

## TABLE OF CONTENTS

	<u>Page</u>
I. INTRODUCTION .....	1
II. THE GOVERNING EQUATIONS USED IN THE STUDY AND THEIR DIMENSIONLESS FORM .....	7
III. ONE DIMENSIONAL ILLUSTRATIVE CALCULATIONS USING THE MOMENTS OF THE BOLTZMANN TRANSPORT EQUATIONS .....	14
IV. INTRINSIC SCALING AND THE MOMENTS OF THE BOLTZMANN TRANSPORT EQUATION .....	17
V. CALCULATIONS WITH CONSTANT GOVERNING DIMENSIONLESS PARAMETERS AND VARIABLE SCATTERING RATES TIED TO EXTRINSIC PARAMETERS .....	22
VI. CALCULATIONS WITH CONSTANT GOVERNING DIMENSIONLESS PARAMETERS AND CONSTANT SCATTERING RATES TIED TO INTRINSIC MATERIAL PROPERTIES .....	24
VII. CALCULATIONS WITH CONSTANT GOVERNING DIMENSIONLESS PARAMETERS AND VARIABLE SCATTERING RATES TIED TO INTRINSIC MATERIAL PROPERTIES .....	26
VIII. CALCULATIONS WITH VARIABLE DONOR DENSITY .....	29
IX. NONUNIFORM FIELDS, LENGTH SCALING .....	30
X. TWO DIMENSIONAL SCALING CONSIDERATIONS .....	34
XI. TWO DIMENSIONAL TRANSPORT WITH MATERIAL SCALING WITHIN THE FRAMEWORK OF THE DRIFT AND DIFFUSION EQUATIONS .....	37
XII. SMALL SIGNAL DEVICE BEHAVIOR .....	41
XIII. SPACE CHARGE INJECTION FIELD EFFECT TRANSISTORS .....	42
XIV. SUMMARY .....	43
FIGURE CAPTIONS .....	44
REFERENCES .....	48
FIGURES	
APPENDIX A - THE ROLE OF BOUNDARY CONDITIONS TO NEAR AND SUBMICRON LENGTH GALLIUM ARSENIDE STRUCTURES	
APPENDIX B - SCALING BAND STRUCTURE AND MATERIAL CHARACTERISTICS OF HIGH SPEED SUBMICRON LENGTH DEVICES	

SEMICONDUCTOR MATERIALS FOR HIGH  
FREQUENCY SOLID STATE SOURCES  
FINAL REPORT: R85-920016-F

H.L. Grubin, J.P. Kreskovsky, M. Meyyappan and B.J. Morrison

Defense Advanced Research Project Agency

ARPA ORDER NO.: 4599

CONTRACT NO.: N00014-82-C-0697

EFFECTIVE DATE OF CONTRACT: 1 September 1982

EXPIRATION DATE OF CONTRACT: 31 August 1984

PRINCIPAL INVESTIGATOR: Dr. Harold L. Grubin

TELEPHONE NO.: (203) 659-0333

SHORT TITLE OF WORK: Semiconducting Materials

REPORTING PERIOD: 1 June 1982 - 31 August 1984

Accession For	
NTIS GRA&I	<input checked="" type="checkbox"/>
DTIC TAB	<input type="checkbox"/>
Unannounced	<input type="checkbox"/>
Justification	
By _____	
Distribution/	
Availability Codes	
Dist	Avail and/or Special
A-1	

FISCAL STATUS:

- (1) Amount currently provided on contract: 199,768
- (2) Expenditures and commitments to date: 196,423
- (3) Funds required to complete work: 3,345



Scientific Research Associates, Inc.  
P.O. Box 498  
Glastonbury, CT 06033

SCALING AND BAND STRUCTURE DEPENDENT TRANSPORT IN NEAR  
AND SUBMICRON LENGTH SEMICONDUCTOR DEVICES

H.L.Grubin, J.P.Kreskovsky, M. Meyyappan and B.V. Morrison  
Scientific Research Associates, Inc.  
P.O.Box 498  
Glastonbury, Connecticut 06033

I. INTRODUCTION

The trend in the semiconductor device industry has been to higher density chips and faster devices. This technology has been accomplished by scaling down present devices using a variety of scaling procedures, some of which are now taught as part of the standard undergraduate curricula. There is, however, a dilemma, and of course and accompanying challenge. First, why is there difficulty in suitably scaling down the semiconductor gallium arsenide (GaAs)? Second, is GaAs the optimum semiconductor for high frequency application? Third, are there scaling principles, either extrinsic or intrinsic, that may be developed to permit a match between the semiconductor device and the semiconductor in question? Fourth, is the FET as commonly configured, the optimum design for high frequency and high speed operation? Each of these questions has been addressed, with varying degrees of completeness during the past two years under a DARPA sponsored study (ONR Contract No.:N00014-82-C-0697). Several key results have emerged from the study:

1. The optimum choice of semiconductor material is dependent upon the application envisioned. For example, a low noise two terminal high frequency local oscillator requirement would require a semiconductor with a region of negative differential mobility that persisted at frequencies well in excess of 100GHz. In this case GaAs may be of marginal use, but a material such as indium phosphide may be the semiconductor of choice. For the three terminal device, in particular the FET, the region of negative differential mobility is not the key to device operation and does not enter as a figure of merit. Rather, the low field mobility is a key issue. Thus, GaAs is likely to be one of the best compromises for high speed performance, when compared to such materials as indium phosphide (InP). Improvements may be expected when materials such as GaInAs are considered; where the key is to obtain materials with high values for the low field mobility, and decreased intervalley transfer.
2. High field saturated drift velocity, often regarded as a key figure of merit for semiconductor FETs is not likely to be a relevant parameter for submicron FETs. The more significant parameter is the low field mobility of the semiconductor.
3. Band structure and material scaling are effective means for the understanding operation of present submicron semiconductor devices and establishing a set of guidelines for the engineering of new semiconductor materials.

With regard to scaling, guidance can be provided by discussions extant in undergraduate texts. Here, under conditions of constant field scaling feature sizes are reduced by scaling down the critical lengths and voltages, while the background density is increased. Additionally, improvements in the transconductance arise with improvements in mobility, and for long devices,

improvements in the saturated drift velocity. Thus, the scaling arguments discussed below incorporate systematic changes in

- i. length,
- ii. voltage,
- iii. background density
- iv. band structure parameters designed to produce alterations in the low field mobility, saturated drift velocity, intervalley transfer, etc.

Scaling discussion are, of course, well known to workers in the semiconductor device field. We are reminded here of the work of Dennard [1]. The unique feature of the study summarized below, is that the scaling arguments are predicated upon application of the moments of the Boltzmann transport equation. Thus, implicit in the discussion, is the inclusion of nonequilibrium transport and velocity overshoot effects. As a result, the conclusions of the study have an immediate application to present semiconductor technology, and the choice of materials, thereof.

But from a long term viewpoint the significance of the scaling arguments used below is even more direct. An example considered during the Contract period was the effect of the variation of the intervalley deformation potential coupling coefficient on the device behavior. While these results are discussed below they may be of potential significance to the design of semiconductor strained superlattices [2]. For example, it is conceptually possible to construct a strained layer superlattice from alternate layers of n-type materials, such as GaAs and GaAlAs. Each of these host semiconductors possesses its own lattice constant (they are nearly the same for both), its own periodicity and its own Brillouin zone size. The strained layer superlattice has a periodicity that is significantly greater than that of either host element and consequently a Brillouin zone size that is smaller than either host element. If the mean free path of the majority carriers, in the strained superlattice, is larger than the periodicity of the superlattice, it is anticipated that the resultant deformation potential coupling coefficient will be a perturbation of the coupling coefficient of the dominant host element. For this case, the results of the scaling arguments given during this study are directly applicable. On the other hand, if the mean free path of the majority carriers is less than that of the superlattice periodicity, or if neither host semiconductor is dominant, then a complete band structure calculation is required; and only general principles emerging from this study are relevant.

The philosophy of the study involved over the course of the Contract period. Initially, the emphasis was to select materials that would be intrinsically suitable as active elements for high frequency application. It became quickly apparent, however, that materials exhibiting the desirable attribute of high mobility would not necessarily be synonymous with active high frequency performance. Here, when referring to a active device, the paradigm structure is the two terminal transferred electron coplanar Gunn oscillator currently being pursued at NRL, for 94GHz operation [3]. However, since two terminal structures are not likely to be the first choice for high frequency operation the structure towards which emphasis was directed was the field effect transistor, as reflected in the final report.

The study reported below is numerical and reflects the essential device physics guidelines established during the Contract period. The results of the study have been prepared for publication in the form of two long comprehensive studies, one of which has already been accepted for publication. The second is being prepared for publication. These studies contain the critical details and results of a significant portion of the study performed under the DARPA sponsored program. Both of these studies are included as Appendix A and B of this document. However, the body of the final report has been written as a 'stand-alone' document and the relevant portion of these papers have been included, to assure continuity of discussion. Thus section II, which contains a discussion of the equations used in the study, includes only brief descriptions of how these equations are altered during the course of the scaling study. It is noted that two sets of equations were used in the course of the study: the moments of the Boltzmann transport equation, and the semiconductor drift and diffusion equations. The equations of choice are clearly the moment equations, but their state of development, and associated costs, precludes performing as many two dimensional calculations as is customary when implementing the semiconductor drift and diffusion equations.

Section III provides a brief description of the one dimensional transient calculations using the moments of the Boltzmann transport equation. The section is designed to introduce some of the language used in the report. Details of the calculation form the core of Appendix A.

Section IV is concerned with illustrating how scaling is applied to the Boltzmann transport equation. Here the concepts of constant scattering scaling as applied to transient transport, and introduced by Thornber [4], are discussed. Specific application is made to the semiconductors GaAs and InP whose scattering rates are introduced. The point is that materials such as InP and InGaAs can be approximately represented as scaled GaAs elements, and the relative advantages of one against another immediately assessed. Again, assessment rests upon specific device application. Additionally, the significant contribution of nonuniform fields in scaling is also introduced, and shown that necessarily, material scaling must be accompanied by density scaling.

Section V is an introductory discussion of scaling as applied to the semiconductor GaAs. Here on the basis of trends in the semiconductor industry in which intrinsic material changes are almost always accompanied by suitable scaling of such extrinsic variables as length and doping level, the following generic type of problem is addressed: If a material could be constructed whose low field mobility is a constant multiple,  $\lambda$ , of the low field mobility of GaAs, and whose remaining steady state field dependent velocity is a compressed version of that of GaAs; can the steady state and transient characteristic of the scaled device be predicted. On the basis of the discussion in section III, the answer to this question is immediately relevant to the semiconductors InP and InGaAs and their use as substitutes or replacements for GaAs.

The discussion of section V was chosen to serve as an intuitive guide and reference point for additional scaling. For example, the situation may arise when a particular feature size of a device is a specification of the problem; and the task then becomes determining what changes in the electrical characteristics may be expected when there is a choice of materials. This problem is treated in two parts. In section VI a two terminal structure of length 0.25 microns and a doping level of  $8 \times 10^{16}/\text{cm}^3$  is examined. Material

variations are considered by altering the scattering rates by the constant  $\lambda$ . In section VI, the choices of  $\lambda$  are:  $\lambda=1$ , 2 and 4.

The discussion of section VI is continued in section VII, where isolated band structure alterations are introduced. In this case the scattering rates as used with the moments of the Boltzmann transport equation, are changed by a constant amount, but are nonuniformly altered. For example, in section VIIa, the deformation coupling coefficient for intervalley transfer is altered. That is, starting from the value used in the calculations for GaAs, the deformation coupling coefficient  $D_{FL}$  is multiplied by the factors '2' and '1/2'. The resulting steady state nonuniform field calculations are then compared to that of GaAs. The calculations are performed for the same extrinsic values as those used in section VI, and a direct comparison is offered. As anticipated, the uniform field calculations show an increase in the saturated drift velocity with increased coupling coefficient. When this result is folded into earlier studies using the drift and diffusion equation (see e.g., Grubin [5]), higher values of IDSS may be anticipated. However, when transport in submicron devices is considered it is determined, that the significant figure of merit is the low field mobility of the semiconductor; and if the improvements in velocity saturation are not accompanied by improvements in the low field mobility, there is little to be gained by choosing materials with high field velocity saturation.

The situation that tends to show both a satisfactory low field mobility and a high saturated drift velocity occurs when the intervalley energy separation in GaAs is doubled. The dimensions and scaling of this calculation, which are discussed in section VIIb, are best understood when placed in the context of the GaAs calculations of section V. The results of this calculation are designed to show the trends that should be expected when the energy separation is increased, and tends to suggest significant advantages for GaInAs over GaAs for high speed transport in three terminal devices.

All of the calculations performed through section VIIb have ignored the effects of ionized impurity scattering. There are indeed conceptual difficulties in dealing with high donor densities and ionized impurity scattering in submicron devices, each of which have been addressed in previous discussions (see e.g., Grubin and Ferry [6]), but are ignored here. From the point of view of the discussion of scaling, the effect of ionized impurity scattering is regarded as introducing nonuniform contributions to the scattering rates; here the effects of ionized impurity scattering influences only the momentum scattering rate. This discussion of ionized impurity contributions is contained in section VIIc.

One of the critical issues associated with device transport is whether an increase in the carrier density by a constant value,  $\lambda$ , will lead to an increase in the current density by the same factor,  $\lambda$ . The answer to this question is a negative one, and the principle reason that classical scaling, which ignores the spatial variations in the density, leads to over-optimistic predictions. The question of carrier density dependence is addressed in section VIII.

While the calculations of the previous sections emphasized the effects of intrinsic scaling and included calculations for structures of different lengths, little emphasis was placed on length scaling and its effects on device performance. In section IX the effects of length scaling are discussed for two situations. The first situation is for a uniformly doped structure with a comparison of results for structures of length 0.25 and 1.00 microns. The

second structure considered is that of a  $N^+N^-N^+$  device, with a one-micron cathode-to-anode spacing but with a variable length  $N^-$  region. At this point, the two terminal  $N^+N^-N^+$  structure is examined for several reasons. First, it provides a realistic assessment of submicron structures that are likely to be fabricated. Second, the results point to the fact that care must be exercised in interpreting results with devices that are loosely referred to as submicron devices. In particular we have found, that one micron long devices with sub-micron features under 0.1 micron cannot necessarily be regarded as submicron structures. The details are reported below. Third, current transients associated with these devices completely confuse the issue of temporal velocity overshoot. The results as discussed below show that initial transients may have their origin in displacement current contributions. Thus, this last two-terminal structure offers the most serious example of the interplay of the interface and the length of the critical submicron region on the electrical characteristics of the submicron structures.

Two dimensional scaling considerations are addressed in the remaining portions of the study. Section X addresses typical scaling in two dimensions as discussed by Bar-Lev [7], and ties these concepts to those addressed during the course of the study. Weaknesses in predictions of high frequency operation are addressed in section X, through solutions to the drift and diffusion equations for a low and high frequency GaAs FET. The clear implication of these studies is that scaling will lead to improved performance, but that the predictions based upon simple scaling will tend to be over-optimistic.

Section XI reviews already published studies, that tie the role of saturation in the drift velocity to FET performance, and connects the results to the discussion of the earlier chapters on scaling. Additionally, preliminary computations using the DDE with GaAs parameters yielding a cutoff frequency of 9.0GHz, demonstrate that scaling down the critical feature size by an order of magnitude is likely to increase the cutoff frequency to values near 90GHz. Section XI also contains the first preliminary results of a comparison of FET computations using the BTE and the DDE. The principle conclusion is that the submicron FET is likely to be better characterized by a transconductance that is mobility dominated rather than saturated drift velocity dominated.

A number of small signal one dimensional calculations were performed during the course of the study and are summarized in section XII. Several were performed on uniform field two terminal devices and several on devices where the space charge distribution were nonuniform. The question was asked as to whether a window of frequency existed for two terminal small signal active device applications. The study herein nonuniformities in the field were retained through an injecting contact and advantage was taken of a paper by workers in Japan [8] who predicted, from solutions to moments of the Boltzmann transport equation that if transfer was avoided a window of gain could be obtained at frequencies well in excess of 800GHz. A critical feature of these studies is that the results require that terms ignored in the drift and diffusion term, but present in the MBTE and the Boltzmann transport equation be retained. Preliminary calculations to date, through joint support of ONR, indicate that frequencies within the terahertz region can lead to gain.

It was the view of this study that a key element of the program was the ability to suggest new and novel device structures. A structure of particular

significance that was discussed during the Contract period was the three terminal  $N^+N^-N^+$  device, which is commonly referred to as the space charge injection FET [9]. And calculations using the MBTE algorithm was used to ascertain its effectiveness and are summarized in section XIII. A key issue here is that the active region is undoped and thus ionized impurity scattering can, for all purposes, be disregarded. Thus, an immediate benefit is accrued. The second feature is the high injection level. For three terminal studies efforts by other [10] have demonstrated that the presence of space charge injection can lead to improvements in the transconductance. These improvements exist even without the benefits of overshoot in velocity. However, the results of previous sections demonstrate that overshoot is present in two terminal injection devices, thus the benefits of overshoot should be present in the FET. This is demonstrated.

Finally, section XII is a summary of the conclusions of the study, part of which have been addressed above.

## II. THE GOVERNING EQUATIONS USED IN THE STUDY AND THEIR DIMENSIONLESS FORM

### IIa. Introduction

The principle objective of all studies of charge transport in semiconductor devices is the ability to predict the distribution in space and time of the net charge density within any give device structure. Thus essential to all analyses are the solutions to Poisson's equation:

$$\nabla^2 \phi = -\frac{\rho}{\epsilon} \quad (1)$$

where  $\rho$  is the net charge density within the device and  $\phi$  is the self-consistently computed potential. The equations that are coupled to Poissons equation, represent the essential physics that is deemed acceptable for the study under discussion. Thus, in the present study there were two sets of equations used. The first are the semiconductor drift and diffusion equations. The second are the moments of the Boltzmann transport equations. Each are subject to a different set of approximations; each being capable of accurately describing the relevant physics subject to the agreed set of approximations. For example, the drift and diffusion equations (DDE) ignore all acceleration effects, both spatially and temporally, and assume that the carriers are instantaneous functions of the self-consistent field. This approximation has been very successful, but a host of studies have scrutinized this assumption and found it to be severely lacking particularly as device size shrinks and high frequency and speed is sought. The breakdown of this assumption is indeed relevant for devices that are currently being fabricated today, and new means of predicting device behavior are currently being developed. The method used below starts from the Boltzmann transport equation, assumes a form for the distribution function and then proceeds to develop a set of moment equations to describe transport in the structure. Effects such as overshoot are implicit in the study, as overshoot arises from a combination of acceleration and differences in the energy and momentum relaxation times. From a conceptual point of view, if a choice between use of the moment equations and the DDE arises, the moment equations should always be favored as they are, in principle, capable of a more accurate description of transport. The reason for the choice is that the development of algorithms for the moment equations is new, and considerable work remains before the moment equations will replace the DDE. Thus, engineering approximations and decisions are instituted in making the relevant choices.

### IIb. The Drift and Diffusion Equations

The semiconductor drift and diffusion equations consist of the continuity equation and the constitutive equations. For electron and hole transport these equations are:

$$(electrons) \quad e \frac{\partial N}{\partial t} = \nabla \cdot \vec{J}_n \quad (2)$$

$$(holes) \quad e \frac{\partial P}{\partial t} = -\nabla \cdot \vec{J}_p \quad (3)$$

where

$$(electrons) \quad \bar{J}_n = -e(N\mu_n \nabla \phi - D_n \nabla N) \quad (4)$$

$$(holes) \quad \bar{J}_p = -e(P\mu_p \nabla \phi + D_p \nabla P) \quad (5)$$

where  $\mu_n$ ,  $\mu_p$ ,  $D_n$ , and  $D_p$ , are phenomenological field dependent mobilities and diffusivities. The above equations can, in principle, be as rich as is necessary, and include additionally, trap kinetics, carrier generation, etc. For the purpose of this study each of these contributions are ignored. Only the basic transport mechanisms are explored.

From the viewpoint of simulation, scaling is a natural consequence of preparing the governing equations for numerical computations; and the key step is placing the equations in dimensionless form. The working dimensionless form is often arrived at arbitrarily and generally depends on the practitioners performing the task of numerical simulation. The dimensionless form arrived at in the study is based upon the assignment of several key extrinsic parameters referred to as 'reference' quantities. For the drift and diffusion equations these reference quantities are:

- (i) the nominal carrier density,  $N_{ref}$ ,
- (ii) a reference potential,  $\phi_{ref}$ ,
- (iii) a reference velocity,  $V_{ref}$ ,
- (iv) a reference length,  $X_{ref}$ ,
- (v) a reference mobility,  $\mu_{ref}$ .

The dimensionless form of Poisson's equation is:

$$\nabla^2 \phi^* = S_n (N^{**} - P^{**}) \quad (6)$$

and that of the governing drift and diffusion equations, after introducing the terms  $N' = N - N_0$ ,  $P' = P - P_0$ , is:

$$\begin{aligned} \frac{\partial N'}{\partial t} &= -C_n \nabla (\mu_n^* N^{**}) \cdot \nabla \phi^* - C_n S_n \mu_n^* N^{**} (N^{**} - P^{**}) + \frac{1}{R_n} \nabla \cdot D_n^* \nabla N^{**} \\ &\quad - C_n \nabla (\mu_n^* N_0^*) \cdot \nabla \phi^* - C_n S_n \mu_n^* N_0^* (N^{**} - P^{**}) + \frac{1}{R_n} \nabla \cdot D_n^* \nabla N_0^* \end{aligned} \quad (7a)$$

$$\begin{aligned}\frac{\partial P'}{\partial t} = & -C_n \nabla (\mu_p^* P'^*) \cdot \nabla \phi^* - C_n S_n \mu_p^* P'^* (N'' - P'^*) + \frac{1}{R_n} \nabla \cdot D_p^* \nabla P'^* \\ & - C_n \nabla (\mu_{p_0}^* P_0'^*) \cdot \nabla \phi^* - C_n S_n \mu_{p_0}^* P_0'^* (N'' - P'^*) + \frac{1}{R_n} \nabla \cdot D_{p_0}^* \nabla P_0'^*\end{aligned}\quad (7b)$$

All starred quantities in equations (6) and (7) are dimensionless quantities. The symbols in the above equations represent the following collection of parameters:

$$C_n = [\mu \Psi_r / X_r V_r]$$

$$S_n = [e X_r^2 N_r / \epsilon \Psi_r]$$

$$R_n = [X_r V_r / D_r]$$

and have the following significance:  $C_n$  is the ratio of the velocity of a carrier, under constant mobility assumptions, to the value of the reference velocity. In many cases this quantity is of the order of magnitude of unity, and is often chosen to be equal to unity. The quantity  $S_n$  is the 'square' of the ratio of the reference length to 'twice' the depletion width of a Schottky barrier obtained within the framework of the depletion layer approximation. Under many scaling procedures this quantity is kept constant [7]. The third quantity is often referred to, in the field of computational fluid dynamics as the 'Reynolds' number. It is most often ignored in all analysis of scaling. However, its importance increases in those areas where it is ignored, namely when device feature size is reduced. Calculations in the later sections will illustrate its effect.

### IIIc. Moments of the Boltzmann Transport Equation

The second set of governing equations incorporated in this study are the moments of the Boltzmann transport equation (MBTE). The detailed discussion of these equations is contained in Appendix A. For materials exhibiting electron transfer, the only materials considered in this study, there are three groups of equations to consider: the continuity equations, and the equations for momentum and energy balance. These equations are written for two species of carriers, representing, e.g., two sections of the conduction band,  $\Gamma$  and L. Thus,

$$n = n_1 + n_2 \quad (8)$$

where  $n_1$  designates the population of the  $\Gamma$  valley and  $n_2$  denotes the population of the L valley. Poisson's equation is coupled to the moment equations, the first set of which involves continuity. For the  $\Gamma$  valley

$$\frac{\partial n_1}{\partial t} = - \frac{\partial}{\partial x_j} \frac{n_1 n_k^j}{m_1} - n_1 \Gamma_1 + (n - n_1) \Gamma_2 \quad (9)$$

where  $\Gamma_1$  denotes the rate at which carriers are scattered from the  $\Gamma$  valley to all sections of the  $\Gamma$  valley.  $\Gamma_2$  denotes return scattering. It is noted that for parabolic bands, an assumption made below

$$\frac{\hbar k_1^j}{m_1} = m_1 v_1^j \quad (10)$$

An equation similar to (9) describes transient population changes in the L valley. When the two are combined, a global continuity equation results.

$$\frac{\partial n}{\partial t} = -\frac{\partial}{\partial x_1} \left[ n_1 \frac{\hbar k_1^j}{m_1} + (n - n_1) \frac{\hbar k_2^j}{m_2} \right] \quad (11)$$

The quantity

$$n_1 \frac{\hbar k_1^j}{m_1} + (n - n_1) \frac{\hbar k_2^j}{m_2} \equiv C^j \quad (12)$$

is the velocity flux density of the system and is related to a mean spatially dependent drift velocity:

$$v^j = C^j/n \quad (13)$$

When carrier velocities are discussed, reference is to equation (13). It is noted that the total current density

$$J^j = -eC^j + e \frac{\partial F^j}{\partial t} \quad (14)$$

is conserved.

The second pair of moment equations is that of momentum balance. For the  $\Gamma$  valley carrier

$$\frac{\partial}{\partial t} n_1 \hbar k_1^j + \frac{\partial}{\partial x_1} \frac{\hbar k_1^j}{m_1} n_1 \hbar k_1^j = e n_1 \frac{\partial \phi}{\partial x_1} - \frac{\partial}{\partial x_1} \psi_1^{jj} - n_1 \hbar k_1^j \Gamma_3 \quad (15)$$

$\Gamma_3$  represents the net rate of momentum scattering and  $\Psi$  represents the components of the pressure tensor

$$\Psi_i^{ij} = \frac{1}{4\pi^3} \frac{\hbar^2}{m_i} \int (\vec{k} - \vec{k}_i)_j (\vec{k} - \vec{k}_i)_j f d\vec{k} \quad (16)$$

For the situation where the distribution function represents a displaced Maxwellian (see appendix A for details):

$$\Psi_i^{ij} = n_i k_B T_i \delta_{ij} \quad (17)$$

where  $T_i$  is the electron temperature of the  $i$  valley carriers. For the L valley an equation similar to that of equation (15) emerges.

The third and final pair of moment equations is that associated with energy transport:

$$\frac{\partial}{\partial t} W_i = - \frac{\partial}{\partial x_j} \frac{\hbar k_2^j}{m_i} W_i + n_i e \frac{\hbar k_i^j}{m_i} \frac{\partial \phi}{\partial x_j} - \frac{\partial}{\partial x_j} \frac{\hbar k_i^j}{m_i} \Psi_i^{ij} - \frac{\partial}{\partial x_j} Q_i^j - n_i U_i \Gamma_5 + (n - n_i) U_2 \Gamma_6 \quad (18)$$

where

$$U_i = \frac{3}{2} k_B T_i \quad (19)$$

$$W_i = n_i \left[ \frac{1}{2} \frac{\hbar^2 k_L^2}{2m_i} + U_i \right] \quad (20)$$

and

$$Q_i^j = \frac{\hbar^3}{8\pi^3 m_i^2} \int (k - k_i)_j (k - k_i)_i^2 f d\vec{k} \quad (21)$$

where the summation convention over (i) is assumed.  $Q_i^j$  is zero for spherically symmetric distribution functions. For nonspherical situations it represents a flow of heat and is treated phenomenologically through analogy to Fourier's law

$$Q_i^j = -\kappa_i \frac{\partial}{\partial x_j} T_i \quad (22)$$

It is important to note, at this point, that the specific form of the stress tensor, equation (16), and the form of equation (21), used in this study are not fundamentally determined. Rather, they are expressions of ignorance of the detailed role of the distribution on transport, particularly near the boundaries. Additionally, in the calculations of this paper a spherically symmetric distribution is not assumed. Rather a distribution function that is asymmetric in  $k$  space is assumed. The details are discussed in appendix A.

Before continuing it is worthwhile to digress and connect the DDE formulation to that of the MBTE. First, it is noted that the current flux used in the DDE, as given by equations (4) and (5), is replaced in the MBTE formulation by the expression  $-eNV$  (see equation (13) and (14)). Thus, the mean velocity computed under steady state spatially-nonuniform field conditions has a different significance than that normally associated with a field dependent velocity. The commonly used field dependent velocity, as discussed in the DDE formulation, is obtained under steady state uniform field conditions by setting the right hand side of equation (15) to zero. The second important feature is the presence of the spatial and temporal derivatives on the left hand side of equation (15). These derivatives constitute the nonequilibrium overshoot that is present in submicron-high speed devices.

As, in the case of the DDE formulation, the MBTE is cast into dimensionless form. The continuity equations (9) and (10) are expressed as

$$\frac{\partial n_i^*}{\partial t^*} = -\frac{\partial n_i^* v_i^{*j}}{\partial x_j^*} - n_i^* f_1 + (n^* - n_i^*) f_2 \quad (23)$$

and

$$\frac{\partial n^*}{\partial t^*} = -\frac{\partial}{\partial x_j^*} (n_i^* v_i^{*j} + (n^* - n_i^*) v_2^{*j}) \quad (24)$$

The dimensionless variables (starred quantities) are identified in table 1, where

$$t_{ref} = x_{ref} / V_{ref}$$

$$\Gamma_{ref} = 1 / t_{ref} \quad (25)$$

The  $\Gamma$  valley momentum balance equations in dimensionless form is:

$$\frac{\partial n_i^* V_1^{*i}}{\partial t^*} = - \frac{\partial n_i^* V_1^{*j} V_1^{*i}}{\partial x_j^*} + Pf \frac{n_i^*}{m_i^*} \frac{\partial \phi^*}{\partial x_i^*} - \frac{1}{\gamma M^2} \frac{\partial}{\partial x_i^*} n_i^* R_i T_i^* + \frac{\mu_i^*}{Re \cdot m_i^*} \frac{\partial^2 V_1^{*i}}{\partial x_j^*} - n_i^* V_1^{*i} f_3$$

(26)

with a similar equation for the L valley. The quantity  $\hat{\mu}$  represents a dimensionless viscous contribution, and represents the nonspherical nature of the distribution function (see appendix A). The dimensionless parameters associated with the momentum balance equations are identified in table 2.

The  $\Gamma$  valley energy balance equation in dimensionless is expressed as:

$$\begin{aligned} \frac{\partial (n^* - n_i^*) T_2^*}{\partial t^*} = & - \frac{\partial (n^* - n_i^*) T_2^* V_2^{*j}}{\partial x_j^*} - (\gamma - 1)(n^* - n_i^*) T_2^* \frac{\partial V_2^{*j}}{\partial x_j^*} + \frac{1}{Re \cdot Pr} \frac{1}{m_2^* c_2^*} \frac{\partial}{\partial x_j^*} \left( \kappa_2^* \frac{\partial T_2^*}{\partial x_j^*} \right) \\ & + \gamma(\gamma - 1)M^2 \frac{V_2^{*j} V_2^{*i}}{\partial x_i^*} (2(n^* - n_i^*) f_4 + n_i^* f_1 - (n^* - n_i^*) f_2) - (n^* - n_i^*) T_2^* f_7 + n_i^* T_1^* f_8 \end{aligned}$$

(27)

with a similar for the L valley. The dimensionless parameters associated with the energy balance equations are identified in table 3.

The critical feature of the nondimensionalization lies in the relative values of the dimensionless parameters. Thus, for the DDE the important quantities are the relative values of  $R_n$  and  $C_n$ ; and the value of  $S_n$  that appears in the dimensionless Poisson equation. It is noted that typical scaling arguments generally ignore diffusive contributions and hence  $R_n$  (see e.g., Bar-Lev [7]). Instead, the quantities of interest are  $C_n$  and  $S_n$ . Unfortunately, on a submicron scale when nonuniform fields enter the diffusive contributions are a first order and neglecting them is incorrect. This is discussed in more detail in this paper.

For the moment equation formulation the relative values of  $Pf$  and  $\gamma M^2$  are of significance. In particular, if the term multiplying  $(\gamma M^2)^{-1}$  is regarded as a diffusive contribution, a reduction in  $\Phi_{ref}$  increases the relative contribution of the diffusive term. In the DDE formulation, where an increase in the diffusive term may result in lowered current levels as the feature size is reduced, for the moment equation, a reduction in feature size increases the relative contribution of the  $\Gamma$  valley and improvements in device performance may be expected.

### III. ONE DIMENSIONAL ILLUSTRATIVE CALCULATIONS USING THE MOMENTS OF THE BOLTZMANN TRANSPORT EQUATIONS

#### IIIa. Uniform Fields

The purpose of this section is to provide an illustration and a reference point for solutions to the Moments of the Boltzmann Transport Equation Calculations for uniform fields are discussed first, as they offer an important starting point for examining transients under nonuniform field conditions. Uniform fields result from assuming a donor level  $n_0$  that is spatially constant to the boundary and specifying:

$$n_x = n_{1x} = v_{1x} = v_{2x} = T_{1x} = T_{2x} = 0$$

(28)

at both the cathode and anode boundaries. In the above, the subscript x denotes a first derivative. Figure 1 displays the current transient (which for uniform fields is the same as the velocity transient) for a one-micron long element with a doping level of  $5.0 \times 10^{15}/\text{cm}^3$ . The length specification is artificial. For each calculation, the bias was raised in a one time step from 0.01 volts to the value indicated in the figure. One notes the current transient occurring at approximately 0.5 picosecond and the long-term asymptotic lower steady state value. Also apparent in the figure, is the presence of a region of negative differential mobility. Figure 2 displays the time rate of change of carriers in the  $\Gamma$  valley. Electron transfer is apparent at times following the peak velocity. Figure 3 displays the time dependence of the electron temperature following application of the voltage pulse. The feature to be noted from this figure is that for uniform fields all time dependence in  $T_1$  is due entirely to scattering events and is thus, a measure of when ballistic transport may be ignored.

### IIIb. Nonuniform Fields, Uniform Doping

Nonuniform fields and space charge layers are expected in all devices, and their origin in uniformly doped structures lies in the conditions imposed at the up and downstream boundaries. In the discussion that follows, a very simple set of boundary conditions is imposed and taken to represent the effects of the physical boundary. The importance of these boundary conditions is discussed in Appendix A. The calculations are performed for a GaAs structure with the same material parameters as that of the uniform field calculations. Here, however, the boundary conditions are different. At the cathode

$$n_{xx} = n_{1xx} = 0, \quad V_1 = 15,625 \frac{\partial \phi}{\partial x}, \quad V_{2x} = 0, \quad T_1 = 300^\circ K, \quad T_{2x} = 0 \quad (29)$$

and the anode

$$n_{xx} = n_{1xx} = V_{1xx} = V_{2xx} = T_{1xx} = T_{2xx} = 0 \quad (30)$$

where the double x subscript denotes a second derivative. The consequences of this set of boundary conditions is that the  $\Gamma$  valley electrons enter the structure with a velocity in excess of the steady state uniform field value. Specification of the  $\Gamma$  valley temperature at  $300^\circ K$  assures that the relative cathode carrier contribution of the L valley is negligible.

The steady state time dependent distributions of electric field, carrier density,  $\Gamma$  valley velocity and electron temperature are displayed in figures 4 through 7 for various bias levels. While the calculation displays the excess carrier velocity at elevated bias levels, there is also an enhanced electron transfer and the dc current shows saturation. The clear consequence of the transfer is that the current does not scale the velocity. This latter feature is reflected in the current-voltage relation shown in figure 8.

With regard to the current-voltage characteristic, while the current does not scale the velocity and, thus, does not fully reflect overshoot contributions, its high bias level is above that associated with the equilibrium steady state velocity field relation, while below that associated with the  $\Gamma$  valley velocity. The excess above the equilibrium steady state value is due predominantly to the cathode boundary condition that allows for a high level of injected charge. The depression below the  $\Gamma$  valley velocity is due to electron transfer. Figure 9 displays the current transient following application of a voltage pulse. The first point we emphasize is that the plot consists of current rather than velocity. The second point is that while current transient is ostensibly similar to that associated with velocity overshoot, there is a fundamental difference between the two. For uniform and nonuniform fields, during the first time step, the field throughout the structure is increased by an amount equal to the change in applied voltage divided by device length. This introduces a one time step displacement current whose magnitude is computationally dependent and, therefore, nonphysical. For uniform field, all displacement current contributions cease after the initial time step. For nonuniform fields all time dependent field evolution is accurately calculated following the initial time step. Here, with the cathode boundary introducing a

cathode adjacent accumulation layer, the time dependence introduces a layer that propagates toward the anode boundary. This propagation is accompanied by field rearrangement and internal point-by-point displacement current contributions.

#### IV. INTRINSIC SCALING AND THE MOMENTS OF THE BOLTZMANN TRANSPORT EQUATION

The concept of scaling is introduced with a set of simple examples, the first of which is based on a discussion given by Thornber [4], under the idea of constant parameter scaling. This is first applied under uniform field conditions.

Currently, semiconductor materials are classified with parameters extracted from uniform field considerations in which all space charge nonuniformities are neglected. While this approach is unfortunate because all semiconductor devices are operated under nonuniform space charge conditions, its use will be continued below. In particular, insofar as scaling arises from variations of known parameters the discussion begins with a description of GaAs under uniform field conditions and the consequences thereof in which all scattering rates are altered by the same constant. The situation of nonuniform fields, which is the thrust of this paper follows in the remaining sections.

The relevance of altering all scattering rates by the same constant is moot. It is different from the classical scaling discussed, e.g., by Bar-Lev [7], insofar as it focuses attention on alterations in the mobility rather than the extrinsic characteristics of the structure, although the latter will clearly enter the picture. The advantage of the constant scaling is that it provides an initial introduction into the work of this study.

In principle the scattering rates are the signatures of the semiconductors from which all transport properties are identified. Specific semiconducting elements in this study are identified by an assumed set of scattering events, e.g., LO phonon, intervalley phonon, acoustic phonon, impurity scattering, etc. From these events a field dependent velocity emerges. For GaAs, assuming only two levels of transfer (between the  $\Gamma$  and L valleys) the steady state uniform field dependent properties are shown in figure 10. The band structure parameters used for the calculation are identified in table 4. There are eight frames associated with figure 10. Figures 10a and 10b, display the field dependent velocity over a range of field values varying from zero to 92kv/cm and 20kv/cm, respectively. This field dependence is approximately what is seen experimentally [11]).

In addition to the field dependent velocity the fractional density of carriers in the  $\Gamma$  and L valleys are displayed in figures 10c and 10d, respectively. It is noted that electron transfer while rapid, occurs continuously, beginning at a field of approximately 3 kv/cm. The mean carrier velocity for electrons within the  $\Gamma$  and L valleys are displayed in figures 10e and 10f, respectively. For the parameters chosen, there is an apparent onset of saturation in the  $\Gamma$  velocity. The parameters for the L valley have been chosen such that the mobility of the L valley is relatively constant over a wide range of fields.

It may be anticipated that the mobility of the L valley would also exhibit nonlinearities at high fields. However, for the calculations discussed in this paper, the L valley carriers, over the field range of 90 kv/cm, are approximately at the equilibrium with the lattice and all nonlinearities associated with the velocity field curve are due primarily to 'k' - space transfer. Finally, figures 10g and 10f display the field dependence of the electron temperature in the  $\Gamma$  and L valleys, respectively. It is noted that the L valley temperature is approximately equal to the ambient over the field

range of interest; whereas the  $\Gamma$  valley temperature increases significantly with field. The variation of temperature with field is a consequence of relaxation mechanisms (see e.g., Grubin and Kreskovsky [12]).

Since we have chosen scattering rate scaling as the principle means of assessing semiconductor materials for device applications it is critical to determine the degree of predictability that emerges when these scattering parameters are systematically altered. Unfortunately, there are not many tests that can be used to accurately assess the effectiveness of these alterations. The one that we focus on is the semiconductor InP, and its relationship to GaAs as a scaled semiconductor material. The semiconductor InP is of interest as a candidate two terminal millimeter wave material (see e.g., Binari, et al., [3]) and because over certain electron temperature ranges its scattering rates are approximate multiples of that for GaAs. It must, however, be noted that the specific parameter alteration from GaAs is of less importance, in its detail, than the observed alteration in transport that is predicted. Thus, the simplest and first question to be addressed is how will the field dependent velocity relation change as scattering rates are altered, by a constant, over the entire range of energy, or 'k' value. In this case, the analysis of section B and Thornber [4] lead to the following simple rule:

$$V_\lambda(F) = V_0(F/\lambda)$$

(31a)

$$V_\lambda(\lambda F) = V_0(F)$$

(31b)

Thus, if  $\lambda=2$ , the scaled and unscaled field dependent velocity relations take the form shown in figure 11. It is noted, that with the exception of the region of negative differential mobility, the scaled  $\lambda=2$  curve is remarkably similar to that of InP. Additionally, the  $\lambda=1/2$  curve, while not shown, bears a strong resemblance to  $GaxIn_{1-x}As$  ( $x=.5$ ) [11].

The case for InP as a 'limited scaled GaAs' is further addressed in figures 12 through 14, where calculations for both InP and GaAs are displayed. For example, figure 12 is a repeat of figure 10a, but for the semiconductor InP. The parameters used in this calculation are listed in table 5.

Insofar as the calculations performed during the course of the study involve altering the scattering rates for GaAs, the scattering rates for GaAs are displayed in figure 13.

Figure 13a displays the scattering rates of electrons in GaAs being transferred from the  $\Gamma$  to L valley. The scattering rates are defined in terms of their dependence on the electron temperature, which in these figures varies from  $300^{\circ}\text{K}$  to  $4800^{\circ}\text{K}$ . With the exception of strong nonlinearities below approximately  $1500^{\circ}\text{K}$  the scattering rates show an approximate linear dependence on electron temperature. For the return L to  $\Gamma$  scattering displayed in figure 13b, the nonlinearity is weak and the electron temperature dependence appears to be approximately linear.

The momentum scattering rates for carriers in GaAs are displayed in figure 13c for the  $\Gamma$  valley and figure 13d for the L valley. The low field mobility for GaAs is dominated by  $\Gamma$  valley carrier transport; and at an electron temperature equal to the ambient, the momentum scattering rate is  $0.325 \times 10^{13}$ /sec and is dominated by LO phonon scattering. The L valley scattering rates are more than an order of magnitude greater than that for the  $\Gamma$  valley electrons and indicates corresponding low values of the L valley carrier mobility.

The energy scattering rates for  $\Gamma$  valley carriers in GaAs are displayed in figure 13e. It is noted that figure 13e shows an energy scattering rate that is a monotonically increasing function of electron temperature. Because intervalley scattering is included, effects associated with catastrophic breakdown does not occur. Return scattering, shown in figure 13f, is associated with the transfer of energy when a carrier makes a transition from the L to the  $\Gamma$  valley. Similar remarks apply to figures 13g and 13h, however, when considering figure 13g, it must be noted that the effectiveness of energy scattering within the L valley decreases for carrier temperatures in excess of  $900^{\circ}\text{K}$ . The results here are qualitatively similar to those obtained by Butcher, et al., [13], Bosch and Thim [14] and Grubin, et al., [15].

The InP rates are discussed in Appendix B and summarized in figure 14 which displays the ratio of the scattering rates of InP to GaAs. The following points are noted: substantial intervalley carrier scattering in the InP does not occur until the  $\Gamma$  valley electron temperature reaches approximately  $900^{\circ}\text{K}$ , the latter reflecting the larger energy separation between the  $\Gamma$  and L portions of the conduction band than that of GaAs. Second, the  $\Gamma$  valley momentum scattering rate is approximately twice that of GaAs and reflects the presence of enhanced LO scattering. The net effect of these differences is to provide scattering rates that scale over select sections of the entire electron temperature range.

It would clearly be stretching the point to conclude that constant parameter scaling applies to the semiconductors InP and GaAs. On the other hand, constant parameter scaling for the individual events does occur over meaningful variations in electron temperature. The significant points associated with scaling are: (i) starting from GaAs parameters, constant scaling will yield a field dependent velocity curves very similar to that of InP (when the scaling is greater than unity) or curves similar to that of GaInAs (when the scaling is less than unity); (ii) starting from first principles, where the scattering rates for InP are not constant multiples of GaAs a field dependent velocity curve for InP can be constructed that is very similar to one that may be obtained by scaling GaAs. The significant implication is that the uniform field dependent velocity field curves discussed in the literature to characterize individual semiconductors may not be uniquely determined. Thus in the absence of knowing, apriori, what the material parameters are that characterize a semiconductor, it must be accepted that various combinations of material parameters will yield the same results. Of interest then, as carried in the discussion of this paper are (i) determining the trends that may reasonably be expected if material parameter identification is uncertain, and (ii) the general direction one must proceed in attaining high frequency materials. Thus, the approach taken is first to identify the trends associated with constant parameter scaling, regarding them as providing bounds for device behavior.

The general situation as summarized above is that variations in the semiconductor material properties will not be accomplished by constant parameter scaling. Rather, individual scattering rates will be altered nonuniformly, with effects as shown in figure 15, and discussed in the later sections. For the moment, however, we return to constant parameter scaling and uniform fields.

For uniform fields attention is given to the MBTE under transient conditions. Again, the term containing the spatial derivations is once again ignored. For this case, the effect of constant scaling is as follows: For a given value of uniform field  $F_0$ , the mean velocity of the electrons is computed. The carriers are then subjected to a controlled change in electric field  $\delta F_0$ , which reaches a new steady state value  $F_0(t) + \delta F_0(t)$ , as shown in figure 16a. The task at hand is to calculate the transient response of the mean carrier velocity figure 16b. Under the assumption that the scattering rates are not explicit functions of time, scaling is direct and leads to the following simple rule: If  $V_0(F(t), t)$  represents the transient response of the unscaled field dependent velocity, to a time dependent change in field, then the scaled and unscaled velocities bear the following relation

$$V_\lambda[F(t), t] \geq V_0\left[\frac{F}{\lambda}(\lambda t), \lambda t\right] \quad (32)$$

where the equality is true beyond the first time step. For this case the transient response of the unscaled and scaled velocity is as shown in figure 17. The principle result of figure 17, is that the response of a scaled device for  $\lambda > 1$ , is faster than that of the unscaled device, but that additionally larger fields are required. This latter result is intuitively accessible: The ordinary differential equation describing the motion of a single carrier subjected to uniform fields and scattering rates has a solution given by  $V_0(F, t) = -e\tau F m^{-1} [1 - e^{-t/\tau}]$ , where  $\tau$  is a relaxation time. If the scattering rate is increased by  $\lambda$ , the relaxation time is reduced by the factor  $\lambda$ , and the scaled velocity becomes  $V_\lambda(F, t) = -e\tau F(m\lambda)^{-1} [1 - e^{-t\lambda/\tau}] = V_0(F/\lambda, t\lambda)$ . The clear implication is that relaxation effects are more rapid for  $\lambda$  greater than or equal to unity.

Another viewpoint may be expressed by examining the response of the scaled semiconductor to a sinusoidal electric field. In this case, the rule of equation (32) teaches that if power gain is obtained with an unscaled device at, e.g., 110GHz, then power gain will be obtained with the scaled device at  $\lambda \times 110$ GHz, provided the field across the scaled device is increased by the amount  $\lambda F_0$ . This particular situation was examined for self-excited oscillations in two terminal uniform field structures.

For the self excited oscillations the unscaled GaAs was in the circuit of figure 18 and the maximum frequency of oscillation was approximately 130GHz. A  $\lambda=2$  scaled device, according to the rule of equation (32) would have an upper frequency limit of 260GHz. It is immediately apparent that the scattering rates of InP dictate that its upper frequency limit should be higher than that of GaAs. Indeed, from a variety of experimental observations two terminal InP structures yield useable power at frequencies substantially higher than that of GaAs. Calculations performed during the course of this study demonstrate frequencies of self excited oscillations for InP in excess of 180GHz. A result

consistent with the rule of equation (32) and the experimental observations. A description of the self excited oscillations is obtained in figure 19.

The situation with spatial scaling is similar to that of temporal scaling and is discussed in Appendix B. The result is that if the spatial velocity variations are computed for an unscaled but spatially varying electric field, then similar velocity variations will occur for the scaled element. For the scaled element the velocity variations will occur over the distance  $L/\lambda$ , providing the amplitude of the applied field is increased by the factor  $\lambda$ . Thus, for  $\lambda > 1$ , higher switching speeds, due to shorter transit times, are possible.

## V. CALCULATIONS WITH CONSTANT GOVERNING DIMENSIONLESS PARAMETERS AND VARIABLE SCATTERING RATES TIED TO EXTRINSIC PARAMETERS

For purposes of illustration the dimensionless equations are first manipulated under conditions of constant governing dimensionless parameter scaling. For this case the unscaled device is GaAs discussed in the previous section.

The concept of constant parameter scaling and constant reference potential scaling as applied to this one dimensional structure is as follows. First, the reference potential is held fixed at 1.0 volt. Second, all of the scattering rates,  $\Gamma_1$  through  $\Gamma_8$  are altered by the multiplicative constant  $\lambda$ . Then the dimensionless continuity equations are unchanged when  $\Gamma_{ref} \rightarrow \lambda \Gamma_{ref}$ ,  $t_{ref} \rightarrow t_{ref}/\lambda$ ,  $X_{ref} \rightarrow X_{ref}/\lambda$  (thus,  $V_{ref}$  is unchanged). Then, if  $\lambda$  is doubled, the scaled length, is halved.

The scaling of the momentum balance equation is similar. Here, if  $\Phi_{ref}$  is kept unchanged, the dimensionless equations are unaltered when the the following parameter changes are made:  $N_{ref} \rightarrow \lambda^2 N_{ref}$ ,  $\hat{\mu}_{ref} \rightarrow \lambda \hat{\mu}_{ref}$ . For this case  $Re$  and  $Pf$  are unchanged. To see the connection between this computation and the discussion for uniform fields, we express the field as the gradient of potential. Then equation (6) is re-expressed as

$$V_\lambda(\phi, X, t) = V_0(\phi, \lambda X, \lambda t) \quad (33)$$

For the energy equation, the only scaling required is on the thermal conductivity, which becomes  $\kappa_{ref} \rightarrow \lambda \kappa_{ref}$ . Poisson's equation requires no additional alteration. The new boundary condition at the cathode requires that  $\mu_c \rightarrow \mu_c/\lambda$ . A summary of the above scaling is displayed in table 6.

The constant governing dimensionless parameter scaling is illustrated in the earlier figures 4 through 7. In these calculations for both the scaled and unscaled structures the potential is kept fixed and is not altered in going from scaled to unscaled structures. A simple illustration of the effect of scaling is provided through the following approximation, where the field dependent velocity and temperature is given by the following expressions:

$$V = \frac{e\tau_m}{m} \frac{\Delta\phi}{\Delta X}, \quad T_e = \frac{2e\tau_e}{3k_B} V \frac{\Delta\phi}{\Delta X} \quad (34)$$

Here  $\tau_m$  and  $\tau_e$  are, respectively, constant momentum and energy relaxation times.

In equation (34) when the scattering rates are altered by the constant  $\lambda$ , the relaxation time is altered by the constant  $1/\lambda$ . Then under uniform field conditions with the potential difference specified at a given value, the carriers obtain values of velocity and temperature equal to the unscaled value, over a distance that is a factor of  $\lambda$  larger than that of the unscaled values. The situation of interest below, is for spatially dependent nonuniform fields, but the example just discussed is intuitively relevant.

The detailed calculations were performed for the unscaled GaAs and are extracted from an earlier study (Grubin and Kreskovsky [12]). The scaled results are determined from the above discussion and are implicit in the illustrations of the unscaled results. Thus, figure 5 displays calculations for the distribution of total and  $\Gamma$  valley carriers for  $\lambda=1, 2$ , and  $4$ . The  $\lambda=1$  results are for GaAs. The boundary conditions chosen are representative of a highly injecting contact. The scaled results are in accordance with table 6. It is noted that for  $\lambda=2$ , identical transfer occurs over 0.5 microns as against 1.0 microns for the unscaled structure.

Figure 4 displays the field distribution for this scaled calculation. Of significance here, is the fact that for the unscaled GaAs the peak anode field is  $33\text{kv/cm}$  @ 1.0 volts, and is reached at 1.0 microns. For  $\lambda=2$ , the peak anode field is  $66\text{kv/cm}$  and is reached at 0.5 microns. Here, if reference is made to InP as a " $\lambda=2\times\text{GaAs}$ " semiconductor where the threshold field for NDM is of the order of twice that of GaAs, then the results are intuitively relevant. Thus, the high field region at the anode offers the potential problem of introducing avalanching at premature voltage levels. Similar arguments apply to InGaAs, when regarded as a " $\lambda=1/2\times\text{GaAs}$ " structure where the anode fields are lower.

The velocity and temperature distributions are displayed in figures 6 and 7, respectively. No scaling on the magnitudes of either occurs, although the spatial scaling is apparent, a result that is consistent with the discussion associated with equation (34).

The temporal transient to steady state is shown in figure 9, which displays current density versus time. Two points are noted: First, the time to equilibrium is shorter for  $\lambda=2$ , than for  $\lambda=1$ . Here it may be anticipated the scaled InP is capable of higher switching speeds. Second, because of the increase in  $N_{ref}$ , the reference current drive is increased by a factor of four.

Before the significance of this scaling is considered it is noted that the scaling procedure involves an alteration of the reference carrier density, length and low field mobility. In terms of the reference current density, it is increased by the scale factor  $\lambda^2$ . The reference total current is unchanged. In equation form, if an unscaled current voltage relation is linear, i.e.,

$$I_0 = \Psi_0 / R_0 \quad (35)$$

the scaled current voltage relation is the same, as the resistance  $R_0$  is unchanged with this scaling.

## VI. CALCULATIONS WITH CONSTANT GOVERNING DIMENSIONLESS PARAMETER AND CONSTANT SCATTERING RATES TIED TO INTRINSIC MATERIAL PROPERTIES

The above type of scaling serves as an intuitive guide and as a reference point for additional scaling. The manipulation of the extrinsic parameters in the last section followed the alteration associated with that of the material parameters. The more general situation may arise when a particular feature size of a device is a specification of the problem. The task is then to determine the variations in the electrical characteristics that may be expected if there is a choice of materials. The simplest way to proceed here is to perform a series of numerical calculations in which the device length is fixed but the material scattering rates are altered. This is considered below.

The calculations performed are in the same spirit as those in the previous section are discussed in detail in Appendix B, and are briefly summarized below. The calculations are performed for a 0.25 micron long structure with a doping of  $8 \times 10^{16} / \text{cm}^3$ , an applied potential of 0.6 volts (for an average field of 24kv/cm) and materials with three different scaling constants. The  $\lambda=1$  calculations are the unscaled GaAs results. The  $\lambda=2$  case is relevant to InP. It is noted that the calculations are being performed for high doping levels, in which the background is treated as jellium. This latter assumption is likely to be a poor one (Grubin and Ferry [6]). Additionally, scattering events due to ionized impurities are not included in this calculation. They are discussed in section VII.

The calculations reflect that fact that the scaled devices exhibit different percentages of electron transfer at a given value of field, and the fact that the contributions of the  $\Gamma$  valley tend to dominate transport. For example, the distribution of charge within the device reveals that the transfer increases as  $\lambda$  decreases from 4 to 2. The observation is made that the increase transfer rate is a consequence of the fact that at a given value of field the rate of electron transfer is greater for the scaled  $\lambda=2$  structure than for the scaled  $\lambda=4$  structure (Grubin and Kreskovsky [16], to be published). It is noted that a clear description of the trends with respect to increased scaled scattering is not yet possible, insofar as the higher donor density often results in free carrier densities levels that are below background. While a full range of calculations is discussed in Appendix B, below we concentrate on the  $\Gamma$  valley velocity and the total current.

The distribution of  $\Gamma$  valley carrier velocity for these calculations is shown in figure 20. The critical result here is that  $\Gamma$  valley carrier velocity decreases as  $\lambda$  increases. This is a statement of the fact that the mobility of the  $\Gamma$  valley is decreasing with increased scattering rate. When this result is coupled to the fact that carriers in the  $\Gamma$  valley carry most of the current, improvements in the current response can be anticipated (see figure 21).

The dc current levels with the scattering rates doubled and then redoubled is shown in figure 21. It is noted that, at the bias level of 0.6 volts there is a progressive decrease in current level as the scaling parameter increases. This result is anticipated, as the bias levels chosen tend to enhance the contributions from the  $\Gamma$ -valley, whose mobility is smallest for the highest  $\lambda$  structure. As the discussion in Appendix B indicates, unlike the uniform calculations where an increase in the scattering rate results in a reduction in the time to steady state, here the relaxation time is less certain. Indeed,

this result is additional evidence that caution must be applied before extrapolating uniform field results to nonuniform submicron transport. (We note that the scaled GaAs calculation with a scaled scattering rate of 4 provides results that are identical to that of a 1.0 micron device with a doping of  $5.0 \times 10^{15}/\text{cm}^3$ ).

## VII. CALCULATIONS WITH CONSTANT GOVERNING DIMENSIONLESS PARAMETERS AND VARIABLE SCATTERING RATES TIED TO INTRINSIC MATERIAL PROPERTIES

The calculations in this section are similar to those already performed, with one key difference: The calculations of the previous sections were performed for cases in which the material scattering rates were all changed by the same constant. In this section individual scattering components are altered, and the emphasis moves closer to realistic alterations in material parameters of semiconductor devices.

### 7a. Deformation Potential Coupling Coefficient Alterations

This set of calculations is performed to highlight the role of velocity saturation on near and submicron-scale device performance. The motivation for this is as follows: Presently, individual semiconductors are accepted or rejected as candidate device materials based, in large measure, upon the value of their high field saturation drift velocity. Indeed, the material silicon carbide, apart from its high temperature advantages is under consideration as for FET applications because of its high field saturation drift velocity. It is noted that the low field mobility of silicon carbide is considerably smaller than that of GaAs. The question then arises as to whether an increase in saturation drift velocity is a sufficient criteria for submicron device semiconductor material selection, or whether the key figure of merit is the low field mobility. The question is addressed through alterations of the intervalley deformation potential coupling coefficient, where it is observed that an increase in saturation that is accomplished by an increased in the intervalley deformation coupling coefficient also reduces the low field mobility. When this result is coupled to the results of section 6, such alterations may be of less use for submicron-structure devices. Indeed one of the obvious recommendations that arises from the results presented below is a clear need to search for materials with both a high saturation drift velocity and a high low field mobility.

Alterations in the saturated drift velocity of the carriers accomplished by altering the deformation potential coupling coefficient have been indicated in figures 7a and 7b. Figure 7 displays the steady state characteristics for the situation where the intervalley deformation potential coupling coefficient is increased by a factor of 2.0, and decreased by the factor 1/2. As is noted, increasing the deformation potential has the twin effect of increasing the saturated drift velocity, while decreasing the low field mobility. The opposite occurs when the coupling coefficient is reduced by a factor of 2.0. It is noted that alterations in the  $\Gamma$  valley mobility do not set in until fields near the threshold for negative differential mobility are reached. The detailed calculations under alterations of the deformation potential coupling coefficient are discussed in Appendix B. Of significance here are the  $\Gamma$  valley carrier velocity profiles, figures 22 through 24. The  $\Gamma$  valley carrier velocity is highest for the element with the lowest deformation potential coupling coefficient, as is the steady state current level. A summary of this result is displayed in figure 25a which shows the dc current voltage relation. Clearly the element with the highest saturated drift velocity is not the element with the highest submicron current level.

The above result does not contradict what has been taught about saturated drift velocity results and associated current levels. Earlier teachings were, however, incomplete. It is anticipated, that as the device length increases, the element with the highest saturated drift velocity will dominate, if the dominant part of the structure, sustains fields well into velocity saturation. This statement is backed-up by a series of calculations summarized in figure 25b which displays the current voltage relations for two pairs of nonuniform field calculations. One for a device feature size of 1.0 microns and a second, for 2.0 microns; the carrier density for both was  $5 \times 10^{15}/\text{cm}^3$ . Two points are noted: First, as the device length increases the steady current level decreases. Second, the difference in the steady state current level between the high and low deformation potential coupling coefficients decreases as the device length increases. It is anticipated that for structures greater than five microns in length the current level for the higher deformation potential coupling coefficient will be the highest.

#### 7b. Intervalley Energy Separation Alterations

Because of the importance of the  $\Gamma$  valley carrier to transport in submicron devices, a set of calculations was performed in which all of the coefficient with respect to GaAs were held fixed, but the intervalley separation was increased. The steady state uniform field characteristics were displayed in figure 15, and reflect the fact the: (i) the mobility of the  $\Gamma$  valley carrier is virtually unchanged at low values of electric field from that obtained with GaAs, but is higher than that of GaAs at higher field values; (ii) electron transfer is delayed beyond that of that associated with GaAs, a result that is consistent with that of InP; (iii) the peak steady state velocity, prior to negative differential mobility is higher than that for GaAs.

Calculations for nonuniform field were performed for a 1.0 micron structure with a donor concentration of  $5 \times 10^{15}/\text{cm}^3$ . These are displayed in figures 26 and 27. Additional discussion is contained in Appendix B. There are several points that should be noted. First, because of the increased energy separation there is a delay in field value at which intervalley transfer occurs. (This effect has been known for sometime from studies of InP). There is a corresponding increase in the threshold field for negative differential mobility, as well as a corresponding increase in the saturation drift velocity. But most important, from the point of view of submicron structures, is the fact that the low field mobility is virtually unaltered. Thus the benefits of high saturation drift velocity and high-low field mobility emerge. A particularly important comparison is the steady state  $\Gamma$  valley velocity, the current voltage relation and it's comparison to GaAs, figures 15 and 27. There is a clear, and remarkable improvement with the higher intervalley separation. This is perhaps one of the most desirable features that should be sought after in choosing high frequency devices. And InGaAs begins to look attractive.

#### 7c. Calculations Including Ionized Impurity Scattering

The calculations in the previous discussion ignored the influence of ionized impurity scattering on the results. Clearly the effect of ionized impurity scattering is to reduced the mobility. The effects of ionized impurity scattering were not included initially, because they detract from the basic concepts associated with scaling. From the point of view of this paper,

ionized impurity scattering has the effect of selectively altering the scattering rates. In this case only two scattering rate components are altered: the  $\Gamma$  and L valley momentum scattering rates.

The results of the calculations are discussed in Appendix B, and as expected, are qualitatively similar to that obtained without any impurity scattering. There is, however, the expected degradation in the  $\Gamma$  valley velocity and the consequent reduction in current voltage relation. The results, however, are of more general significance insofar as they forecast the result that improvements in the momentum scattering rate will improve device performance.

## VIII. CALCULATIONS WITH VARIABLE DONOR DENSITY

The calculations of the preceding sections were specifically concerned with scaling and its relation to variations in band structure. The results demonstrated that it was possible to scale the scattering rates and the doping such that no alteration in the electrical results occurs (see section 5). The topic of interest is then: What occurs when the doping level is varied? It may be argued, that this question has already been considered in papers that initially dealt with velocity overshoot. Here, reference is to the study of, e.g., Frey et al., [16]. In these studies, however, the effects of varying the donor density was not addressed. The only question considered was the alteration in the transient velocity due to changes in the ionized impurity scattering.

To examine the effects of varying the magnitude of the uniform donor density a series of calculations were performed, again for the submicron structure with an active region length of 0.25 microns. The calculations were performed for doping levels of  $5 \times 10^{15} / \text{cm}^3$ ,  $2 \times 10^{16} / \text{cm}^3$  and  $8 \times 10^{16} / \text{cm}^3$ , and again, ionized impurity scattering was not incorporated. The detailed results are discussed in Appendix B. Here the  $\Gamma$  valley velocity is shown in figure 28, for the donor level of  $5 \times 10^{15} / \text{cm}^3$ ; figure 29, for the donor level of  $2 \times 10^{16} / \text{cm}^3$ ; and figure 24, for a donor level of  $8 \times 10^{16} / \text{cm}^3$ .

There are two important features to be noted from these calculations as discussed in Appendix B: First, as the donor density increases the field distribution within the device becomes more nonuniform. This result is a direct consequence of the fact that the dimensionless parameter  $S_n$  used in Poisson's equation (equation (6)) increases linearly with donor density. Second: as a consequence of the increased spatial nonuniformities the steady state currents at a given value of bias do not scale linearly with carrier density. Rather the scaling is sublinear. This last result should be apparent from the summary of figure 30, where the normalized current density versus potential is plotted as a function of donor density. Of greater importance is the fact that the sublinear current scaling will have a significant influence on all scaled FET results, as will be apparent from the later discussions.

## IX. NONUNIFORM FIELDS, LENGTH SCALING

### IXa. Length Scaling - Uniform Donor Density

While the calculations of the previous sections emphasized the effects of intrinsic scaling and included calculations for structures of different lengths, little emphasis was placed on length scaling and its effects on device performance. In this section the effects of length scaling are discussed for two situations. The first situation is for a uniformly doped structure with the same boundary conditions as given by equation (29), but with a comparison of results for structures of length 0.25 and 1.00 microns. The second structure considered is that of a  $N^+N^-N^+$  device, with a one-micron cathode-to-anode spacing but with a variable length  $N^-$  region.

The detailed calculations for the 0.25 micron-long device are discussed in Appendix A where it is noted that for the same average field for the 0.25 micron device and the 1.0 micron device, the detailed spatially dependent field distributions are quantitatively different. Additionally, the carrier and velocity distributions for the two structures are different. These differences are, in part, a result of the fact that conditions at the upstream boundary are sensitively dependent upon the proximity of the collecting contact.

Figure 31 is a comparison of the current-versus voltage for the 0.25 and 1.0 micron-long device. Again, two points are emphasized: the first shows the absence of any negative differential conductance. The second point is that the presence of increased levels of charge injection yield an increase in the drive current over that of the one-micron long device.

The transient characteristics of the 0.25 and 1.0 micron structures are also discussed in Appendix A. The results are quantitatively different. It is noted here that although the time to steady state is shorter for the  $0.25\mu m$  electron, it is not a factor of 4 shorter. The time scales involved in the approach to steady state involves nontransit time contributions.

### IXb. Length Scaling - Nonuniform donor doping

The next structure considered is the  $N^+N^-N^+$  device it is of interest because as a three terminal device it is regarded as a candidate for high frequency FET operation and has been given the name space charge injection FET [9]. Calculations for this structure have been initiated under this program and will be summarized in a later section. At this point, the two terminal  $N^+N^-N^+$  structure is examined for several reasons. First, it provides a realistic assessment of submicron structures that are likely to be fabricated. Second, the study points to the fact that care must be exercised in interpreting results with devices that are loosely referred to as submicron devices. In particular, it is found that 1.0 micron long devices with submicron features under 0.1 microns cannot necessarily be regarded as submicron structures. The details are reported below. Third, current transients associated with these devices completely confuse the issue of temporal velocity overshoot. The results as discussed below show that initial transients may have their origin in displacement current contributions. Thus, this last two-terminal structure offers the most serious example of the interplay of the interface and the length of the critical submicron region on the electrical characteristics of the submicron structures.

The boundary conditions for this structure were chosen to minimize their influence on transport within the nonuniformly doped structure. The boundary conditions at the cathode are:

$$n = n_0, \quad n_i = n_{i\text{eq}}, \quad V_{ixx} = 0, \quad V_{2x} = 0, \quad T_i = 300^\circ\text{K}, \quad T_{2x} = 0 \quad (36)$$

At the anode all second derivatives were set to zero.

The  $\text{N}^+\text{N}^-\text{N}^+$  calculations performed were for the one-dimensional structure of figure 32, in which the  $\text{N}^-$  region was assigned a nominal doping level of  $10^{15}/\text{cm}^3$  and the  $\text{N}^+$  region was at  $10^{17}/\text{cm}^3$ . The length of the  $\text{N}^-$  region is specified at the doping level of  $10^{16}/\text{cm}^3$ , and varied from 0.416 microns to 0.116 microns. The entire structure was fixed at a length of 1.0 microns. The design of the structure dictates that nonuniform fields and charge densities form within it. Thus, again the relevant experimental quantity is current density rather than velocity. The first set of results is shown in figure 33. Figure 33 displays the total current flowing through the device following application of a voltage pulse of magnitude 1.0v.

Before discussing the effects of length scaling on this structure, we report on the transient characteristics insofar as they highlight the inadequacy of temporal velocity transients to explain initial time dependence associated with electron devices. These calculations, when placed in context of current experimental efforts to measure transient temporal overshoot, indicate that much of the conclusions of the experimental results must be rethought before definitive statements are made accepting or rejecting temporal velocity overshoot.

As seen in figure 33, the current displays an initial peak at approximately 0.15ps, followed by a drop in current and a subsequent rise toward a steady state value. This initial peak as the calculations demonstrate is dominantly displacement current as seen below. Figure 34 displays the particle current through the device at select instants of time. A comparison of the magnitude of the particle and total current indicates that within certain key regions of the device, particularly near the interface regions, that the displacement current dominates the current level. The general conclusion is that since the initial transient is strongly influenced by displacement current contributions it is inappropriate to assume that the initial current transient is a measure of velocity overshoot.

The details of the transient, specifically as it relates to displacement current contributions, are reflected in the time dependence of the electric field and potential profiles and are discussed in detail in Appendix A.

Notwithstanding the displacement current contributions, it is necessary to determine the extent to which the carrier velocity can exceed the equilibrium values. For the structure considered herein with  $L_{\text{N}^-} = 0.416$  microns, most of the current is transported by the  $\Gamma$  valley carriers. For this case, the mean carrier velocity, thereby, exceeds the steady state value. The results clearly indicate the presence of spatial velocity overshoot under nonuniform steady state field conditions. This is discussed in Appendix A and in a later figure 39.

We next consider the dependence of the results on the length of the N<sup>-</sup> region and note the expectation that the shorter the active region the higher the dc drive current. For the N<sup>+</sup>N<sup>-</sup>N<sup>+</sup> structure, as in the uniform N<sub>0</sub> structure with injecting contacts a significant contribution to the current arises from the excess charge injected into the N<sup>-</sup> region. The point was also made in [17] where the dependence of current and voltage on N<sup>-</sup> region length was also examined. A second point of importance here, concerns determining which portion of the structure dominates its transport. It may be intuitively expected that for the structure considered it is the N<sup>-</sup> regions that dominates. This appears to be the case for the above discussion. But one may expect that for a sufficiently small N<sup>-</sup> region, no single region dominates. In the calculations reported here, the absence of a single dominating region becomes apparent at higher voltage levels and for the case when L<sub>N</sub> = 0.116 microns. These results are illustrated in figures 35 through 41, with particular attention paid to voltage sharing and electron transfer in the N<sup>+</sup> region as the N<sup>-</sup> region is reduced in size. Figure 35 is a sketch of the background doping level associated with the variable N<sup>-</sup> region. Within these regions and at a bias of 1 volt, the potential is calculated self-consistently and is displayed in figure 36. It is noted, that for N<sup>-</sup> regions of length 0.266 and 0.416 microns, most of the potential drop is across the N<sup>-</sup> region. For the smallest region a substantial potential drop falls across the N<sup>+</sup> region. The origins of this enhanced potential drop may be found in examining the self-consistently computed charge distribution figure 37 which shows the presence of an excess charge accumulation at the downstream N<sup>-</sup>N<sup>+</sup> interface, resulting in a change in sign of the curvature of the potential. The distribution of Γ valley carriers is displayed in figure 38, where the presence of substantial electron transfer in the N<sup>+</sup> region is noted. The carrier velocity, figure 39, displays the expected increases for the shorter N<sup>-</sup> region. The electric field distribution, shown in figure 40 displays higher field values within the N<sup>+</sup> region.

The significance of the above result is that while variations in the total charge density tend to screen variations in the doping profile of the structure, the potential drop across the N<sup>-</sup> region may be small enough to allow a substantial drop across the downstream N<sup>+</sup> regions thereby permitting electron transfer to occur away from the N<sup>-</sup> region. This, of course, is not unexpected. It is implicit in the design of Gunn oscillators with doping variations assigned the task of domain nucleation sites. The current-voltage characteristics are, therefore, expected to reflect a complex set of electrical phenomena. These are displayed in figure 41.

Figure 41 displays a series of current versus voltage curves for N<sup>+</sup>N<sup>-</sup>N<sup>+</sup> structures with the indicated N<sup>-</sup> region length. Each curve displays J/J<sub>ref</sub> versus Φ/Φ<sub>ref</sub>. J<sub>ref</sub> is the computed value of current at Φ<sub>ref</sub>=0.25 volts. The value J<sub>ref</sub> is indicated in the figure caption. Because of the intuitive relation between the space charge injection properties of the submicron N<sup>+</sup>N<sup>-</sup>N<sup>+</sup> structure and those associated with Child's law, J ∝ Φ<sup>γ</sup> was extracted. It is noted that J<sub>ref</sub> increases as the N<sup>-</sup> regions decrease in length. At low bias levels the current voltage relation appears to follow a power relation that is slightly less than J/J<sub>ref</sub>=(Φ/Φ<sub>ref</sub>)<sup>γ</sup> = 1.7 (as compared to a Child's law relation where γ=1.5). At higher values of bias is enhanced sublinearity in the current voltage relation, due in part to electron transfer to the satellite valleys.

As indicated above, a considerable amount of electron transfer occurs in the downstream portion of the N<sup>+</sup> region when the N<sup>-</sup> region is decreased in length. Indeed, the detailed calculations indicate that the relative amount of electron transfer increases as the N<sup>-</sup> region decreases in length. At first glance, this result appears to contradict all that has been discussed about transport in submicron devices. But it is not unusual when it is realized that as the N<sup>-</sup> region decreases in length a greater fraction of the voltage drop falls across the N<sup>+</sup> regions of the device. It is this latter feature that is responsible for the enhanced transfer. To place this in different terms, the active region length of the device increases as the N<sup>-</sup> region becomes insignificantly small.

## X. TWO DIMENSIONAL SCALING CONSIDERATIONS

To qualify the scaling discussions to two space dimensions, it is useful to recall the classical scaling arguments as applied to n-channel MOSFETs. The discussion for this scaling can be found in many texts and reference is to the text of Bar-Lev [7]. The basic scaling principle invoked is to retain a constant average electric field across the structure, while reducing the critical feature size of the device. As discussed in [7] all extrinsic dimensions are reduced by a constant  $\lambda$ , and all critical intrinsic linear dimensions are expected to be reduced by the same constant. To achieve this the voltages are scaled down by  $\lambda$ , while the substrate doping is increased by this same constant. Thus the depletion width surrounding the drain diffusion is reduced as follows:

$$d_{dep} = \left[ \frac{2\epsilon\phi_t}{qN_A} \right]^{1/2} \rightarrow d_{dep}/\lambda \quad (37)$$

and such characteristics as the source-drain current (not current density) within the gradual channel approximations is reduced as follows:

$$I_{DS} = \frac{\mu C_{ox} W}{L} [(\phi_{GS} - \phi_t)\phi_{DS} - \phi_{DS}^2/2] \rightarrow I_{DS}/\lambda \quad (38)$$

In the above the usual definitions apply [7], with  $V_t$  being the threshold voltage at the drain, and  $C_o$  the gate oxide capacitance:

$$C_o = \frac{\epsilon}{t_{ox}} \rightarrow \lambda C_o \quad (39)$$

Under these scaling constraints, the transconductance is unchanged, while the power, delay time, speed-power product and power dissipation per unit area are changed as follows:

$$(power) \quad I_\phi \rightarrow I_\phi/\lambda^2 \quad (40a)$$

$$(delay time) \quad T \rightarrow T/\lambda \quad (40b)$$

$$(speed-power product) \quad (I_\phi T) \rightarrow (I_\phi T)/\lambda^3 \quad (40c)$$

(power dissipation per unit area)

$$\left[ \frac{I\phi}{A} \right] \rightarrow \left[ \frac{I\phi}{A} \right]$$

(40d)

A brief discussion of the role of the above scaling within the general arguments of the preceding section is given below. It is noted, however, that Poisson's equation in dimensionless form, equation (6), contains the parameter  $S_n$ . Under constant average field scaling, considered in the first paragraph of this section,  $S_n$  is unchanged.

The impact of the above type of scaling upon the moments of the Boltzmann transport equation has already been indicated, but is reviewed within the context of the present discussion. First it is noted that the Poisson scaling factor,  $S_n$ , is the same for both the DDE and the moment equations. Second, the importance of the dimensionless parameters lies in their relative values. Thus, for the DDE formulation the important quantities are the relative values of  $R_n$  and  $C_n$ , where it was noted that  $R_n$  decreases with decreasing feature size. For the moment equation formulation, equation (31), and the relative values of  $P_f$  and  $\gamma M^2$  are of significance. In particular, if the term multiplying  $(\gamma M^2)^{-1}$  is regarded as a diffusive contribution, and constant average field scaling is invoked, a reduction in  $\Phi_{ref}$  increases the relative contribution of the diffusive term. In the DDE formulation, where an increase in the diffusive term may result in lowered current levels as the feature size is reduced, for the moment equation, a reduction in feature size increases the relative contribution of the  $\Gamma$  valley and improvements in device performance may be expected. While a full range of two dimensional scaling calculations have not yet been performed information can be garnered from the one dimensional calculations; particularly with reference to assessing expected reductions in power, delay time, and speed power product as device feature size is reduced.

The calculation of interest are displayed in two groups: The first group is contained in figures 4 through 6, where attention is focused on the unscaled GaAs. In these figures, the relevant features are:

$$x_{ref} = 1.0 \text{ micron}$$

$$\Phi_{ref} = 1.0 \text{ volts}$$

$$N_{ref} = 5 \times 10^{15} / \text{cm}^3$$

The second group of calculations is represented by figure 30. In this representation the relevant features are:

$$x_{ref} = 0.25 \text{ microns}$$

$$\Phi_{ref} = 0.25 \text{ volts}$$

$$N_{ref} = 2 \times 10^{16} / \text{cm}^3$$

These numbers satisfy the criteria of Bar-Lev [7] and constant average field scaling (the average field is 10kv/cm). The steady state current density level for each is indicated in the figures. For the one micron long device, the normalized current density is 0.29. For the 0.25 micron device the normalized current density is 0.45. The last result is not surprising; it is one of the reasons for moving to submicron feature sizes. It does, however, emphasize the obvious; namely increased current drive leads to increased power levels. The results, if extrapolated, teach that the power dissipation, the speed power product, and the power dissipation per unit area are likely to be in excess of 50% of that predicted by classical scaling theory.

## XI. TWO DIMENSIONAL TRANSPORT WITH MATERIAL SCALING WITHIN THE FRAMEWORK OF THE DRIFT AND DIFFUSION EQUATIONS

### XIa. Silicon, GaAs, Scaled GaAs

Of all of the internal parametric changes that were made to the scattering intergals, as discussed in the earlier sections, three broad features changed in the field dependent velocity curves: (i) the low field mobility, (ii) the peak velocity, and (iii) the saturation velocity. The effects of each are predictable and have been routinely used to assess semiconductor materials. In particular, the reader is referred to a review article by Eden [18]. But the first detailed calulations of this appeared in a study by Grubin in 1980 [5]. Because of the relevance of this study to the discussion of the earlier sections and to the later discussion, the study is briefly summarized.

The study was in two parts. The first was an assessment of the role of the saturated drift velocity on the electrical characteristics of the FET, in particular IDSS. Thus a sequence of three terminal calculations were performed for GaAs, and then for two other 'fictitious' materials as shown in figure 42. As is clear from figure 42, one curve was chosen to represent a material without negative differential mobility, but with a saturated drift velocity that was equal to that of the GaAs structure in the figure. The second was chosen similarly, but with a saturated drift velocity equal to the peak velocity value of GaAs. The calculation explored the effect of these parameter changes on the IDSS of a three terminal structure. It is noted that all three materials had the same low field mobility as that for GaAs. The structure for the calculation is shown in figure 43.

The structure in figure 43 is a three terminal device with source and drain contacts placed on parallel ends of the device. The gate was centrally placed. For each of these calculations the ratio of channel height to channel length was 5/41, and the ratio of gate length to channel length was 8/41. The doping level for this set of calculations was  $1.0 \times 10^{15}/\text{cm}^3$ . The reference quantities for this calculation are indicated in below.

$$X_{\text{ref}} = 10.0 \text{ microns}$$

$$\Phi_{\text{ref}} = 3.25 \text{ volts}$$

$$\mu_{\text{ref}} = 6,770 \text{ cm}^2/\text{v-s}$$

$$V_{\text{ref}} = 2.2 \times 10^7 \text{ cm/s}$$

$$F_{\text{ref}} = 3.25 \text{ kv/cm}$$

$$N_{\text{ref}} = 1.0 \times 10^{15}/\text{cm}^3$$

The above choices lead to a set of dimensionless constants equal to:

$$C_n = 1.0$$

$$S_n = 45.0$$

$$R_n = 120.0$$

The results of the calculation are clear and are shown in figure 44. The current voltage relation for 'HiV' yields a saturation current that exceeds that of GaAs, while that for 'LoV' is depressed below that of GaAs. The results indicate that even in materials possessing a nonlinear 'N' shaped negative differential conductivity, saturation in current is likely to be above that associated with the saturated drift velocity. This result should dispell any notion, that since Si has a higher saturation drift velocity than GaAs, it will perform better.

The next set of calculations is a comparison of Si to GaAs. Here, however, a comparison is not made to structures with similar extrinsic parameters; enough has been said in this paper to indicate that Si will not perform speed-wise in a matter similar to GaAs. Rather the question is, are there scaling procedures that permit the design of Si devices, which with respect to reference quantities are as good as that of GaAs? The answer to this question is yes, the significance, of which is discussed below.

Numerical simulations were performed for a Si device with the field dependent velocity and diffusivity shown in figure 45. The parameters for this calculation were deliberately chosen so that the dimensionless constants for the Si device were nearly equal to that of GaAs. This criteria leads to the reference quantities given below:

$$\begin{aligned}X_{\text{ref}} &= 4.4 \text{ microns} \\ \Phi_{\text{ref}} &= 3.14 \text{ volts} \\ \mu_{\text{ref}} &= 1400 \text{ cm}^2/\text{v-s} \\ V_{\text{ref}} &= 1.0 \times 10^7 \text{ cm/sec} \\ F_{\text{ref}} &= 7.14 \times 10^3 \text{ v/cm} \\ N_{\text{ref}} &= 5.0 \times 10^{15}/\text{cm}^3\end{aligned}$$

The dc electrical characteristics of the Si FET are shown in figure 46, and are as good as the "HiV" element when the silicon is doped to higher levels and reduced in feature size. This result is simply a statement that higher doping is needed to compensate for the low mobility of silicon, and that shorter crucial length scales are required to compensate for the low carrier velocity of Si.

With regard to the power delay produced, GaAs and the scaled Si are within a factor of two of each other [5]), implying that more energy must be dissipated through the smaller Si device to achieve the same electrical characteristics.

#### XIb. Scaling and High Frequency FETs

The goal of each of the above scaling procedures is to assist in the realistic design of a high frequency three terminal oscillator. The most useful method to obtain design information is through application of the moments of the Boltzmann transport equation. Unfortunately, the MBTE development as indicated

earlier precludes a full scale procedure. Instead, we expand upon results of an earlier study, where a full transient small signal analysis of an FET was presented [19], and then speculate with preliminary calculations on the short channel effects. In the [19] study the three terminal device discussed in the previous section was taken to a steady state time independent state; upon which the gate and drain voltage levels were, respectively and separately, pulsed. The resulting current transient, subsequently Fourier analyzed and the small signal 'Y' parameters computed. Of significance here is the cut-off frequency, which is defined as

$$f_T = \frac{\Omega \operatorname{Re} Y_{21}}{2\pi |\operatorname{Im}(Y_{11} + Y_{12})|} \quad (41)$$

For the structure of figure 43, the peak cut-off frequency as seen in figure 47, is bias dependent and peaks near 9GHz. The implication of scaling with the drift and diffusion code is that if diffusive effects are to be ignored, then a reduction in the critical length parameters by the scale factor ' $\lambda$ ' is expected to increase the cut-off frequency by the same scale factor. This, of course, is the basis of all FET scaling procedures; and is a major motivating factor for going to submicron structures. This scaling was tested with the following set of parameters:

$$x_{ref} = 1.0 \text{ microns}$$

$$\phi_{ref} = 0.325 \text{ volts}$$

$$N_{ref} = 1.0 \times 10^{16}/\text{cm}^3$$

However, in testing, rather than perform a full scale calculation, only a limited and preliminary set of dc current voltage characteristics were obtained.

The electrical characteristics of the scaled and unscaled GaAs structures are shown in figure 48, and somewhat surprising the expected degradation with increased donor level did not appear. While additional scaling work here is needed, the preliminary conclusion is that if 9GHz is possible, a scaled cut-off frequency of 90GHz is feasible.

The situation with submicron FET is complicated by determining the key design significance of the submicron feature size. This is a more difficult problem and has been examined by Frey and coworkers [20] using a highly approximate set of equations whose applicability to submicron devices is somewhat uncertain. The results of our previous one dimensional study have indicated that as device feature size is reduced transport is dominated by  $\Gamma$  valley carriers. The immediate implication is that the early transport models in which transconductance was defined in terms of low field mobility is the more relevant quantity. A preliminary estimate of this effect is examined in the next calculation of this study.

#### XIc. MBTE versus DDE

Figure 49 is a sketch of the dc current voltage relation for a GaAs FET with the feature size shown in the diagram. Two sets of calculations were performed: one using the drift and diffusion equations, and the second using

the moments of the Boltzmann transport equation. The calculations were done at zero bias on the gate along with a zero dc current boundary condition on the gate contact. The calculations show current voltage relationships that are virtually identical at low values of bias, with substantial deviations at high values of bias. It is noted that at high values of bias the DDE over estimates the amount of electron transfer within the device and thereby under estimates the dc current level. Rather, at high bias levels, the dc current is dominated by  $\Gamma$  valley carriers with a corresponding high field dependent mobility. The charge distribution within the device, of course, reflects the variations in the current levels, but the differences between the DDE and the MBTE carrier density calculations, as seen in the contour plots the figures 50 and 51, indicate them to be of secondary importance. The result, of course, is that scaling down improves the performance of the structure.

## XII. SMALL SIGNAL DEVICE BEHAVIOR

A number of small signal one dimensional calculations were performed during the course of the study. Several were performed on uniform field two terminal devices and several on devices where the space charge distributions were nonuniform. The question was asked as to whether a window of frequency existed for two terminal small signal active device applications. Here it is known that with a nonuniformity in the doping the two terminal structure can behave as though uniform field exists across the active region, thereby leading to small signal gain at high frequencies. In the study herein, nonuniformities in the field were retained through an injecting contact, and advantage was taken of a paper by workers in Japan [8] who predicted, from solutions to moments of the Boltzmann transport equation that if transfer was avoided a window of gain could be obtained at frequencies well in excess of 800GHz. A critical feature of these studies is that the results require that terms ignored in the drift and diffusion term, but present in the MBTE and the Boltzmann transport equation be retained. Preliminary calculations to date, through joint support of ONR, indicate that frequencies within the terahertz region can lead to gain. A critical element is thus to determine whether a set of parameters can be found to reduce the frequency window.

### XIII. SPACE CHARGE INJECTION FIELD EFFECT TRANSISTORS

It was the view of this study that a key element of the program was the ability to suggest new and novel device structures. A structure of particular significance that was discussed during the Contract period was the three terminal  $N^+N^-N^+$  device, which is commonly referred to as the space charge injection FET [24]. And calculations using the MBTE algorithm was used to ascertain its effectiveness. It is noted, however, that due to budget limitations a full range of calculations were not undertaken; and the results must, therefore, be regarded as preliminary in nature. Nevertheless, several key ideas emerge from calculations performed during the course of the study, as well as those of others.

The structure under consideration is shown in figure 52. It is a three terminal structure with an essentially undoped center region. Its two terminal counterpart has been discussed in earlier sections. A key issue here is that the active region is undoped and thus ionized impurity scattering, can for all purposes be disregarded. Thus, an immediate benefit is accrued. The second feature is the high injection level. For three terminal studies efforts by others [25] have demonstrated that the presence of space charge injection can lead to improvements in the transconductance. These improvements exist even without the benefits of overshoot in velocity. However, the results of the previous section demonstrate that overshoot is present in two terminal injection devices, thus the benefits of overshoot should be present in the FET. This has been established through the Monte Carlo calculations of [24], and through the calculations performed under the present study, as seen below. Figures 53, 54, and 54 show, respectively, the distribution of potential;, carrier density and  $T$  valley velocity. Overshoot is clearly present. The space charge injection FET is likely to be a major high frequency candidate device, and additional work on this device is warrented. It is noted that predictions of cut-off frequencies of 360 GHz, have emerged from the original studies.

#### XIV. SUMMARY

The present study was undertaken to establish a set of systematic procedures for assessing the material characteristics of near and submicron length semiconductor devices structures. The first point of note, is that the assessment of the semiconductor materials requires a decision as to how they will be used. For example, semiconductor materials that are optimum for two terminal active device applications are not necessarily the ones to be sought after for three terminal application. In the case of two terminal active devices rapid scattering is sought; however, this normally leads to low values of mobility. For three terminal structures, submicron devices are dominated by the  $\Gamma$  valley scattering; and materials with high values of mobility are sought. Another important conclusion, was the role of carrier density in scaling. Of particular importance here was the fact that increased donor concentration often led to current levels below that anticipated. The study suggests that a hierarchy of material parameters exists for device applications. For two terminal active devices the three materials in order of significance are InP, GaAs, and GaInAs. For three terminal structures materials in order of significance are GaInAs, GaAs, InP, Ge, Si, and SiC.

The conclusions were drawn from a broad range of calculations that involved altering the band structure parameters, both uniformly and nonuniformly; and altering the doping profile both uniformly and nonuniformly. Additionally, supplementary two dimensional three terminal calculations were performed to test the concepts.

Several important features emerged: First, scaling as currently applied has been inadequate for examining submicron devices. In particular, features associated with field nonuniformities are generally ignored, and are crucial for submicron devices. The absence of suitable scaling basically arises because of a limited number of calculations that emphasize scaling. The study demonstrated that scaling procedures can be envisioned, through which small signal steady state analysis can effectively lead to devices whose, e.g., cut-off frequency can be increased by the factor  $\lambda$  if the carrier density is increased, and the scaling length decreased by the same factor.

While small signal parameter studies of the three terminal FET have begun, there is a clear need for further assessing the relative merits of GaAs coplanar devices from both a small and large single viewpoint, particularly through solutions to the moments of the Boltzmann transport equation. The MBTE has not yet been completely applied to assessing the high frequency performance of the standard GaAs FET and such studies are necessary before a realistic comparison can be made to such novel devices as the space charge injection FET. Additionally, new insight can be obtained through small signal analysis, as was revealed in this study in which high frequency gain in the terahertz region arose from phase delays in the carrier density. This phenomena is new to solid state semiconductor devices.

## FIGURE CAPTIONS

- Figure 1. Magnitude of the current transient following application of a sudden change in bias. Parameters for this calculation are listed in the Appendix A and include a carrier density of  $5 \times 10^{15} / \text{cm}^3$ . The terminus of each calculation reflects the physical time required for steady state. The longest time duration is that associated with the lowest bias level. For this calculation 2.0 volts corresponds to an average field of 20kv/cm 1.0 volts yields 10kv/cm, etc.
- Figure 2. Distribution of  $\Gamma$  valley carriers as a function of time for the parameters of figure 1. Note the delay in electron transfer, a delay that is shortest for the highest bias level.
- Figure 3. Transient distribution of temperature following application of a sudden change in bias for the parameters of figure 1. The presence of a temperature overshoot is noted, a feature resulting from the enhanced scattering at elevated temperatures. The inset displays the temperature during the first 0.4ps and demonstrates through application of equation 27 of the onset of scattering.
- Figure 4. Total and  $\Gamma$  valley carrier density obtained as a solution to the MBTE with the boundary conditions of equations (29) and (30). Inset denotes scaling parameters as introduced in section V;  $\lambda=1$  unscaled GaAs,  $\lambda=1/2$ , 2 and 4, are scaled results.
- Figure 5. As in figure 4, but for the total and  $\Gamma$  valley carrier density.
- Figure 6. As in figure 4, but for  $\Gamma$  valley carrier velocity.
- Figure 7. As in figure 4, but for  $\Gamma$  valley electron temperature.
- Figure 8. Steady state current density versus applied voltage and average field for the 1.0 cm long structure with the parameters of figure 4.
- Figure 9. Transient current response of the 1.0 micron long gallium arsenide one dimensional structure subjected to a sudden change in bias.
- Figure 10. Steady state uniform field characteristics for electrons in gallium arsenide assuming two levels of transfer. The parameters for this calculation are shown in table 4. (a) and (b) are the magnitudes of the mean carrier velocity over different ranges of electric field. (c) and (d) display the field dependence of the fractional population of carriers in the  $\Gamma$  and L valleys. (e) and (f) display the magnitudes of the mean carrier velocity in the  $\Gamma$  and L valleys. (g) and (h) display the carrier temperatures in the  $\Gamma$  and L valleys.
- Figure 11. Steady state uniform field dependent drift velocities using the scaling principles of equation (34). Scaling parameters are indicated.

Figure 12. As in figure 10, but for indium phosphide.

Figure 13. Two level moment equation scattering rates for gallium arsenide.

Figure 14. Ratio of the scattering rates of indium phosphide to gallium arsenide.

Figure 15. Effects of parameter variation, as indicated, on the field dependent velocity of gallium arsenide.

Figure 16. Response of the mean carrier velocity in gallium arsenide to a controlled change in electric field.

Figure 17. Transient mean velocity response of scaled and unscaled gallium arsenide.

Figure 18. Circuit for high frequency study

Figure 19. Steady state oscillation for gallium arsenide in the circuit of figure 18 with an average applied field of  $4 \times 10^3$  kv/cm. Figure shows time dependent field and  $\Gamma$  valley density. The  $\Gamma$  valley carries density exhibit hysteresis and is responsible for limiting the upper frequency limit. For this calculation the steady oscillation frequency was 98GHz. A similar calculation for InP with a scaled bias of  $4 \times 10^4$  kv/cm yielded oscillation at 138GHz.

Figure 20.  $\Gamma$  valley carrier velocity for a 0.25 micron long scaled and unscaled gallium arsenide device. The potential across the structure is 0.6 volts, and the donor density is  $8 \times 10^{16}$ /cm<sup>3</sup>.

Figure 21. Steady state current voltage relation for the calculation of figure 20.

Figure 22. Steady state  $\Gamma$  valley carrier velocity for a 0.25 micron long device with indicated values of potential. For this calculation the deformation coupling coefficient of gallium arsenide is increased by a factor of 2. The donor density for this calculation is  $8 \times 10^{16}$ /cm<sup>3</sup>.

Figure 23. As in figure 22, but for the deformation coupling coefficient reduced by a factor of 2.

Figure 24. As in figure 22, but for gallium arsenide.

Figure 25. (a) Current density versus potential for a 0.25 micron long structure with injecting contacts and a donor density of  $8.0 \times 10^{16}$ . The potential variations are as indicated. Calculations are for different values of the coupling coefficients.

(b) As in (a) but for a 1.0 and 2.0 microns long structures.

- Figure 26.** Steady state  $\Gamma$  valley carrier velocity for a 1.0 micron long device with a donor level of  $5 \times 10^{15}/\text{cm}^3$ , and an intervalley energy separation increased to 0.66ev. Potential levels are indicated.
- Figure 27.** Comparison of steady state current levels for gallium arsenide and an element in which the intervalley energy separation is increased to 0.66ev.
- Figure 28.** As in figure 24, but for a donor level of  $5 \times 10^{15}/\text{cm}^3$ .
- Figure 29.** As in figure 24, but for a donor level of  $2 \times 10^{16}/\text{cm}^3$ .
- Figure 30.** Steady state current voltage relation for different donor densities for the calculations of figures 24, 28, and 29.
- Figure 31.** Length dependence of steady state current voltage characteristics for a 0.25 and 1.0 micron gallium arsenide element doped  $5 \times 10^{15}/\text{cm}^3$ .
- Figure 32.** Donor distribution of the  $N^+N^-N^+$  structure used in the study. In the calculations, the width of the  $N^-$  region (defined at a donor level of  $10^{16}/\text{cm}^3$ ) varied from  $0.416\mu\text{m}$  to  $0.116\mu\text{m}$ . In all calculations the width of the upstream  $N^+$  region was unchanged.
- Figure 33.** Time dependent current following application of a step change in bias to 1.0 volts for the  $N^+N^-N^+$  structure with an  $N^-$  region of  $0.416\mu\text{m}$ . The structure of the current profile displays significant quantitative differences from that of the uniform donor calculations. First, the peak in the current occurs within 0.10ps, which is below that of the uniform donor calculations. Second, there is a strong current minima, followed by relaxation. Steady state requires approximately 15ps. Parameters for the calculation are listed in the Appendix A.
- Figure 34.** Spatial distribution of particle current at different instants of time for the parameters of figure 32. Also shown is the donor distribution. The largest spatial variation in particle current occurs near the interfacial boundaries.
- Figure 35.** Donor concentration for  $N^+N^-N^+$  structure with three different  $N^-$  region lengths. For A,  $L_{N^-} = 0.116\mu\text{m}$ , for B,  $L_{N^-} = 0.266\mu\text{m}$ , for C,  $L_{N^-} = 0.416\mu\text{m}$ . The calculations for C have already been presented and are included for completeness.
- Figure 36.** Steady state distribution of potential for structures A, B, and C subject to bias of 1.0 volt. For structures B and C the potential drop is confined mainly to the  $N^-$  region. For structure A, a significant fraction of potential falls across the  $N^+$  region.
- Figure 37.** Steady state distribution of total carrier concentration for structures A, B, and C. Note, for all three structures, the free carrier concentration closely traces the donor variation.

**Figure 38.** Distribution of  $\Gamma$  valley carriers. The least amount of electron transfer occurs for the widest structure C. For structure A, transfer continues to the anode contact and is a consequence of a large potential falling across the downstream  $N^+$  region.

**Figure 39.** Distribution of  $\Gamma$  valley carriers velocity for structures A, B, and C. Peak velocity gradually increases as the  $N^-$  region decreases in length. Additionally, the up and downstream carrier velocity increases as the  $N^-$  region decreases in length.

**Figure 40.** Steady state distribution of electric field for the three structures A, B, and C. It is noted that for structure A, a large residual field remains across the downstream  $N^+$  layer.

**Figure 41.** Steady state current voltage characteristics for the three structures A, B, and C. The current level for structure A is higher than that of B, which in turn, than C. Note that the low field resistance of structure A is the lowest of the three. Also included for reference is the Child's law curves.

**Figure 42.** Field dependent velocity relationships used to determine the relevance of the saturated drift velocity to the IDDS of FETs.

**Figure 43.** Sketch of three terminal FET structure used in calculations.

**Figure 44.** Current-voltage relation for the field dependent velocities of figure 42.

**Figure 45.** Field dependent velocity and diffusivity for a silicon unipolar FET calculation.

**Figure 46.** Current-voltage relation for silicon and 'HiV' drawn on the same scale.

**Figure 47.** Small signal cutoff frequency in gallium arsenide FET with  $X_{ref}=10.0$  microns.

**Figure 48.** Drain current versus drain bias for scaled and unscaled gallium arsenide FET. Also shown in the velocity field characteristic sealed current.

**Figure 49.** Comparison of the FET characteristics using the DDE and MBTE formulation structure is indicated with length in microns.

**Figure 50.** Comparison of DDE and MBTE contour for indicated bias.

**Figure 51.** As in figure 51.

**Figure 52.** Space charge injection FET.

**Figure 53.** Velocity distribution for the space charge injection FET.

**Figure 54.** Density distribution for the space charge injection FET.

**Figure 55.** Potential distribution for the space charge injection FET.

#### REFERENCES

1. See review, R.J. Dennard, J. Vac., Sci., Tech., Vol. 19, 537 (1981)
2. See e.g., G.C. Osborne, Journal Applied Physics 53, 1586 (1982)
3. S.C. Binari, H.L. Grubin, and P.E. Thompson, 1982 IEDM Technical Digest 770 (1982)
4. K. Thornber, Journal Applied Physics 51, 2127 (1982)
5. H.L. Grubin, IEEE Trans. Micro. Th. Tech., MTT-28, 442 (1980)
6. H.L. Grubin and D.K. Ferry, J. Vac. Sci. Tech. No.1, 19, 540 (1981)
7. A. Bar-Lev, Semiconductors and Electric Devices (2nd edition) Prentice Hall International, N.J. (1984)
8. A. Aishima and Y. Fukushima, J. Appl. Phys. 56, 1088 (1984)
9. R. Fauquembergue, M. Pernisek and E. Constant, in Physics of Submicron Structures (H.L. Grubin, K. Hess, G.J. Iafrate, and D.K. Ferry, editions) 171 Plenum Press, N.Y. (1984)
10. C. Lyden and J.S. Campbell, IEEE Electron Dev. LeHs., EDL-5, 40, (1984)
11. T.H. Windhorn, L.W. Cook, T.S. Roth, and G.E. Stillman, in Physics of Submicron Structures (H.L. Grubin, K. Hess, G.J. Iafrate, D.K. Ferry editions) 253 Plenum Press, N.Y. (1984)
12. H.L. Grubin and J.P. Kreskovsky, in VLSI Electronics (N.G. Einspruch, edition) 10, 237 Academic Press, FL (1985)
13. P.N. Butcher, Rept. Prog. Phys. 30, 97 (1967)
14. R. Bosch and H. Thien, IEEE Trans. Electron Devices, ED-21, 16 (1974)
15. H.L. Grubin, D.K. Ferry, G.J. Iafrate, and J.R. Barker, in VLSI Electronics (N.G. Einspruch, edition) 3, 198 Academic Press, N.Y. (1982)
16. See e.g., S. Kratzer and J. Frey, Journal Applied Physics, 49, 4064 (1978)
17. H.L. Grubin and J.P. Kreskovsky, J. Vac. Sci. Tech., Vol. 20, 610 (1984)
18. R.C. Eden, Proc. IEEE Trans. Micro. Tech., 70 5 (1982)
19. H.L. Grubin and J.P. Kreskovsky, Scientific Research Associates, Inc. Report R930007-F (1983)
20. See e.g., F.A. Buot and J. Frey, in Physics of Submicron Structures (H.L. Grubin, K. Hess, G.J. Iafrate, and D.K. Ferry editions) 77 Plenum Press, N.Y. (1984)

FIG. 1

920010 31684 - 5

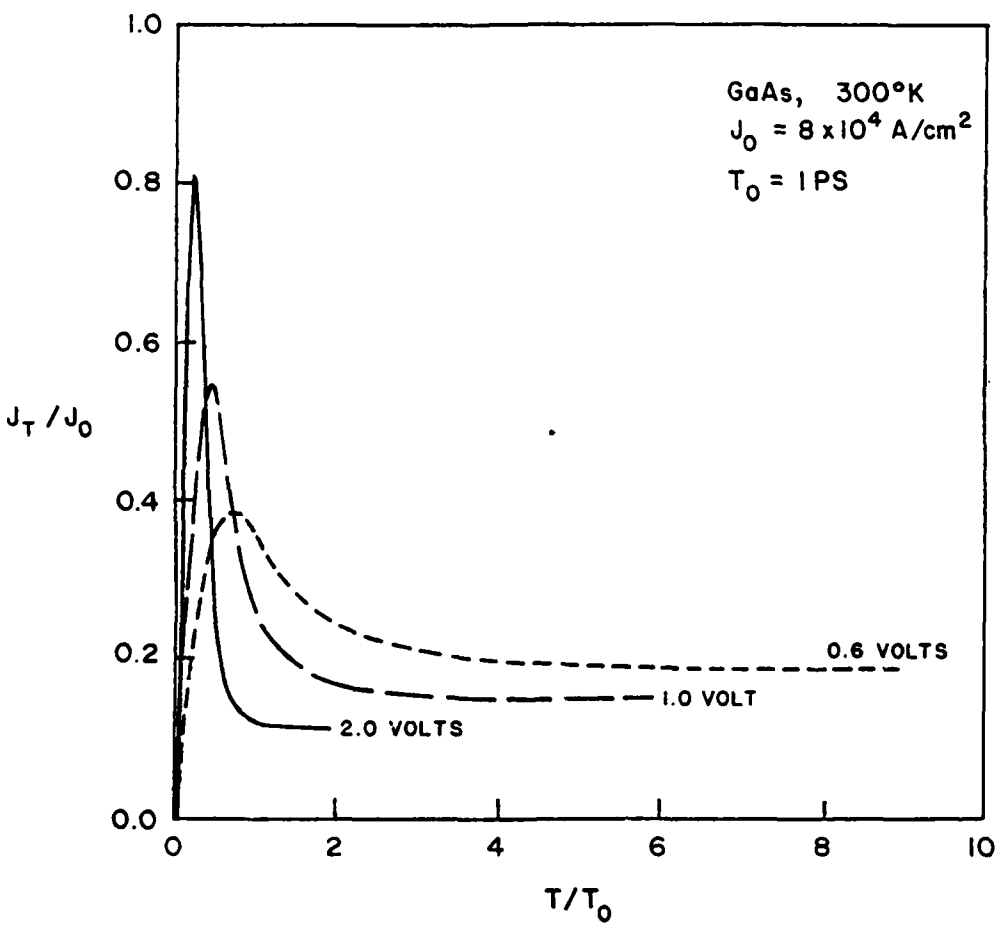


FIG. 2

920010 316 84-6

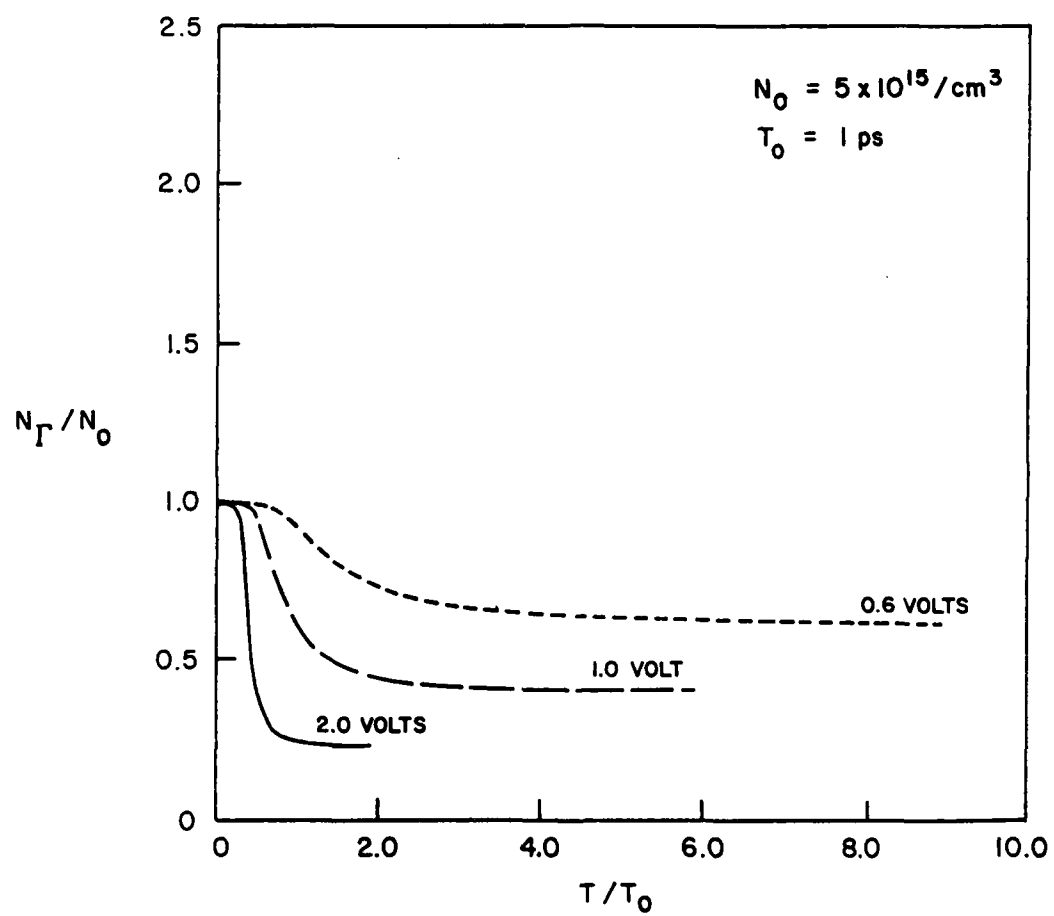


FIG. 3

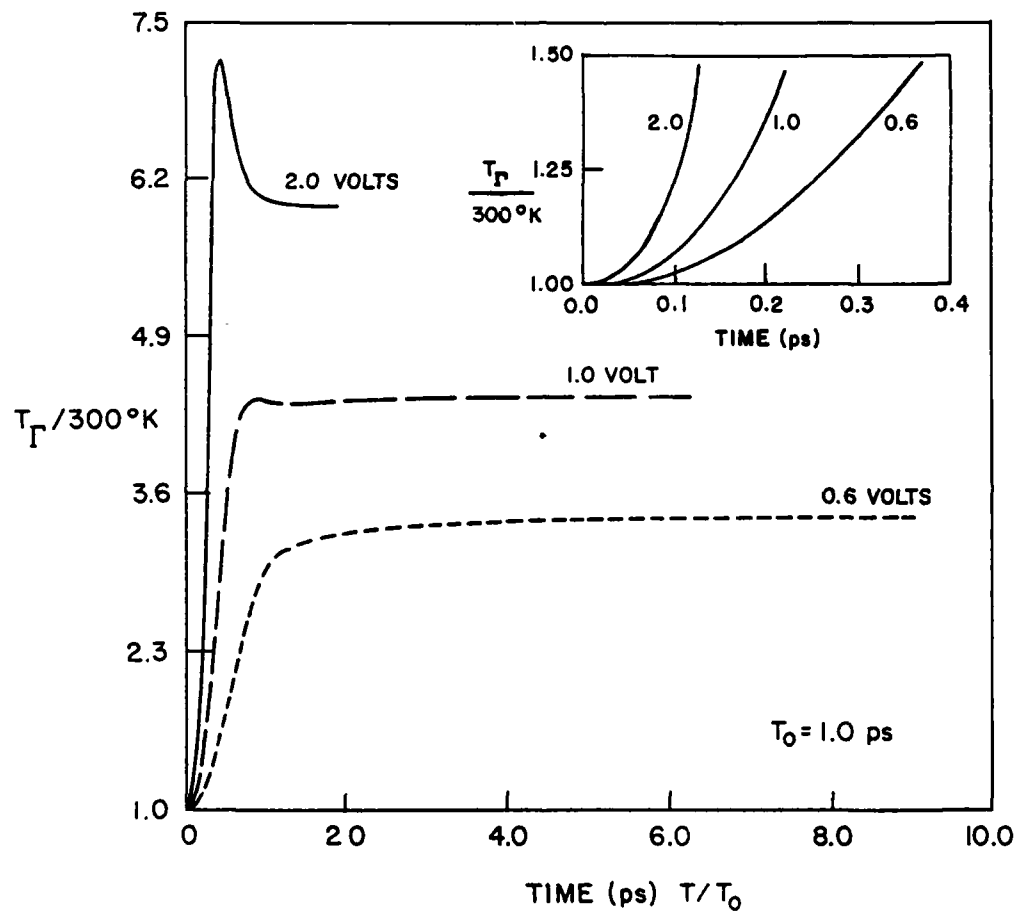
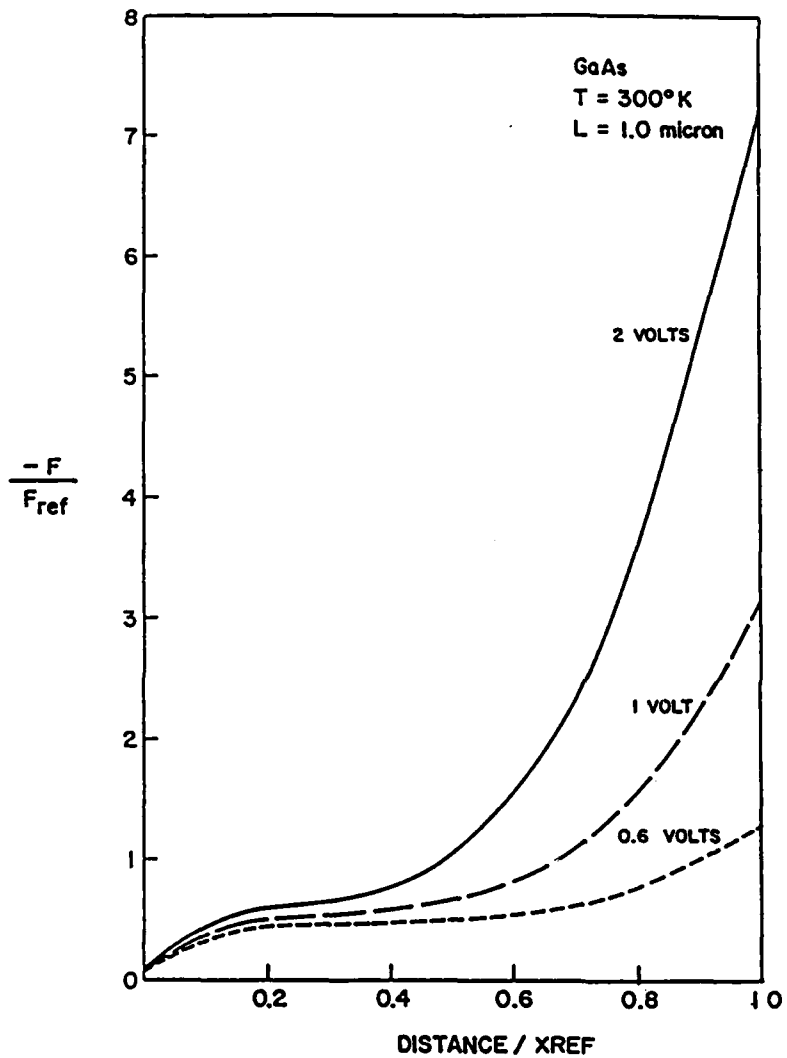
316 84-7  
920010

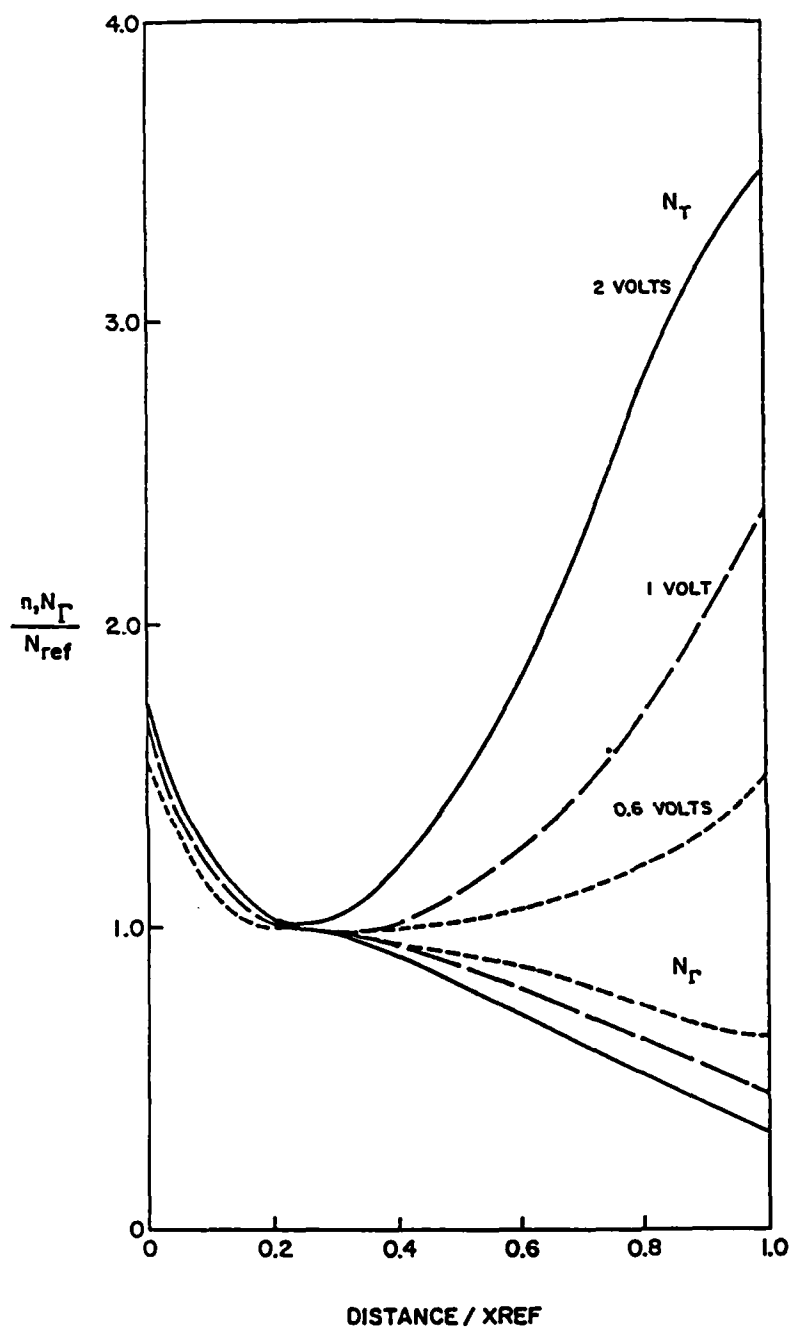
FIG. 4

920016 31484 -1



SCALING	$X_{\text{ref}}$	$F_{\text{ref}}$
$\lambda = 1$	$1.0 \mu\text{m}$	$10 \text{ kv/cm}$
$\lambda = 2$	$0.5 \mu\text{m}$	$20 \text{ kv/cm}$
$\lambda = 0.5$	$2.0 \mu\text{m}$	$5 \text{ kv/cm}$
$\lambda = 4$	$0.25 \mu\text{m}$	$40 \text{ kv/cm}$
$\phi_{\text{ref}} = 1.0 \text{ volts}$		
$T_{\text{ref}} = 300^\circ \text{K}$		
COMMENT - GaAs = $\lambda = 1$		

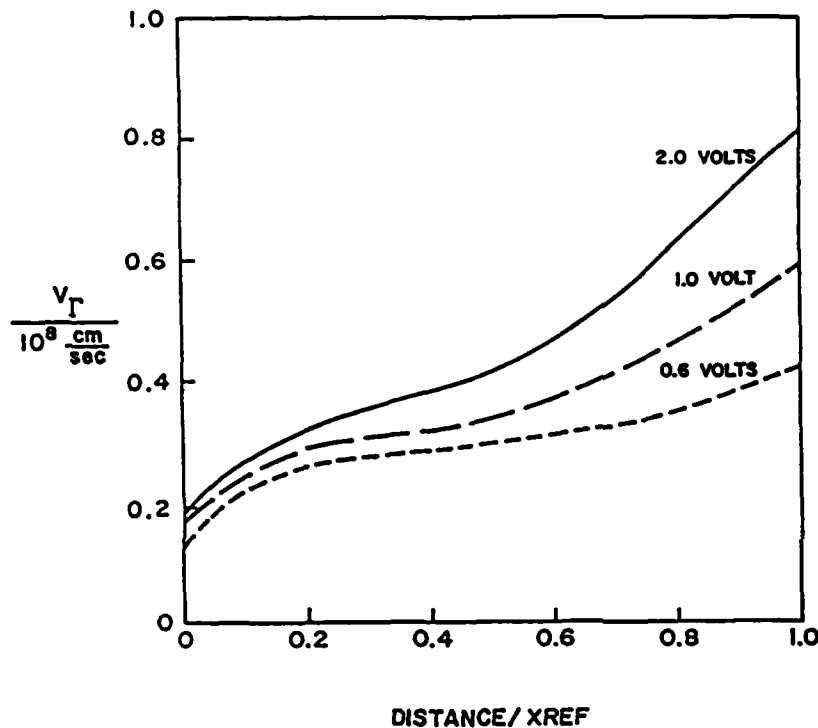
FIG. 5



SCALING	$X_{ref}$	$N_{ref}$
$\lambda = 1$	$1.0 \mu\text{m}$	$5 \times 10^{15} / \text{cm}^3$
$\lambda = 2$	$0.5 \mu\text{m}$	$2 \times 10^{16} / \text{cm}^3$
$\lambda = 0.5$	$2.0 \mu\text{m}$	$1.25 \times 10^{15} / \text{cm}^3$
$\lambda = 4$	$0.25 \mu\text{m}$	$8 \times 10^{16} / \text{cm}^3$
$\phi_{ref} = 1.0 \text{ volts}$		
$T_{ref} = 300^\circ\text{K}$		
COMMENT - GaAs = $\lambda = 1$		

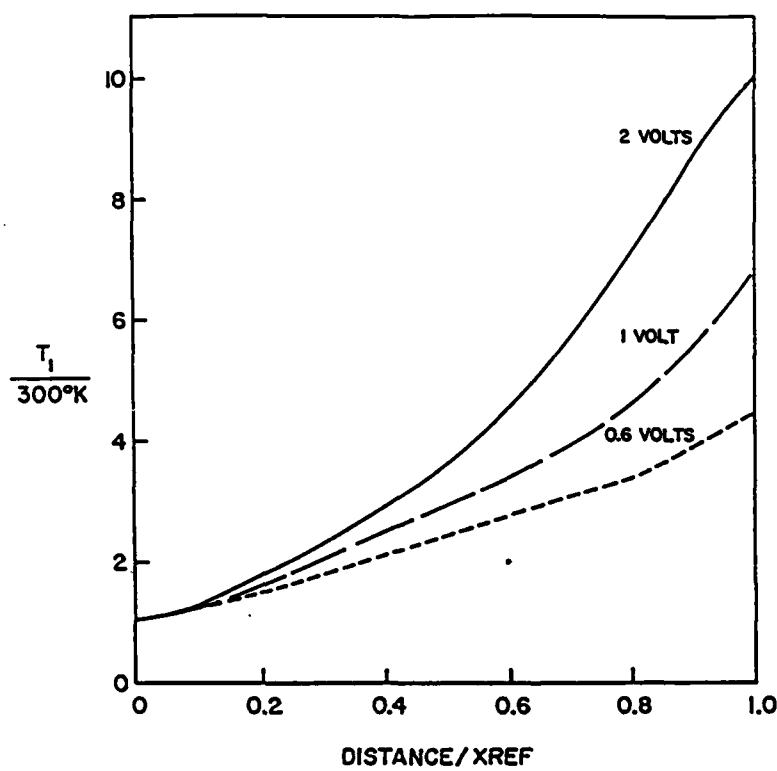
FIG. 6

920016 31584 I



SCALING	$x_{\text{ref}}$
$\lambda = 1$	$1.0 \mu\text{m}$
$\lambda = 2$	$0.5 \mu\text{m}$
$\lambda = 0.5$	$2.0 \mu\text{m}$
$\lambda = 4$	$0.25 \mu\text{m}$
$\phi_{\text{ref}} = 1.0 \text{ volts}$	
$T_{\text{ref}} = 300^\circ \text{K}$	
COMMENT - GaAs = $\lambda = 1$	

FIG. 7



SCALING	$X_{\text{ref}}$
$\lambda = 1$	$1.0 \mu\text{m}$
$\lambda = 2$	$0.5 \mu\text{m}$
$\lambda = 0.5$	$2.0 \mu\text{m}$
$\lambda = 4$	$0.25 \mu\text{m}$
$\phi_{\text{ref}} = 1.0 \text{ volts}$	
COMMENT - GaAs = $\lambda = 1$	

FIG. 8

redrawn 12-

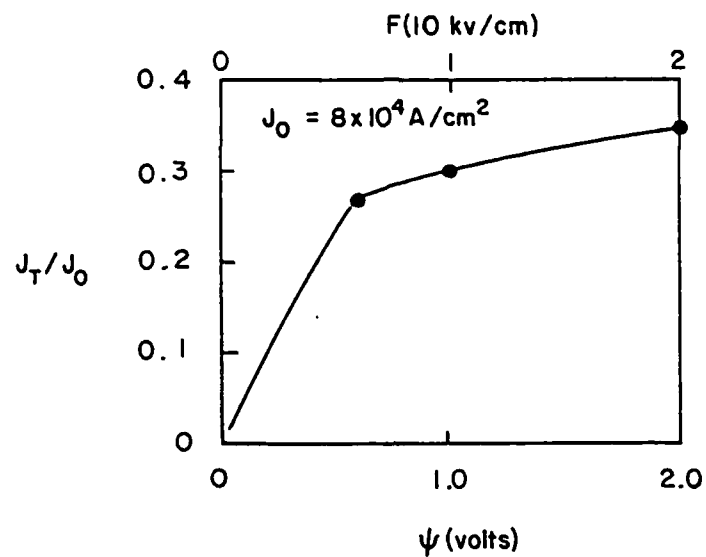
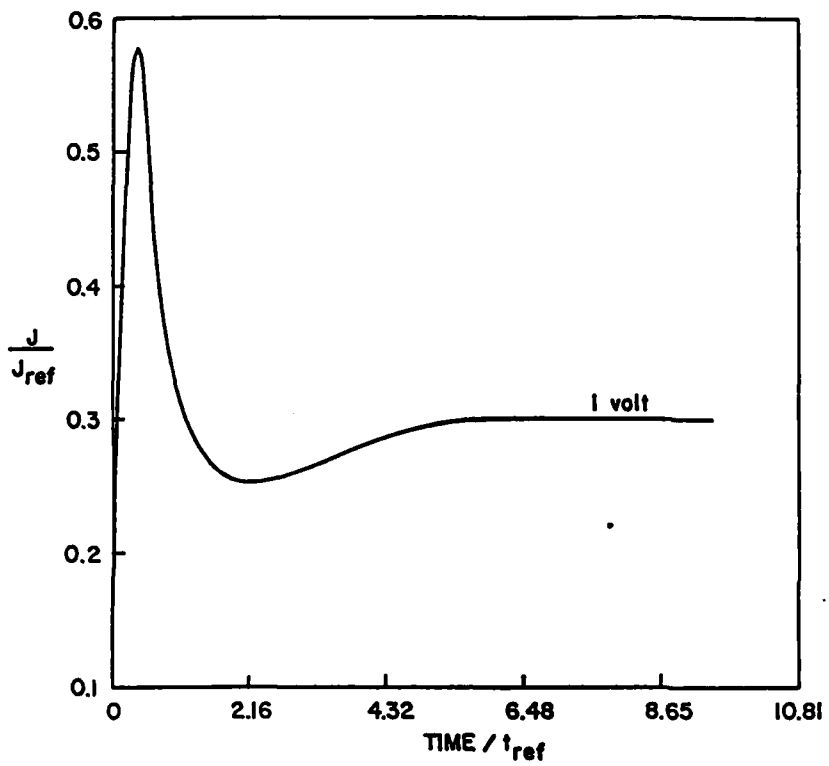


FIG. 9

920016 31584-4



SCALING	$J_{\text{ref}}$	$t_{\text{ref}}$
$\lambda = 1$	$8 \times 10^4 \text{ A/cm}^2$	1 ps
$\lambda = 2$	$32 \times 10^4 \text{ A/cm}^2$	0.5 ps
$\lambda = 0.5$	$2 \times 10^4 \text{ A/cm}^2$	2 ps
$\lambda = 4$	$128 \times 10^4 \text{ A/cm}^2$	0.25 ps
$\Phi_{\text{ref}} = 1.0 \text{ volts}$		
$T_{\text{ref}} = 300^\circ\text{K}$		
COMMENT - GaAs = $\lambda = 1$		

FIG. 10

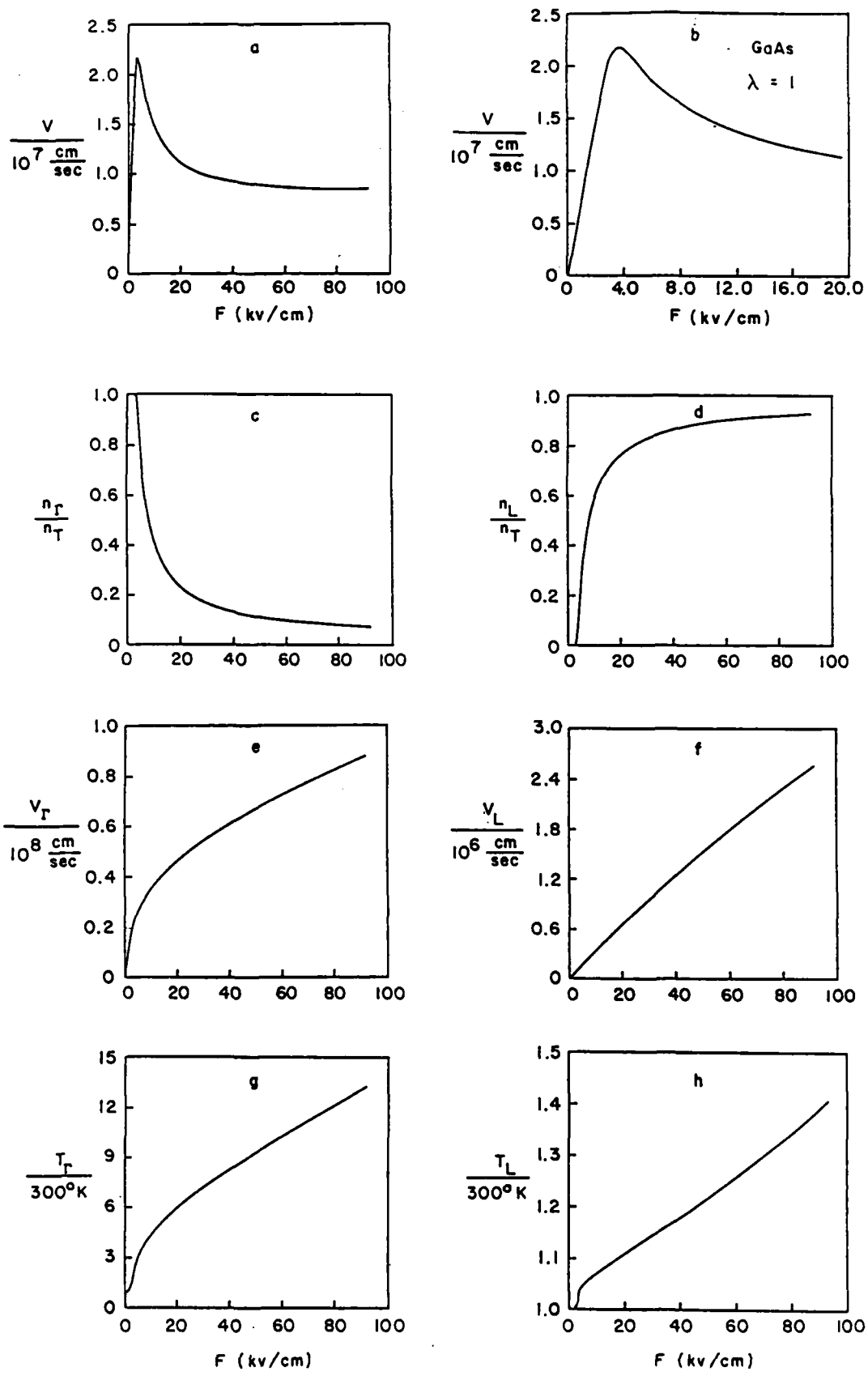
II 30 84 - 5  
J / HG 920016

FIG. 11

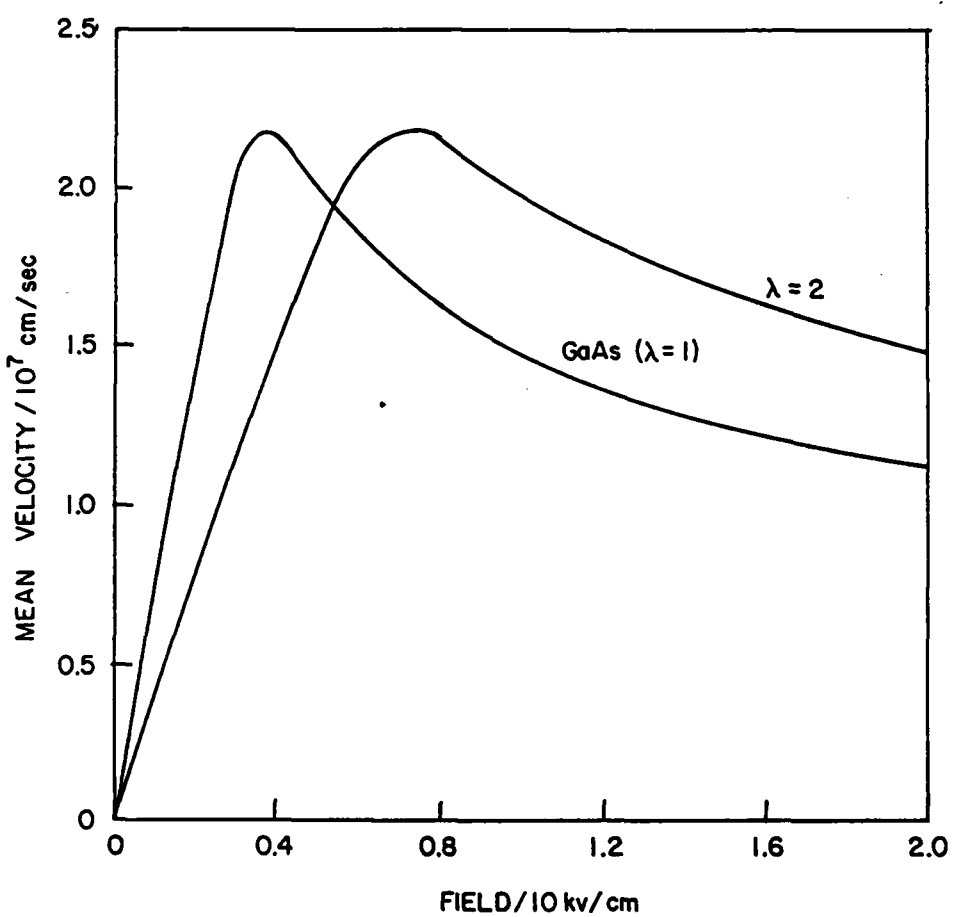


FIG. 12

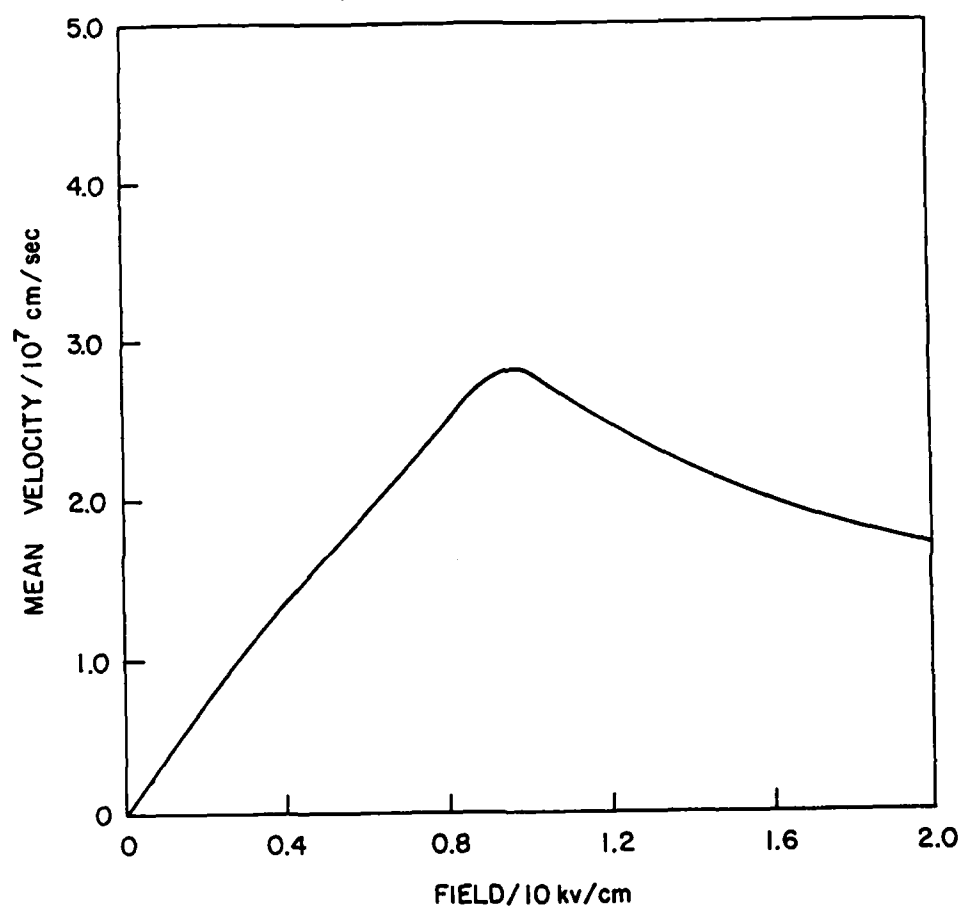


FIG. 13

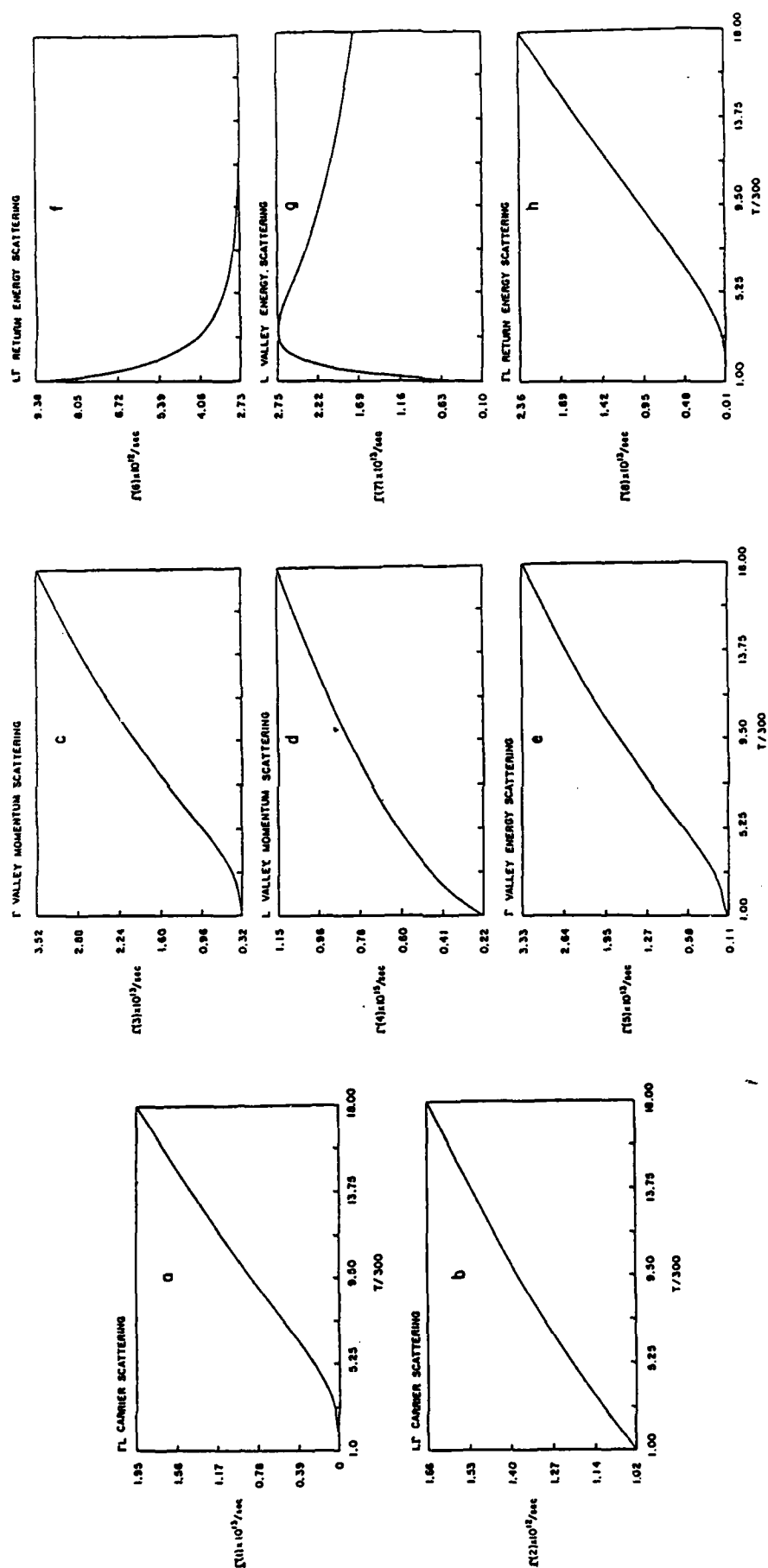


FIG. 14

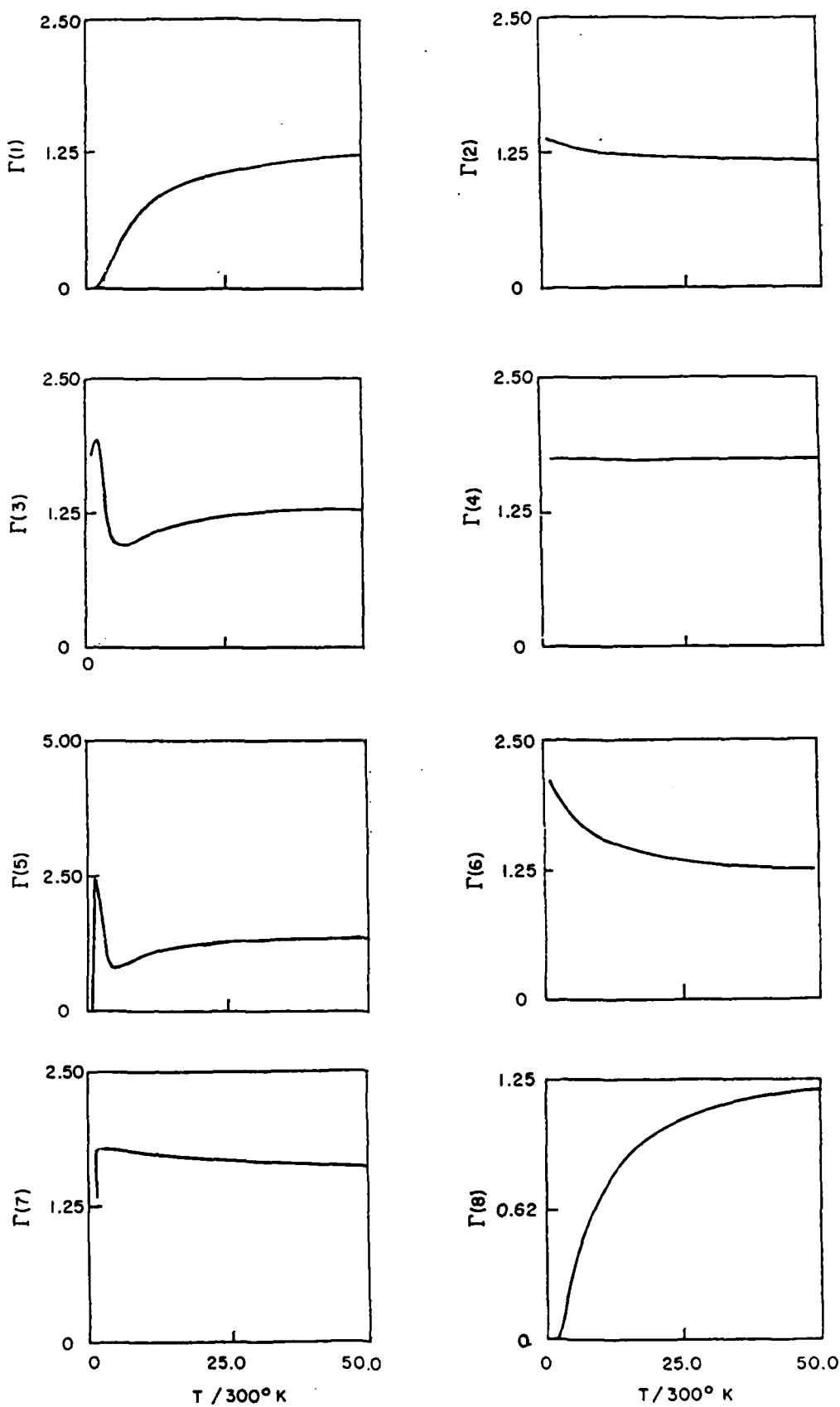
12 21 84 - 1  
920010

FIG. 15

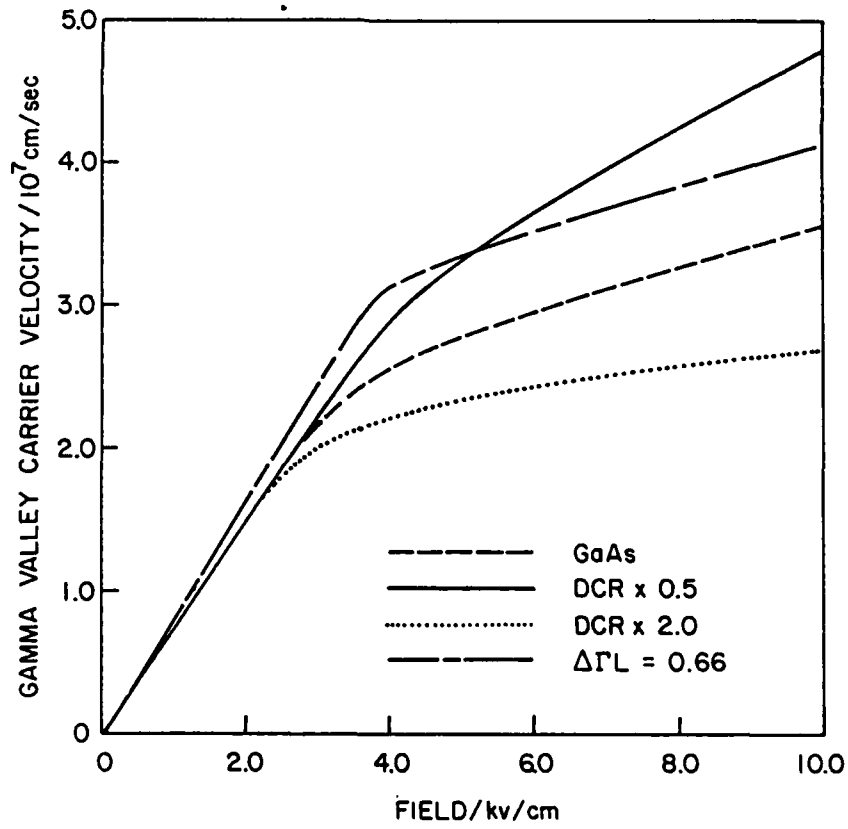
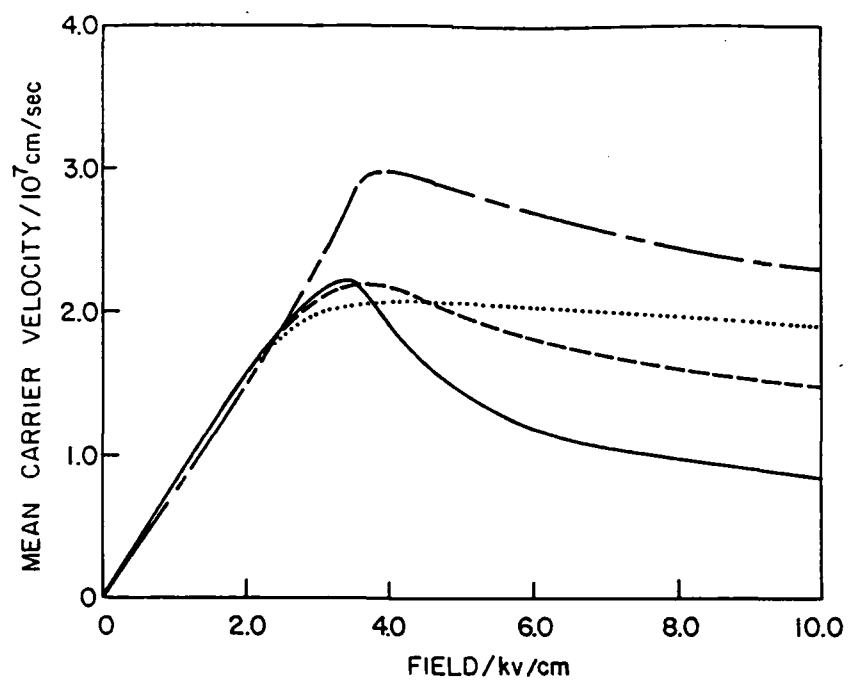
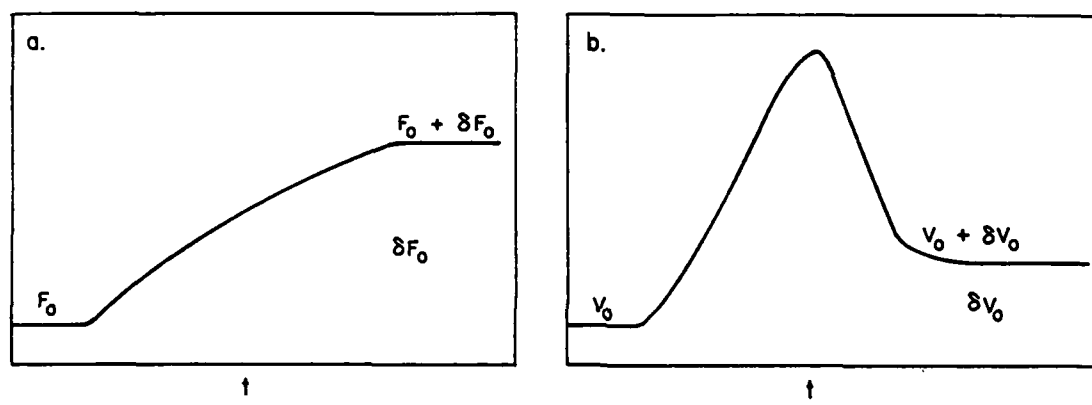
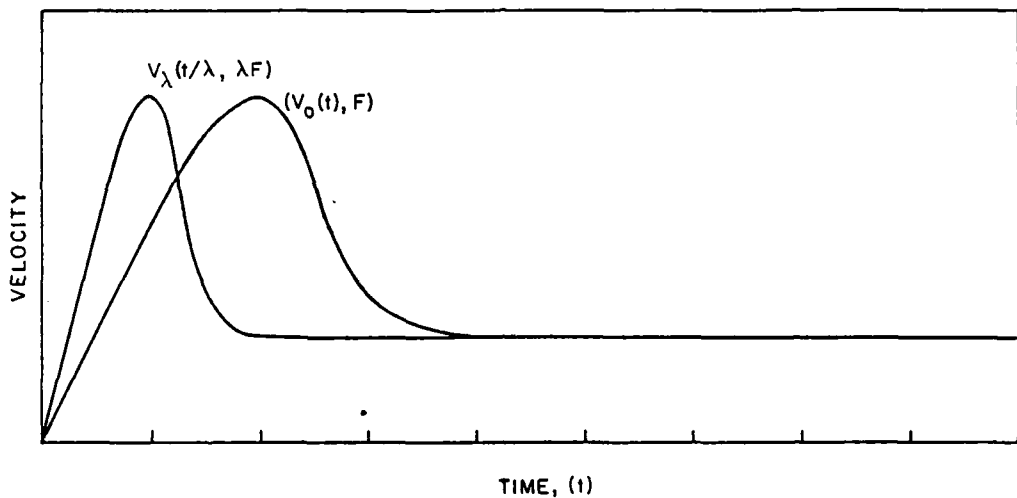


FIG. 16



920010 1286-2



11085-3 920010

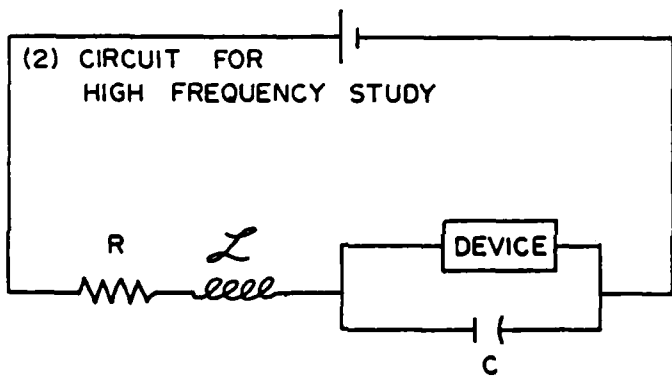


FIG. 19

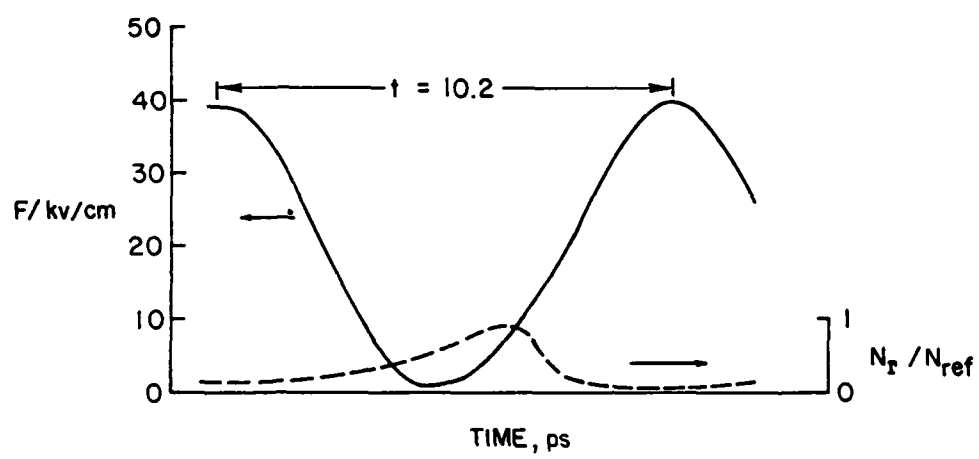


FIG. 20

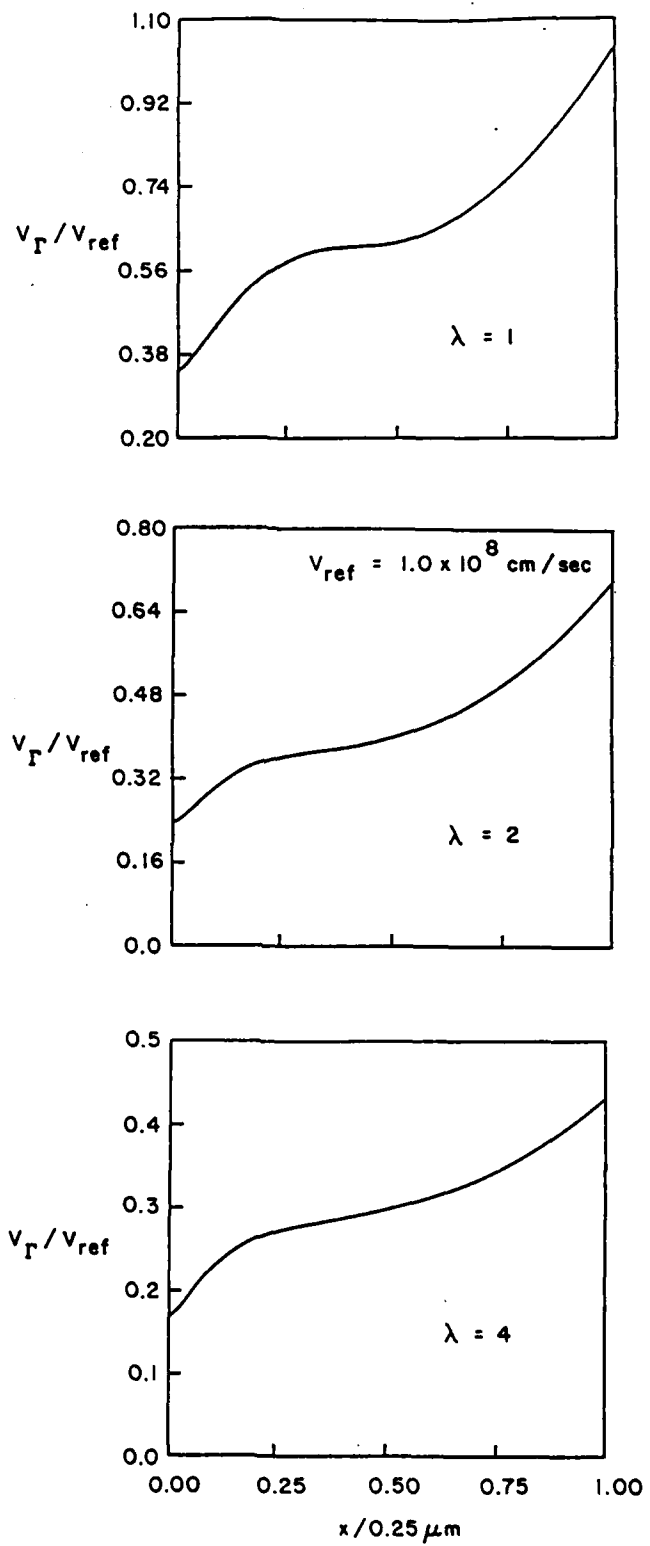
II 30 84 - 2  
920016

FIG. 21

920010 17 85-4

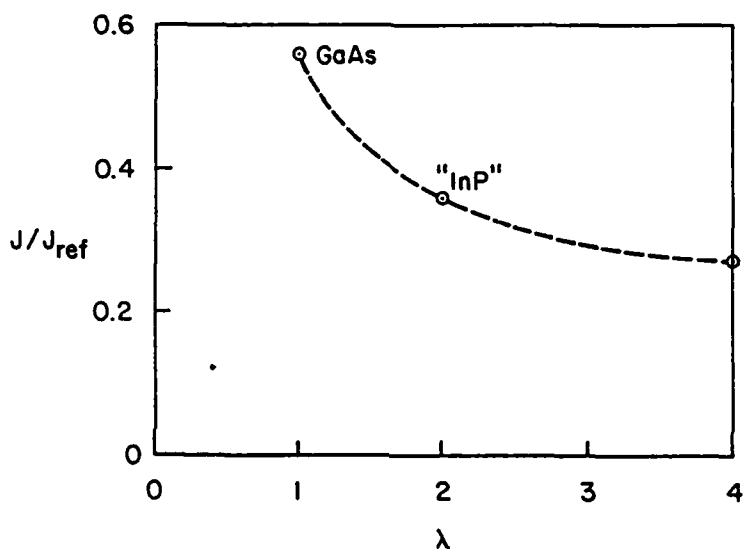


FIG. 22

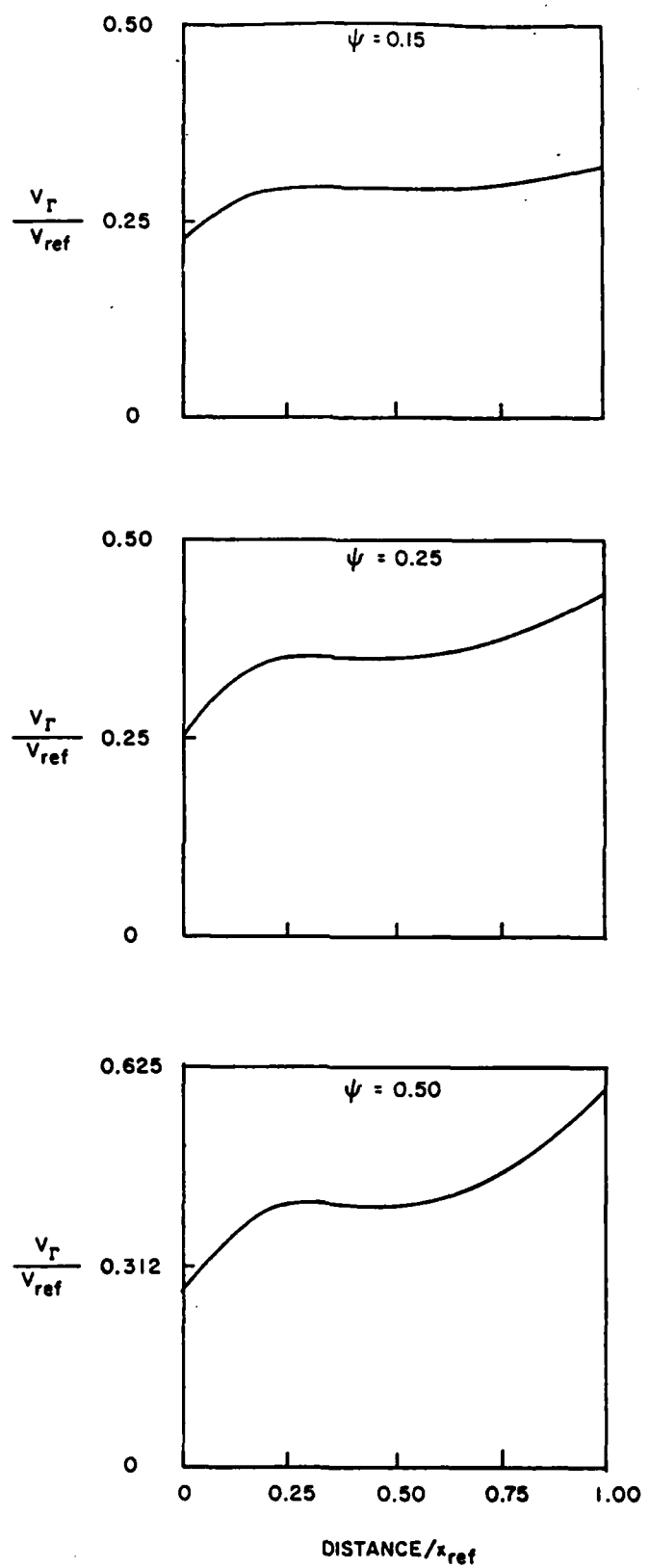


FIG. 23

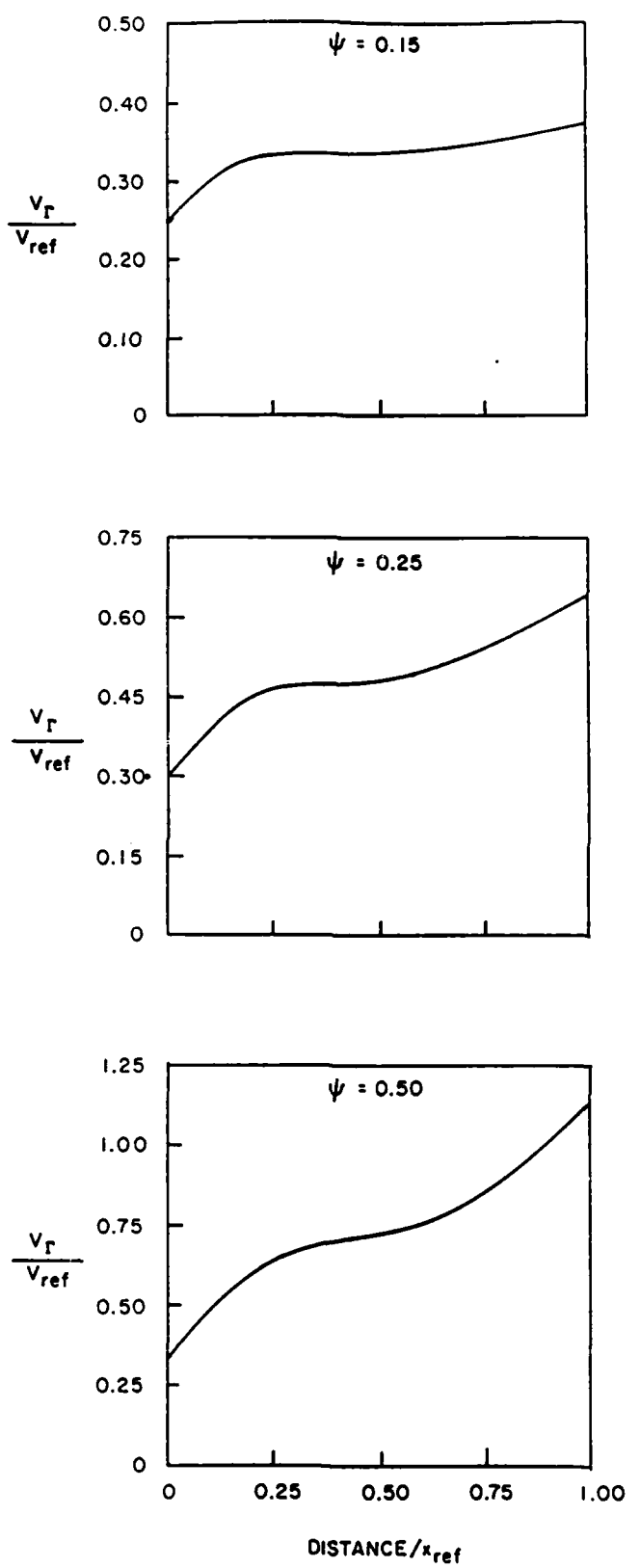


FIG. 24

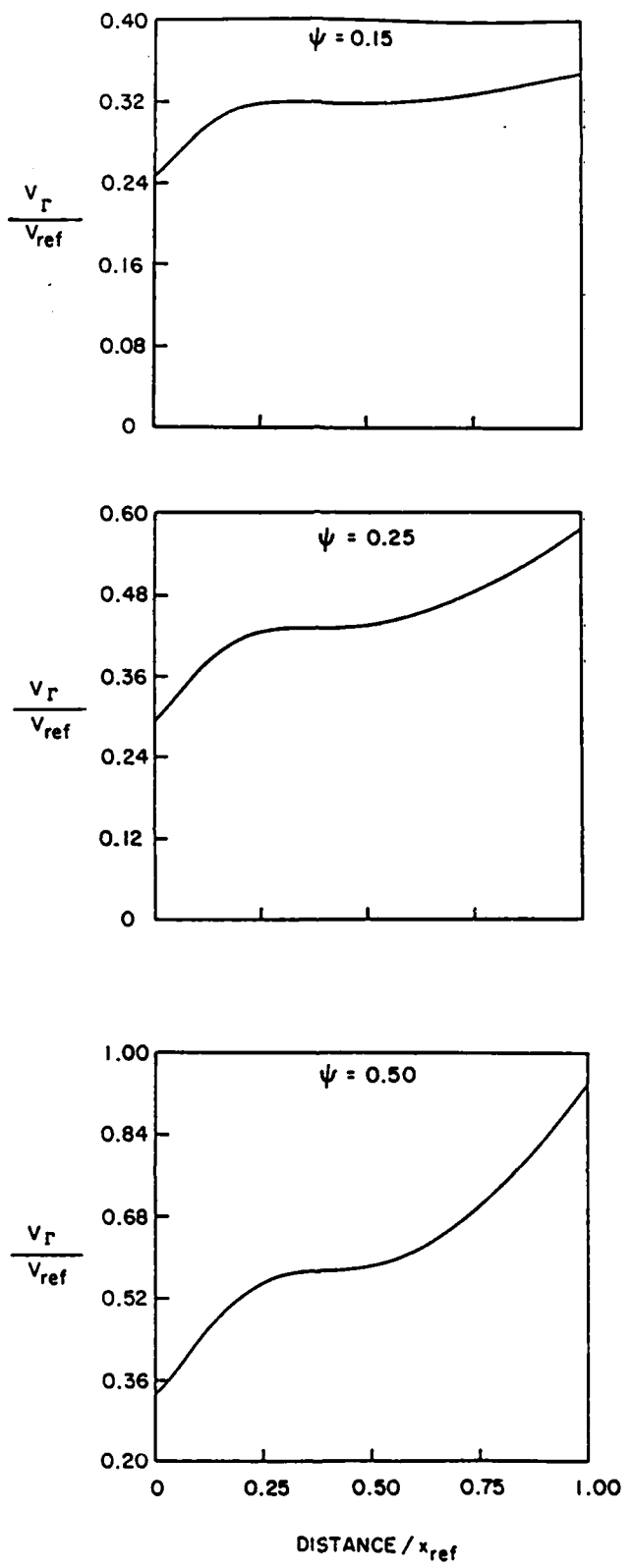


FIG. 25

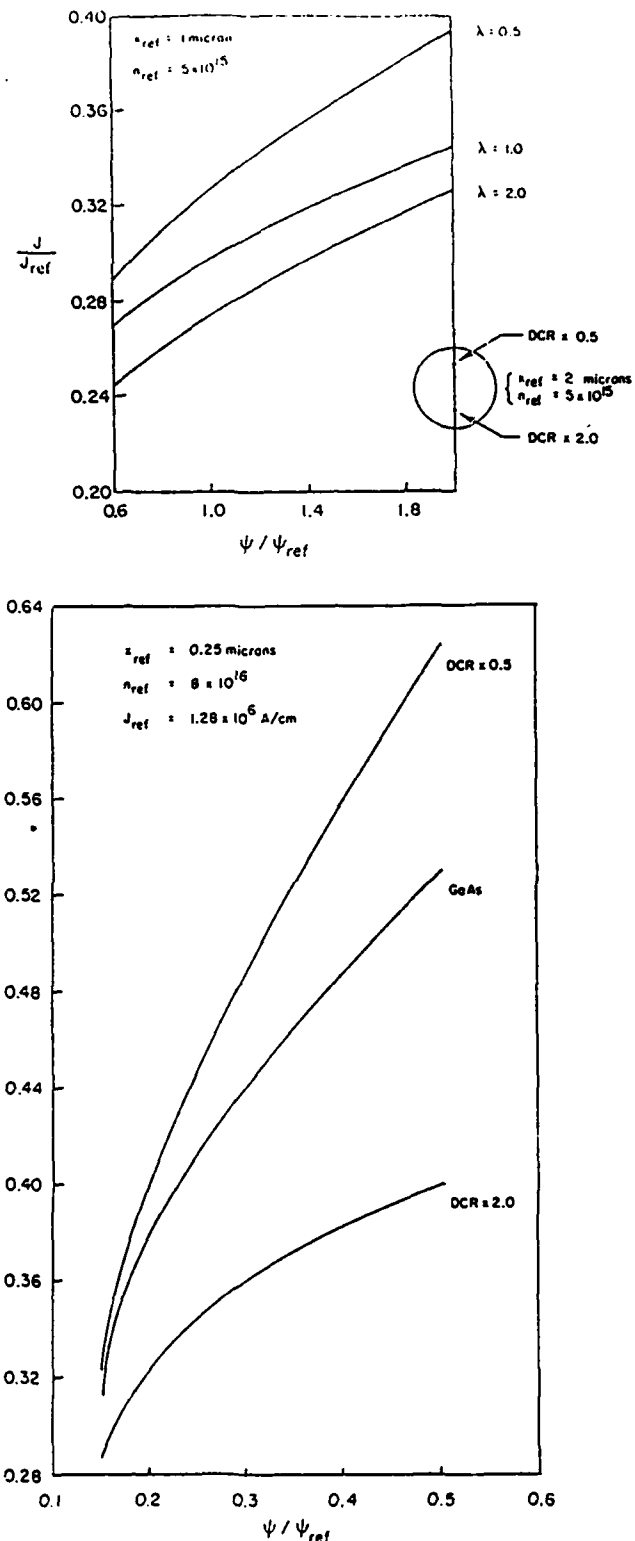


FIG. 26

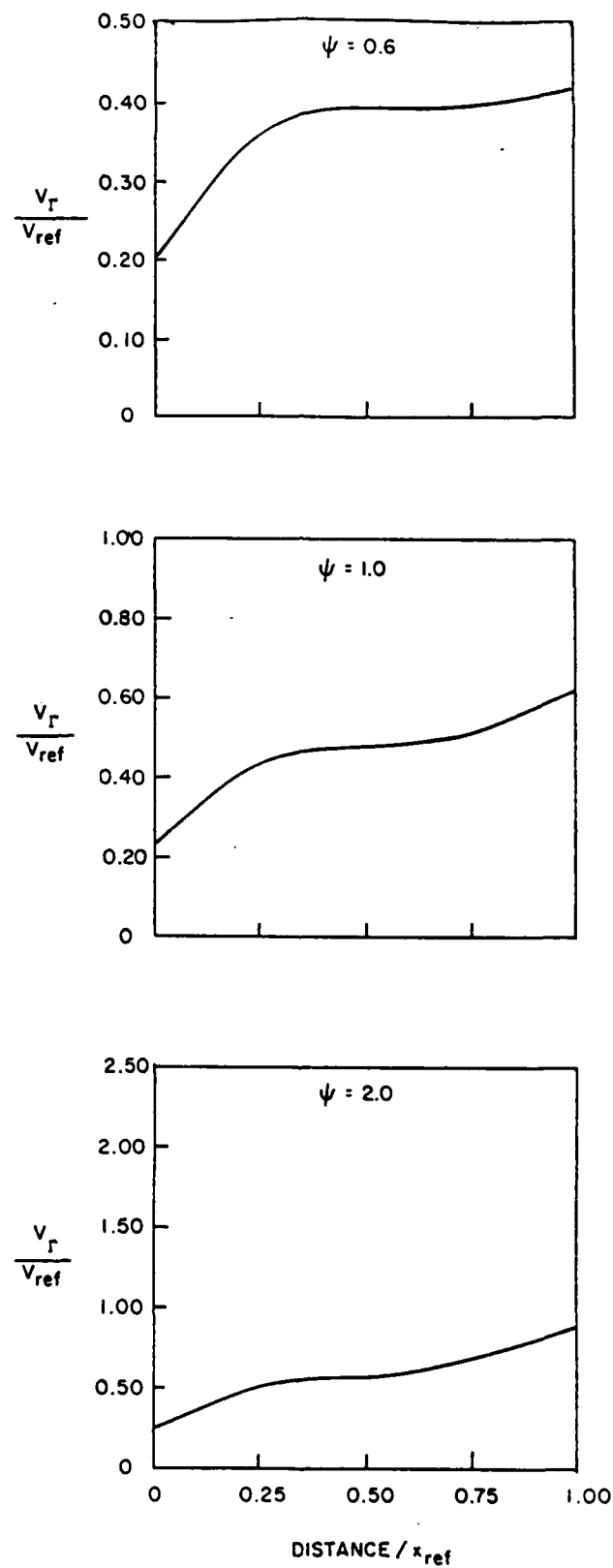


FIG. 27

modified 10/85 Redrawn 12-19-84 -1

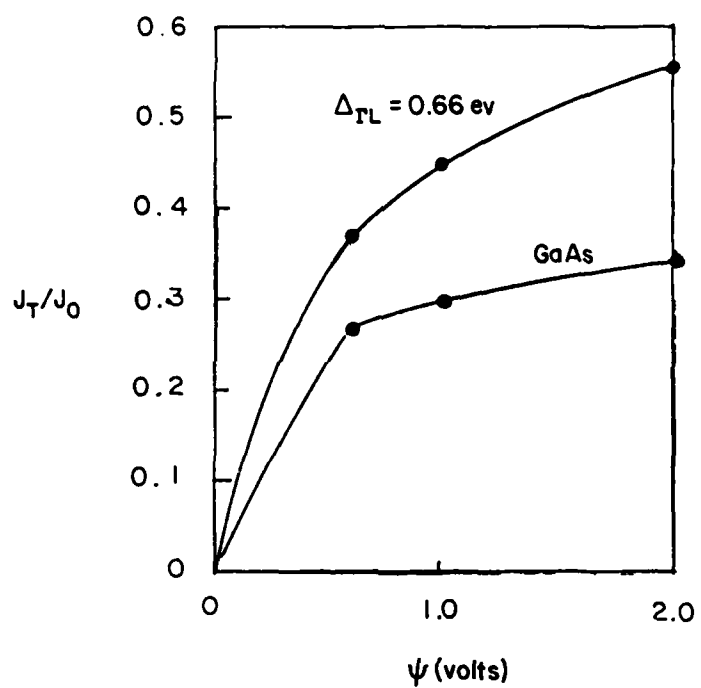


FIG. 28

920010 32084-1

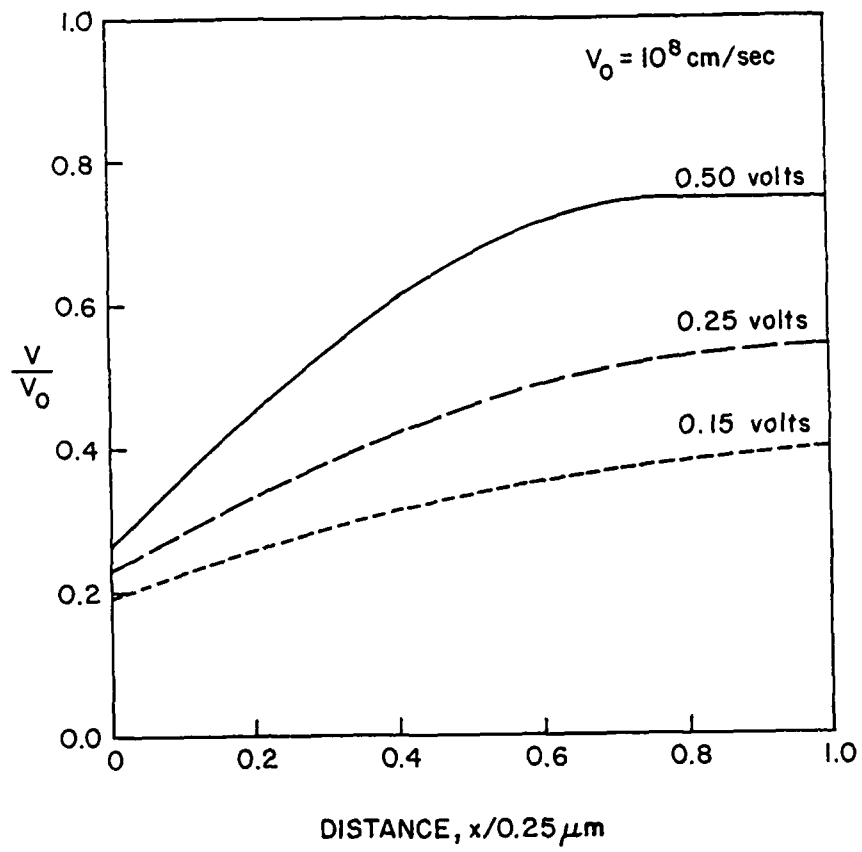


FIG. 29

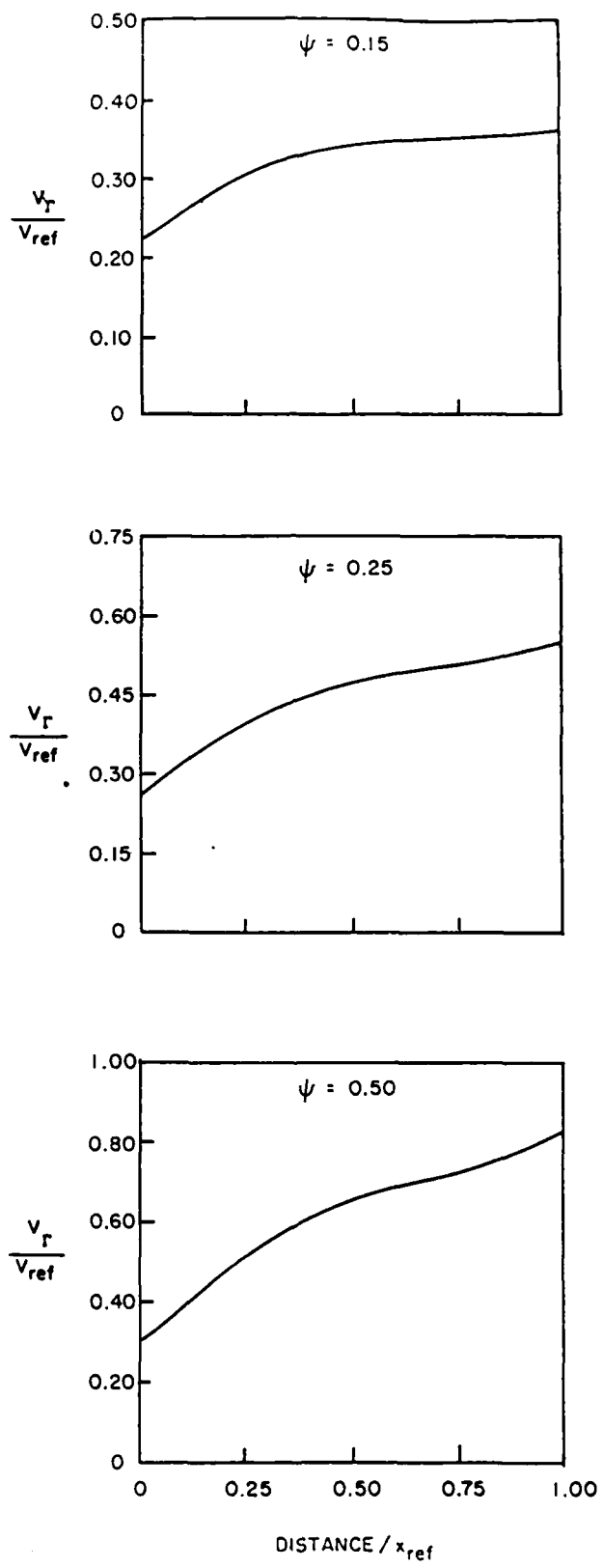
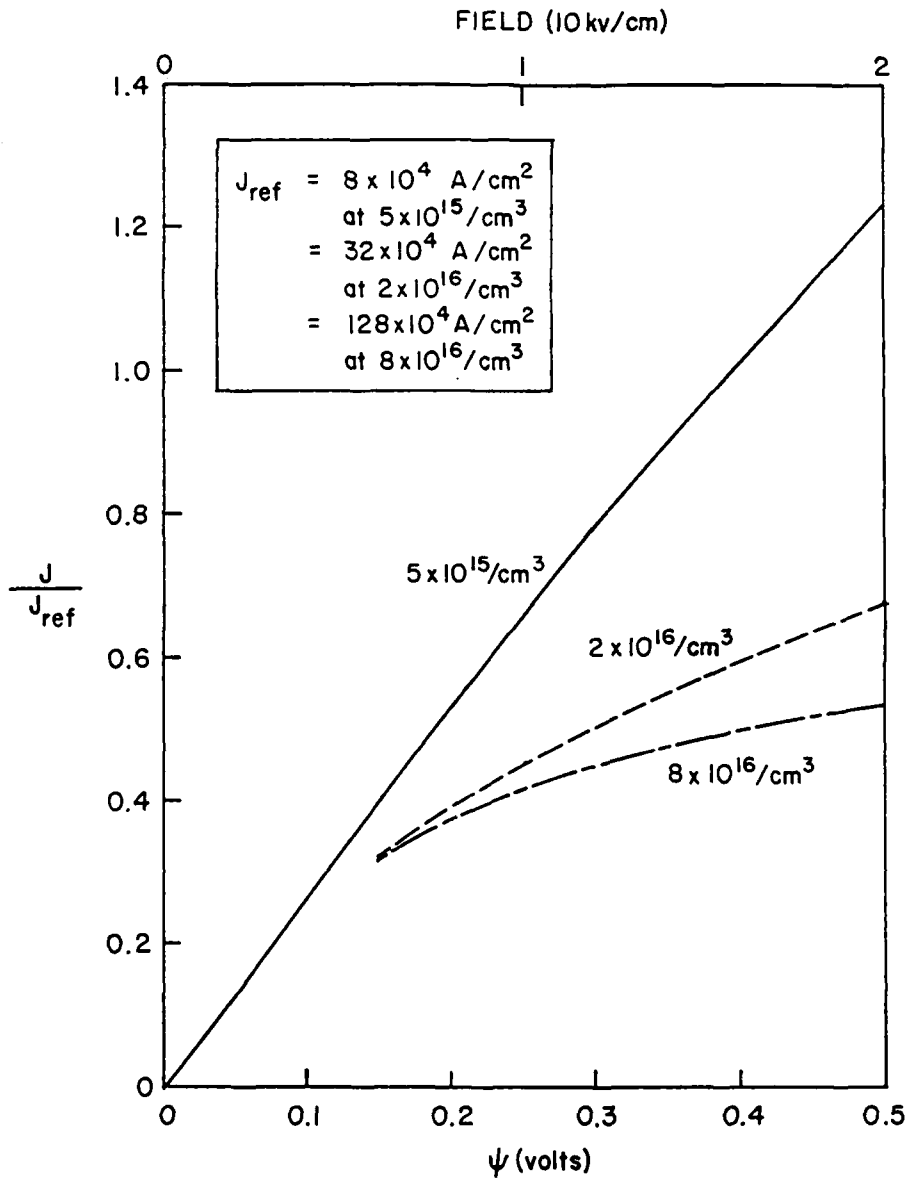


FIG. 30



920010 32084-2 386-2

FIG. 31

920010 1985-1

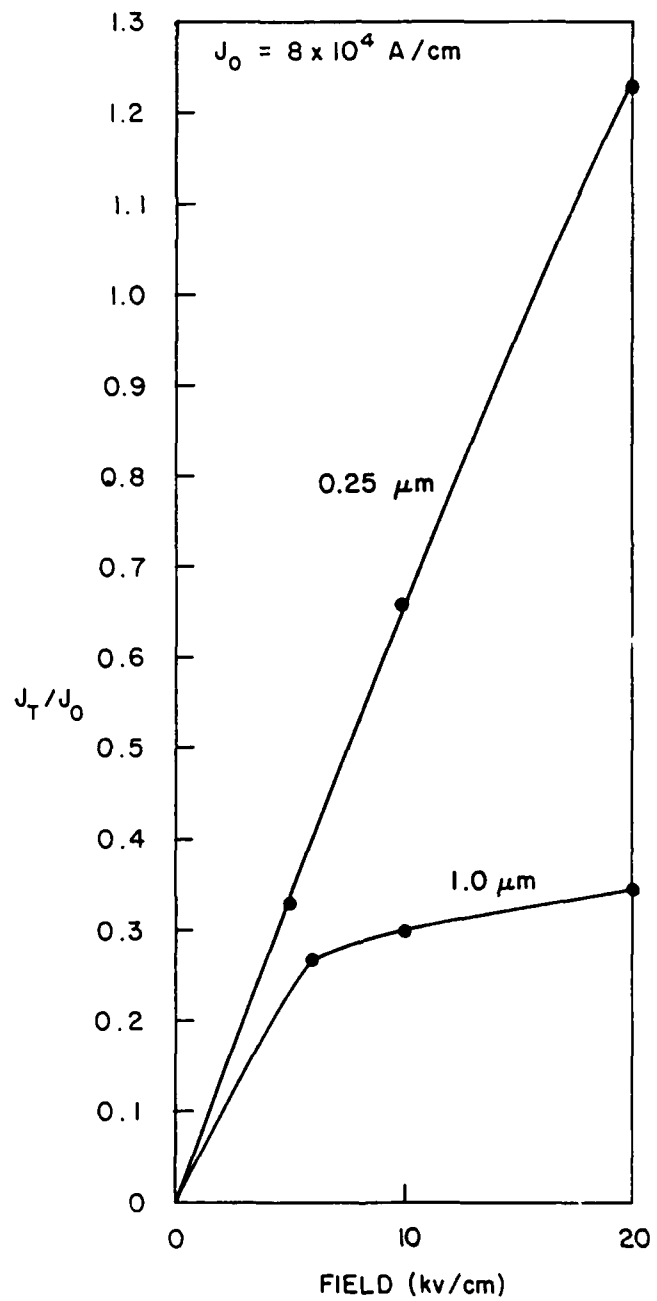


FIG. 32

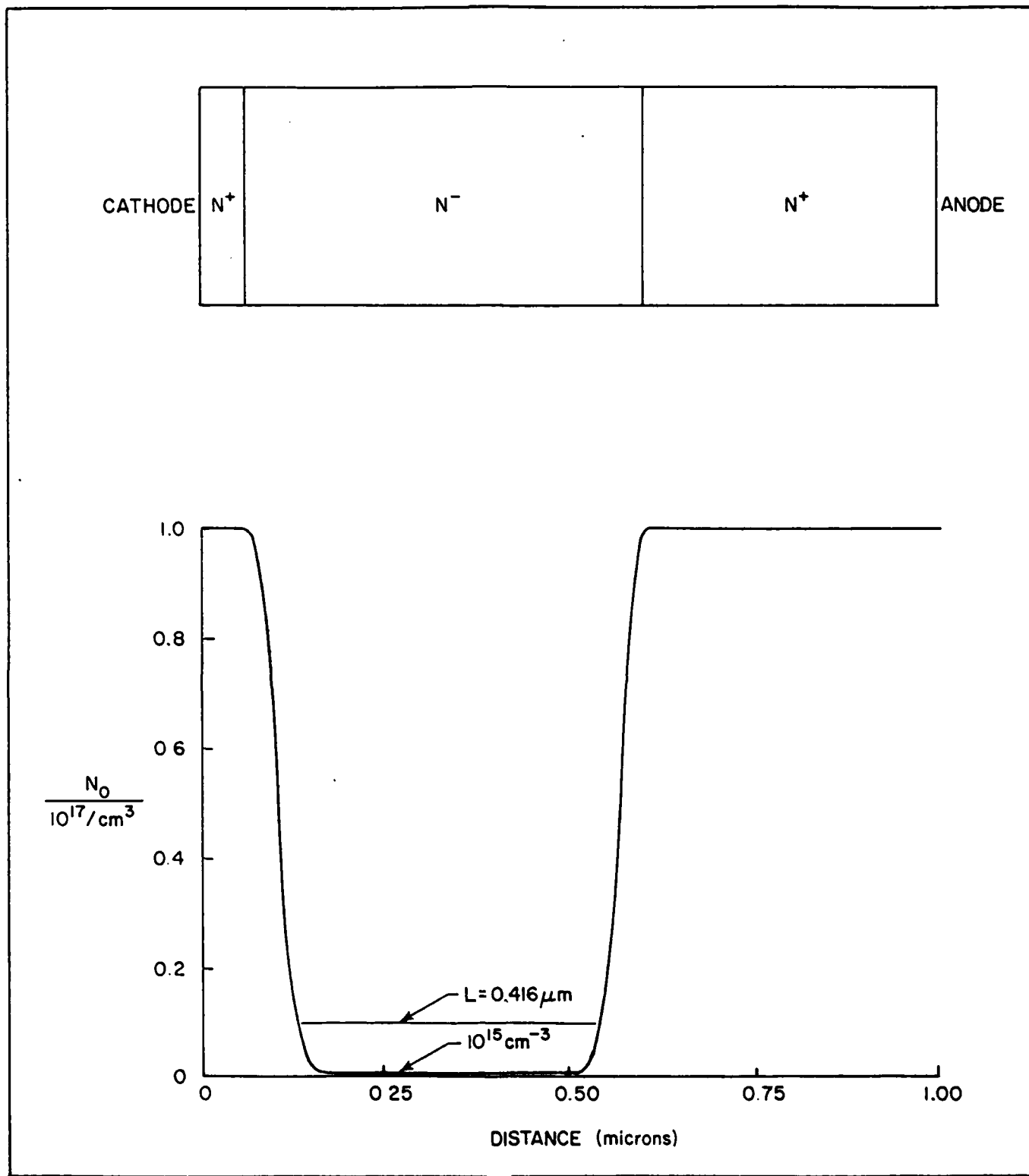


FIG. 33

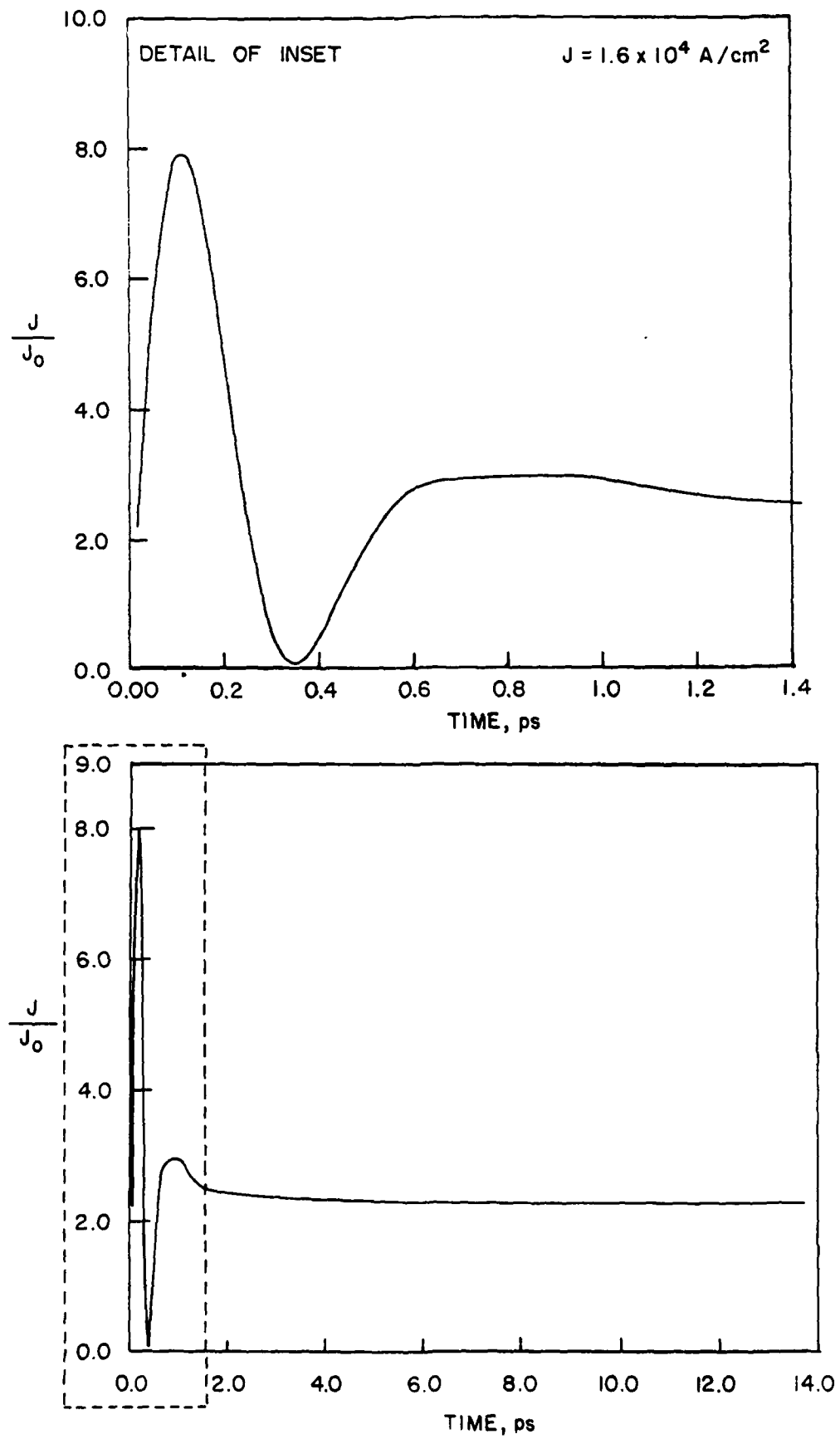


FIG. 34

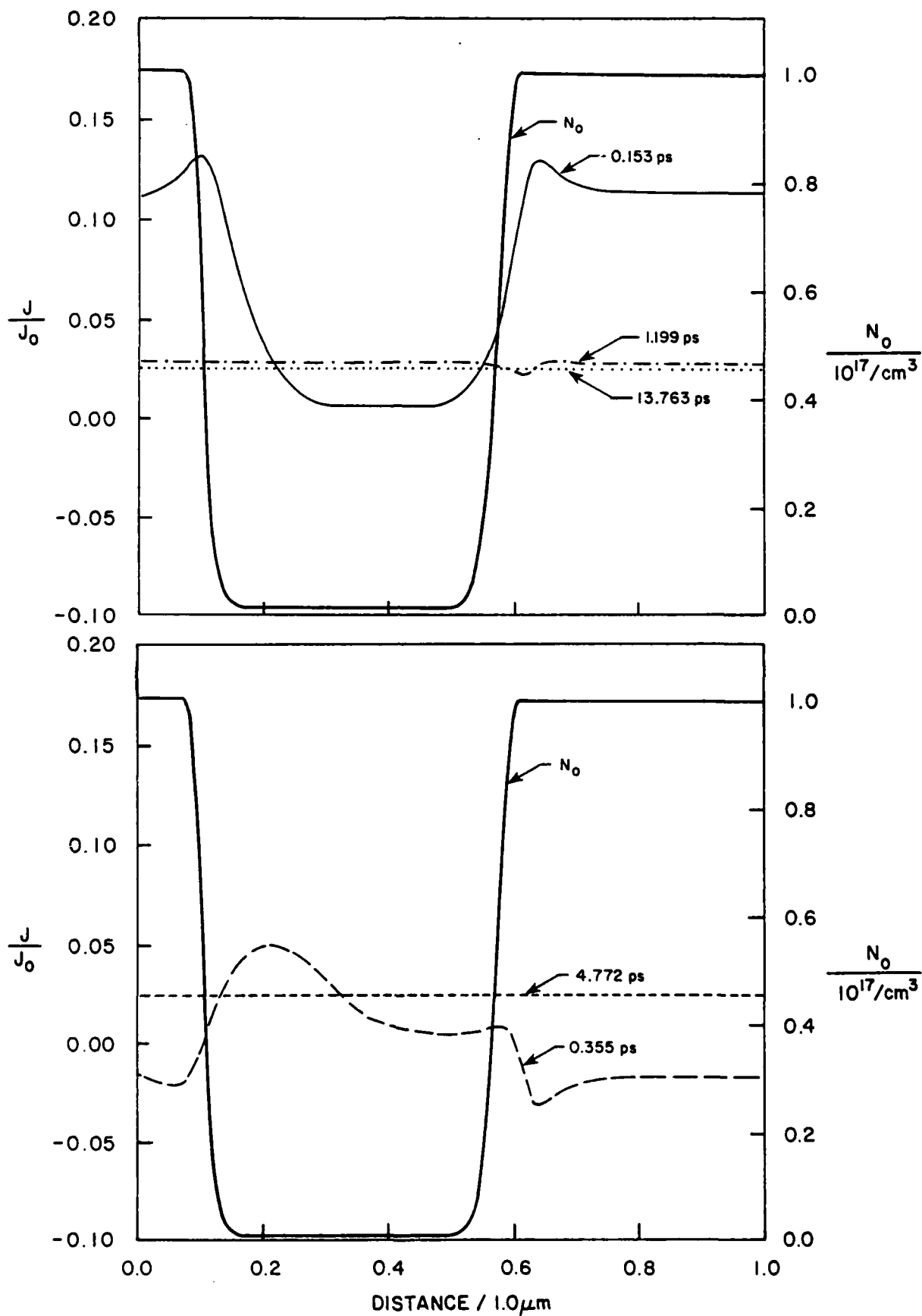


FIG. 35

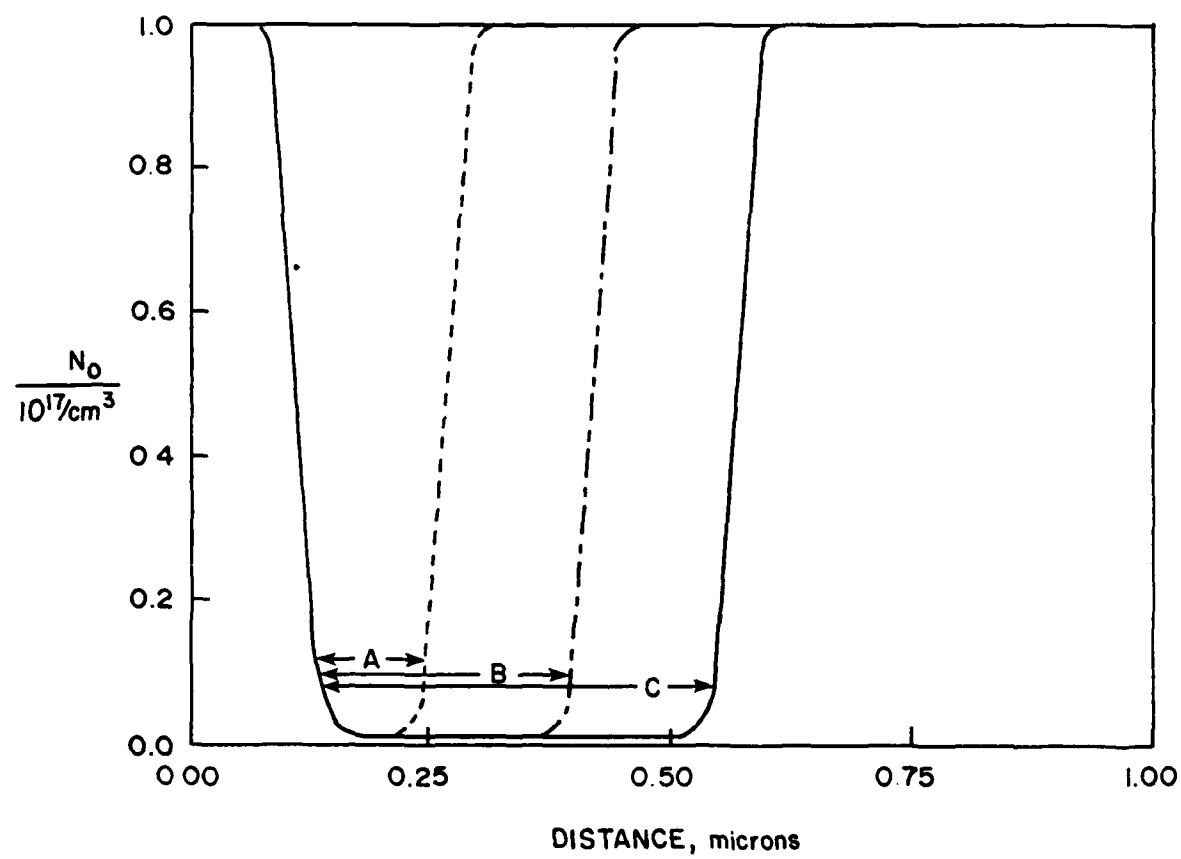


FIG. 36

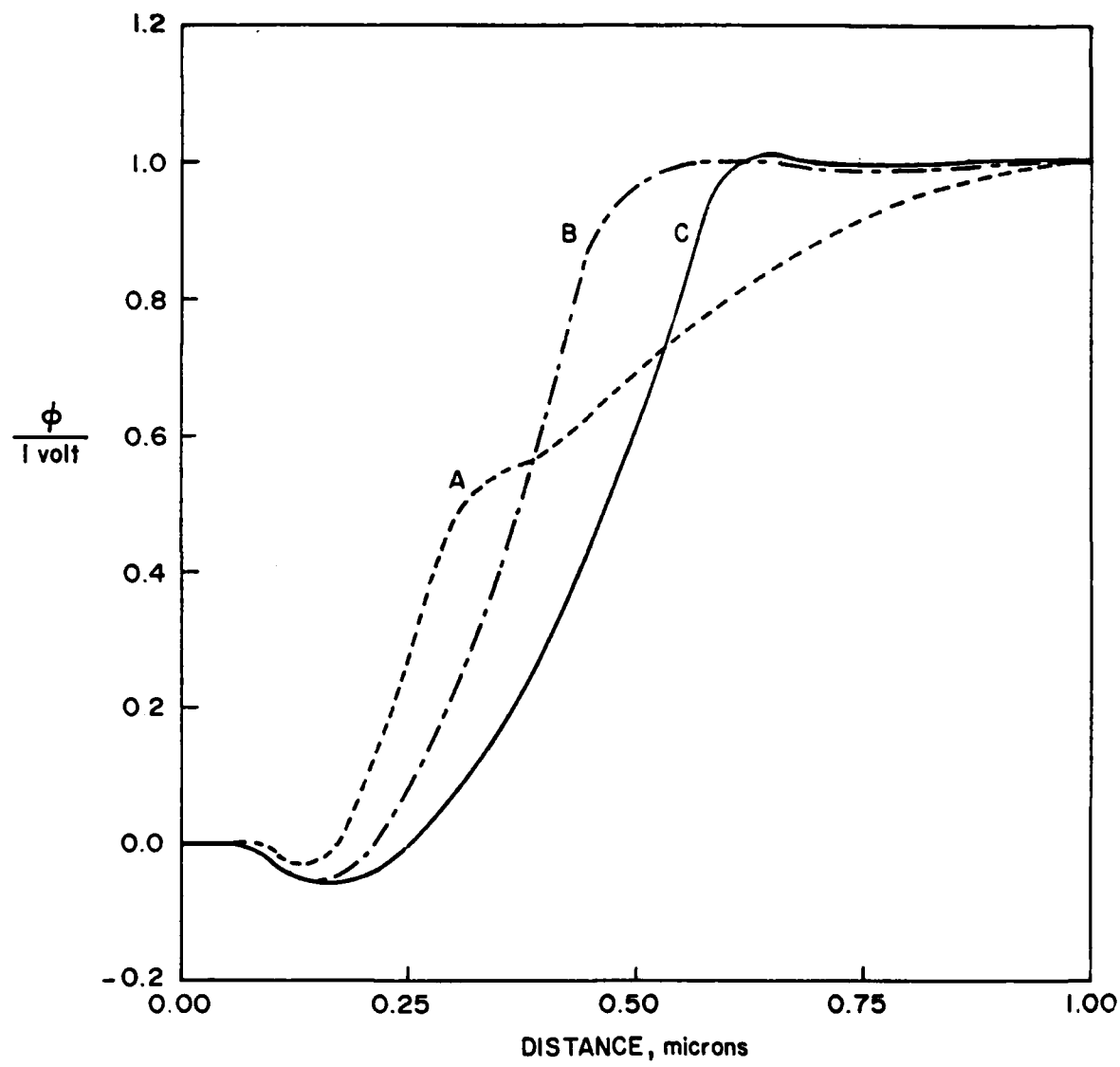
214.84-2  
920017

FIG. 37

920017 2-14-64-3

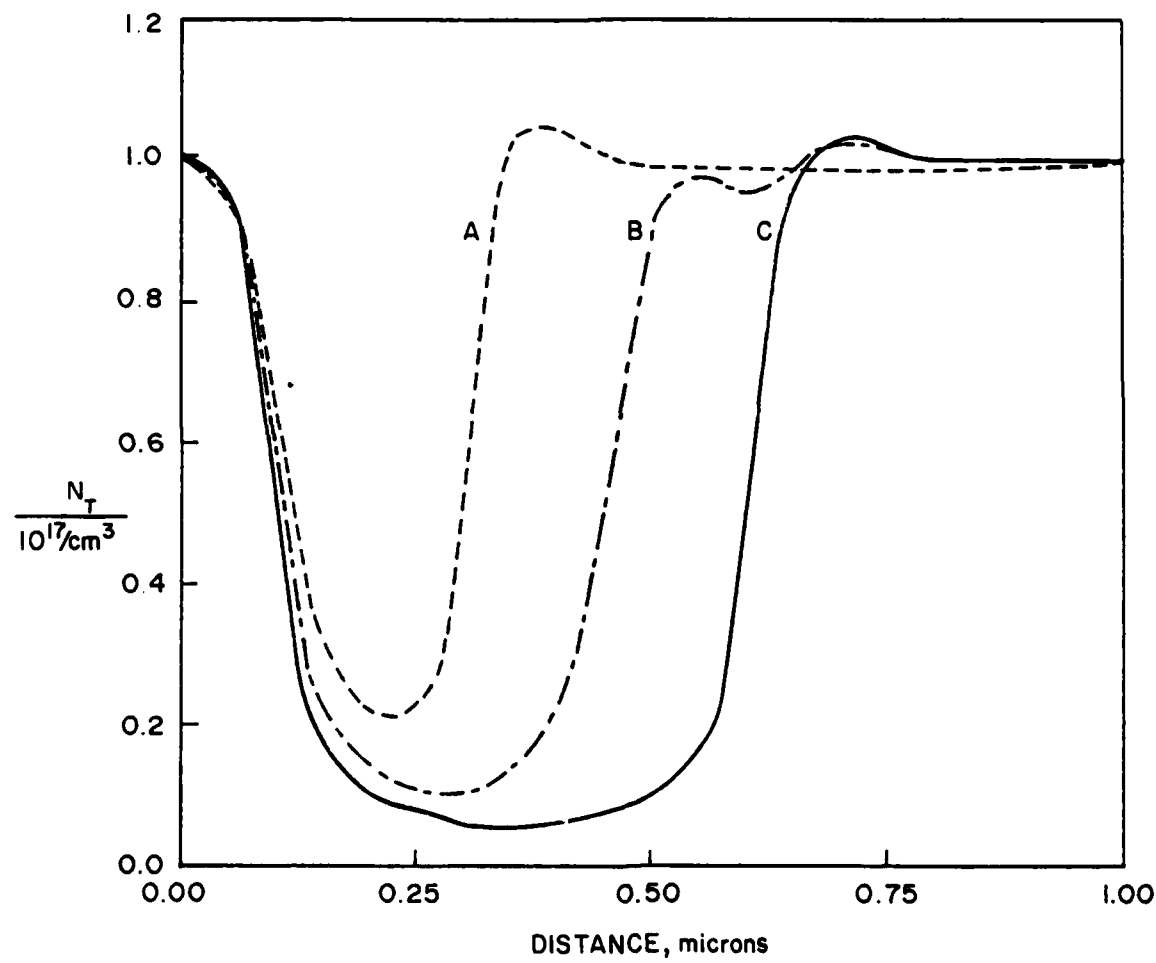


FIG. 38

2-14-84-4  
920017

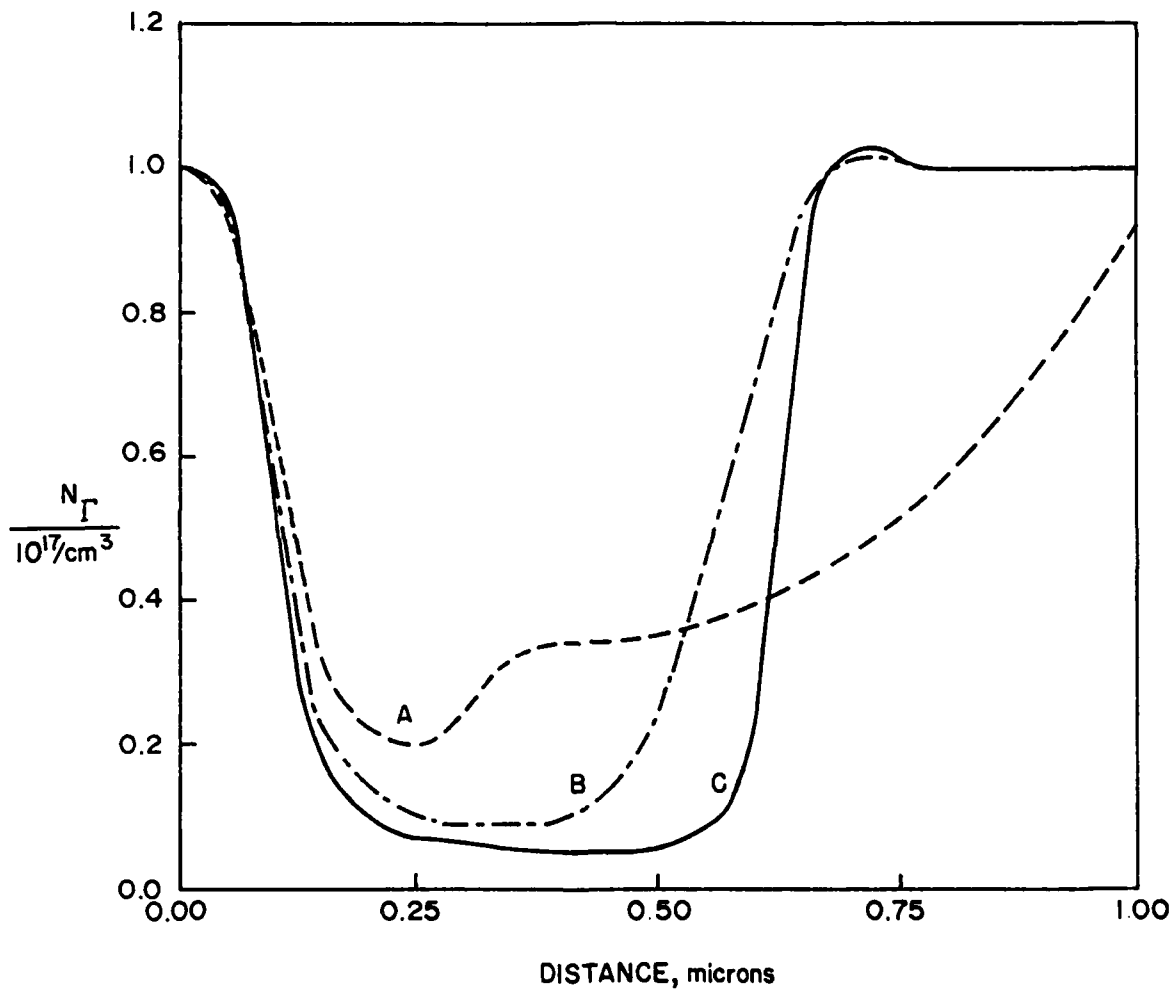


FIG. 39

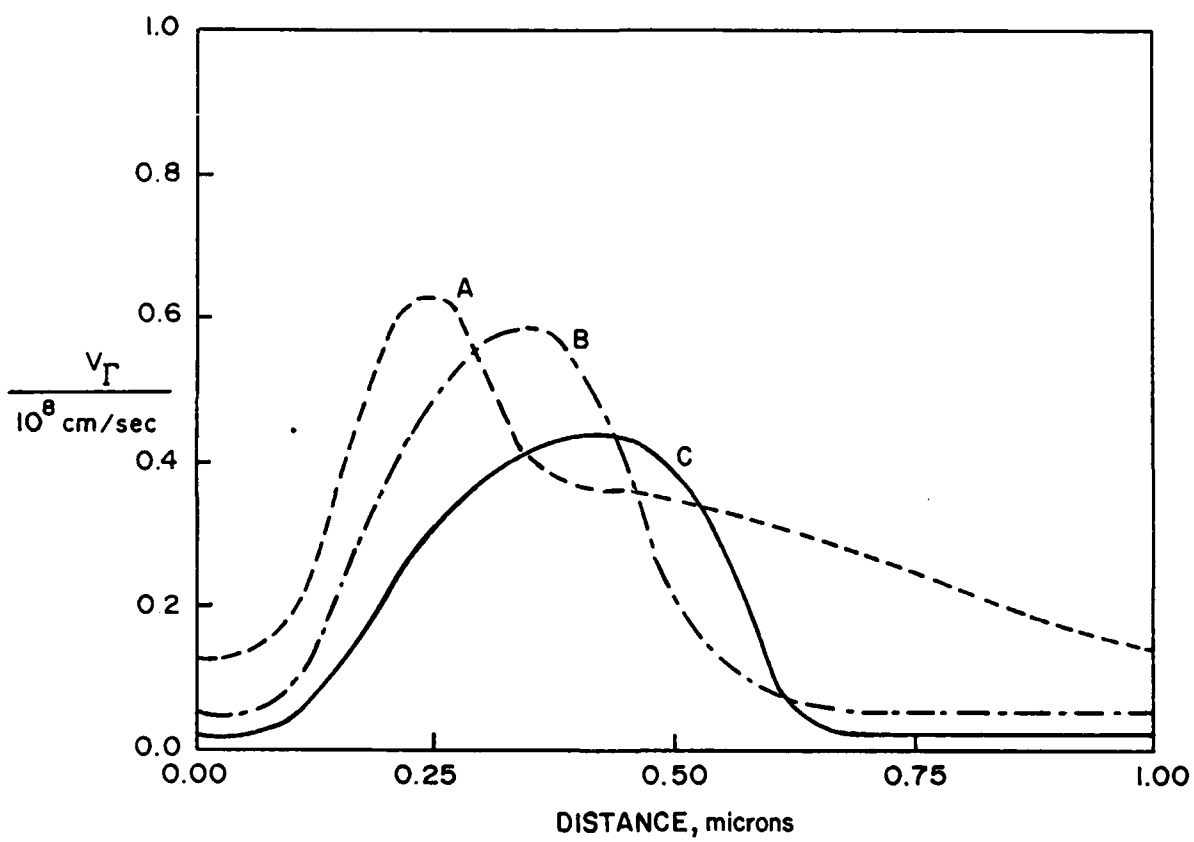


FIG. 40

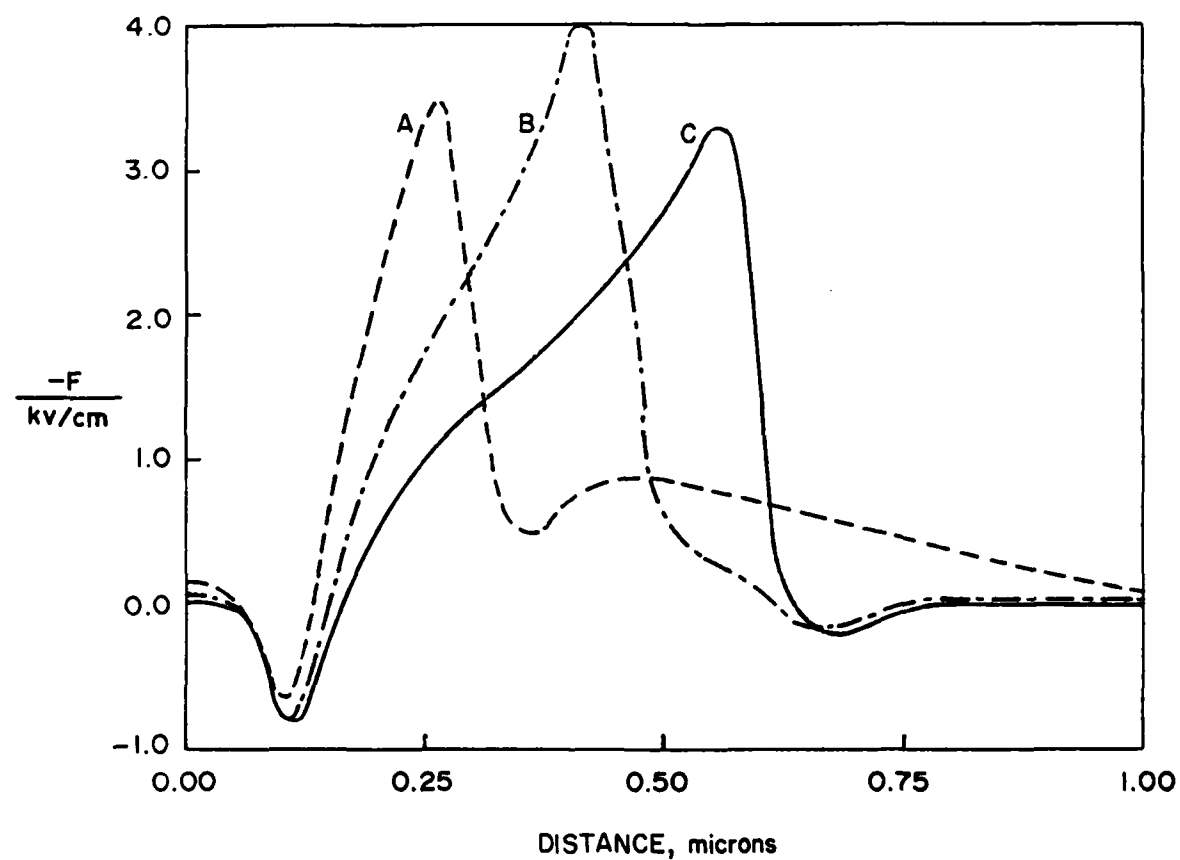


FIG. 41

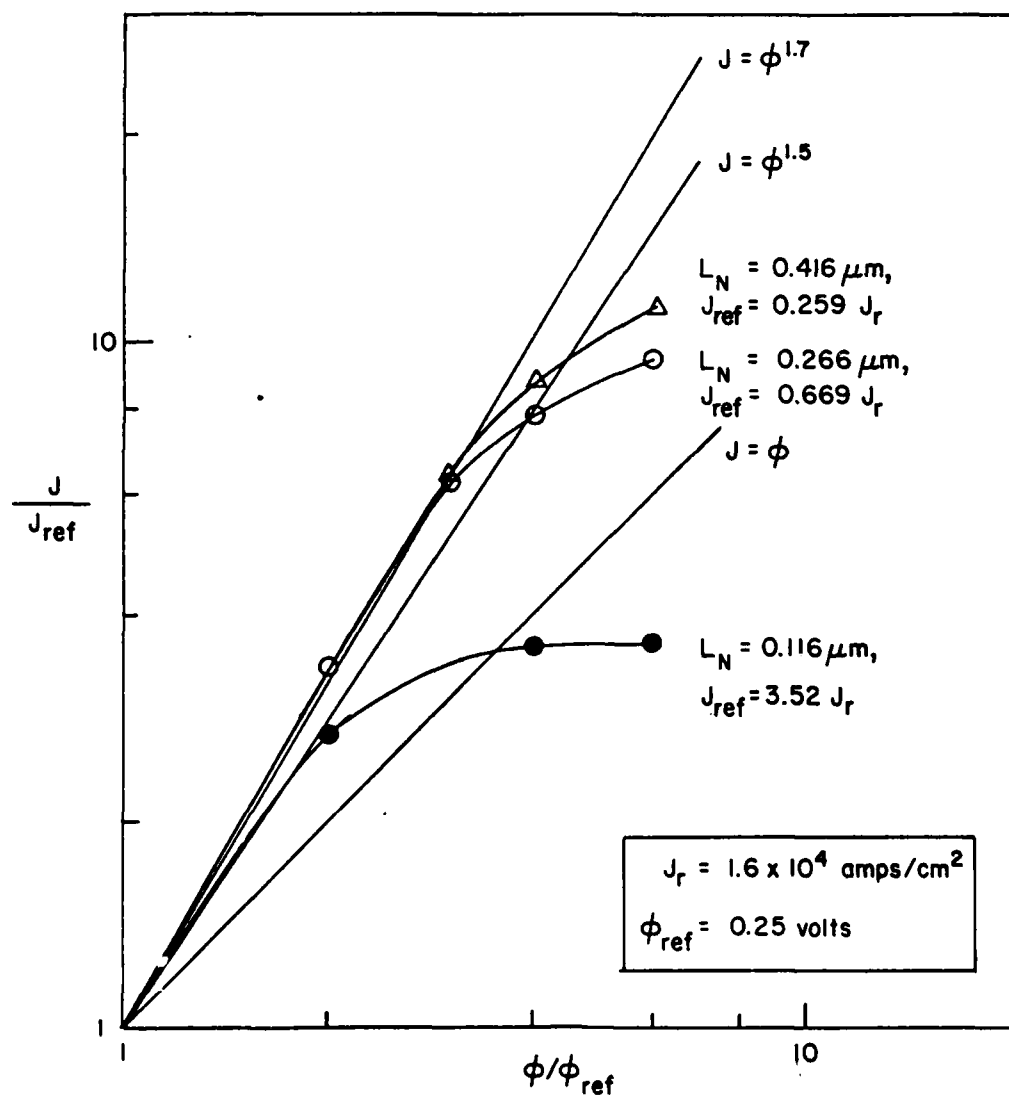


FIG. 42

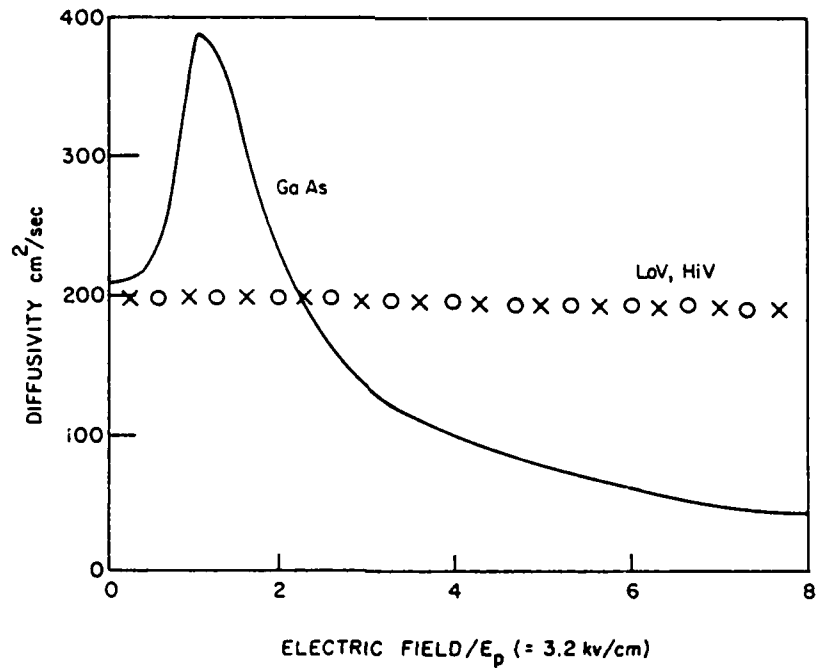
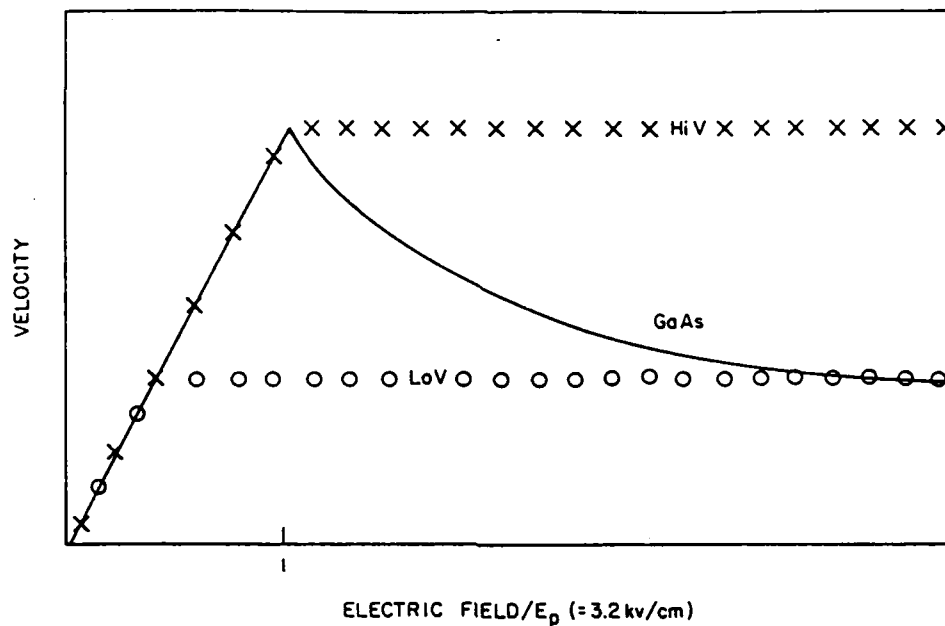


FIG. 43

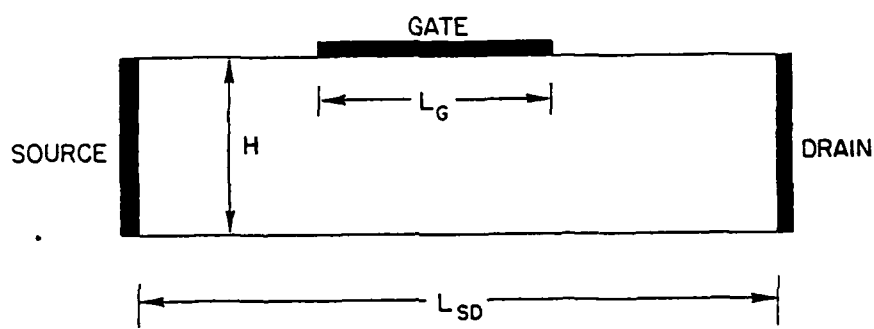
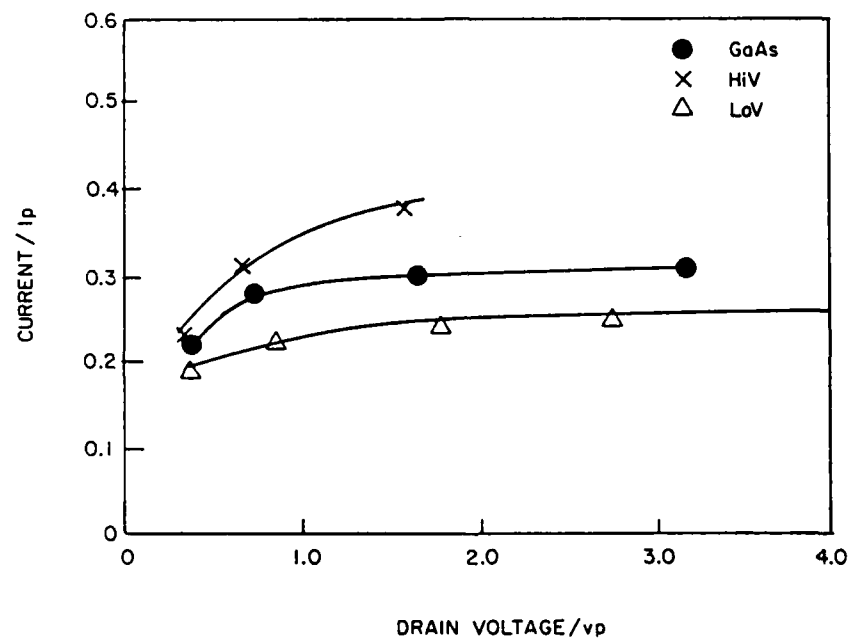
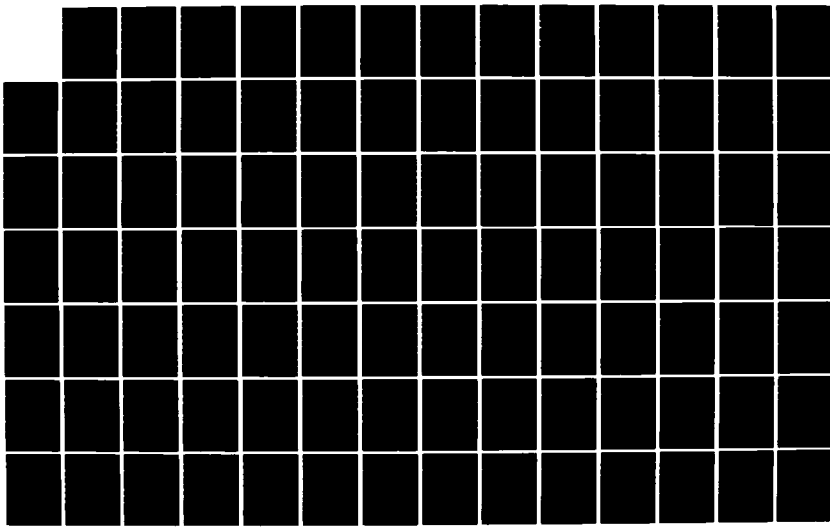
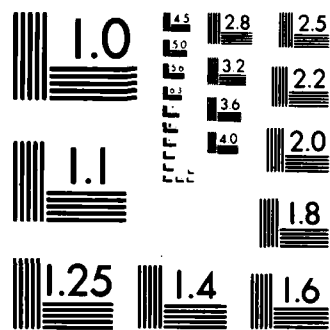


FIG. 44



✓ AD-A150 020 SEMICONDUCTOR MATERIALS FOR HIGH FREQUENCY SOLID STATE 2/4  
SOURCES(U) SCIENTIFIC RESEARCH ASSOCIATES INC  
GLASTONBURY CT H L GRUBIN ET AL 18 JAN 85  
UNCLASSIFIED SRA-R85-920016-F N00014-82-C-0697 F/G 28/12 NL





MICROCOPY RESOLUTION TEST CHART  
NATIONAL BUREAU OF STANDARDS 1963 A

FIG. 45

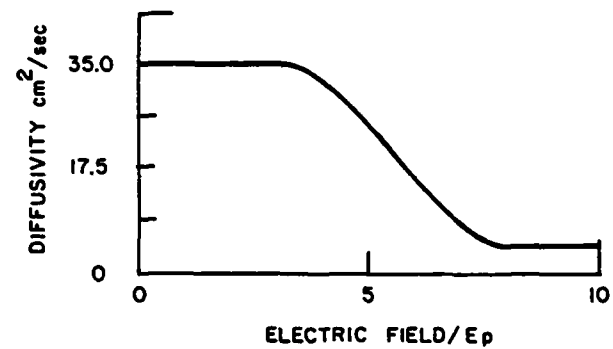
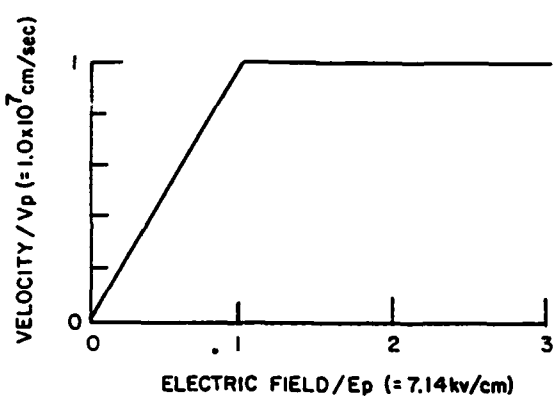


FIG. 46

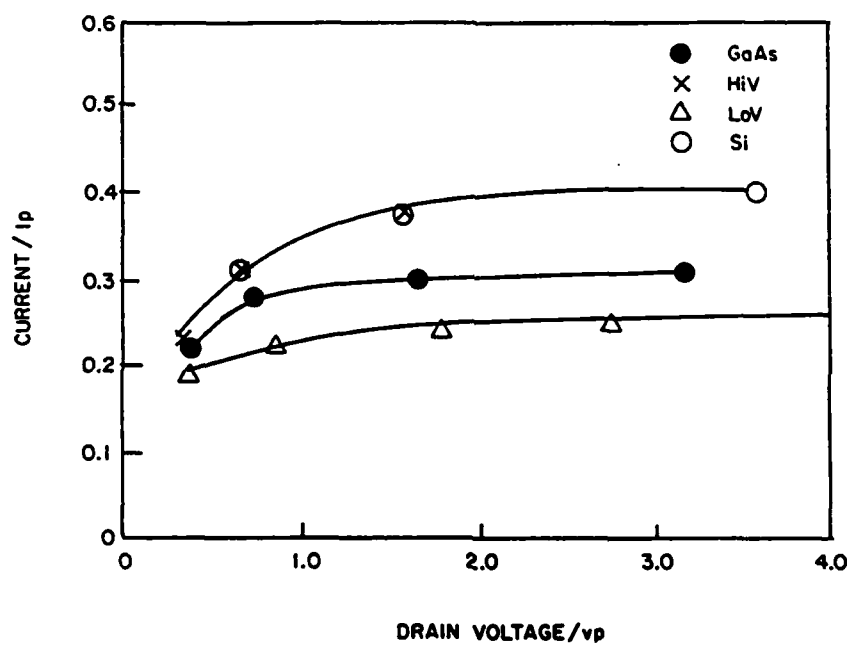


FIG. 47

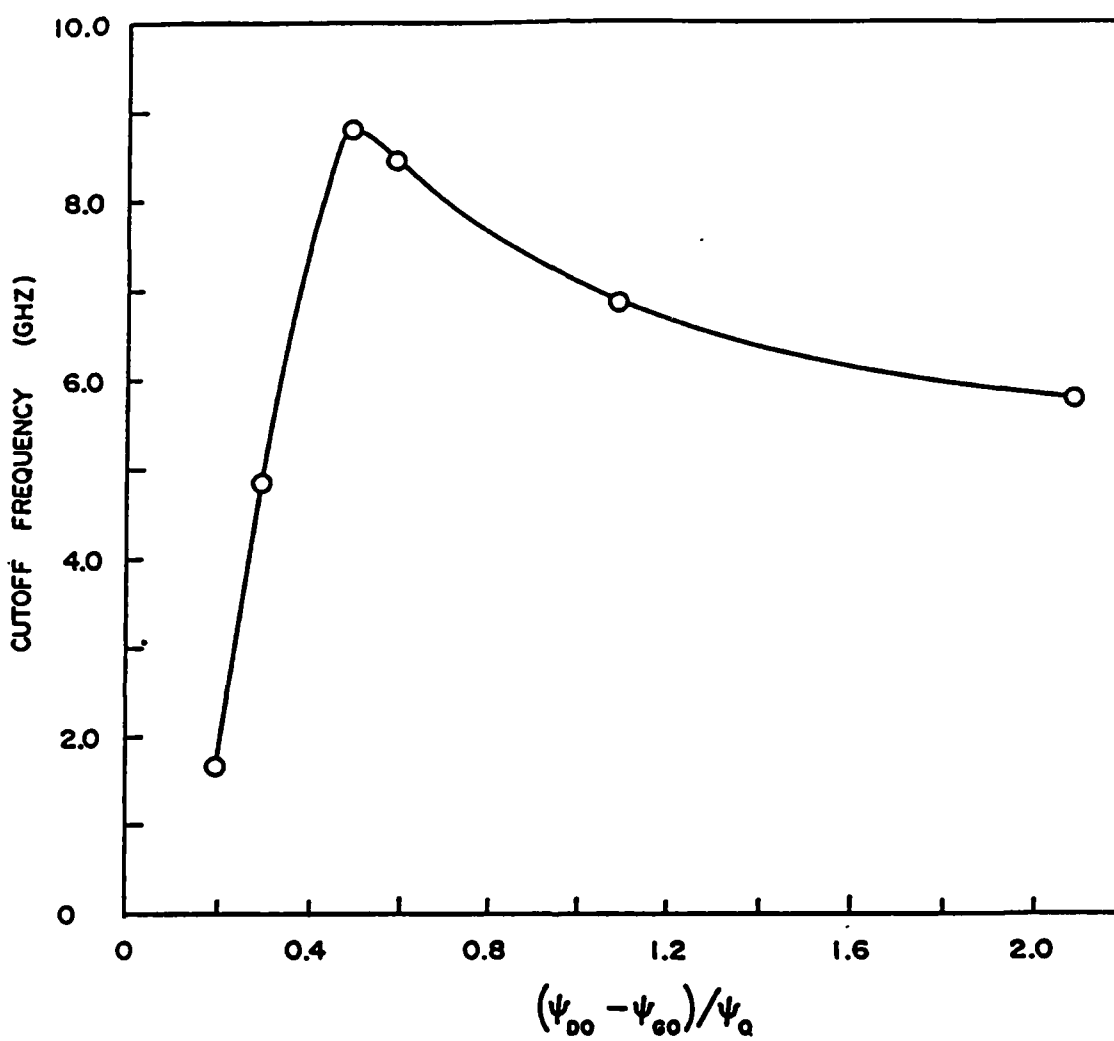
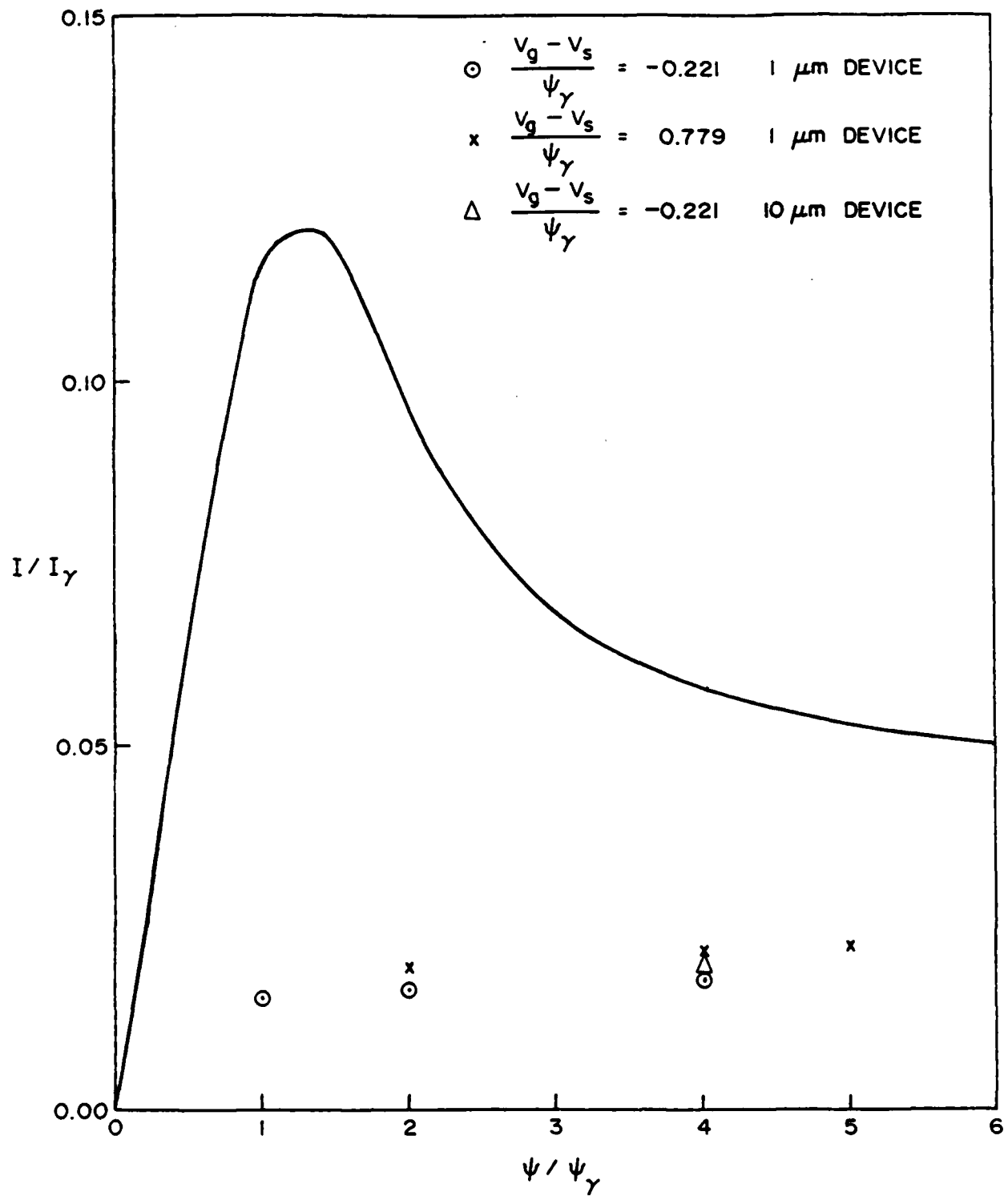


FIG. 48



PLOT OF  $\frac{V_d - V_s}{\psi_\gamma}$  VS.  $\frac{I_d}{I_\gamma}$

FIG. 49

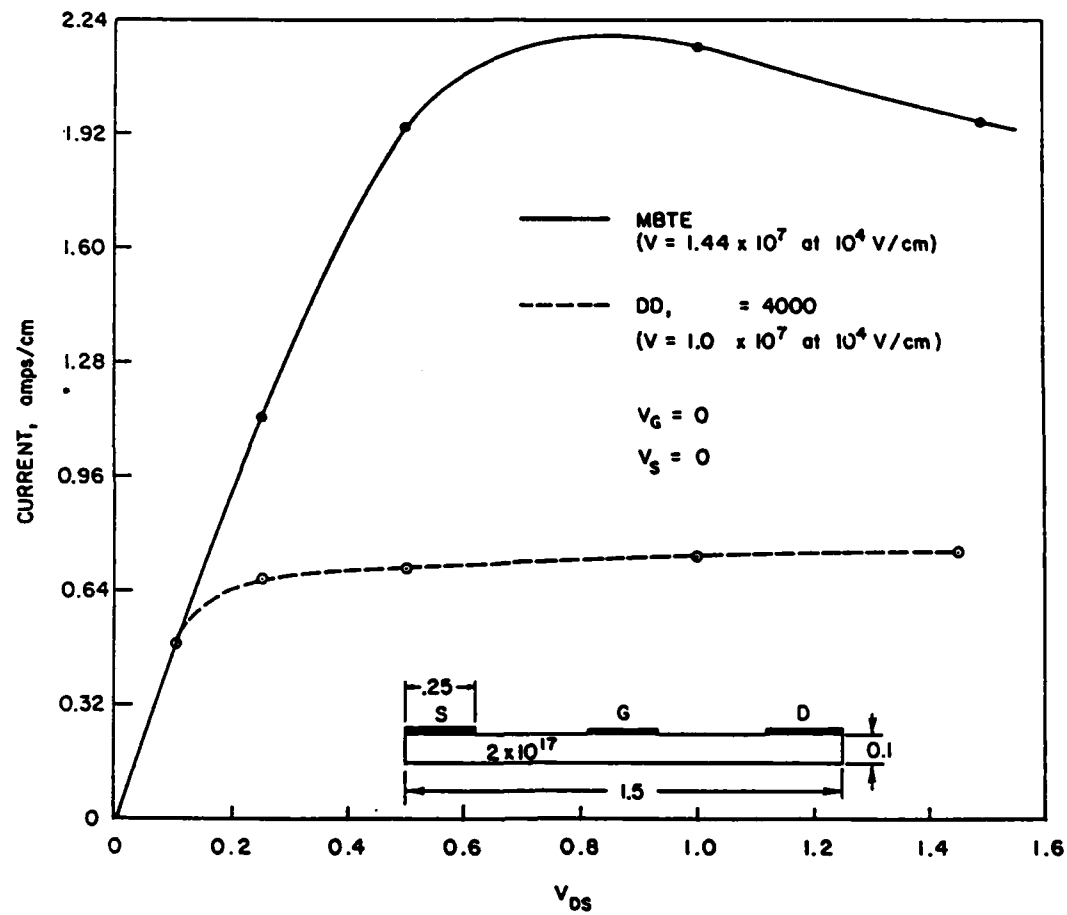


FIG. 50

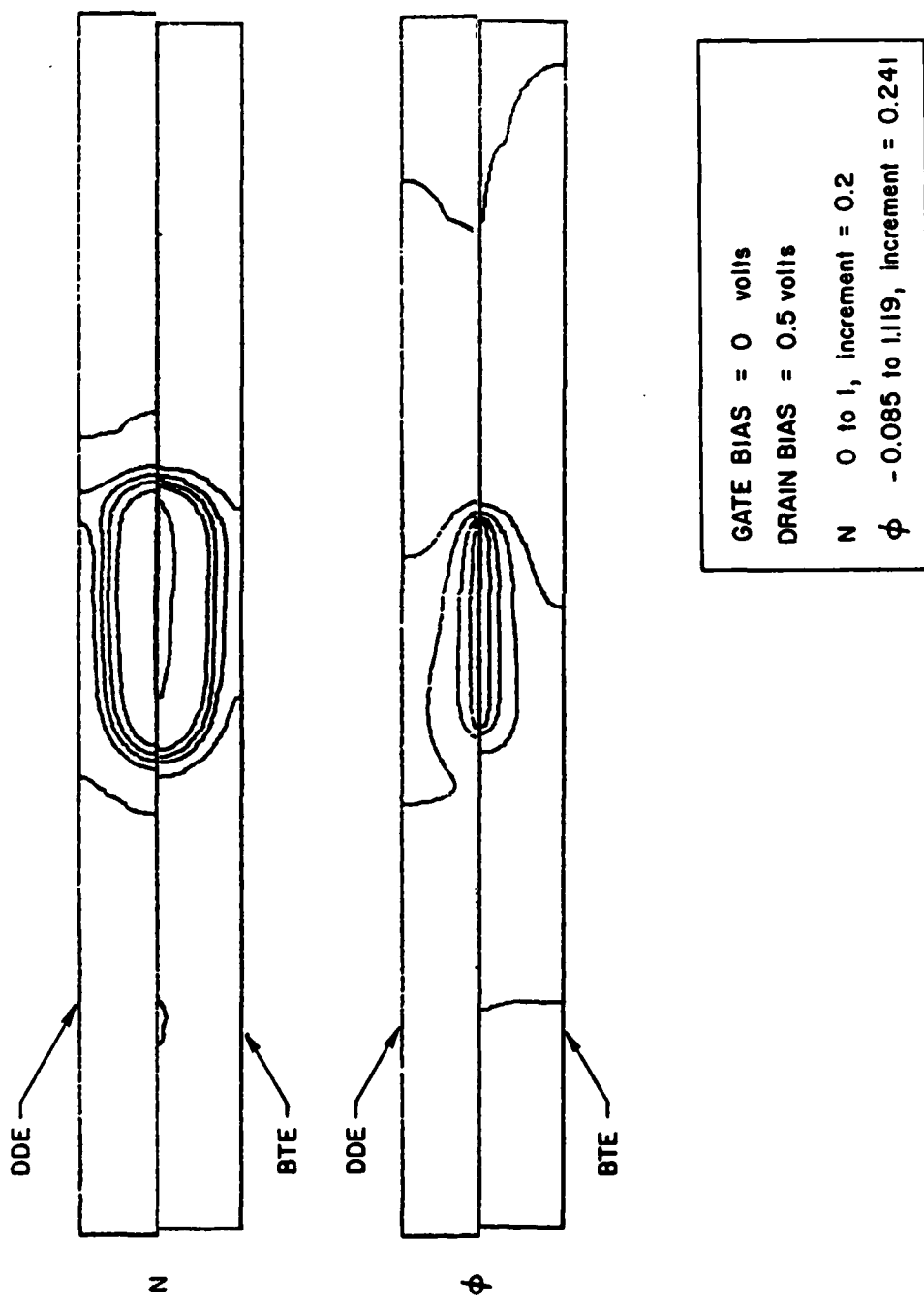
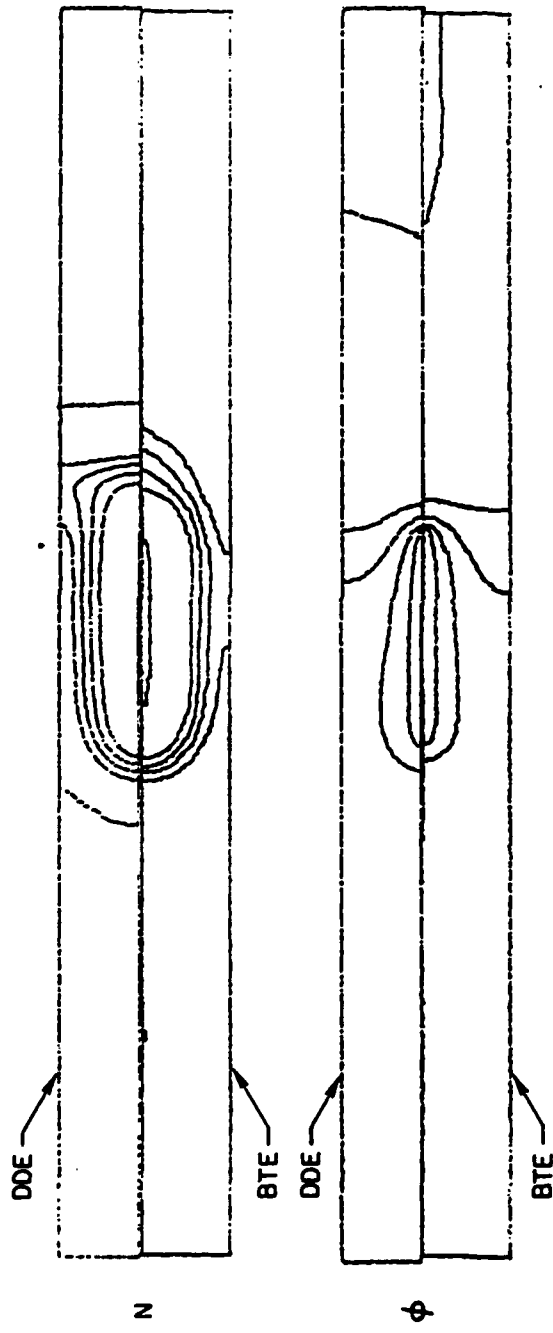


FIG. 51

920010 1780-3



GATE BIAS = 0 volts  
DRAIN BIAS = 1 volt  
N 0 to 1, increment = 0.2  
 $\phi$  - 0.085 to 1.619, increment = 0.341

FIG. 52

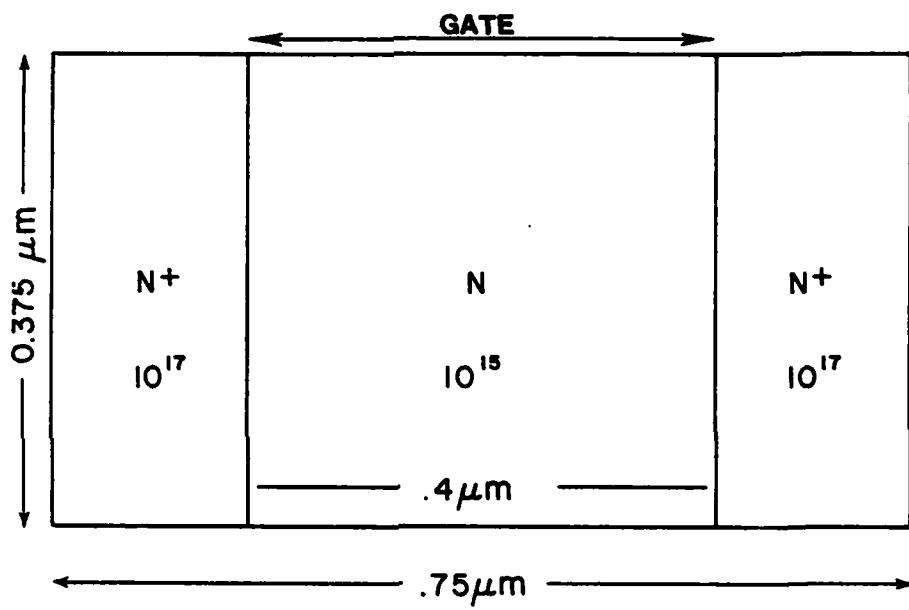


FIG. 53

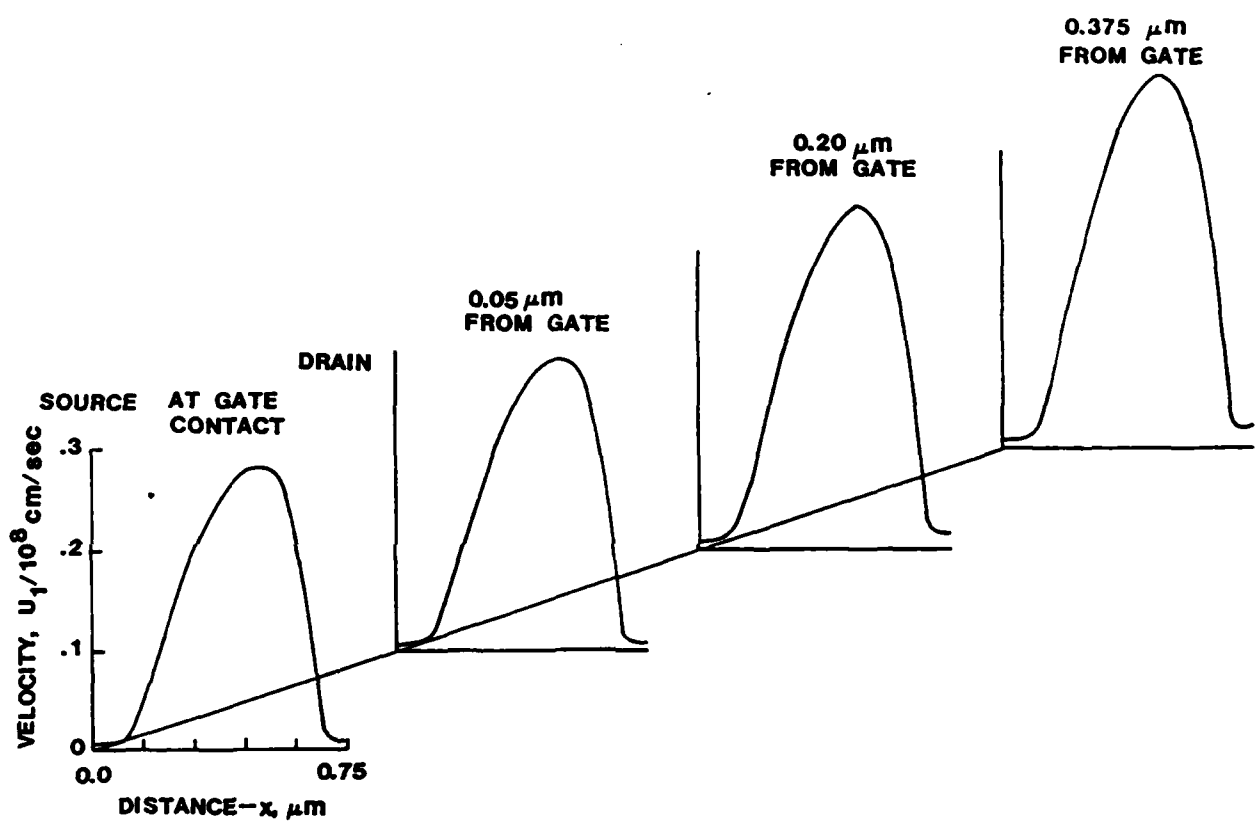


FIG. 54

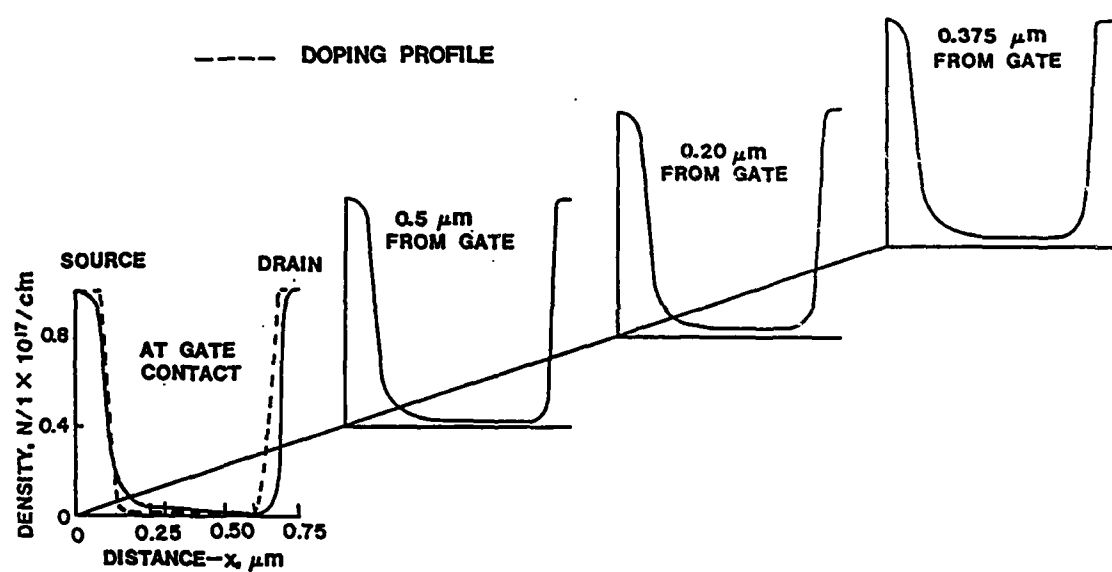


FIG. 55

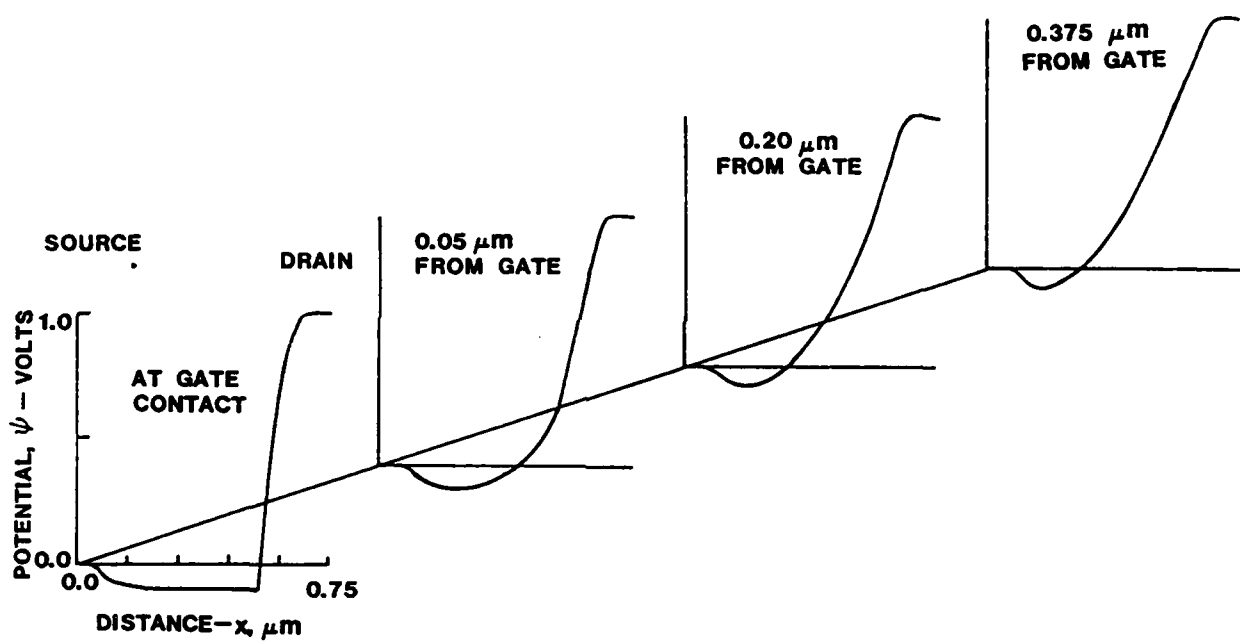


TABLE I

$$n_1^* = n_1 / n_{ref}, \quad v_1^* = v_1 / v_{ref}$$

$$n^* = n / n_{ref}, \quad v_2^* = v_2 / v_{ref}$$

$$f_1 = \Gamma_1 / \Gamma_{ref}, \quad f_2 = \Gamma_2 / \Gamma_{ref}$$

$$x^* = x / x_{ref}, \quad t^* = t / t_{ref}$$

$$\Gamma_{ref} = 1/t_{ref}$$

TABLE I. DIMENSIONLESS VARIABLES CONNECTED WITH THE CONTINUITY EQUATIONS

TABLE 2

$$\phi^* = \phi / \phi_{ref}$$

$$m_1^* = m_1 / m_{ref} , \quad m_2^* = m_2 / m_{ref}$$

$$R_1 = k_B / m_1 , \quad R_2 = k_B / m_2$$

$$R_{ref} = k_B / m_{ref}$$

$$R_1^* = R_1 / R_{ref} = \frac{1}{m_1^*} , \quad R_2^* = R_2 / R_{ref} = \frac{1}{m_2^*}$$

$$f_3 = \Gamma_3 / \Gamma_{ref} , \quad f_4 = \Gamma_4 / \Gamma_{ref}$$

$$\mu_1^* = \dot{\mu}_1 / \dot{\mu}_{ref} , \quad \mu_2^* = \dot{\mu}_2 / \dot{\mu}_{ref}$$

$$P_f = e\phi_{ref}/m_{ref} V_{ref}^2$$

$$M = V_{ref}/V_a$$

$$V_a = \left( \frac{5}{3} R_{ref} T_{ref} \right)^{1/2}$$

$$\gamma = 5/3$$

$$Re = x_{ref} V_{ref} n_{ref} m_{ref} / \dot{\mu}_{ref}$$

TABLE 2. DIMENSIONLESS PARAMETERS ASSOCIATED WITH THE MOMENTUM BALANCE EQUATIONS

TABLE 3

$f_5 = \Gamma_5 / \Gamma_{ref}$	$f_6 = \Gamma_6 / \Gamma_{ref}$
$f_7 = \Gamma_7 / \Gamma_{ref}$	$f_8 = \Gamma_8 / \Gamma_{ref}$
$\kappa_1^* = \kappa_1 / \kappa_{ref}$	$\kappa_2^* = \kappa_2 / \kappa_{ref}$
$C_{V1} = \frac{3}{2} R_1$	$C_{V2} = \frac{3}{2} R_2$
$C_{V1}^* = C_{V1} / C_{Vref}$	$C_{V2}^* = C_{V2} / C_{Vref}$
$P_r = C_{Vref} \mu_{ref} / \kappa_{ref}$	

TABLE 3. DIMENSIONLESS PARAMETERS ASSOCIATED WITH THE ENERGY BALANCE EQUATIONS

TABLE 4  
GALLIUM ARSENIDE  
PARAMETERS AND BOUNDARY CONDITIONS USED IN CALCULATION

PARAMETERS	$\Gamma$	L	COMMON
NUMBER OF EQUIVALENT VALLEYS	1	4	
EFFECTIVE MASS ( $m_e$ )	0.067	0.222	
$\Gamma$ -L SEPARATION (ev)			0.33
POLAR OPTICAL SCATTERING			
STATIC DIEL. CONST.			12.90
HIGH FREQ. DIEL. CONST.			10.92
LO PHONON (ev)			0.0354
$\Gamma$ -L SCATTERING			
COUPL. CONS. (ev/cm)			$0.800 \times 10^9$
PHONON ENERGY (ev)			0.0278
L-L SCATTERING			
COUPL. CONST. (ev/cm)			$2.0 \times 10^9$
PHONON ENERGY (ev)			0.0354
ACOUSTIC SCATTERING			
DEFORM. POT. (ev)	7.0	9.2	
NONPOLAR SCATTERING (L)			
COUPLING CONSTANT (ev/cm)			$0.300 \times 10^9$
PHONON ENERGY (ev)			0.0343

TABLE 4. SCATTERING PARAMETERS USED IN THE GALLIUM ARSENIDE CALCULATION.

TABLE 5  
INDIUM PHOSPHIDE  
PARAMETERS AND BOUNDARY CONDITIONS USED IN CALCULATION

PARAMETERS	$\Gamma$	L	COMMON
NUMBER OF EQUIVALENT VALLEYS	1	4	
EFFECTIVE MASS ( $m_e$ )	0.080	0.300	
$\Gamma$ -L SEPARATION (ev)			0.52
POLAR OPTICAL SCATTERING			
STATIC DIEL. CONST.		12.35	
HIGH FREQ. DIEL. CONST.		9.52	
LO PHONON (ev)		0.0432	
$\Gamma$ -L SCATTERING			
COUPL. CONS. (ev/cm)		0.700 $\times 10^9$	
PHONON ENERGY (ev)		0.0278	
L-L SCATTERING			
COUPL. CONST. (ev/cm)		5.0 $\times 10^9$	
PHONON ENERGY (ev)		0.0432	
ACOUSTIC SCATTERING			
DEFORM. POT. (ev)	7.0	12.3	
NONPOLAR SCATTERING (L)			
COUPLING CONSTANT (ev/cm)		0.670 $\times 10^9$	
PHONON ENERGY (ev)		0.0343	

TABLE 5. SCATTERING PARAMETERS USED IN THE INDIUM PHOSPHIDE CALCULATION.

TABLE 6

## CONSTANT SCATTERING AND POTENTIAL SCALING

 $\phi_{ref} = 1.0, \text{ GaAs}$ 

SCATTERING SCALING PARAMETER $\lambda$	0.5	1.0	2.0	4.0
REFERENCE LENGTH (microns)	2.0	1.0	0.5	0.25
$\kappa_{ref}$ (joules / $^{\circ}\text{K} \cdot \text{cm} \cdot \text{sec}$ )	$4.0 \times 10^{-6}$	$2.0 \times 10^{-6}$	$1.0 \times 10^{-6}$	$0.5 \times 10^{-6}$
$\mu_{ref}$ ( $\text{gm} / \text{cm} \cdot \text{sec}$ )	$11.48 \times 10^{-11}$	$5.74 \times 10^{-11}$	$2.87 \times 10^{-11}$	$1.44 \times 10^{-11}$
$n_{ref}$ ( $\text{cm}^{-3}$ )	$1.25 \times 10^{15}$	$5 \times 10^{15}$	$2 \times 10^{16}$	$8 \times 10^{16}$
$\mu_c$ (CATHODE MOBILITY) $\text{cm}^2/\text{v} \cdot \text{sec}$	31,270	15,635	7,817.5	3,909

TABLE 6. REFERENCE QUANTITIES FOR CONSTANT SCATTERING AND POTENTIAL SCALING (BEGINNING WITH GaAs).

## APPENDIX A

### THE ROLE OF BOUNDARY CONDITIONS TO NEAR AND SUBMICRON LENGTH GALLIUM ARSENIDE STRUCTURES\*

H. L. Grubin and J.P. Kreskovsky  
Scientific Research Associates, Inc.  
P.O. Box 498  
Glastonbury, CT 06033

To Appear in VLSI Electronics, Volume 10

\*This study was supported by ONR and DARPA

## 1. INTRODUCTION

It is now generally accepted that electrical instabilities in bulk III-V semiconductors are controlled by the details of the boundary as well as details of the interior regions. By boundary we mean the metal-semiconductor interface, the  $N^+N^-$  interface, the semiconductor-vacuum interface, etc. The situation with submicron devices is such, that by virtue of the thin interior region, the interface is expected to exercise principle control over transport within the semiconductor and devices constructed thereof.

Transport within any device, particularly with regard to boundaries is three dimensional. The distribution function within the device mirrors scattering events at the boundaries, particle confinement and a host of detailed surface properties. Difficulties arise simply in describing the role of the boundary theoretically and identifying its influence experimentally. In this volume, there are several papers dealing with the role of the boundary for transport parallel to the interface. Here, however, the discussion will be confined to transport normal to the interface. Particular emphasis will rest with identifying the role of the boundary in controlling transport in near and submicron length devices.

In examining the role of the boundary, cognizance is taken of the review article by Hess, et al. (Ref. 1) on the dependence of transport on the energy and velocity distribution of electrons entering a uniform field region. In the discussion below, however, emphasis is on spatially dependent transport in which both the space charge and the field distribution within the device are nonuniform. The reason for including nonuniformities in the discussion is that they are consequences of the presence of contacts and/or the existence of nonuniformities in the doping profile. The significance of including them in the study lies in the fact that transient effects in the presence of spatial inhomogeneities are both qualitatively and quantitatively different from those calculated under uniform field conditions. Several examples illustrate these differences. First, under uniform field conditions, long-time steady-state velocities show the presence of a dc negative differential conductivity in gallium arsenide arising from electron transfer. Under nonuniform field conditions where current rather than velocity is the relevant quantity,

calculations for devices with injecting, partially blocking contacts and highly nonuniform  $N^+ N^- N^+$  structures show highly nonlinear current-voltage relations. These IV characterisations do not, however, display negative differential conductivity (Ref. 2). Another point of importance involves the character of the transient. For uniform fields the signature of velocity overshoot lies in an initial high peak velocity followed by electron transfer and a rapid settling toward steady state. Under nonuniform field conditions, the initial transient is dependent upon the structure of the device. For  $N^+ N^- N^+$  regions, the initial transient sustains major position displacement current contributions. These displacement current contributions arise from the internal rearrangement of electric field and have the effect of increasing the lapsed time before the field reaches its steady state value. This results in a decreased velocity overshoot transient but not a decreased spatial overshoot, as discussed below.

In another matter, it must be recognized that the role of metal boundaries and/or properly designed heterostructure interfaces is significantly different than the role of the  $N^+ N$  or  $NN^+$  interface on device operation. The key element here, even for transport normal to the interface may be carrier confinement. A quarter micron structure with carriers confined to this region will behave differently than a one-micron long  $N^+ N^- N^+$  element in which the  $N^-$  region is only  $0.25\mu m$  in length. For the  $N^+ N^- N^+$  structure at sufficiently high fields enough of the potential can fall across the downstream  $N^+$  region to cause it to maintain high current densities and electron transfer.

A key element in the study of these electron devices lies in the description of the interface and how it is modeled. Here, it may be argued that there are several philosophical approaches one may take. In one dimensional descriptions, the metal semiconductor interface may be treated as a mathematical boundary, with the variables chosen to represent the boundary dictated by the form of differential equations chosen to describe transport within the semiconductor. For example: in the drift and diffusion formulation of transport, the equation for total current is often expressed in terms of a second order partial differential equation in field. Thus, the boundary condition involves specifying the field at the cathode and anode. In one study (Ref. 3) the electric field was specified at a time-independent value and the resulting dc current voltage characteristic and time dependent behavior, when it occurred, was shown to be a sensitive function of the chosen

boundary value. More general discussions have included a time-dependent cathode field (Refs. 4).

Another point of view may tend to ignore the mathematical boundary as an appropriate representation of the interface effect. Instead, at a position far removed from the boundary, an effective field may be introduced to account for the consequences of e.g., a dipole layer, or indeed the dipole layer may be introduced, (Ref. 5). The region must then be coupled to a set of time-dependent rate equations that account either for thermionic emission or field assisted tunneling through the generated barrier (Ref. 6).

Independent of the point of view taken to model the effect of the interface in the presence of an applied field, the carriers will enter the semiconductor with a well defined distribution of energies that are likely to be significantly different from those far from the interface. A case in point is gallium arsenide where the following question may be asked: When the distribution of carriers, velocity and energy in the  $\Gamma$ , L & X valleys are known at the up and downstream interface, then through solution to the governing interior equations, it may be expected that the current-voltage relation and transient behavior of the structure in principle is predictable. Given this, can the obverse side be seen. Namely, can one extract from a given set of electrical measurements on near and submicron structures a family of interfacial characteristics within which material variations lead to predictive device behavior. This approach is clearly iterative, and has been attempted. It may also be necessary if one has any hopes of engineering structures for high-speed applications. Indeed, there are already indications that this approach may be successful. The evidence lies in the success of the boundary field models to explain, on one level, the broad range of electrical behavior of gallium arsenide and indium phosphide (Ref. 7) and the apparent relation of these boundary field models to the energy, momentum and carrier distribution of entering electrons.

The above discussion expresses the construction and viewpoint of this article. Namely, device boundaries and interfaces dictate that transport must reflect their presence. The purpose of the present paper is to illustrate this. The discussion is separated into two distinct parts, with the first part dealing with the equations governing near and submicron transport.

The description of transport is through moments of the Boltzmann transport equation. The second part of the discussion deals with boundary and length dependent transport. Initially, several uniform field transient calculations are included to introduce the language of transient transport and to form a basis for comparison with the nonuniform field results.

The nonuniform field results are discussed in section III. Here, two distinct classes of devices are considered. The first consists of a uniformly doped structure in which all space charge nonuniformities arise from variations in the upstream boundary (cathode) conditions. The second device structure is the  $N^+ N^- N^+$  structure in which nonuniformities in the space charge arise primarily from the  $N^+ N^-$  and  $N^- N^+$  interfaces. Transient calculations with both structures show distinct local displacement current contributions, which will, in many cases, camouflage the presence of transient overshoot.

A brief summary of the basic findings of the study is contained in Section IV.

## II

### Transport Through Moment of the Boltzmann Transport Equation

Spatial and temporal transients are determined through solution to a set of coupled equations. These include Poisson's equation

$$\nabla^2 \phi = + \frac{e}{\epsilon} (n - n_0) \quad (1)$$

where  $n_0$  is a prespecified background concentration and  $n$  denotes the free carrier contribution arising from various portions of the conduction band. For the discussion below, only two sections of the conduction band are considered,  $\Gamma$  and  $L$ . Thus,

$$n = n_1 + n_2 \quad (2)$$

where  $n_1$  designates the population of the  $\Gamma$  valley and  $n_2$  the population of the  $L$  valley.

Poisson's equation is coupled to the first three moments of the Boltzmann transport equation, the first set of which involves continuity. For the  $\Gamma$  valley

$$\frac{dn_1}{dt} = -\frac{\partial}{\partial x_j} \frac{n_1 \hbar k_1^j}{m_1} - n_1 \Gamma_1 + (n - n_1) \Gamma_2 \quad (3)$$

where  $\Gamma_1$  denotes the rate at which carriers are scattered from the  $\Gamma$  valley to all sections of the L valley.  $\Gamma_2$  denotes return scattering. It is noted that for parabolic bands, an assumption made below

$$\frac{\hbar k_1^j}{m_1} = m_1 v_i^j \quad (4)$$

An equation similar to (3) describes transient population changes in the L valley. When the two are combined, a global continuity equation results.

$$\frac{dn}{dt} = -\frac{\partial}{\partial x_j} \left[ n_1 \frac{\hbar k_1^j}{m_1} + (n - n_1) \frac{\hbar k_2^j}{m_2} \right] \quad (5)$$

The quantity

$$n_1 \frac{\hbar k_1^j}{m_1} + (n - n_1) \frac{\hbar k_2^j}{m_2} \equiv C^j \quad (6)$$

is the velocity flux density of the system. It is convenient to relate this term to a mean spatially dependent drift velocity:

$$v^j = C^j/n \quad (7)$$

It is noted that the total current density

$$J^j = -eC^j + e \frac{\partial F^j}{\partial t} \quad (8)$$

is conserved, i.e.,

$$\frac{\partial J^j}{\partial x_j} = 0 \quad (9)$$

The second pair of moment equations is that of momentum balance. For the  $\Gamma$  valley carrier

$$\frac{\partial}{\partial t} n_i \hbar k_i^I = - \frac{\partial}{\partial x_i} \frac{\hbar k_i^I}{m_i} n_i \hbar k_i^I + e n_i \frac{\partial \phi}{\partial x_i} - \frac{\partial}{\partial x_i} \psi_i^{II} - n_i \hbar k_i^I \Gamma_3 \quad (10)$$

Here,  $\Gamma_3$  represents the net rate of momentum scattering and  $\psi_i^{II}$  represents the components of the pressure tensor

$$\psi_i^{II} = \frac{1}{4\pi^3} \frac{\hbar^2}{m_i} \int (\bar{k} - \bar{k}_i)_i (\bar{k} - \bar{k}_i)_j f d\bar{k} \quad (11)$$

For the situation where  $f$  represents a displaced Maxwellian

$$\psi_i^{II} = n_i k_B T_i \delta_{II} \quad (12)$$

where  $T_i$  is the electron temperature of the  $\Gamma$  valley carriers. For the situation where there are nonspherical contributions to  $f$ , additional diagonal as well as off-diagonal components of the pressure tensor arise. For the calculations below, the distribution function has been generalized from the displaced Maxwellian

$$f_0 = A \exp - \frac{\hbar^2 (k - k_i)^2}{2 m_i k_B T_i} \quad (13)$$

into the form (Ref. 8)

$$f = \left( 1 + a_i \frac{\partial}{\partial k_i} + a_{ij} \frac{\partial^2}{\partial k_i \partial k_j} + a_{ijk} \frac{\partial^3}{\partial k_i \partial k_j \partial k_k} \dots \right) f_0 \quad (14)$$

subject to the conditions

$$\frac{1}{4\pi^3} \int f d\bar{k} = \frac{1}{4\pi^3} \int f_0 d\bar{k} \quad (15)$$

$$\frac{1}{4\pi^3} \frac{\hbar^2}{m_1} \int f(\mathbf{k}-\mathbf{k}_1)^2 d\mathbf{k} = \frac{1}{4\pi^3} \frac{\hbar^2}{m_1} \int f_0(\mathbf{k}-\mathbf{k}_1)^2 d\mathbf{k} \quad (16)$$

The nonspherical nature of the distribution function suggests the separation

$$\psi_1^{ij} = \psi_{01}^{ij} + \hat{\psi}_1^{ij} \quad (17)$$

where  $\psi_{01}^{ij}$  is given by equation 12 and  $\hat{\psi}_1^{ij}$  represents the additional contribution. The nonspherical contributions are not calculated from first principles. Instead, the treatments of fluid dynamics are followed with

$$\hat{\psi}_1^{ij} = -\mu_1 \left[ \frac{\partial v_1^i}{\partial x_j} + \frac{\partial v_1^j}{\partial x_i} - \frac{2}{3} \frac{\partial v_1^k}{\partial x_k} \delta_{ij} \right] \quad (18)$$

where it is noted that

$$\sum_{i=1}^3 \hat{\psi}_1^{ii} = 0 \quad (19)$$

In one dimension (along x)

$$\hat{\psi}_1^{ij} = -\frac{4}{3} \mu_1 \frac{\partial v_1^x}{\partial x} \quad (20)$$

In two dimensions, the derivative of the stress tensor is

$$\begin{aligned} \frac{\partial}{\partial x_i} \hat{\psi}_1^{ij} &= i \left\{ (-\mu_1) \left[ \frac{4}{3} \frac{\partial^2 v^x}{\partial x^2} + \frac{\partial^2 v^y}{\partial x^2} + \frac{\partial^2 v^z}{\partial x \partial y} - \frac{2}{3} \frac{\partial^2 v^y}{\partial x \partial y} \right] \right. \\ &\quad \left. + i \left\{ (-\mu_1) \left[ \frac{4}{3} \frac{\partial^2 v^y}{\partial y^2} + \frac{\partial^2 v^x}{\partial y^2} + \frac{\partial^2 v^z}{\partial y \partial x} - \frac{2}{3} \frac{\partial^2 v^x}{\partial y \partial x} \right] \right\} \right\} \end{aligned} \quad (21)$$

In the discussion below, an even simpler version of equation 21 is assumed

$$\frac{\partial}{\partial x_i} \psi_i^{ij} = -\mu_i \frac{\partial^2 v_i^j}{\partial x_i^2} \quad (22)$$

with the constraint equation 15 only approximately satisfied. Thus, the relevant equation for momentum balance is

$$\frac{\partial}{\partial t} n_i \hbar k_i^j = -\frac{\partial}{\partial x_i} \frac{\hbar k_i^j}{m_i} n_i \hbar k_i^j + e n_i \frac{\partial \phi}{\partial x_j} - \frac{\partial}{\partial x_j} n_i k_B T_i + \frac{\mu_i \hbar}{m_i} \frac{\partial^2 k_i^j}{\partial x_i^2} - n_i \hbar k_i^j \Gamma_3 \quad (23)$$

For the L valley the relevant momentum balance equation is

$$\begin{aligned} \frac{\partial}{\partial t} (n - n_i) \hbar k_2^j &= -\frac{\partial}{\partial x_i} \frac{\hbar k_2^j}{m_2} (n - n_i) \hbar k_2^j + e(n - n_i) \frac{\partial \phi}{\partial x_j} - \frac{\partial}{\partial x_j} (n - n_i) k_B T_2 \\ &\quad + \frac{\mu_2 \hbar}{m_2} \frac{\partial^2 k_2^j}{\partial x_i^2} - (n - n_i) \hbar k_2^j \Gamma_4 \end{aligned} \quad (24)$$

The third and final pair of balance equations is that associated with energy transport. Straight forward application of the moment equations yields

$$\frac{\partial}{\partial t} W_i = -\frac{\partial}{\partial x_j} \frac{\hbar k_2^j}{m_i} W_i + n_i e \frac{\hbar k_2^j}{m_i} \frac{\partial \phi}{\partial x_j} - \frac{\partial}{\partial x_j} \frac{\hbar k_i^j}{m_i} \psi_i^{ij} - \frac{\partial}{\partial x_j} Q_i^j - n_i U_i \Gamma_5 + (n - n_i) U_2 \Gamma_6 \quad (25)$$

where

$$U_i = \frac{3}{2} k_B T_i \quad (26)$$

$$W_i = n_i \left[ \frac{\hbar^2 k_2^2}{2m_i} + U_i \right] \quad (27)$$

and

$$Q_1^j = \frac{\hbar^3}{8\pi^3 m_1^2} \int (k - k_1)_j (k - k_1)_i^2 f dk \quad (28)$$

where the summation convention over  $i$  is assumed.  $Q_1^j$  is zero for spherically symmetric distribution functions. For nonspherical situations it represents a flow of heat and is treated phenomenologically through analogy to Fourier's law

$$Q_1^j = -\kappa_1 \frac{\partial}{\partial x_j} T_1 \quad (29)$$

It is important to note at this point that the use of the relationships given by equations 18 and 29 are not fundamental. Rather, they are expressions of ignorance of the detailed role of the distribution on transport, particularly near the boundaries.

In the analysis that follows, equation 25 is not solved. Rather it is combined with equations (3) and (24) to yield

$$\begin{aligned} \frac{\partial}{\partial t} n_1 U_1 &= -\frac{\partial}{\partial x_j} \frac{\hbar k_1^j}{m_1} n_1 U_1 - \frac{2}{3} n_1 U_1 \frac{\partial}{\partial x_j} \frac{\hbar k_1^j}{m_1} + \kappa_1 \frac{\partial^2}{\partial x_j^2} T_1 \\ &+ \frac{\hbar^2 k_1^2}{2m_1} [2n_1 \Gamma_3 - n_1 \Gamma_1 + (n-n_1) \Gamma_2] - n_1 U_1 \Gamma_5 + (n-n_1) U_2 \Gamma_6 \end{aligned} \quad (30)$$

In the above, the nonspherical contributions of the stress tensor, equation 10, are ignored. For the second species of carriers

$$\begin{aligned} \frac{\partial}{\partial t} (n-n_1) U_2 &= -\frac{\partial}{\partial x_j} \frac{\hbar k_2^j}{m_2} (n-n_1) U_2 - \frac{2}{3} (n-n_1) U_2 \frac{\partial}{\partial x_j} \frac{\hbar k_2^j}{m_2} + \kappa_2 \frac{\partial^2}{\partial x_j^2} T_2 \\ &+ \frac{\hbar^2 k_2^2}{2m_2} [2(n-n_1) \Gamma_4 + n_1 \Gamma_1 - (n-n_1) \Gamma_2] - (n-n_1) U_2 \Gamma_7 + n_1 U_1 \Gamma_6 \end{aligned} \quad (31)$$

Equation 1, 3, 5, 23, 24, 30 and 31 are the equations governing transport in the systems considered in this review. The equations are more general than others in that nonspherical contributions to the BTE moments have been included. The scattering integrals  $\Gamma_1$  through  $\Gamma_8$  and the form they

take have been discussed in the past where these evaluations have been in terms of the displaced Maxwellian only. These integrals have not been generalized to include nonspherical contributions.

The governing equations are expressed in dimensionless form prior to transformation into difference equations. The dimensionless equations are discussed in the appendix. Solution of the governing equation requires imposition of boundary conditions. These represent a crucial aspect of the study and are discussed as they are needed. The band structure parameters used in the study for two-level transfer are also discussed in the appendix.

### III

#### Solution of the Governing Equations

##### IIIa. Uniform Fields

Calculations for uniform fields are discussed first, as they offer an important starting point for examining transients under nonuniform field conditions. Uniform fields result from assuming a donor level  $n_0$  that is spatially constant to the boundary and specifying that

$$n_x = n_{1x} = V_{1x} = V_{2x} = T_{1x} = T_{2x} = 0 \quad (32)$$

at both the cathode and anode boundaries. In the above, the subscript x denotes a first derivative. Figure 1 displays the velocity transient for a one-micron long element with a doping level of  $5.0 \times 10^{15}/\text{cm}^3$ . The length specification is artificial. For each calculation, the bias was raised in one time step from 0.01 volts to the value indicated in the figure. One notes the high carrier velocity occurring at approximately 0.5p sec. and the long-term asymptotic lower steady state value. Also apparent in the figure is the presence of a region of negative differential mobility. Figure 2 displays the time rate of change of carriers in the gamma valley. Electron transfer is apparent at times following the peak velocity. Figure 3 displays the time

dependence of the electron temperature following application of the voltage pulse. The feature to be noted from this figure and equation 30 is that for uniform fields any time dependence in  $T_1$  is due entirely to scattering events - and is thus a measure of when ballistic transport may be ignored. Another point of interest is that under uniform field conditions the population of carriers in either the central or satellite valley is governed by the scattering rates which are in turn governed by the value of the carrier temperature. This will be featured prominently below when contacts effects are considered. The time dependence of the  $\Gamma$  valley velocity is displayed in figure 4. Note: the long-time asymptotic values do not and should not display negative differential mobility. The mean steady state distribution of velocities as well as that within the  $\Gamma$  valley is shown in figure 5. It is noted that nonparabolic effects are not included here.

### IIIb Nonuniform Fields, Uniform Doping

The origin of nonuniform fields and space charge layers in uniformly doped structures lies in the conditions imposed at the up and downstream boundaries. Under conditions in which current is flowing through the structure, the upstream boundary conditions manifest themselves as cathode boundary current-field relations. It is the influence of the cathode boundary that will dominate the following discussion. To develop the concept of boundary controlled transport several qualitative features of the mathematics governing transport are considered.

Under time independent steady state conditions, the velocity flux density

$$C = n_1(x)v_1(x) + [n(x) - n_1(x)]v_2(x) \equiv n(x)v(x) \quad (33)$$

is a constant independent of position. Denoting, through the subscript 'C' the carrier density and the mean velocity at the first computed point within

the semiconductor, the following exercise is performed:

$$C - n_0 V_c = (n_c - n_0) V_c \quad (34)$$

where  $n_0$  is the uniform background doping level. For the purpose of specificity  $V_c$  is assigned to be a monotonically increasing function of field and to have the form represented by the curve  $n_0 V_0$  in figure 6. Note that for uniform field conditions,  $V_c$  would necessarily be the same as the bulk field dependent velocity and exhibit negative differential mobility. Also included in figure 6 is a sketch of one possible variation of  $n_c V_c$ . The field dependence of  $n_c$  is thereby defined implicitly in figure 6. It is also noted that  $n_0 V_c$  and  $n_c V_c$  are chosen to intersect, although there is no a priori reason to assume any universality to this property. Figure 6 also includes a schematic of the velocity flux density,  $n_0 V_n$ , (assuming negative differential mobility) associated with uniform fields and two horizontal lines representing two different values of the current flux density within the device.

Figure 6a takes on significance when the intersection of the line of constant current  $C$  and the neutral field characteristic  $n_0 V_n$  is taken to represent uniform field region values within the interior of the semiconductor; and the intersection of  $C$  with the cathode characteristic  $n_c V_c$ , is taken to represent field values at the boundary of the semiconductor (Ref. 10).

Consider first the low current case  $C_1$ . Here, the assumed current field relations are such that for

$$F_c < F_{bl} \quad (35)$$

$n_0 > n_c$ . And for a specific distance between the upstream boundary and the interior of the structure, a range of charge depletion forms, as sketched in figure 6b.

Consider next the higher current case  $C_2$ . For this situation

$$n_0 V_c(F_c) < n_c V_c(F_c) \quad (36)$$

and a region of local charge accumulation forms at the upstream boundary. Because the field dependence of the mean carrier velocity exhibits a region of negative differential mobility, the downstream interior field is either greater than or less than the cathode field and either a range of charge accumulation forms within the interior of the structure or a range of charge depletion forms within the interior. The latter is illustrated in figure 6b. It is important to note that nothing has been said about the stability of these profiles. Indeed, in some cases the profiles are electrically unstable (Ref. 7).

Consider figure 7a with a different set of upstream boundary characteristics. For the low current case

$$F_c > F_{bi} \quad (37)$$

and a region of charge accumulation layer forms over a specific distance between the upstream boundary and the interior of the structure. However, at the upstream boundary

$$n_0 V_c(F_c) > n_c V_c(F_c) \quad (38)$$

indicating that a region of local charge depletion forms at the upstream boundary. A sketch of a possible space charge profile is shown in figure 7b. For the high current case, both within the interior and at the upstream boundary regions of charge accumulation form. A sketch of this charge layer is also shown in figure 7b.

The discussion above indicates that the interplay between the boundary and the interior of the semiconductor is able to introduce a rich variation in the space charge distribution. A situation evoking considerable interest with respect to this interplay is one that may be regarded as a singular solution. This occurs when the current flux density  $C_2$  intersects the neutral characteristic at two points and the curves  $N_c V_c$ ,  $n_0 V_c$  and  $N_o V_n$  intersect

at the same value of field (thus,  $V_n = V_c$  and  $n_o = n_c$ ). The general description and consequences of the approach to this event in long samples, as a precursor for nucleation of high electric field traveling dipole layers has been broadly delineated in a variety of publications (Ref. 7 and 10). The consequence of this in terms of solutions to the BTE moments is discussed in section IIe.

It should be apparent from the above discussion that the detailed description of the influence of the boundary requires a description of the field dependence of the mean entrance velocity and carrier distributions. In the calculations below in which transport is described through solutions to moments of the BTE, these field dependencies are constrained by the boundary conditions to the governing equation and are expressed as solutions to the following equation.

$$C = n_c V_c(F_c) \Rightarrow F_c = g(C) \quad (39)$$

When  $F_c$  is a double valued function of  $C$  a regional approach is taken.

### IIIc The Effect of Device Length

Up to this point, nothing has been discussed concerning the influence of device length on the cathode characteristic properties, nor on the transport properties through the structure. There are, however, several points of note. First, in the calculations, the field at the cathode is not specified but is computed self consistently from the governing equation subject to the constraints of the boundary conditions. For constant  $n_o$  the details of transport from the cathode are dominated by the uniform field neutral velocity characteristic. For uniform fields and long devices, the velocity exhibits negative differential mobility as displayed in figure 5. However, as the device decreases in length, the mean carrier velocity for uniform fields is altered as displayed in figure 8. (See reference 11 for a discussion of how the calculation was performed along with the imposed condition). Perhaps the most significant phenomena occurring as the semiconductor length is reduced is the progressive decrease in negative differential mobility of GaAs

and the increase in the velocity and hence current. These effects are illustrated below.

#### IIId Steady State and Transient Behavior Injecting Cathode (L=1.0 microns)

The discussion above is independent of the detailed description provided by the governing equations chosen to represent device transport. The governing equations and their associated boundary conditions provide a mechanism by which a set of contact "descriptors" can be extracted. For example, it is expected that the specific properties of the physical contact or boundary will influence the distribution of carriers within the valence and conduction bands of the semiconductor in the vicinity of the boundary. (Ref. 12). Further, under conditions of finite bias in which current is transported through the device, the influence of the contact is expected to affect the entrance velocities (Ref. 3). In the discussion that follows, a very simple set of boundary conditions is imposed to represent the effects of the physical boundary. The importance of these boundary conditions is to create nonuniform fields. As will be seen, the boundary conditions chosen are not the result of an exhaustive study. Rather, they are associated with an initial effort. For example, in the discussion below, the initial sharing of carriers between the  $\Gamma$  and L portions of the conduction band is controlled by specifying a value for the electron temperature at the cathode boundary. In addition, a representation of the entrance velocity is through a cathode contact mobility. This is identified in the calculation beginning with figure 9.

Figures 9 through 12 are calculations performed for a gallium arsenide structure with the same material parameters as that of the uniform field calculations. Here, however, the boundary conditions are different. At the cathode

$$n_{xx} = n_{ixx} = 0, \quad V_i = -15,625 F, \quad V_{zx} = 0, \quad T_i = 300^\circ K, \quad T_{zx} = 0 \quad (40)$$

and at the anode

$$n_{xx} = n_{1xx} = V_{1xx} = V_{2xx} = T_{1xx} = T_{2xx} = 0 \quad (41)$$

where the double x subscript denotes a second derivative. The consequences of this set of boundary conditions is that the  $\Gamma$  valley electrons enter the structure with a velocity in excess of the steady state uniform field value. Specification of the  $\Gamma$  valley temperature at 300° K assures that the relative cathode carrier contribution of the L valley is negligible. Further, the fact that the mean velocity of the L valley carriers is significantly below that of the  $\Gamma$  valley carriers provides the demonstration that the cathode current field relation is dominated by the  $\Gamma$  valley carriers:

$$J_c = -e[nV_{1c} + (n-n_1)V_{2c}] \approx ne\mu_c F \quad (42)$$

While equation 42 is significant in providing a description of the dominating carrier at the cathode, alone it will not determine whether the cathode is carrier depleted, neutral or accumulated. The moment equations coupled to Poisson's equation must be solved. Qualitative information, can, however, be obtained for the specific set of boundary conditions given by equation (40) through use of the mobility approximation. Because of the inherent limitations of the mobility approximation the consequences of its use must be regarded as relevant only if insight is provided in the interpretation of the exact solution.

The qualitative information is obtained through a calculation of the transit time of a carrier within the vicinity of the cathode. Because the transit time is necessarily a positive quantity, inequalities arise which express cathode depletion, neutrality and accumulation. The transit time between the cathode and an interior point X is

$$\tau(X) = \int_0^X \frac{dx'}{V(x)} \quad (43)$$

Assuming a constant mobility for the  $\Gamma$  valley carriers and the significant approximation

$$nV \approx n_i V_i \quad (44)$$

then for carriers within the vicinity of the cathode, the arguments leading to equation (42) imply that  $V \approx -\mu_1 F$ . This last statement, when coupled to Poisson's equation yields

$$t(X) = \tau_0 \log \left\{ \frac{J - n_0 e \mu_c F_c}{J - n_0 e \mu_i F(X)} \right\} \quad (45)$$

where

$$\tau_0 = \frac{\epsilon}{n_0 e \mu_i} \quad (46)$$

is the dielectric relaxation time of the gamma valley carriers. For a cathode boundary condition consistent with  $J = N_c e \mu_c F_c$

$$t(X) = \tau_0 \log \left\{ \left( 1 - \frac{n_0 \mu_i}{n_c \mu_c} \right) / \left( 1 - \frac{n_0 \mu_i F(X)}{n_c \mu_c F_c} \right) \right\} \quad (47)$$

Since the requirement that the transit time be positive must be met, two inequalities emerge:

$$n_c \mu_c > n_0 \mu_i, \quad F(X) > F_c \quad (48)$$

$$n_c \mu_c < n_0 \mu_i, \quad F(X) < F_c$$

For case (a) of equation (48) local charge accumulation is present at the cathode. Note that the condition  $F(X) > F_c$  is stronger than the first inequality and requires that  $N_c > N_0$ . In case (b) cathode depletion occurs with  $N_c < N_0 \mu_i / \mu_c$ . The results of the simulation discussion below are consist-

ent with case (a) as demonstrated in figure 9. For case (b), reference is made to the discussion of Grubin and Kreskovsky (Ref. 13). Figure 9 is a plot of the computed dc current versus field relation at the cathode boundary. It is approximately linear with only a marginal variation in field. The cathode field is effectively pinned. For reference purposes, the current field relation for the uniform field structure is also shown.

The characteristics of the uniform field curve and the cathode current field relation are different and for a constant current through the semiconductor at least two different field values result at intersections. The cathode boundary field is lower than that of the neutral field intersection; a result that is consistent with cathode accumulation.

The steady state time independent distributions of electric field, carrier density,  $\Gamma$  valley velocity and electron temperature are displayed in figures 10 through 13, for various bias levels. While the calculation displays the excess carrier velocity at elevated bias levels, there is also an enhanced electron transfer and the dc current shows saturation. The clear consequence of the transfer is that the current does not scale the velocity. This latter feature is reflected in the current-voltage relation shown in figure 14.

With regard to the current-voltage characteristic, while the current does not scale the velocity and thus does not fully reflect overshoot contributions, its high bias level is above that associated with the equilibrium steady state velocity field relation, while below that associated with the  $\Gamma$  valley velocity. The excess above  $V_n$  is due predominantly to the cathode boundary condition that allows for a high level of injected charge. The depression below  $V_n$  is due to electron transfer. It is also noted that there is virtually no electron transfer near the cathode. Most of it occurring near the anode and it is the effect of electron transfer that leads to saturation in the current density. Another feature of the nonuniform field calculation lies in the clear absence of negative differential conductivity; a phenomena present in uniform field calculations.

The significant qualitative differences between the steady state uniform field characteristics and those associated with nonuniform fields suggests some differences in the transient characteristics. This is indeed the case as discussed below.

Figure 15 displays the current transient following application of a

voltage pulse. The first point we emphasize is that the plot consists of current rather than velocity. The second point is that the current transient is ostensibly similar to that associated with velocity overshoot. There is, however, a fundamental difference between the two. For uniform and nonuniform fields, during the first time step, the field throughout the structure is increased by an amount equal to the change in applied voltage divided by device length. This introduces a one time step displacement current whose magnitude is computationally dependent and therefore nonphysical. For uniform fields, all displacement current contributions cease after the initial time step. For nonuniform fields all time dependent field evolution is accurately calculated following the initial time step. Here, with the cathode boundary introducing a cathode adjacent accumulation layer, the time dependence introduces a layer that propagates toward the anode boundary. This propagation is accompanied by field rearrangement and internal point-by-point displacement current contributions.

Figure 16 shows the space and time dependent evolution of the electric field with the device. The effect of the boundary condition is to introduce a propagating accumulation layer originating at the cathode, while downstream from the anode the field is approximately uniform during the first 0.5ps, becoming highly nonuniform as steady state is approached. The early time transients dictate that displacement current contributions will be significant within the vicinity of the propagating accumulation layer, as shown in figure 17 and will be insignificant downstream from the layer. In the latter regions, the familiar velocity transients obtained from uniform field calculations arises. At later times propagation continues but is accompanied by electron transfer. The long-time transient differs from that of uniform fields. (One notes from figures 18 and 19 the absence, for  $t < 0.5$ ps, of any significant transfer downstream from the moving space charge layer. Hereto, the carrier velocity (figure 20) downstream from the moving space charge layer sustains high values common to overshoot).

There are three dominating features of the above calculations. The first two are the boundary conditions on the  $\Gamma$  valley temperature and mean carrier velocity. The third is the length of the structure. As discussed earlier, the specification of the  $\Gamma$  valley electron temperature provides dominant control in these calculations of the relative population of the  $\Gamma$

valley carriers at the cathode. For the calculations of figures 10 through 17, specifying  $T_1$  at  $300^\circ K$  resulted in virtually the entire sea of cathode carriers as  $\Gamma$  valley carriers. In a study performed earlier (Ref. 13) in which the device length was 2.0 microns and the  $\Gamma$  valley velocity was subject to a mobility boundary condition as in equation (40), the results were qualitatively similar for  $T_1=300^\circ K$  and a  $\Gamma$  valley boundary mobility greater than that of the low field steady state mobility of the  $\Gamma$  valley carriers. In those calculations, the total set of boundary conditions was somewhat different than those employed in the discussion of figures 10 through 20 but there were several definite trends. For example, by retaining a suitably high cathode mobility and by elevating the electron temperature, space charge accumulation at the cathode was retained but the relative proportion of  $\Gamma$  valley carriers at the cathode decreased. Again, on the obverse side, retaining a cathode temperature of  $T_1=300^\circ K$  but reducing the boundary mobility of the  $\Gamma$  valley carriers to a value below that of the low field mobility of the  $\Gamma$  valley carrier in steady state results in a partial depletion of carriers at the cathode and a concomitant increase in the cathode field to values in excess of that within neutral regions interior to the device. Each of these results are consistent with the qualitative arguments contained in equations 43 to 48.

The immediate conclusion that can be drawn from the set of referenced results is that the presence of space charge accumulation or depletion at the cathode is dominated by the field dependence of the entering carrier velocity vis-a-vis, that within the interior of the device. This conclusion is applied to a problem of high visibility, transit time Gunn domain instabilities in GaAs.

#### IIe Steady State and Transient Behavior, Partially Blocking Cathode ( $L = 5.00$ microns) Gunn Oscillations

The structure under consideration is 'long' with respect to submicron dimension. The device length is 5.00 microns. The boundary conditions here are different than those used for figures 10 through 20. In this case, those of equation 30 are repeated, with two critical variations:

$$V_i = -4000 F, \quad T_1 = 1200^\circ K \quad (49)$$

As in the case of the accumulated cathode, the situation represented by equation (49) can be described qualitatively by equations (43) through (47) with the modification:

$$nV \approx n_i V_i \cong \beta n V_i \quad (50)$$

where  $\beta$  represents an average of the fraction of  $\Gamma$  valley to total carriers within the cathode region. With this change

$$t(X) = \tau_0 \log \left\{ \left( 1 - \frac{\beta n_0 \mu_i}{n_c \mu_c} \right) / \left( 1 - \frac{\beta n_0 \mu_i F(X)}{n_c \mu_c F_c} \right) \right\} \quad (51)$$

The requirement that the transit time be positive lead to the inequalities

$$\begin{aligned} n_c \mu_c &> \beta n_0 \mu_i, \quad F(X) > F_c \\ n_c \mu_c &< \beta n_0 \mu_i, \quad F(X) < F_c \end{aligned} \quad (52)$$

Inequality (b) of equation (52) is represented in detail below and shows the presence of cathode depletion.

Figure 21 displays the field distribution, whose most obvious characteristic is that of a broad depletion region adjacent to the cathode. The characteristics of this depletion region are that with increasing bias, the depletion zone broadens, the cathode field increases and the downstream field begins to approach a constant value. This latter feature manifests itself as hard saturation in current versus voltage.

Figure 22 is a display of the carrier density in the  $\Gamma$  valley as well as total carrier density. It is first noted that for all of the bias value chosen, the  $\Gamma$  valley carrier density displays partial depletion in the vicinity of the cathode boundary. This, it may be anticipated, will manifest itself as an excess carrier velocity at the cathode. It is also noted that as the bias level increases, the total charge at the cathode shows a diminished depletion, while downstream, there is a weak region of charge accumulation. With regard to the  $\Gamma$  valley velocity, this follows the pattern dictated by current continuity and cathode adjacent charge depletion. The carrier velocity at the cathode sustains values in excess of that within the neutral interior regions of the semiconductor.

Figure 24 displays the dc current voltage-relation for this structure. Several points are noteworthy: The first is the absence of negative differ-

ential conductivity even though the neutral interior region is characterized by a region of negative differential mobility. The second point to note is that current saturation occurs at values below that associated with the one-micron long device.

The cathode current field relation is displayed against the neutral field characteristic in figure 25. In addition, the cathode boundary neutral field characteristic is also shown. The curves display an apparent tendency to intersect within the region of negative differential mobility, resulting in two approximately neutral regions sustaining different values of field and velocity. Under a well defined set of conditions, this configuration is electrically unstable and leads to the nucleation and propagation of high field domains. For the configuration under consideration, an increase in bias level from 2.0 to 3.0 volts resulted in transient local cathode adjacent accumulation and subsequent dipolar propagation as displayed in figure 26. The details of figure 26 show the transient transformation of the space charge layer, as reflected in the electric field distribution, from a depletion layer to a dipole propagating layer. The dipole layer is quenched at the anode boundary and repeated transit time oscillations occur. The time dependent oscillations are displayed in figure 27 and occur after an initial transient that is qualitatively similar in structure to that associated with the accumulation cathode and the uniform field transients. Indeed, the peak current is both a reflection of overshoot and the influence of the cathode boundary condition which reduces its value to a level below that of the uniform field transient. It is important to note this point, that while the development of a set of conditions for initiating a propagating domain is of clear technological significance, they play a secondary role to the thrust of this paper, which is that conditions at the cathode are likely to be the single most pervasive influence on near and submicron length semiconductor devices; much as they are for longer devices.

#### IIIf Nonuniform Fields, Length Scaling

While the calculations in sections IIId and e were for structures of different length, the emphasis was on the effects of the boundary. However, the effects of length scaling, insofar as they affect the velocity field relation, vis-a-vis figure 8, will influence the electrical transient and the steady state field profiles. This is illustrated for two situations. The

first situation is for a uniformly doped structure with the same boundary conditions as given by equations 27 but with a length of 0.25 microns. The second structure considered is that of a  $N^+ N^- N^+$  device, with a one-micron cathode-to-anode spacing but with a variable length  $N^-$  region.

The calculations for the 0.25 micron-long device are displayed in figures 28 through 36. The steady state electric field distribution is displayed in figure 28, for the indicated bias levels. It is noted that although the average fields for the 0.25 micron device and the 1.0 micron device are the same, the field distributions are quantitatively different. The difference lies in the fact that at the lower bias levels only a marginal amount of electron transfer occurs within the shorter structure. It is noted that the electric field at the cathode is low, as for the one-micron long device.

Figure 29 displays the steady state population of the  $\Gamma$  valley as well as the total carrier density. The first point to note here is that the density of carriers for the given bias level exceeds that for the one-micron long element. The second point is that considerably less electron transfer occurs downstream from the cathode. There is, however, a far more significant aspect to the quantitative differences between the results of the 0.25 and 1.0 micron. The carrier and velocity distributions for the two structures are different. These differences are, in part, a result of the fact that conditions at the upstream boundary are sensitively dependent upon the proximity of the collecting contact. Further evidence for this is provided by the velocity distribution displayed in figure 30 which shows higher entrance velocities, but lower exit velocities.

Figure 31 is a plot of current-versus voltage for the 0.25 micron-long device. Again, two points are emphasized: the first shows the absence of any negative differential conductance. The second point is that the presence of increased levels of charge injection yield an increase in the drive current over that of the one-micron long device.

The transient characteristics at 0.25 microns are displayed in figures 32 through 36. The results are quantitatively different from that associated with the one-micron device. The first difference is displayed in the current transient (figure 32) which shows a higher peak current and a smaller current dropback. As revealed in the time dependent distributions of field (figure

33) the higher peak current (greater than 25%) is in large part due to displacement current contributions. The higher long-time steady state current level reflects the increased injection level (figures 34 and 35) over that of the 1.0 $\mu\text{m}$  calculation. In this regard, it is again pointed out that the exit velocity for the 0.25  $\mu\text{m}$  structure is below that for 1.0 $\mu\text{m}$ . (figure 36) The final point of interest involves the time to steady state. This time is shorter for the 0.25 $\mu\text{m}$  electron, but not a factor of 4 shorter. The time scales involved in the approach to steady state involves nontransit time contributions.

### IIIg. Transients in $\text{N}^+\text{N}^-\text{N}^+$ Structures, Length Scaling

The final two-terminal structure considered is the  $\text{N}^+\text{N}^-\text{N}^+$  device, and there are several key features to note. The first is that the dominant interfaces for this structure, the  $\text{N}^+\text{N}^-$  and  $\text{N}^-\text{N}^+$  interface are not the physical boundaries of the device and are thus likely to have a different effect on the electrical behavior of the device. The second feature of importance lies in the fact that the electric field profile is highly nonuniform in the steady state, may dominate the transient and completely camouflage all sub-micron effects. Third, for a sufficiently small  $\text{N}^-$  regions, the influence of the  $\text{N}^+\text{N}^-$  and  $\text{N}^-\text{N}^+$  interfaces for carrier confinement may be less prominent. Thus, this last two-terminal structure offers the most serious example of the interplay of the interface and the length of the critical submicron region on the electrical characteristics of the submicron structures. To avoid conflict with the influence of the true metal confining contacts, the physical boundary conditions at the cathode were taken as

$$n = n_0, \quad n_i = n_{i\text{eq}}, \quad V_{ix} = 0, \quad V_{2x} = 0, \quad T_i = 300^\circ\text{K}, \quad T_{2x} = 0 \quad (53)$$

At the anode all second derivatives were set to zero.

The  $\text{N}^+\text{N}^-\text{N}^+$  calculations performed were for the one-dimensional structure of figure 37, in which the  $\text{N}^-$  region was assigned a nominal doping level of  $10^{15}/\text{cm}^3$  and the  $\text{N}^+$  region was at  $10^{17}\text{cm}^3$ . The length of the  $\text{N}^-$  region is

specified at the doping level of  $10^{16}/\text{cm}^3$ , and varied from 0.416 microns to 0.116 microns. The entire structure was fixed at a length of 1.0 microns. The design of the structure dictates that nonuniform fields and charge densities form within it. Thus, again the relevant experimental quantity is current density, rather than velocity. The first set of results is shown in figure 38. Figure 38 displays the total current flowing through the device following application of a voltage pulse of magnitude 1.0v.

As in the uniform  $N_0$  studies, the calculation is performed in two stages. The first involves obtaining a steady state solution at 0.01v. For the second, using this as an initial condition the bias is raised in one time step, to 1.0v. Application of the bias in one time step replicates the procedure of most of the uniform field calculations.

As seen in figure 38, the current displays an initial peak at approximately 0.15ps, followed by a drop in current and a subsequent rise toward a steady state value. For uniform field calculations in which the voltage is increased in one time step, as discussed earlier, there is an initial displacement current whose magnitude is determined entirely by the computational time step. Thereafter, all displacement currents are zero and all transients are particle current transients. (It is noted that with a load line, displacement currents would exist). The situation with the nonuniform field calculation and displacement current contributions is different. Figure 39 displays the particle current through the device at select instants of time. A comparison of the magnitude of the particle and total current indicates that within certain key regions of the device, particularly near the  $N^+N^-$  and  $N^-N^+$  micron regions, that the displacement current dominates the current level. The general conclusion of this calculation is that since the initial transient is strongly influenced by displacement current contributions it would be inappropriate to assume that the initial current transient is a measure of velocity overshoot.

The details of the transient, specifically as it relates to displacement current contributions, are reflected in the time dependence of the electric field and potential profiles, figures 40, 41 and the spatially dependent charge density profiles, figures 42 and 43. It is noted, however, that as in the uniform field calculations, immediately following the voltage

step, the electric field increases everywhere by the ratio of the applied bias to the length of the structure, in this case 10kv/cm. This initial increase introduces a displacement current whose magnitude does not correctly represent the physical transient but rather the impulsive change in the applied potential over a single, small but finite time step. Physically accurate calculations follow the initial time step and are discussed below.

Prior to the application of the step potential a retarding field is formed at the upstream  $N^+N^-$  interface limiting further injection of space charge into the  $N^-$  region. This retarding field, which at its maximum is positive in sign, is significantly reduced following application of the step potential; carrier injection into the  $N^-$  region is thereby resumed. Two events accompany this enhanced injection. First, to accomodate the increased charge within the  $N^-$  region Gauss's law dictates that the electric field within the region must become increasingly negative. Second, the space charge injection is self-limiting in that as the process of injection proceeds, the retarding field begins to reform and positive field values result at the upstream  $N^+N^-$  interface. The process of an increased and positive retarding field accompanied by an increasingly negative field within the  $N^-$  region and the constraint of the fixed potential leads to the spatially dependent displacement currents inferred from figure 39. It is noted that in steady state a significant amount of injected charge resides at the downstream  $N^-N^+$  interface and results in the presence of a downstream retarding field.

Notwithstanding the displacement current contributions, it is necessary to determine the extent to which the carrier velocity can exceed the equilibrium values. For the structure considered herein with  $L_N^- = 0.416$  microns, most of the current is transported by the gamma valley carriers. For this case, the mean carrier velocity thereby exceeds the steady state value. This is seen in figure 44 and in figure 45, the latter displaying a plot of the gamma valley temperature. The steady state distribution is qualitatively similar to that reported in a number of different studies (Ref. 15 through 17). In particular, the presence of a local cooling at the  $N^+N^-$  interface is noted (Ref. 15).

There are several noteworthy features associated with figure 44. First, there is the progressive movement of the velocity layer toward the downstream  $N^-N^+$  interface. This migration is associated with the spatial and temporal derivatives on the left-hand side of equation (2). Second, there is a pro-

gressive decrease in the velocity in the  $N^+$  regions as dictated by the decreasing field within these regions. Indeed, the possibility exists for the carriers to sustain a transient separation at the  $N^+N^-$  interface, with carriers on the upstream portion of the interface moving toward the cathode and carriers at the downstream portion of the interface moving toward the downstream boundary. This separation is accompanied by compensating displacement current contributions.

The results clearly indicate the presence of velocity overshoot under nonuniform field conditions. Under uniform field conditions, the transient following the peak velocity is dominated by electron transfer. The question becomes; does similar phenomena occur when nonuniform fields are present? Figure 46 is a plot of the time evolution of the total carrier density and the gamma valley and the gamma valley carrier density at two points within the  $N^+N^-N^+$  structure. It is seen that as in the uniform donor calculations at the upstream portion of the structure very little transfer occurs. Most of the transfer is at the downstream portion of the structure. One necessary conclusion as before is that the uniform field calculations bear little resemblance to the transients occurring in the  $N^+N^-N^+$  structure.

We next consider the dependence of the results on the length of the  $N^-$  region and note the expectation that the shorter the active region the higher the dc drive current (Ref. 12). For the  $N^+N^-N^+$  structure, as in the uniform  $N_0$  structure with injecting contacts a significant contribution to the current arises from the excess charge injected into the  $N^-$  region. This point was also made in Ref. 17 where the dependence of current and voltage on  $N^-$  region length was also examined. A second point of importance here concerns determining which portion of the structure dominates its transport. It may be intuitively expected that for the structure considered it is the  $N^-$  region that dominates. This appears to be the case for the above discussion. But one may expect that for a sufficiently small  $N^-$  region, no single region dominates. In the calculations reported here, the absence of a single dominating region becomes apparent at higher voltage levels and for the case when  $L_N = 0.116$  microns. These results are illustrated in figures 47 through 53, with particular attention paid to voltage sharing and electron transfer in the

$N^+$  region as the  $N^-$  region is reduced in size. Figure 47 is a sketch of the background doping level associated with the variable  $N^-$  region. Within these regions and at a bias of 1 volt, the potential is calculated self-consistently and is displayed in figure 48. It is noted that for  $N^-$  regions of length 0.266 and 0.416 microns, most of the potential drop is across the  $N^-$  region. For the smallest region a substantial potential drop falls across the  $N^+$  region. The origins of this enhanced potential drop may be found in examining the self-consistently computed charge distribution (figure 49) which shows the presence of an excess charge accumulation at the downstream  $N^-N^+$  interface, resulting in a change in sign of the curvature of the potential. The distribution of  $\Gamma$  valley carriers is displayed in figure 50, where the presence of a substantial electron transfer in the  $N^+$  region is noted. The carrier velocity (figure 51) and electron temperature (figure 52) within the  $\Gamma$  valley display the expected increases for the shorter  $N^-$  region. The electric field distribution, shown in figure 53 displays higher field values within the  $N^+$  region.

The significance of the above result is that while variations in the total charge density tend to screen variations in the doping profile of the structure, the potential drop across the  $N^-$  region may be small enough to allow a substantial drop across the downstream  $N^+$  regions thereby permitting electron transfer to occur away from the  $N^-$  region. This, of course, is not unexpected. It is implicit in the design of Gunn oscillators with doping variations assigned the task of domain nucleation sites. The current-voltage characteristics are, therefore, expected to reflect a complex set of electrical phenomena. These are displayed in figure 54.

Figure 54 displays a series of current versus voltage curves for  $N^+N^-N^+$  structures with the indicated  $N^-$  region length. Each curve displays  $J/J$  versus  $\phi/\phi_{ref}$ .  $J_{ref}$  is the computed value of current at  $\phi_{ref} = 0.25$  volts. The value of  $J_{ref}$  is indicated in the figure caption. Because of the intuitive relation between the space charge injection properties of the submicron  $N^+N^-N^+$  structure and those associated with Child's law, a power law,  $J \propto \phi^\gamma$  was extracted. It is noted that  $J_{ref}$  increases as the  $N^-$  region decreases in length. At low bias levels the current voltage relation appears to follow a power relation that is slightly less than  $J/J_{ref} = (\phi/\phi_{ref})^\gamma$  with  $\gamma = 1.7$  (as compared to a Childs' law relation where  $\gamma = 1.5$ ). At higher values of bias there is

enhanced sublinearity in the current voltage relation, due in part to electron transfer to the satellite valleys.

As indicated above, a considerable amount of electron transfer occurs in the downstream portion of the  $N^+$  region when the  $N^-$  region is decreased in length. Indeed, the detailed calculations indicate that the relative amount of electron transfer increases as the  $N^-$  region decreases in length. At first glance, this result appears to contradict all that has been discussed about transport in submicron devices. But it is not unusual when it is realized that as the  $N^-$  region decreases in length a greater fraction of the voltage drop falls across the  $N^+$  regions of the device. It is this latter feature that is responsible for the enhanced transfer. To place this in different terms, the active region length of the device increases as the  $N^-$  region becomes insignificantly small.

IV

Conclusions

The major technological interest in transient transport arises from the predictions of unusually high mean carrier velocities. The initial discussions of these high velocity values was for uniform space charge distributions, but the results were thought to be relevant for those situations where the mean carrier energy was insufficient to lead to substantial electron transfer in gallium arsenide. Thus the trend developed toward submicron scaled devices. The complication that arises in submicron devices is that the boundary conditions will be the determinant as to whether high velocities will be attained. Additionally, the constraints of current continuity dictates whether high velocities will be accompanied by high carrier densities. For example, in the case of injecting contacts the velocity of the entering carriers was significantly below that within the interior of the semiconductor. The situation was reversed for the case of partially blocking contact conditions.

Several critical results emerged from the discussion: (1) Transient overshoot in submicron structures reflects the presence of velocity overshoot and displacement current effects. It is not possible, in a simple way to separate the two, with the result that transient measurements of overshoot require extreme care in interpretation. (2) Relaxation times to steady state are dominated by the dominating boundary; e.g. either the metal contact or the critical interface. Relaxation times do not scale linearly with device length. The relaxation time scales monotonically with length. (3) Transient overshoot effects are dependent upon rise times and the time for relevant field rearrangement within the structure.

V

Acknowledgements

The authors benefited greatly from many discussions with their colleagues, particularly, G.J. Iafrate, D.K. Ferry, K. Hess, R.F. Greene, M. Silver and

M.P. Shaw. This work was supported by ONR and DARPA to whom the authors  
are grateful.

## REFERENCES

1. K. Hess et al. in VLSI Electronics, (Academic Press, N.Y.).
2. The absence of dc negative differential conductivity (NDC) from the calculations reported below does not imply the universal absence of dc NDC from transferred electron semiconductors. It is possible to envision the mathematical possibility of a boundary with a region of NDC, which when coupled to a transferred electron semiconductor, will yield a dc NDC.
3. M.P. Shaw, P.R. Solomon and H.L. Grubin, IBM J. Res. Dev. 13, 587 (1969).
4. H.L. Grubin, IEEE Trans. Electron Devices ED-25, 511 (1978).
5. A.Zur, T.C. McGill and D.L. Smith Surface Science 132, 456 (1983)
6. A.W. DeGroot, G.C. McGonigal, D.J. Thomson and H.C. Card, J. Appl. Phys. 55, 312 (1984).
7. M.P. Shaw, P.R. Solomon and H.L. Grubin, The Gunn Hilsum Effect, Academic Press, N.Y. (1979).
8. See, e.g., A. Sommerfield, Thermodynamics and Statistical Mechanics (Academic Press, N.Y., 1956) Section 43.
9. J.G. Ruch, IEEE Trans. Electron Devices, ED-19, 652 (1972).
10. H. Kroemer, IEEE Trans. Electron Devices, ED-15, 819 (1968).
11. H.L. Grubin, D.K. Ferry, G.J. Iafrate and J.. Berker, in VISI Electronics, Vol. 3. 198 (Academic Press, N.Y., 1982).
12. One of the earliest studies involving the role of the boundaries on transient transport through solutions to the Boltzmann transport equation was that of K.W. Gray J.. Pattison, H.D. Rees, B.A. Prew, R.C. Clarke and L.D. Irving, Proc. Fifth Biennial Cornell Conf. 215, (Cornell Univ. N.Y. 1975).
13. H.L. Grubin and J.P. Kreskovsky, Surface Science 132, 594 (1983).
14. H.L. Grubin and J.P. Kreskovsky. J. Vac. Sci. Tech.
15. R.K. Cook and J. Frey, IEEE Trans. Electron Devices, ED-28, 951 (1981).
16. K. Tomizawa, Y. Aveno, N. Hashizume, M. Kawashima, IEEE Proc., 129, 131 (1982).
17. J.R. East and P.A. Blakey, Proc. 1982 Workshop on the Physics of Submicron Structures, in press.

TABLE I

## PARAMETERS AND BOUNDARY CONDITIONS USED IN CALCULATION

PARAMETERS	$\Gamma$	L	COMMON
NUMBER OF EQUIVALENT VALLEYS	1	4	
EFFECTIVE MASS ( $m_e$ )	0.067	0.222	
$\Gamma$ -L SEPARATION (ev)			0.33
POLAR OPTICAL SCATTERING			
STATIC DIEL. CONST.			12.90
HIGH FREQ. DIEL. CONST.			10.92
LO PHONON (ev)			0.0354
$\Gamma$ -L SCATTERING			
COUPL. CONS. (ev/cm)			$0.800 \times 10^9$
PHONON ENERGY (ev)			0.0278
L-L SCATTERING			
COUPL. CONST. (ev/cm)			$2.0 \times 10^9$
PHONON ENERGY (ev)			0.0354
ACOUSTIC SCATTERING			
DEFORM. POT. (ev)	7.0	9.2	
NONPOLAR SCATTERING (L)			
COUPLING CONSTANT (ev/cm)			$0.300 \times 10^9$
PHONON ENERGY (ev)			0.0343

## Appendix A

### Dimensionless Equations Used in the Numerical Simulations

The Continuity Equations in Dimensionless Form:

1. Equation (3)

$$\frac{\partial n_i^*}{\partial t^*} = - \frac{\partial n_i^* v_i^{*j}}{\partial x_j^*} - n_i^* f_1 + (n^* - n_i^*) f_2 \quad (A-1)$$

2. Equation (5)

$$\frac{\partial n^*}{\partial t^*} = - \frac{\partial}{\partial x_j^*} (n_i^* v_i^{*j} + (n^* - n_i^*) v_2^{*j}) \quad (A-2)$$

The dimensional terms are identified in Table A1:

TABLE A1

$n_i^* = n_i / n_{ref}$	,	$v_i^* = v_i / v_{ref}$
$n^* = n / n_{ref}$	,	$v_2^* = v_2 / v_{ref}$
$f_1 = \Gamma_1 / \Gamma_{ref}$	,	$f_2 = \Gamma_2 / \Gamma_{ref}$
$x^* = x / x_{ref}$		$t^* = t / t_{ref}$

with

$$t_{ref} = x_{ref} / v_{ref}$$

(A-3)

$$\Gamma_{ref} = 1 / t_{ref}$$

The Momentum Balance Equations in Dimensionless Form :

I. Equation (23)

$$\frac{\partial n_i^* V_i^{*i}}{\partial t^*} = - \frac{\partial n_i^* V_i^{*j} V_i^{*i}}{\partial x_j^*} + P_f \frac{n_i^*}{m_i^*} \frac{\partial \phi^*}{\partial x_i^*} - \frac{1}{\gamma M^2} \frac{\partial}{\partial x_i^*} n_i^* R_i^* T_i^* + \frac{\mu_i^*}{Re \cdot m_i^*} \frac{\partial^2 V_i^{*i}}{\partial x_j^* \partial x_i^*} - n_i^* V_i^{*i} f_3 \quad (A-4)$$

2. Equation (24)

$$\begin{aligned} \frac{\partial (n^* - n_i^*) V_2^{*i}}{\partial t^*} = & - \frac{\partial}{\partial x_j^*} (n^* - n_i^*) V_2^{*i} V_2^{*j} + P_f \frac{(n^* - n_i^*)}{m_2^*} \frac{\partial \phi^*}{\partial x_i^*} - \frac{1}{\gamma M^2} \frac{\partial}{\partial x_i^*} (n^* - n_i^*) R_2^* T_2^* \\ & + \frac{\mu_2^*}{Re \cdot m_2^*} \frac{\partial^2 V_2^{*i}}{\partial x_j^* \partial x_i^*} - (n^* - n_i^*) V_2^{*i} f_4 \end{aligned} \quad (A-5)$$

The dimensionless terms and parameters are identified in Table A2 :

TABLE A2

$\phi^* = \phi / \phi_{ref}$	
$m_i^* = m_i / m_{ref}$	, $m_2^* = m_2 / m_{ref}$
$R_i = k_B / m_i$	, $R_2 = k_B / m_2$
$R_{ref} = k_B / m_{ref}$	
$R_i^* = R_i / R_{ref} = \frac{1}{m_i^*}$	, $R_2^* = R_2 / R_{ref} = \frac{1}{m_2^*}$
$f_3 = \Gamma_3 / \Gamma_{ref}$	, $f_4 = \Gamma_4 / \Gamma_{ref}$
$\mu_i^* = \bar{\mu}_i / \bar{\mu}_{ref}$	, $\mu_2^* = \bar{\mu}_2 / \bar{\mu}_{ref}$
$P_f = e \psi_{ref} / m_{ref} V_{ref}^2$	
$M = V_{ref} / V_0$	
$V_0 = \left( \frac{5}{3} R_{ref} T_{ref} \right)^{1/2}$	
$\gamma = 5 / 3$	
$Re = x_{ref} V_{ref} n_{ref} m_{ref} / \bar{\mu}_{ref}$	

with

The Energy Balance Equations in Dimensionless Form :

I. Equation (30)

$$\frac{\partial n_i^* T_i^*}{\partial t^*} = - \frac{\partial n_i^* T_i^* V_i^{*j}}{\partial x_j^*} - (\gamma - 1) n_i^* T_i^* \frac{\partial V_i^{*j}}{\partial x_j^*} + \frac{1}{Re \cdot Pr} \frac{1}{m_i^* c_{V_i}^*} \frac{\partial}{\partial x_j^*} \left( \kappa_i^* \frac{\partial T_i^*}{\partial x_j^*} \right) - n_i T_i f_5 + (n - n_i) T_2 f_6 \\ + \gamma(\gamma - 1) M^2 \frac{V_i^{*j} V_i^{*j}}{2c_{V_i}^*} (2n_i^* f_3 - n_i^* f_1 + (n^* - n_i^*) f_2) \quad (A-6)$$

2. Equation (31)

$$\frac{\partial (n^* - n_i^*) T_2^*}{\partial t^*} = - \frac{\partial (n^* - n_i^*) T_2^* V_2^{*j}}{\partial x_j^*} - (\gamma - 1) (n^* - n_i^*) T_2^* \frac{\partial V_2^{*j}}{\partial x_j^*} + \frac{1}{Re \cdot Pr} \frac{1}{m_2^* c_{V_2}^*} \frac{\partial}{\partial x_j^*} \left( \kappa_2^* \frac{\partial T_2^*}{\partial x_j^*} \right) \\ + \gamma(\gamma - 1) M^2 \frac{V_2^{*j} V_2^{*j}}{\partial x_j^*} (2(n^* - n_i^*) f_4 + n_i^* f_1 - (n^* - n_i^*) f_2) - (n^* - n_i^*) T_2^* f_7 + n_i^* T_1^* f_8 \quad (A-7)$$

The dimensionless terms and parameters are identified in Table A3 :

TABLE A3

$$f_5 = \Gamma_5 / \Gamma_{ref}$$

$$f_6 = \Gamma_6 / \Gamma_{ref}$$

$$f_7 = \Gamma_7 / \Gamma_{ref}$$

$$f_8 = \Gamma_8 / \Gamma_{ref}$$

$$\kappa_i^* = \kappa_i / \kappa_{ref}$$

$$\kappa_2^* = \kappa_2 / \kappa_{ref}$$

$$C_{V_1} = \frac{3}{2} R_1$$

$$C_{V_2} = \frac{3}{2} R_2$$

$$C_{V_{ref}} = \frac{3}{2} R_{ref}$$

$$C_{V_1}^* = C_{V_1} / C_{V_{ref}}$$

$$C_{V_2}^* = C_{V_2} / C_{V_{ref}}$$

$$P_r = C_{V_{ref}} \tilde{\mu}_{ref} / \kappa_{ref}$$

Poisson's Equation in Dimensionless Form :

I. Equation (1)

$$\frac{\partial^2 \phi^*}{\partial x_j^{*2}} = S_n (n_i^* + (n^* - n_i^*) - n_o^*) \quad (A-8)$$

The dimensionless terms and parameters are identified in Table A4 :

TABLE A4

$$S_n = \frac{x_{ref}^2 n_{ref}}{\phi_{ref} \epsilon}$$

$$n_o^* = n_o / n_{ref}$$

TABLE A5  
Boundary Conditions in Dimensionless Form

**Equation (32)**

$$\frac{\partial n^*}{\partial x^*} = \frac{\partial n_1^*}{\partial x^*} = \frac{\partial V_1^*}{\partial x^*} = \frac{\partial V_2^*}{\partial x^*} = \frac{\partial T_1^*}{\partial x^*} = \frac{\partial T_2^*}{\partial x^*} = 0 \quad ] \quad \text{at} \quad x = 0, \phi^* = 0 \\ x = L, \phi^* = \phi_0$$

**Equation (40)**

$$\frac{\partial^2 n^*}{\partial x^{*2}} = \frac{\partial^2 n_1^*}{\partial x^{*2}} = 0, \quad V_1^* = \mu_c^* \frac{\partial \phi^*}{\partial x^*}, \quad \mu_c^* = \frac{\mu_c \phi_{ref}}{x_{ref} V_{ref}}, \quad \frac{\partial V_2^*}{\partial x^*} = 0, \quad T_1 = T_c^*, \quad \frac{\partial T_2^*}{\partial x^*} = 0, \quad \phi^* = 0$$

**Equation (41)**

$$\frac{\partial^2 n^*}{\partial x^{*2}} = \frac{\partial^2 n_1^*}{\partial x^{*2}} = \frac{\partial^2 V_1^*}{\partial x^{*2}} = \frac{\partial^2 V_2^*}{\partial x^{*2}} = \frac{\partial^2 T_1^*}{\partial x^{*2}} = \frac{\partial^2 T_2^*}{\partial x^{*2}} = 0, \quad \phi^* = 0$$

**Equation (53)**

$$n^* = n_0^*, \quad n_1^* = \frac{f_2}{f_1 + f_2} n_0^*, \quad \frac{\partial^2 V_1^*}{\partial x^{*2}} = \frac{\partial V_2^*}{\partial x^*} = 0, \quad T_1^* = T_c^*, \quad \frac{\partial T_2^*}{\partial x^*} = 0, \quad \phi^* = 0$$

where  $f_1$  and  $f_2$  are evaluated at  $T = T_{ref}$ .

TABLE A-6  
DIMENSIONLESS REFERENCE QUANTITIES

FIGURES	1-4	9-19	21-27	28-36	37-53
Device Length, (microns)	1.0	1.0	5.0	0.25	1.0
$x_{ref}$ (microns)	1.0	1.0	5.0	0.25	0.75
$n_{ref}$ ( $\text{cm}^{-3}$ )	$5. \times 10^{15}$	$5. \times 10^{15}$	$5. \times 10^{15}$	$5. \times 10^{15}$	$1. \times 10^{17}$
$t_{ref}$ (psec)	1.0	1.0	5.0	0.25	0.75
$\Gamma_{ref}$ ( $10^{12}/\text{sec}$ )	1.0	1.0	0.2	4.0	1.33
$\kappa_{ref}$ (Joules/ $^{\circ}\text{K} \cdot \text{cm} \cdot \text{sec}$ )	$2.0 \times 10^{-6}$	$2.0 \times 10^{-6}$	$2.0 \times 10^{-6}$	$2.0 \times 10^{-6}$	$4.14 \times 10^{-5}$
$\hat{\mu}_{ref}$ (gm/cm $\cdot$ sec)	$5.74 \times 10^{-11}$	$5.74 \times 10^{-11}$	$5.74 \times 10^{-11}$	$5.74 \times 10^{-11}$	$1.15 \times 10^{-9}$
DIMENSIONLESS PARAMETERS					
Re	53.17	53.17	265.86	13.29	39.88
Sn	8.16	8.16	204.00	0.51	91.84
$\psi^*$	0.6	0.6	0.5	0.15	1.0
	1.0	1.0	1.0	0.25	
	2.0	2.0	1.5	0.50	
			2.0		
			3.0		
$T_c^*$	N.A.	1.0	4.0	1.0	1.0
$\mu_c^*$	N.A.	1.56	0.08	6.25	N.A.

COMMON PARAMETERS	COMMON DIMENSIONLESS PARAMETERS
$v_{ref} = 10^8 \text{ cm/sec}$	$m_1^* = 1$
$\phi_{ref} = 1.0 \text{ volts}$	$m_2^* = 3.31$
$m_{ref} = 6.10 \times 10^{-29} \text{ gm}$	$R_1^* = 1.0$
$k_B = 1.38 \times 10^{-23} \text{ J}/^{\circ}\text{K}$	$R_2^* = 1.0$
$R_{ref} = 2.26 \times 10^5 \text{ J}/^{\circ}\text{K} \cdot \text{gm}$	$\mu_1^* = 1.0$
$T = 300 \text{ }^{\circ}\text{K}$	$\mu_2^* = 1.0$
$V_a = 3.36 \times 10^7 \text{ cm/sec}$	

Figure Captions

- Figure 1.** Magnitude of the current transient (equation 8) following application of a sudden change in bias. Parameters for this calculation are listed in the appendix. The results of this calculation are qualitatively similar to those obtained in many studies, the first for GaAs being Ruch (Ref. 9). The terminus of each calculation reflects the physical time required for steady state. The longest time duration is that associated with the lowest bias level. For this calculation 2.0 volts corresponds to an average field of 20kv/cm 1.0 volts yields 10kv/cm, etc.
- Figure 2.** Distribution of  $\Gamma$ -valley carriers as a function of time for the parameters of figure 1. Note the delay in electron transfer, a delay that is shortest for the highest bias level.
- Figure 3.** Transient distribution of temperature following application of a sudden change in bias for the parameters of figure 1. The presence of a temperature overshoot is noted, a feature resulting from the enhanced scattering at elevated temperatures. The inset displays the temperature during the first 0.4ps and demonstrates through application of equation 30. of the onset of scattering.
- Figure 4.** Transient  $\Gamma$ -valley velocity distribution for the parameter of figure 1. The initial velocity peak corresponds closely in value to the peak current transient prior to electron transfer. The decreased velocity represents enhanced scattering at elevated temperatures.
- Figure 5.** Steady state field dependent velocity for electrons in  $p$ -valley of gallium arsenide for the parameters of Table 1. Also, steady state mean field dependent electron velocity,  $V_n$  (See equation 6).
- Figure 6a.** Schematic representation of a current field relation within the interior of the semiconductor,  $n_o V_o$ ; and a possible current field relation at the first computed point following the boundary of the semiconductor,  $n_o V C_1$  and  $C_2$  represent constant current levels in the device. The cathode field for the low current level case is denoted by  $F_{cl}$ . The neutral interior field is represented by  $F_{bl}$ . Similar remarks apply to the higher current level. (It is important to note that studies using the drift and diffusion equations indicate that for  $\phi \approx 0$  at the boundary, the transition from cathode depletion to cathode accumulation requires all three characteristics,  $n_o V_c$ ,  $N V_c$  and  $n_o V_n$  to intersect at the same point (Ref. 10).

**Figure 6b.** Schematic of possible cathode adjacent depletion and accumulation, followed by broad depletion, for the two bias current levels of figure 6a.

**Figure 7a.** As in figure 6a but for a different set of  $n_o V_c$  and  $n_c V_c$  curves.

**Figure 7b.** Schematic of possible cathode adjacent depletion and accumulation followed by broad accumulation for the two bias levels of figure 7a.

**Figure 8.** Velocity versus distance for the uniform field velocity transient. For these calculations, as in figures 1 through 4, velocity transient is in response to a sudden change in electric field. Initial velocity is zero and

(From Ref. 11)

**Figure 9.** Repeat of figure 5, plus the cathode current field relation for the accumulation layer boundary.

**Figure 10.** Steady state distribution of field within a one-micron long GaAs element at three bias values. (See appendix for boundary conditions). Electron transfer occurs downstream from the cathode resulting in a downstream accumulation of carriers. (See also Ref. 2).

**Figure 11.** Distribution of total and  $\Gamma$  valley carrier density for the parameters of figure 10. Electron transfer begins within 0.2 microns downstream from the cathode. By comparing figures 2 and 11, it is noted that electron transfer at 6, 10 and 20Kv/cm significantly lags the uniform field value.

**Figure 12.** Distribution of  $\Gamma$  valley velocity for the parameters of figure 10. At a bias of 2 volts and a field of 20 Kv/cm the  $\Gamma$  valley velocity is slightly in excess of the uniform field calculation. At a bias of 1 volt and a field of 10 Kv/cm, the difference between the nonuniform and uniform field velocity is even greater. This excess is a consequence of a lower value of electron temperature at these given field values.

**Figure 13.** Temperature distribution within the  $\Gamma$  valley for the parameters of figure 10. See comments associated with figure 12.

**Figure 14.** Steady state current density versus applied voltage and average field for the 1.0 cm long structure with the parameters of figure 10.

**Figure 15.** Magnitude of current transient following application of a step change in bias to 1.0volt for a 1.0μm long device with the parameters of figure 10. Current peak is similar to that of figure 1. Steady state velocity is above that of the uniform field case. It is noted that the time to steady state is approximately 50% longer than that associated with the steady state calculation of figure 1.

**Figure 16.** Distribution of electric field at successive instants of time following application of a step change in voltage for the parameters of figure 15. During the first time step, the field increases from its steady state value at a bias of 0.01 volt, by an amount equal to 9.99 Kv/cm [ $(1-0.01)V / 1\mu m$ ]. Subsequent time dependence shows a space charge layer propagating toward the anode. During the first 0.5 ps the field downstream from the propagating accumulation layer is spatially uniform. Within this region transients are governed by the uniform field velocity overshoot transients. During the long-time transients, electron transfer occurs and relaxation differs from that of the uniform field transient.

**Figure 17a & b**

Displacement current at 5 instants of time for the parameters of figure 15. Initial displacement currents are strong and accompany the moving accumulation layer.

**Figure 17c & d**

Particle current,  $J_p = eNV$  at five instants of time for the parameters of figure 15. Strong spatial variations dominate the initial cathode region and reflect the propagating accumulation layer. Downstream from the propagating accumulation layer, the particle current transient almost completely traces the total current transient for the first 0.5ps.

**Figure 18.** Transient distribution of total charge following application of a step change in potential for the parameters of figure 15. It is noted that downstream from the propagating accumulation layer, the charge distribution is flat as reflected, additionally in the flat field profile of figure 16a. Space charge accumulation occurs during the longer time interval.

**Figure 19.** Transient distribution of  $\Gamma$  valley carrier density for the parameters of figure 15. It is noted that within the first 0.5 ps, very little transfer occurs.

**Figure 20.** Transient distribution of the  $\Gamma$  valley velocity following application of a voltage pulse for the parameters of figure 15. The velocity layer propagates and shows a tendency to lead the transient changes in the  $\Gamma$  valley carrier density. Downstream, the velocity transient is relatively uniform for  $t < 10.5$ ps and tends to follow the uniform field transient of figure 4. Differences from the uniform field calculations occur during the long-time transient.

- Figure 21.** Steady state distribution of electric field within the interior of a 5.00 micron-long uniformly doped GaAs structure. Parameters are given in the appendix. The bias levels are 0.5, 1.0, 1.5 and 2.0 volts. It is noted that the field at the cathode, in response to the boundary conditions, is qualitatively different than that associated with figures 10 through 20. Here, the field decreases from the cathode to the anode. In the vicinity of the anode the field is uniform. The net decrease in field is consistent with a cathode region partially depleted of carriers. It is noted that prior to reaching the downstream portion of the structure, the field displays a minimum followed by a change in slope. This change in slope represents the presence of a region of local charge accumulation.
- Figure 22.** Distribution of total and gamma valley carriers within the device for the parameter of figure 21. It is noted that there is a net depletion of total charge within the vicinity of the cathode and that this partial depletion is reduced as the bias level is raised. For all bias levels the  $\Gamma$  valley population is below that of the total carrier density.
- Figure 23.** Steady state velocity distribution of  $\Gamma$  valley carriers for the parameters of figure 21. It is noted that unlike the velocity distribution for the  $\Gamma$  valley electrons of an injecting contact where the carrier velocity is greatest at the anode, for this length structure, the  $\Gamma$  valley velocity is greatest at the cathode. It is further noted that the change in cathode velocity with increased bias is very small at high bias levels and reflects the presence of current saturation.
- Figure 24.** Steady state current voltage characteristics  $j(\phi)$  for the partially depleted cathode structure with a length of 5.00 microns. Parameters are those of figures 21. Of significance here is that saturation in current occurs at an average field significantly below that of the 1.0 $\mu$ m device, and that the current in saturation is approximately 1/2 that of the 1.0 $\mu$ m long device. Also shown is the cathode current field relation  $J_c(F_e)$  and the neutral field characteristic.
- Figure 25.** Neutral current field relation for gallium arsenide  $n^o V$ , the cathode current field relation  $n^o V$  and the neutral cathode field relation  $n^o V$ . All three curves show a tendency to intersect with the negative differential mobility region. When they do, as discussed in reference 11, a condition for a domain instability occurs. Parameters are those of figure 21.
- Figure 26a.** Transient electric field profile showing nucleation and propagation of high field domain. It is noted that propagation is accompanied by low downstream field values and residual cathode adjacent depletion. Parameters are those of figure 21.
- b. Details of transiting domains.

- Figure 27.** Current transient following application of a step change in potential to 3.0 volts. Initial transient is a reflection of nonequilibrium transient transport. The steady long-time transient reflects the nucleation, propagation and the quenching of a propagating high-field dipole layer. Parameters are those of figure 21.
- Figure 28.** Steady state distribution of electric field for 0.25 micron uniform structure with injecting cathode contacts. Average field across structure is the same as that of figure 10 for 1.0 micron-long device. Parameters for this calculation are listed in the appendix.
- Figure 29.** Distribution of total and  $\Gamma$  valley carrier density. Only marginal transfer occurs for the lowest bias level. Substantial transfer occurs at the higher bias levels. At all bias levels, injection level is extremely high, and  $N_p$  exceeds  $N_o$ . Parameters are those of figure 28.
- Figure 30.** Steady state distribution of the  $\Gamma$  valley carrier velocity at three values of bias. It is noted that the velocity increases from cathode to anode, corresponding to a decrease in the  $\Gamma$  valley carrier density. Parameters are those of figure 28.
- Figure 31.** Steady state current density versus applied voltage and average field for a 0.25  $\mu\text{m}$  long structure with injecting contacts. Excessively high current levels are primarily due to high levels of space charge injection. Also shown is the cathode current field relation. Parameters are those of figure 28.
- Figure 32.** Magnitude of current transient following application of a step change in potential for a 0.25  $\mu\text{m}$  long device with injecting contacts. Current peak exceeds that of both the uniform field structure and the 1.0 $\mu\text{m}$  device with injecting contacts. Steady state current level is above that of the 1.0 $\mu\text{m}$  device with injecting contacts. Note: the time to relaxation is 4.9ps which is approximately 40% less than that of the 1.0 $\mu\text{m}$  device with the same average field. Given the fact that the structure is 0.25 $\mu\text{m}$  in length, this result provides evidence that the relaxation effects are influenced by nontransit time effects. Parameters are those of figure 28.
- Figure 33.** Time dependent evolution of electric field distribution for the 0.25 $\mu\text{m}$  device subject to a step change in bias of 0.25 volts. During the first 0.1ps, the field propagates downstream from the cathode, indicating a propagating accumulation layer. The field downstream from the cathode is relatively uniform. To satisfy the constraints of constant voltage across the device there are displacement current contributions at the bottom half of the structure and account for much of the difference in the peak currents associated with the 0.25 $\mu\text{m}$  and 1.0 $\mu\text{m}$  devices. Parameters are those of figure 32.

- Figure 34.** Time dependent evolution of total carrier density within the  $0.25\mu\text{m}$  device. Initial propagation characteristics are similar to those of the  $1.0\mu\text{m}$  devices. Proximity effects are introduced after 0.1ps and differences in the  $0.25\mu\text{m}$  and  $1.0\mu\text{m}$  calculations arise. Parameters are those of figure 32.
- Figure 35.** Time dependent evolution of the  $\Gamma$  valley for the parameters of figure 32. Note the electron transfer after 2ps.
- Figure 36.** Distribution of  $\Gamma$  valley carrier velocity following application of a step change in bias of  $0.25\text{v}$ . The initial velocity distribution is similar to that found in the  $1.0\mu\text{m}$  transient study. Downstream velocity values during the first 0.1ps are higher than that of the  $1.0\mu\text{m}$  calculation and correspond in part to the presence of slightly higher downstream fields. Parameters are those of figure 32.
- Figure 37.** Donor distribution of the  $\text{N}^+\text{N}^-\text{N}^+$  structure used in the study. In the calculations, the width of the  $\text{N}^-$  region (defined at a donor level of  $10^{16}/\text{cm}^3$ ) varied from  $0.416\mu\text{m}$  to  $0.116\mu\text{m}$ . In all calculations the width of the upstream  $\text{N}^+$  region was unchanged.
- Figure 38.** Time dependent current following application of a step change in bias to 1.0 volts for the  $\text{N}^+\text{N}^-\text{N}^+$  structure with an  $\text{N}^-$  region of  $0.416\mu\text{m}$  (From Ref. 14). The structure of the current profile displays significant quantitative differences from that of the uniform donor calculations. First, the peak in the current occurs within 0.10ps, which is below that of the uniform donor calculations. Second, there is a strong current minima, followed by relaxation. Steady state requires approximately 15ps. Parameters for the calculation are listed in the appendix.
- Figure 39.** Spatial distribution of particle current at different instants of time for the parameters of figure 38. Also shown is the donor distribution. The largest spatial variation in particle current occurs near the interfacial boundaries.
- Figure 40.** Distribution of electric field following application of a bias pulse. Note the strong temporal variation in field at the upstream interface and within the  $\text{N}^-$  region. The propagation characteristics associated with the electric field distribution under uniform donor conditions are camouflaged here by the spatial rearrangements within the interface region (Ref. 14). In addition, note the presence of the strong regarding field, one that is characteristic of  $\text{N}^+\text{N}^-\text{N}^+$  structures (see also Ref. 15). Parameters are as in figure 38.
- Figure 41.** Spatial distribution of potential within the  $\text{N}^+\text{N}^-\text{N}^+$  structures at different instants of time. Note that in the steady state approximately  $1.0\text{v}$  falls across the  $0.41\mu\text{m}$  long region. It may

**Figure 41.(cont.)**

be anticipated that this will lead to large scale injection into the  $N^-$  region. Parameters are as in figure 38.

**Figure 42.** Time dependent evolution of the total carrier concentration within the  $N^+N^-N^+$  structure (Ref. 14). During the early transient, space charge layer displays a characteristic propagation downstream from the cathode, as seen in the uniform donor calculations. Insofar as the form of the electric field profile is controlled by differences between  $n$  and  $n_0$ , these propagation characteristics lose the distinction that emerges from the uniform donor calculations. Note: the injection level is almost an order of magnitude higher than the  $N^-$  donor level. Parameters are as in figure 38.

**Figure 43.** Time dependent evolution of the distribution of satellite valley carrier. An inconsequential number of carriers are scattered into the satellite valley during the early transient ( $t < 0.45\text{ps}$ ). Electron transfer is apparent in the steady state. Parameters are as in figure 38.

**Figure 44.** Time dependent evolution of the spatial distribution of the  $\Gamma$  valley carrier velocity. Note the initial propagation of the velocity layer downstream from the  $N^+N^-$  interface. It is noted that while the peak field for this calculation is approximately  $44\text{Kv/cm}$ , the peak velocity is only near  $5 \times 10^7\text{cm/sec}$ , a value considerably below that of the  $0.25\text{ micron}$  long uniform donor calculations. It is also noted that during the early time transient the carriers outside the  $N^-$  region drift in a direction opposite to carriers within the  $N^-$  region. Here, displacement current contributions dominate. Parameters are as in figure 38.

**Figure 45.** Time dependent evolution of the spatial distribution of  $\Gamma$  valley temperature within the  $N^+N^-N^+$  structure. It is noted that in steady state an apparent cooling of the carriers occurs within the region near the  $N^+N^-$  interface where a large excess of carriers is present (see also Ref. 15). Parameters are as in figure 38.

**Figure 46.** Transient distribution of total and  $\Gamma$  valley carrier density at two points within the  $N^+N^-N^+$  structure. At  $0.2\mu\text{m}$ , there is no electron transfer of any significance. At  $0.5\mu\text{m}$ , electron transfer occurs at the end of the transient. Parameters are as in figure 38.

**Figure 47.** Donor concentration for  $N^+N^-N^+$  structure with three different  $N^-$  region lengths. For A,  $L_{N^-} = 0.116\mu\text{m}$ , for B,  $L_{N^-} = 0.266\mu\text{m}$ , for C,  $L_{N^-} = 0.416\mu\text{m}$ . The calculations for C have already been presented and are included for completeness.

- Figure 48.** Steady state distribution of potential for structures A, B and C subject to a bias of 1.0 volt. For structures B and C and potential drop is confined mainly to the N<sup>-</sup> region. For structure A a significant fraction of potential falls across the N<sup>-</sup> region.
- Figure 49.** Steady state distribution of total carrier concentration for structures A, B and C. Note, for all three structures, the free carrier concentration closely traces the donor variation.
- Figure 50.** Distribution of  $\Gamma$  valley carriers. The least amount of electron transfer occurs for the widest structure C. For structure A transfer continues to the anode contact and is a consequence of a large potential falling across the downstream N<sup>+</sup> region.
- Figure 51.** Distribution of  $\Gamma$  valley carrier velocity for structures A, B and C. Peak velocity gradually increases as the N<sup>-</sup> region decreases in length. Additionally, the up and downstream carrier velocity increases as the N<sup>-</sup> region decreases in length.
- Figure 52.** Distribution of  $\Gamma$  valley electron temperature for the three structures A, B and C. Electron temperature distribution is qualitatively different for structure A. A longer downstream N<sup>+</sup> region is needed before the temperature approaches 300°K.
- Figure 53.** Steady state distribution of electric field for the three structures A, B and C. It is noted that for structure A a large residual field remains across the downstream N<sup>+</sup> layer.
- Figure 54.** Steady state current voltage characteristics for the three structures A, B and C. The current level for structure A is higher than that of B which in turn is higher than C. Note that the low field resistance of structure A is the lowest of the three. Also included for reference are the Child's law  $J = \phi^{1.5}$  curve and  $J = \phi$  curves.

FIG. I

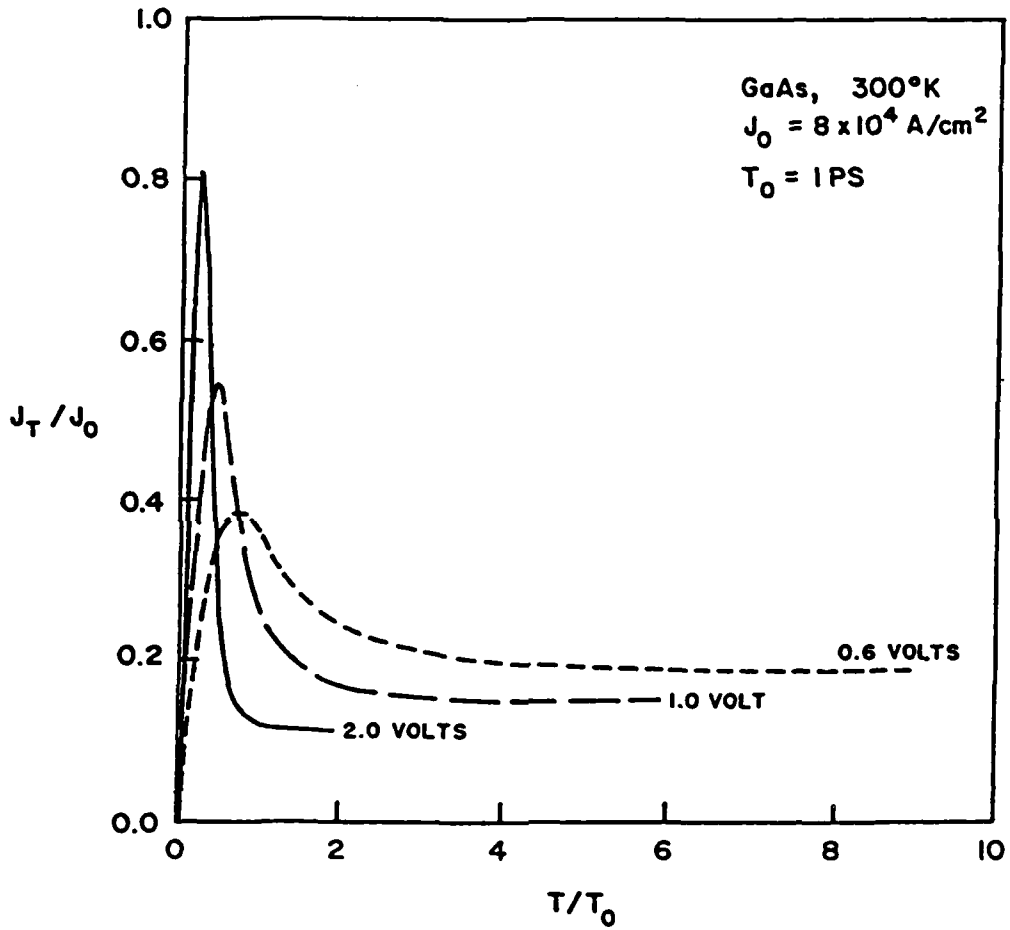


FIG. 2

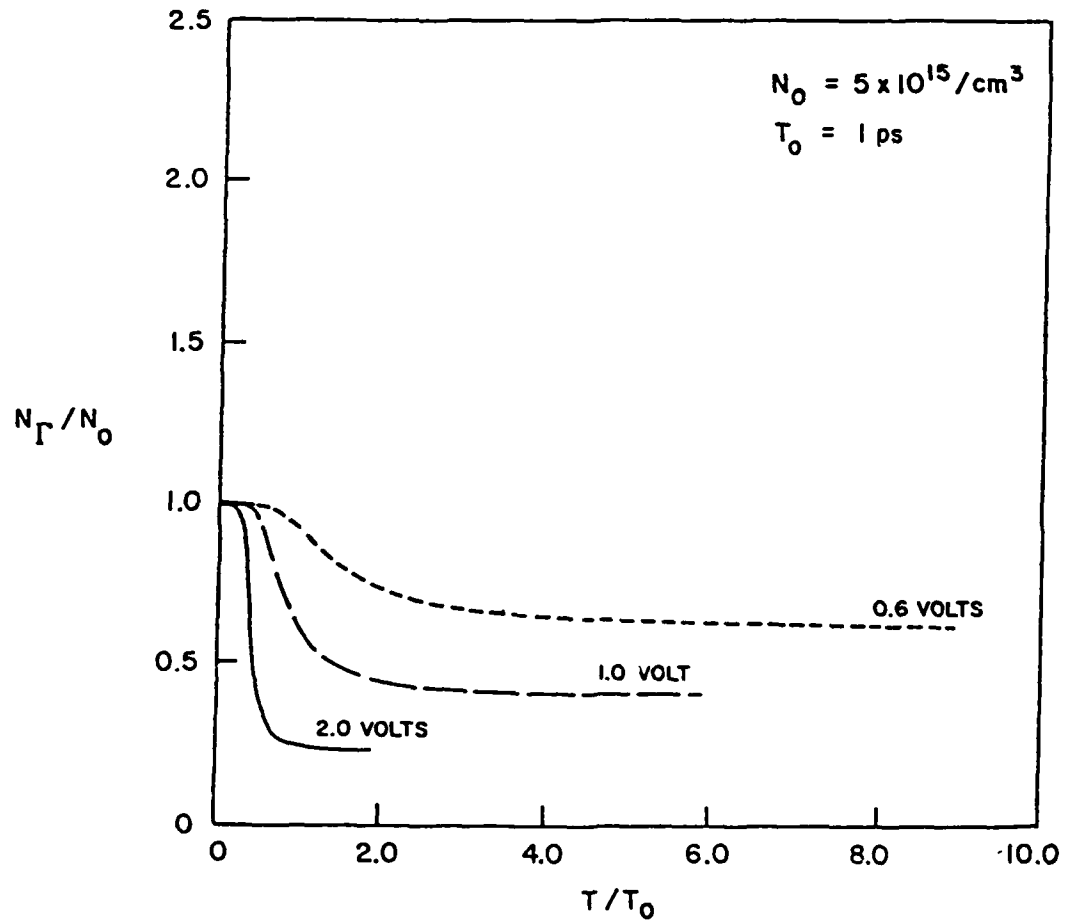


FIG. 3

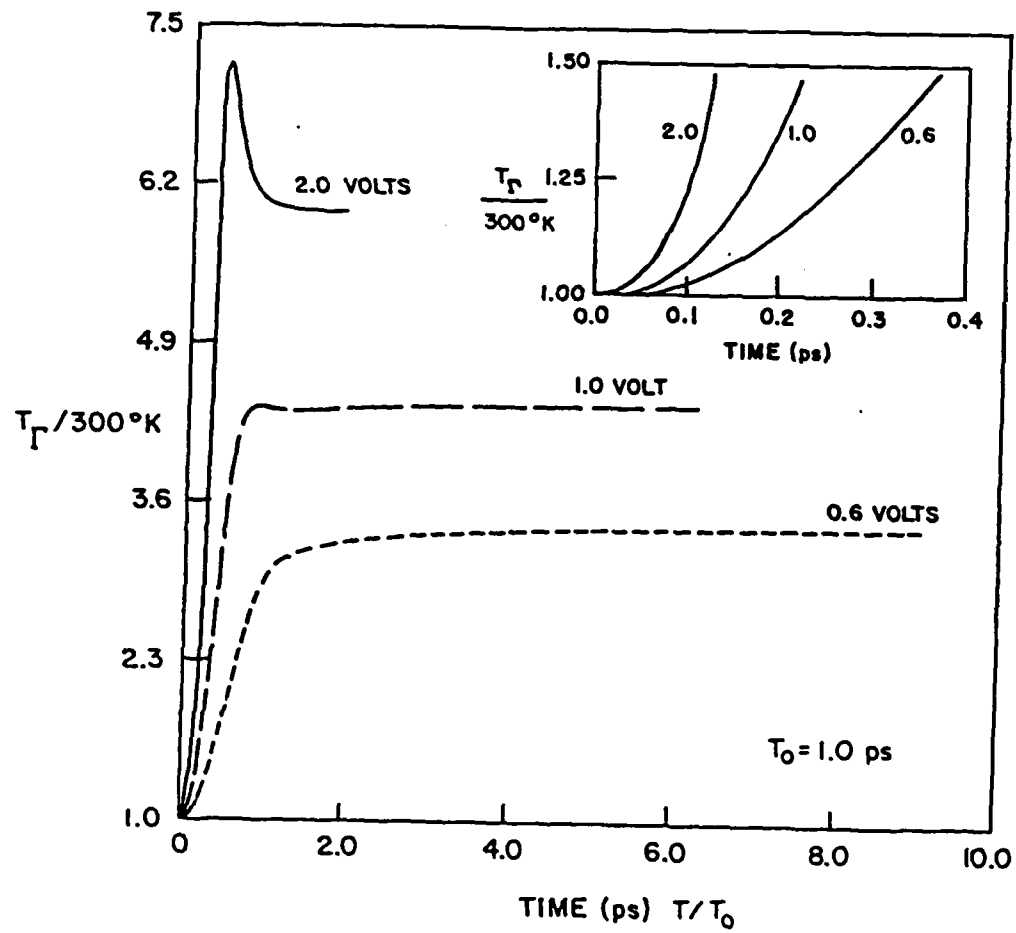


FIG. 4

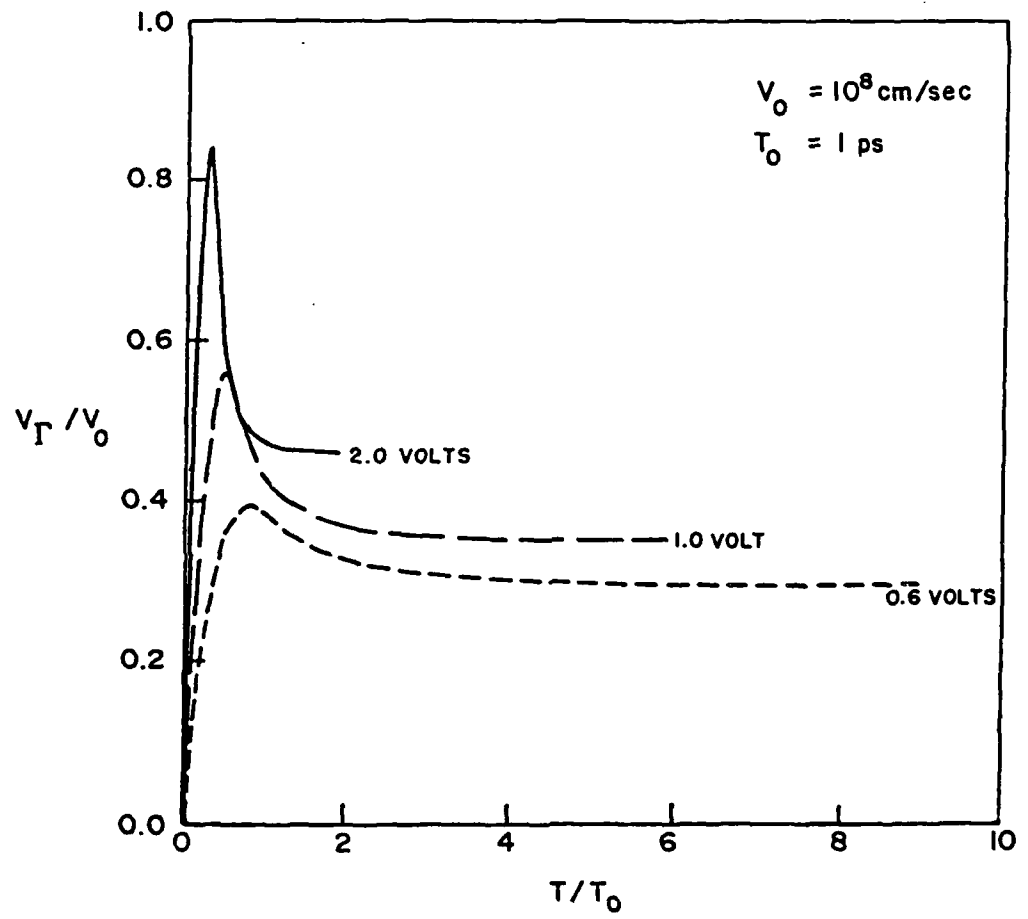


FIG. 5

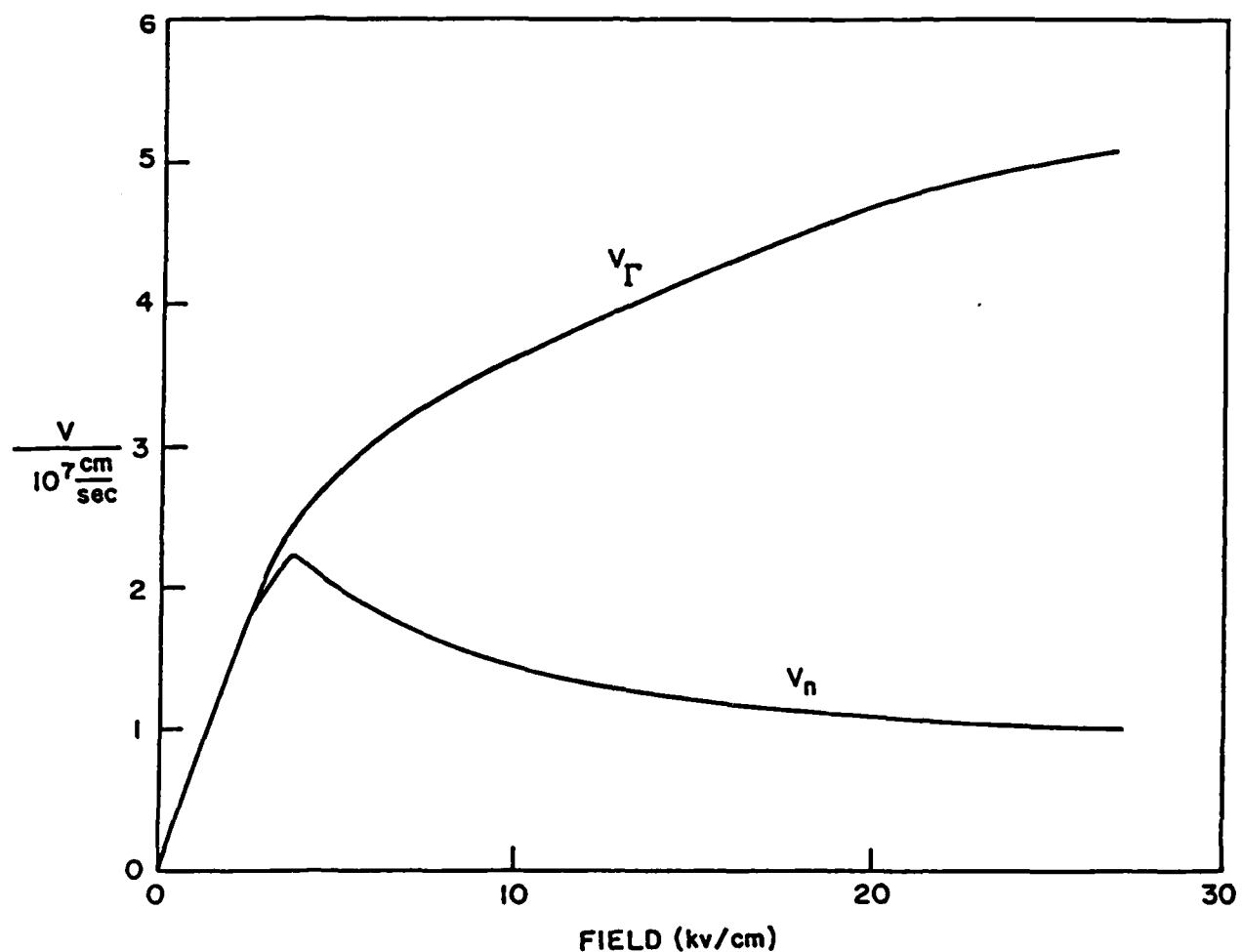


FIG. 6

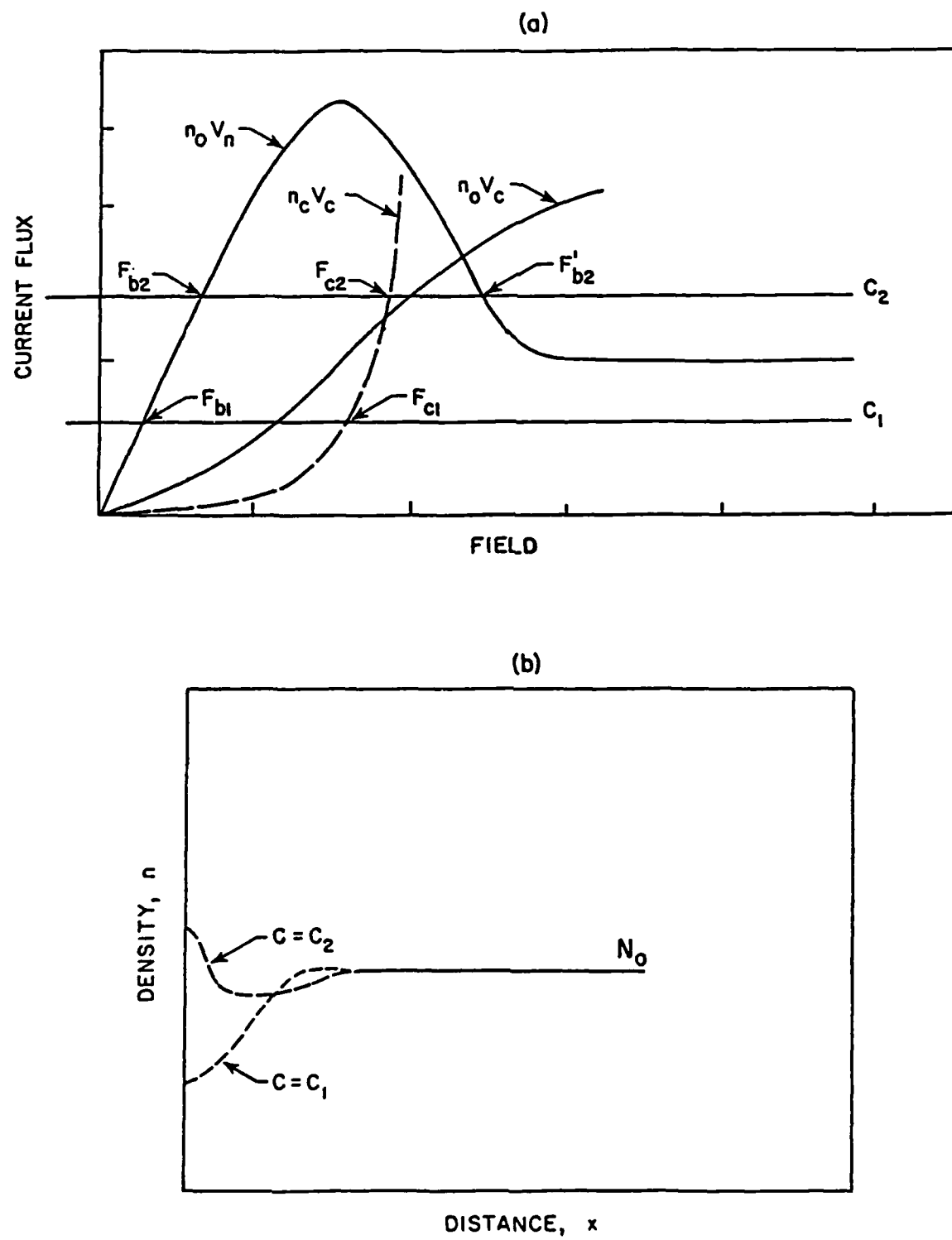


FIG. 7

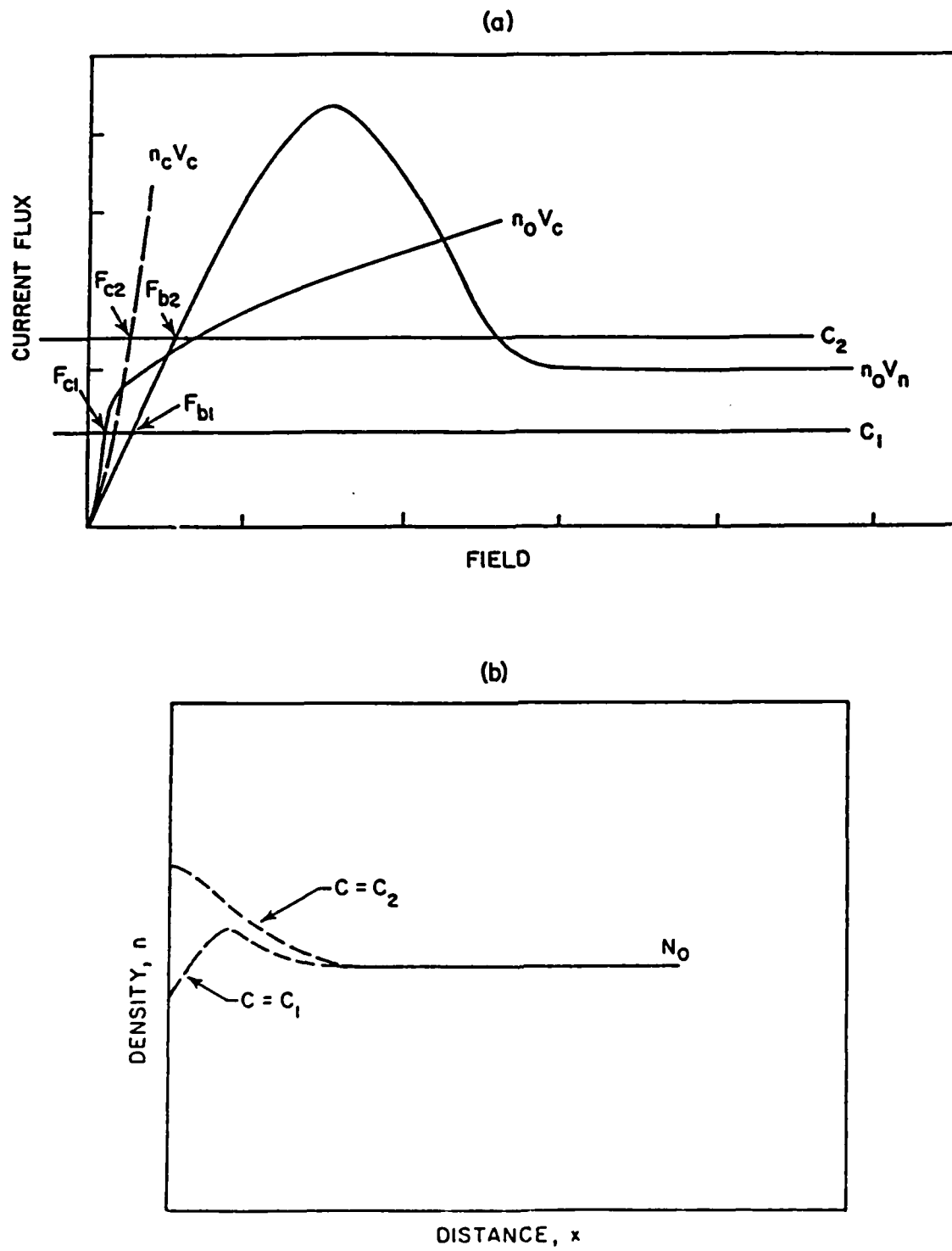


FIG. 8

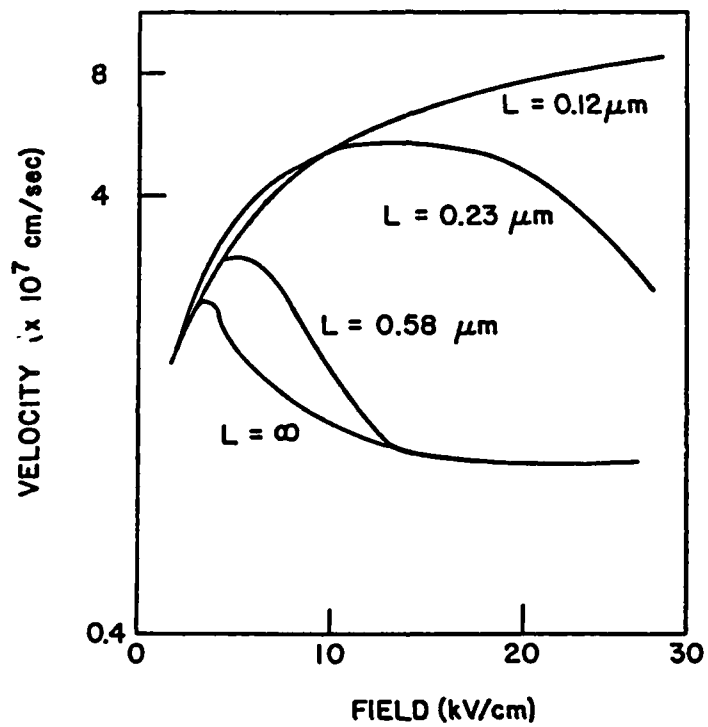


FIG. 9

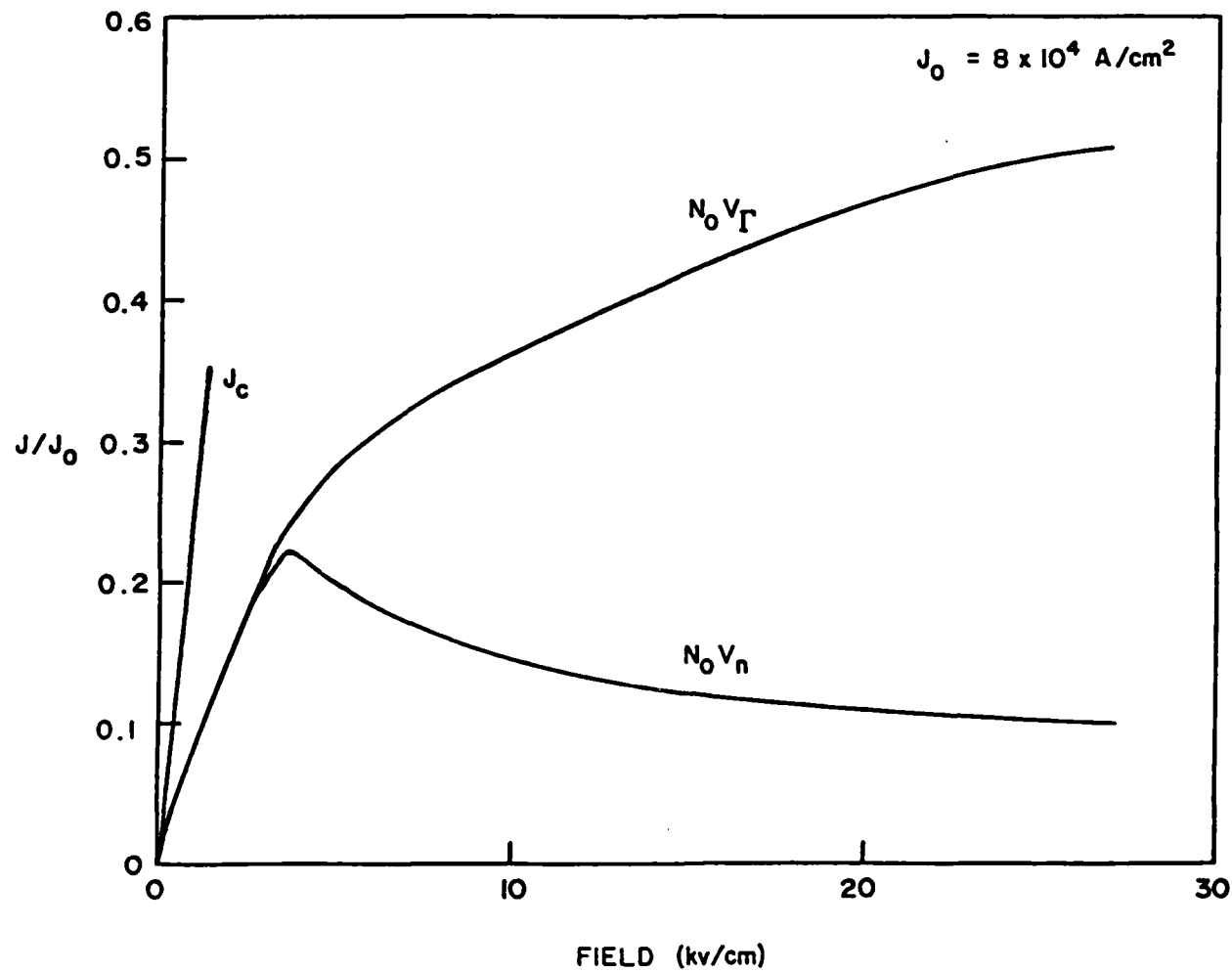


FIG. 10

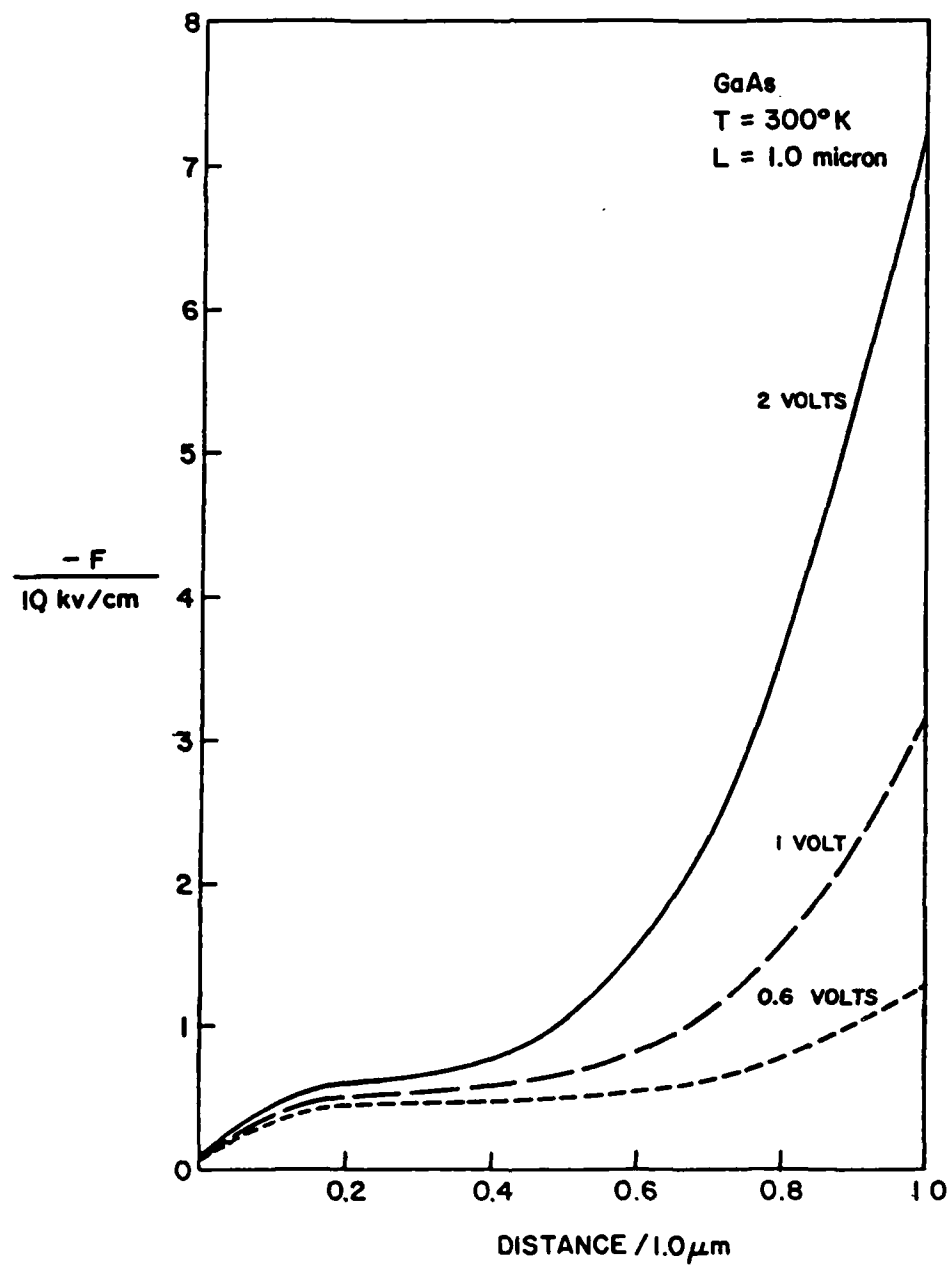


FIG. 11

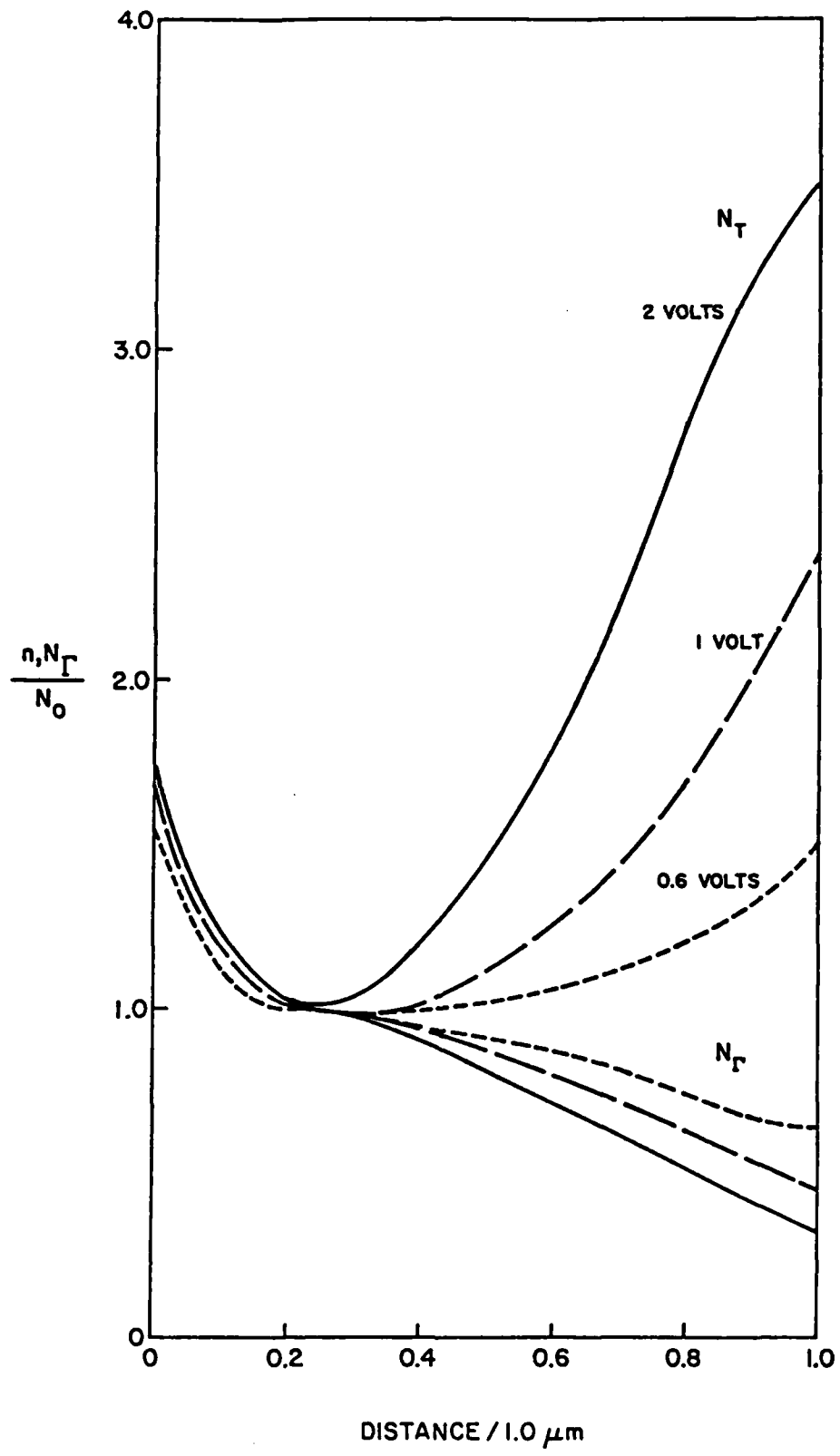


FIG. 12

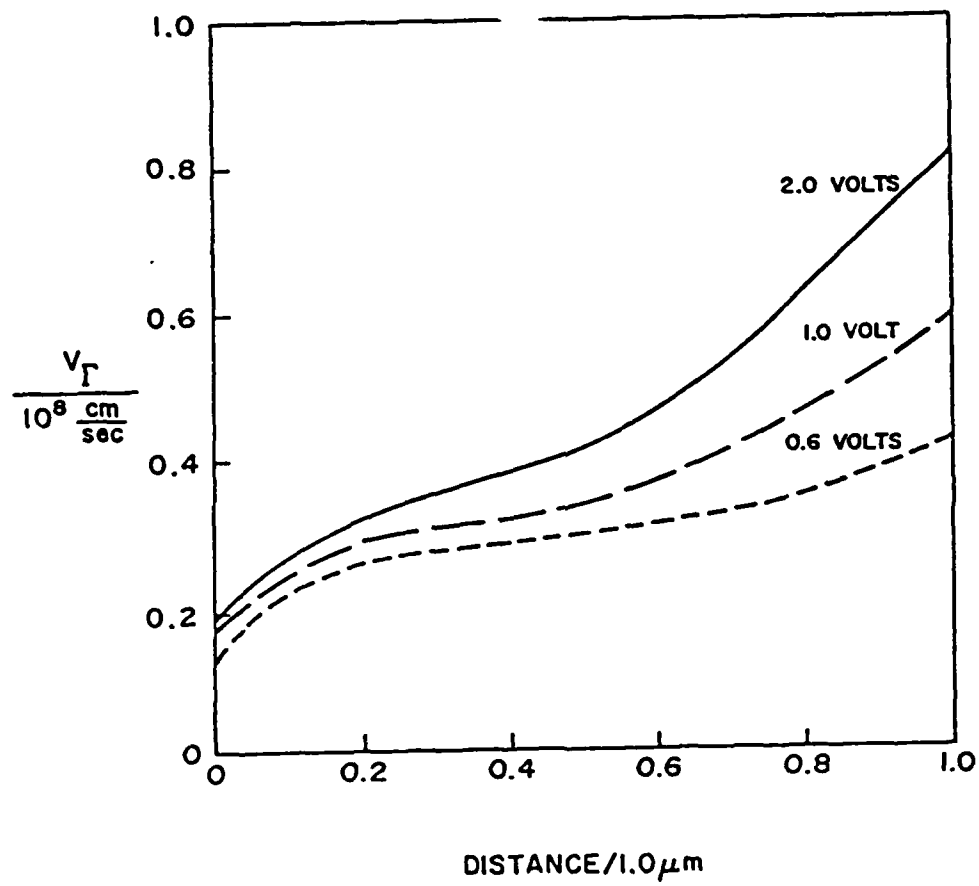


FIG. 13

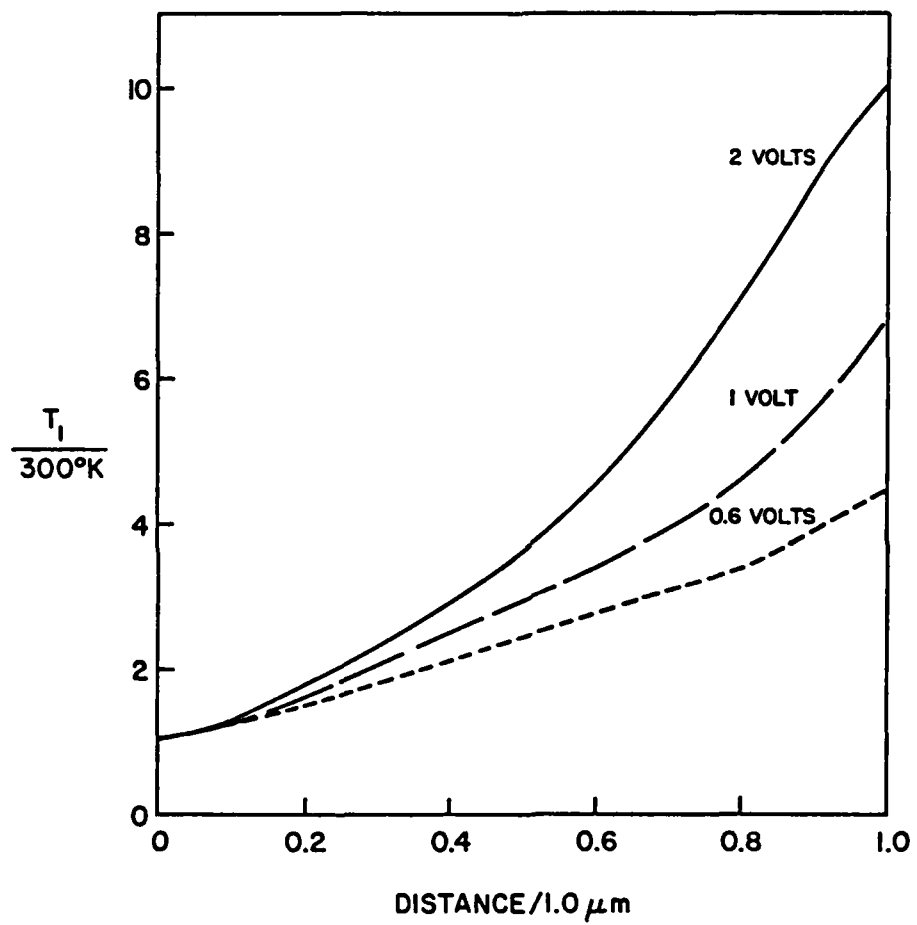


FIG. 14

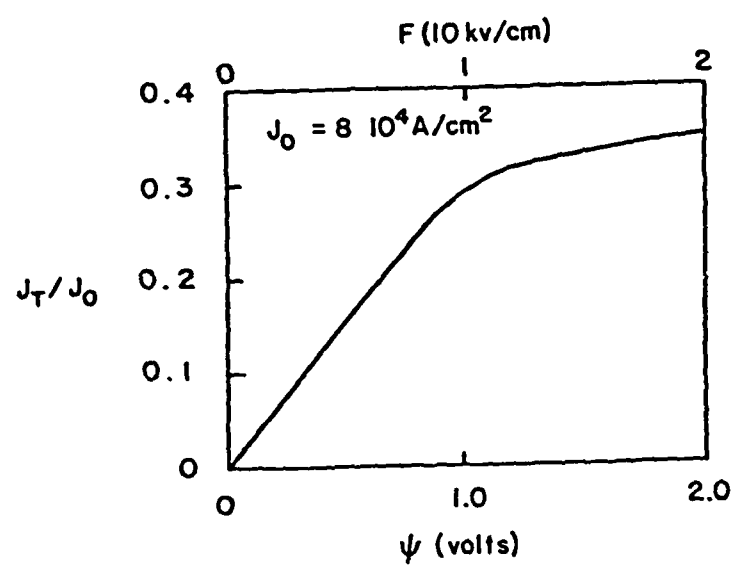


FIG. 15

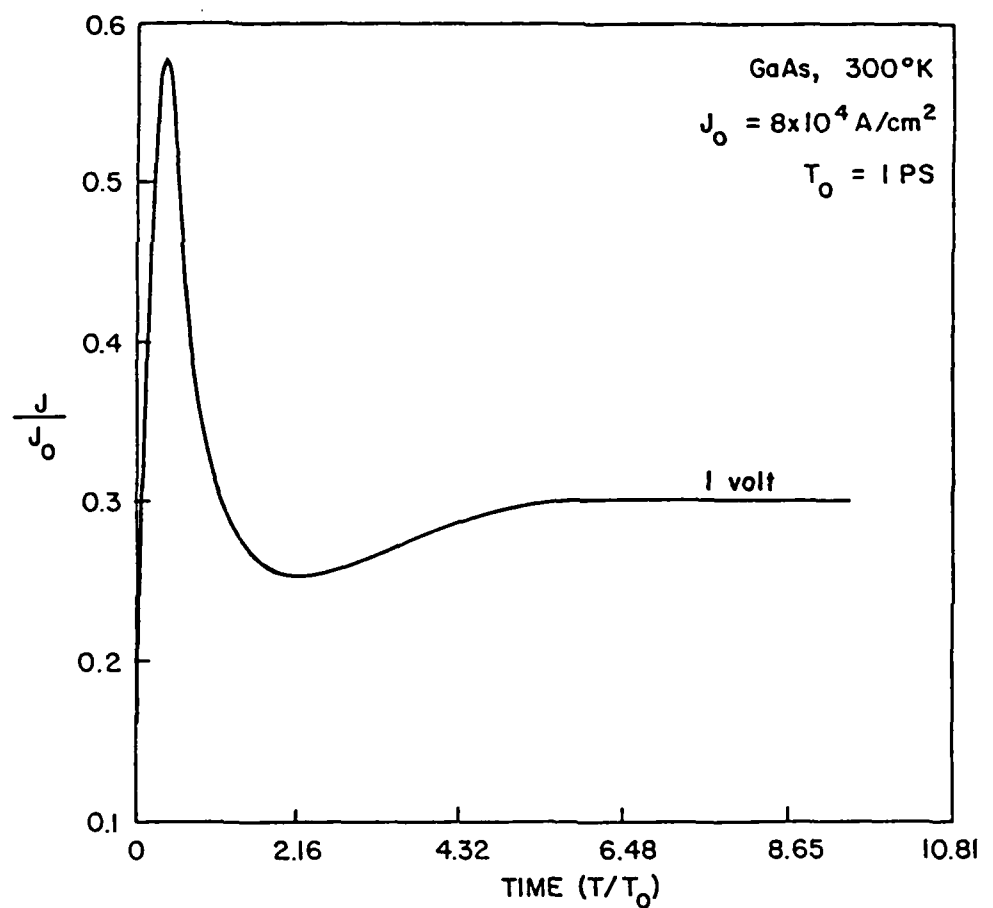


FIG. 16

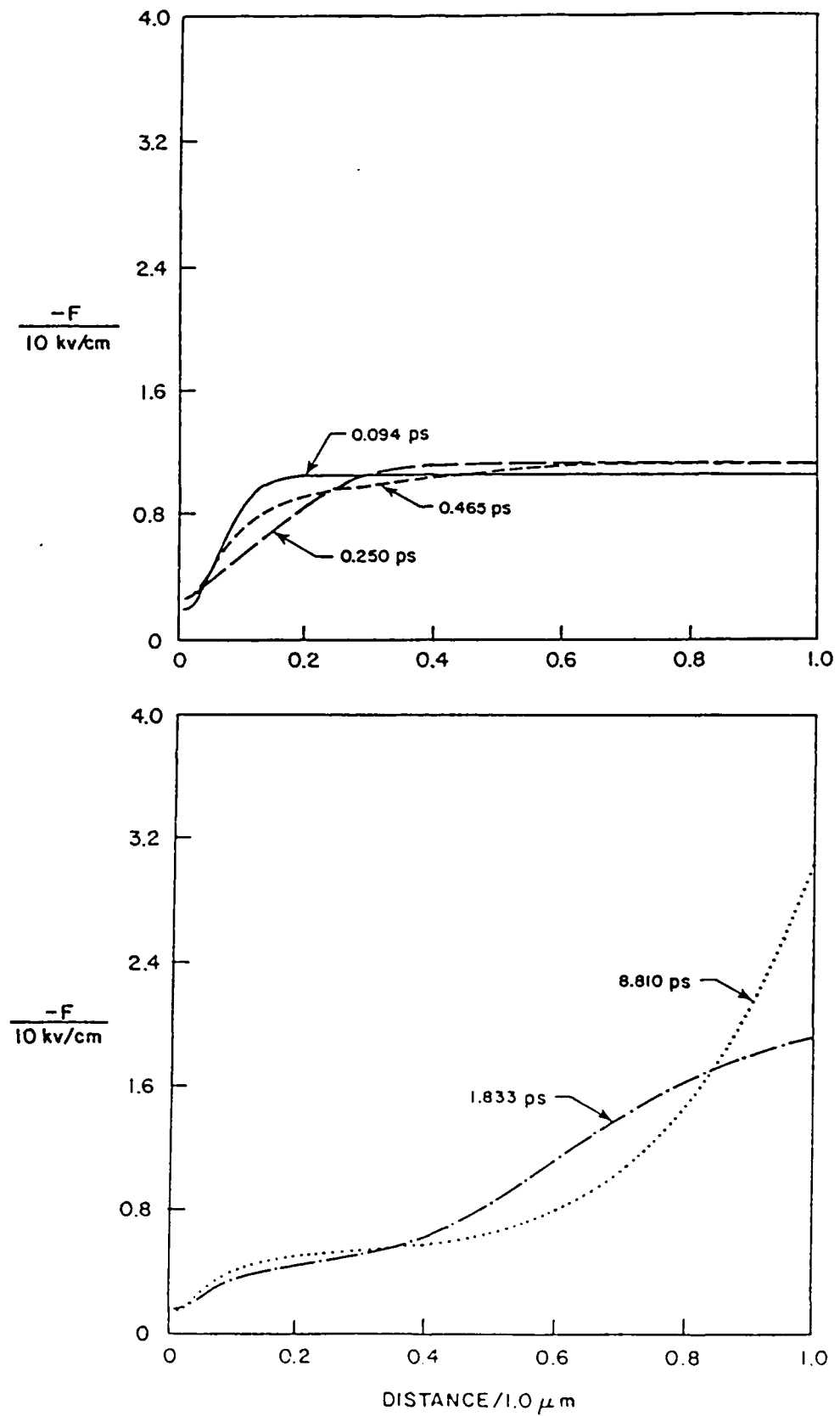


FIG. 17 a,b

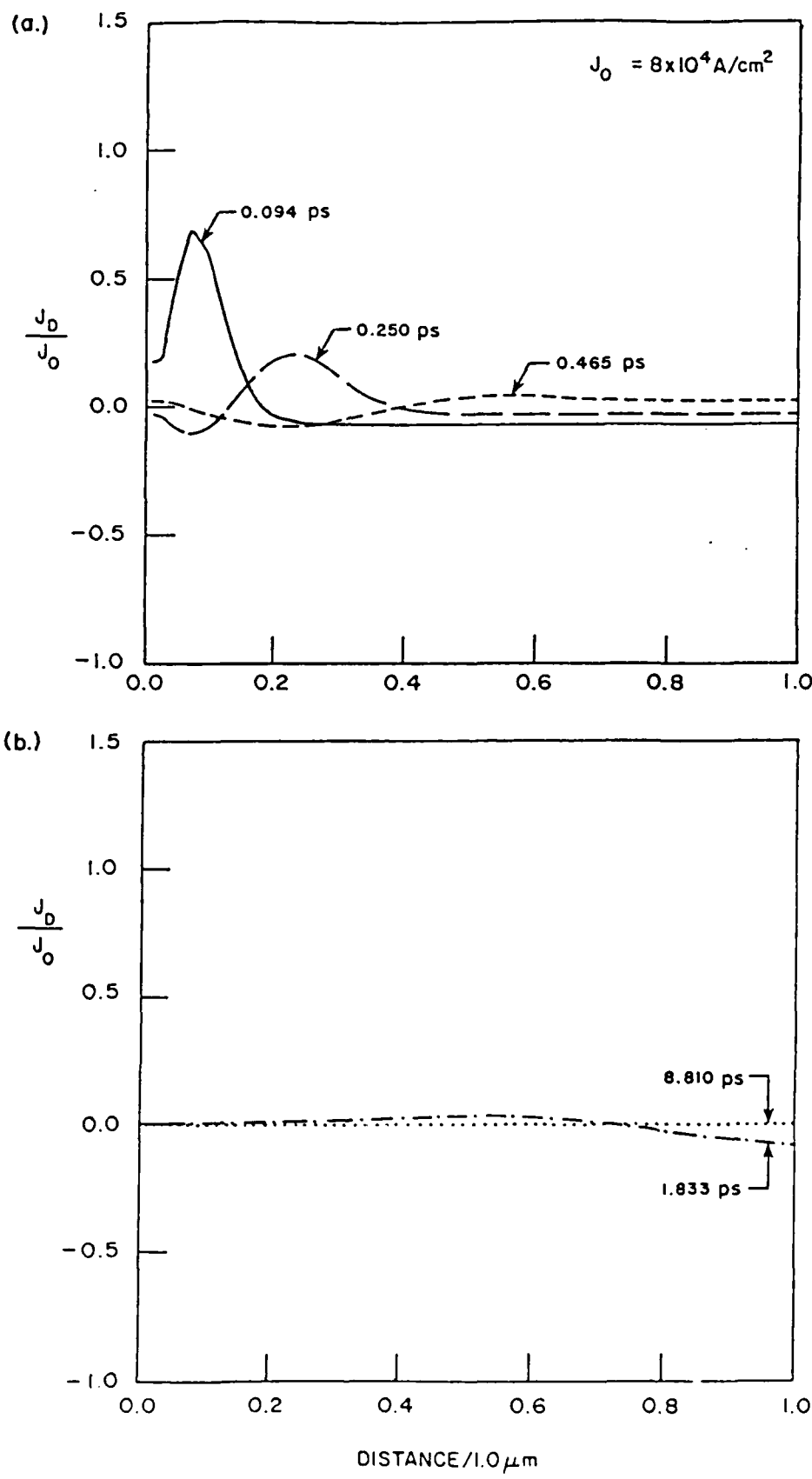


FIG. 18

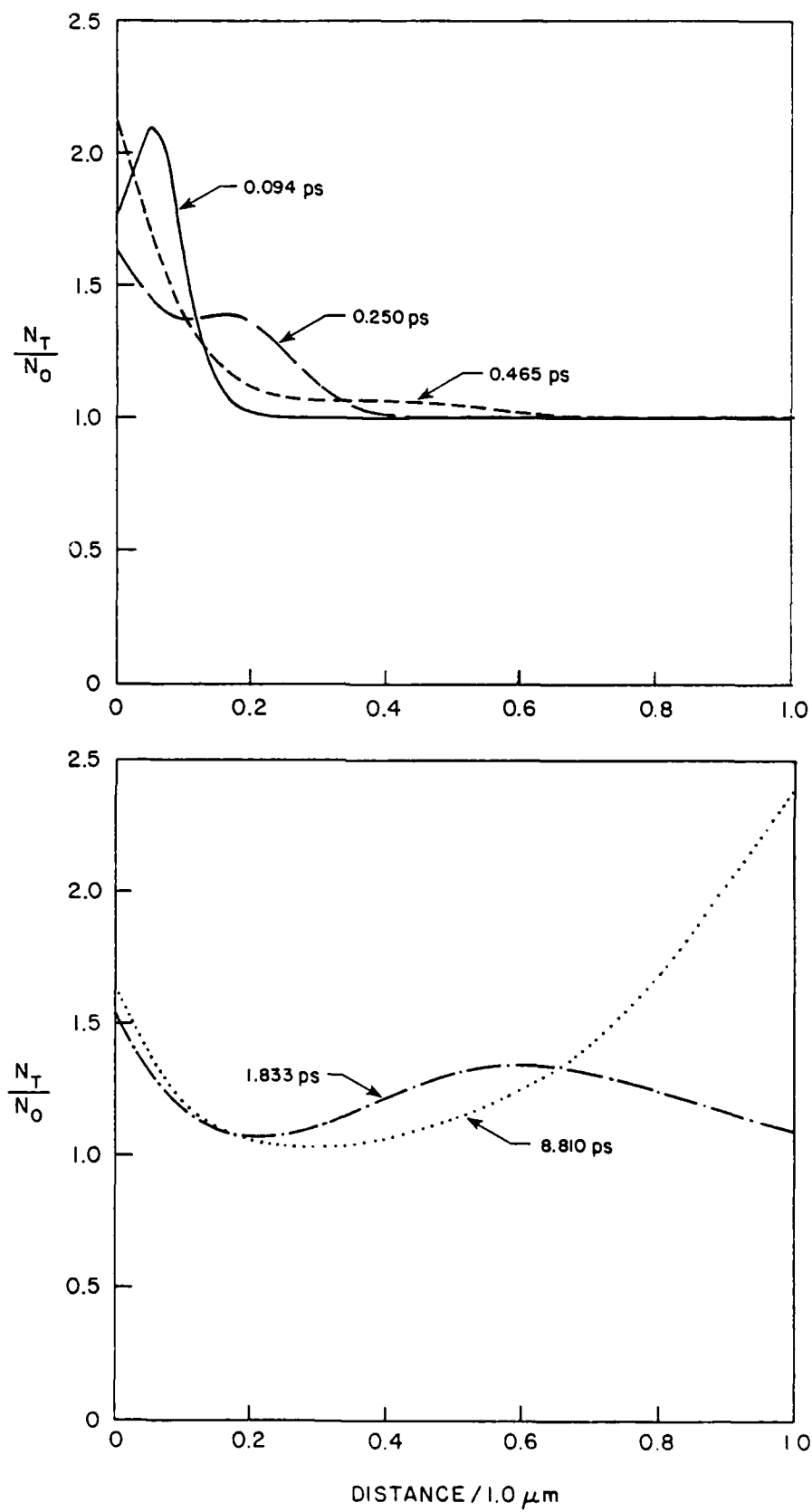


FIG. 20

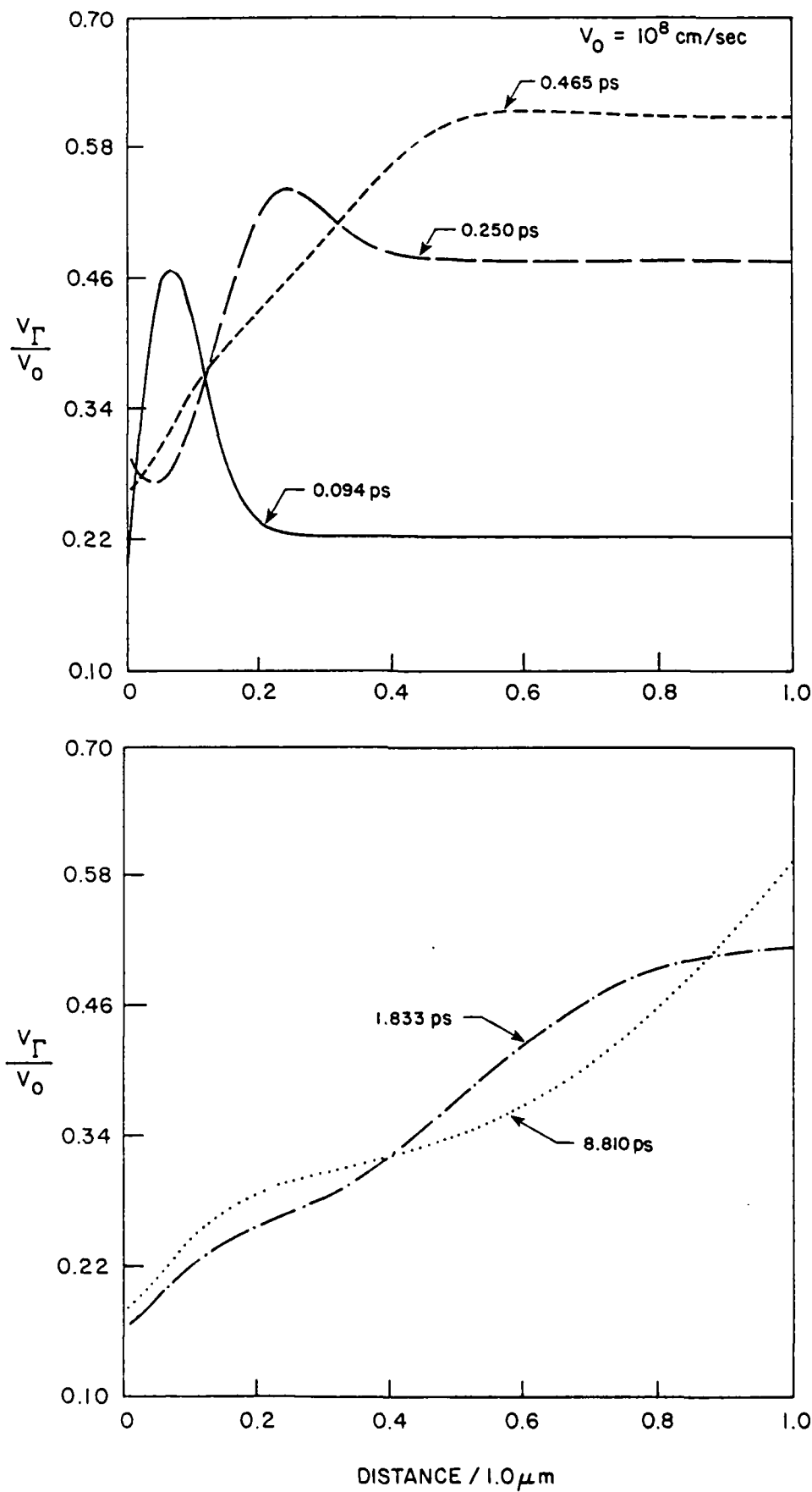


FIG. 21

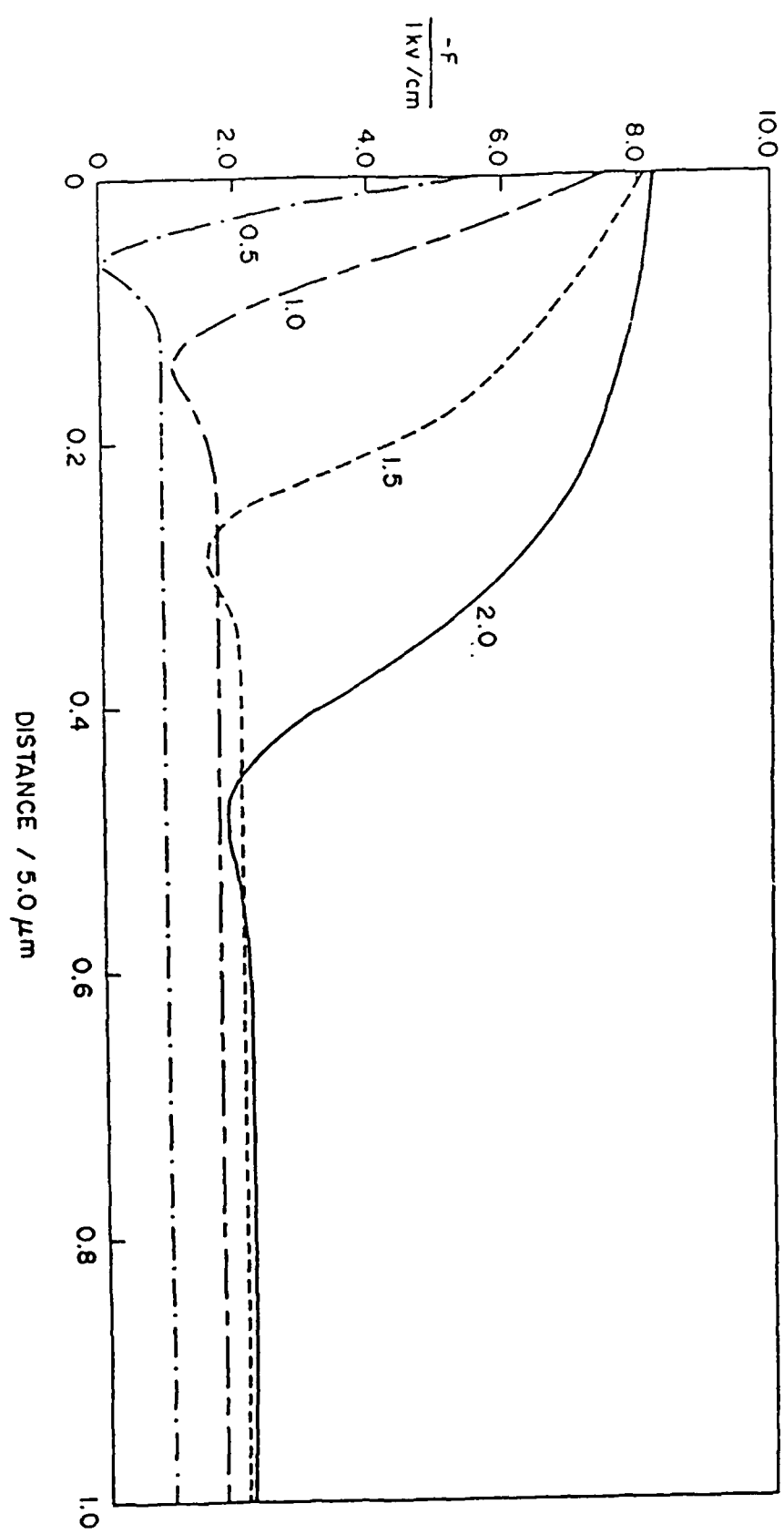
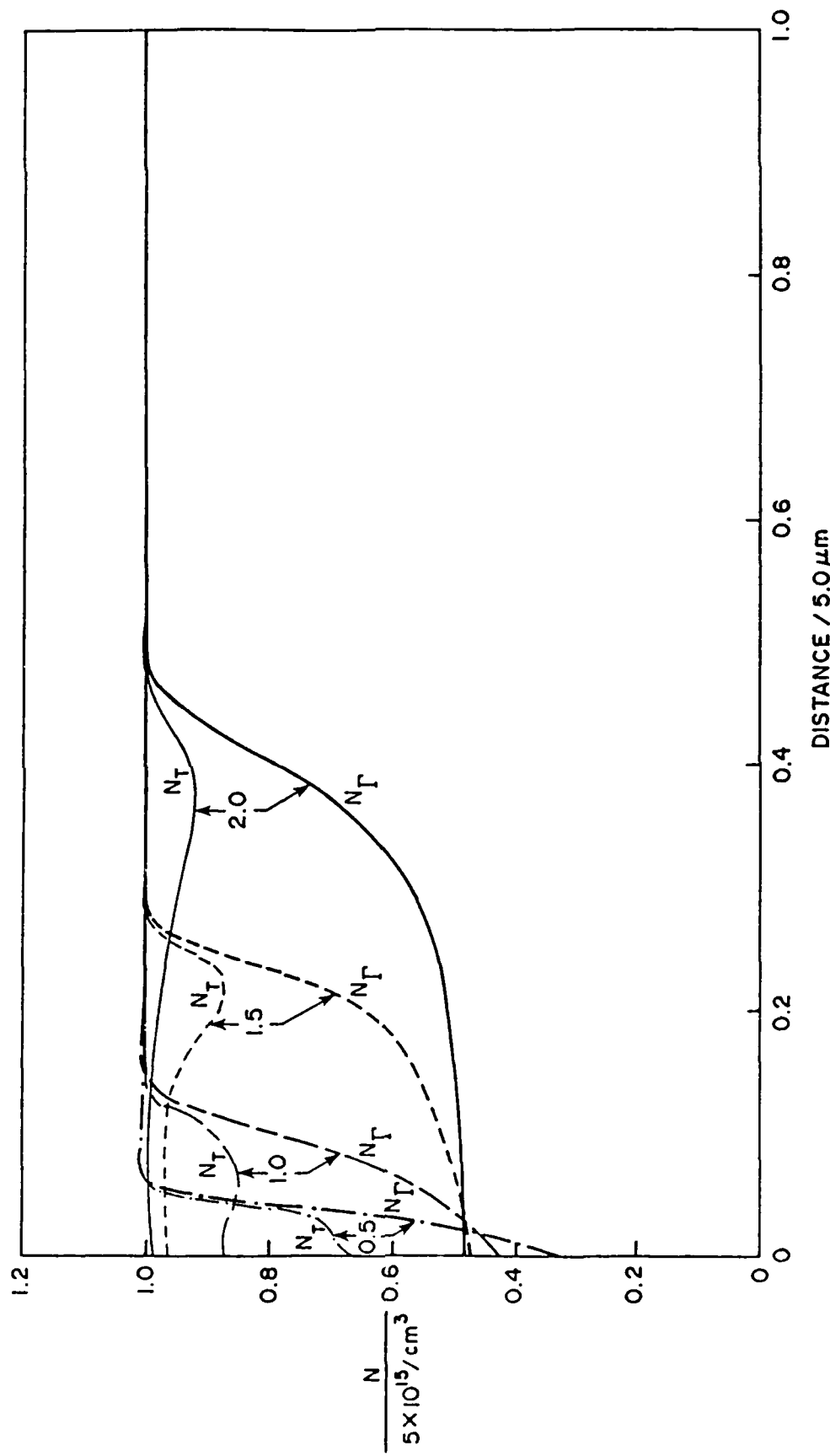


FIG. 22



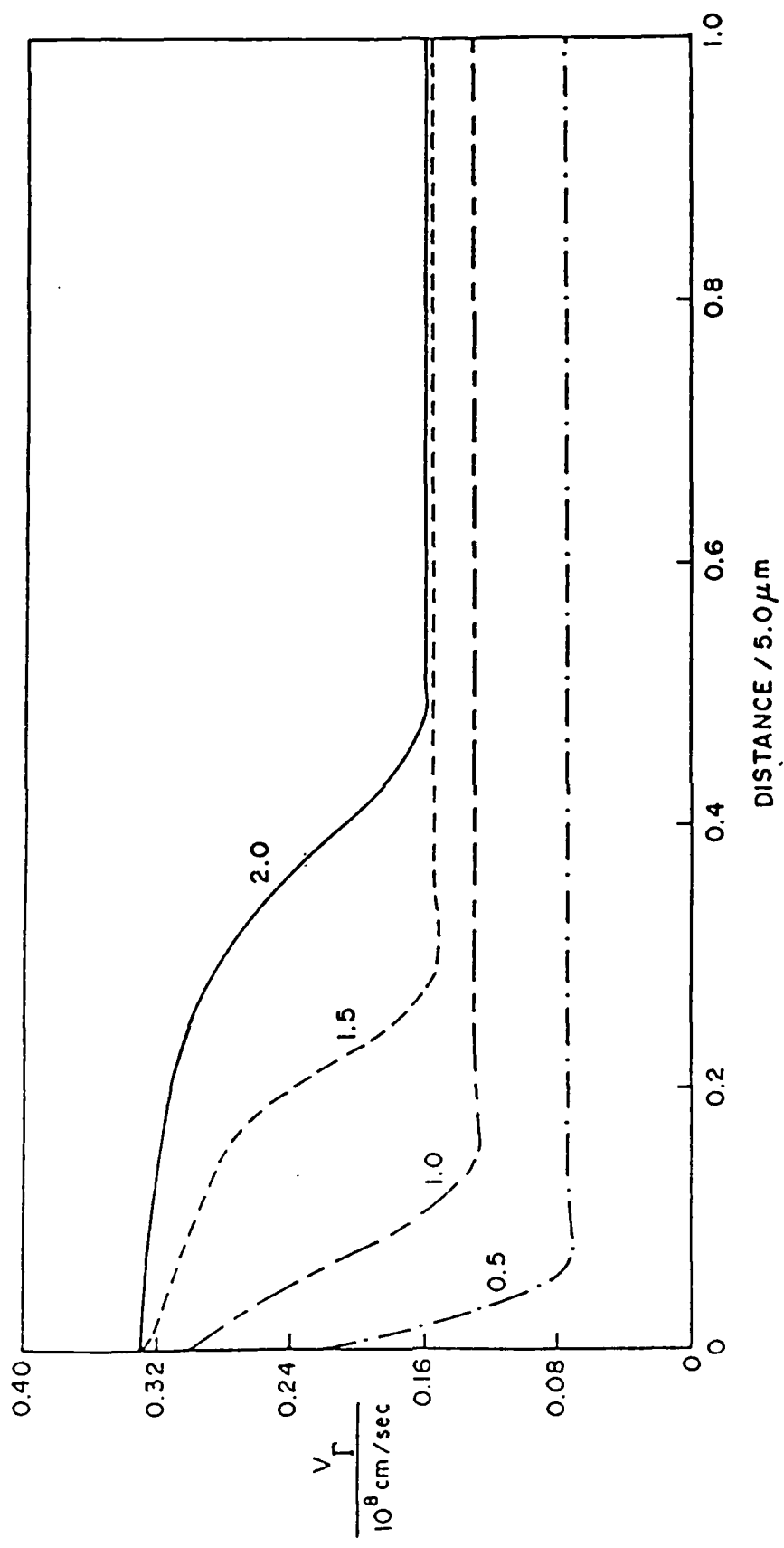


FIG. 23

FIG. 24

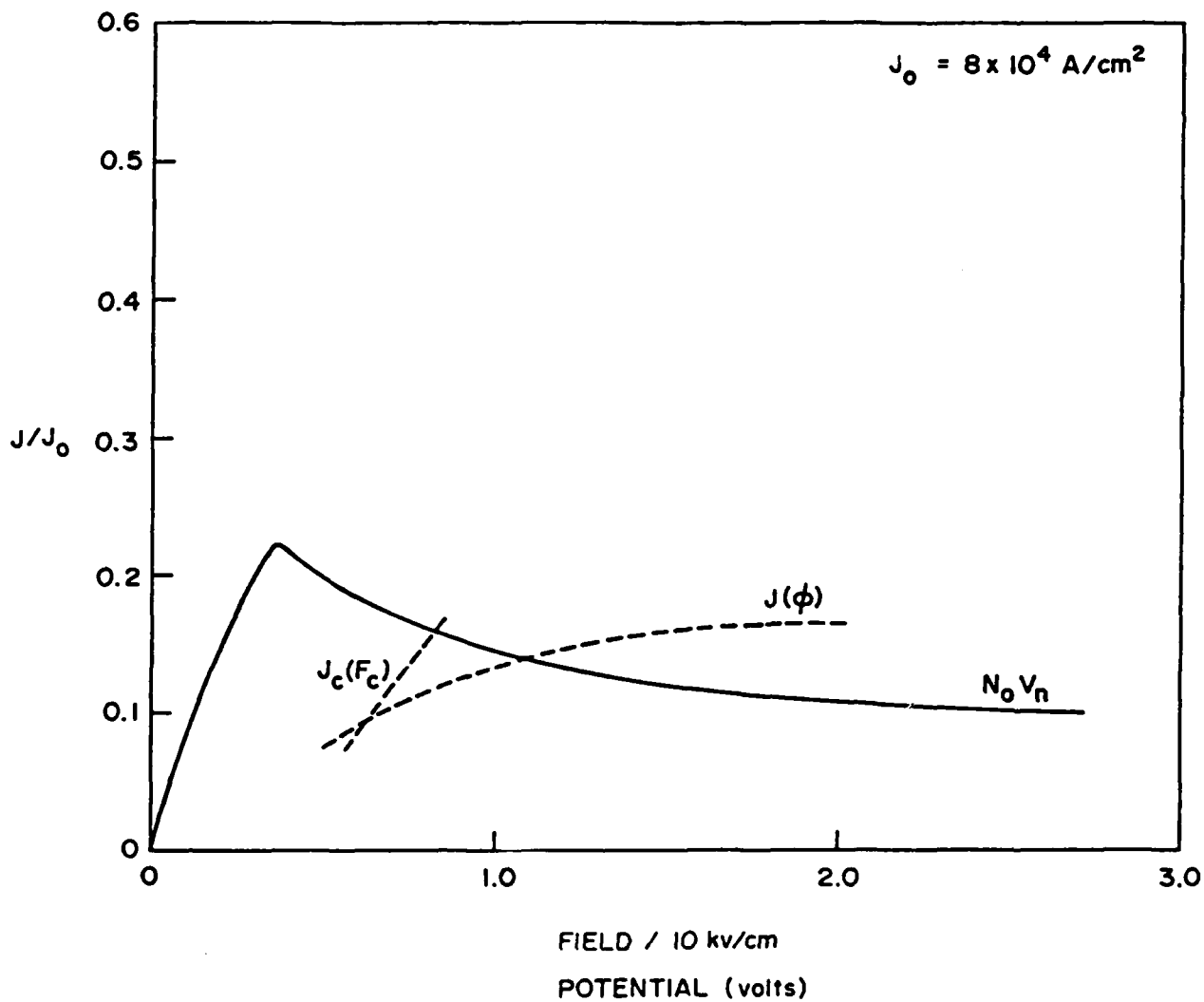


FIG. 25

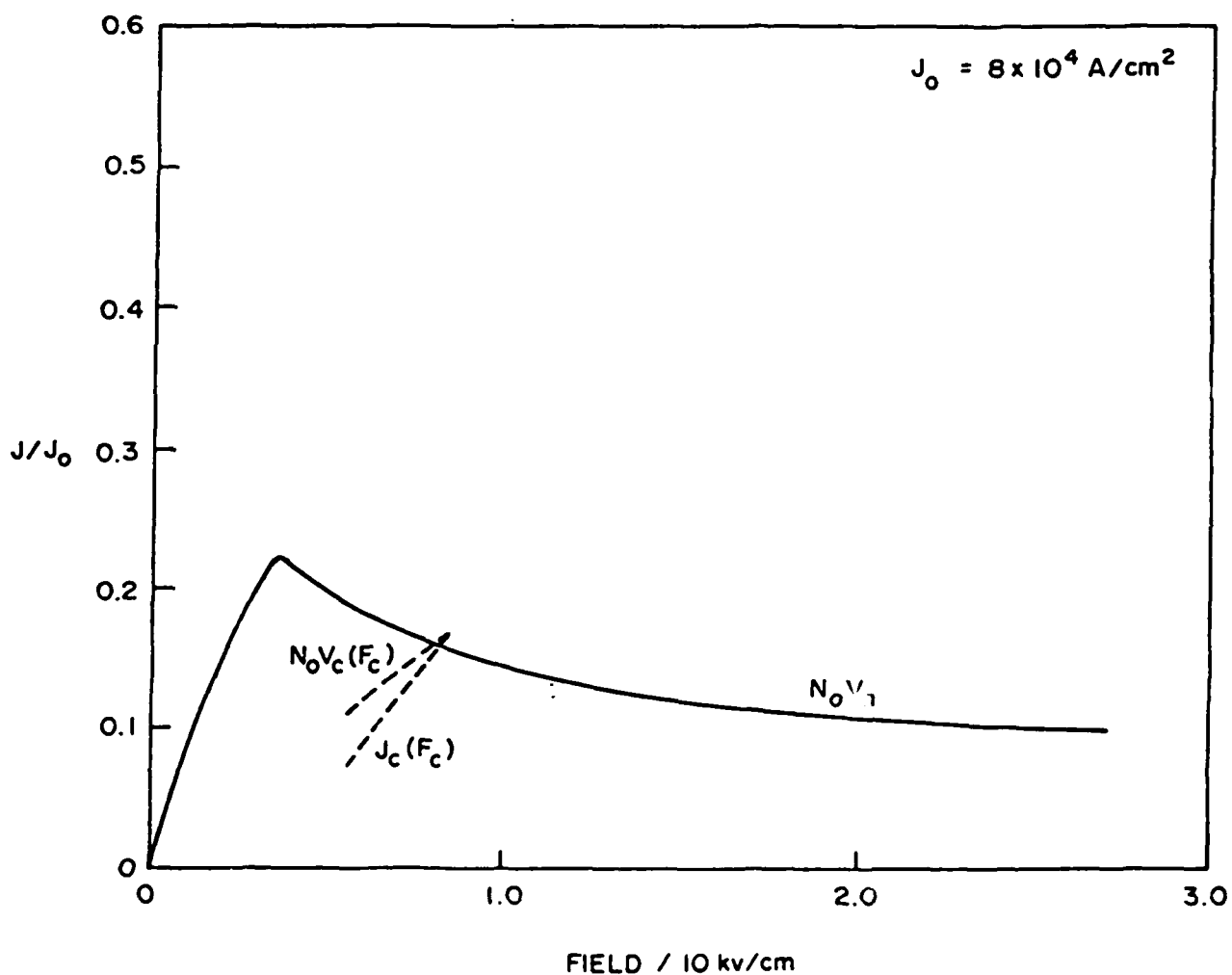


FIG. 26a.

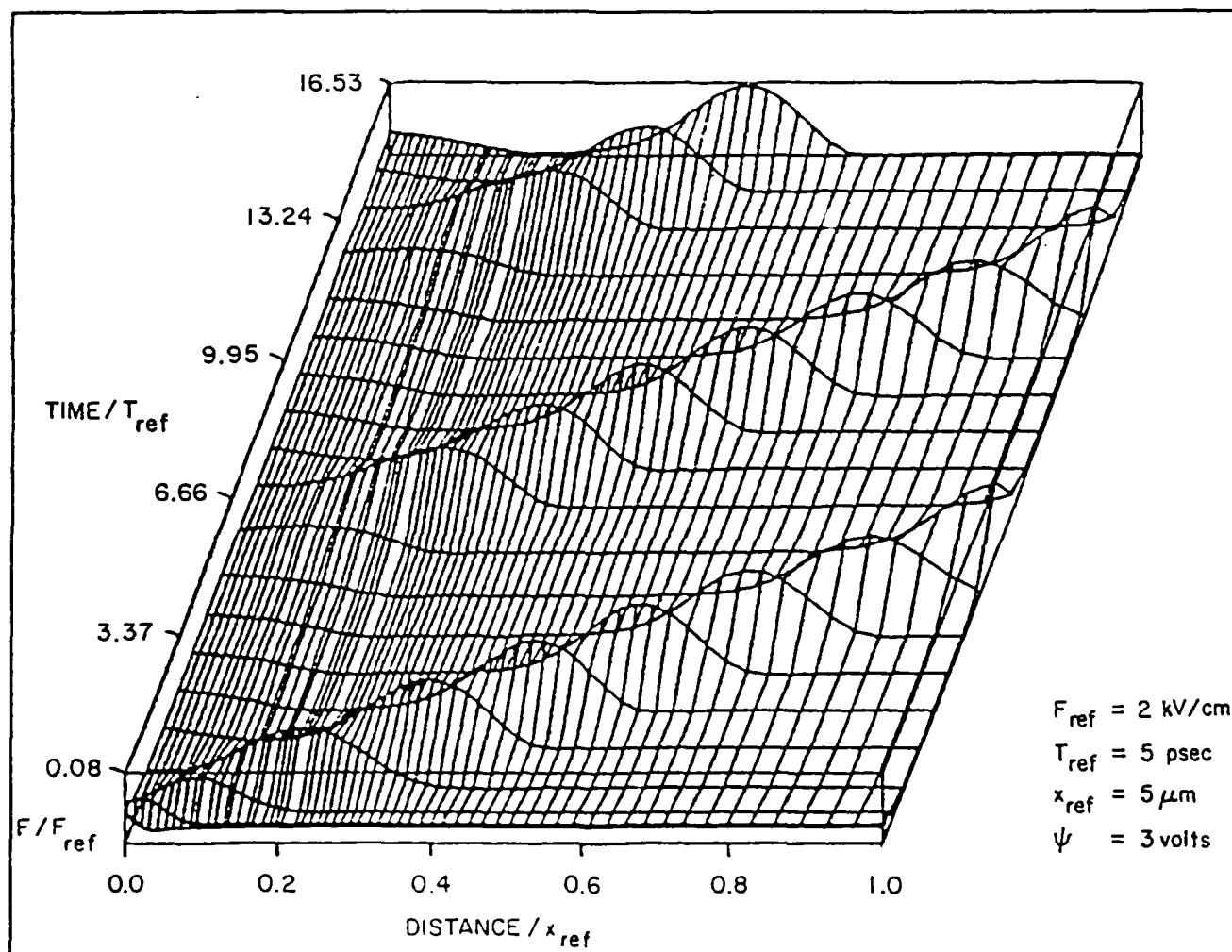


FIG. 26b.

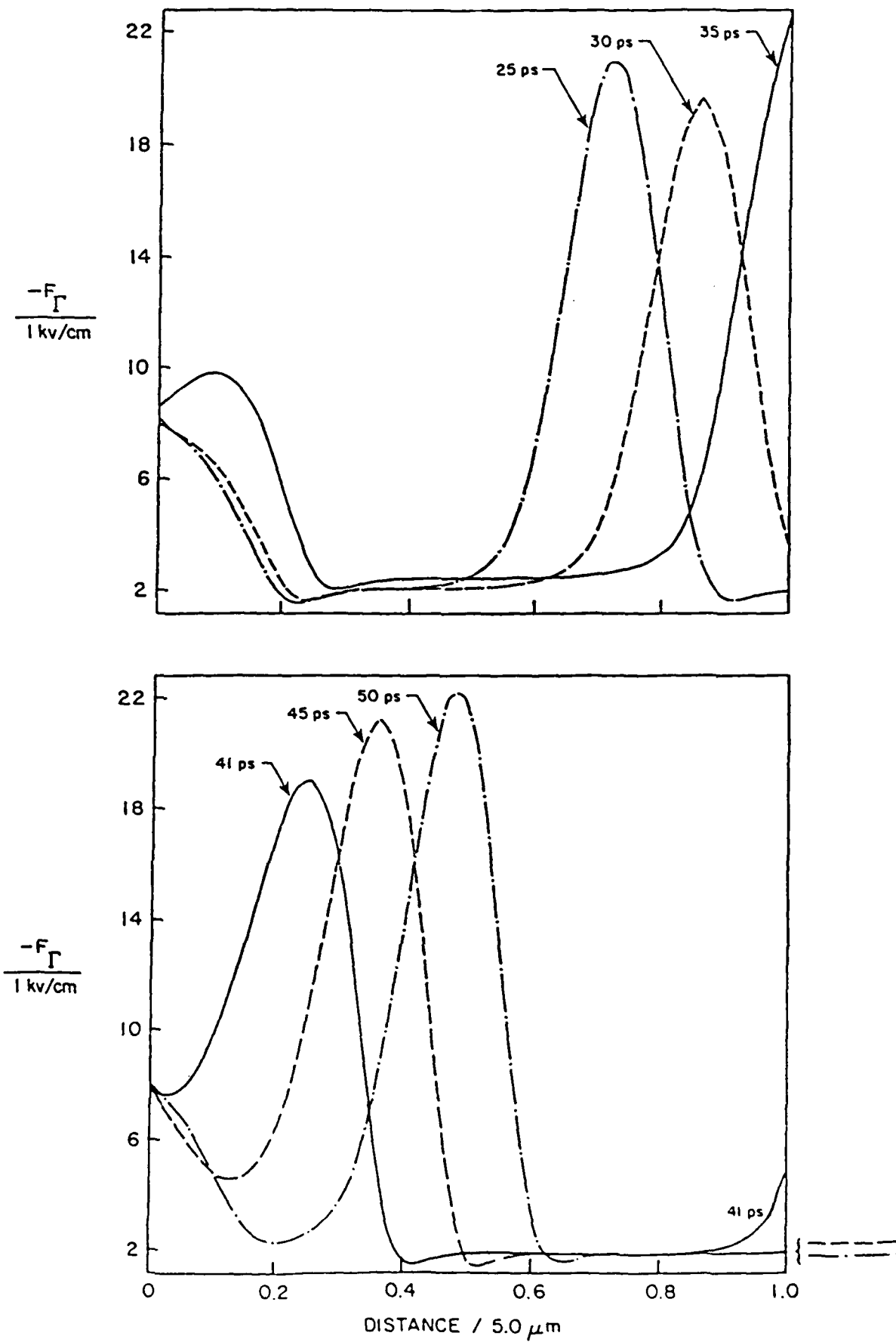


FIG. 27

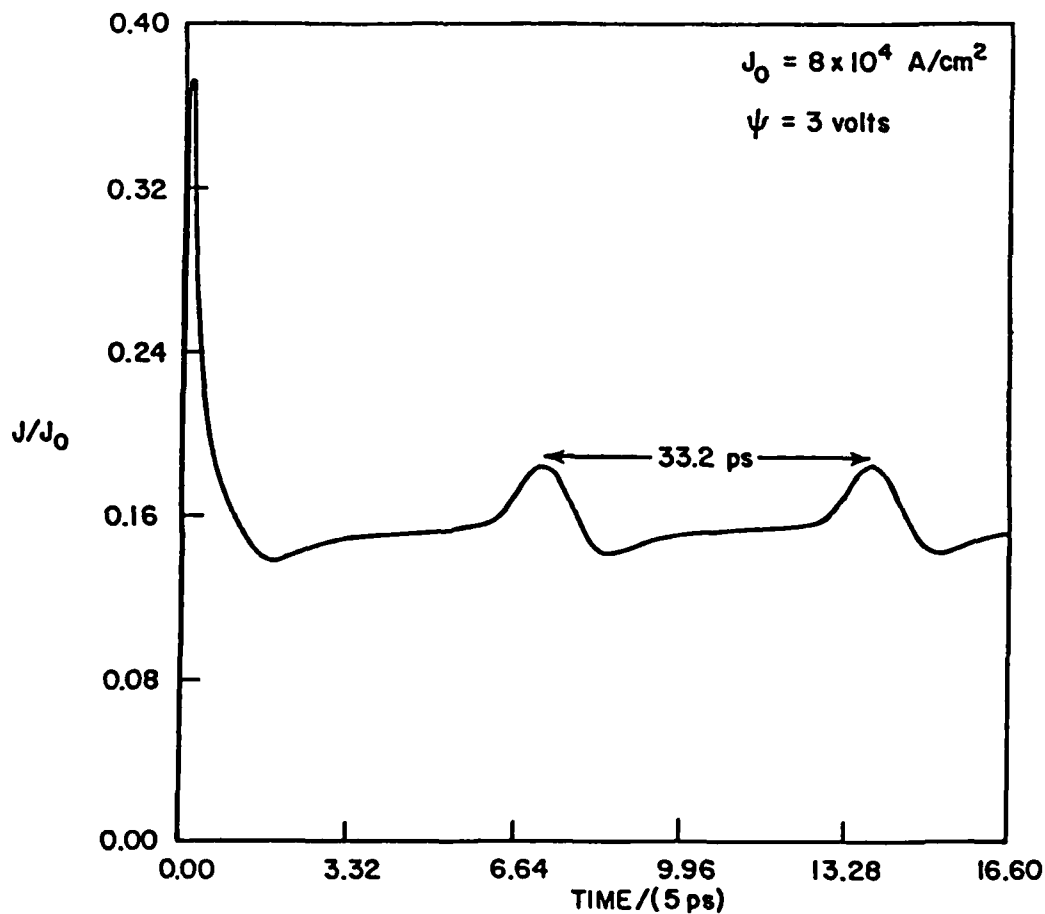


FIG. 28

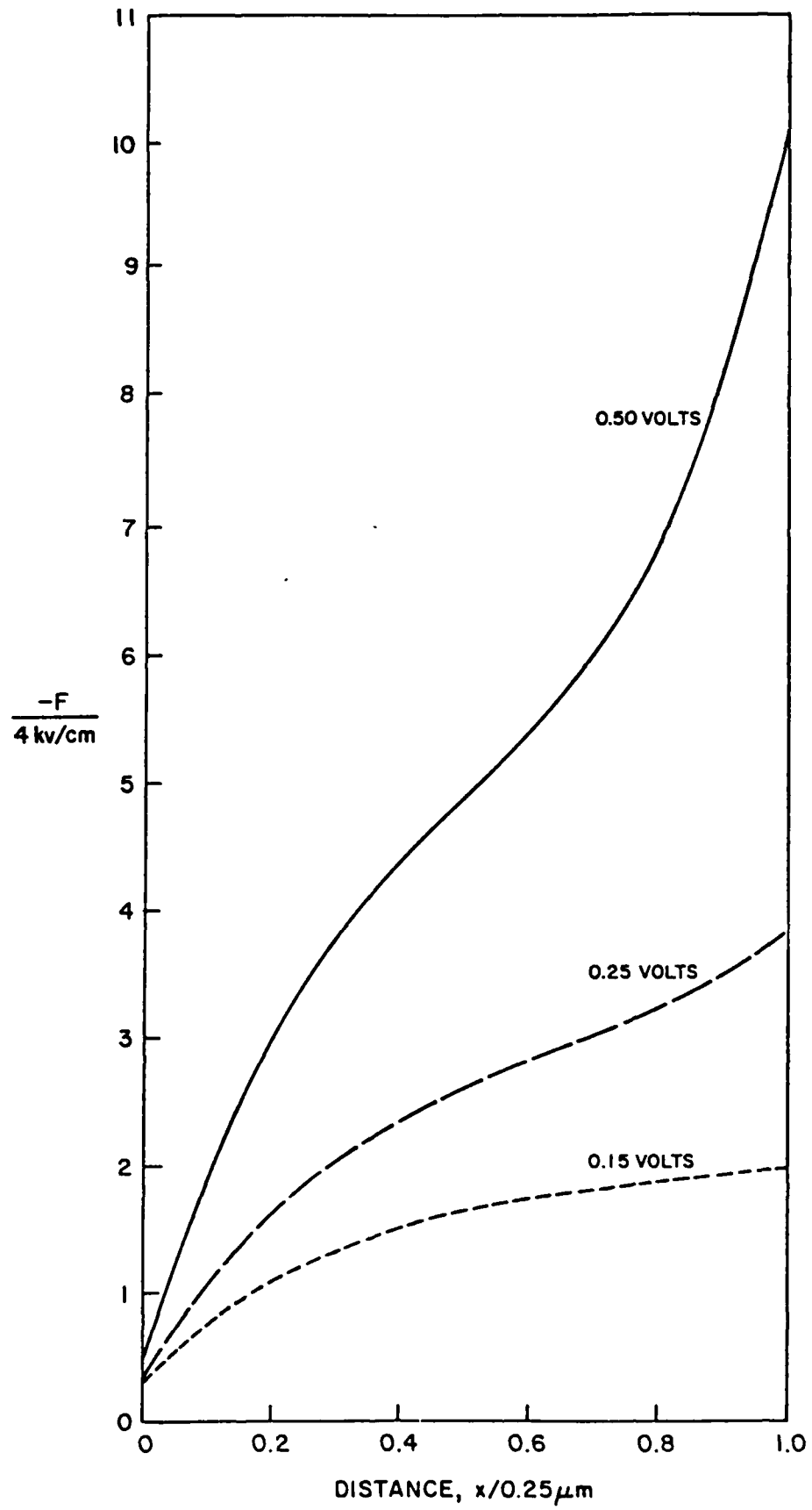


FIG. 29

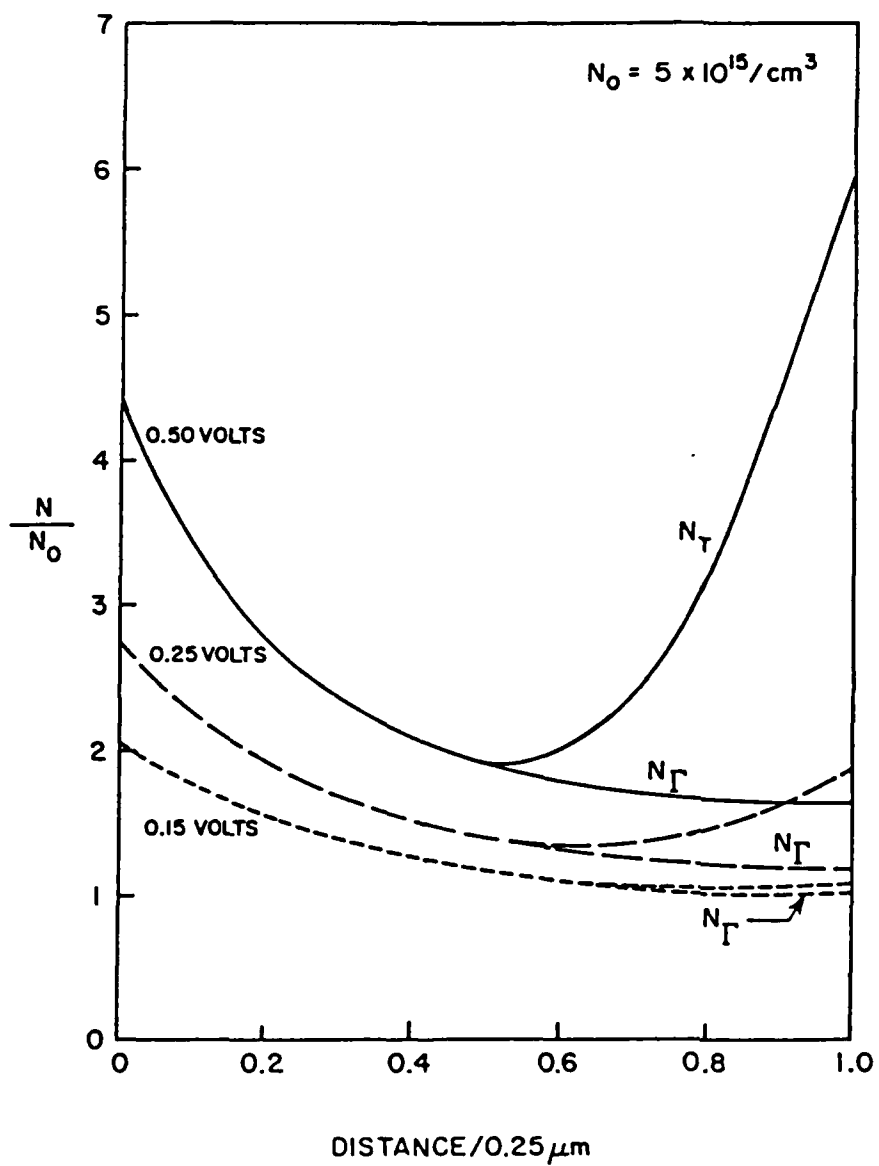


FIG. 30

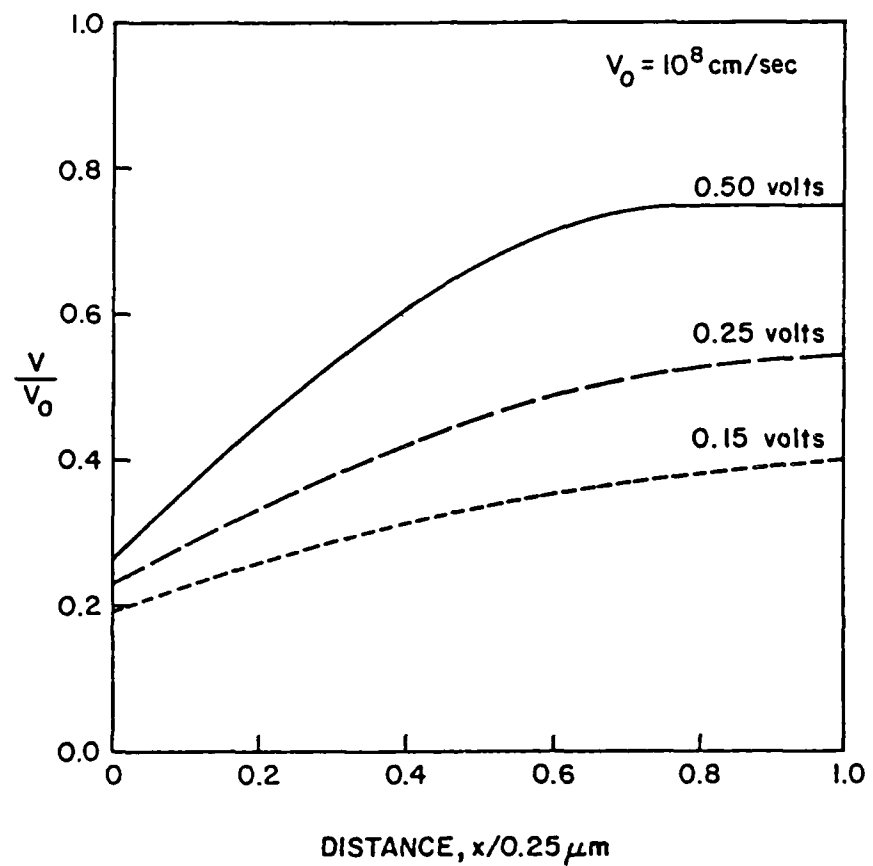
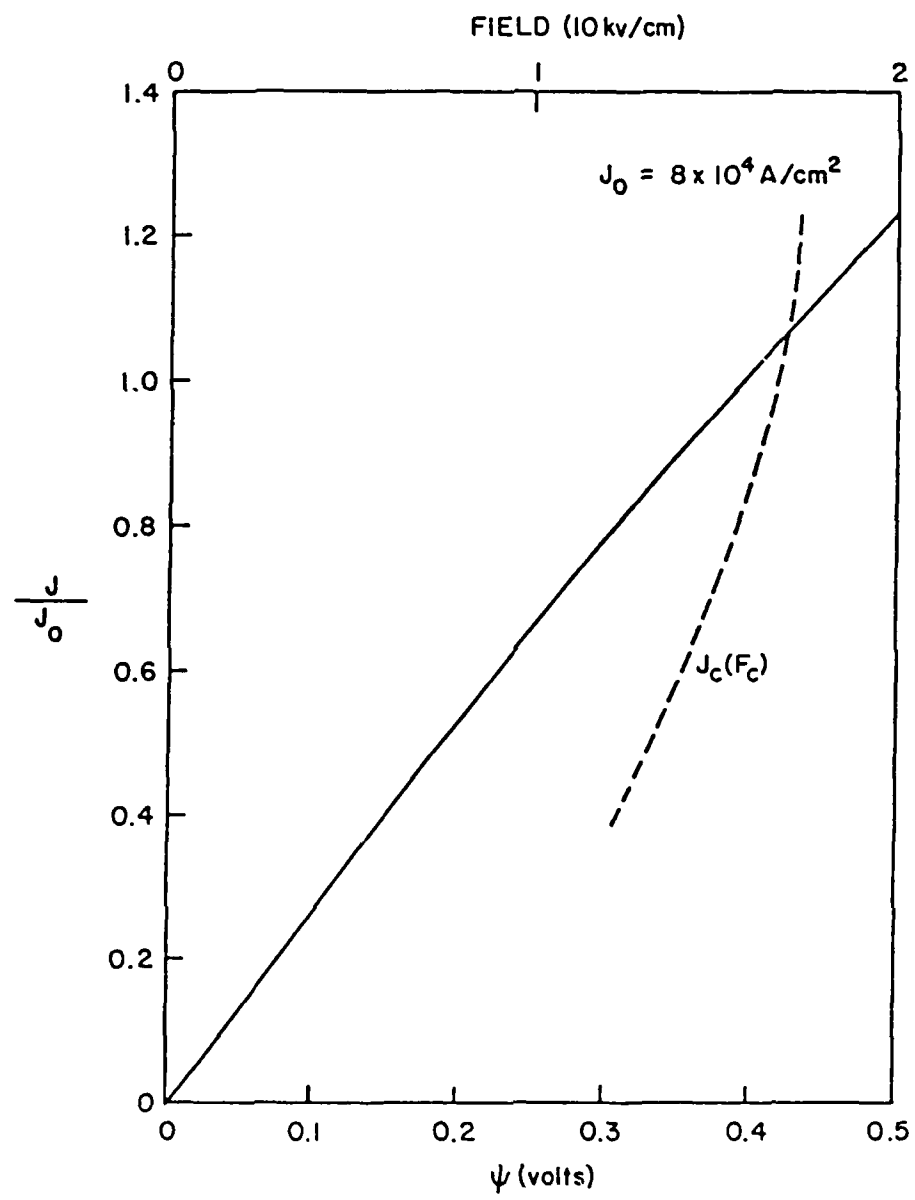


FIG. 31



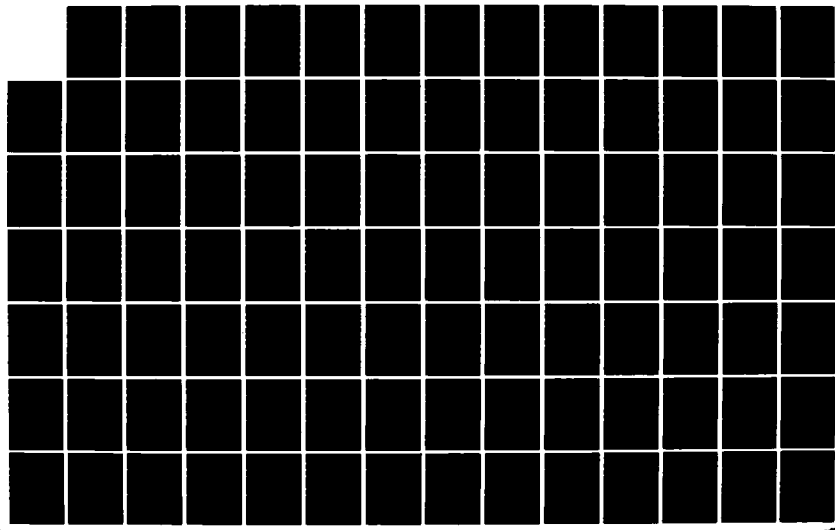
✓ RD-A150 020 SEMICONDUCTOR MATERIALS FOR HIGH FREQUENCY SOLID STATE 3/4  
SOURCES(U) SCIENTIFIC RESEARCH ASSOCIATES INC  
GLASTONBURY CT H L GRUBIN ET AL. 18 JAN 85

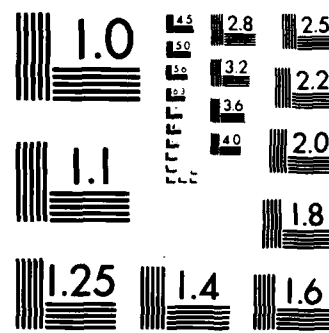
UNCLASSIFIED

SRA-R85-920016-F N80014-82-C-8697

F/G 20/12

NL





MICROCOPY RESOLUTION TEST CHART  
NATIONAL BUREAU OF STANDARDS-1963 A

FIG. 32

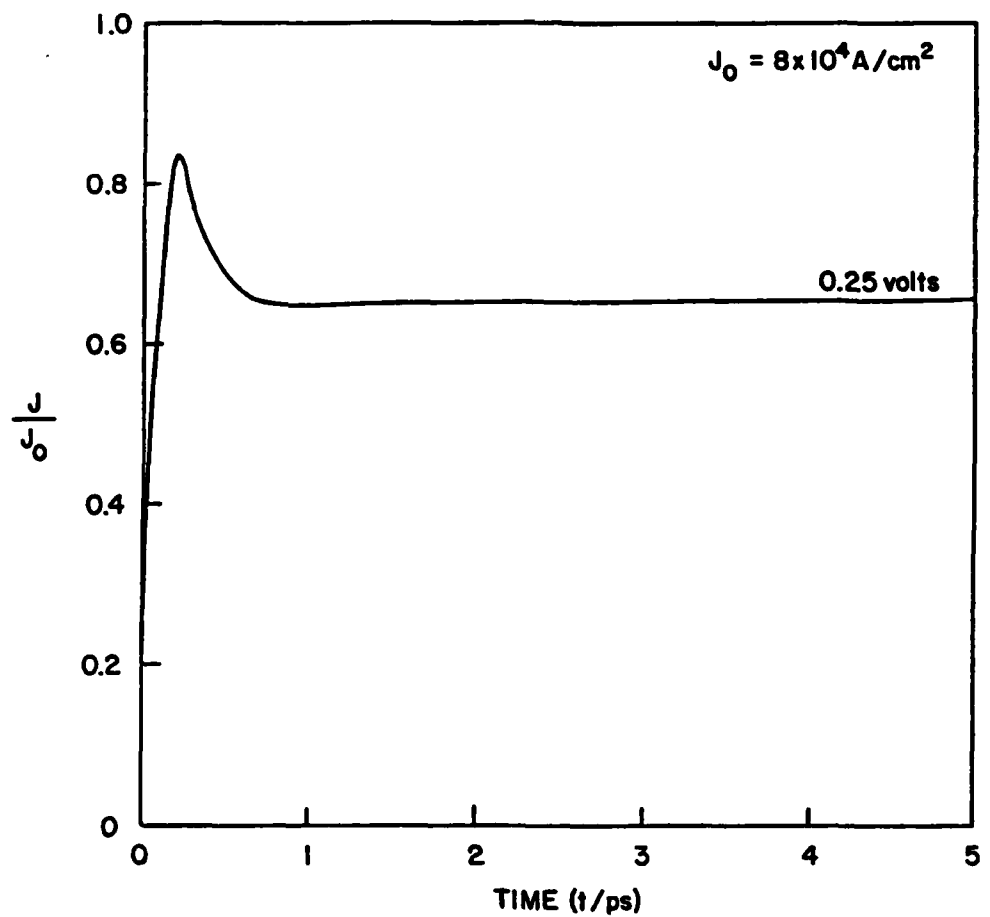


FIG. 33

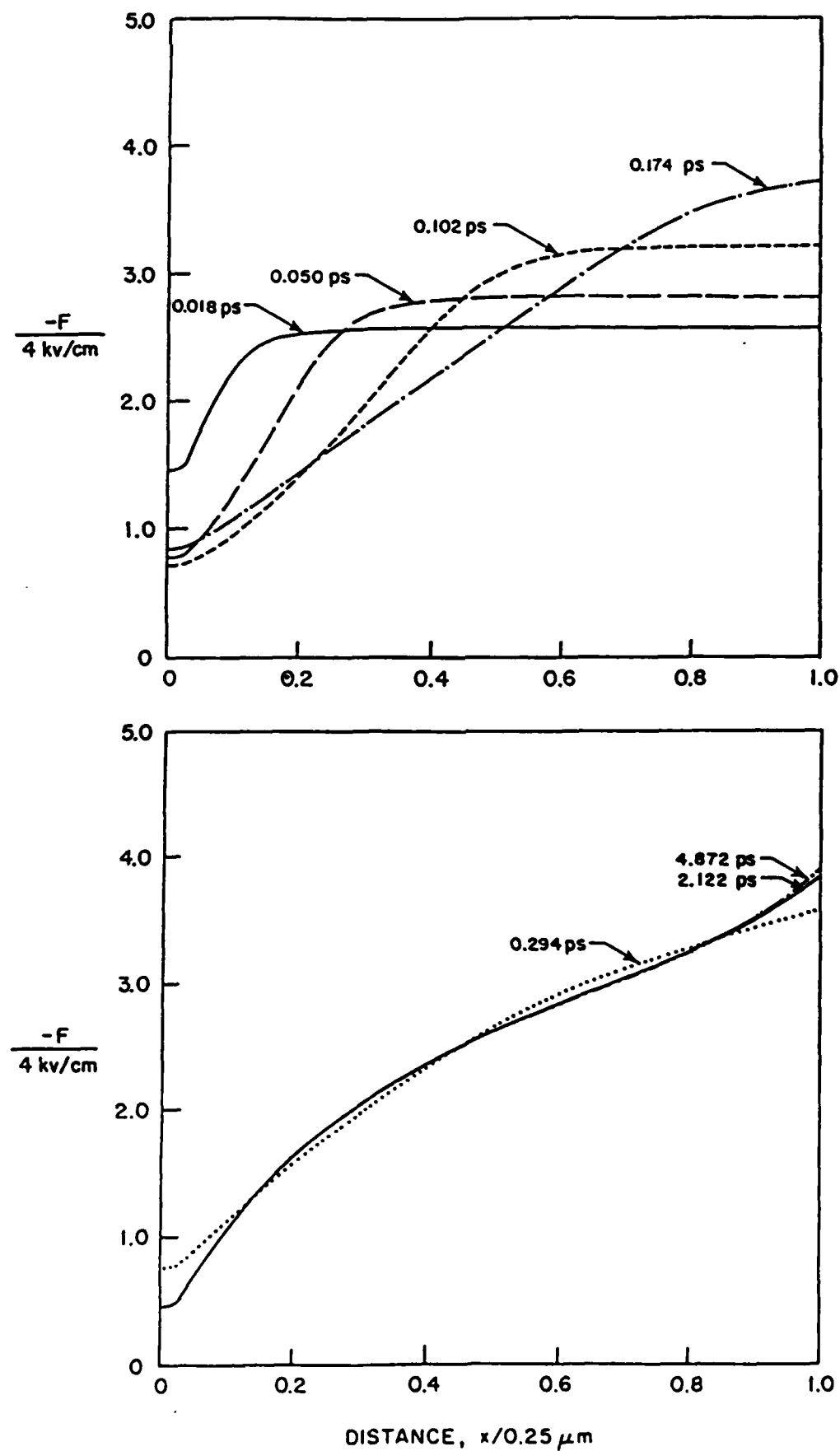


FIG. 34

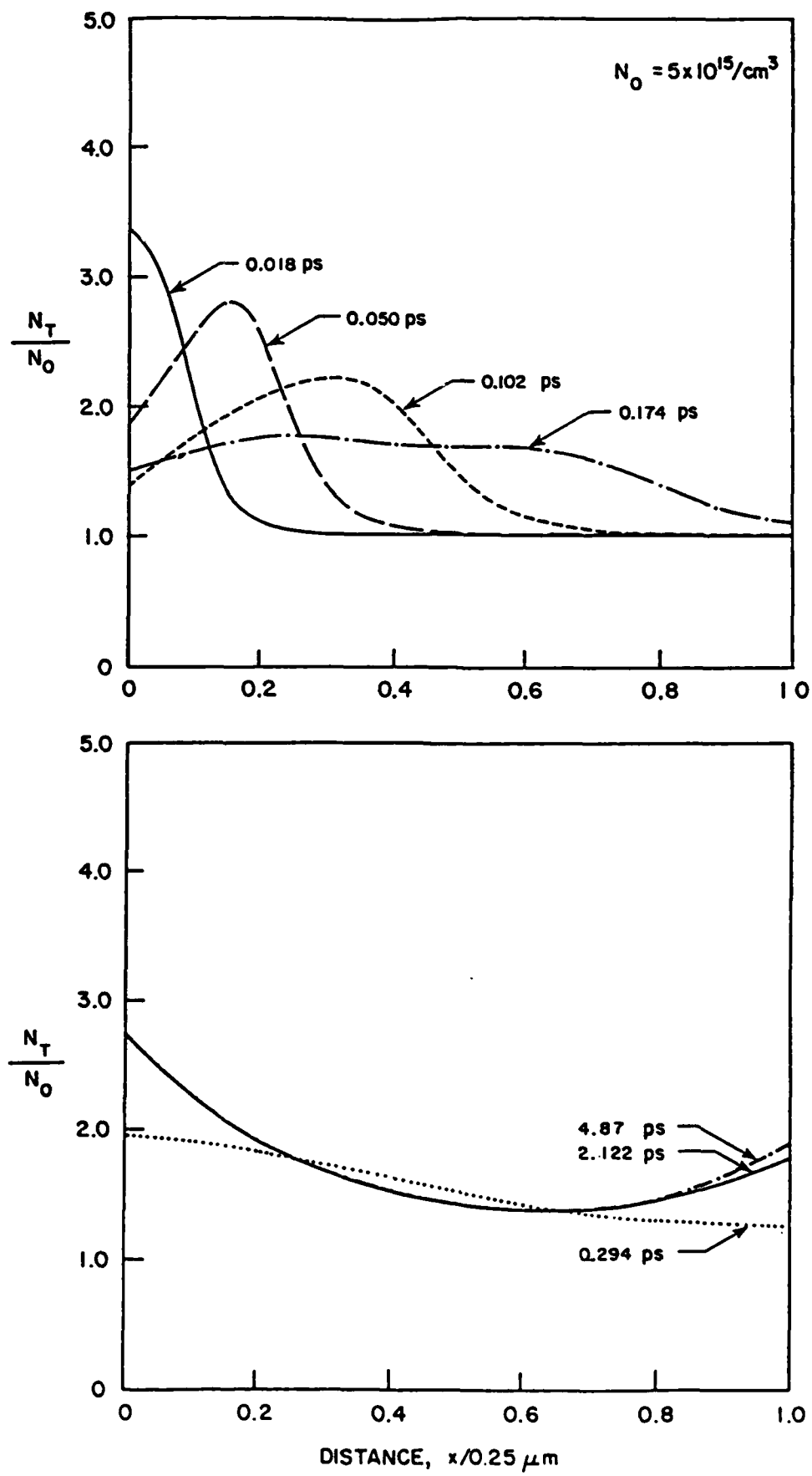


FIG. 35

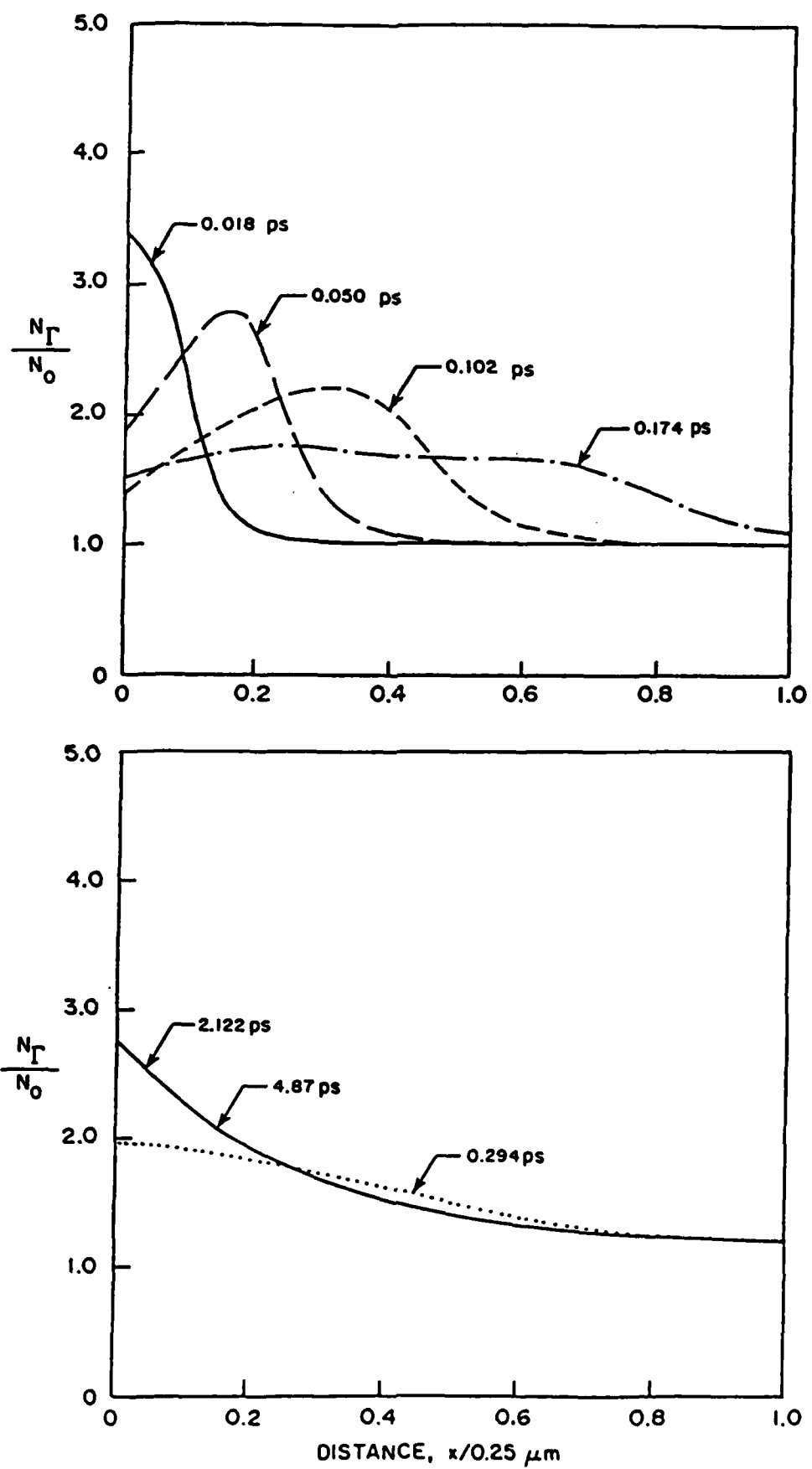


FIG. 36

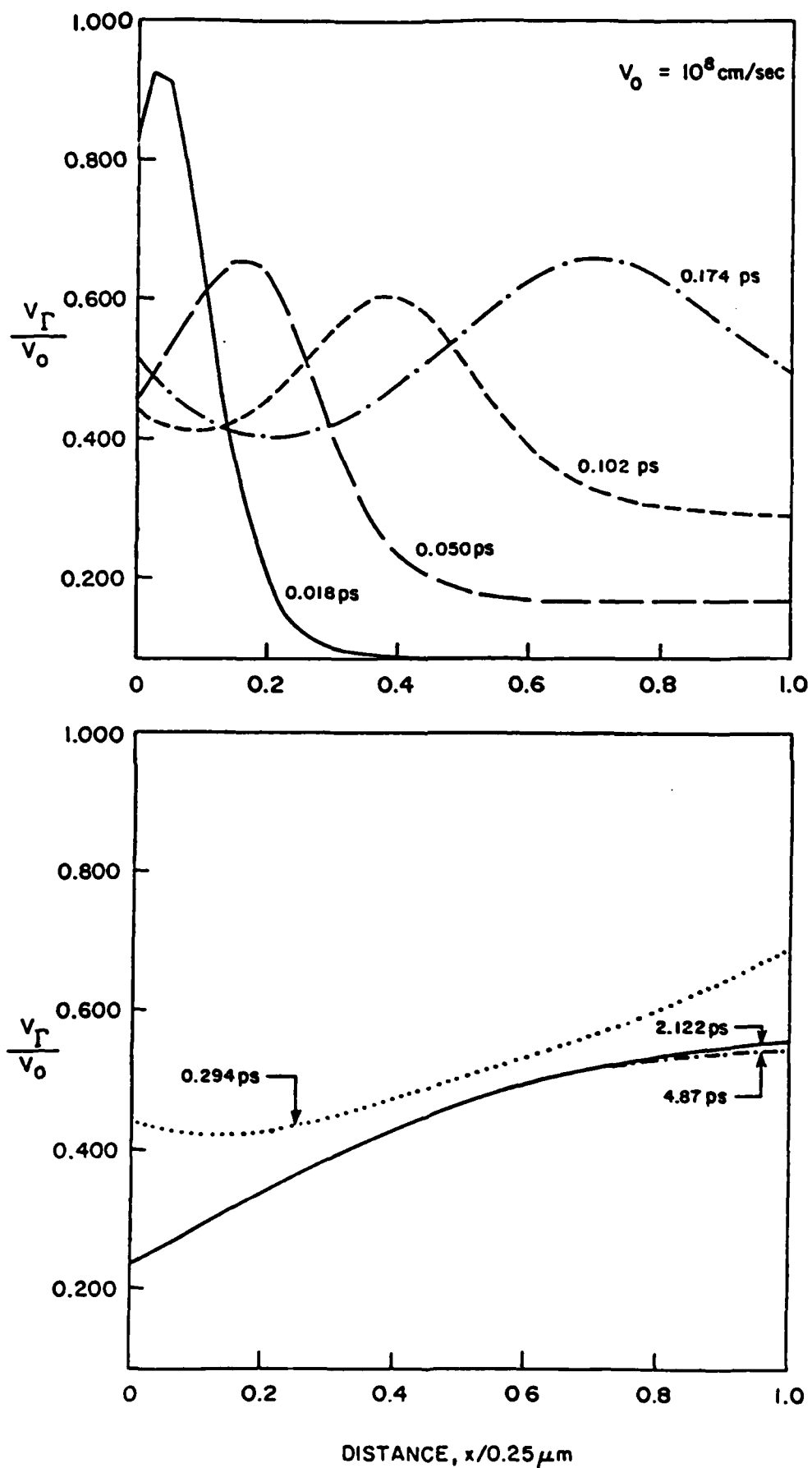


FIG. 37

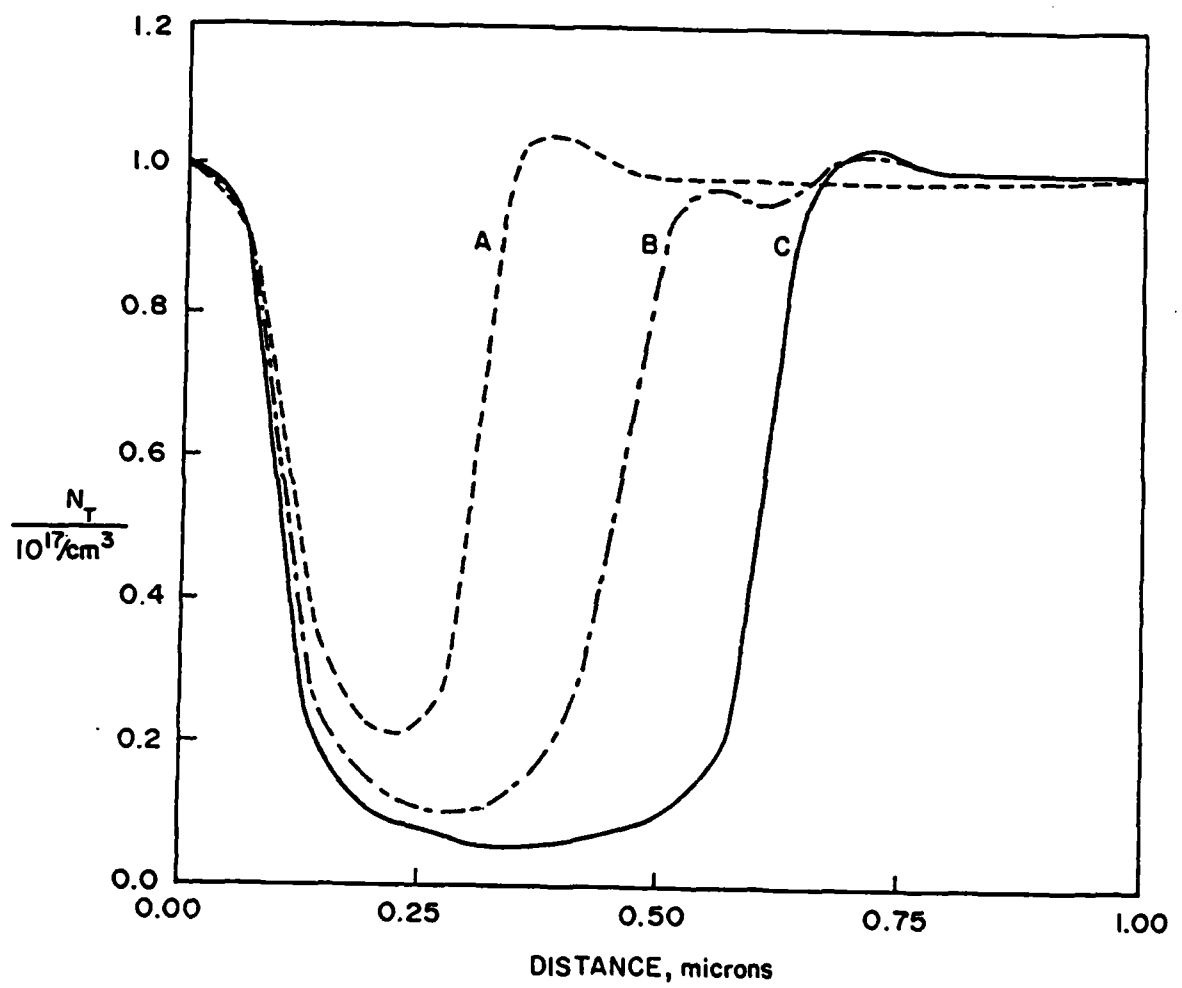


FIG. 38

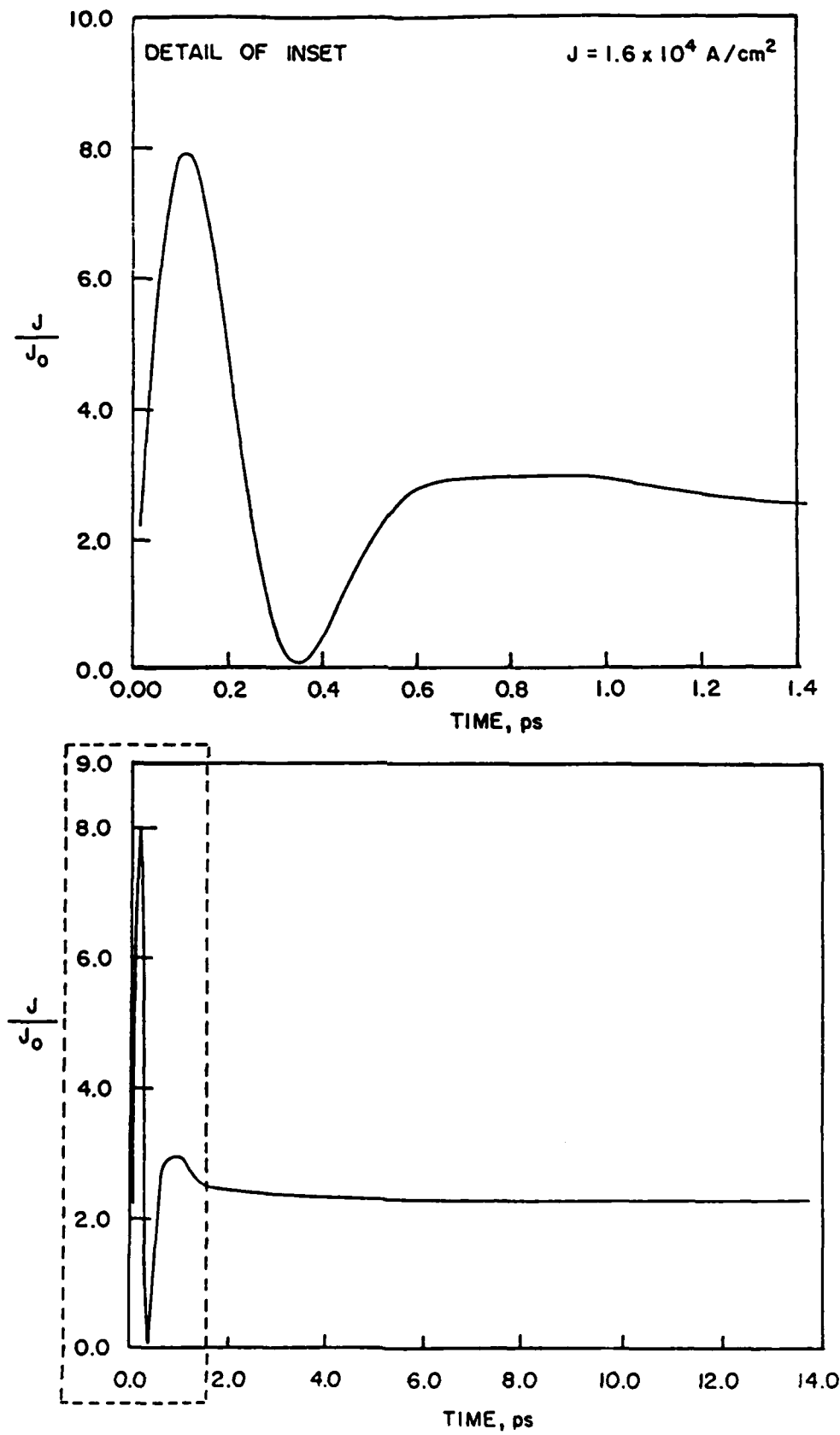


FIG. 39

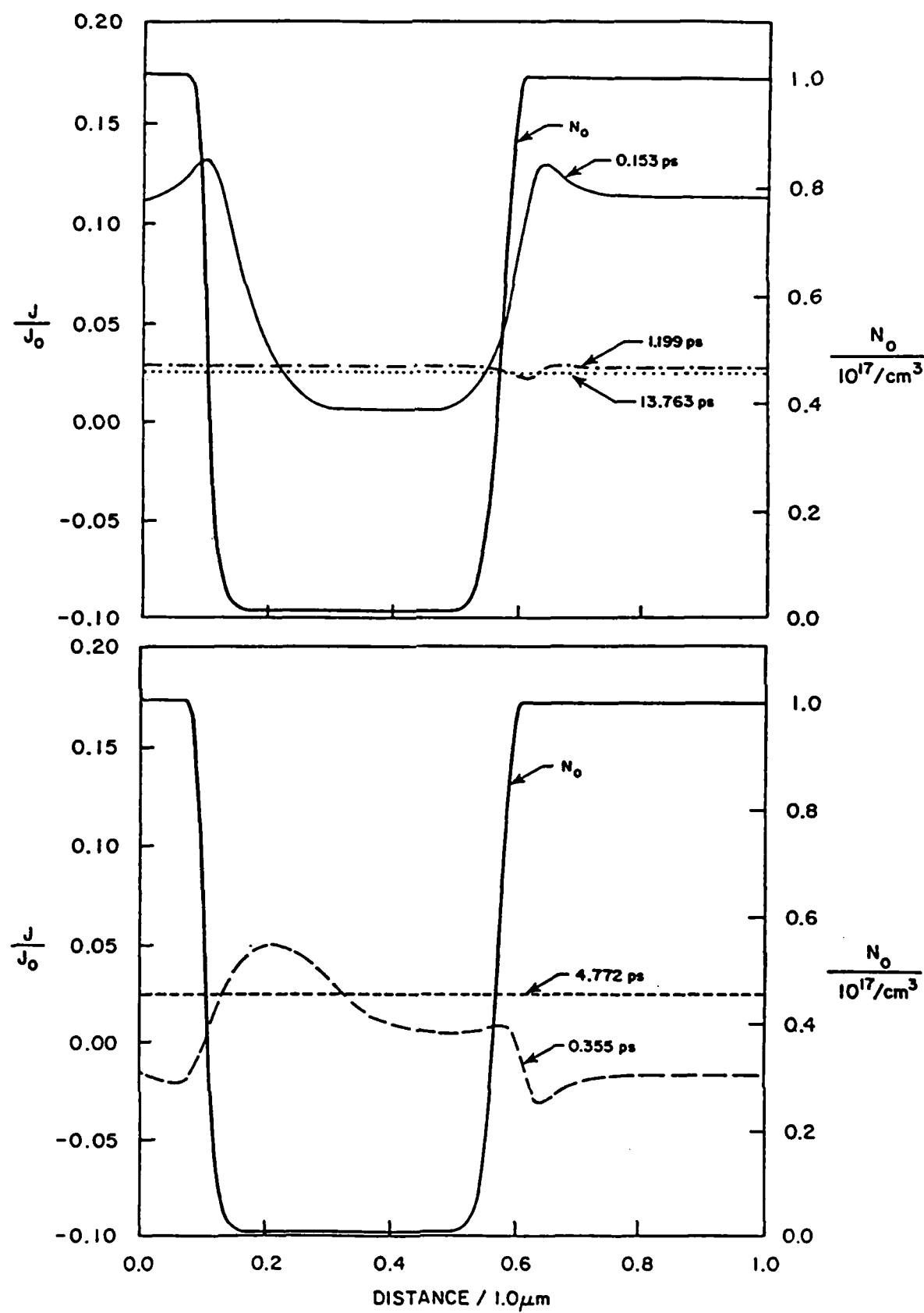


FIG. 40

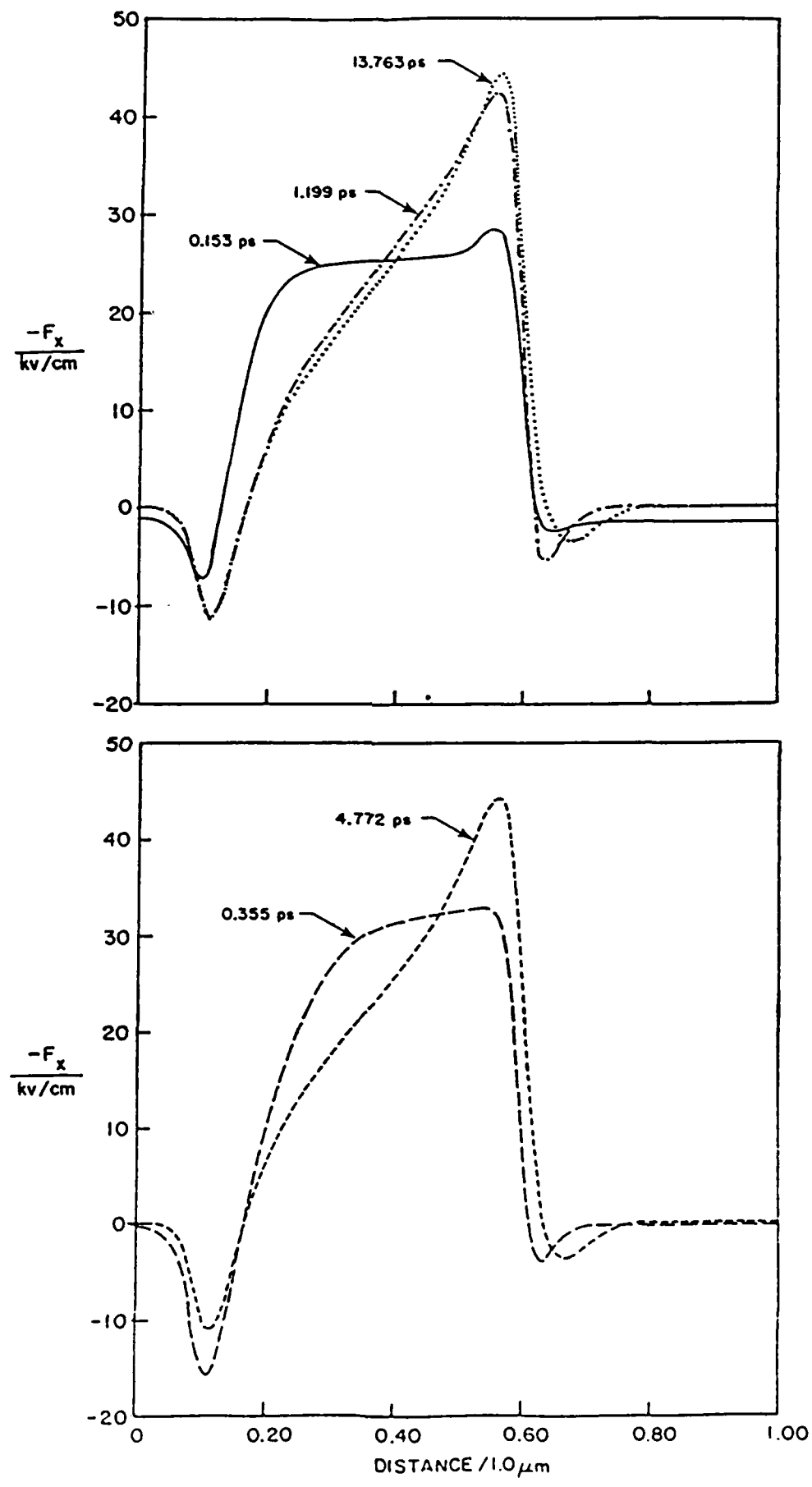


FIG. 41

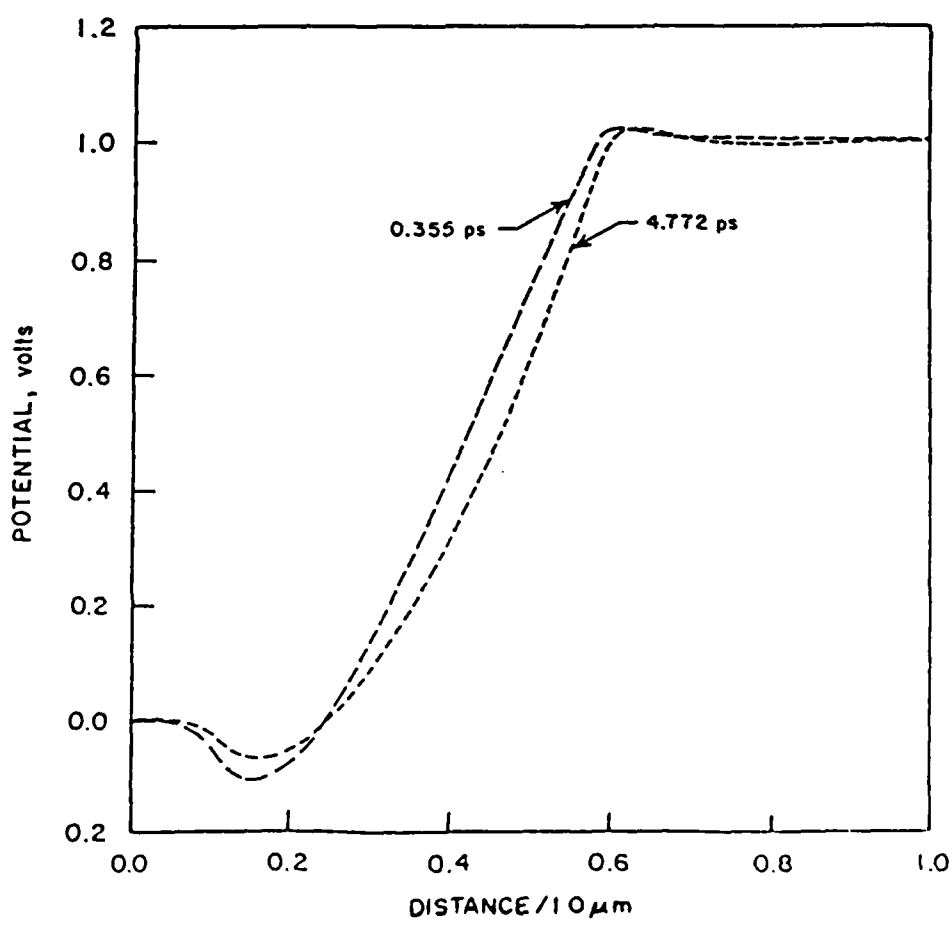
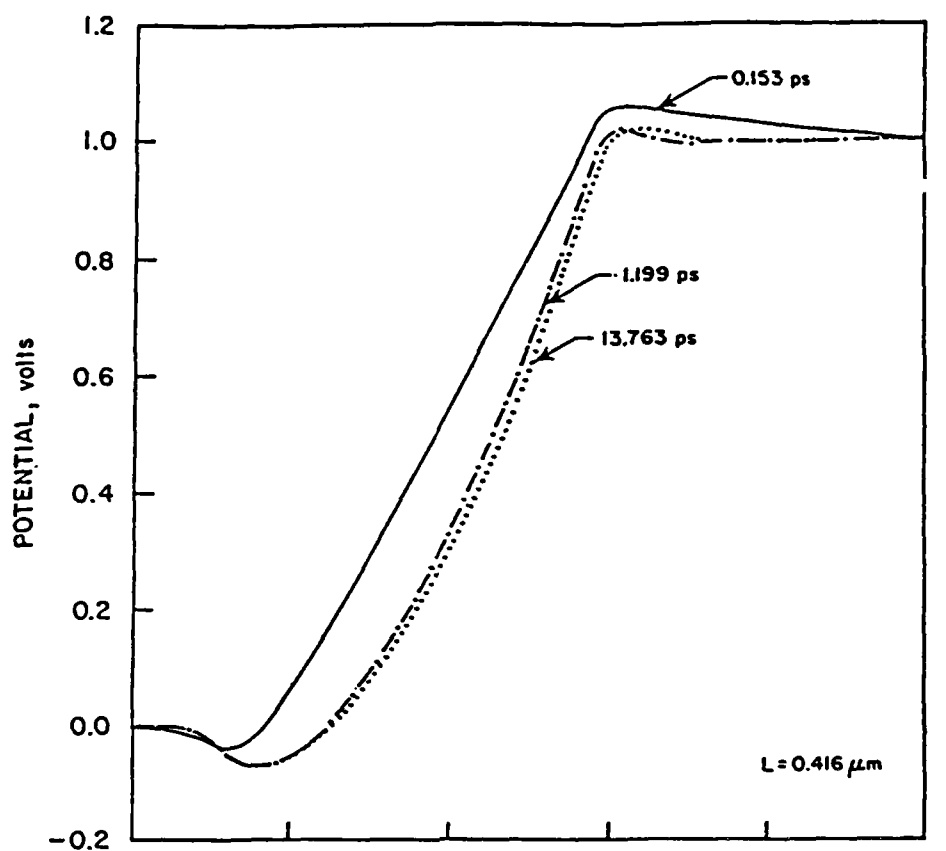


FIG. 42

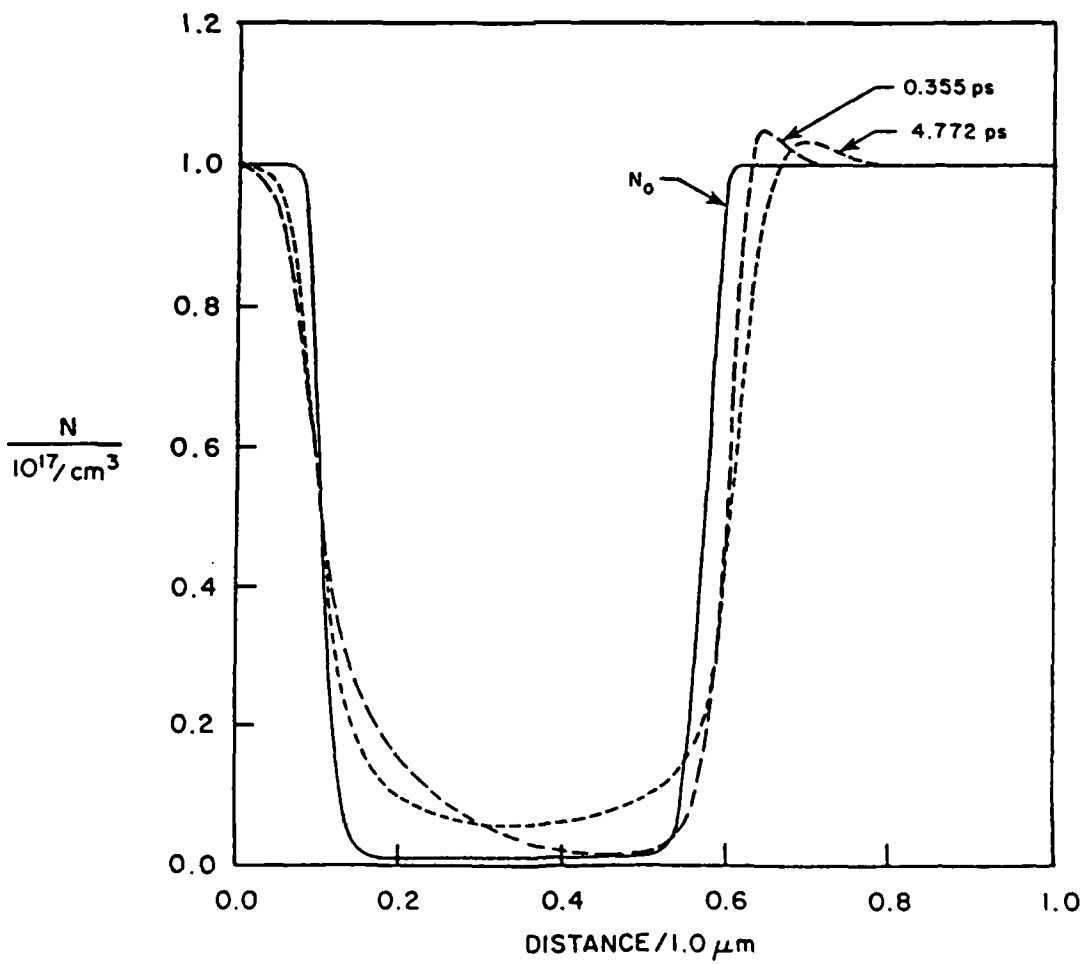
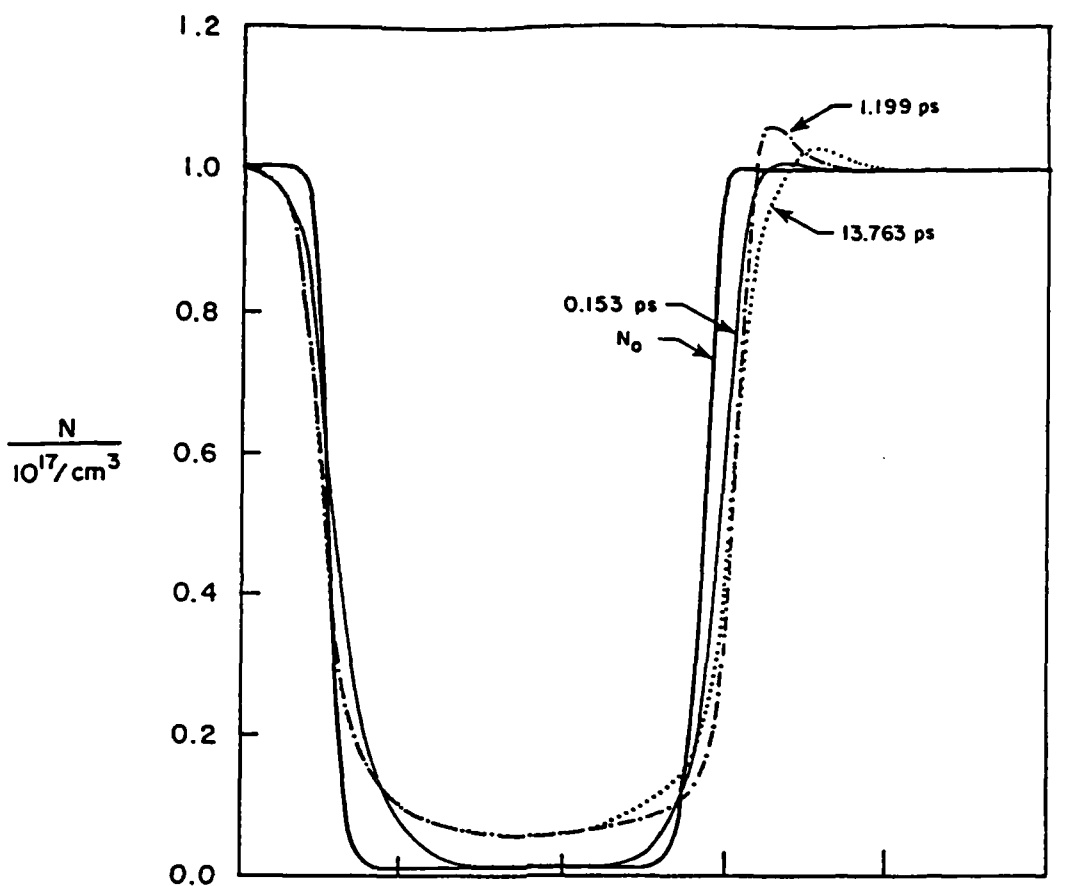


FIG. 43

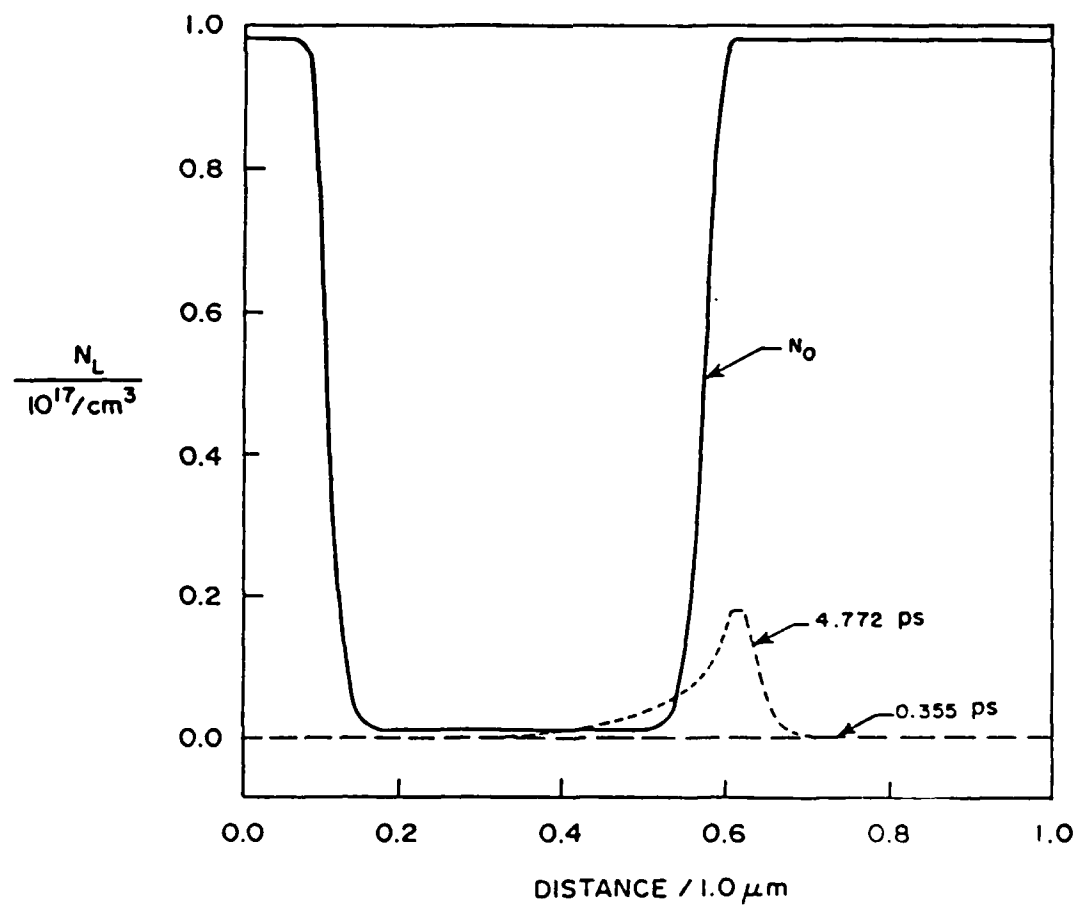
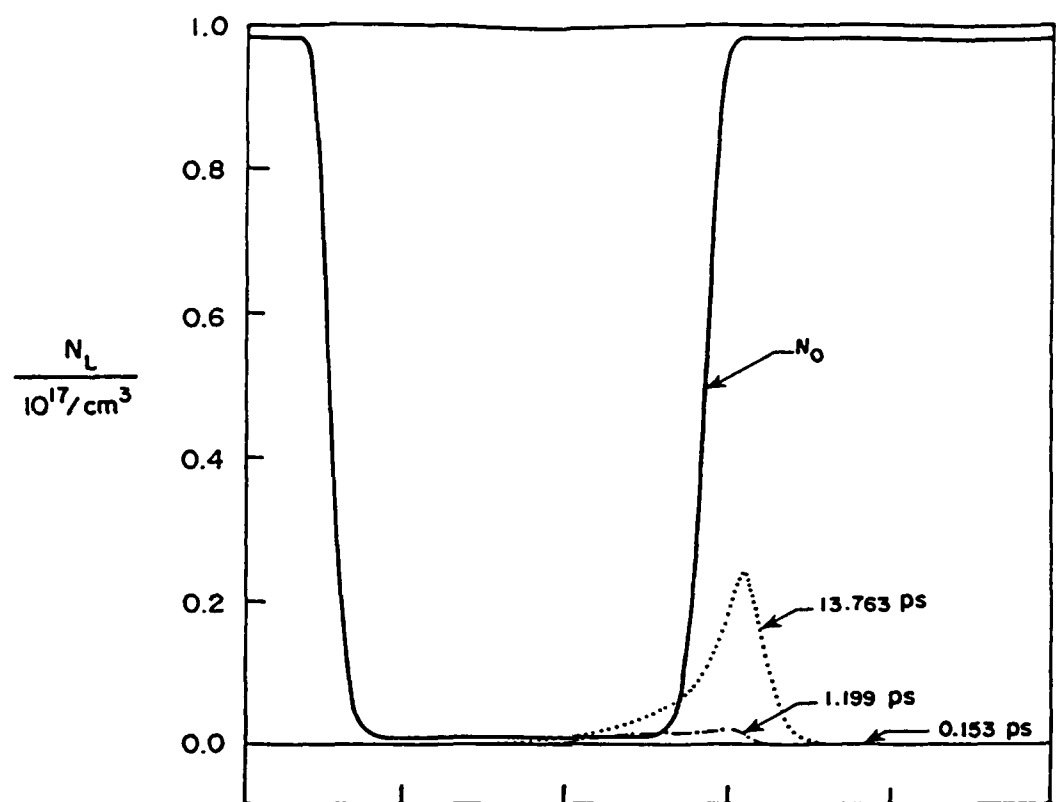


FIG. 44

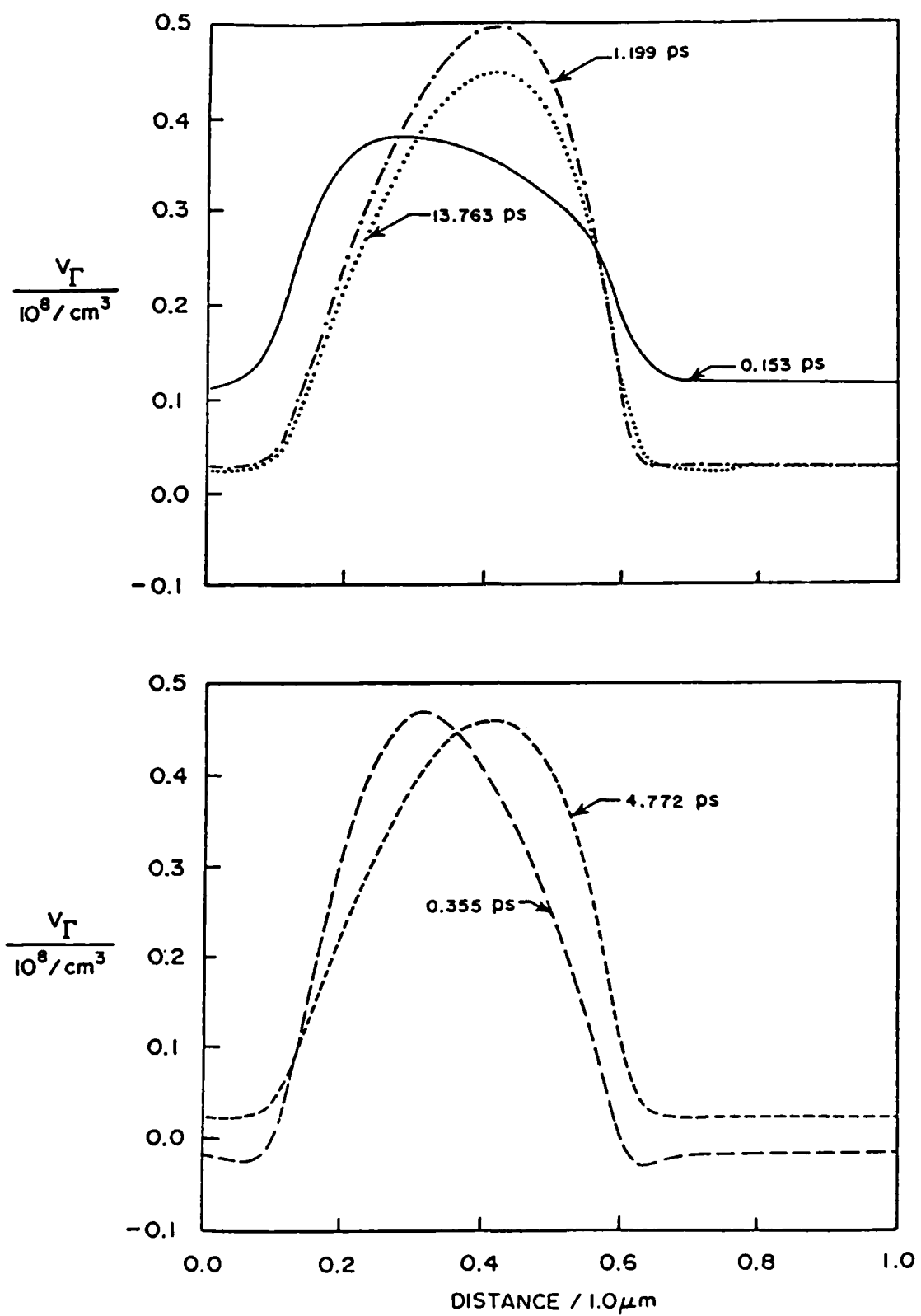


FIG. 45

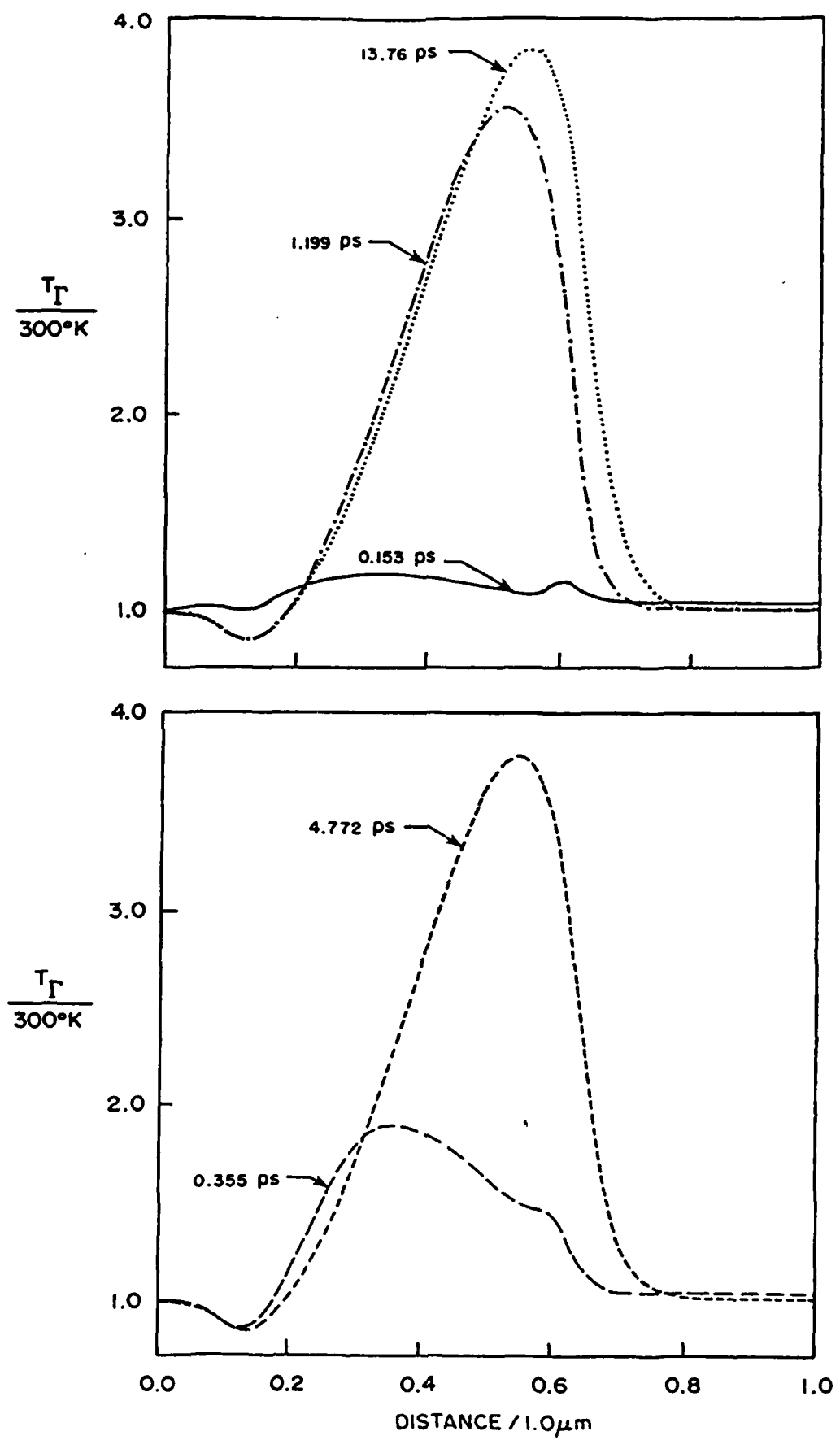


FIG. 46

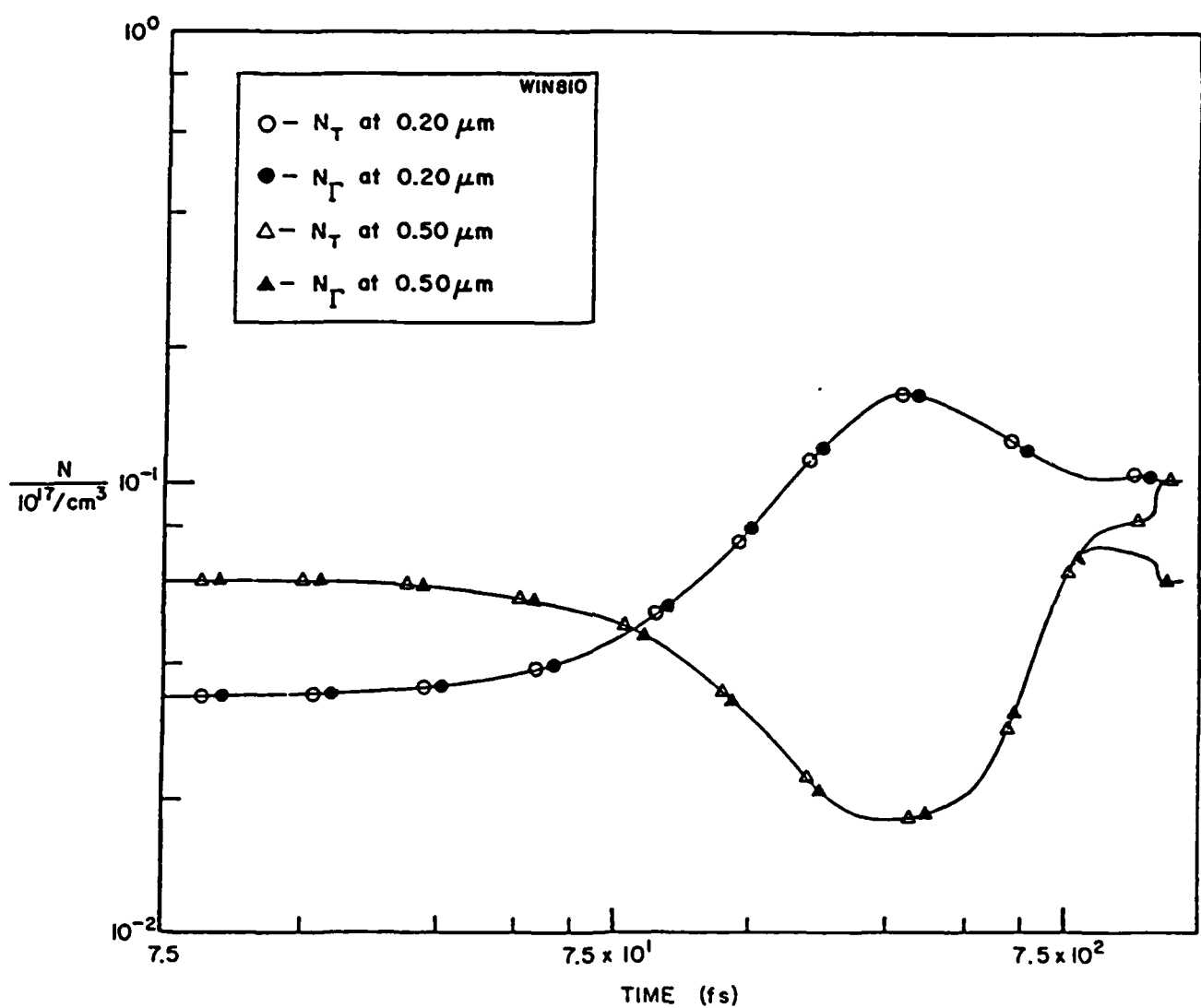


FIG. 47

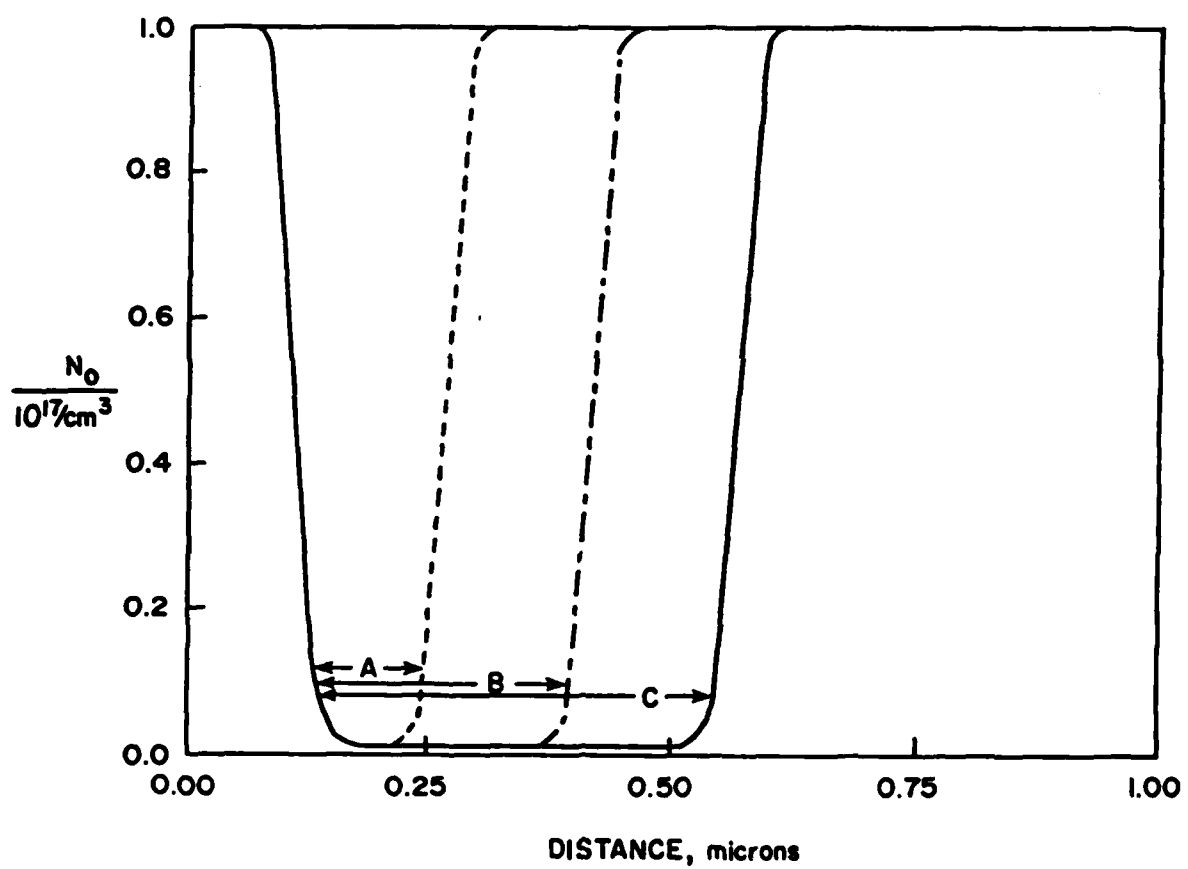


FIG. 48

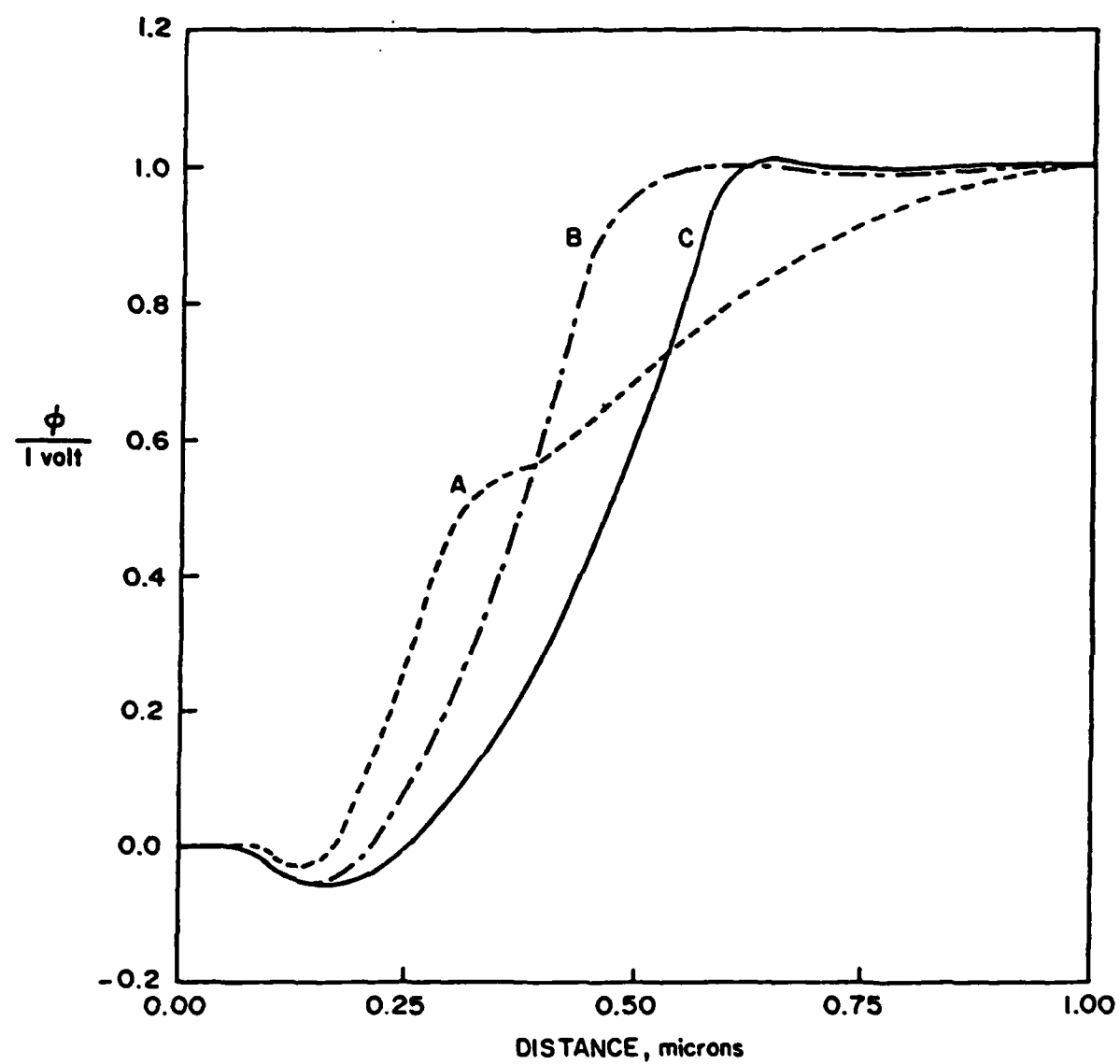


FIG. 49

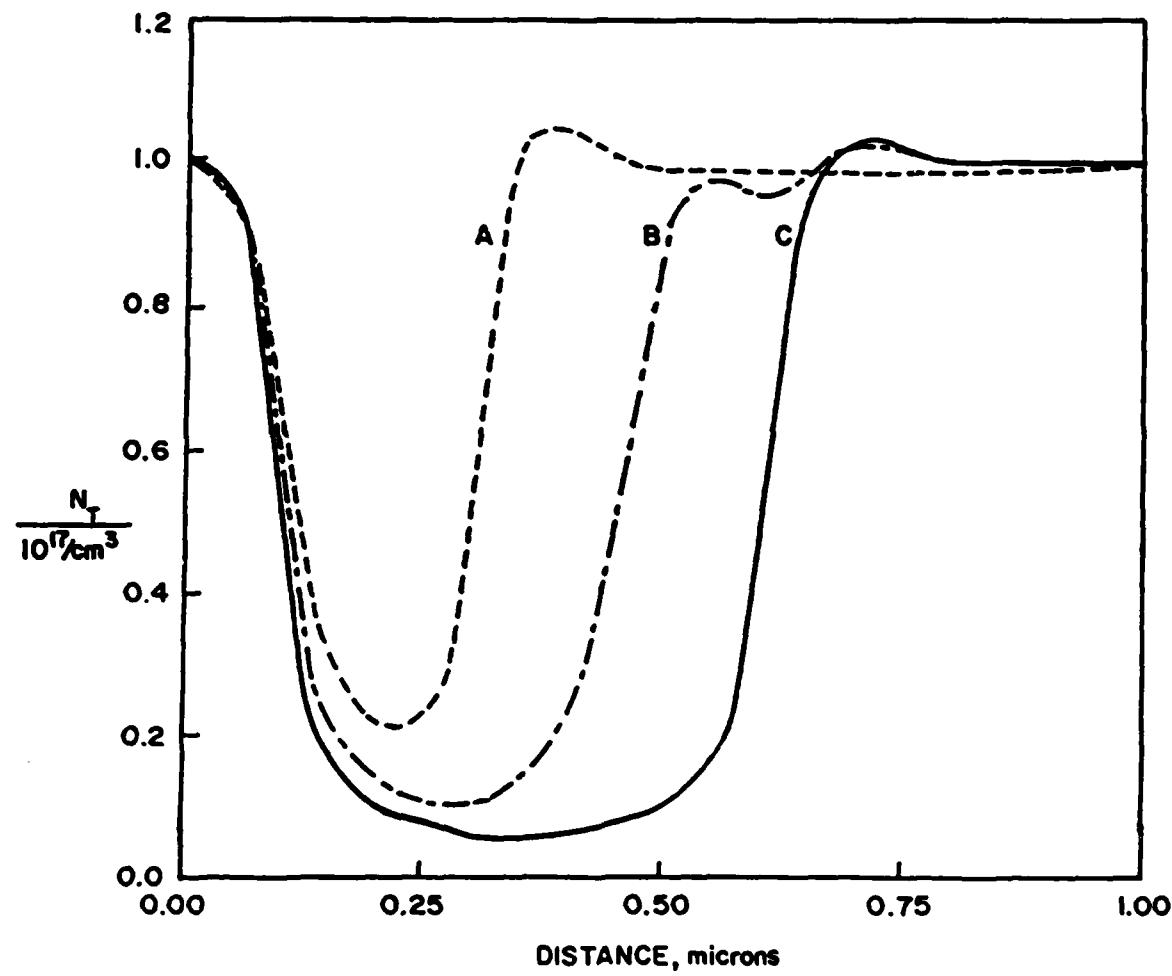


FIG. 50

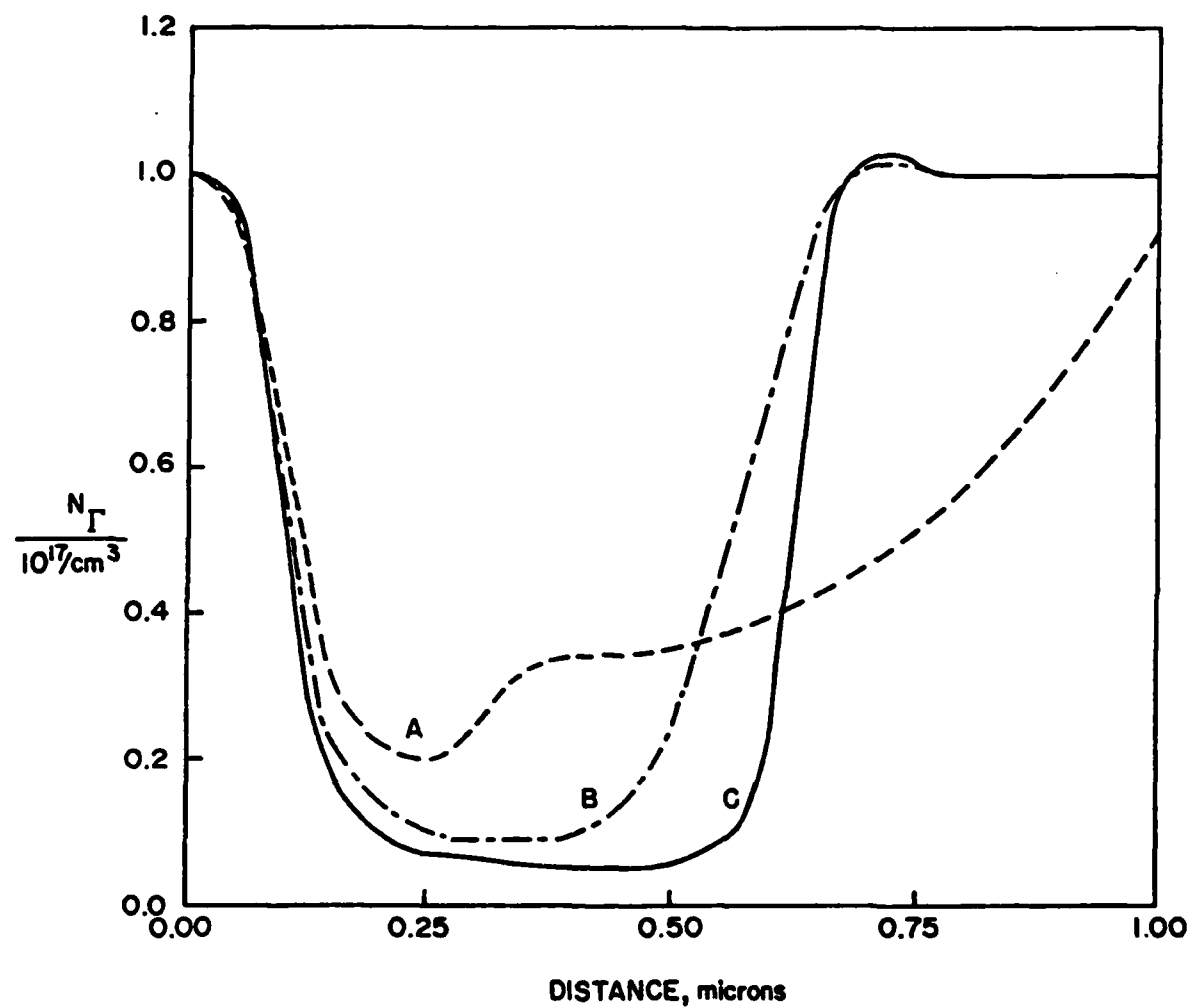


FIG. 5

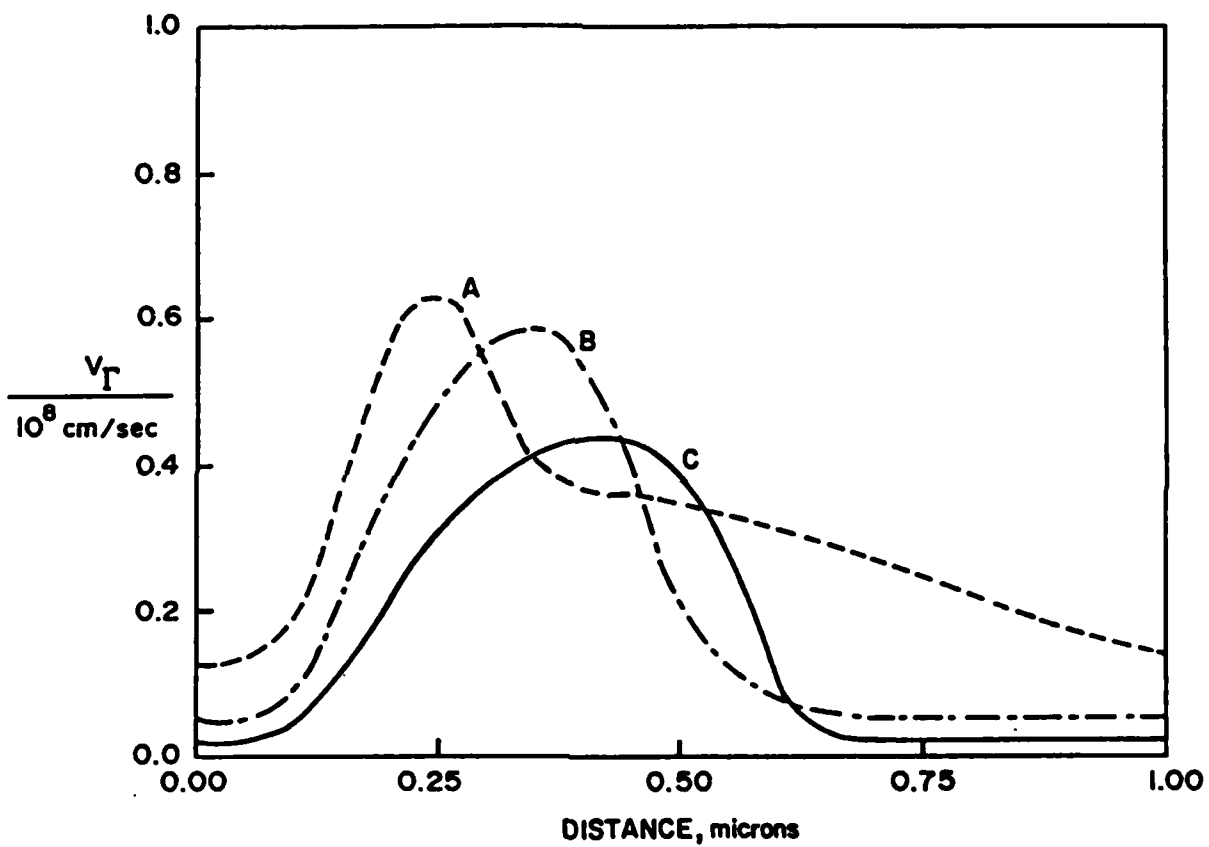


FIG. 52

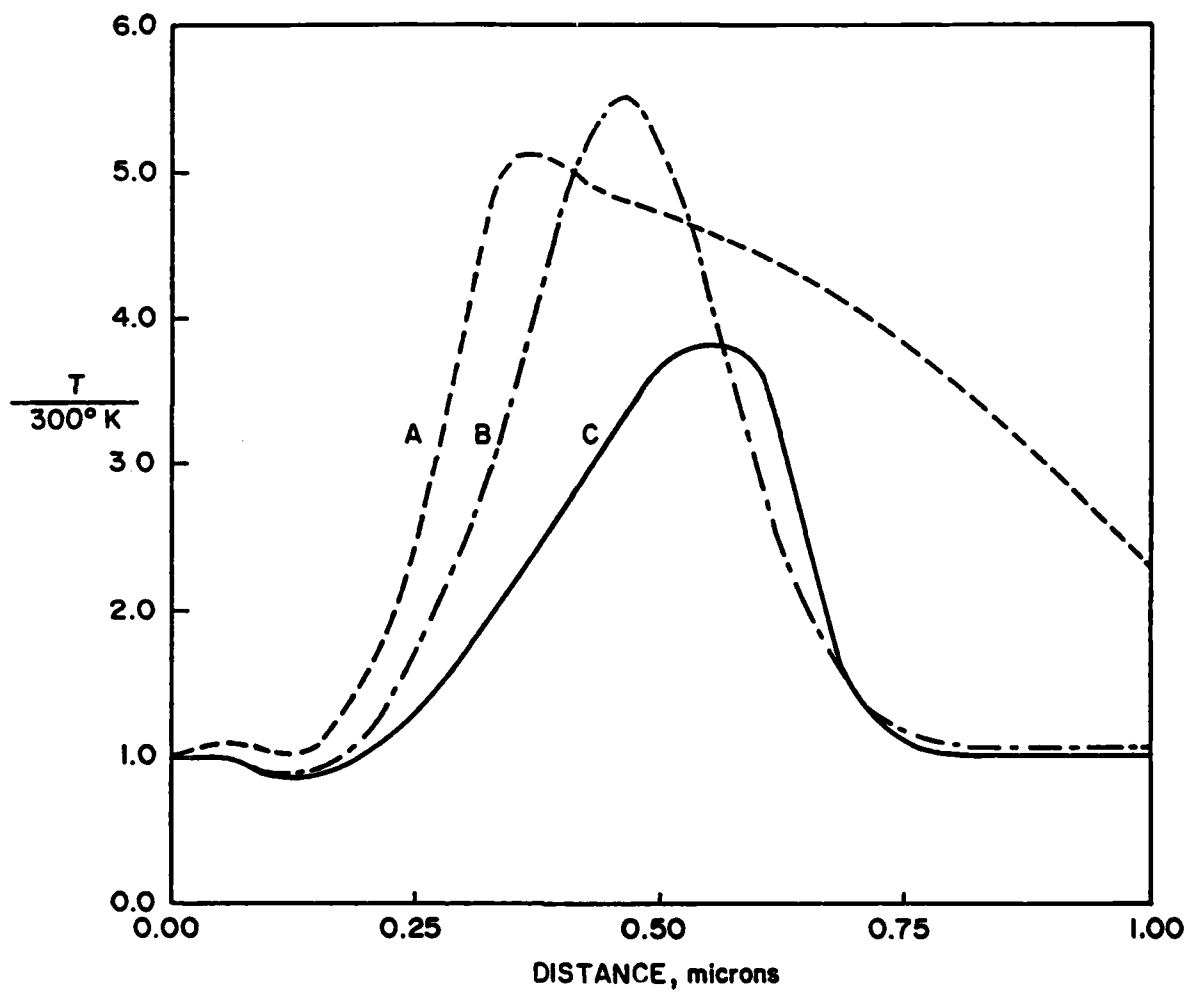


FIG. 53

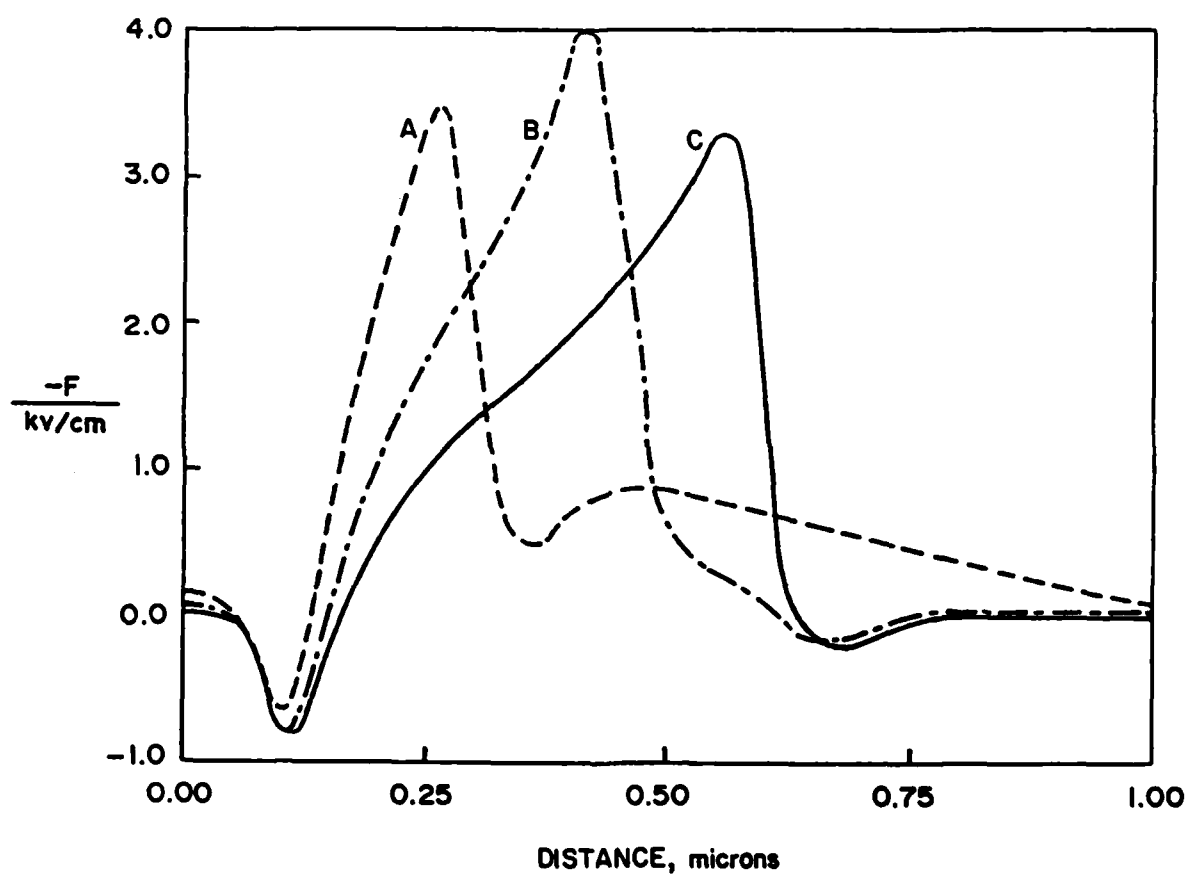
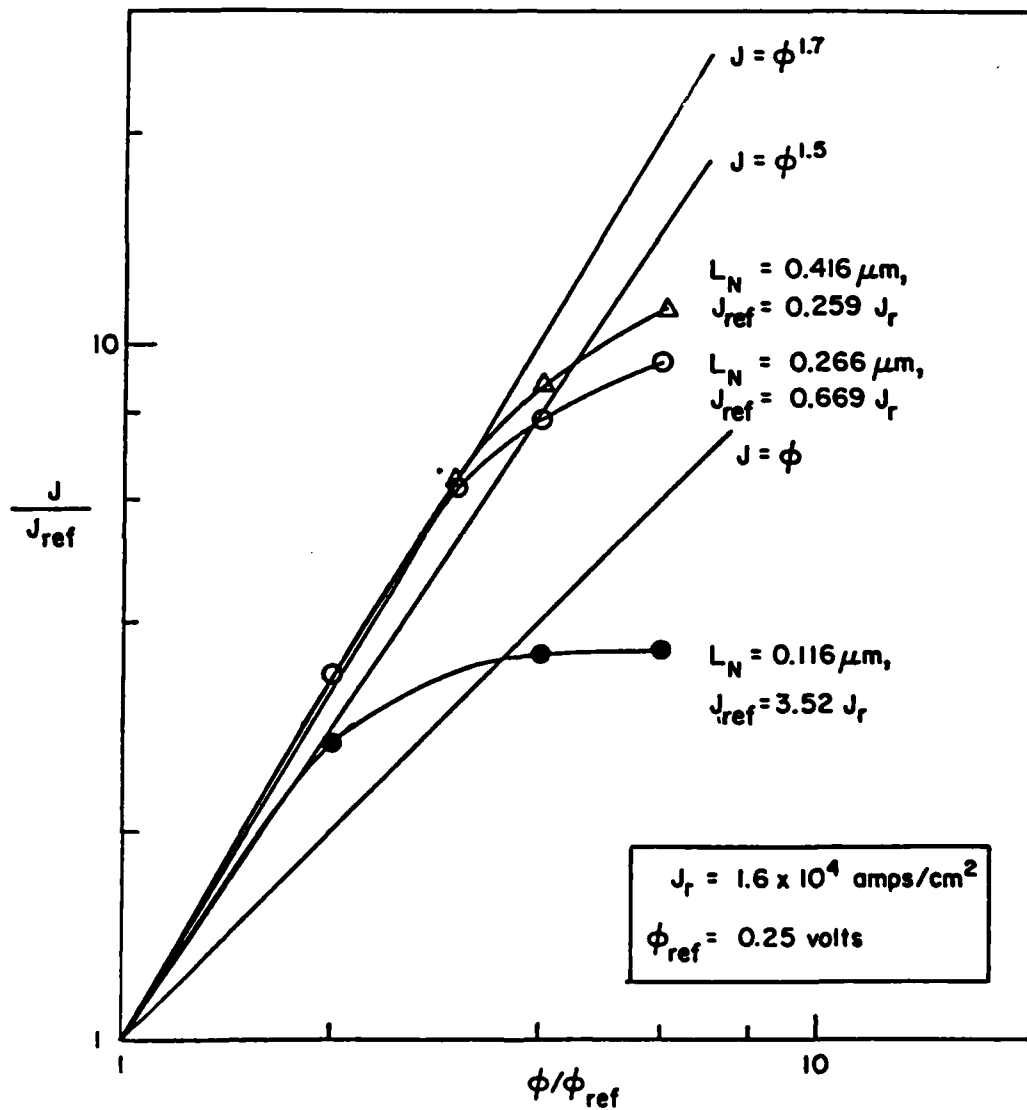


FIG. 54



**APPENDIX B**

**SCALING BAND STRUCTURE AND MATERIAL CHARACTERISTICS  
OF HIGH SPEED SUBMICRON LENGTH DEVICES**

**H. L. Grubin, J.P. Kreskovsky and M. Meyyappan  
Scientific Research Associates, Inc.  
P.O. Box 498  
Glastonbury, CT 06033**

**\*This study was supported by ONR and DARPA**

## I. INTRODUCTION

The performance characteristics of semiconductor devices are generally expressed in terms of a few key quantities, the transconductance, the delay time, the speed-power product. The material parameter dependence of these quantities has been determined under a wide variety of assumptions (see e.g., Shockley [1]) and has been the key element in the choice of semiconductor used. The device figures of merit are expressed in terms of such quantities as the mobility, saturated drift velocity, structure feature size and substrate doping. The role of each of these parameters is intrinsically different and tendencies to connect them for near and submicron length devices have often led to ostensibly confusing statements such as:

1. Gallium Arsenide is superior to silicon because of its higher electron mobility;
2. Silicon is superior to gallium arsenide because of its higher saturated drift velocity;
3. The results will tend to average out, and sometimes silicon is superior, while at other times gallium arsenide is superior.

The above statements tend to over simplify the issue as they are based on material characterization only and ignore the extrinsic as well as intrinsic features of the device being analyzed, e.g., n-channel MOSFET versus unipolar MESFET. But the debate does tend to highlight the critical role that the material properties play on the operation of the device and they also ask implicitly whether scaling as commonly practiced (see e.g., Bar-Lev [2]) is meaningful for submicron structures.

In the spirit of the above discussion a study was undertaken to examine the role that band structure (hence material characteristics), device feature size and density play in obtaining such quantities as the field dependent velocity and mobility, the current-voltage relations, and the general electrical characteristics of submicron structures. However, the interest in this study is broader than the debate of 'silicon versus gallium arsenide'. (Here, because of the strong commercial and military interest in both these semiconductors occupy an entrenched place in the semiconductor market place). Rather, attention was focused on the question: How does one proceed to make choices of new materials? And here, the question inspires additional significance in view of the attention given to the strained super-lattices discussed by Osbourne and coworkers [3], the ternary and quaternary III-V semiconductors, and of course, indium phosphide.

The study that resulted from addressing the above questions rested heavily on solutions to the moments of the Boltzmann transport equation (MBTE), and there were a few surprises. Perhaps the most significant is that the field dependent velocity that is used to represent the signature of a particular semiconductor is not uniquely determined. This conclusion was of relatively little significance in a practical way for lower frequency devices, but has a profound effect on submicron feature size devices, as discussed below. A second issue of interest, is the role of the saturated drift velocity as a figure of merit. Presently, high saturated drift velocities are regarded as positive attributes of a semiconductor (see e.g., Eden [4] and Grubin [5]). However, if the structure of interest is scaled down to submicron feature

sizes, and the material chosen is one in which high saturation drift velocity is achieved at the expense of a reduced low field mobility then device performance can be seriously degraded. A third issue is the effect of scaling-up the carrier density as the device feature size is reduced. Here, the important result is that increasing the carrier density does not lead to a corresponding scaled increase in the current density, as the uniform field calculations implicitly imply. Rather, increased carrier densities lead to greater nonuniformities in the spatially dependent field distribution and lower current levels than that predicted from the uniform field concepts.

The task of material scaling follows the general philosophy discussed by Thornber [6] as well as the scaling principles routinely used by workers in the area of computational fluid dynamics. The key conclusion of the study is that classical scaling arguments as currently applied to semiconductors provide incorrect assessments of the upper frequency limits of submicron - high speed semiconductor devices.

The approach taken to systematically analyze the role of band structure on the material characteristics of the semiconductor device involves performing a number of key baseline one dimensional calculations for the semiconductor gallium arsenide with a given channel length and doping level. The calculations are performed at several values of bias. The question is then asked: How do the results change, when the scattering rates, structure length, density, deformation potential coupling coefficient, intervalley energy separation, etc., are altered, either collectively, or separately. The results, as expected form an interesting mosaic, as discussed below.

The discussion below consists of a number of widely disparate elements each of which are brought into focus at the end of the paper. For example section II is concerned with illustrating how scaling is applied to the Boltzmann transport equation. Here the concepts of constant scattering scaling as applied to transient transport, and introduced by Thornber [6], are discussed. Specific application is made to the semiconductors gallium arsenide and indium phosphide whose scattering rates are introduced. The point is that materials such as indium phosphide and indium gallium arsenide can be approximately represented as scaled gallium arsenide elements, and the relative advantages of one against another immediately assessed. Again, assessment rests upon specific device application. Additionally, the significant contribution of nonuniform fields in scaling is also introduced, and shown that necessarily, material scaling must be accompanied by density scaling.

The calculations of this study were performed using the moments of the Boltzmann transport equation. The moment equations and their associated scattering integrals are briefly discussed in section III. A more detailed description is contained in a recent paper by Grubin and Kreskovsky [7]. The point of view of the scaling procedure is contained implicitly in section IV, where the moment equations are prepared for the nondimensionalization necessary for numerical procedures. Critical dimensionless scaling constants (DSC) are also introduced in this section; but the core of the study begins in section V.

Section V is an introductory discussion of scaling as applied to the semiconductor gallium arsenide. Here on the basis of trends in the semiconductor industry in which intrinsic material changes are almost always accompanied by

suitable scaling of such extrinsic variables as length and doping level, calculations are performed in which all DSC are held fixed. Thus, the following generic type of problem is addressed: If a material could be constructed whose low field mobility is a constant multiple,  $\lambda$ , of the low field mobility of gallium arsenide, and whose remaining steady state field dependent velocity is a compressed version of that of gallium arsenide; can the steady state and transient characteristic of the scaled device be predicted. On the basis of the discussion in section II, the answer to this question is immediately relevant to the semiconductors indium phosphide and indium gallium arsenide and their use as substitutes or replacements for gallium arsenide.

The discussion of section V was restricted, by choice, to calculations in which all DSC were fixed. Scaling in section V is designed to serve as an intuitive guide and reference point for additional scaling. For example, the situation may arise when a particular feature size of a device is a specification of the problem; and the task then becomes determining what changes in the electrical characteristics may be expected when there is a choice of materials.ials. This problem is treated in two parts. In section VI a two terminal structure of length 0.25 microns and a doping level of  $8 \times 10^{16}/\text{cm}^3$  is examined. Material variations are considered by altering the scattering rates by the constant  $\lambda$ . In section VI, the choices of  $\lambda$  are:  $\lambda=1, 2$  and  $4$ .

The discussion of section VI is continued in section VII, where isolated band structure alterations are introduced. In this case the scattering rates as used with the moments of the Boltzmann transport equation, are changed by a constant amount, but are nonuniformly altered. For example, in section VIIa the deformation coupling coefficient for intervalley transfer is altered. That is, starting from the value used in the calculations for gallium arsenide, the deformation coupling coefficient  $D_{PL}$  is multiplied by the factors '2' and '1/2'. The resulting steady state nonuniform field calculations are then compared to that of gallium arsenide. The calculations are performed for the same extrinsic values as those used in section VI, and a direct comparison is offered. As anticipated, the uniform field calculations show an increase in the saturated drift velocity with increased coupling coefficient. When this result is folded into earlier studies using the drift and diffusion equation (see, e.g., Grubin [5]), higher values of IDSS may be anticipated. However, when transport in submicron devices is considered it is determined, that the significant figure of merit is the low field mobility of the semiconductor; and if the improvements in velocity saturation are not accompanied by improvements in the low field mobility, there is little to be gained by choosing materials with high field velocity saturation.

The situation that tends to show both a satisfactory low field mobility and a high saturated drift velocity occurs when the intervalley energy separation in gallium arsenide is doubled. The dimensions and scaling of this calculation, which are discussed in section VIIb, are best understood when placed in the context of the gallium arsenide calculations of section V. The results of this calculation are designed to show the trends that should be expected when the energy separation is increased, and tends to suggest significant advantages for gallium indium arsenide over gallium arsenide for high speed transport in three terminal devices.

All of the calculations performed through section VIIb have ignored the effects of ionized impurity scattering. There are indeed conceptual difficulties in dealing with high donor densities and ionized impurity scattering in submicron

devices, each of which have been addressed in previous discussions (see e.g., Grubin and Ferry [8]), but are ignored here. From the point of view of the discussion of scaling, the effect of ionized impurity scattering is regarded as introducing nonuniform contributions to the scattering rates; here the effects of ionized impurity scattering influences only the momentum scattering rate. This discussion of ionized impurity contributions is contained in section VIIc.

One of the critical issues associated with device transport is whether an increase in the carrier density by a constant value,  $\lambda$ , will lead to an increase in the current density by the same factor,  $\lambda$ . The answer to this question is a negative one, and the principle reason that classical scaling, which ignores the spatial variations in the density, leads to over-optimistic predictions. The question of carrier density dependence is addressed in section VIII.

Two dimensional scaling considerations are addressed in the remaining portions of the study. Section IX addresses typical scaling in two dimensions as discussed by Bar-Lev [2], and ties these concepts to those addressed during the course of the study. Weaknesses in predictions of high frequency operation are addressed in section X, through solutions to the drift and diffusion equations for a low and high frequency gallium arsenide FET. The clear implication of these studies is that scaling will lead to improved performance, but that the predictions based upon simple scaling will tend to be over-optimistic.

Section XI reviews already published studies, that tie the role of saturation in the drift velocity to FET performance, and connects the results to the discussion of the earlier chapters on scaling. Additionally, preliminary computations using the DDE with GaAs parameters yielding a cutoff frequency of 9.0GHz, demonstrate that scaling down the critical feature size by an order of magnitude is likely to increase the cutoff frequency to values near 90 Ghz. Section XI also contains the first preliminary results of a comparison of FET computations using the BTE and the DDE. The principle conclusion is that the submicron FET is likely to be better characterized by a transconductance that is mobility dominated rather than saturated drift velocity dominated. Section XII is a summary of the conclusions of the study, part of which have been addressed above.

## II. SCALING AND THE BOLTZMANN TRANSPORT EQUATION

The Boltzmann transport equation for electrons responding to a field  $F$ , and scattering sites, while being transported in a parabolic band with effective mass  $m$  is

$$\frac{\partial f}{\partial t} + \frac{\hbar \vec{k}}{m} \cdot \nabla_r f - \frac{e\vec{F}}{\hbar} \cdot \nabla_k f = -\frac{V}{4\pi^3} \left\{ \int d^3 k' W(\vec{k}, \vec{k}') f(\vec{k}) (1-f(\vec{k}')) - \int d^3 k' W(k', k) f(k') (1-f(k)) \right\} \quad (1)$$

In equation (1),  $W(k, k')$  is the probability of a carrier undergoing a transition from the state  $k$  to the state  $k'$ .  $W(k, k')$  is generally complex in form and as used below is separated into contributions from individual sections of the conduction band, as in the cases of gallium arsenide and indium phosphide.

Currently, semiconductor materials are classified with parameters extracted from uniform field considerations in which all space charge nonuniformities are neglected. While this approach is unfortunate because all semiconductor devices are operated under nonuniform space charge conditions, its use will be continued below. In particular, the discussion begins with a description of gallium arsenide under uniform field conditions and the consequences thereof in which all scattering rates are altered by the same constant. The situation of nonuniform fields, which is the thrust of this paper follows in the remaining sections.

The relevance of altering all scattering rates by the same constant is moot. It is different from the classical scaling discussed, e.g., by Bar-Lev [2], insofar as it focuses attention on alterations in the mobility rather than the extrinsic characteristics of the structure, although the latter will clearly enter the picture. The advantage of the constant scaling is that it provides an initial introduction into the work of this study.

Under spatially uniform, time independent conditions, electron transport in the presence of an electric field is described by the equation

$$\frac{e\vec{F}}{\hbar} \nabla_k f = \frac{V}{4\pi^3} \left\{ \int d^3 k' W(k, k') f(k) (1-f(k')) - \int d^3 k' W(k', k) f(k') (1-f(k)) \right\} \quad (2)$$

and statistical mean quantities such as the carrier velocity

$$v \equiv \int \frac{\hbar \vec{k}}{m} f d^3 k / \int f d^3 k \quad (3)$$

In principle the scattering rates are the signatures of the semiconductors from which all transport properties are identified. In examining high field transport in semiconductors a number of different approaches have been taken to identify the relevant physics. The approach taken in this study is to

utilize the first three moments of the Boltzmann transport equation, as discussed in section III. Thus, an apology is in order here: In referring to computed velocities in this section, it is noted that they were not obtained through solution to the Boltzmann transport equation. Rather, they were obtained from solutions of the moment equations. The scaling arguments as applied to the Boltzmann transport equation are, however, also the same as those applicable to the moment equations. The conceptual results are thus interchangable.

Specific semiconducting elements in this study are identified by an assumed set of scattering events, e.g., LO phonon, intervalley phonon, acoustic phonon, impurity scattering, etc. From these events a field dependent velocity emerges. For gallium arsenide, assuming only two levels of transfer (between the  $\Gamma$  and L valleys) the steady state uniform field dependent properties are shown in figure 1. The band structure parameters used for the calculation are identified in table 1. There are eight frames associated with figure 1. Figures 1a and 1b, display the field dependent velocity over a range of field values varying from zero to 92kv/cm and 20kv/cm, respectively. This field dependence is approximately what is seen experimentally [9]).

In addition to the field dependent velocity the fractional density of carriers in the  $\Gamma$  and L valleys are displayed in figures 1c and 1d, respectively. It is noted that electron transfer while rapid, occurs continuously, beginning at a field of approximately 3 kv/cm. The mean carrier velocity for electrons within the  $\Gamma$  and L valleys are displayed in figures 1e and 1f, respectively. For the parameters chosen, there is an apparent onset of saturation in the  $\Gamma$  velocity. The parameters for the L valley have been chosen such that the mobility of the L valley is relatively constant over a wide range of field values. It may be anticipated that the mobility of the L valley would also exhibit nonlinearities at high fields. Indeed, using the  $\Gamma$  - X ordering originally discussed by Butcher, et al., [10] it is apparent that such nonlinearities exist. However, for the calculations discussed in this paper, the L valley carriers, over the field range of 90 kv/cm, are approximately at the equilibrium with the lattice and all nonlinearities associated with the velocity field curve are due primarily to 'k' - space transfer. Finally, figures 1g and 1f display the field dependence of the electron temperature in the  $\Gamma$  and L valleys, respectively. It is noted that the L valley temperature is approximately equal to the ambient over the field range of interest; whereas, the  $\Gamma$  valley temperature increases significantly with field. The variation of temperature with field is a consequence of relaxation mechanisms (see e.g., Grubin and Kreskovsky [7]).

The principal topic of interest is to determine the degree of predictability that emerges when these scattering parameters are systematically altered. Unfortunately, there are not many tests that can be used to accurately assess the effectiveness of these alterations. The one that we focus on is the semiconductor indium phosphide, and its relationship to gallium arsenide as a scaled semiconductor material. The semiconductor indium phosphide is of interest as a candidate millimeter wave material (see e.g., Binari, et al., [11]) and because over certain electron temperature ranges it's scattering rates are approximate multiples of that for gallium arsenide. It must, however, be noted that the specific parameter alteration from gallium arsenide is of less importance, in its detail, than the observed alteration in transport that is predicted. Thus, the simplest and first question to be

addressed is how will the field dependent velocity relation change as scattering rates are altered, by a constant, over the entire range of energy, or 'k' value. In this case, simple algebra indicates that if

$$W(\vec{k}, \vec{k}') \Rightarrow \lambda W(\vec{k}, \vec{k}') \quad (4)$$

the uniform field BTE takes the form

$$\frac{eF}{\hbar\lambda} \nabla_k f = \frac{V}{4\pi^3} \left\{ \int d^3 k' W(k, k') f(k) (1 - f(k')) - \int d^3 k W(k', k) f(k') (1 - f(k)) \right\} \quad (5)$$

and leads to the following simple rule (Thornber [6]):

$$v_\lambda(F) = v_0(F/\lambda) \quad (6a)$$

$$v_\lambda(\lambda F) = v_0(F) \quad (6b)$$

Thus, if  $\lambda=2$ , the scaled and unscaled field dependent velocity relations take the form shown in figure 2. It is noted that with the exception of the region of negative differential mobility, the scaled  $\lambda=2$  curve is remarkably similar to that of indium phosphide. Additionally, the  $\lambda=1/2$  curve, while not shown, bears a strong resemblance to  $Ga_xIn_{1-x}As$  ( $x=.5$ ) [12].

The case for indium phosphide as a 'limited scaled gallium arsenide' is further addressed in figures 3 through 6, where calculations for both indium phosphide and gallium arsenide are displayed. For example, figures 3 is a repeat of figure 1b, but for the semiconductor indium phosphide. The parameters used in this calculation are listed in table 2.

Figure 4 shows the scattering rates for gallium arsenide, whereas figure 5 displays the results for indium phosphide. The rates depicted in figures 4 and 5 are those used in the moment equation (7) and are discussed next.

Figure 4a displays the scattering rates of electrons in gallium arsenide being transferred from the  $\Gamma$  to L valley. The scattering rates are defined in terms of their dependence on the electron temperature, which in these figures varies from 3000K to 4800K. With the exception of strong nonlinearities below approximately 1500K the scattering rates show an approximate linear dependence on electron temperature. For the return L to  $\Gamma$  scattering displayed in figure 4b the nonlinearity is weak and the electron temperature dependence appears to be approximately linear.

The momentum scattering rates for carriers in gallium arsenide are displayed in figure 4c for the  $\Gamma$  valley and figure 4d for the L valley. The low field mobility for gallium arsenide is dominated by  $\Gamma$  valley carrier transport; and at an electron temperature equal to the ambient, the momentum scattering rate

is  $0.325 \times 10^{13}$ /sec and is dominated by LO phonon scattering. The L valley scattering rates are more than an order of magnitude greater than that for the  $\Gamma$  valley electrons and indicates corresponding low values of the L valley carrier mobility.

The energy scattering rates for  $\Gamma$  valley carriers in gallium arsenide are displayed in figure 4e. It is noted that figure 4e shows an energy scattering rate that is a monotonically increasing function of electron temperature. Because intervalley scattering is included, effects associated with catastrophic breakdown does not occur. Return scattering, shown in figure 4f is associated with the transfer of energy when a carrier makes a transition from the L to the  $\Gamma$  valley. Similar remarks apply to figures 4g and 4h; however, when considering figure 4g, it must be noted that the effectiveness of energy scattering within the L valley decreases for carrier temperatures in excess of 900°K. The results here are qualitatively similar to those obtained by Butcher, et al., [10], Bosch and Thim [12] and Grubin, et al., [13].

The indium phosphide scattering rates which are displayed in figure 5 reflect a number of significant differences in value from that of gallium arsenide. These differences are summarized in figure 6, which displays the ratio of the scattering rates of indium phosphide to gallium arsenide. First, substantial intervalley carrier scattering in the indium phosphide does not occur until the  $\Gamma$  valley electron temperature reaches approximately 900°K. The latter reflects the larger energy separation between the  $\Gamma$  and L portions of the conduction band than that of gallium arsenide. Second, the  $\Gamma$  valley momentum scattering rate is approximately twice that of gallium arsenide and reflects the presence of enhanced LO scattering. The net effect of these differences is to provide scattering rates that scale over select sections of the entire electron temperature range. For example, the ratio of the  $\Gamma$  valley momentum scattering rates is approximately equal to '2', for a range of values of electron temperature from the ambient to values slightly in excess of 600°K. For values of temperature in excess of 1200°K the ratio of the scattering rates is approximately equal to unity. The variation from one value to the next occurs over the range where the intervalley transfer is dominant. As in the case of gallium arsenide, the indium phosphide L valley momentum scattering rate is approximately constant over the entire temperature range. While the  $\Gamma$  to L valley carrier transfer was discussed before, the return L to  $\Gamma$  transfer rates are approximately constant and 30% in excess of unity over a range somewhat in excess of 1800°K.

It would clearly be stretching the point to conclude that constant parameter scaling applies to the semiconductors indium phosphide and gallium arsenide. On the other hand, constant parameter scaling for the individual events does occur over meaningful variations in electron temperature. The significant points associated with scaling are: (i) starting from gallium arsenide parameters, constant scaling will yield a field dependent velocity curves very similar to that of indium phosphide (when the scaling is greater than unity) or curves similar to that of gallium indium arsenide (when the scaling is less than unity); (ii) starting from first principles, where the scattering rates for indium phosphide are not constant multiples of gallium arsenide a field dependent velocity curve for indium phosphide can be constructed that is very similar to one that may be obtained by scaling gallium arsenide. The significant implication is that the uniform field dependent velocity field curves discussed in the literature to characterize individual semiconductors may not

be uniquely determined. Thus in the absence of knowing, *a priori*, what the material parameters are that characterize a semiconductor, it must be accepted that various combinations of material parameters will yield the same results.

Of interest then, as carried in the discussion of this paper are:

(i) determining the trends that may reasonably be expected if material parameter identification is uncertain, and (ii) the general direction one must proceed in attaining high frequency materials. Thus, the approach taken is first to identify the trends associated with constant parameter scaling, regarding them as providing bounds for device behavior.

The general situation as summarized above is that variations in the semiconductor material properties will not be accomplished by constant parameter scaling. Rather, individual scattering rates will be altered nonuniformly, with effects as shown in figure 7. For the moment, however we return to constant parameter scaling and uniform fields.

For uniform fields attention is given to the BTE with the term containing the spatial derivations once again ignored. For this case, the effect of constant scaling is as follows: For a given value of uniform field  $F_0$ , the mean velocity of the electrons is computed. The carriers are then subjected to a controlled change in electric field  $\delta F_0$ , which reaches a new steady state value  $F_0(t) + \delta F_0(t)$ , as shown in figure 8a. The task at hand is to calculate the transient response of the mean carrier velocity figure 8b. Under the assumption that the scattering rates and the distribution functions are not explicit functions of time, scaling is direct and leads to the following modified equation:

$$\frac{\partial f}{\partial(\lambda t)} - \frac{eF}{\hbar\lambda} \nabla_k f = - \frac{V}{4\pi^3} \left\{ \int d^3 k' W(k, k') f(k) (1 - f(k')) - \int d^3 k' W(k', k) f(k') (1 - f(k)) \right\} \quad (7)$$

and the following simple rule: If  $v_0(F(t), t)$  represents the transient response of the unscaled field dependent velocity, to a time dependent change in field, then the scaled and unscaled velocities bear the following relation

$$v_\lambda[F(t), t] \geq v_0\left[\frac{F}{\lambda}, \lambda t\right] \quad (8)$$

where the equality is true beyond the first time step. For this case the transient response of the unscaled and scaled velocity is as shown in figure 9. The principle result of figure 9 is that the response of a scaled device, for  $\lambda > 1$ , is faster than that of the unscaled device, but that additionally larger fields are required. This latter result is intuitively accessible: The ordinary differential equation describing the motion of a single carrier subjected to uniform fields and scattering rates has a solution given by  $v_0(F, t) = -etFm^{-1}[1 - e^{-t/\tau}]$ , where  $\tau$  is a relaxation time. If the

scattering rate is increased by  $\lambda$  the relaxation time is reduced by the factor  $\lambda$ , and the scaled velocity becomes  $v_\lambda(F,t) = -e\tau F(m\lambda)^{-1}[1-e^{-t\lambda/\tau}] = v_0(F/\lambda,t\lambda)$ . The clear implication is that relaxation effects are more rapid for  $\lambda$  greater than or equal to unity.

Another viewpoint may be expressed by examining the response of the scaled semiconductor to a sinusoidal electric field. In this case, the uniform field BTE becomes

$$\frac{\partial f}{\partial(\lambda t)} - \frac{eF}{\hbar\lambda} \sin\lambda t \nabla_k f = -\frac{V}{4\pi^3} \left\{ \int d^3 k' W(\vec{k}, \vec{k}') f(\vec{k}) (1-f(\vec{k}')) - \int d^3 k W(k', k) f(k') (1-f(k)) \right\}$$
(9)

The significance of equation (9) is that if power gain is obtained with an unscaled device at, e.g., 110GHz, then power gain will be obtained with the scaled device at  $\lambda \times 110\text{GHz}$ , provided the field across the scaled device is increased by the amount  $\lambda F_0$ .

The situation with spatial scaling is similar to that of temporal scaling and for simplicity the scaled BTE is written for a sinusoidal field as

$$\frac{\hbar\vec{k}}{m} \left( \frac{\partial f}{\partial \lambda \vec{x}} \right) - \frac{eF}{\hbar\lambda} \sin\lambda x \nabla_k f = -\frac{V}{4\pi^3} \left\{ \int d^3 k' W(\vec{k}, \vec{k}') f(\vec{k}) (1-f(\vec{k}')) - \int d^3 k W(k', k) f(k') (1-f(k)) \right\}$$
(10)

The significance of equation (10) for spatial variations is that if the spatial velocity variations are computed for an unscaled but sinusoidally varying electric field, then similar velocity variations will occur for the scaled element. For the scaled element the velocity variations will occur over the distance  $L/\lambda$ , providing the amplitude of the applied field is increased by the factor  $\lambda$ . Thus for  $\lambda > 1$ , higher switching speeds, due to shorter transit times, are possible.

The situation with respect to equation (10) is, however, more complicated than it appears, for self-consistency has been ignored. To include self-consistency, Poissons equation must be solved. Here

$$\nabla^2 \phi = +\frac{e}{\epsilon} (n - n_0)$$
(11)

or

$$\frac{\partial F}{\partial x} = -\frac{e}{\epsilon} (n - n_0) \quad (12)$$

in one dimension. The scaled Poisson equation is of the form

$$\frac{\partial F}{\partial x} = -\frac{e\lambda^2}{\epsilon} (n - n_0) \quad (13)$$

implying that scaling, in which, among other things, the potential is kept constant, requires that the background density be decreased by the factor of  $\lambda^2$ . While an alteration in the donor density leaves the scaled semiconductors unchanged with respect to transport; the effects of variable donor density on unscaled gallium arsenide is significant, and is discussed in section VIII.

### III. MOMENTS OF THE BOLTZMANN TRANSPORT EQUATION

The discussion above was concerned with demonstrating that a broad set of guidelines for spatial and temporal scaling of semiconductor devices can be developed. Were the discussion confined to constant scaling parameters alone that analysis while useful would be of restricted applicability. To be as general as possible, while remaining within the framework of practicality, nonuniform scaling is also examined in considerable detail. The nonuniform scaling involves applying nonuniform weights to the gallium arsenide scattering integrals. Transport can then be examined by solving the BTE using any of the widely accepted methods: iterative, Monte Carlo, and moment methods (see e.g., Grubin, et al., [13]). The approach taken below employs the moment methods for two species of carriers:  $\Gamma$  and L valley (or more generally satellite) carriers. The moment equations have been discussed in detail in the past (see e.g., Grubin and Kreskovsky [7]). They are included for completeness in the discussion below. It is important to note that all of the scaling included in the moment equation formulation are part of all solutions to the Boltzmann transport equation.

The essential feature of the moment equation, as used below, is that Poisson's equation with

$$n = n_1 + n_2 \quad (14)$$

is coupled to the first three moments of the BTE, the first, of which, involves continuity. For valley '1'

$$\frac{\partial n_1}{\partial t} = - \frac{\partial}{\partial x_1} \frac{n_1 \hbar k_1^j}{m_1} - n_1 \Gamma_1 + (n - n_2) \Gamma_2 \quad (15)$$

where  $\Gamma_1$  denotes the rate at which carriers are scattered from valley 1 to all sections of the valley 2.  $\Gamma_2$  denotes return scattering. It is noted that for parabolic bands, an assumption made below

$$\frac{\hbar k_1^j}{m_1} = m_1 v_1^j \quad (16)$$

An equation similar to (15) describes transient population changes in the L valley 2. When the two are combined, a global continuity equation results.

$$\frac{\partial n}{\partial t} = - \frac{\partial}{\partial x_1} \left[ n_1 \frac{\hbar k_1^j}{m_1} + (n - n_1) \frac{\hbar k_2^j}{m_2} \right] \quad (17)$$

The quantity

$$n_1 \frac{\hbar k_1^j}{m_1} + (n - n_1) \frac{\hbar k_2^j}{m_2} \equiv C^j \quad (18)$$

is the velocity flux density of the system. It is convenient to relate this to a mean spatially dependent drift velocity:

$$v^j = C^j/n \quad (19)$$

It is noted that the total current density

$$J^j = -eC^j + e \frac{\partial F^j}{\partial t} \quad (20)$$

is conserved, i.e.,

$$\frac{\partial J^j}{\partial x_j} = 0 \quad (21)$$

The second pair of moment equations is that of momentum balance. By incorporating nonspherical contributions to the distribution function the momentum balance equation for valley '1' is:

$$\frac{\partial}{\partial t} n_1 \hbar k_1^j = - \frac{\partial}{\partial x_i} \frac{\hbar k_1^j}{m} n_1 \hbar k_1^j + e n_1 \frac{\partial \phi}{\partial x_j} - \frac{\partial}{\partial x_j} n_1 k_B T_1 + \hat{\mu}_1 \frac{\partial^2 k_1^j}{\partial x_i^2} - n_1 \hbar k_1^j \Gamma_3 \quad (22)$$

For valley 2 the relevant momentum balance equation is

$$\frac{\partial}{\partial t} (n - n_1) \hbar k_2^j = - \frac{\partial}{\partial x_i} \frac{\hbar k_2^j}{m_2} (n - n_1) \hbar k_2^j + e(n - n_1) \frac{\partial \phi}{\partial x_j} - \frac{\partial}{\partial x_j} (n - n_1) k_B T_2 + \hat{\mu}_2 \frac{\hbar}{m_2} \frac{\partial^2 k_2^j}{\partial x_i^2} - (n - n_1) \hbar k_2^j \Gamma_4 \quad (23)$$

where  $\hat{\mu}$  is a phenomenological 'viscous' contribution [7].

The final set of moment equations used in the discussion below is that for energy transport. This can be written in a variety of forms [7]. The form chosen for valley '1', with

$$U_1 = \frac{3}{2} k_B T_1 \quad (24)$$

is

$$\begin{aligned} \frac{\partial}{\partial t} n_1 U_1 = & - \frac{\partial}{\partial x_j} \frac{\hbar k_1^j}{m_1} n_1 U_1 - \frac{2}{3} n_1 U_1 \frac{\partial}{\partial x_j} \frac{\hbar k_1^j}{m_1} + \kappa_1 \frac{\partial^2}{\partial x_j^2} T_1 \\ & + \frac{\hbar^2 k_1^2}{2m_1} [2n_1 \Gamma_3 - n_1 \Gamma_1 + (n-n_1) \Gamma_2] - n_1 U_1 \Gamma_5 + (n-n_1) U_2 \Gamma_6 \end{aligned} \quad (25)$$

For valley '2'

$$\begin{aligned} \frac{\partial}{\partial t} (n-n_1) U_2 = & - \frac{\partial}{\partial x_j} \frac{\hbar k_2^j}{m_2} (n-n_1) U_2 - \frac{2}{3} (n-n_1) U_2 \frac{\partial}{\partial x_j} \frac{\hbar k_2^j}{m_2} + \kappa_2 \frac{\partial^2}{\partial x_j^2} T_2 \\ & + \frac{\hbar^2 k_2^2}{2m_2} [2(n-n_1) \Gamma_4 + n_1 \Gamma_1 - (n-n_1) \Gamma_2] - (n-n_1) U_2 \Gamma_7 + n_1 U_1 \Gamma_8 \end{aligned} \quad (26)$$

Equations (11), (15), (17), (22), (23), (25) and (26) are the equations governing transport in near-micron and submicron length semiconductor devices. The equations are more general than others in that nonspherical contributions to the moments of the BTE have been included. The scattering rate have been reviewed elsewhere (Grubin et al., [13]). To more clearly discuss the implications of scaling these governing equations are cast into dimensionless form, as discussed in section IV.

#### IV. DIMENSIONLESS FORM OF THE GOVERNING EQUATIONS

In performing the calculations below the equations are first cast into dimensionless form. While discussions of nondimensionalization are normally relegated to appendices, because of the inherent nature of scaling, they are included below.

The first set of equations cast into dimensionless form are the continuity equations (15) and (17). These are expressed as

$$\frac{\partial n_i^*}{\partial t^*} = - \frac{\partial n_i^* v_i^{*j}}{\partial x_j^*} - n_i^* f_1 + (n^* - n_i^*) f_2 \quad (27)$$

and

$$\frac{\partial n^*}{\partial t^*} = - \frac{\partial}{\partial x_j^*} (n_i^* v_i^{*j} + (n^* - n_i^*) v_2^{*j}) \quad (28)$$

The dimensionless variables (starred quantities) are identified in table 3, where the subscript 'ref' denotes reference quantities, as illustrated below:

$$t_{ref} = x_{ref} / V_{ref} \quad (29)$$

$$\Gamma_{ref} = 1/t_{ref} \quad (30)$$

The momentum balance equations in dimensionless form are taken from equations (22) and (23) and written as

$$\begin{aligned} \frac{\partial n_i^* v_i^{*i}}{\partial t^*} &= - \frac{\partial n_i^* v_i^{*j} v_i^{*i}}{\partial x_j^*} + P_f \frac{n_i^*}{m_i^*} \frac{\partial \phi^*}{\partial x_i^*} - \frac{1}{\gamma M^2} \frac{\partial}{\partial x_i^*} n_i^* R_i T_i^* \\ &+ \frac{\mu_i^*}{Re \cdot m_i^*} \frac{\partial^2 v_i^{*i}}{\partial x_j^*} - n_i^* v_i^{*i} f_3 \end{aligned} \quad (31)$$

and

$$\begin{aligned}
 \frac{\partial(n^* - n_1^*)V_2^{*i}}{\partial t^*} = & -\frac{\partial}{\partial x_j^*}(n^* - n_1^*)V_2^{*i}V_2^{*j} + P_f \frac{(n^* - n_1^*)}{m_2^*} \frac{\partial \phi^*}{\partial x_i^*} \\
 & - \frac{1}{\gamma M^2} \frac{\partial}{\partial x_i^*}(n^* - n_1^*)R_2^* T_2^* + \frac{\hat{\mu}_2^*}{Re \cdot m_2^*} \frac{\partial^2 V_2^{*i}}{\partial x_j^*} - (n^* - n_1^*)V_2^{*i} f_4
 \end{aligned} \tag{32}$$

The dimensionless parameters associated with the momentum balance equations are identified in table 4.

We next consider the energy balance equations. These are taken from equations (25) and (26) and are expressed as

$$\begin{aligned}
 \frac{\partial n_1^* T_1^*}{\partial t^*} = & -\frac{\partial n_1^* T_1^* V_1^{*j}}{\partial x_j^*} - (\gamma - 1)n_1^* T_1^* \frac{\partial V_1^{*j}}{\partial x_j^*} + \frac{1}{Re \cdot Pr} \frac{1}{m_1^* c_{v_1}^*} \frac{\partial}{\partial x_j^*} \left( \kappa_1^* \frac{\partial T_1^*}{\partial x_j^*} \right) \\
 & - n_1 T_1 f_5 + (n - n_1) T_2 f_6 + \gamma(\gamma - 1)M^2 \frac{V_1^{*j} V_1^{*j}}{2c_{v_1}^*} (2n_1^* f_3 - n_1^* f_1 + (n^* - n_1^*) f_2)
 \end{aligned} \tag{33}$$

(33)

and

$$\begin{aligned}
 \frac{\partial(n^* - n_1^*)T_2^*}{\partial t^*} = & -\frac{\partial(n^* - n_1^*)T_2^* V_2^{*j}}{\partial x_j^*} - (\gamma - 1)(n^* - n_1^*)T_2^* \frac{\partial V_2^{*j}}{\partial x_j^*} + \frac{1}{Re \cdot Pr} \frac{1}{m_2^* c_{v_2}^*} \frac{\partial}{\partial x_j^*} \left( \kappa_2^* \frac{\partial T_2^*}{\partial x_j^*} \right) \\
 & + \gamma(\gamma - 1)M^2 \frac{V_2^{*j} V_2^{*j}}{\partial x_j^*} (2(n^* - n_1^*)f_4 + n_1^* f_1 - (n^* - n_1^*)f_2) - (n^* - n_1^*)T_2^* f_7 + n_1^* T_1^* f_8
 \end{aligned} \tag{34}$$

(34)

The dimensionless parameters associated with the energy balance equations are identified in table 5.

Finally, Poisson's equation in dimensionless form is written as

$$\frac{\partial^2 \phi^*}{\partial x_j^{*2}} = Sn(n_l^* + (n^* - n_l^*) - n_o^*) \quad (35)$$

with the dimensionless terms and parameters identified in table 6. The dimensionless transport equations (27), (28), (31) through (35) are the ones that are placed in finite difference form. It is clear that for a range of parameter alterations that leave constant the dimensionless parameters

---

Pf, Re, Pr, Sn,

---

that leave the numerical results are unchanged. This feature is critical and allows us to provide an initial quick assessment of scaling. The above four terms are regarded below as the governing dimensionless parameters. Students of computational fluid dynamics will immediately see a connection between these dimensionless equations and those of CFD. In particular, Re, is the 'Reynolds' number for the system of governing equations. In the discussion that follows scaling will be achieved through manipulation of physical parameters that, in turn: (i) leave the governing dimensionless parameters unaltered, and (ii) selectively alter them. Extrinisic variables that cause alterations in these parameters are carrier density, device length, etc. These calculations appear in sections VI through VIII. Following this, a set of calculations are discussed in which selective scattering parameters are altered. These parameters include such key material parameters as the deformation potential coupling coefficient for intervalley transfer, and the energy separation between the  $\Gamma$  and L valleys.

V. CALCULATIONS WITH CONSTANT GOVERNING DIMENSIONLESS PARAMETERS  
AND VARIABLE SCATTERING RATES TIED TO EXTRINSIC PARAMETERS

For purposes of illustration the dimensionless equations are first manipulated under conditions of constant governing dimensionless parameter scaling. For this case the unscaled device is GaAs doped to  $5 \times 10^{15}/\text{cm}^3$ , with a cathode to anode spacing of 1.0 microns and an applied bias of 1.0 volts. The structure is taken as one dimensional with the following set of boundary conditions at  $x=0$ ,

$$n_{xx} = n_{1xx} = 0, \quad V_1 = 15,625 \frac{\partial \phi}{\partial x}, \quad V_{2x} = 0, \quad T_1 = 300^\circ\text{K}, \quad T_{2x} = 0 \quad (36)$$

and at  $x=1.0$  microns,

$$n_{xx} = n_{1xx} = V_{1xx} = V_{2xx} = T_{1xx} = T_{2xx} = 0, \quad \phi = 1.0 \text{ volts} \quad (37)$$

The dimensionless form of the boundary conditions at  $x=0$  is

$$\frac{\partial^2 n^*}{\partial x^*^2} = \frac{\partial^2 n_1^*}{\partial x^2} = 0, \quad V_1^* = \mu_c^* \frac{\partial \phi^*}{\partial x^*}, \quad \frac{\partial V_2^*}{\partial x^*} = 0, \quad T_1 = T_c^*, \quad \frac{\partial T_2^*}{\partial x^*} = 0, \quad \phi^* = 0 \quad (38)$$

with

$$\mu_c^* = \frac{\mu_c \phi_{ref}}{x_{ref} V_{ref}} \quad (39)$$

The concept of constant parameter scaling and constant reference potential scaling as applied to the one dimensional structure is as follows. First, the reference potential is held fixed at 1.0 volt. Second, all of the scattering rates,  $\Gamma_1$  through  $\Gamma_8$  are altered by the multiplicative constant  $\lambda$ . The dimensionless continuity equations are unchanged when  $\Gamma_{ref} \rightarrow \lambda \Gamma_{ref}$ ,  $t_{ref} \rightarrow t_{ref}/\lambda$ ,  $X_{ref} \rightarrow X_{ref}/\lambda$  (thus,  $V_{ref}$  is unchanged). Then, if  $\lambda$  is doubled, the scaled length, is halved.

The scaling of the momentum balance equation is similar. Here, if  $\phi_{ref}$  is kept unchanged, the dimensionless equations are unaltered when the the following parameter changes are made:  $N_{ref} \rightarrow \lambda^2 N_{ref}$ ,  $\hat{u}_{ref} \rightarrow \lambda \hat{u}_{ref}$ .

For this case  $R_e$  and  $P_f$  are unchanged. To see the connection between this computation and the discussion for uniform fields, we express the field as the gradient of potential. Then equation (6) is re-expressed as

$$V_\lambda(\phi, X, t) = V_0(\phi, \lambda X, \lambda t)$$

For the energy equation, the only scaling required is on the thermal conductivity, which becomes  $\kappa_{ref} + \lambda \kappa_{ref}$ . Poisson's equation requires no additional alteration. The new boundary condition at the cathode requires that  $u_c \rightarrow u_c/\lambda$ . A summary of the above scaling is displayed in table 7.

The constant governing dimensionless parameter scaling is illustrated in figure 10 through 14. In these calculations for both the scaled and unscaled structures the potential is kept fixed and is not altered in going from scaled to unscaled structures. A simple illustration of the effect of scaling is provided through the following approximation, where the field dependent velocity and temperature is given by the following expressions:

$$V = \frac{e\tau_m}{m} \frac{\Delta\phi}{\Delta X}, \quad T_e = \frac{2e\tau_e}{3k_B} V \frac{\Delta\phi}{\Delta X} \quad (40)$$

Here  $\tau_m$  and  $\tau_e$  are, respectively, constant momentum and energy relaxation times.

In equation (40) when the scattering rates are altered by the constant  $\lambda$ , the relaxation time is altered by the constant  $1/\lambda$ . Then under uniform field conditions with the potential difference specified at a given value, the carriers obtain values of velocity and temperature equal to the unscaled value, over a distance that is a factor of  $\lambda$  larger than that of the unscaled values. The situation of interest below, is for spatially dependent nonuniform fields, but the example just discussed is intuitively relevant.

The detailed calculations were performed for the unscaled gallium arsenide and are extracted from an earlier study (Grubin and Kreskovsky [7]). The scaled results are determined from the above discussion and are implicit in the illustrations of the unscaled results. Thus, figure 10 displays calculations for the distribution of total and  $\Gamma$  valley carriers for  $\lambda=1$ , 2, and 4. The  $\lambda=1$  results are for gallium arsenide. The boundary conditions chosen are representative of a highly injecting contact. The scaled results are in accordance with table 7. It is noted that for  $\lambda=2$ , identical transfer occurs over 0.5 microns as against 1.0 microns for the unscaled structure.

Figure 11 displays the field distribution for this scaled calculation. Of significance here, is the fact that for the unscaled gallium arsenide the peak anode field is 33kv/cm @ 1.0 volts, and is reached at 1.0 microns. For  $\lambda=2$ , the peak anode field is 66kv/cm and is reached at 0.5 microns. Here, if reference is made to indium phosphide as a " $\lambda=2$ xGaAs" semiconductor where the threshold field for NDM is of the order of twice that of gallium arsenide, then the results are intuitively relevant. Thus, the high field region at the anode offers the potential problem of introducing avalanching at premature

voltage levels. Similar arguments apply to indium phosphide gallium arsenide, when regarded as a " $\lambda=1/2x$ GaAs" structure where the anode fields are lower.

The velocity and temperature distributions are displayed in figures 12 and 13, respectively. No scaling on the magnitudes of either occurs, although the spatial scaling is apparent, a result that is consistent with the discussion associated with equation (40).

The temporal transient to steady state is shown in figure 14, which displays current density versus time. Two points are noted: First, the time to equilibrium is shorter for  $\lambda=2$ , than for  $\lambda=1$ . Here it may be anticipated the scaled indium phosphide is capable of higher switching speeds. Second, because of the increase in  $N_{ref}$ , the reference current drive is increased by a factor of four.

## VI. CALCULATIONS WITH CONSTANT GOVERNING DIMENSIONLESS PARAMETER AND CONSTANT SCATTERING RATES TIED TO INTRINSIC MATERIAL PROPERTIES

The above type of scaling serves as an intuitive guide and as a reference point for additional scaling. The manipulation of the extrinsic parameters in the last section followed the alteration associated with that of the material parameters. A more general situation may arise when a particular feature size of a device is a specification of the problem. The task is then to determine the variations in the electrical characteristics that may be expected if there is a choice of materials. The simplest way to proceed is to perform a series of numerical calculations in which the device length is fixed, and all of the material scattering rates are altered by the same constant. This is considered below.

The calculations considered below are all performed for a 0.25 micron long structure, a doping of  $8 \times 10^{16}/\text{cm}^3$ , and an applied potential of 0.6 volts (for an average field of 24kv/cm). The  $\lambda=1$  calculations are for gallium arsenide. The  $\lambda=2$  case is relevant to indium phosphide. Note that the calculations discussed are for high doping levels, in which the background is treated as jellium. This latter assumption is likely to be a poor one (Grubin and Ferry [8]). Additionally, scattering due to ionized impurities are not included in this calculation. They are introduced in section VII.

The calculations are summarized in figures 15 through 19. Figure 15 shows the time dependent distribution of current for the gallium arsenide structure figure 15a. The current distribution for the transient with the scattering rates doubled and redoubled are shown in figures 15b and 15c, respectively. There are two points of note: (i) at the bias level of 0.6 volts there is a progressive decrease in normalized current level,  $J/J_{\text{ref}}$  as the scaling parameter increases, (ii) unlike, the uniform field calculations where an increase in the scattering level results in a reduction in the time to steady state, here the relaxation time is less certain. (We note that the scaled gallium arsenide calculation with a scaled scattering rate of 4 provides results that are identical to that of a 1.0 micron device with a doping of  $5.0 \times 10^{15}/\text{cm}^3$ ).

The steady state distribution of charge within the device is shown in figure 16, where it is observed that the transfer increases as  $\lambda$  decreases from 4 to 2. The observation is made here that the increase transfer rate is a consequence of the fact that at a given value of field the rate of electron transfer is greater for the scaled  $\lambda=2$  structure than for the scaled  $\lambda=4$  structure (Grubin and Kreskovsky [14], to be published). It is noted that a clear description of the trends with increased scaled scattering is not possible insofar as the high donor density often results in free carrier density levels that are below background; a result that tends to obscure some of the results. This is apparent from the  $\lambda=1$  and  $\lambda=2$ , calculations.

The distribution of  $\Gamma$  valley carrier velocity for these calculations is shown in figure 17. The critical result here is that the  $\Gamma$  valley carrier velocity decreases as  $\lambda$  increases. This reflects the fact that the mobility of the  $\Gamma$  valley is decreased with increased scattering rate. When this result is coupled to the fact that carriers in the  $\Gamma$  valley carry most of the current, improvements in the current level with lower scattering rates can be anticipated (see figure 15).

The corresponding temperature profile for this calculation are depicted in figure 18. It is noted that the highest electron temperatures are sustained for gallium arsenide at this bias level. It is this result that tends to obscure some of the predictions of the previous section, for several reasons: First, on the basis of the earlier discussion it was anticipated that increased scattering rates resulted in higher electron temperatures. Second, increased scattering rates were expected to lead to higher values of the anode field and higher electron temperatures. These conclusions are drawn form the discussions of section V. Several features were not addressed in that section. The first is that increased values of carrier velocity lead to higher electron temperatures. The second is that the increased scattering rate leads to a higher low field resistance, and thus a larger voltage drop within the device. This in turn leads to a lower anode field and lower anode electron temperature values.

The spatially dependent field profiles are shown in figure 19. It is noted that there is an increase in the anode field as  $\lambda$  goes from 1 to 2. However, the interpretation is not direct insofar as this increase is accompanied by a reduction in the amount of charge depletion that exists within the interior of the structure. The situation with  $\lambda=4$  is clear. There is a significant reduction in the anode field; a reduction that is accompanied by an increase in the voltage drop across the interior of the device.

## VII. CALCULATIONS WITH CONSTANT GOVERNING DIMENSIONLESS PARAMETERS AND VARIABLE SCATTERING RATES TIED TO INTRINSIC MATERIAL PROPERTIES

The calculations in this section are similar to those already performed, with one key difference: The calculations of the previous sections were performed for cases in which the material scattering rates were all changed by the same constant. In this section individual scattering components are altered, and the emphasis moves closer to realistic alterations in material parameters of semiconductor devices.

### VIIa. Deformation Potential Coupling Coefficient Alterations

This set of calculations is performed to highlight the role of velocity saturation on near and submicron-scale device performance. The motivation for this is as follows: Presently, individual semiconductors are accepted or rejected as candidate device materials based, in large measure, upon the value of their high field saturation drift velocity. Indeed, the material silicon carbide, apart from its high temperature advantages is under consideration as for FET applications because of its high field saturation drift velocity. It is noted that the low field mobility of silicon carbide is considerably smaller than that of gallium arsenide. The question then arises as to whether an increase in saturation drift velocity is a sufficient criteria for submicron device semiconductor material selection, or whether the key figure of merit is the low field mobility. The question is addressed through alterations of the intervalley deformation potential coupling coefficient, where it is observed that an increase in saturation velocity that is accomplished by an increase in the intervalley deformation coupling coefficient also reduces the low field mobility. When this result is coupled to the results of section VI, such alterations may be of less use for submicron-structure devices. Indeed one of the obvious recommendations that arises from the results presented below is a clear need to search for materials with both a high saturation drift velocity and a high low field mobility.

Alterations in the saturated drift velocity of the carriers accomplished by altering the deformation potential coupling coefficient are indicated in figures 20 through 23. Figures 20 and 21 display the steady state characteristics, and the scattering rates for the case where the intervalley deformation potential coupling coefficient is increased by a factor of 2.0. As is noted there is the twin effect of increasing the saturated drift velocity, while decreasing the low field mobility. The opposite occurs when the coupling coefficient is reduced by a factor of 2.0. The latter is illustrated in figures 22 and 23. It should be recalled from the results of figure 7, that alterations in the  $\Gamma$ -valley mobility do not set in until fields near the threshold for negative differential mobility are reached.

The situation as depicted for nonuniform fields is displayed in figures 24 through 38, where the three different groups of calculations are summarized. Figures 24 through 28 displays a sequence of calculations for a structure that is 0.25 microns in length, with a donor density of  $8 \times 10^{16}/\text{cm}^3$  and a deformation potential coupling coefficient that is twice that of gallium arsenide. Figures 29 through 33 display a similar set of calculations but for a coupling coefficient that is one-half of that of gallium arsenide. Figures 34 through 38 are for unscaled gallium arsenide. Of significance here are the  $\Gamma$ -valley carrier velocity profiles, figures 26, 31, and 36; and the steady state

current levels, figures 28, 33, and 38. The  $\Gamma$ -valley carrier velocity is highest for the element with the lowest deformation potential coupling coefficient, as is the steady state current level. A summary of this result is displayed in figure 39a which shows the dc current voltage relation. Clearly the element with the highest saturated drift velocity is not the element with the highest submicron current level.

The above result does not contradict what has been taught about saturated drift velocity results and associated current levels. Earlier teachings were, however, incomplete. It is anticipated that as the device length increases the element with the highest saturated drift velocity will dominate if the dominant part of the structure sustains fields well into velocity saturation. This statement is backed-up by a series of calculations, summarized in figure 39b. Figure 39b displays the current voltage relations for two pairs of nonuniform field calculations. One for a device feature size of 1.0 microns, and a second for 2.0 microns. The carrier density for both was  $5 \times 10^{15}/\text{cm}^3$ . Two points are noted: First, as the device length increases the steady current level decreases. Second, the difference in the steady state current level between the high and low deformation potential coupling coefficient elements decreases as the device length increases. It is anticipated that for structures greater than five microns in length the current level for the higher deformation potential coupling coefficient will be the highest.

#### VIIb. Intervalley Energy Separation Alterations

Because of the importance of the  $\Gamma$  valley carrier to transport in submicron devices, a set of calculations was performed in which all of the coefficient with respect to gallium arsenide were held fixed, but the intervalley separation was increased. The steady state uniform field characteristics are displayed in figures 40 and 41. Calculations for nonuniform field were performed for a 1.0 micron structure with a donor concentration of  $5 \times 10^{15}/\text{cm}^3$ . These are displayed in figures 42 through 46.

There are several points that should be noted. First because of the increased energy separation, there is a delay in field value at which intervalley transfer occurs. (This effect has been known for sometime from studies of indium phosphide). There is a corresponding increase in the threshold field for negative differential mobility, as well as a corresponding increase in the saturation drift velocity. But most important, from the point of view of submicron structures, is the fact that the low field mobility is virtually unaltered. Thus, the benefits of high saturation drift velocity and high-low field mobility emerge. A particularly important comparison are the steady state current voltage ralation obtained from figure 46, and their comparison to figure 39b. There is a clear, and remarkable improvement with the higher intervalley separation. This is perhaps one of the most desirable features that should be sought after in choosing high frequency devices. And indium phosphide gallium arsenide begins to look attractive.

#### 7c. Calculations Including Ionized Impurity Scattering

The calculations in the previous discussion ignored the influence of ionized impurity scattering on the results. Clearly the effect of ionized impurity scattering is to reduce the mobility. The effects of ionized impurity

scattering were not included, initially, because they detract from the basic concepts associated with scaling. From the point of view of this paper, ionized impurity scattering has the effect of selectively altering the scattering rates. In this case only two scattering rate components are altered: the  $\Gamma$  and L valley momentum scattering rates.

The results of the calculations are displayed in figures 47 through 53. The results, as expected, are qualitatively similar to that obtained without any impurity scattering. There is, however, the expected degradation in electrical performance that is apparent upon comparison of the steady state current levels of figure 53, with that of figure 38, for which ionized impurity scattering is absent. The results, however, are of more general significance insofar as they forecast the result that improvements in the momentum scattering rate will improve device performance. This last conclusion is consistent with the other calculations of this section.

## VIII. CALCULATIONS WITH VARIABLE DONOR DENSITY

The calculations of the preceding sections were specifically concerned with scaling associated with variations in band structure. Some results demonstrated that it was possible to scale the scattering rates and the doping such that no alteration in the electrical results occurs (see section V). The topic of interest is then: What occurs when the doping level is varied? It may be argued, that this question has already been considered in papers that initially dealt with velocity overshoot. Here, reference is to the study of, e.g., Frey et al., [15]. In these studies, however, the effects of varying the donor density was not addressed. The only question considered was the alteration in the transient velocity due to changes in the ionized impurity scattering.

To examine the effects of varying the donor density, a series of calculations were performed, again, for the submicron structure with an active region length of 0.25 microns. The calculations were performed for doping levels of  $5 \times 10^{15} / \text{cm}^3$ ,  $2 \times 10^{16} / \text{cm}^3$  and  $8 \times 10^{16} / \text{cm}^3$ , and again, ionized impurity scattering was not incorporated. The results of the calculation are shown in figures 54 through 58, for the donor level of  $5 \times 10^{15} / \text{cm}^3$ ; figures 59 through 63 for the donor level of  $2 \times 10^{16} / \text{cm}^3$ ; and figures 34 through 38 for a donor level of  $8 \times 10^{16} / \text{cm}^3$ .

There are two important features to be noted from these calculations: First, as the donor density increases the field distribution within the device becomes more nonuniform. This result is a direct consequence of the fact that the dimensionless parameter  $S_n$  used in Poisson's (equation (35) and table 6)) increases linearly with donor density. Second, as a consequence of the increased spatial nonuniformities the steady state currents at a given value of bias do not scale linearly with carrier density. Rather the scaling is sublinear. This last result should be apparent from the summary of figure 64, where the normalized current density versus potential is plotted as a function of donor density. Of greater importance is the fact that the sublinear current scaling will have a significant influence on all scaled FET results, as will be apparent from the later discussions.

## IX. TWO DIMENSIONAL SCALING CONSIDERATIONS

To qualify the scaling discussions to two space dimensions, it is useful to recall the classical scaling arguments as applied to n-channel MOSFETs. The discussion for this scaling can be found in many texts and reference is to the text of Bar-Lev [2]. The basic scaling principle invoked is to retain a constant average electric field across the structure, while reducing the critical feature size of the device. As discussed in reference [2] all extrinsic dimensions are reduced by a constant  $\lambda$ , and all critical intrinsic linear dimensions are expected to be reduced by the same constant. To achieve this the voltages are scaled down by  $\lambda$ , while the substrate doping is increased by this same constant. Thus, the depletion width surrounding the drain diffusion is reduced as follow:

$$d_{dep} = \left[ \frac{2\epsilon\phi_t}{qN_A} \right]^{1/2} \longrightarrow d_{dep}/\lambda \quad (41)$$

and such characteristics as the source-drain current (not current density) within the gradual channel approximations is reduced as follows:

$$I_{DS} = \frac{\mu C_{ox} W}{L} \left[ (\phi_{GS} - \phi_t) \phi_{DS} - \phi_{DS}^2 / 2 \right] \longrightarrow I_{DS}/\lambda \quad (42)$$

In the above the usual definitions apply [2], with  $V_t$  being the threshold voltage at the drain, and  $C_0$  the gate oxide capacitance:

$$C_0 = \frac{\epsilon}{t_{ox}} \longrightarrow \lambda C_0 \quad (43)$$

Under these scaling constraints, the transconductance is unchanged, while the power, delay time, speed-power product and power dissipation per unit area are all changed as follows:

$$(power) \quad I_\phi \longrightarrow I_\phi/\lambda^2 \quad (44a)$$

$$(delay time) \quad T \longrightarrow T/\lambda \quad (44b)$$

$$(\text{speed-power product}) \quad (I\phi T) \longrightarrow (I\phi T)/\lambda^3 \quad (44c)$$

$$(\text{power dissipation per unit area}) \quad \left[ \frac{I\phi}{A} \right] \longrightarrow \left[ \frac{I\phi}{A} \right] \quad (44d)$$

While the discussion of this study is not concerned with MOSFET scaling it is of importance to determine how this scaling fits into the general arguments of the preceding sections. Thus, a brief discussion of the semiconductor drift and diffusion equations will be given. It is noted, however, that Poisson's equation in dimensionless form, equation (35), contains the parameter  $S_n$ . Under constant average field scaling, considered in the first paragraph of this section,  $S_n$  is unchanged.

The arguments in the next two sections will concentrate on scaling as currently being practiced through application of the drift and diffusion equations. These arguments will be supplemented with a discussion of the modifications to be expected through solutions to the moments of the Boltzmann transport equation.

## X. THE SEMICONDUCTOR DRIFT AND DIFFUSION EQUATIONS

The semiconductor drift and diffusion equations, for electrons and holes consist of the continuity equations:

$$(electrons) \quad e \frac{\partial N}{\partial t} = \nabla \cdot \bar{J}_n \quad (45)$$

$$(holes) \quad e \frac{\partial P}{\partial t} = -\nabla \cdot \bar{J}_p \quad (46)$$

where

$$(electrons) \quad \bar{J}_n = -e(N\mu_n \nabla \phi - D_n \nabla N) \quad (47)$$

$$(holes) \quad \bar{J}_p = -e(P\mu_p \nabla \phi + D_p \nabla P) \quad (48)$$

and Poisson's equation, generalized to include holes:

$$\nabla^2 \phi = -e[(n - n_0) - (p - p_0)]/\epsilon \quad (49)$$

In the above  $\mu_n$ ,  $\mu_p$ ,  $D_n$ , and  $D_p$ , are phenomenological field dependent mobilities and diffusivities; each of which may be obtained from the balance equations of the preceding sections (see e.g., Butcher [10]). Combining equations (45) through (49) yields the following form of the continuity equations:

$$\begin{aligned} \frac{\partial N'}{\partial t} &= -\nabla(\mu_n N') \cdot \nabla \phi - \mu_n \frac{e}{\epsilon} N' (N' - P') + \nabla \cdot D_n \nabla N' \\ &\quad - \nabla(\mu_n N_0) \cdot \nabla \phi - \mu_n \frac{e}{\epsilon} N_0 (N' - P') + \nabla \cdot D_n \nabla N_0 \end{aligned} \quad (50)$$

$$\begin{aligned} \frac{\partial P'}{\partial t} &= \nabla(\mu_p P') \cdot \nabla \phi + \mu_p \frac{e}{\epsilon} P' (N' - P') + \nabla \cdot D_p \nabla P' \\ &\quad + \nabla(\mu_p P_0) \cdot \nabla \phi + \mu_p \frac{e}{\epsilon} P_0 (N' - P') + \nabla \cdot D_p \nabla P_0 \end{aligned} \quad (51)$$

where  $N' = N - N_0$ , and  $P' = P - P_0$ . Then using the nondimensionalization procedures of the previous sections the equations take the following form:

$$\begin{aligned}\frac{\partial N'}{\partial t} &= -C_n \nabla (\mu_n^* N'^*) \cdot \nabla \phi^* - C_n S_n \mu_n^* N'^* (N'^* - P'^*) + \frac{1}{R_n} \nabla \cdot D_n^* \nabla N'^* \\ &\quad - C_n \nabla (\mu_n^* N_0^*) \cdot \nabla \phi^* - C_n S_n \mu_n^* N_0^* (N'^* - P'^*) + \frac{1}{R_n} \nabla \cdot D_n^* \nabla N_0^*\end{aligned}\quad (52)$$

$$\begin{aligned}\frac{\partial P'}{\partial t} &= -C_n \nabla (\mu_p^* P'^*) \cdot \nabla \phi^* - C_n S_n \mu_p^* P'^* (N'^* - P'^*) + \frac{1}{R_n} \nabla \cdot D_p^* \nabla P'^* \\ &\quad - C_n \nabla (\mu_p^* P_0^*) \cdot \nabla \phi^* - C_n S_n \mu_p^* P_0^* (N'^* - P'^*) + \frac{1}{R_n} \nabla \cdot D_p^* \nabla P_0^*\end{aligned}\quad (53)$$

where the dimensionless parameters are identified in table 8. It is recalled that the reference quantities may be chosen arbitrarily. However, when correctly chosen, the resulting dimensionless numbers give an indication of the relative importance of various terms in each equation.

The critical feature to note here is that all reference quantities, with the exception of  $R_n$  are unaltered by the scaling of the previous section IX. Thus, if diffusive quantities are ignored, the reference quantities  $J_{ref}$  and  $I_{ref}$  are altered as in the discussion of Bar-Lev [2]. The difficulty with this procedure is that a reduction of the critical length also reduces the dimensionless variable  $R_n$ . The reduction in  $R_n$  indicates that when the field profiles are spatially nonuniform, diffusive contributions begin to take on a sizeable role. Thus, just when scaling appears to be useful, the critical assumptions breakdown.

The impact of this type of scaling upon the moments of the Boltzmann transport equation has already been indicated, but is reviewed within the context of the present discussion. First, it is noted that the Poisson scaling factor,  $S_n$ , is the same for both the DDE and the moment equations. Second, the importance of the dimensionless parameters lies in their relative values. Thus for the DDE formulation the important quantities are the relative values of  $R_n$  and  $C_n$ , where it was noted, that  $R_n$  decreases with decreasing feature size. For the moment equation formulation, equation (31), and the relative values of  $P_f$  and  $\gamma M^2$  are of significance. In particular, if the term multiplying  $(\gamma M^2)^{-1}$  is regarded as a diffusive contribution, and constant average field scaling is invoked, a reduction in  $\Phi_{ref}$  increases the relative contribution of the diffusive term. In the DDE formulation, where an increase in the diffusive term may result in lowered current levels as the feature size is reduced, for the moment equation, a reduction in feature size increases the relative contribution of the  $\Gamma$  valley and improvements in device performance may be expected. While a full range of two dimensional scaling calculations have not yet been performed, see below for preliminary results, information can be garnered from the one dimensional calculations; particularly with reference to

assessing expected reductions in power, delay time, and speed power product as device feature size is reduced.

The calculation of interest have already been performed and are displayed in two groups: The first group is contained in figures 10 through 14, where attention is focused on the unscaled gallium arsenide. In these figures, the relevant features are:

$$x_{ref} = 1.0 \text{ micron}$$

$$\Phi_{ref} = 1.0 \text{ volts}$$

$$N_{ref} = 5 \times 10^{15}/\text{cm}^3$$

The second group of calculations is that shown in figures 59 through 63. In this collection of figures, the relevant features are:

$$x_{ref} = 0.25 \text{ microns}$$

$$\Phi_{ref} = 0.25 \text{ volts}$$

$$N_{ref} = 2 \times 10^{16}/\text{cm}^3$$

These numbers satisfy the criteria of Bar-Lev [2] and constant average field scaling (the average field is 10kv/cm). The steady state current density level for each is indicated in the figures. For the one micron long device, the normalized current density is 0.29. For the 0.25 micron device the normalized current density is 0.45. The last result is not surprising; it is one of the reasons for moving to submicron feature sizes. It does, however, emphasize the obvious; namely increased current drive leads to increased power levels. The results, if extrapolated, teach that the power dissipation, the speed power product, and the power dissipation per unit area are likely to be in excess of 50% of that predicted by classical scaling theory.

## XI. TWO DIMENSIONAL TRANSPORT WITH MATERIAL SCALING WITHIN THE FRAMEWORK OF THE DRIFT AND DIFFUSION EQUATIONS

### XIa. Silicon, GaAs, Scaled GaAs

Of all of the internal parametric changes that were made to the scattering integrals, as discussed in the earlier sections, three broad features changed in the field dependent velocity curves: (i) the low field mobility, (ii) the peak velocity, and (iii) the saturation velocity. The effects of each are predictable and have been routinely used to assess semiconductor materials. In particular, the reader is referred to a review article by Eden [4]. But the first detailed calculations of this appeared in a study by Grubin in 1980 [5]. Because of the relevance of this study to the discussion of the earlier sections and to the later discussion, the study is briefly summarized.

The study was in two parts. The first was an assessment of the role of the saturated drift velocity on the electrical characteristics of the FET, in particular IDSS. Thus a sequence of three terminal calculations were performed for gallium arsenide, and then for two other 'fictitious' materials as shown in figure 65. As is clear from figure 65, one curve was chosen to represent a material without negative differential mobility, but with a saturated drift velocity that was equal to that of the gallium arsenide structure in the figure. The second was chosen similarly, but with a saturated drift velocity equal to the peak velocity value of gallium arsenide. The calculation explored the effect of these parameter changes on the IDSS of a three terminal structure. It is noted that all three materials had the same low field mobility as that for gallium arsenide. The structure for the calculation is shown in figure 66.

The structure in figure 66 is a three terminal device with source and drain contacts placed on parallel ends of the device. The gate was centrally placed. For each of these calculations the ratio of channel height to channel length was 5/41, and the ratio of gate length to channel length was 8/41. The doping level for this set of calculations was  $1.0 \times 10^{15}/\text{cm}^3$ . The reference quantities for this calculation are indicated in below.

$$x_{\text{ref}} = 10.0 \text{ microns}$$

$$\phi_{\text{ref}} = 3.25 \text{ volts}$$

$$\mu_{\text{ref}} = 6,770 \text{ cm}^2/\text{v-s}$$

$$v_{\text{ref}} = 2.2 \times 10^7 \text{ cm/s}$$

$$F_{\text{ref}} = 3.25 \text{ kv/cm}$$

$$N_{\text{ref}} = 1.0 \times 10^{15}/\text{cm}^3$$

The above choices lead to a set of dimensionless constants equal to:

$$C_n = 1.0$$

$$S_n = 45.0$$

$$R_n = 120.0$$

The results of the calculation are clear and are shown in figure 67. The current voltage relation for 'HiV' yields a saturation current that exceeds that of gallium arsenide, while that for 'LoV' is depressed below that of gallium arsenide. The results indicate that even in materials possessing a nonlinear 'N' shaped negative differential conductivity, saturation in current is likely to be above that associated with the saturated drift velocity. This result should dispell any notion, that since silicon has a higher saturation drift velocity than gallium arsenide, it will perform better.

The next set of calculations is a comparison of silicon to gallium arsenide. Here, however, a comparison is not made to structures with similar extrinsic parameters; enough has been said in this paper to indicate that silicon will not perform speed-wise in a matter similar to gallium arsenide. Rather the question is, are there scaling procedures that permit the design of silicon devices, which with respect to reference quantities are as good as that of gallium arsenide? The answer to this question is yes, the significance, of which is discussed below.

Numerical simulations were performed for a silicon device with the field dependent velocity and diffusivity shown in figure 68. The parameters for this calculation were deliberately chosen so that the dimensionless constants for the silicon device were nearly equal to that of gallium arsenide. This criteria leads to the reference quantities given below:

$$x_{ref} = 4.4 \text{ microns}$$

$$\phi_{ref} = 3.14 \text{ volts}$$

$$u_{ref} = 1400 \text{ cm}^2/\text{v-s}$$

$$v_{ref} = 1.0 \times 10^7 \text{ cm/sec}$$

$$F_{ref} = 7.14 \times 10^3 \text{ v/cm}$$

$$N_{ref} = 5.0 \times 10^{15}/\text{cm}^3$$

The dc electrical characteristics of the silicon FET are shown in figure 69, and are as good as the "HiV" element when the silicon is doped to higher levels and reduced in feature size. This result is simply a statement that higher doping is needed to compensate for the low mobility of silicon, and that shorter crucial length scales are required to compensate for the low carrier velocity of silicon.

With regard to the power delay produced, gallium arsenide and the scaled silicon are within a factor of two of each other [5]), implying that more energy must be dissipated through the smaller silicon device to achieve the same electrical characteristics.

#### XIb. Scaling and High Frequency FETs

The goal of each of the above scaling procedures is to assist in the realistic design of a high frequency three terminal oscillator. The most useful method to obtain design information is through application of the moments of the Boltzmann transport equation. Unfortunately, the MBTE development as indicated

earlier precludes a full scale procedure. Instead, we expand upon results of an earlier study, where a full transient small signal analysis of an FET was presented [16], and then speculate with preliminary calculations on the short channel effects. In the [16] study the three terminal device discussed in the previous section was taken to a steady state time independent state; upon which the gate and drain voltage levels were, respectively and separately, pulsed. The resulting current transient, subsequently Fourier analyzed and the small signal 'Y' parameters computed. Of significance here is the cut-off frequency, which is defined as

$$f_T = \frac{\Omega \operatorname{Re} Y_{21}}{2\pi |\operatorname{Im}(Y_{11} + Y_{12})|} \quad (54)$$

For the structure of figure 66, the peak cut-off frequency as seen in figure 70, is bias dependent and peaks near 9GHz. The implication of scaling with the drift and diffusion code is that if diffusive effects are to be ignored, then a reduction in the critical length parameters by the scale factor ' $\lambda$ ' is expected to increase the cut-off frequency by the same scale factor. This, of course, is the basis of all FET scaling procedures; and is a major motivating factor for going to submicron structures. This scaling was tested with the following set of parameters:

$$x_{ref} = 1.0 \text{ microns}$$

$$\phi_{ref} = 0.325 \text{ volts}$$

$$N_{ref} = 1.0 \times 10^{16}/\text{cm}^3$$

However, in testing, rather than perform a full scale calculation, only a preliminary set of dc current voltage characteristics were obtained.

The electrical characteristics of the scaled and unscaled gallium arsenide structures are shown in figure 71. And somewhat surprising the expected degradation with increased donor level did not appear. While additional scaling work here is needed, the preliminary conclusion is that if 9GHz is possible, a scaled cut-off frequency of 90GHz is feasible.

The situation with submicron FET is complicated by determining the key design significance of the submicron feature size. This is a more difficult problem and has been examined by Frey and coworkers [17] using a highly approximate set of equations whose applicability to submicron devices is somewhat uncertain. The results of our previous one dimensional study have indicated that as device feature size is reduced transport is dominated by T-valley carriers. The immediate implication is that the early transport models in which transconductance was defined in terms of low field mobility is the more relevant quantity. An estimate of this effect is examined in the final calculation of this study.

#### XIc. MBTE versus DDE

Figure 72 is a sketch of the dc current voltage relation for a gallium arsenide FET with the feature size shown in the diagram. Two sets of calculations were performed: One using the drift and diffusion equations and

the second using the moments of the Boltzmann transport equation. The calculations were done at zero bias on the gate along with a zero dc current boundary condition on the gate contact. The calculations show current voltage relationships that are virtually identical at low values of bias, with substantial deviations at high values of bias. It is noted that at high values of bias the DDE over estimates the amount of electron transfer within the device and thereby underestimates the dc current level. Rather, at high bias levels, the dc current is dominated by  $\Gamma$  valley carriers with a corresponding high but field dependent mobility. The charge distribution within the device, of course, reflects, the variations in the current levels, but the differences between the DDE and the MBTE carrier density calculations, as seen in the contour plots the figures 73 and 74, indicate them to be of secondary importance. The result, of course, is that scaling down improves the performance of the structure.

#### XIV. SUMMARY

The present study was undertaken to establish a set of systematic procedures for assessing the material characteristics of near and submicron length semiconductor devices structures. The first point of note, is that the assessment of the semiconductor materials requires a decision as to how they will be used. For example, semiconductor materials that are optimum for two terminal active device applications are not necessarily the ones to be sought after for three terminal application. In the case of two terminal active devices rapid scattering is sought, however, this normally leads to low values of mobility. For three terminal structures, submicron devices are dominated by the  $\Gamma$  valley scattering and materials with high values of mobility are sought. Another important conclusion, was the role of carrier density in scaling, of particular importance here was the fact that increase donor concentration often lead to current levels below that anticipated. The study suggests that a hierarchy of material parameters exists for device applications. For two terminal active devices the three materials in order of significance are InP, GaAs, and GaInAs. For three terminal structures materials in order of significance are GaInAs, GaAs, InP, Ge, Si, and SiC.

The conclusions were drawn from a broad range of calculations that involved altering the band structure parameters, both uniformly and nonuniformly; and altering the doping profile both uniformly and nonuniformly. Additionally, supplementary two dimensional three terminal calculations were performed to test the concepts.

Several important features emerged: First, scaling as currently applied has been inadequate for examining submicron devices. In particular, features associated with field nonuniformities are generally ignored, and are crucial for submicron devices. The absence of suitable scaling basically arises because of a paucity of numerical calculations that emphasize scaling. The study reported demonstrated that scaling procedures can be envisioned, through which small signal steady state analysis can effectively lead to devices whose, e.g., cut-off frequency can be increased by the factor  $\lambda$  if the carrier density is increased, and the scaling length decreased by the same factor.

While small signal parameter studies of the three terminal FET has begun, there is a clear need for further assessing the relative merits of GaAs coplanar devices from both a small and large single viewpoint, particularly through solutions to the moments of the Boltzmann transport equation. The MBTE has not yet been completely applied to assessing the high frequency performance of the standard GaAs FET and such studies are necessary before a realistic assessment of the device can be made.

#### FIGURE CAPTIONS

1. Steady state uniform field characteristics for electrons in gallium arsenide assuming two levels of transfer. The parameters for this calculation are shown in table 1. (a) and (b) are the magnitudes of the mean carrier velocity over different ranges of electric field. (c) and (d) display the field dependence of the fractional population of carriers in the  $\Gamma$  and L valleys. (e) and (f) display the magnitudes of the mean carrier velocity in the  $\Gamma$  and L valleys. (g) and (h) display the carrier temperatures in the  $\Gamma$  and L valleys.
2. Steady state uniform field dependent drift velocities using the scaling principles of equation (6). Scaling parameters are indicated.
3. As in figure 1, but for indium phosphide using the parameters of table 2.
4. Two level moment equation scattering rates for gallium arsenide. The scattering rate are keys to the equations of section III.
5. As in figure 4, but for indium phosphide.
6. Ratio of the scattering rates of indium phosphide to gallium arsenide as obtained from the calculations of figures 4 and 5.
7. Effects of parameter variation, as indicated, on the field dependent velocity of gallium arsenide.
8. Response of the mean carrier velocity in gallium arsenide to a controlled change in electric field.
9. Transient mean velocity response of scaled and unscaled gallium arsenide.
10. Total and  $\Gamma$  valley carrier density obtained as a solution, with  $\lambda=1$ , to equations (27), (28), (31) through (35) with the boundary conditions of equations (36).  $\lambda=1/2$ , 2 and 4, are scaled results.
11. As in figure 10, but for the electric field versus distance profile.
12. As in figure 10, but for  $\Gamma$  valley carrier velocity.
13. As in figure 10, but for  $\Gamma$  valley electron temperature.
14. Transient current response of the 1.0 micron long gallium arsenide one dimensional structure subjected to a sudden change in bias. Scale quantities are in accordance with the requirements of table 7.
15. Magnitude of the current transient following application of a step change in potential for 0.25 micron gallium arsenide unscaled and scaled devices. The scaling is indicated.
16. Distribution of charge for the calculation in figure 15.
17. Distribution of  $\Gamma$  valley carrier velocities for the calculation of figure 15.

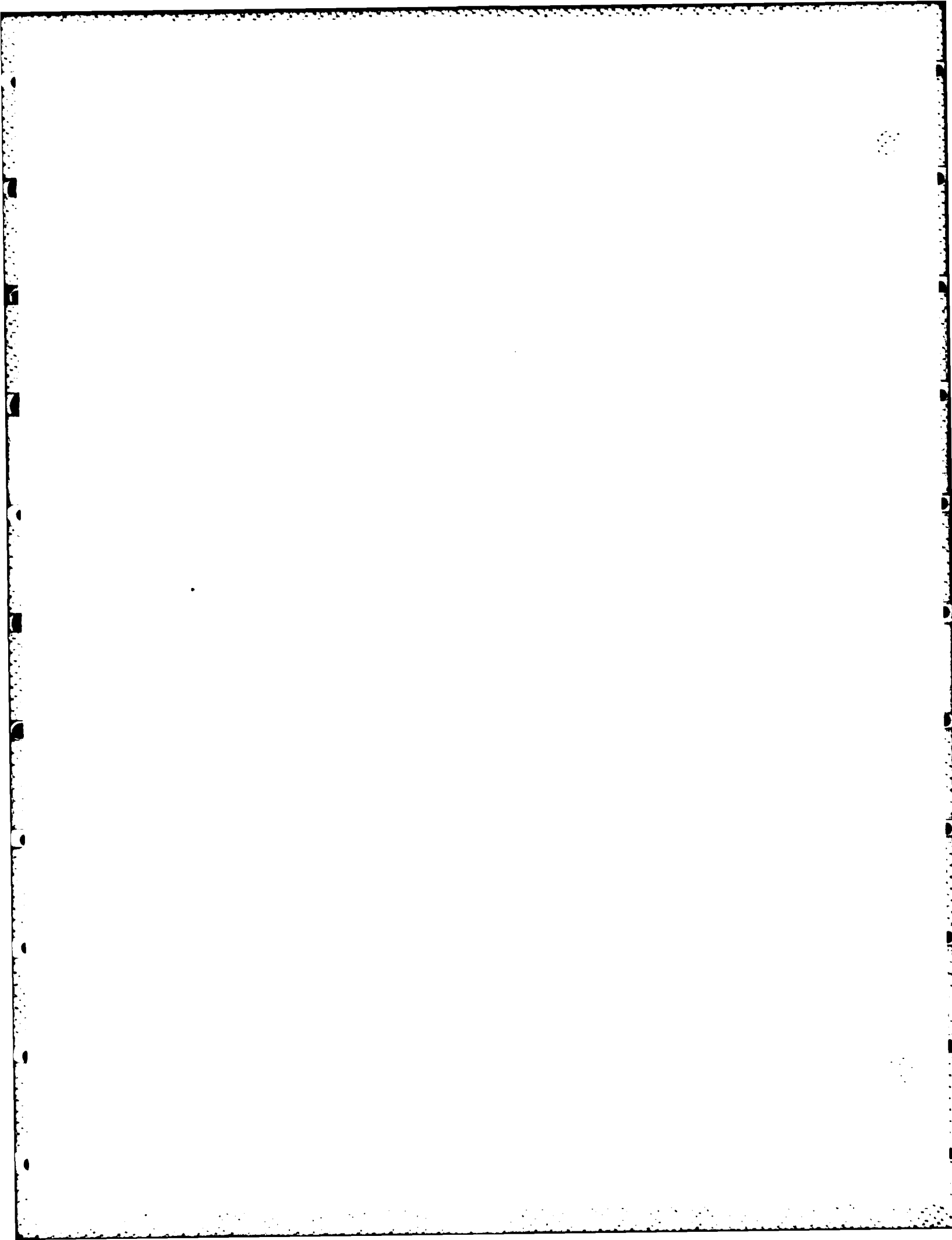
18. As in figure 11, but for the carrier temperature.
19. Distribution of electric field for the calculation of figure 15.
20. As in figure 1, but with DCR increased to twice the value of table 1.
21. The scattering rates associated with figure 20.
22. As in figure 1, but with DCR decreased to one-half the value of table 1.
23. The scattering rates associated with figure 22.
24. Total and  $\Gamma$  valley carrier density obtained for the increased coupling coefficients and scattering rates of figure 20, and  $N_{ref} = 8 \times 10^{16}/\text{cm}^3$ ,  $X_{ref} = 0.25$  microns and indicated values of potential.
25. As in figure 24, but for the electric field versus distance profile.
26. As in figure 24, but for the  $\Gamma$  valley carrier velocity.
27. As in figure 24, but for the  $\Gamma$  valley electron temperature.
28. Magnitude of the transient current response for the structure of figure 24, subject to a sudden change in bias.
29. Total and  $\Gamma$  valley carrier density obtained for the decreased coupling coefficients and scattering rates of figure 22, and  $N_{ref} = 8 \times 10^{16}/\text{cm}^3$ ,  $X_{ref} = 0.25$  microns and indicated values of potential.
30. As in figure 29, but for the electric field versus distance profile.
31. As in figure 29, but for the  $\Gamma$  valley carrier velocity.
32. As in figure 29, but for the  $\Gamma$  valley carrier temperature.
33. As in figure 28, but for the parameters of figure 29.
34. As in figure 24, but for unscaled gallium arsenide.
35. As in figure 34, but for the electric field versus distance profile.
36. As in figure 34, but for the  $\Gamma$  valley carrier velocity.
37. As in figure 34, but for the  $\Gamma$  valley electron temperature.
38. As in figure 28, but for the unscaled gallium arsenide.
39. (a) Current density versus average field for a 0.25 micron long structure with injecting contacts and a donor density of  $5.0 \times 10^{15}$ . The potential variations are as indicated. Calculations are for different values of the coupling coefficients.  
(b) As in (a) but for a 2.0 microns long structures.

40. As in figure 1, but for an energy separation increased to 0.66ev.
41. As in figure 4, but for the parameters associated with figure 40.
42. As in figure 34, but for an energy separation increased to 0.66ev.
43. As in figure 42, but for the electric field versus distance profile.
44. As in figure 42, but for the  $\Gamma$  valley carrier velocity.
45. As in figure 42, but for the  $\Gamma$  valley electron temperature.
46. As in figure 38, but for an energy separation increased to 0.66ev.
47. As in figure 1, but for an inclusion of ionized impurity scattering. Brooks-Herring matrix elements are used and the donor concentration is  $8E+16/cm^3$ .
48. As in figure 4, but only for the momentum scattering rates.
49. As in figure 34, but for ionized impurity scattering.
50. As in figure 49, but for the electric field versus distance profile.
51. As in figure 49, but for the  $\Gamma$  valley carrier velocity.
52. As in figure 49, but for the  $\Gamma$  valley electron temperature.
53. As in figure 38, but for ionized impurity scattering included.
54. As in figure 34, but for a donor density of  $5E+15/cm^3$ .
55. As in figure 54, but for the electric field versus distance profile.
56. As in figure 54, but for the  $\Gamma$  valley carrier velocity.
57. As in figure 54, but for the  $\Gamma$  valley electron temperature.
58. Steady state current versus voltage for a donor density of  $5E+15/cm^3$ .
59. As in figure 54, but for a donor density of  $2E+16/cm^3$ .
60. As in figure 59, but for the electric field versus distance profile.
61. As in figure 59, but for the  $\Gamma$  valley carrier velocity.
62. As in figure 59, but for the  $\Gamma$  valley electron temperature.
63. As in figure 58, but for a donor density of  $2E+16/cm^3$ .
64. Steady state current voltage relation versus donor density  $X_{ref}=0.25\mu m$ .
65. Field dependent velocity relationships used to determine the relevance of the saturated drift velocity to the IDSS of FETs.

66. Sketch of three terminal FET structure used in calculations.
67. Current-voltage relation for the field dependent velocities of figure 65.
68. Field dependent velocity and diffusivity for a silicon unipolar FET calculation.
69. Current-voltage relation for silicon and 'HiV' drawn on the same scale.
70. Small signal cutoff frequency in gallium arsenide FET with  $x_{ref}=10.0$  microns.
71. Drain current versus drain bias for scaled and unscaled gallium arsenide FET.
72. Comparison of FET characteristics using the DDE and MBTE formulation (structure is indicated with length in microns).
73. Comparison of DDE and MBTE contours for indicated bias.
74. As in figure 73.

#### REFERENCES

1. W. Shockley, Proc. IRE 40, 1365 (1952)
2. A. Bar-Lev, Semiconductors and Electric Devices (2nd edition) Prentice Hall International, N.J. (1984)
3. See e.g., G.C. Osborne, Journal Applied Physics 53, 1586 (1982)
4. R.C. Eden, Proc. IEEE 70 5 (1982)
5. H.L. Grubin, IEEE Trans. Micro. Th. Tech., MTT-28, 442 (1980)
6. K. Thornber, Journal Applied Physics 51, 2127 (1982)
7. H.L. Grubin and J.P. Kreskovsky, in VLSI Electronics (N.G. Einspruch, edition) 10, 237 Academic Press, FL (1985)
8. H.L. Grubin and D.K. Ferry, J. Vac. Sci. Tech. No.1, 19, 540 (1981)
9. T.H. Windhorn, L.W. Cook, T.S. Roth, and G.E. Stillman, in Physics of Submicron Structures (H.L. Grubin, K. Hess, G.J. Iafrate, D.K. Ferry editions) 253 Plenum Press, N.Y. (1984)
10. P.N. Butcher, Rept. Prog. Phys. 30, 97 (1967)
11. S.C. Binari, H.L. Grubin, and P.E. Thompson, 1982 IEDM Technical Digest 770 (1982)
12. R. Bosch and H. Thien, IEEE Trans. Electron Devices, ED-21, 16 (1974)
13. H.L. Grubin, D.K. Ferry, G.J. Iafrate, and J.R. Barker, in VLSI Electronics (N.G. Einspruch, edition) 3, 198 Academic Press, N.Y. (1982)
14. H.L. Grubin and J.P. Kreskovsky (in preparation)
15. See e.g., S. Kratzer and J. Frey, Journal Applied Physics, 49, 4064 (1978)
16. H.L. Grubin and J.P. Kreskovsky, SRA Report R930007-F (1983)
17. See e.g., F.A. Buot and J. Frey, in Physics of Submicron Structures (H.L. Grubin, K. Hess, G.J. Iafrate, and D.K. Ferry editions) 77 Plenum Press, N.Y. (1984)



II 30 84 - 5  
920016  
J / H6

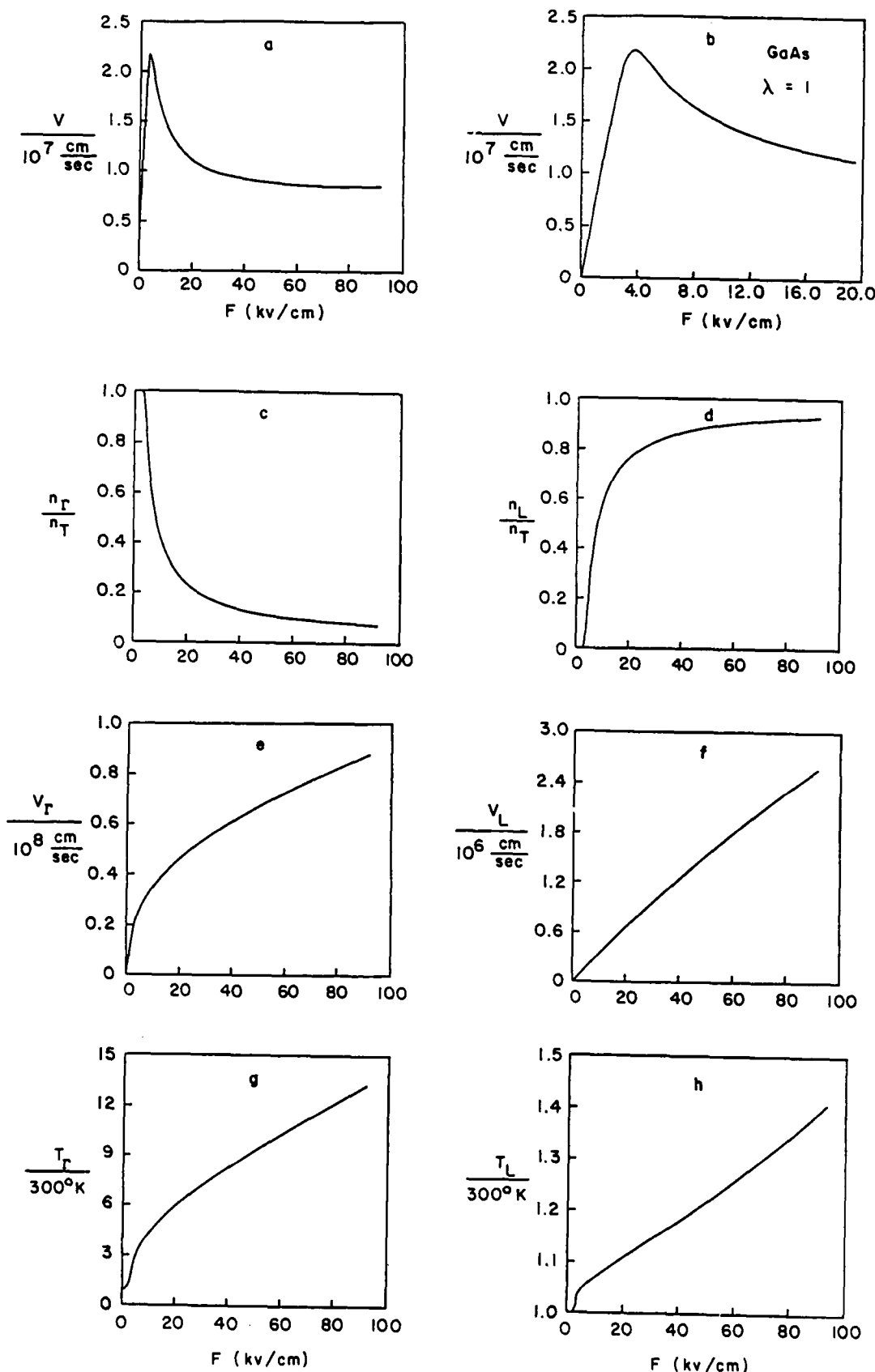


FIGURE 1. STEADY STATE UNIFORM FIELD DEPENDENT DRIFT VELOCITY FOR ELECTRONS IN GALLIUM ARSENIDE, ASSUMING TWO LEVEL TRANSFER.

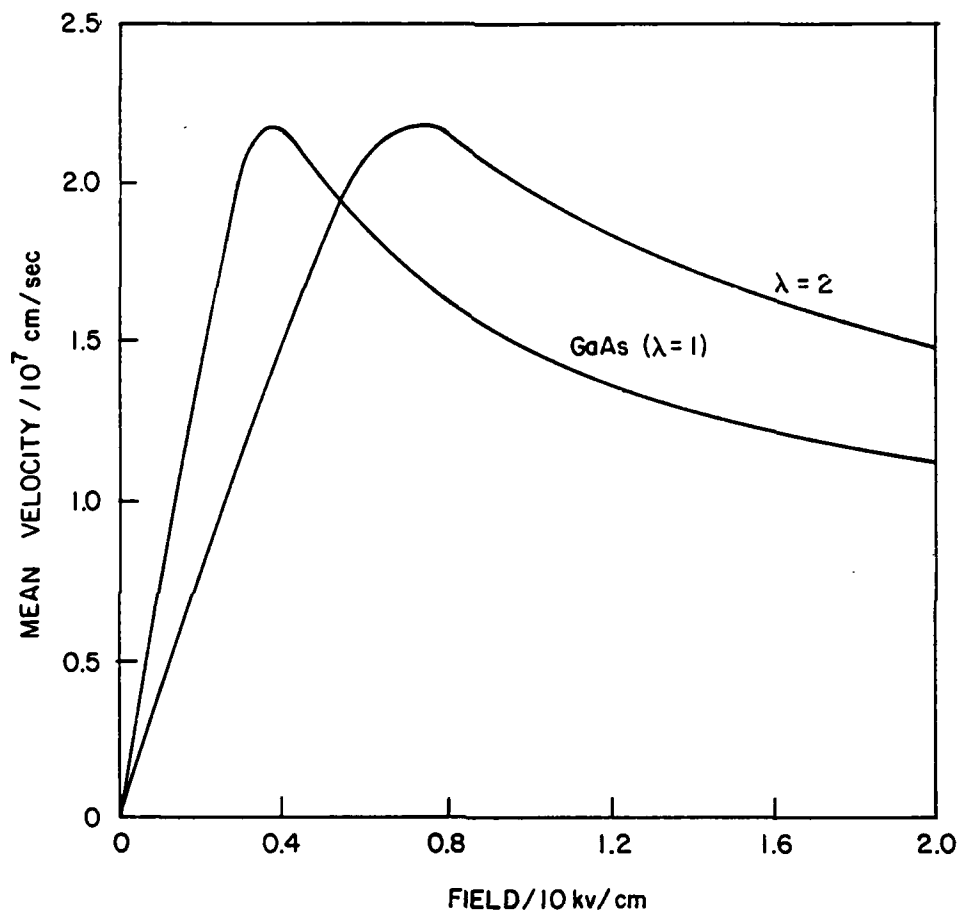


FIGURE 2. STEADY STATE UNIFORM FIELD DEPENDENT DRIFT VELOCITY FOR SCALED AND UNSCALED GALLIUM ARSENIDE STRUCTURE.

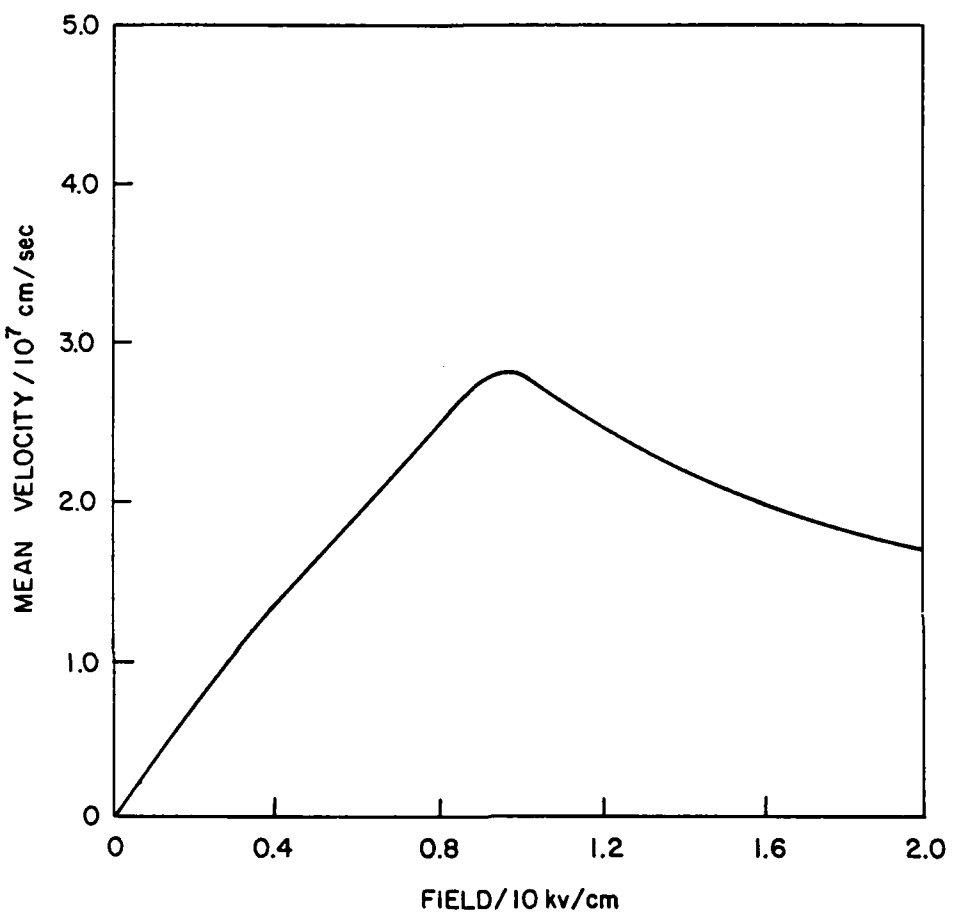


FIGURE 3. STEADY STATE UNIFORM FIELD DEPENDENT DRIFT VELOCITY  
FOR ELECTRONS IN INDIUM PHOSPHIDE, ASSUMING TWO  
LEVEL TRANSFER

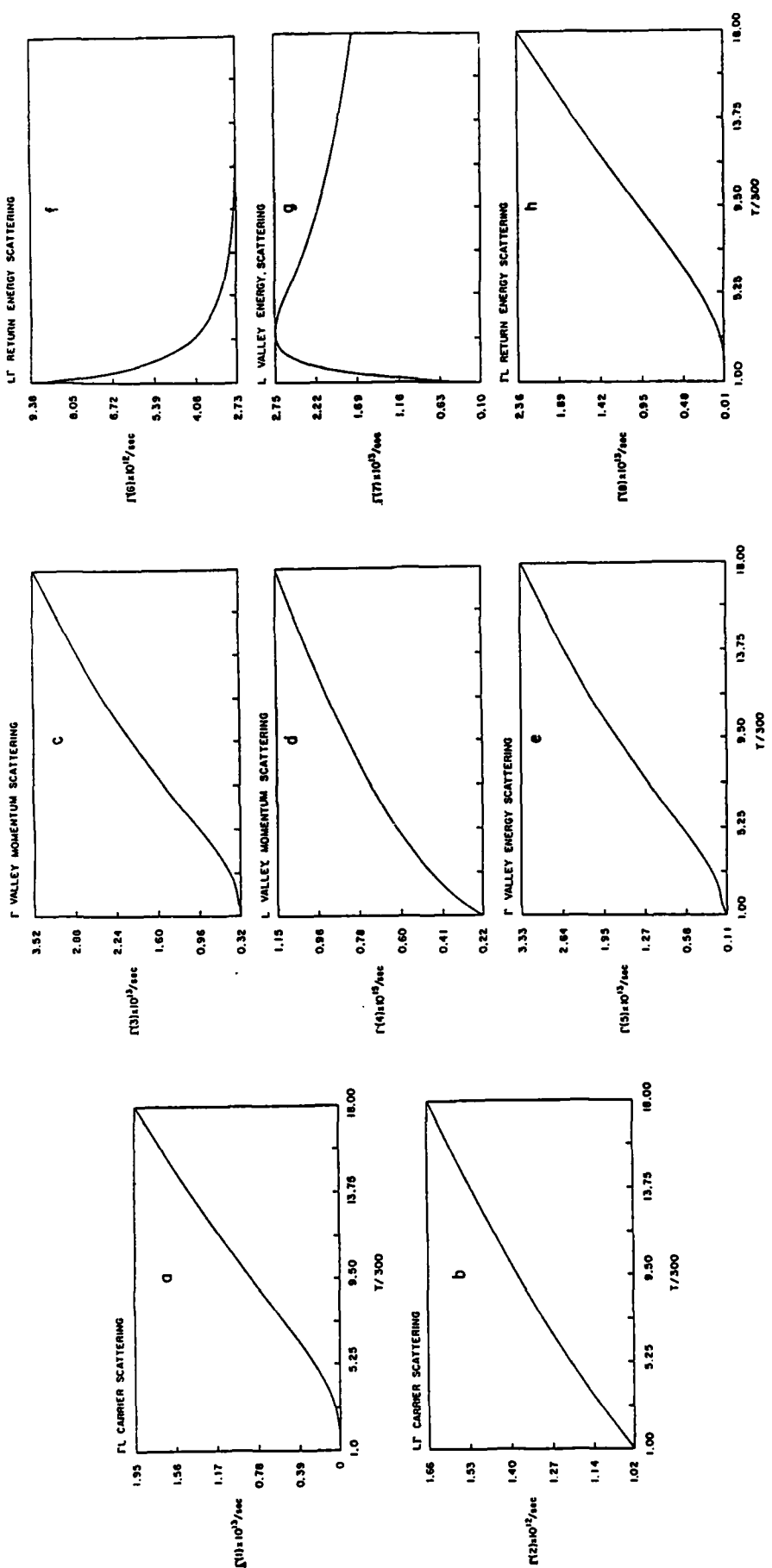


FIGURE 4. TWO LEVEL MOMENT EQUATION SCATTERING SCALES FOR GALLIUM ARSENIDE.

920010 12.2 14.2

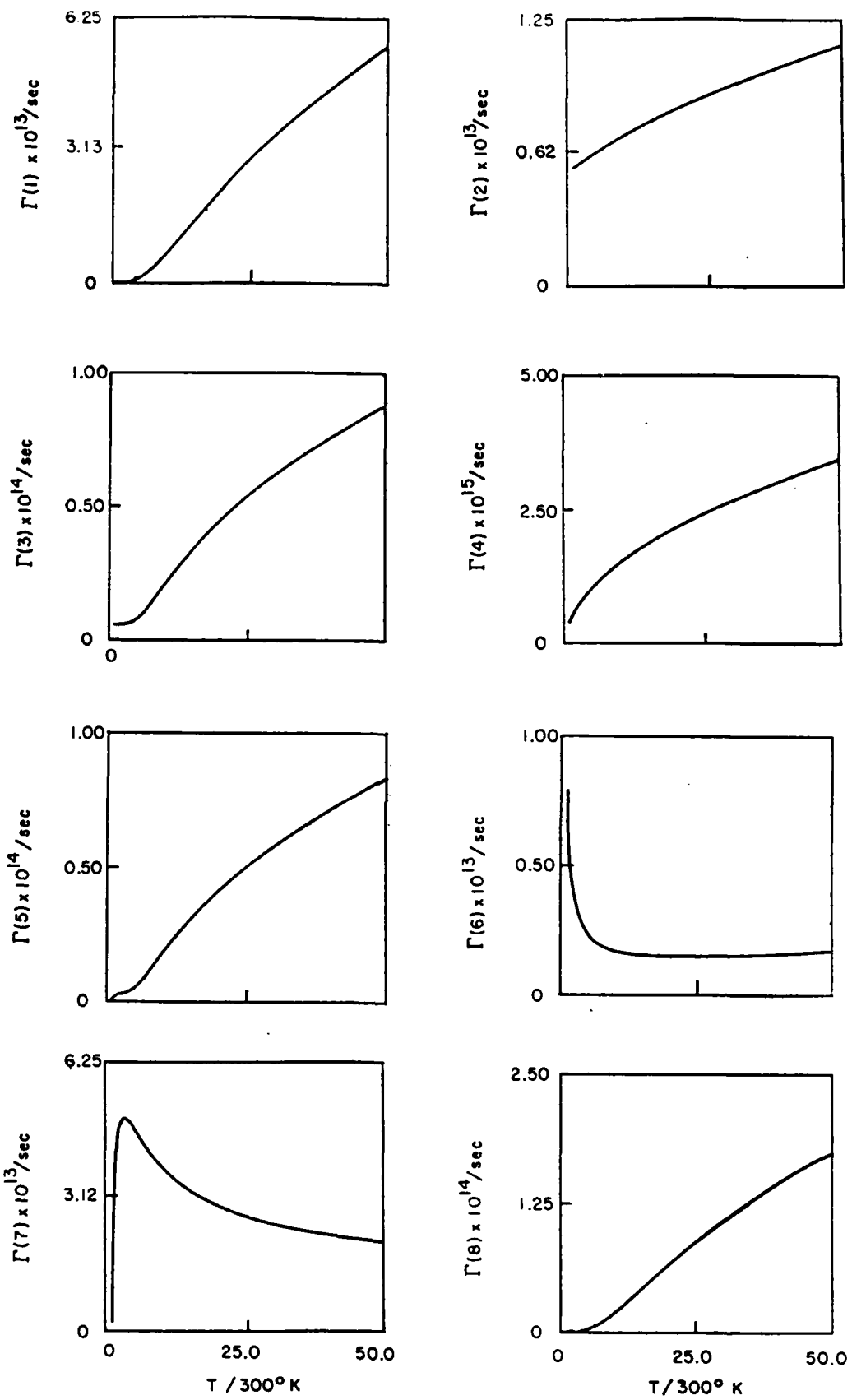


FIGURE 5. TWO LEVEL MOMENT EQUATION SCATTERING SCALES  
FOR INDIUM PHOSPHIDE

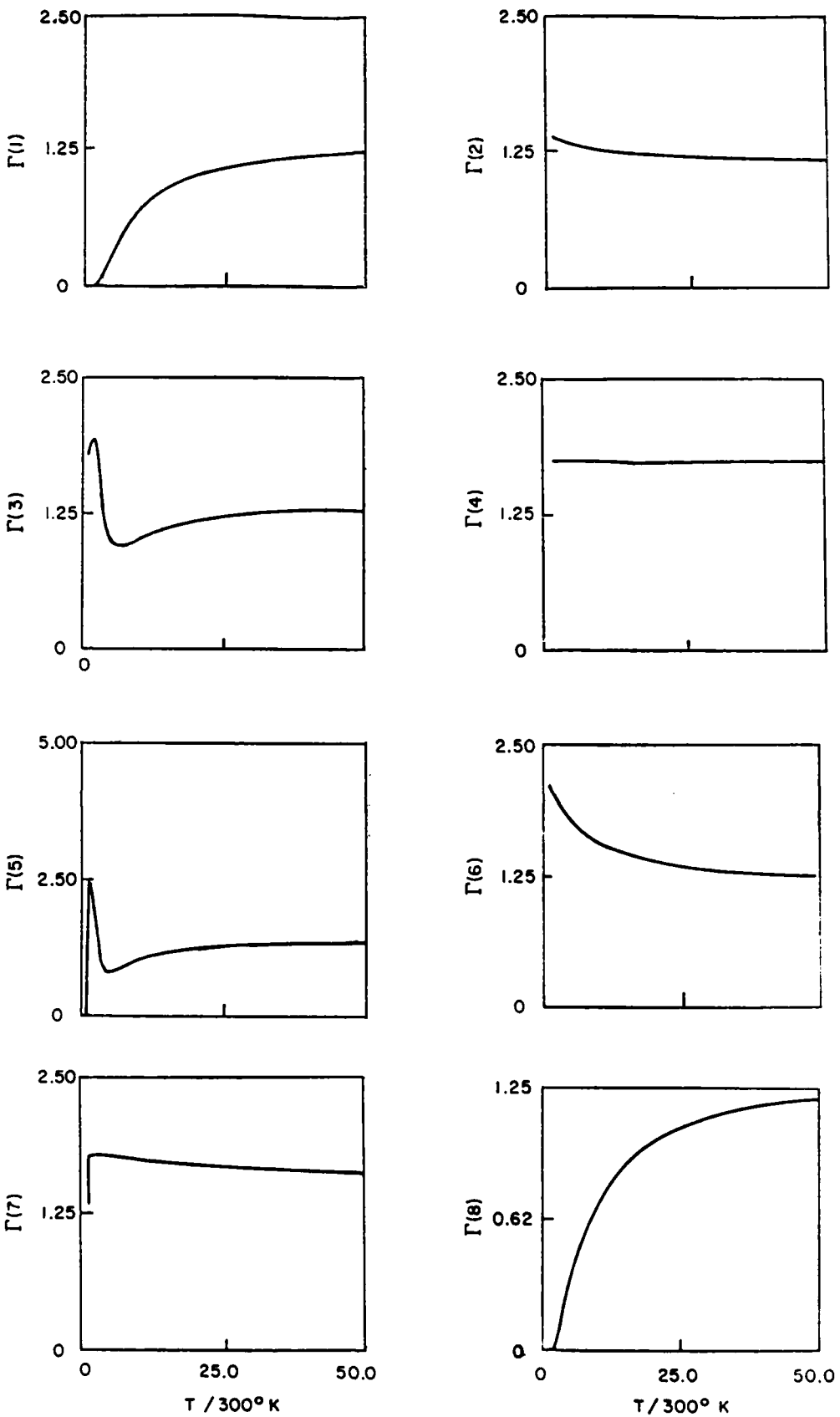


FIGURE 6. RATIO OF THE SCATTERING RATES OF  
INDIUM PHOSPHIDE TO GALLIUM ARSENIDE

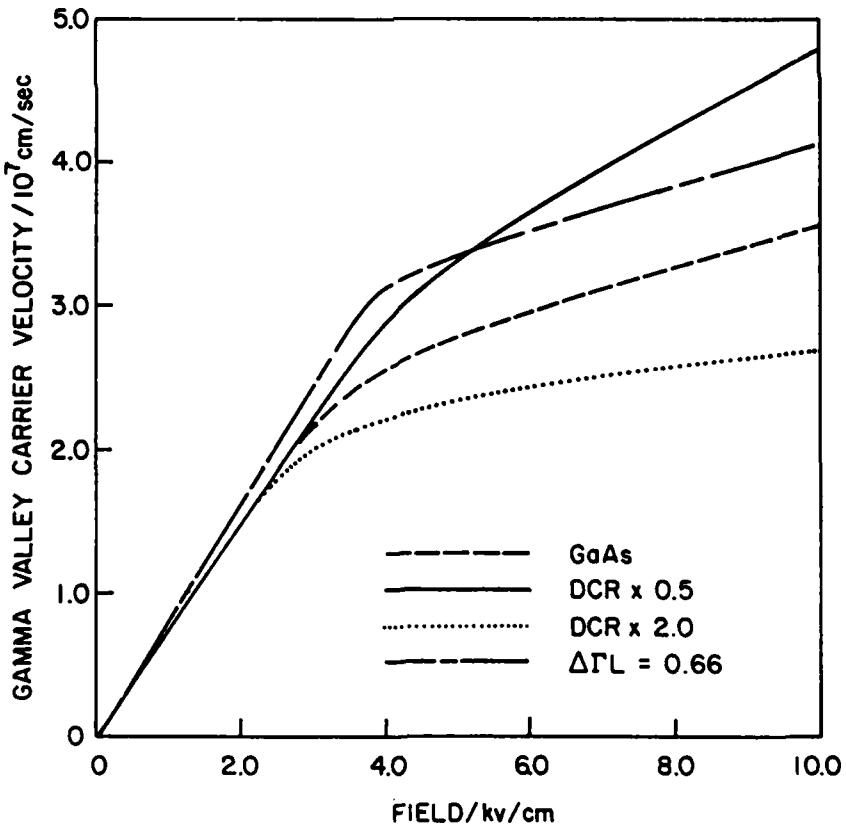
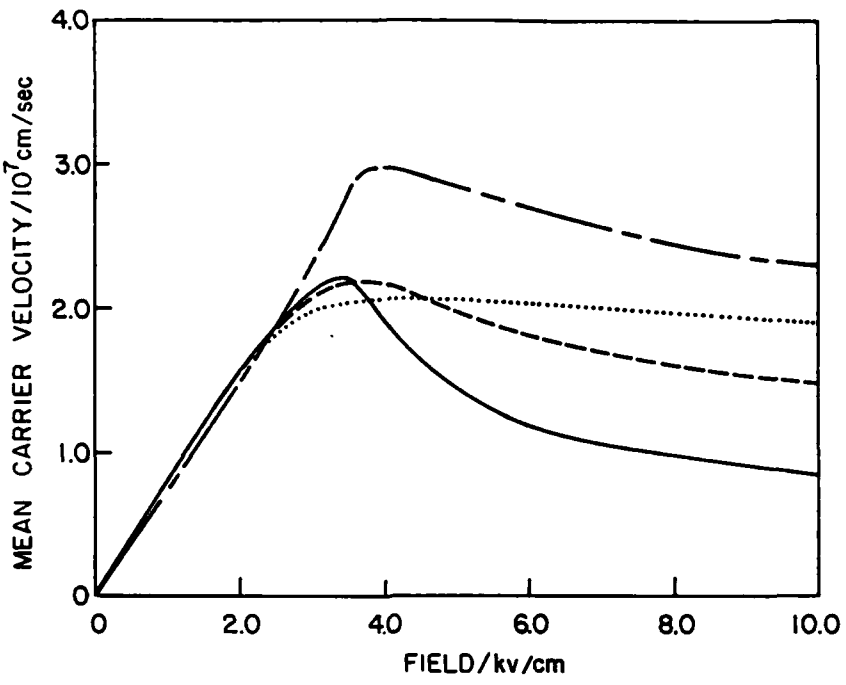


FIGURE 7. EFFECT OF PARAMETER VARIATION ON THE FIELD DEPENDENT VELOCITY OF GALLIUM ARSENIDE

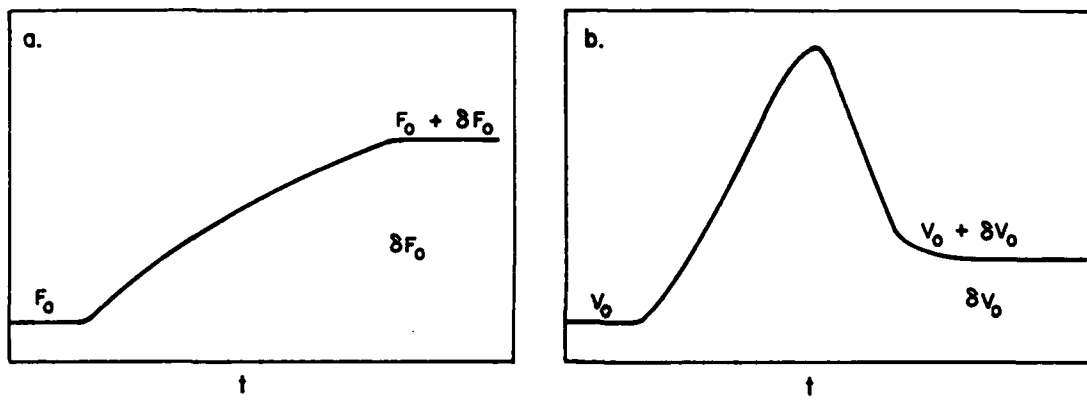


FIGURE 8. RESPONSE OF THE MEAN CARRIER VELOCITY IN GALLIUM ARSENIDE  
TO A CONTROLLED CHANGE IN ELECTRIC FIELD

920010 1285-2

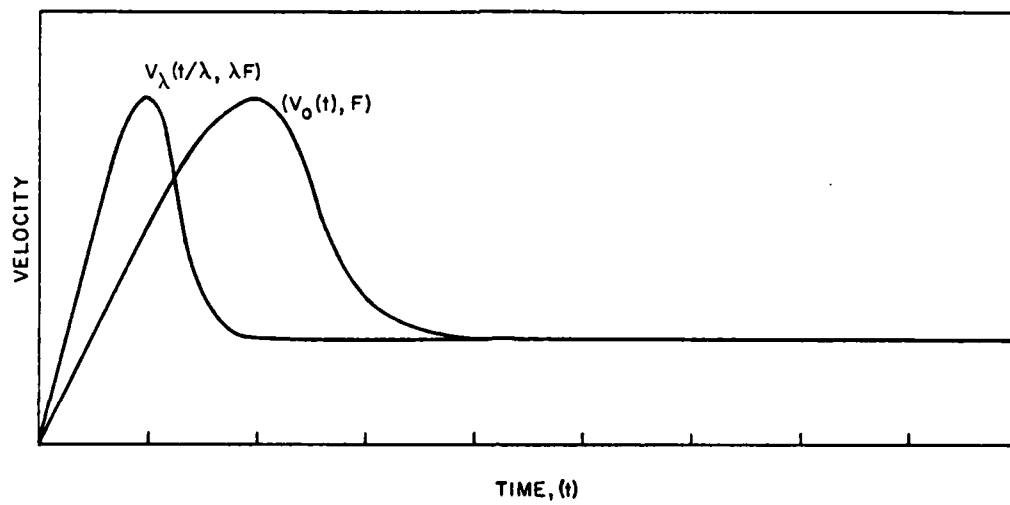
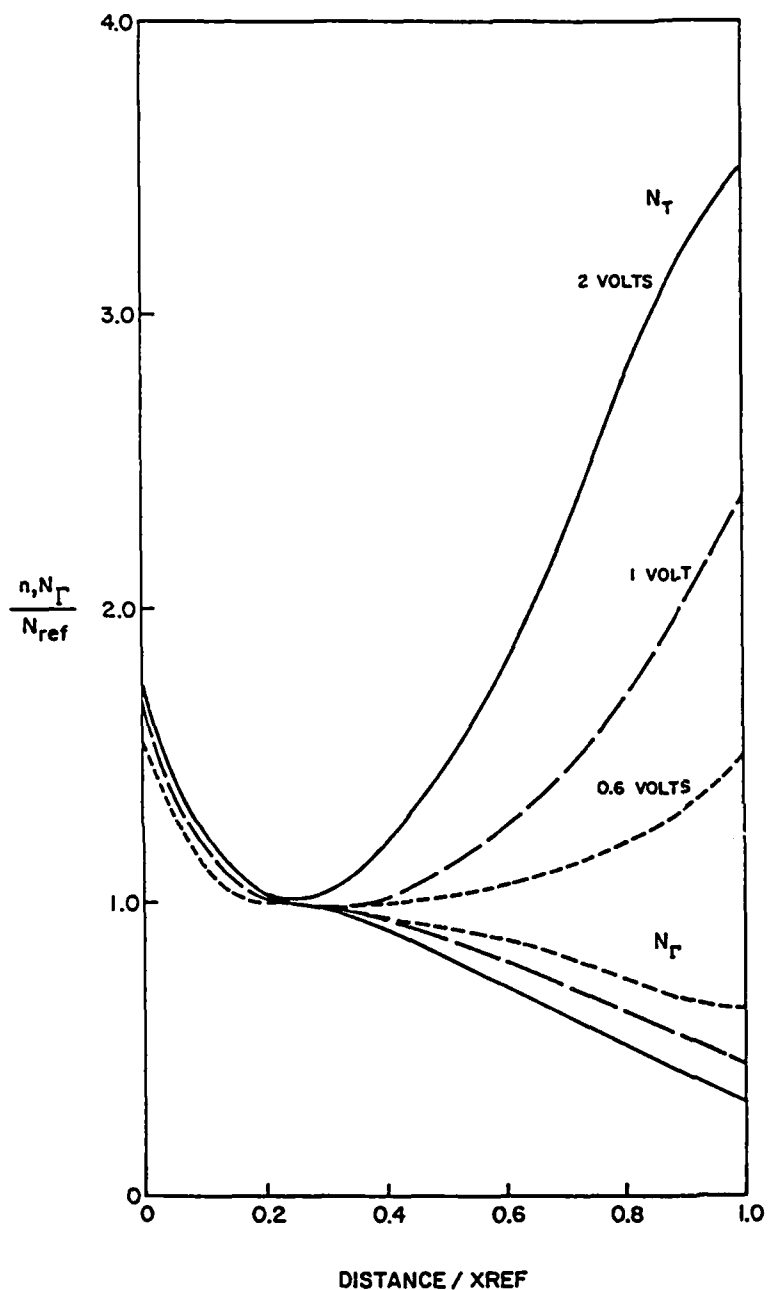


FIGURE 9. TRANSIENT MEAN VELOCITY RESPONSE OF  
SCALED AND UNSCALED CARRIER VELOCITY



SCALING	$x_{ref}$	$N_{ref}$
$\lambda = 1$	$1.0 \mu m$	$5 \times 10^{15}/cm^3$
$\lambda = 2$	$0.5 \mu m$	$2 \times 10^{16}/cm^3$
$\lambda = 0.5$	$2.0 \mu m$	$1.25 \times 10^{15}/cm^3$
$\lambda = 4$	0.25	$8 \times 10^{16}/cm^3$
$\phi_{ref} = 1.0$ volts		
$T_{ref} = 300^\circ K$		
COMMENT - GaAs = $\lambda = 1$		

FIGURE 10. TOTAL AND GAMMA VALLEY CARRIER DENSITY OBTAINED AS A SOLUTION WITH  $\lambda = 1$  TO EQUATIONS 27, 28, 31 TO 35, WITH THE BOUNDARY CONDITIONS OF EQUATIONS 36 AND 37. (FROM REF. 7, WITH PERMISSION).  $\lambda = 0.5, 2.0$  AND  $4.0$  ARE SCALED RESULTS.

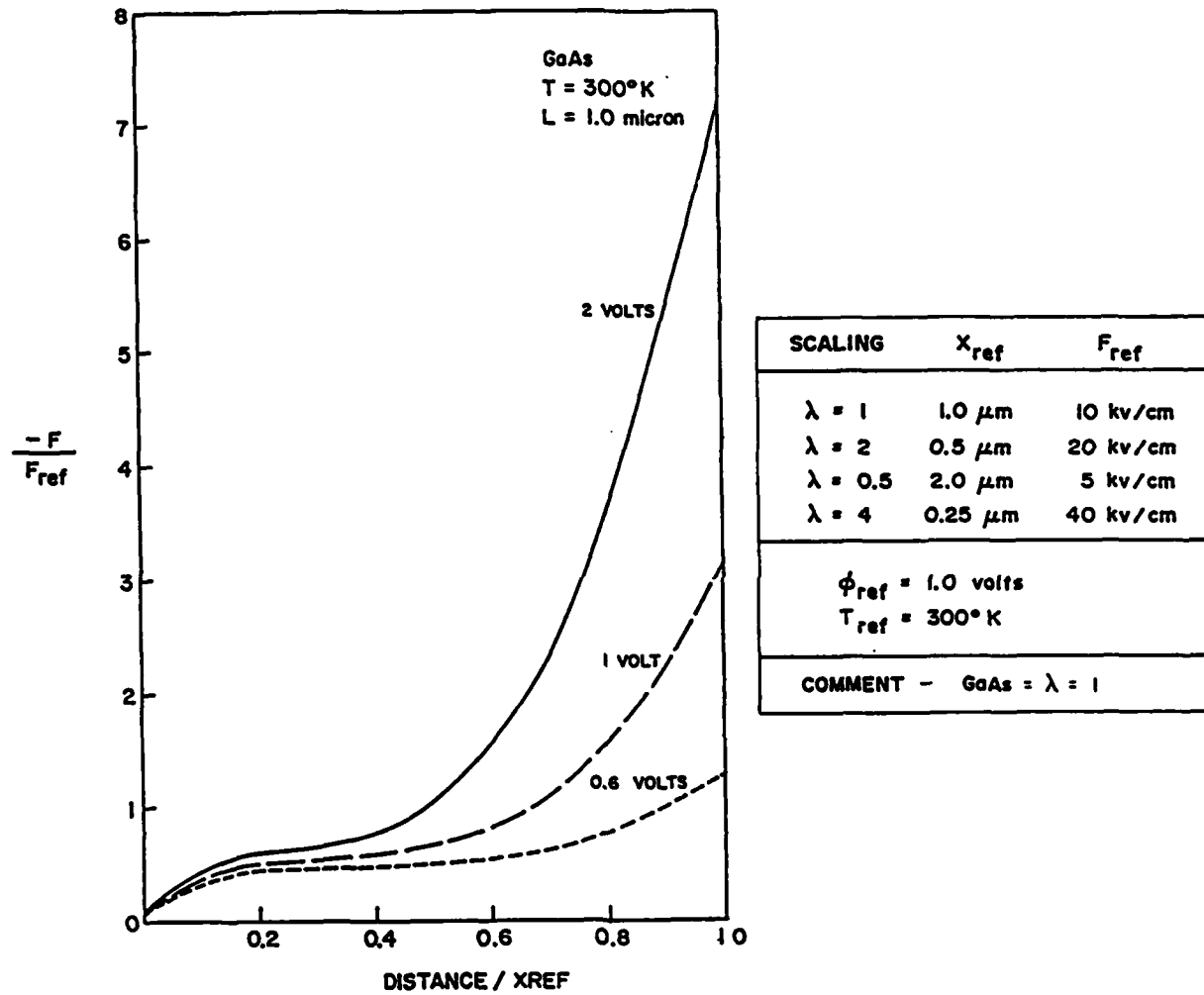
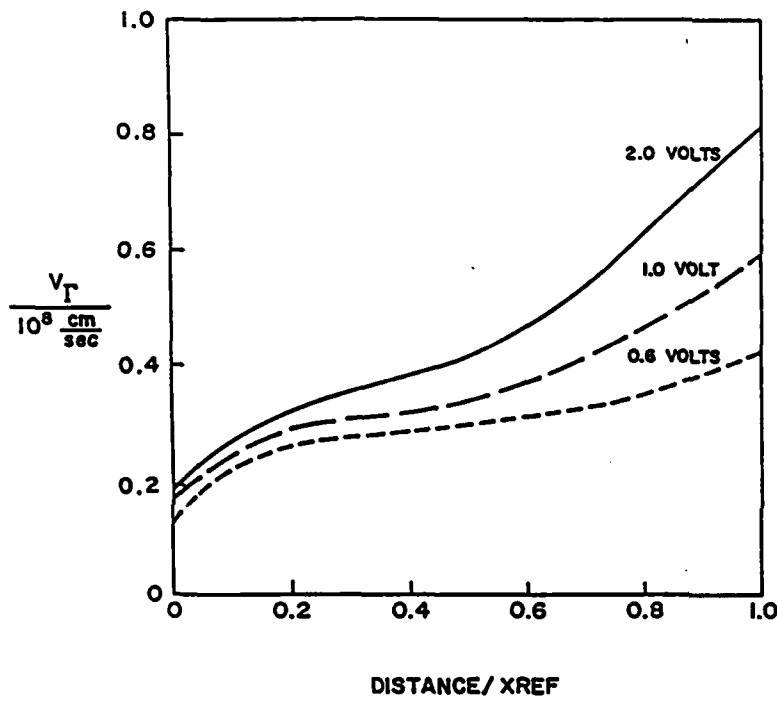


FIGURE 11. AS IN FIGURE 10, BUT FOR THE ELECTRIC FIELD VS. DISTANCE PROFILE.



SCALING	$x_{\text{ref}}$
$\lambda = 1$	$1.0 \mu\text{m}$
$\lambda = 2$	$0.5 \mu\text{m}$
$\lambda = 0.5$	$2.0 \mu\text{m}$
$\lambda = 4$	$0.25 \mu\text{m}$
$\phi_{\text{ref}} = 1.0 \text{ volts}$	
$T_{\text{ref}} = 300^\circ\text{K}$	
COMMENT - GaAs = $\lambda = 1$	

FIGURE 12. AS IN FIGURE 10, BUT FOR  $\Gamma$ -VALLEY CARRIER VELOCITY.

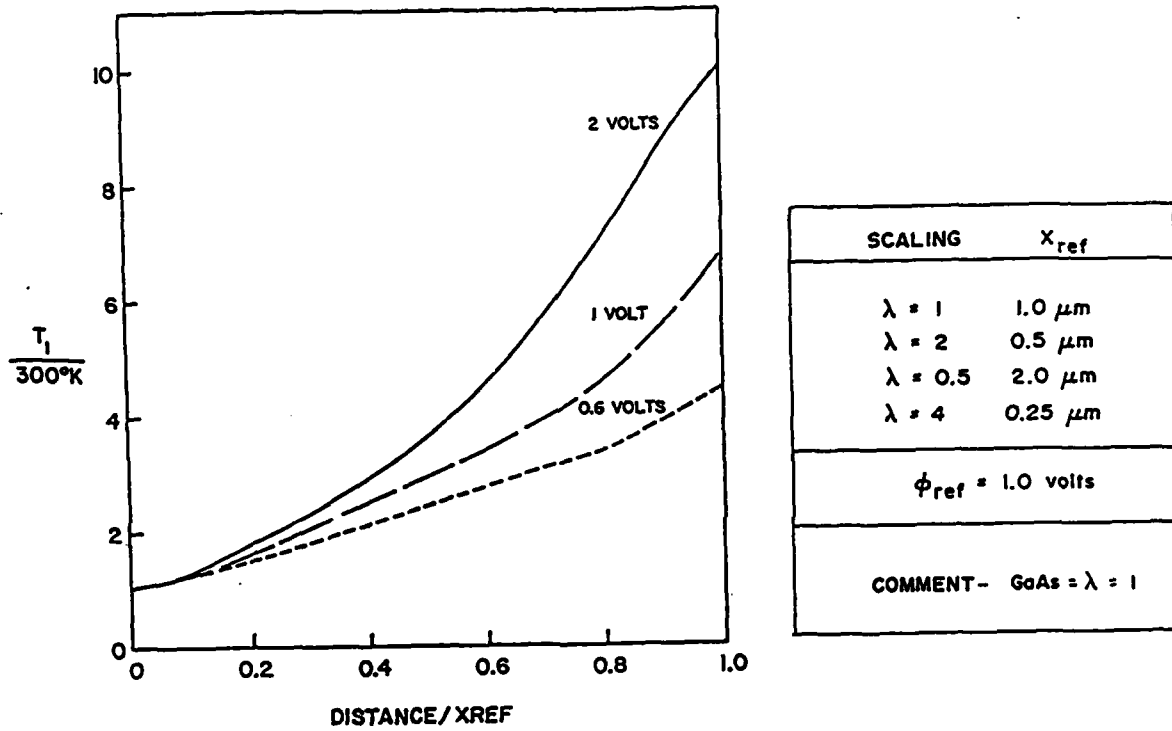
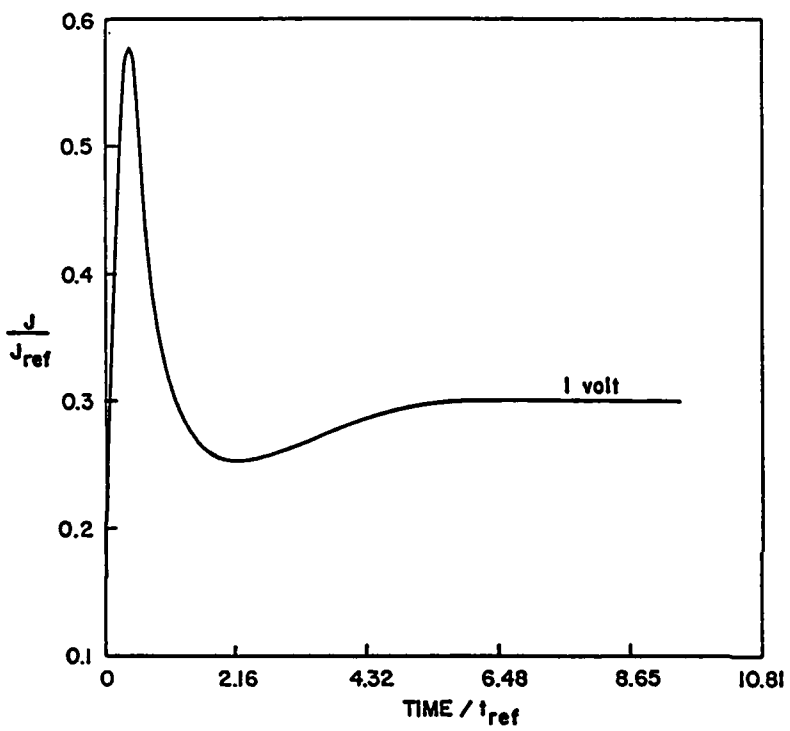


FIGURE 13. AS IN FIGURE 10, BUT FOR  $\Gamma$ -VALLEY ELECTRON TEMPERATURE.



SCALING	$J_{\text{ref}}$	$t_{\text{ref}}$
$\lambda = 1$	$8 \times 10^4 \text{ A/cm}^2$	1 ps
$\lambda = 2$	$32 \times 10^4 \text{ A/cm}^2$	0.5 ps
$\lambda = 0.5$	$2 \times 10^4 \text{ A/cm}^2$	2 ps
$\lambda = 4$	$128 \times 10^4 \text{ A/cm}^2$	0.25 ps
$\phi_{\text{ref}} = 1.0 \text{ volts}$		
$T_{\text{ref}} = 300^\circ\text{K}$		
COMMENT - GaAs = $\lambda = 1$		

FIGURE 14. TRANSIENT CURRENT RESPONSE OF THE  $1.0 \mu\text{m}$  LONG GALLIUM ARSENIDE ONE DIMENSIONAL STRUCTURE SUBJECTED TO A SUDDEN CHANGE IN BIAS. SCALED QUANTITIES ARE IN ACCORDANCE WITH THE REQUIREMENTS OF TABLE 7.

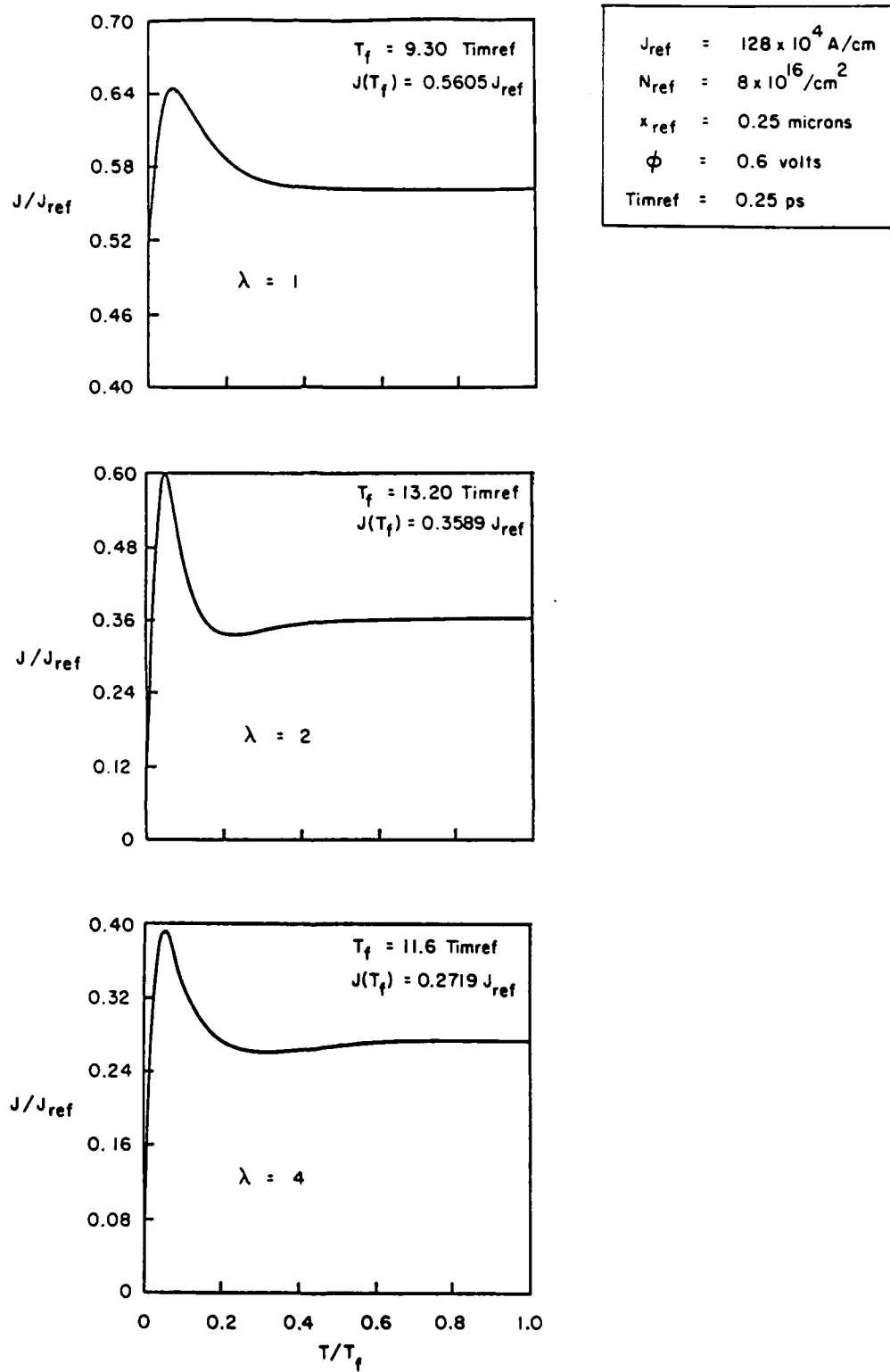


FIGURE 15. MAGNITUDE OF CURRENT TRANSIENTS FOLLOWING APPLICATION OF A STEP CHANGE IN POTENTIAL FOR A  $0.25 \mu\text{m}$  GALLIUM ARSENIDE UNSCALED AND SCALED DEVICE.

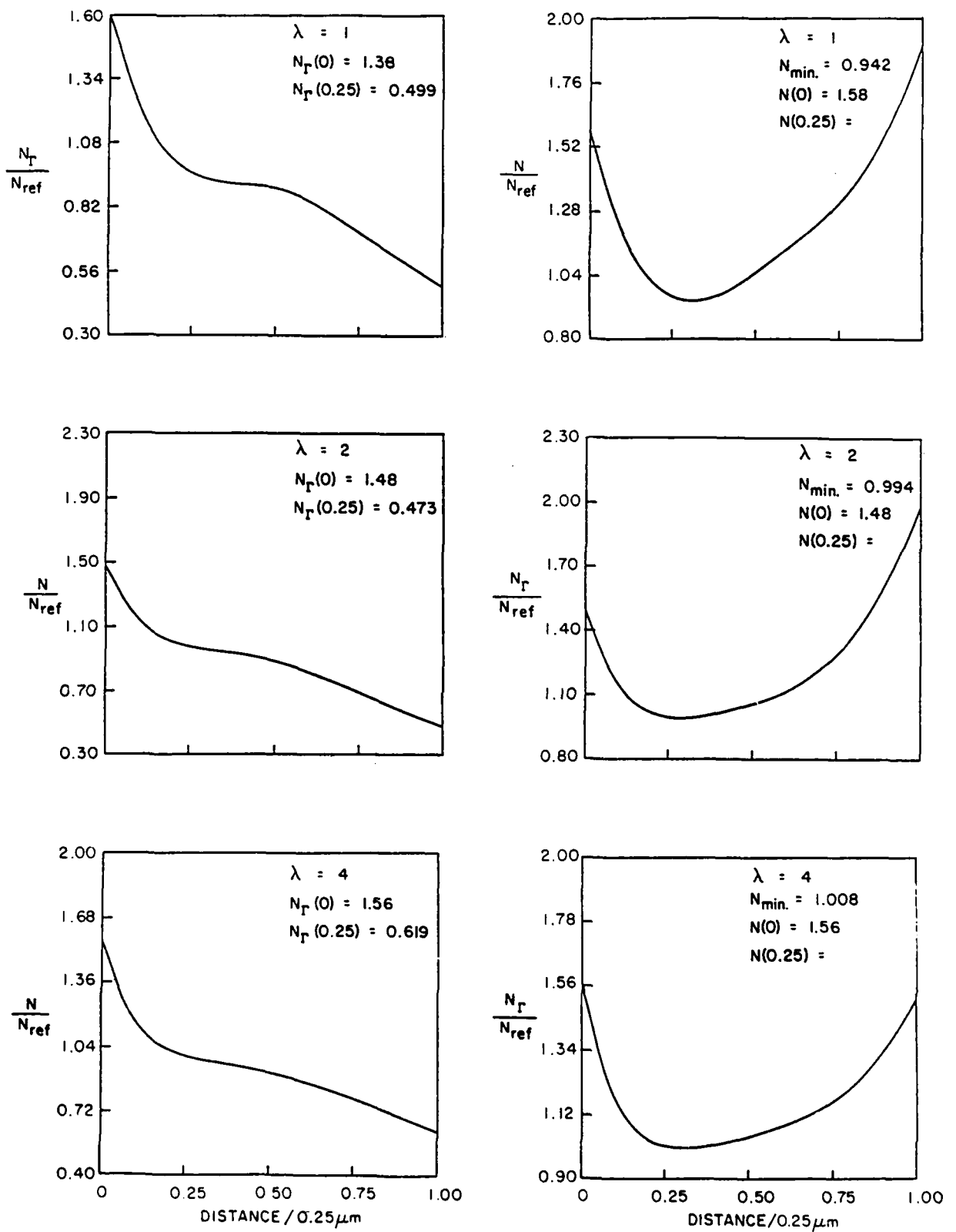


FIGURE 16. DISTRIBUTION OF CHARGE FOR THE CALCULATION OF FIGURE 15.

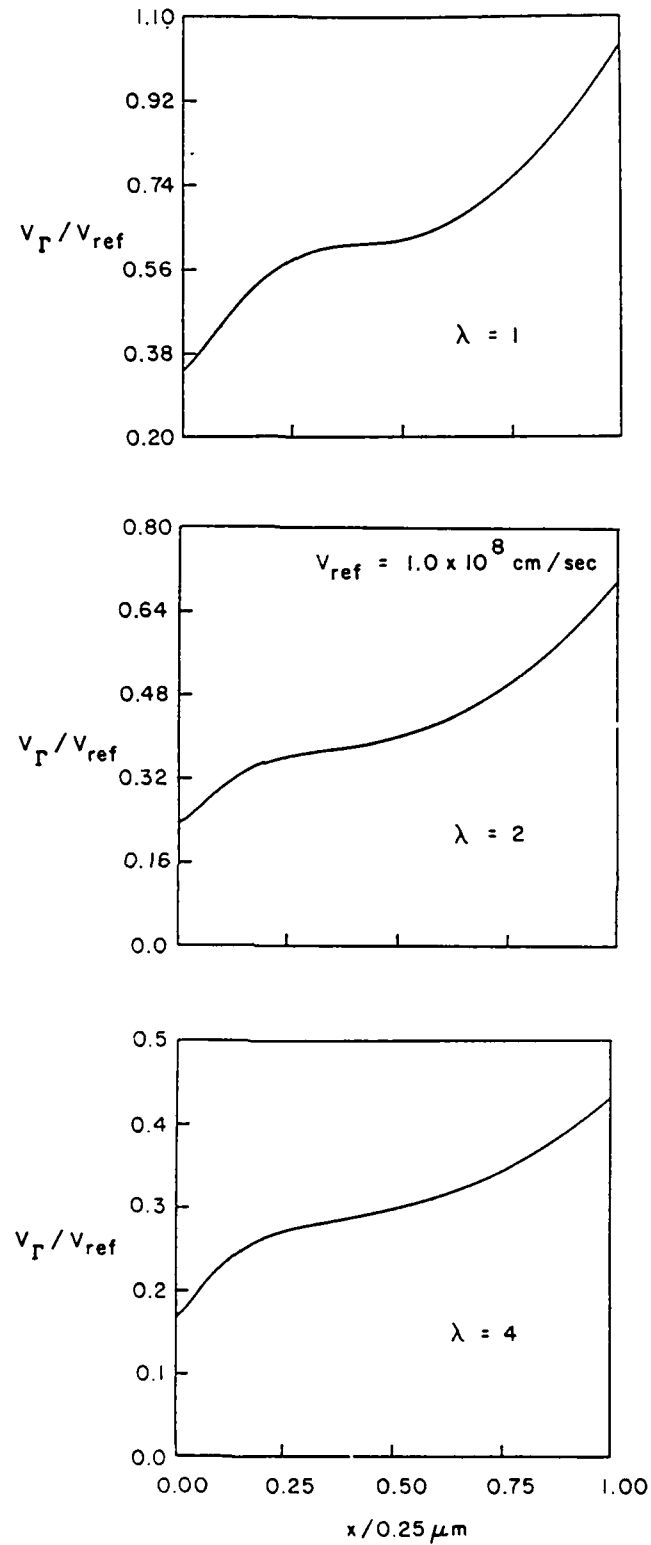


FIGURE 17. DISTRIBUTION OF  $\Gamma$ -VALLEY CARRIER VELOCITIES FOR THE CALCULATION OF FIGURE 15.

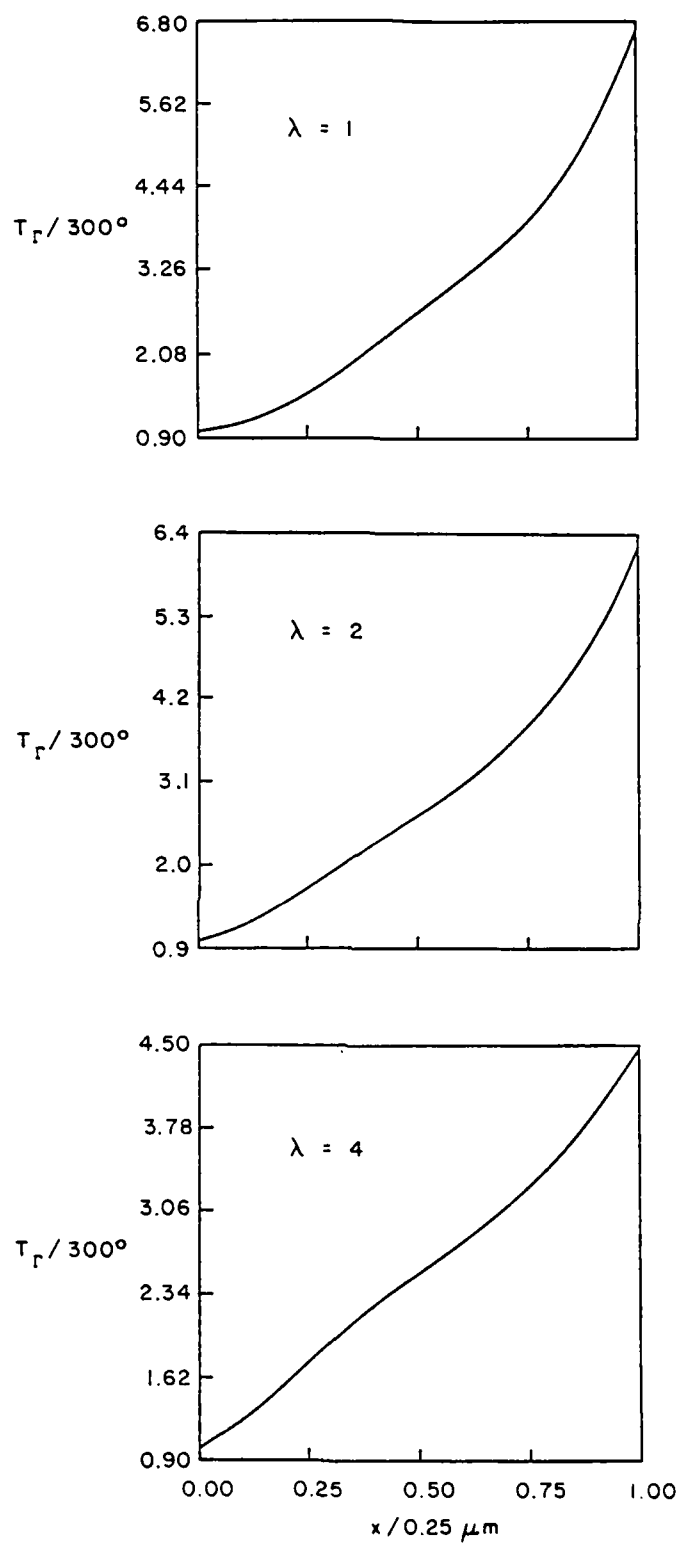


FIGURE 18.  $\Gamma$ -VALLEY ELECTRON TEMPERATURE FOR THE STRUCTURES OF FIGURE 15.

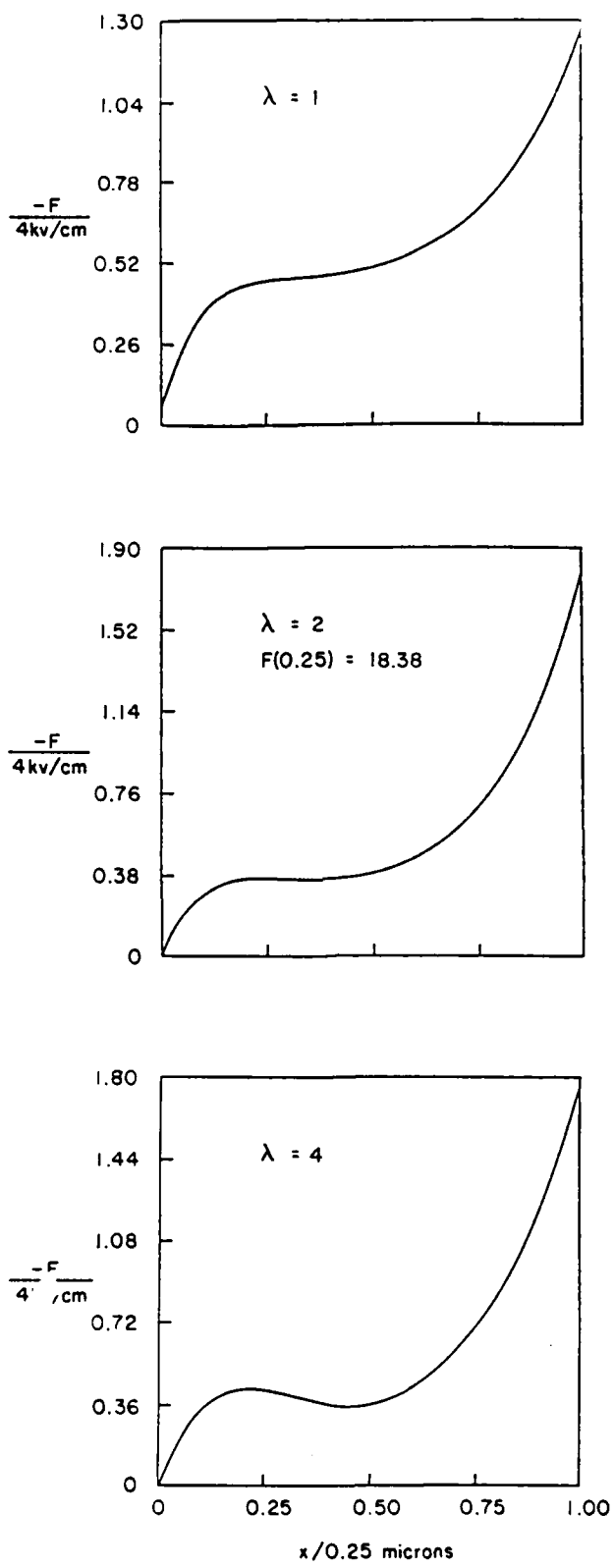


FIGURE 19. ELECTRIC FIELD DISTRIBUTION FOR THE STRUCTURES OF FIGURE 15.

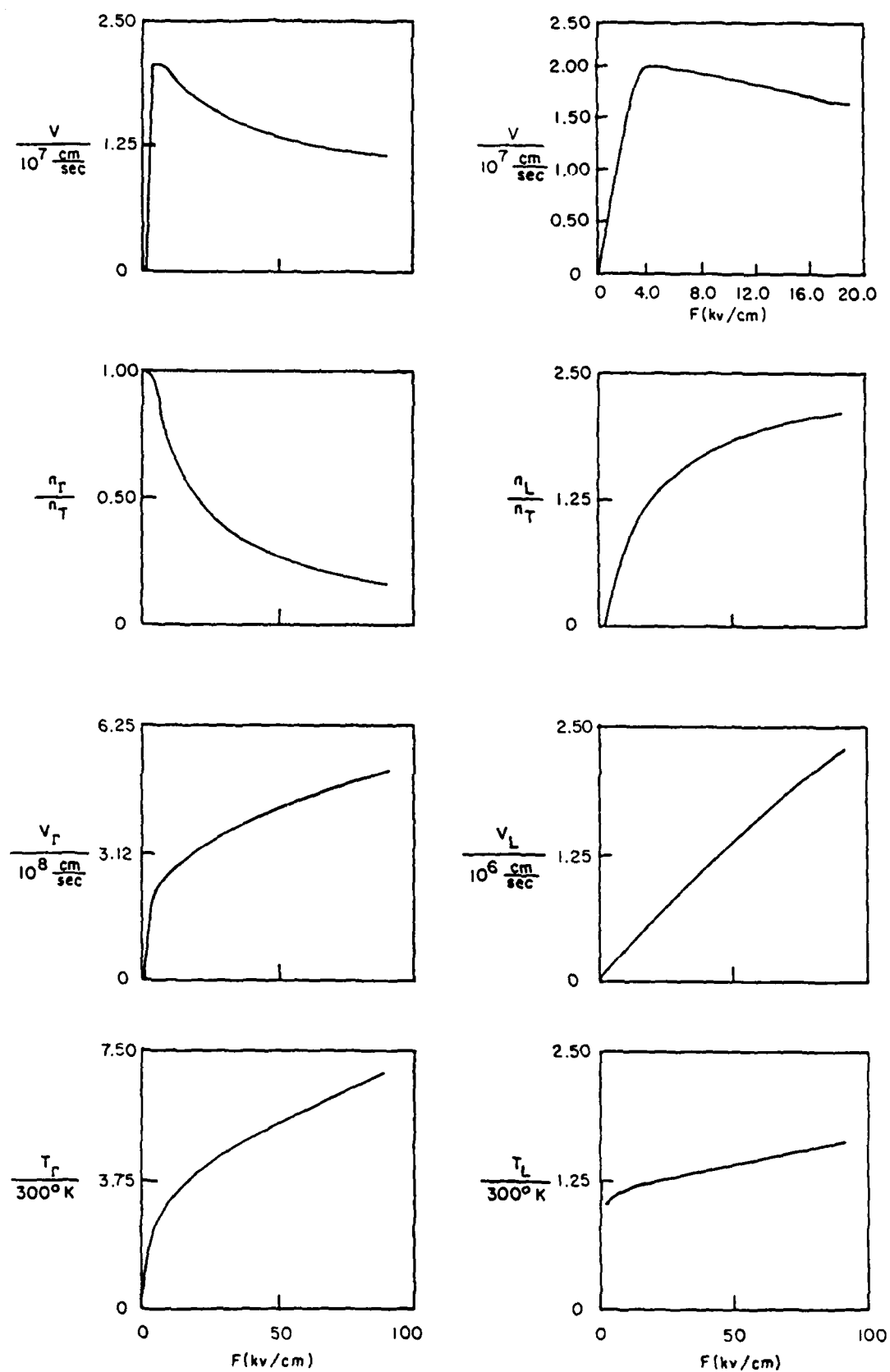


FIGURE 20. AS IN FIGURE 1, BUT WITH DCR INCREASED TO TWICE THE VALUE OF FIGURE 1.

920016 11 30 84-6

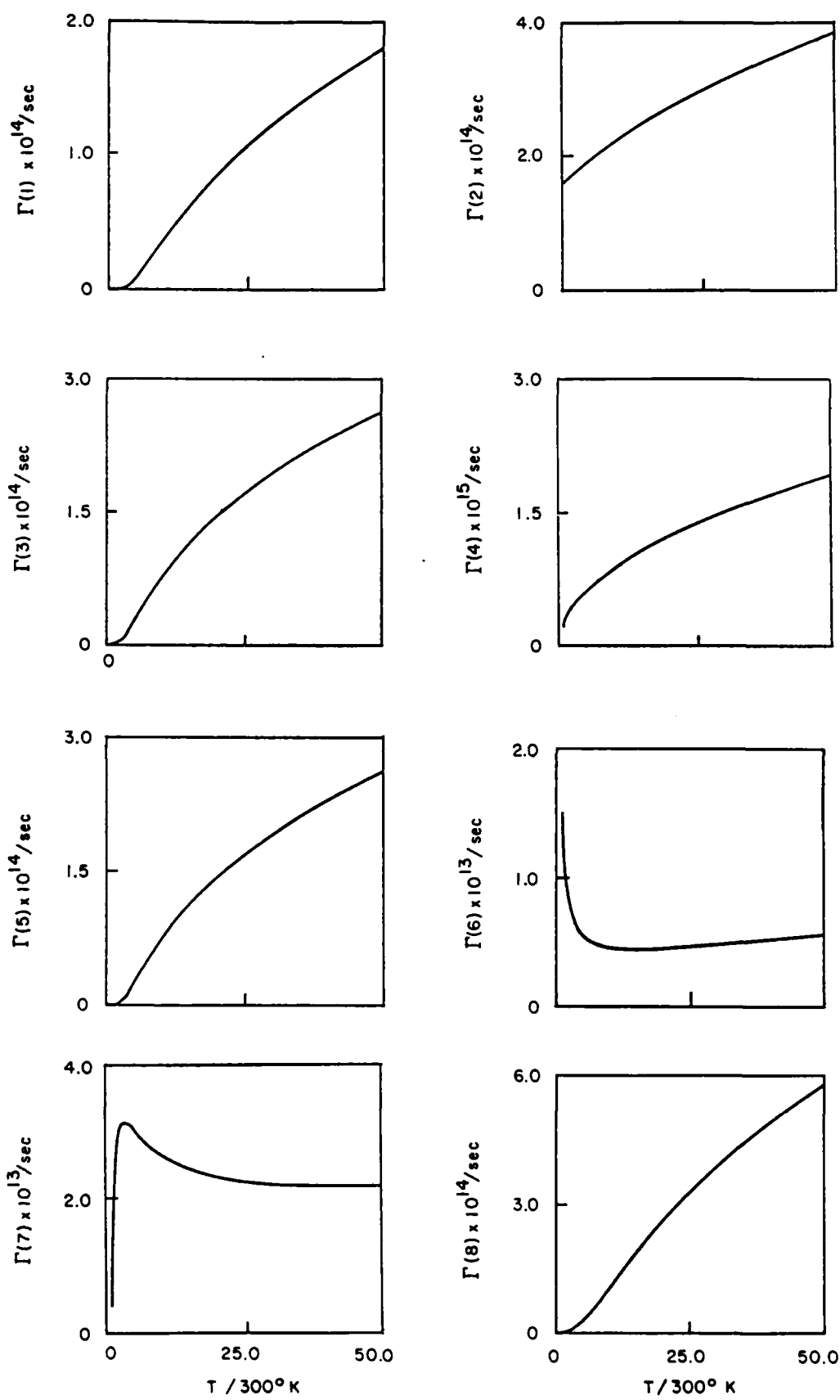


FIGURE 21. THE SCATTERING RATES ASSOCIATED WITH FIGURE 20.

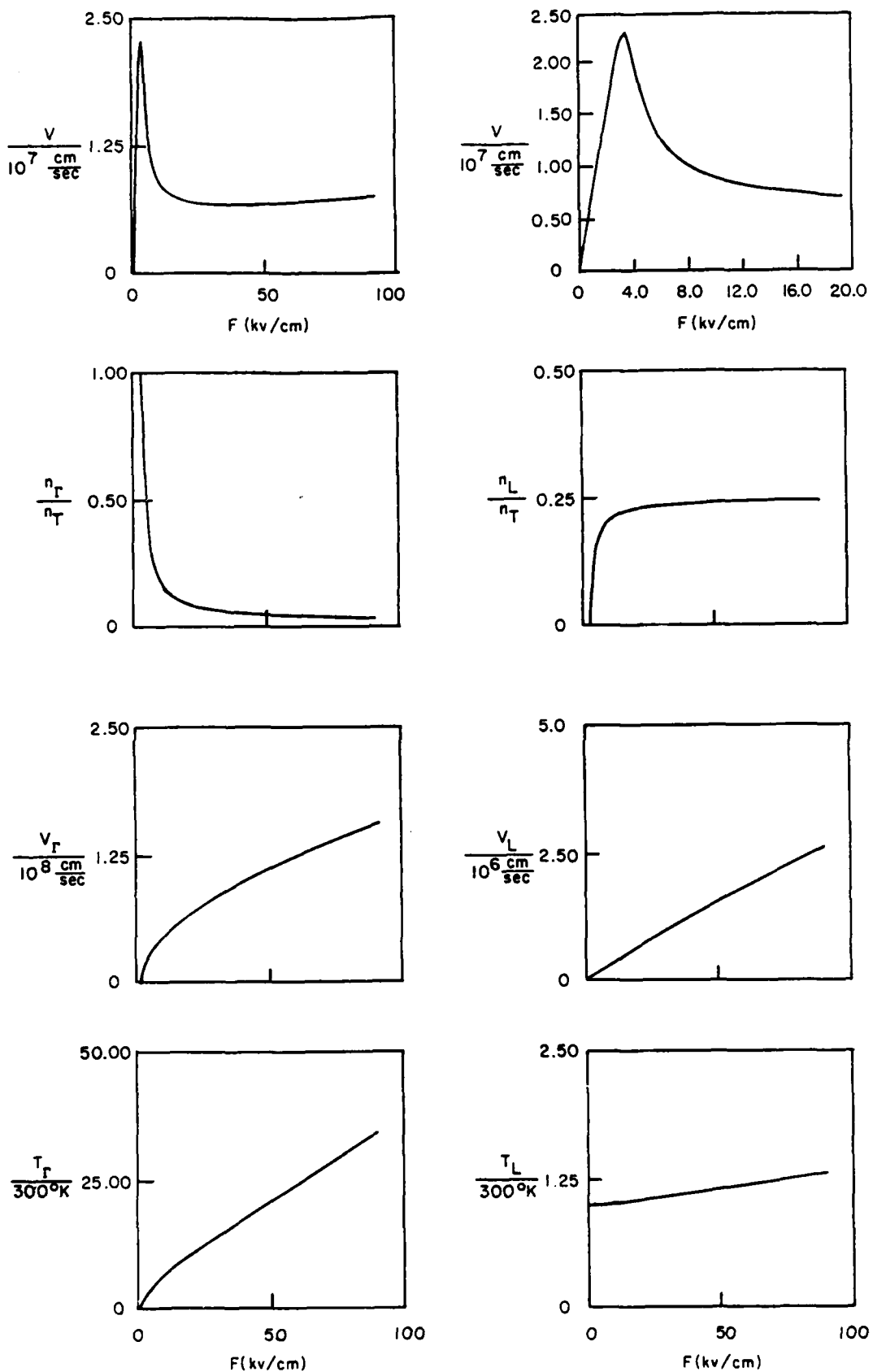


FIGURE 22. AS IN FIGURE 1 BUT WITH DCR DECREASED TO ONE HALF THE VALUE OF TABLE I.

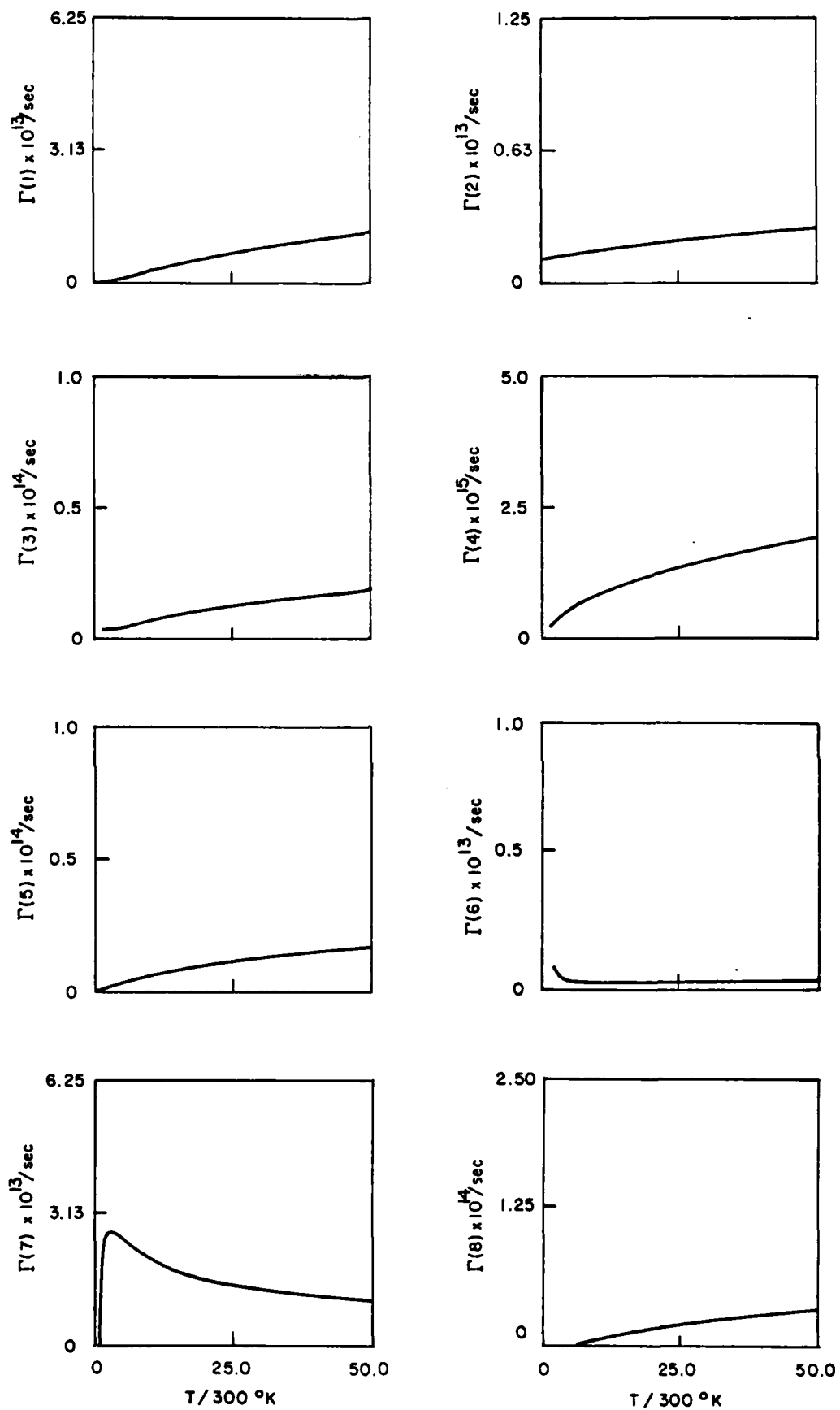


FIGURE 23. THE SCATTERING RATES ASSOCIATED WITH FIGURE 22.

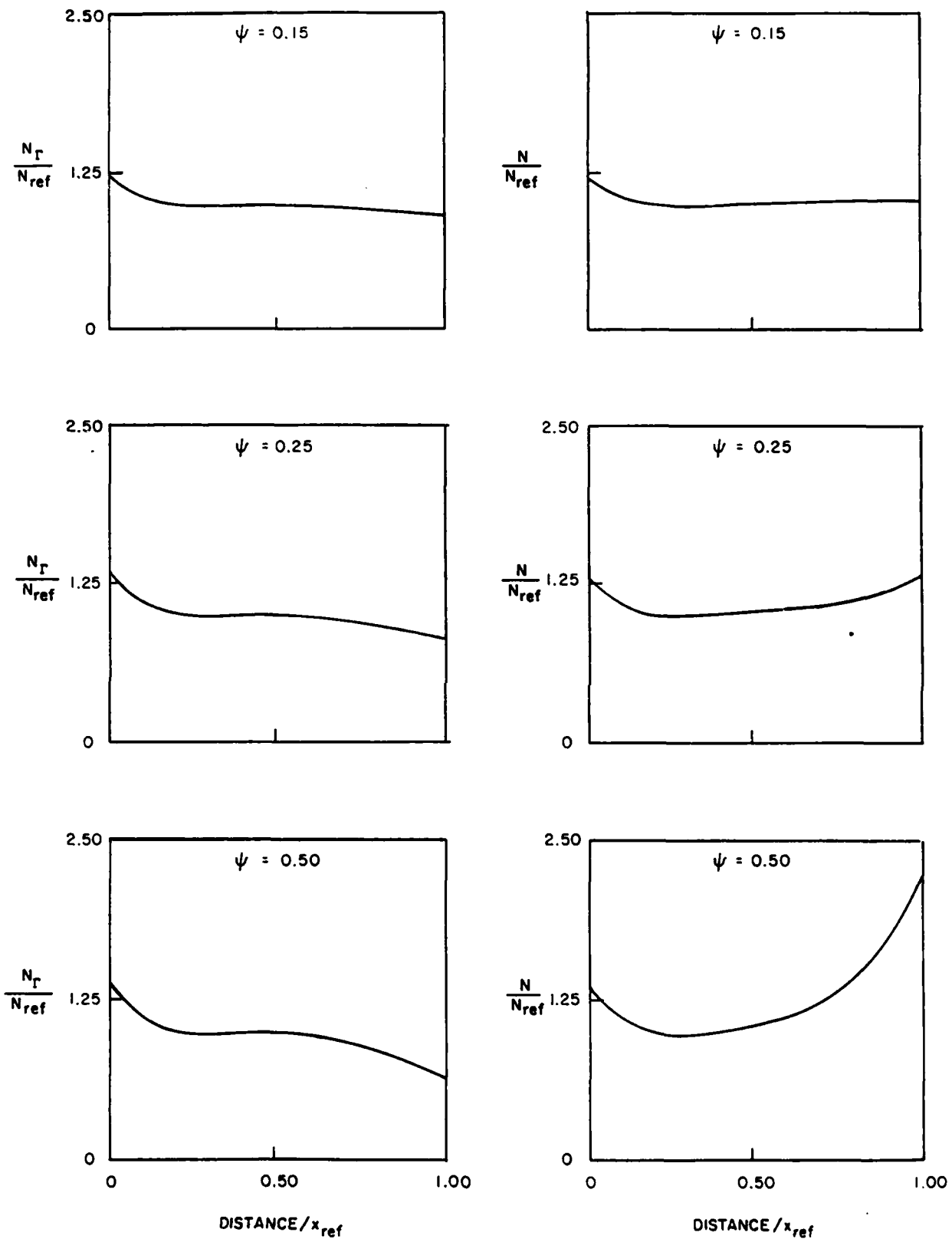


FIGURE 24. TOTAL AND  $\Gamma$ -VALLEY CARRIER DENSITY OBTAINED FOR THE INCREASED COUPLING COEFFICIENTS AND SCATTERING RATES OF FIGURE 20, AND  $N_{ref} = 8 \times 10^{16}/\text{cm}^3$ ,  $x_{ref} = 0.25$  MICRONS AND INDICATED VALUES OF POTENTIAL.

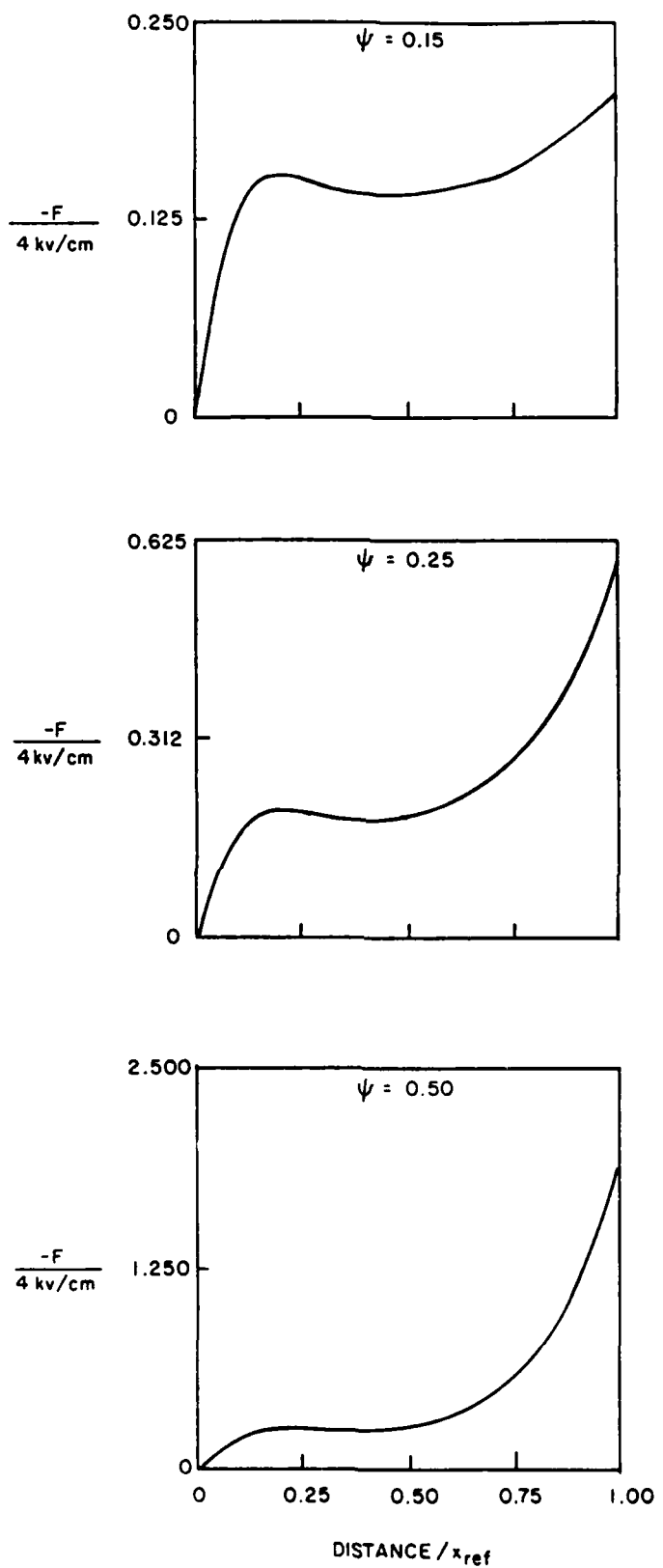


FIGURE 25. AS IN FIGURE 24, BUT FOR THE ELECTRIC FIELD VERSUS DISTANCE PROFILE.

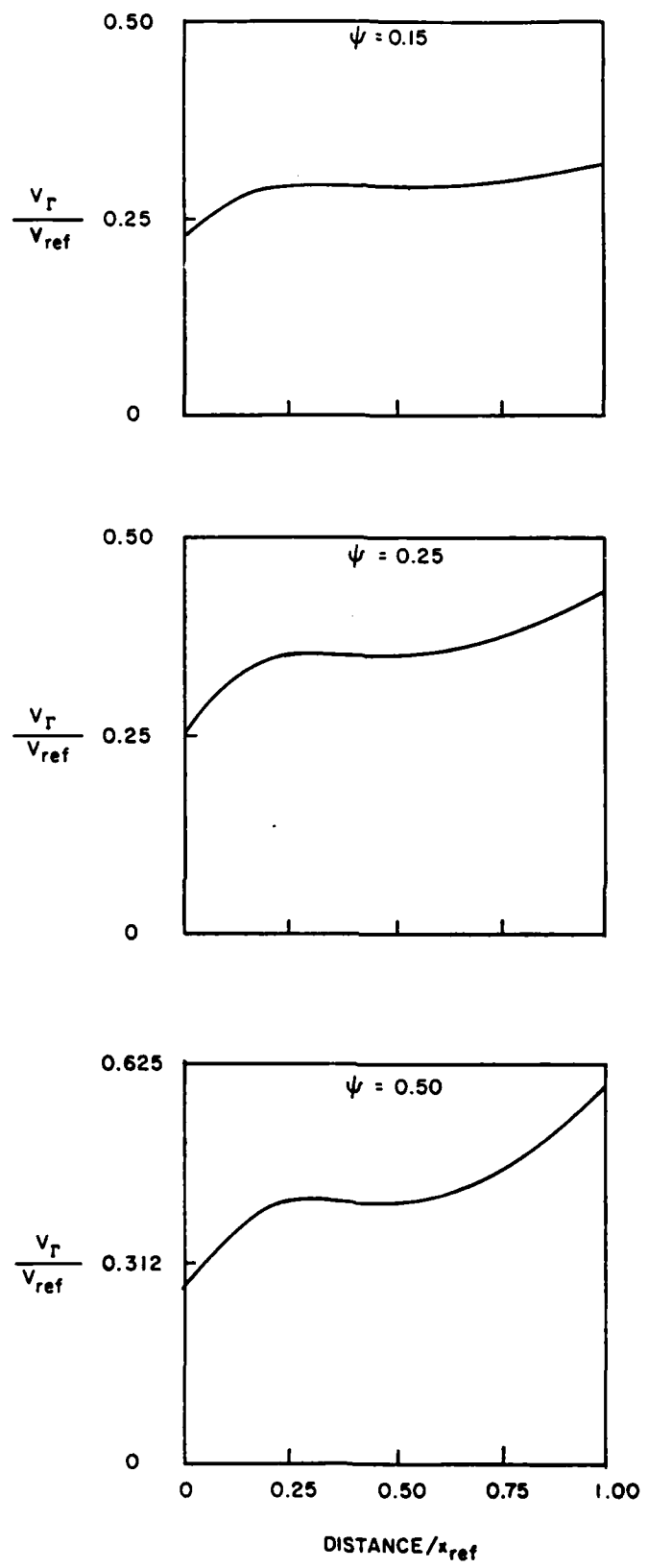


FIGURE 26. AS IN FIGURE 24, BUT FOR THE T-VALLEY CARRIER VELOCITY.

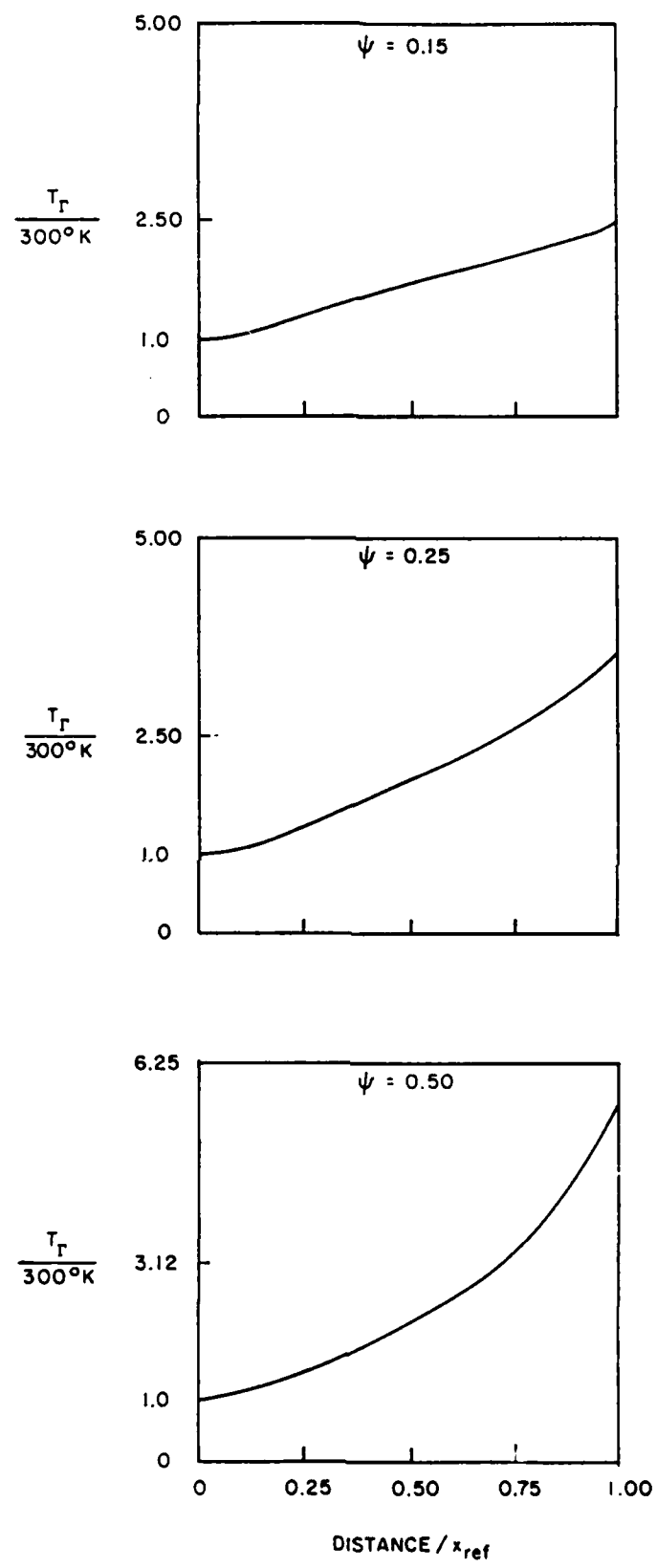


FIGURE 27. AS IN FIGURE 24, BUT FOR THE  $\Gamma$ -VALLEY ELECTRON TEMPERATURE.

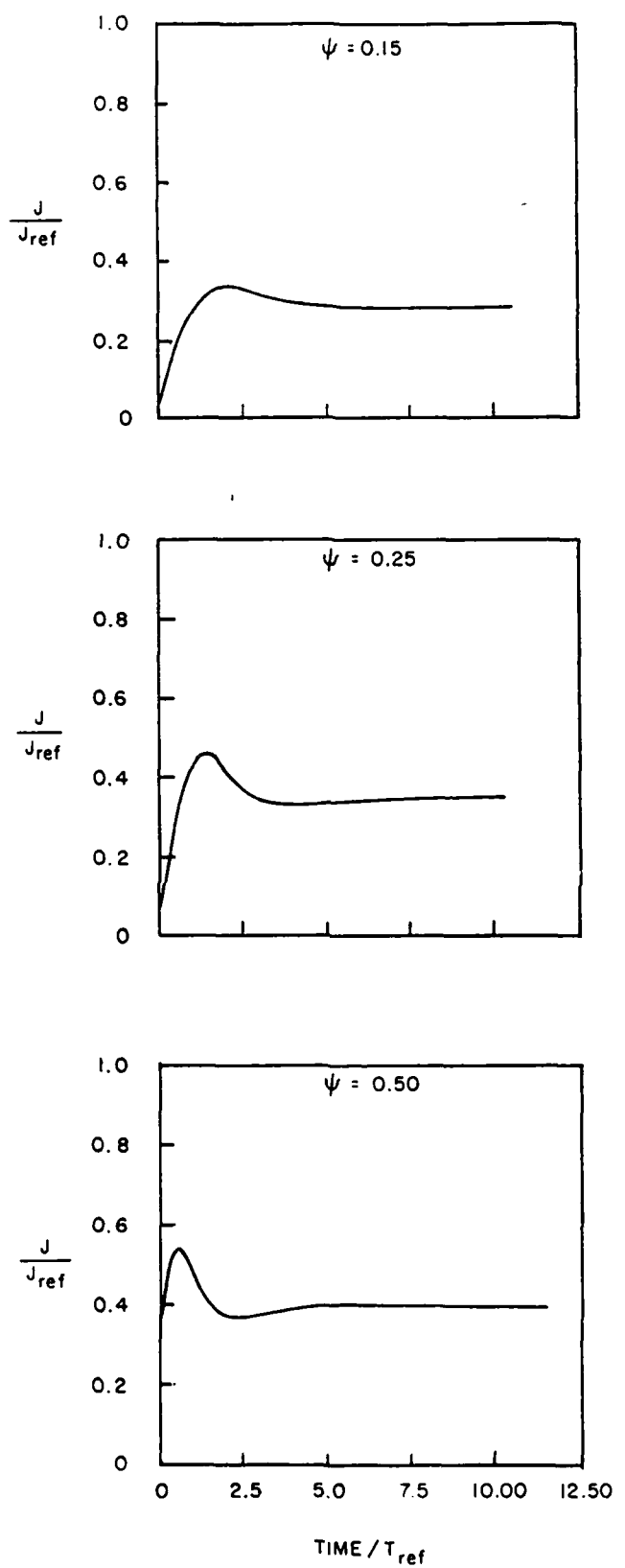


FIGURE 28. MAGNITUDE OF THE TRANSIENT CURRENT RESPONCE FOR THE STRUCTURE OF FIGURE 24, SUBJECT TO A SUDDEN CHANGE IN BIAS. ( $T_{\text{ref}} = 0.25 \text{ ps}$ ).

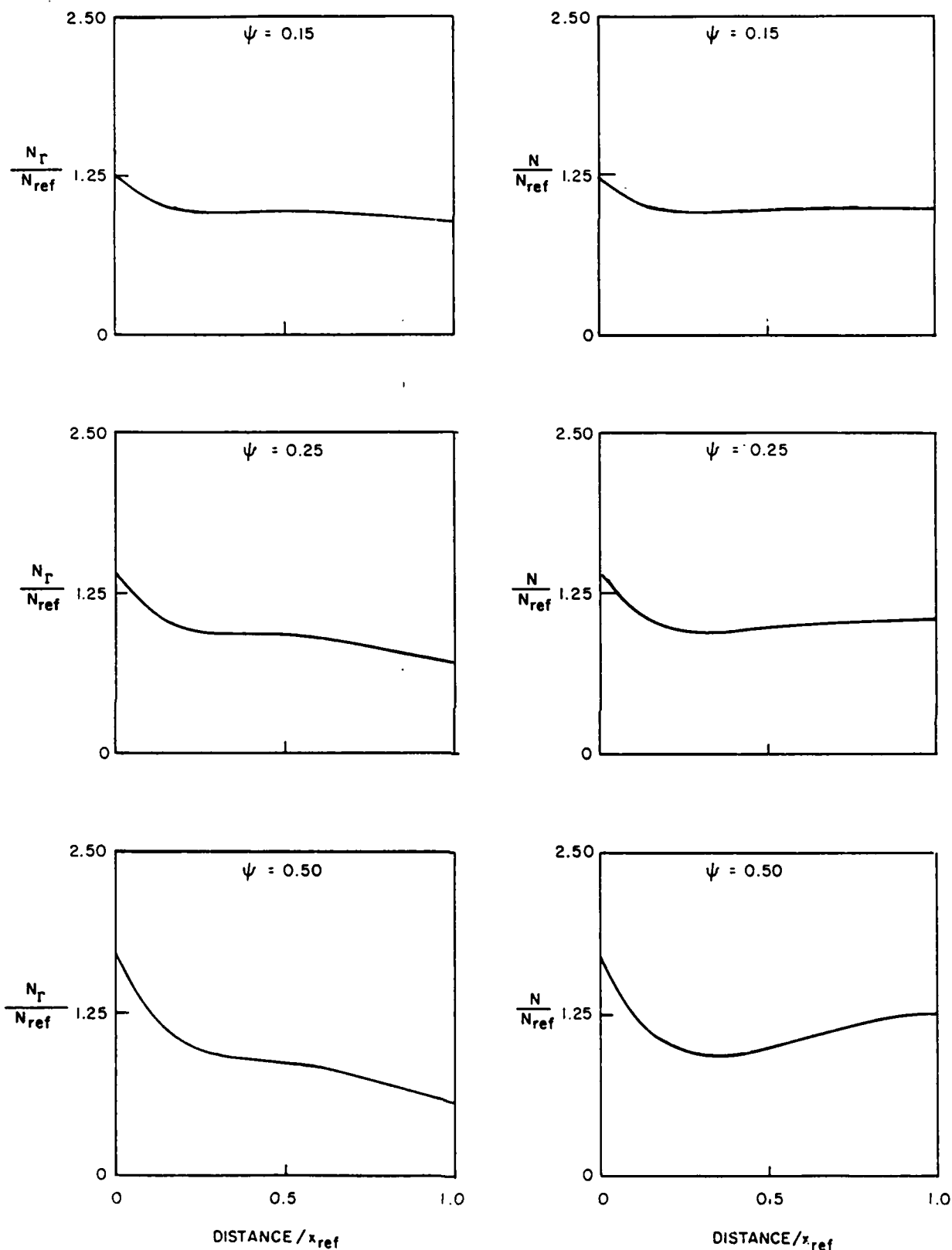


FIGURE 29. TOTAL AND  $\Gamma$ -VALLEY CARRIER DENSITY OBTAINED FOR THE DECREASE COUPLING COEFFICIENTS AND SCATTERING RATES OF FIGURE 22, AND  $N_{ref} = 8 \times 10^{16}/\text{cm}^3$ ,  $x_{ref} = 0.25$  MICRONS AND INDICATED VALUES OF POTENTIAL.

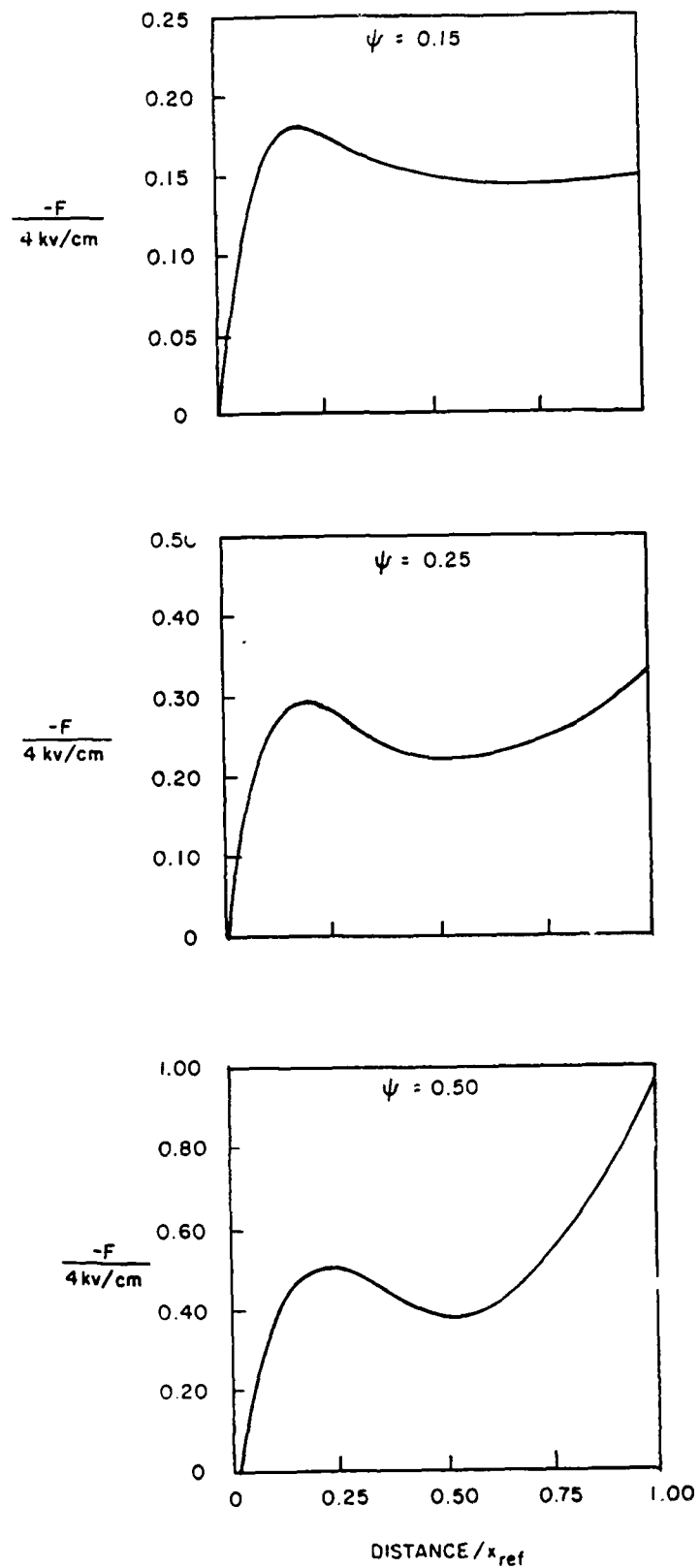
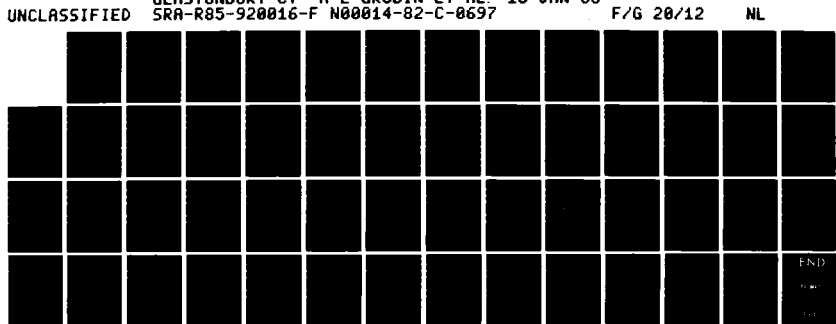


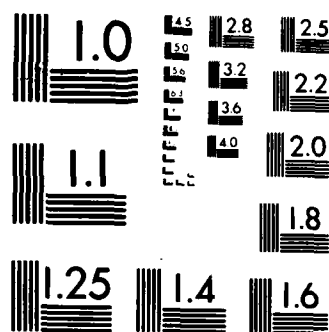
FIGURE 30. AS IN FIGURE 29, BUT FOR THE ELECTRIC FIELD VERSUS DISTANCE PROFILE.

AD-A150 020 SEMICONDUCTOR MATERIALS FOR HIGH FREQUENCY SOLID STATE 4/4  
SOURCES(U) SCIENTIFIC RESEARCH ASSOCIATES INC  
GLASTONBURY CT H L GRUBIN ET AL 18 JAN 85

UNCLASSIFIED SRA-R85-920016-F N00014-82-C-0697 F/G 28/12 NL



END  
RECORDED  
FILED



MICROCOPY RESOLUTION TEST CHART  
NATIONAL BUREAU OF STANDARDS-1963-A

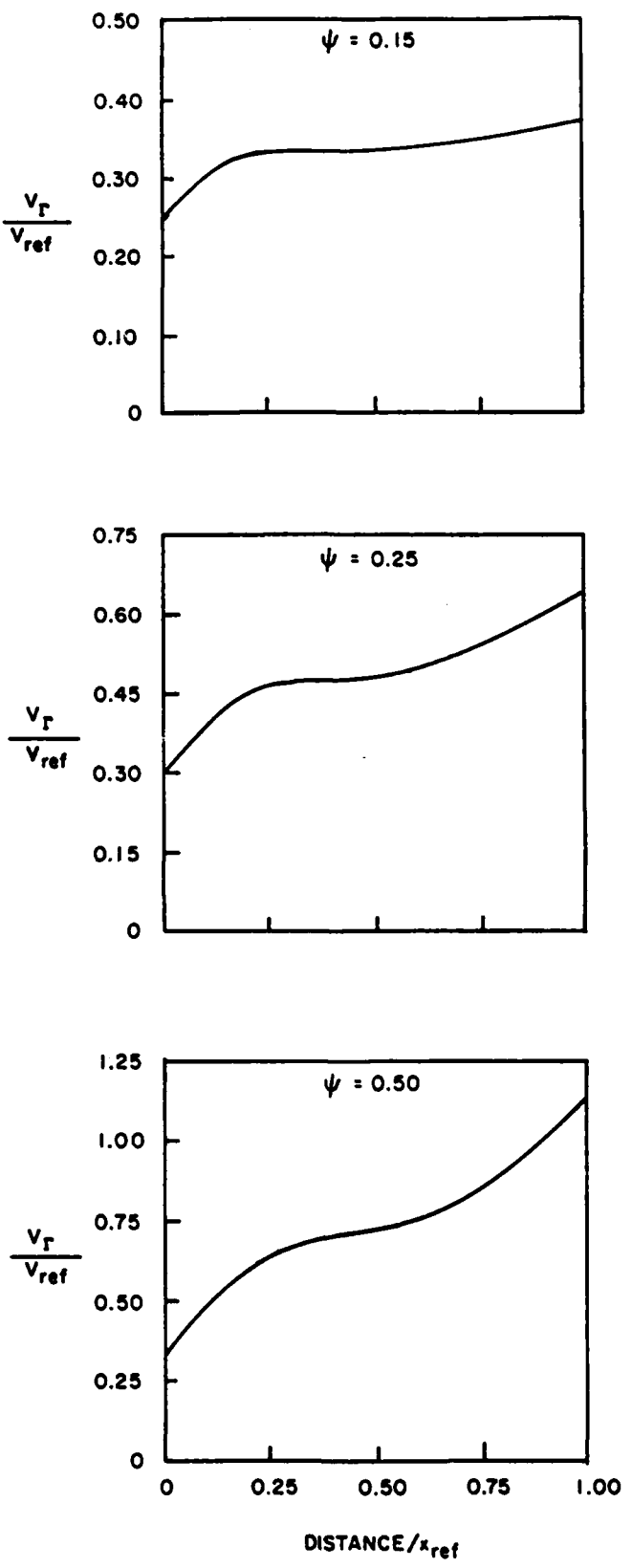


FIGURE 31. AS IN FIGURE 29, BUT FOR THE  $\Gamma$ -VALLEY CARRIER VELOCITY.

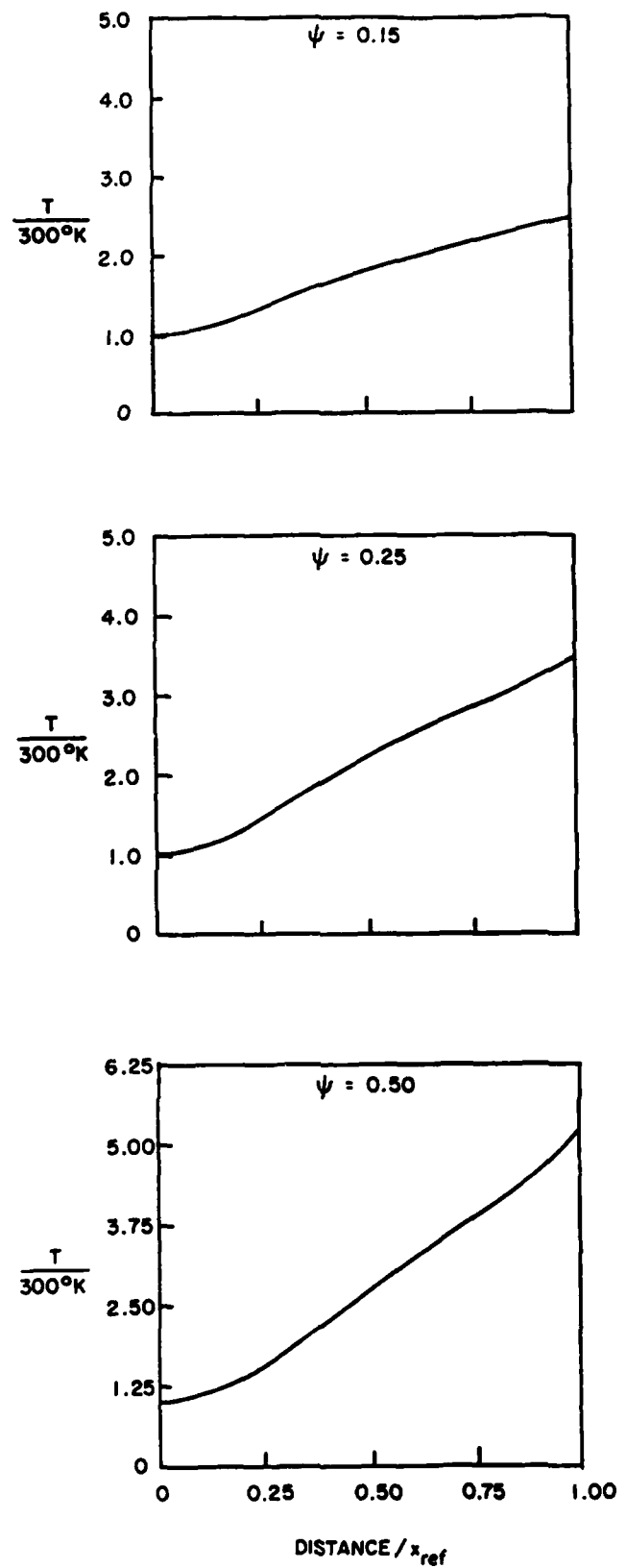


FIGURE 32. AS IN FIGURE 29, BUT FOR THE  $\Gamma$ -VALLEY CARRIER TEMPERATURE.

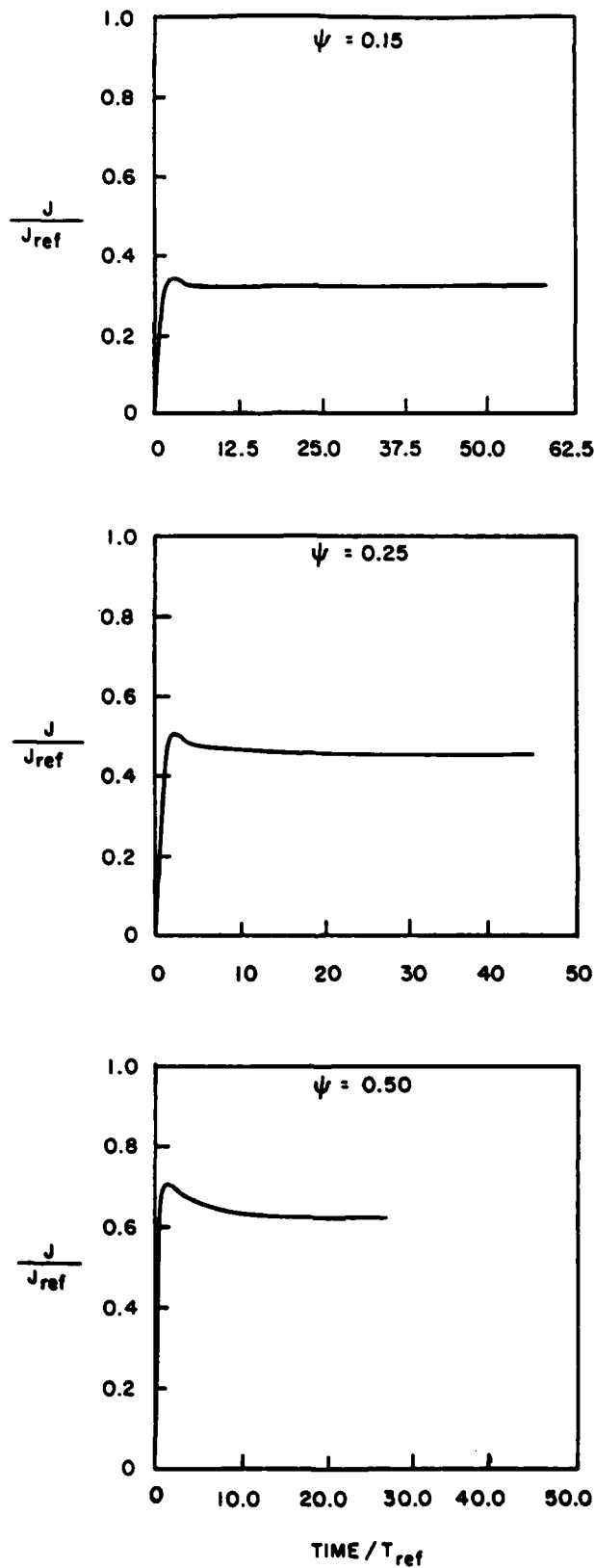


FIGURE 33. AS IN FIGURE 28, BUT FOR THE PARAMETERS OF FIGURE 29.  
 $(T_{\text{ref}} = 0.25 \text{ ps}).$

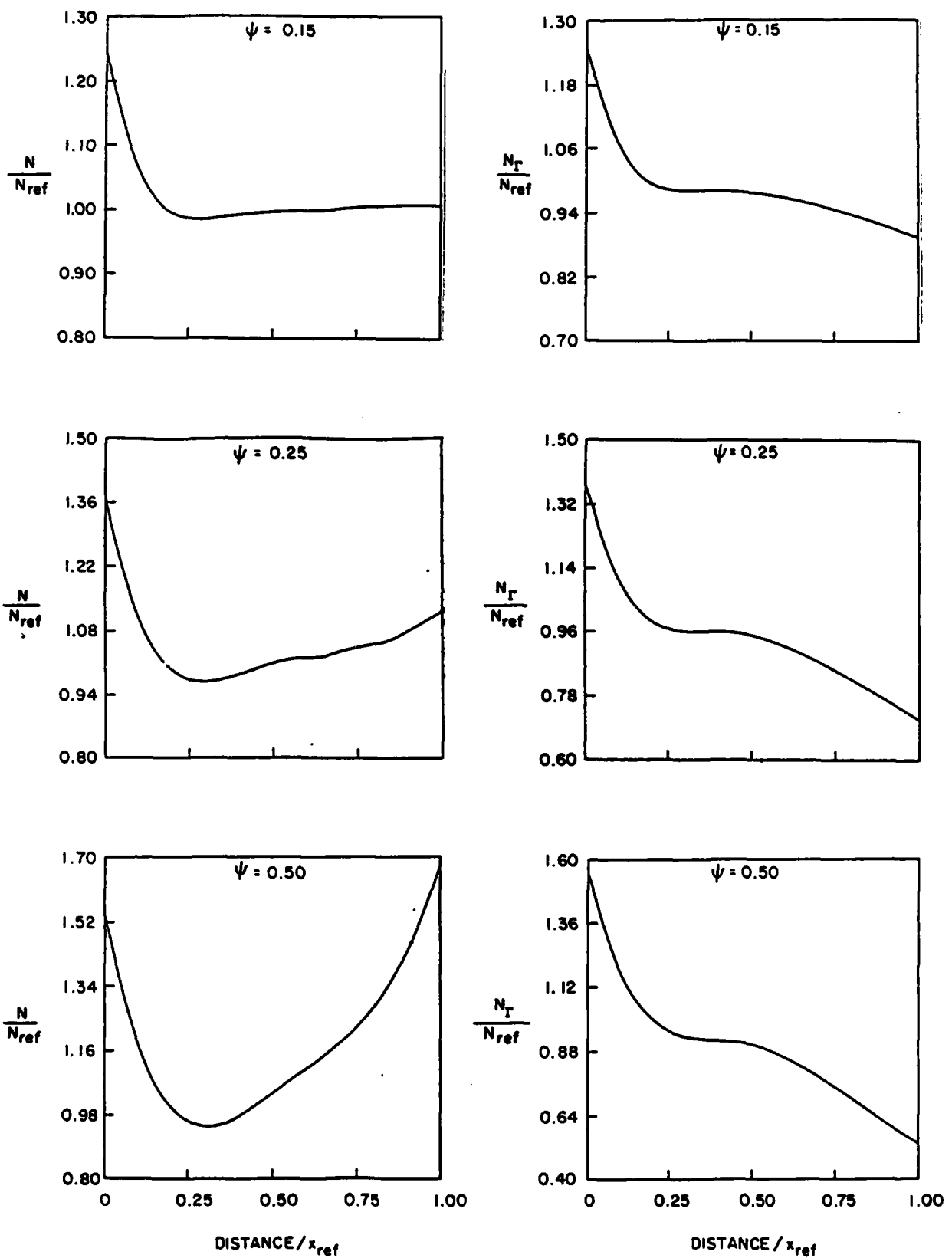


FIGURE 34. AS IN FIGURE 24, BUT FOR UNSCALED GALLIUM ARSENIDE.

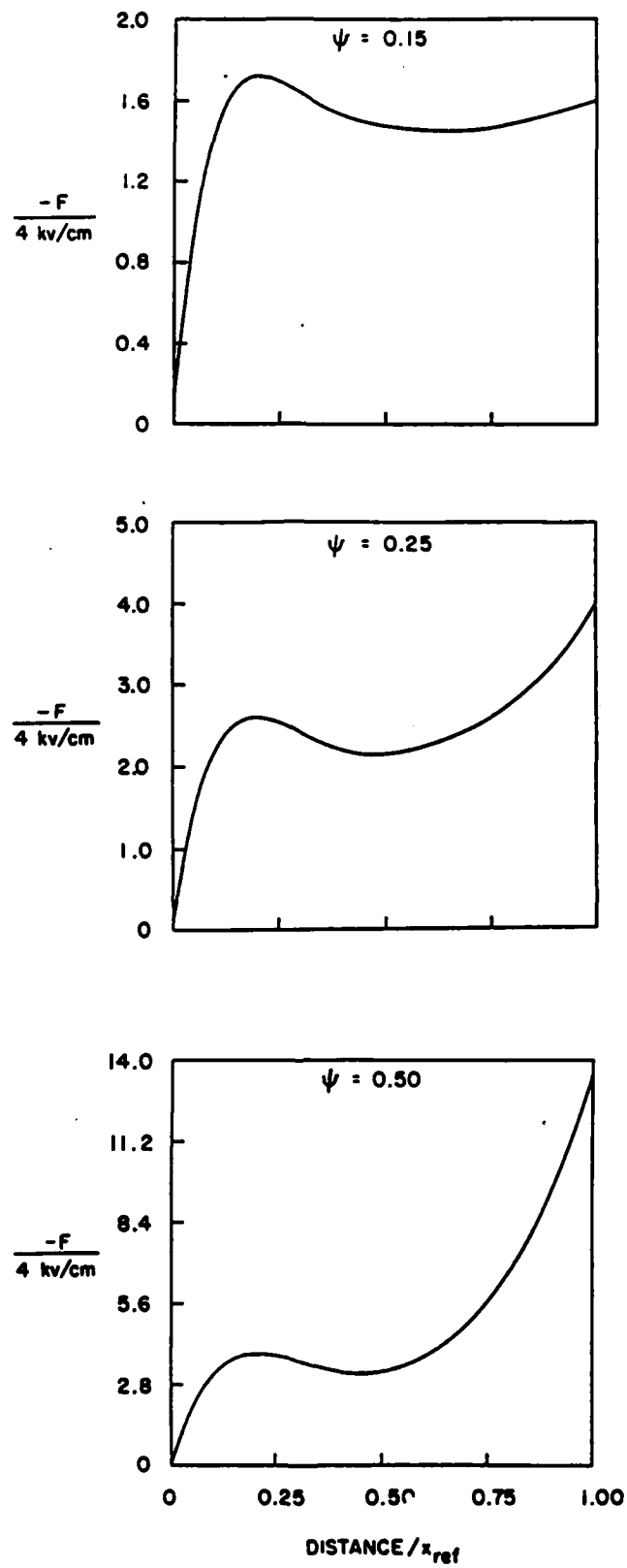


FIGURE 35. AS IN FIGURE 34, BUT FOR THE ELECTRIC FIELD DISTANCE VERSUS PROFILE.

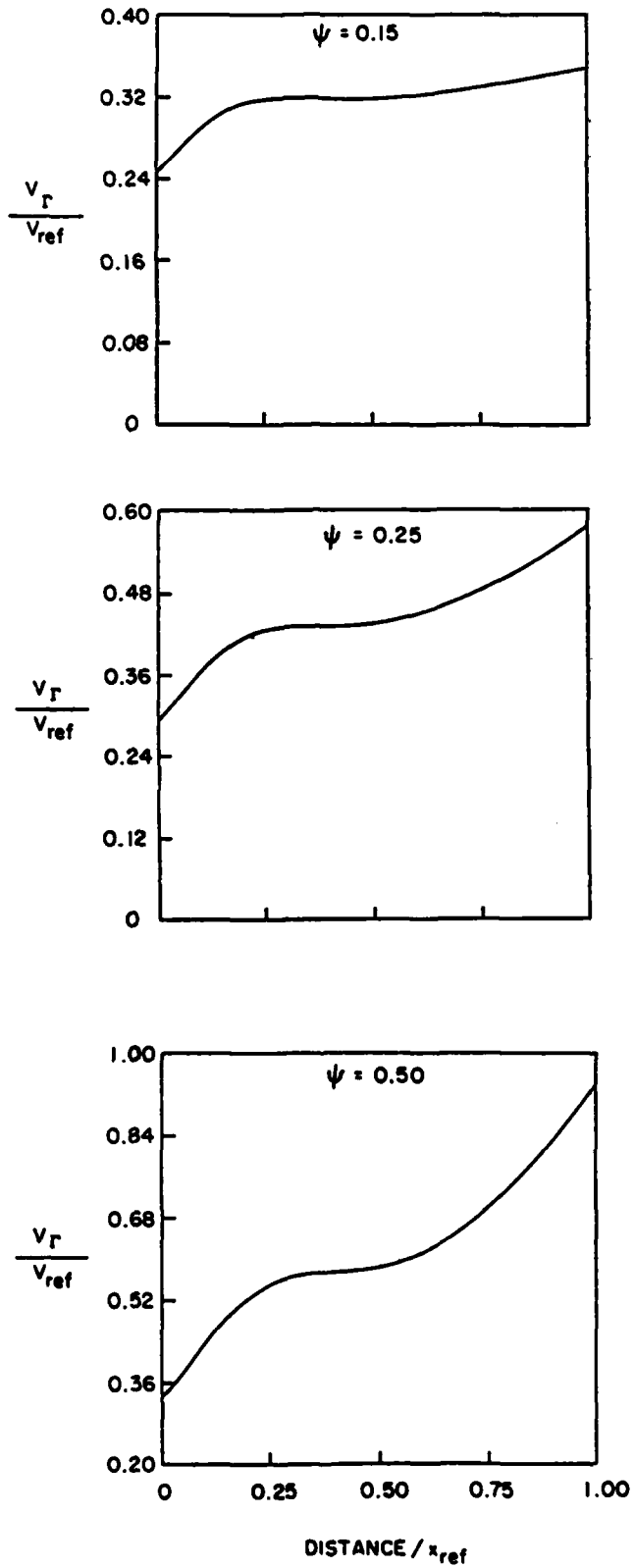


FIGURE 36. AS IN FIGURE 34, BUT FOR THE  $\Gamma$ -VALLEY CARRIER VELOCITY.  
 $(v_{ref} = 1.0 \times 10^8 \text{ cm/sec})$ .

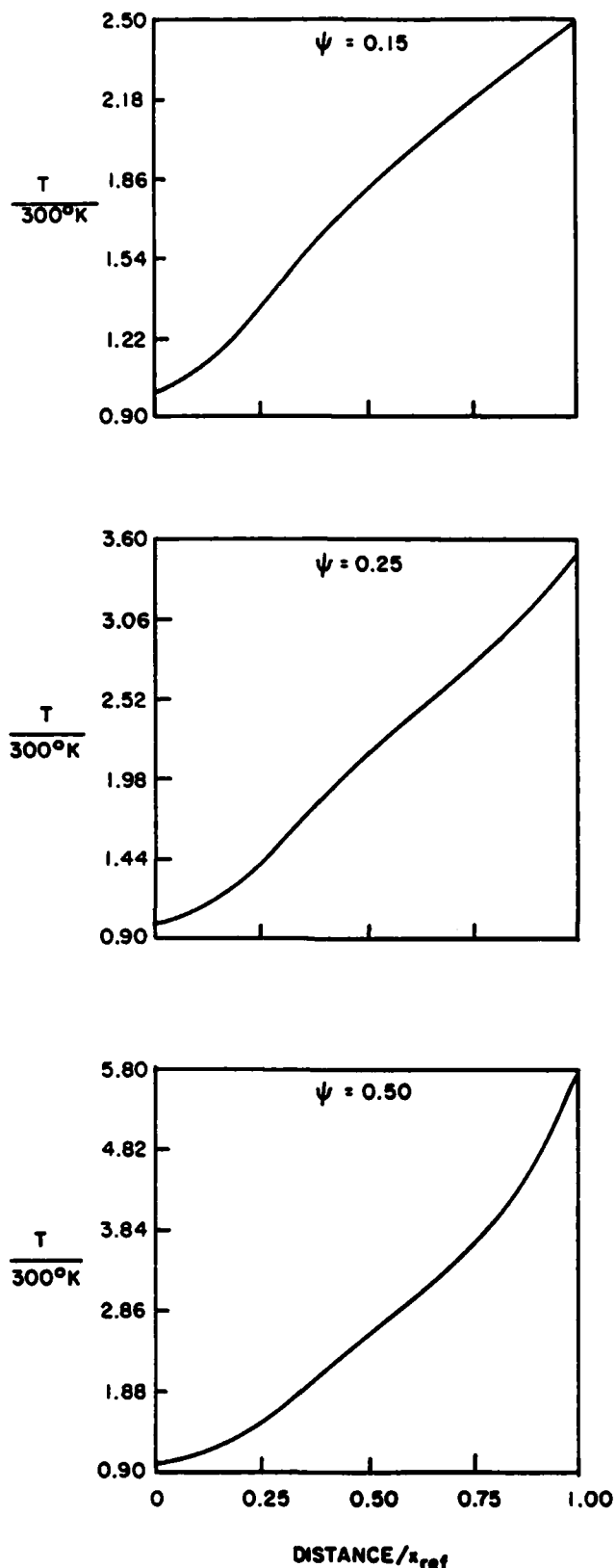


FIGURE 37. AS IN FIGURE 34, BUT FOR THE  $\Gamma$ -VALLEY ELECTRON TEMPERATURE.

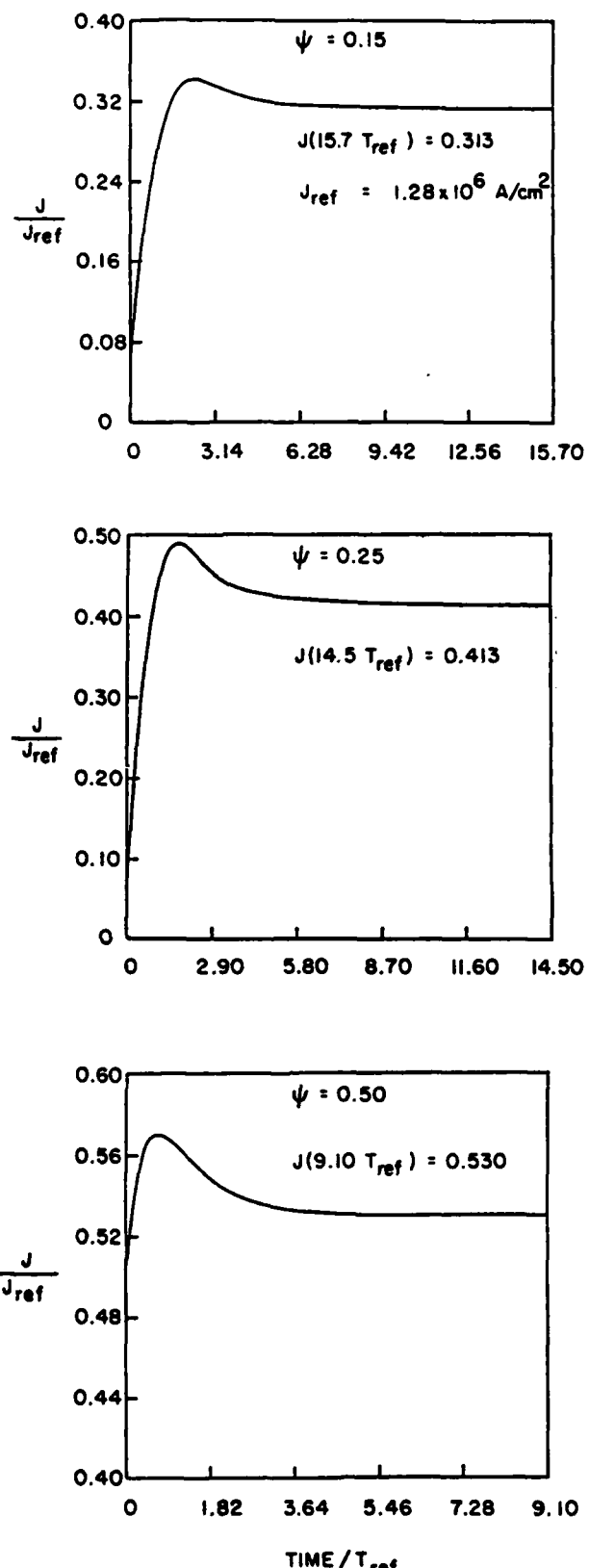


FIGURE 38. AS IN FIGURE 28, BUT FOR THE UNSCALED GALLIUM ARSENIDE.  
 $(T_{\text{ref}} = 0.25 \text{ ps})$ .

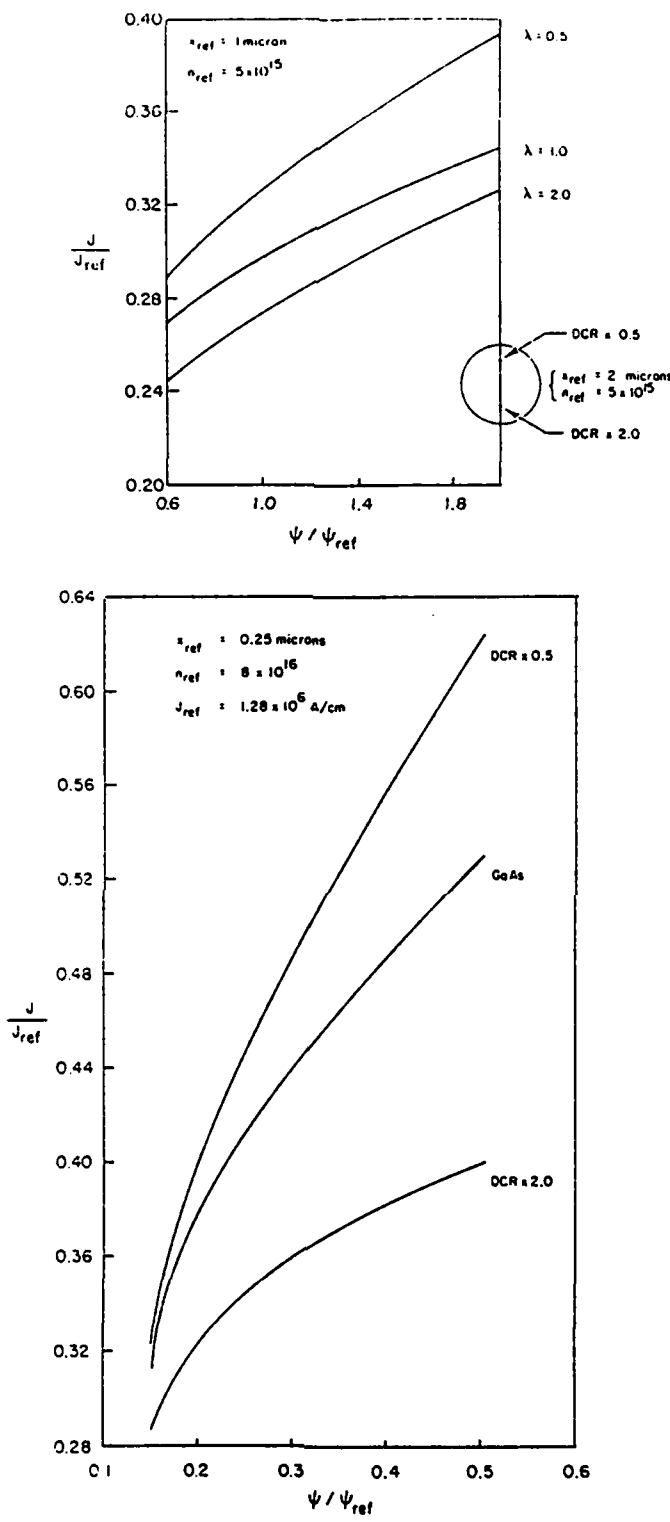


FIGURE 39. (a) CURRENT DENSITY VERSUS AVERAGE FIELD FOR A 0.25 MICRON LONG STRUCTURE WITH INJECTING CONTACTS AND A DONOR DENSITY OF  $8 \times 10^{16}$ . THE POTENTIAL VARIATIONS ARE AS INDICATED. CALCULATIONS ARE FOR DIFFERENT VALUES OF THE COUPLING COEFFICIENTS.  
 (b) AS IN (a) BUT FOR A 2.0 MICRONS LONG STRUCTURE.

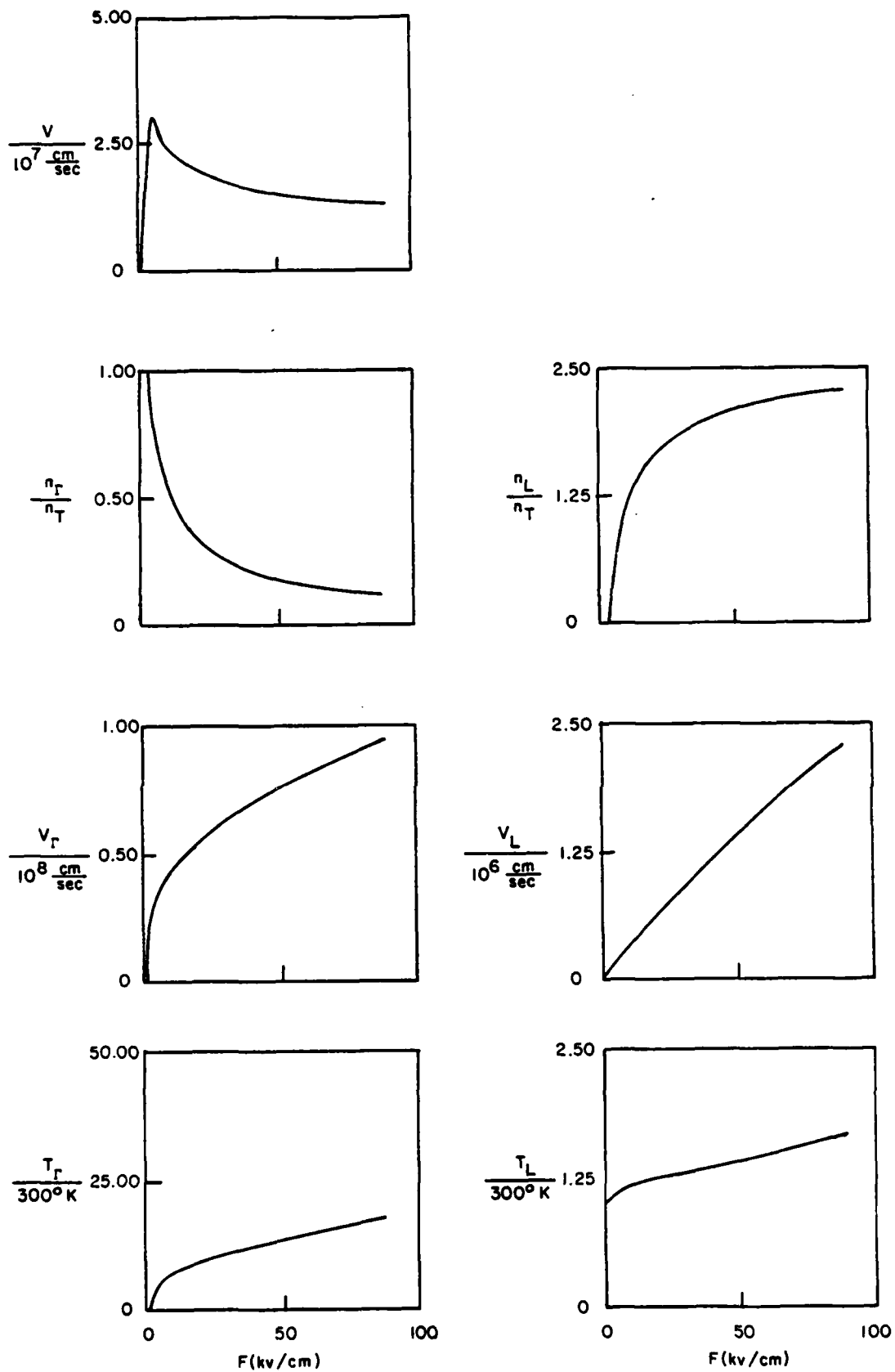


FIGURE 40. AS IN FIGURE 1, BUT FOR AN ENERGY SEPARATION INCREASED TO 0.66 ev.

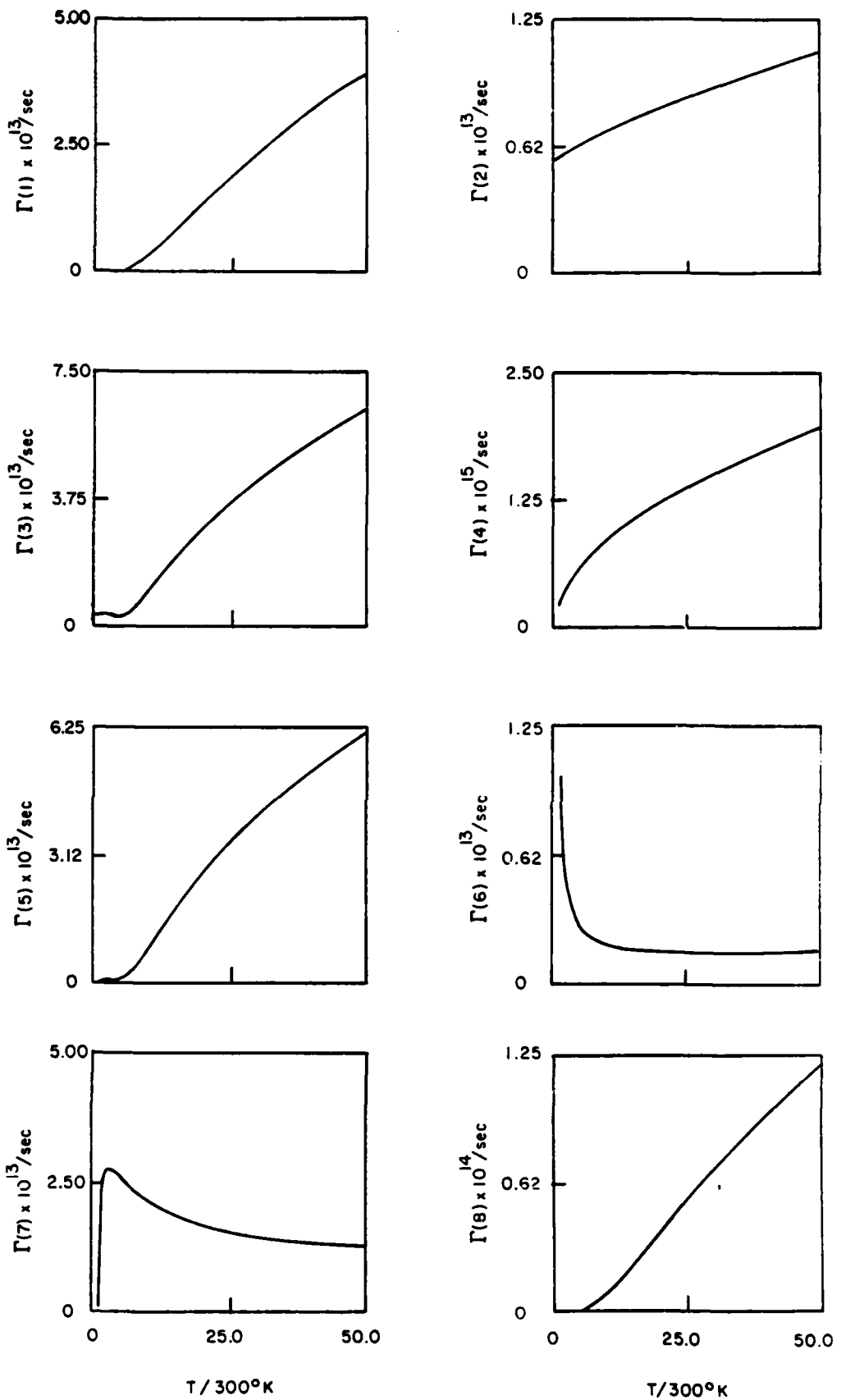


FIGURE 41. AS IN FIGURE 4, BUT FOR THE PARAMETERS ASSOCIATED WITH FIGURE 40.

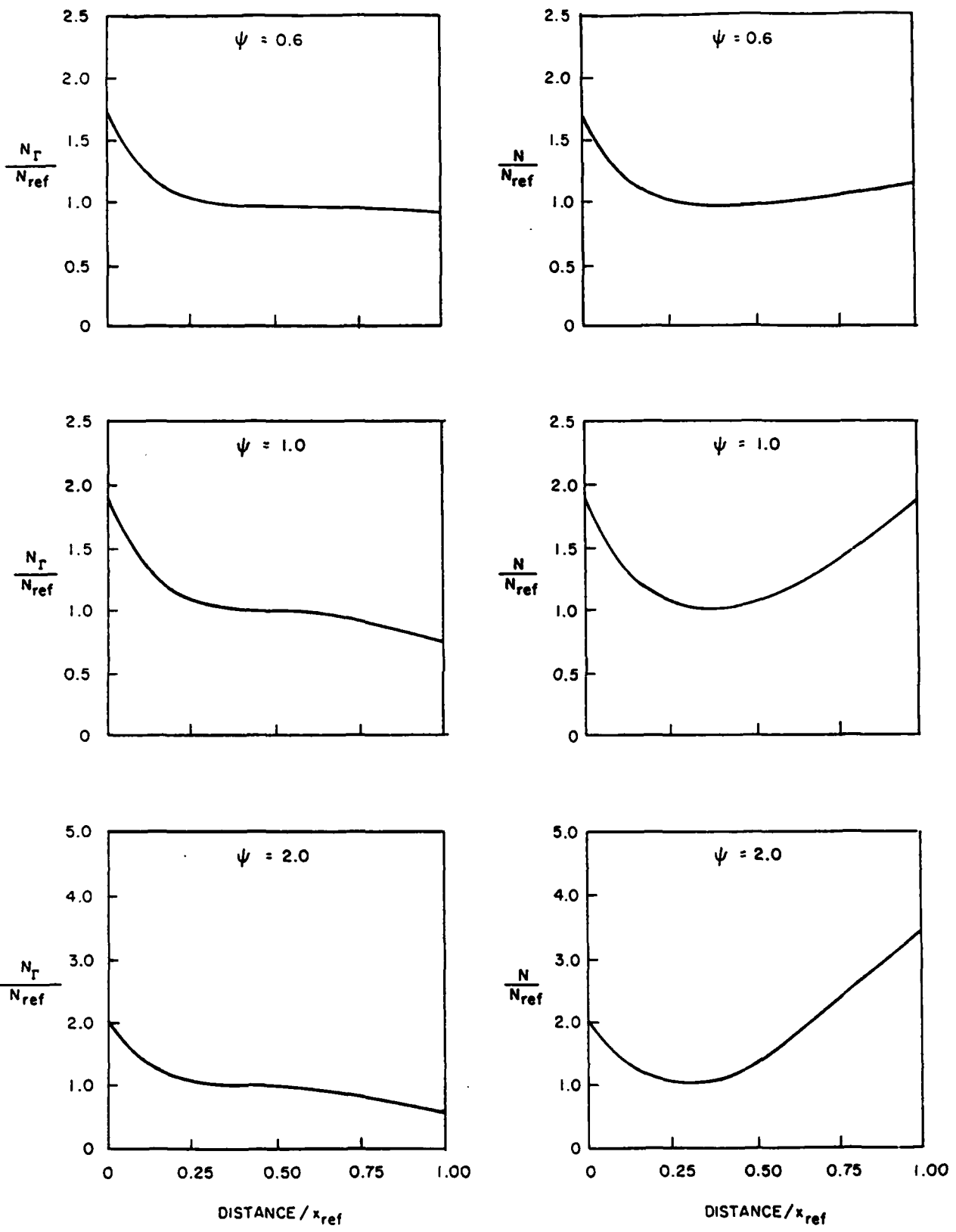


FIGURE 42. AS IN FIGURE 34, BUT FOR AN ENERGY SEPARATION INCREASED TO 0.66 ev.

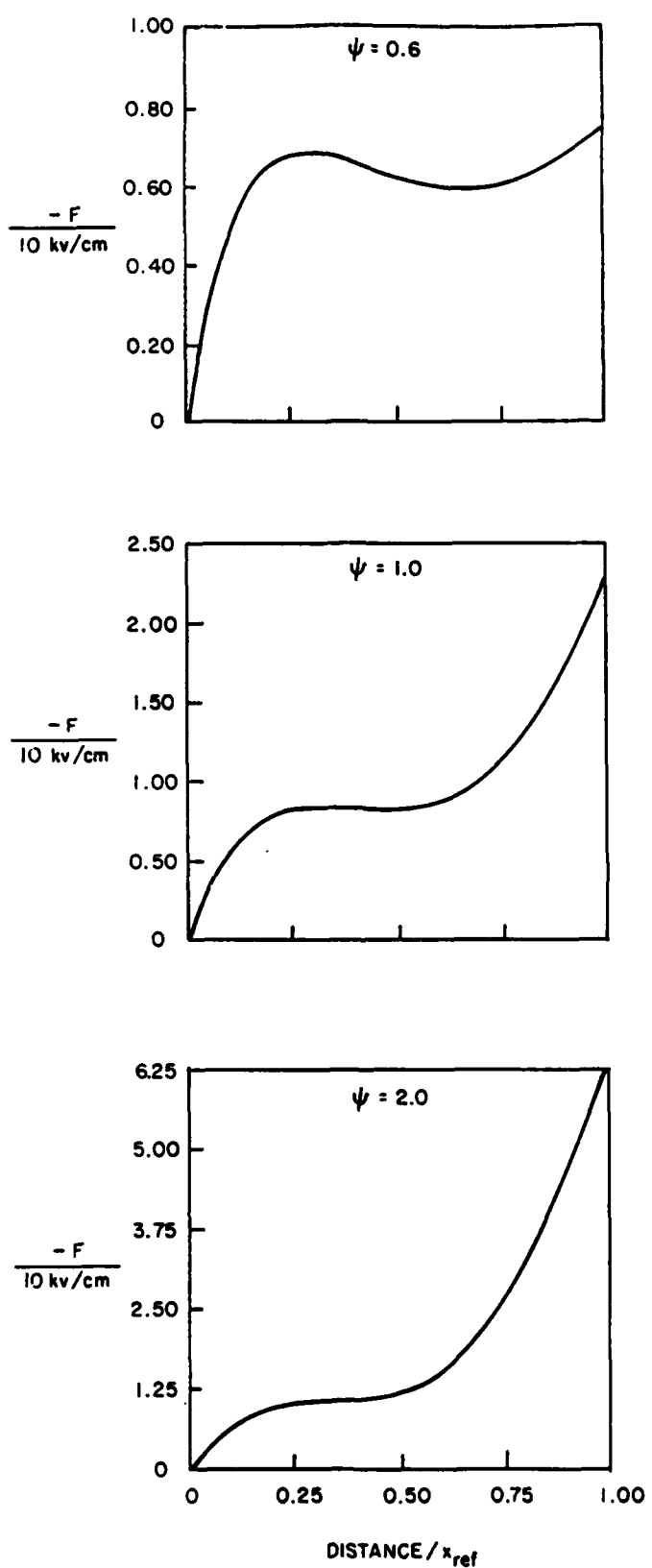


FIGURE 43. AS IN FIGURE 42, BUT FOR THE ELECTRIC FIELD VERSUS DISTANCE PROFILE.

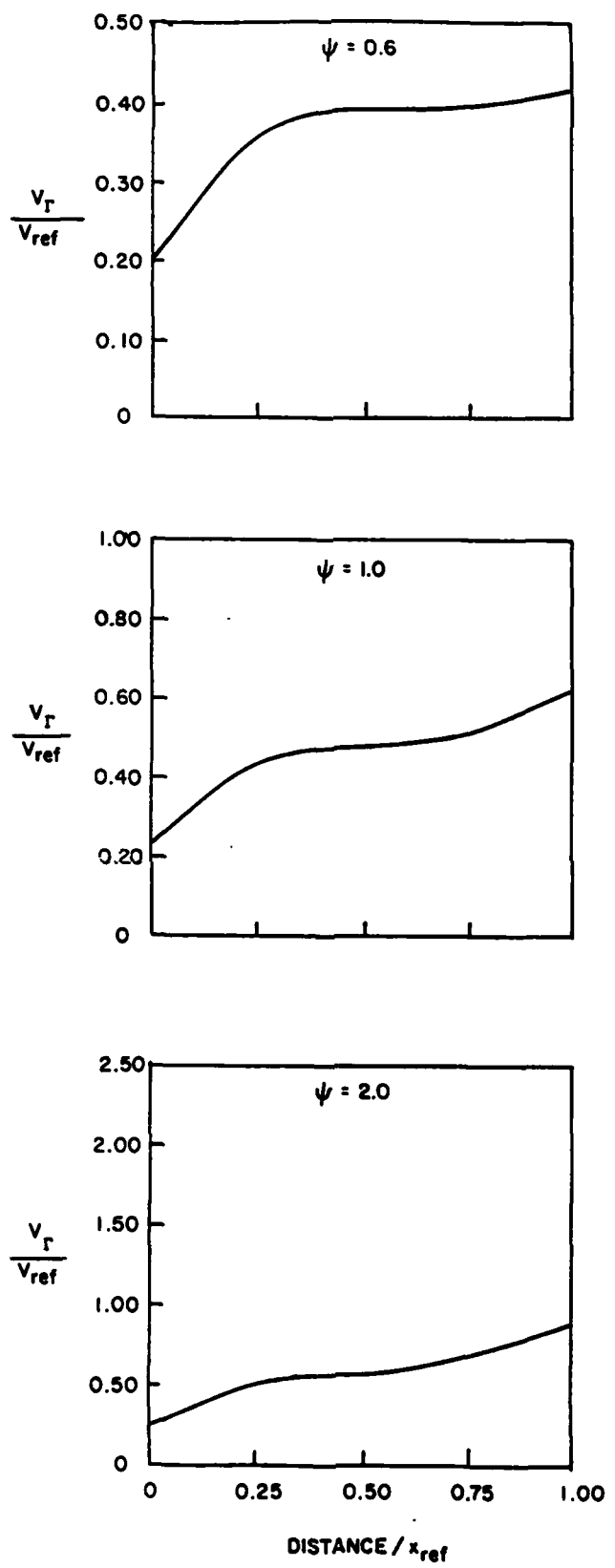


FIGURE 44. AS IN FIGURE 42, BUT FOR THE  $\Gamma$ -VALLEY CARRIER VELOCITY.

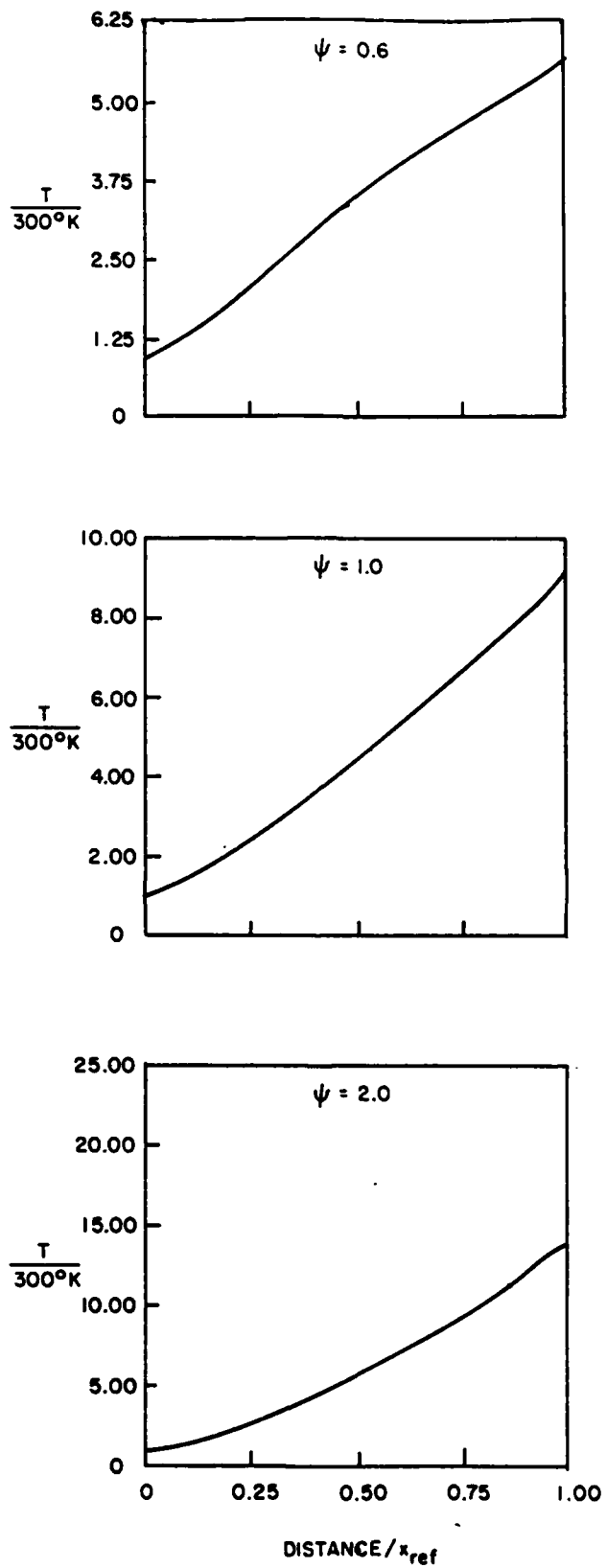


FIGURE 45. AS IN FIGURE 42, BUT FOR THE  $\Gamma$ -VALLEY ELECTRON TEMPERATURE.

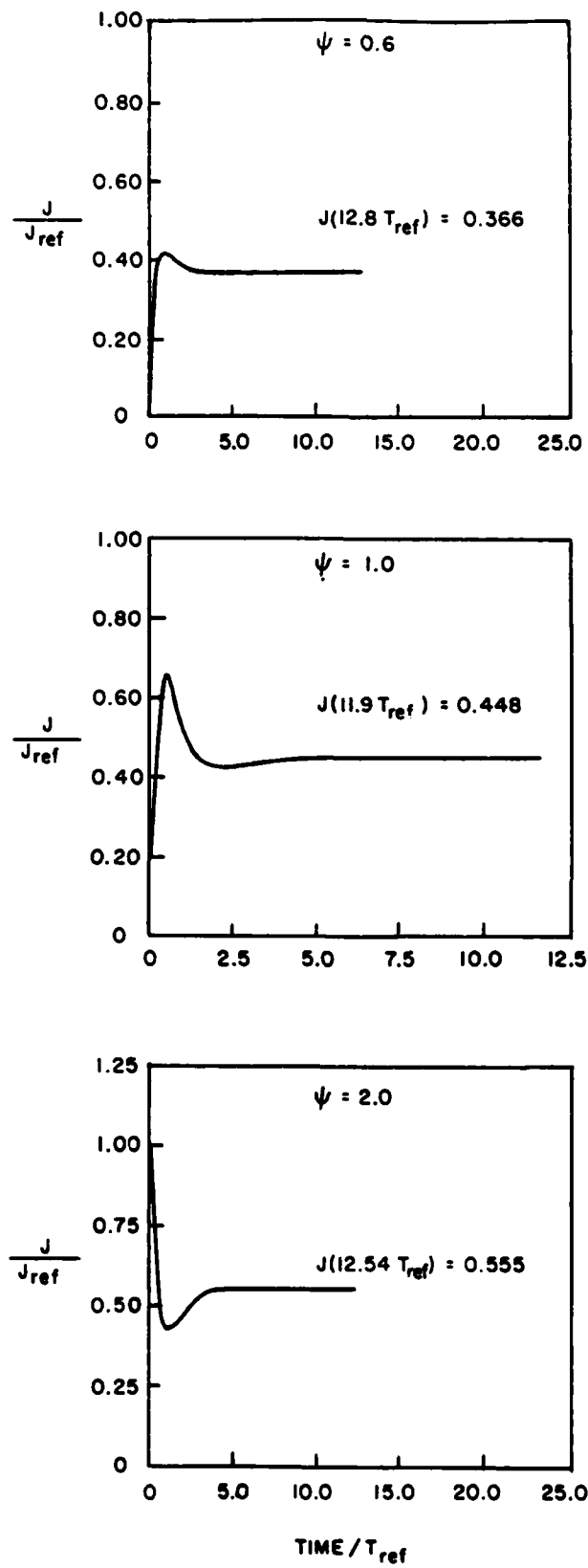


FIGURE 46. AS IN FIGURE 38, BUT FOR AN ENERGY SEPARATION INCREASED TO 0.66 ev.

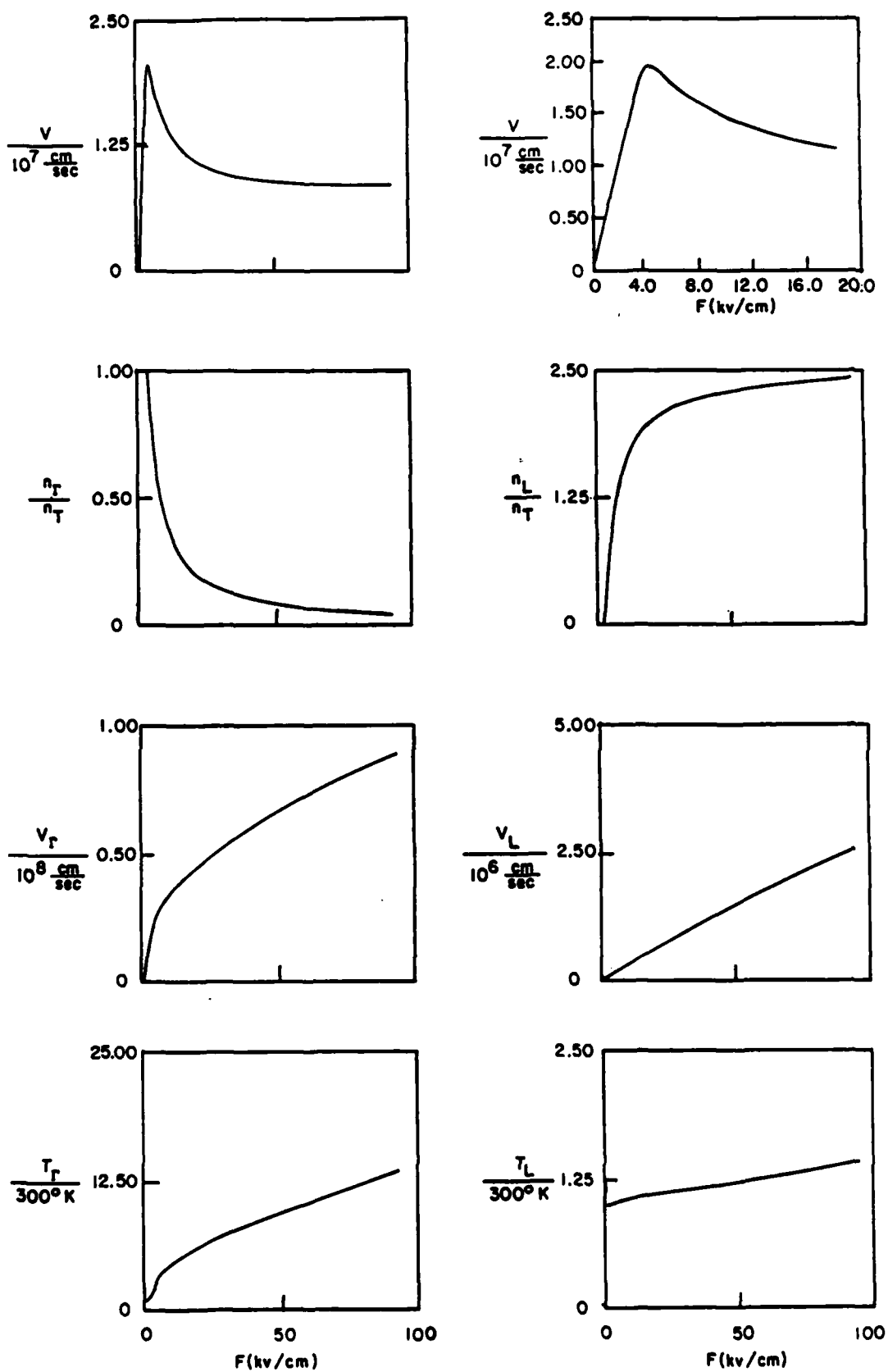


FIGURE 47. AS IN FIGURE 1, BUT FOR AN INCLUSION OF IONIZED IMPURITY SCATTERING. BROOKS-HERRING MATRIX ELEMENTS ARE USED AND THE DONOR CONCENTRATION IS  $8 \times 10^{16}/\text{cm}^3$ .

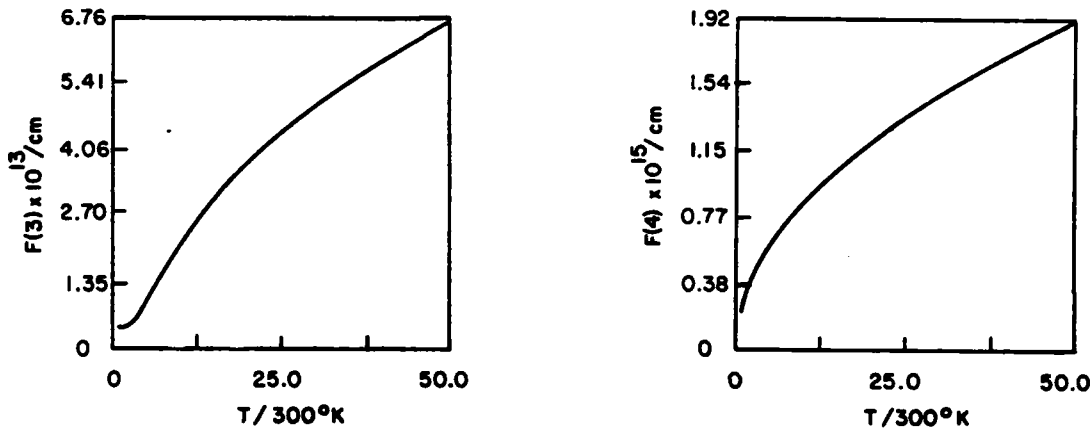


FIGURE 48. AS IN FIGURE 4, BUT ONLY FOR MOMENTUM SCATTERING RATES.

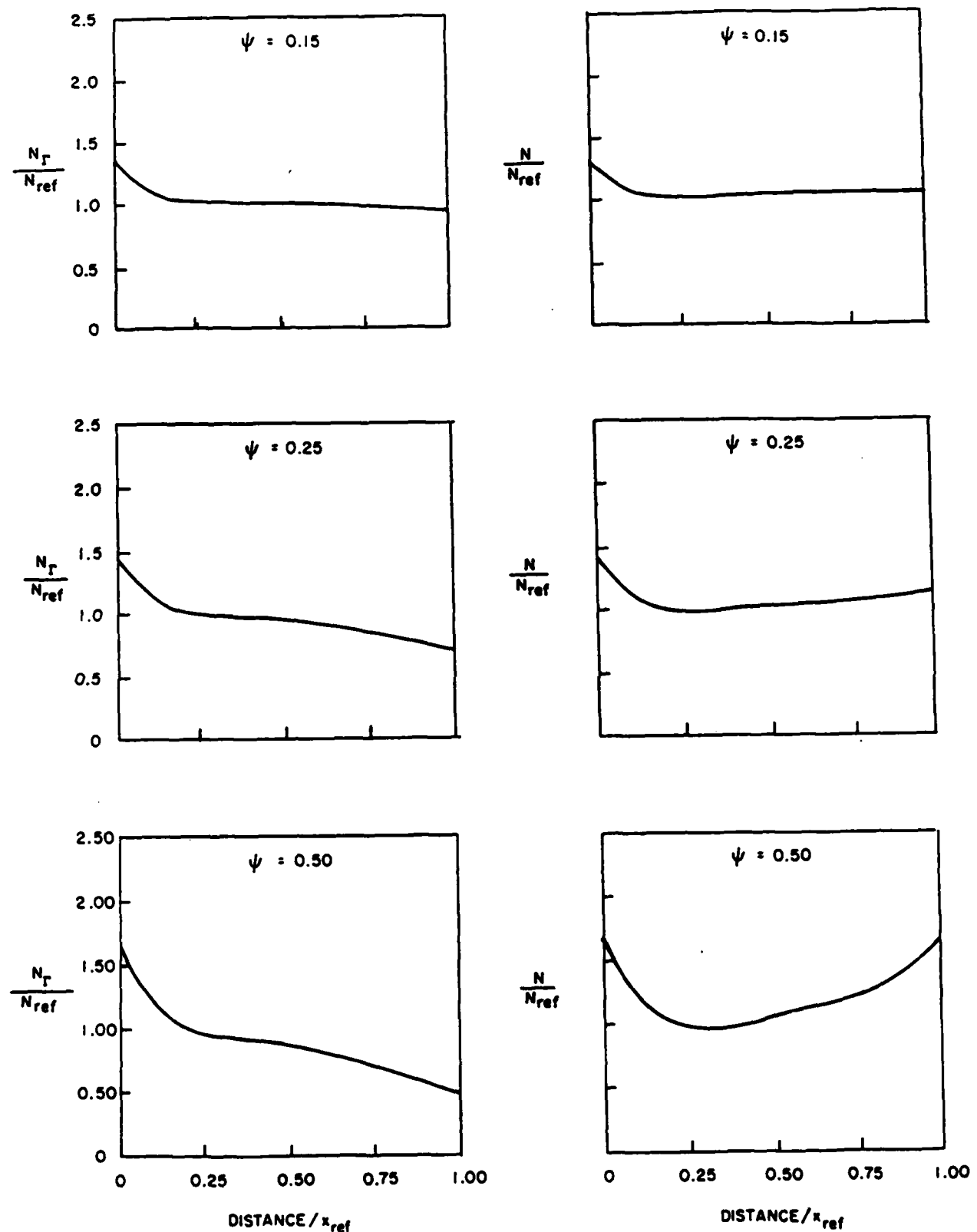


FIGURE 49. AS IN FIGURE 34, BUT FOR IONIZED IMPURITY SCATTERING.  
 $(x_{ref} = 0.25 \mu\text{m}, N_{ref} = 8 \times 10^{16}, \text{B.H.} = 8 \times 10^{16})$ .

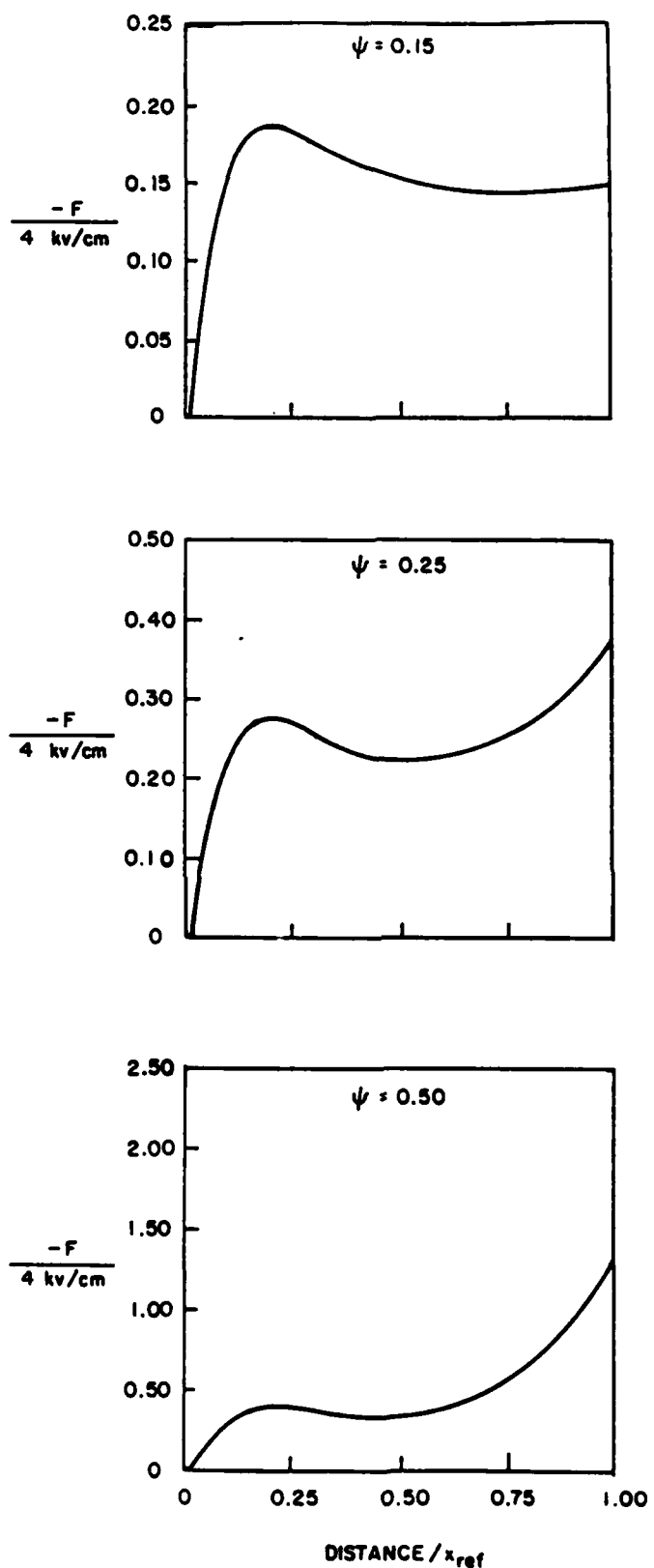


FIGURE 50. AS IN FIGURE 49, BUT FOR THE ELECTRIC FIELD VERSUS DISTANCE PROFILE.

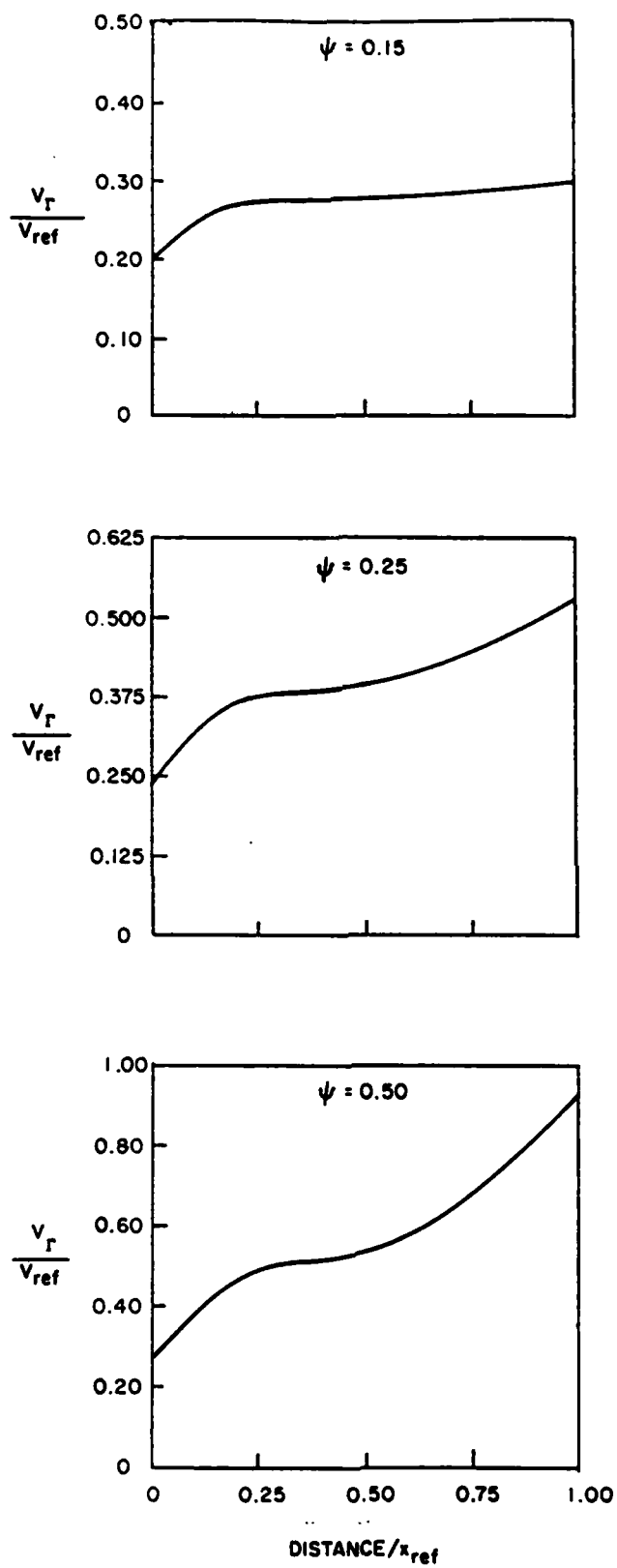


FIGURE 51. AS IN FIGURE 49, BUT FOR THE  $\Gamma$ -VALLEY CARRIER VELOCITY.

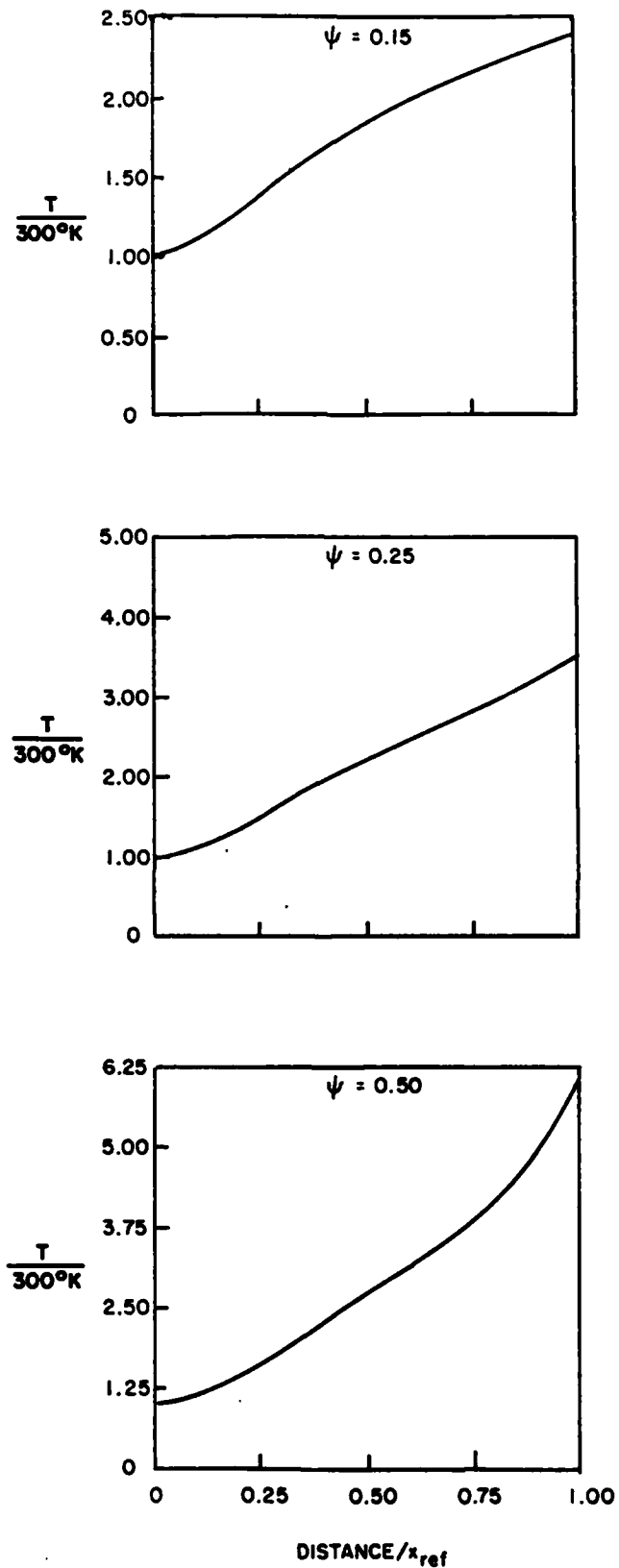


FIGURE 52. AS IN FIGURE 49, BUT FOR THE  $\Gamma$ -VALLEY ELECTRON TEMPERATURE.

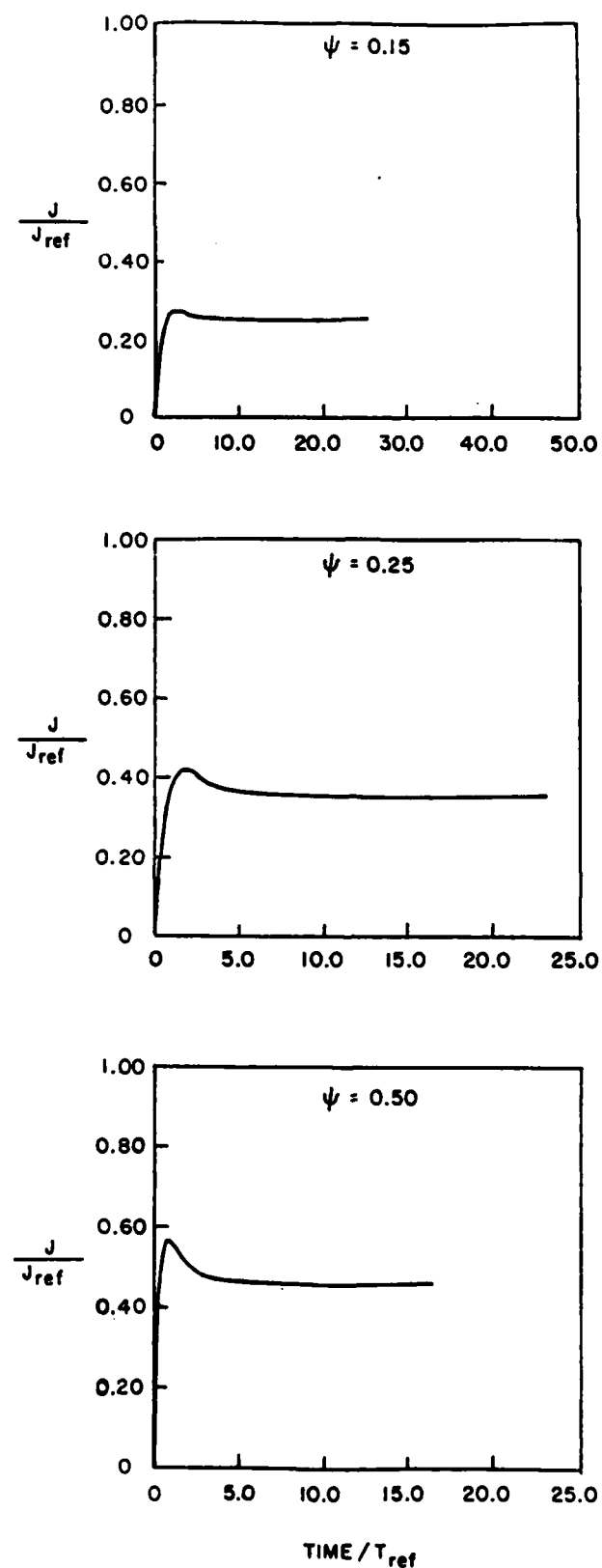


FIGURE 53. AS IN FIGURE 38, BUT FOR IONIZED IMPURITY SCATTERING INCLUDED.

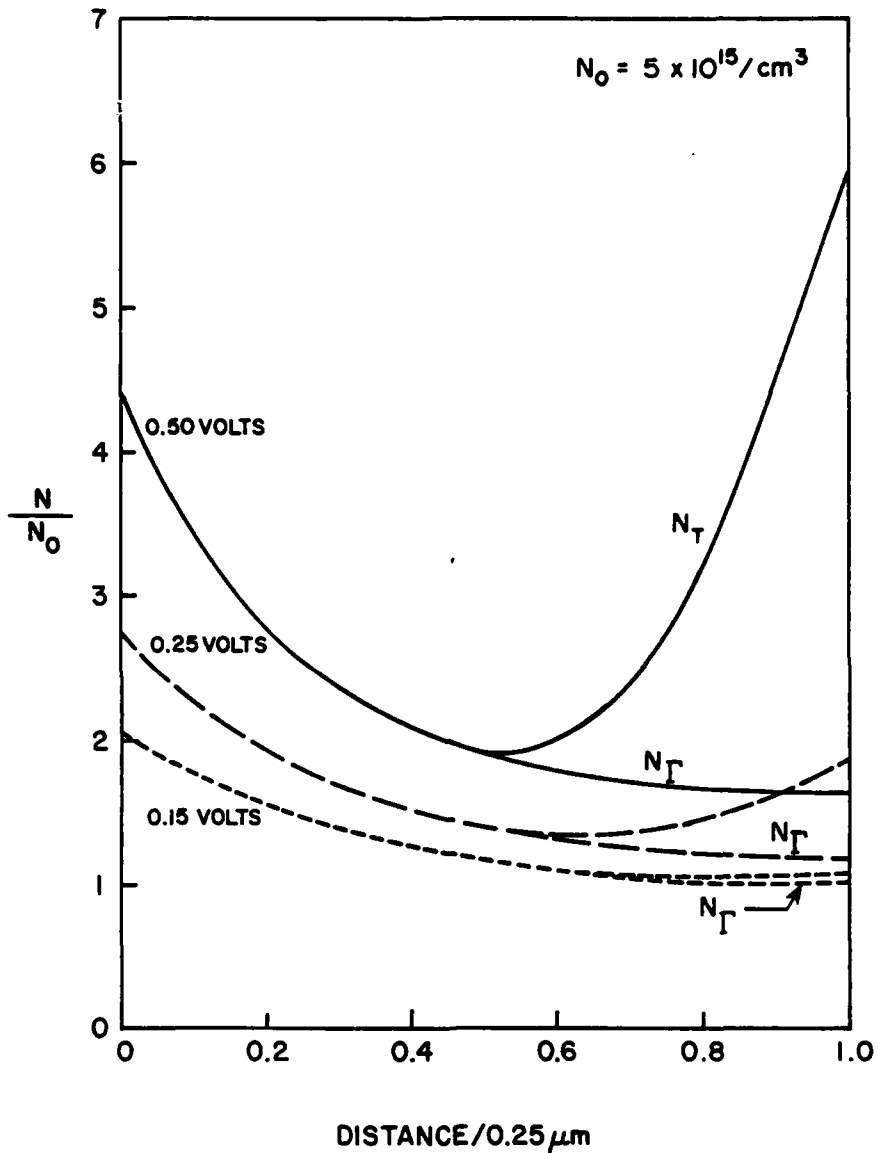


FIGURE 54. AS IN FIGURE 34, BUT FOR A DONOR DENSITY OF  $5 \times 10^{15} / \text{cm}^3$ .

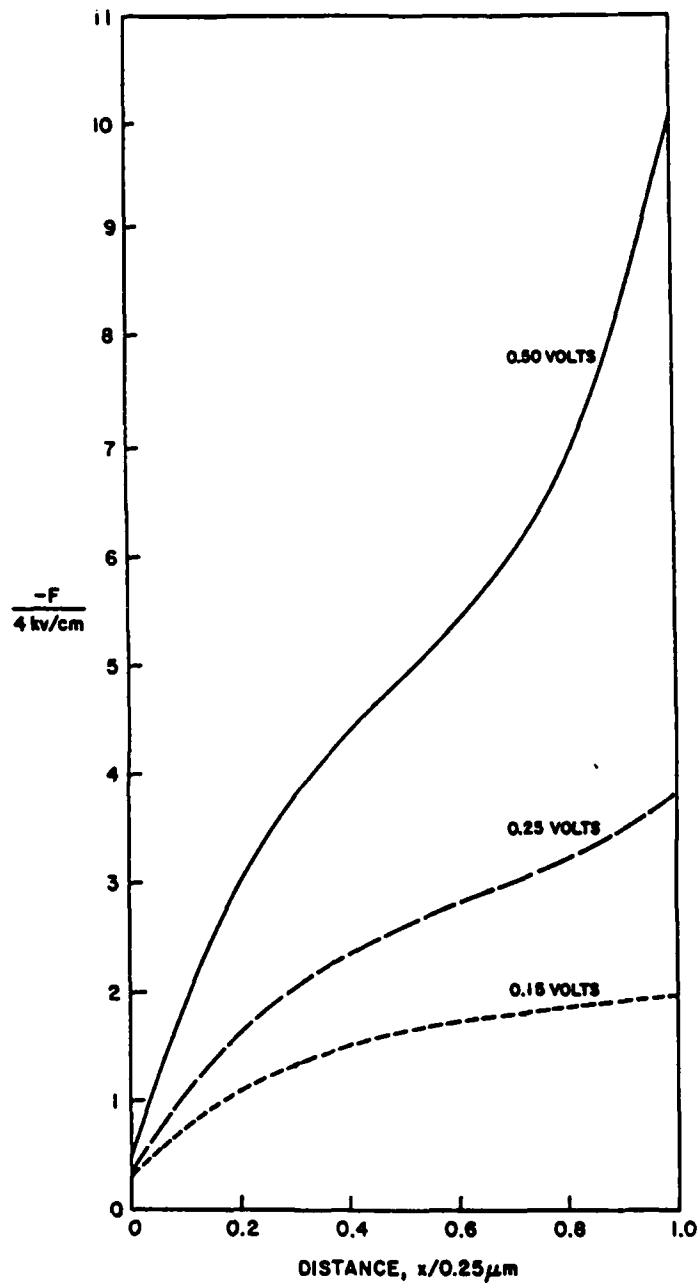


FIGURE 55. AS IN FIGURE 54, BUT FOR THE ELECTRIC FIELD VERSUS DISTANCE PROFILE.

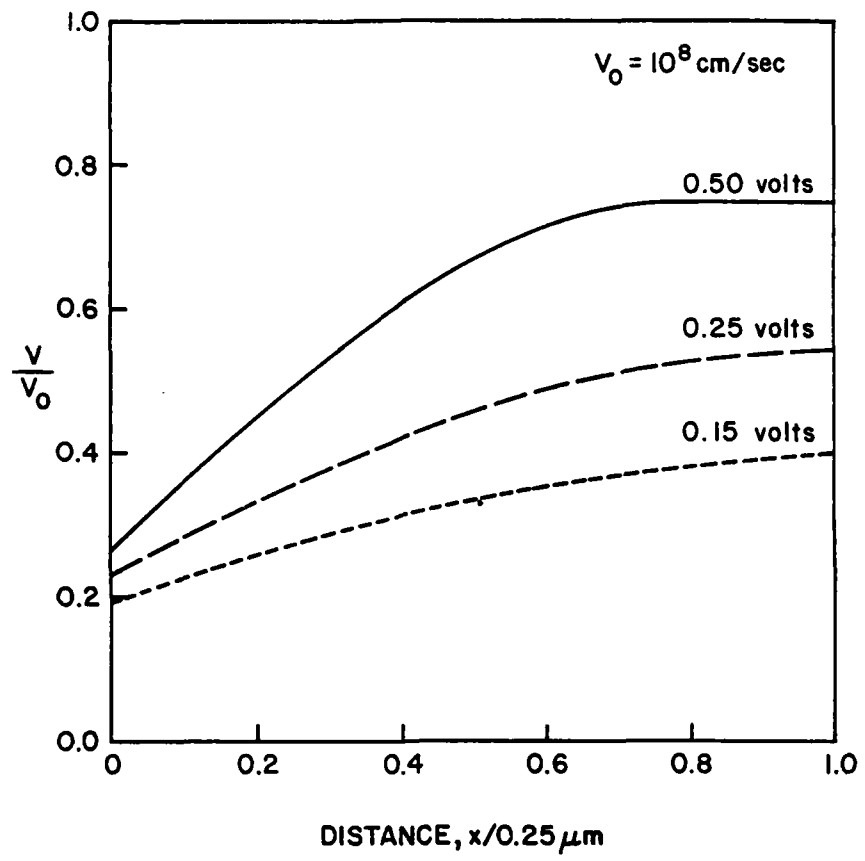


FIGURE 56. AS IN FIGURE 54, BUT FOR THE  $\Gamma$ -VALLEY CARRIER VELOCITY.

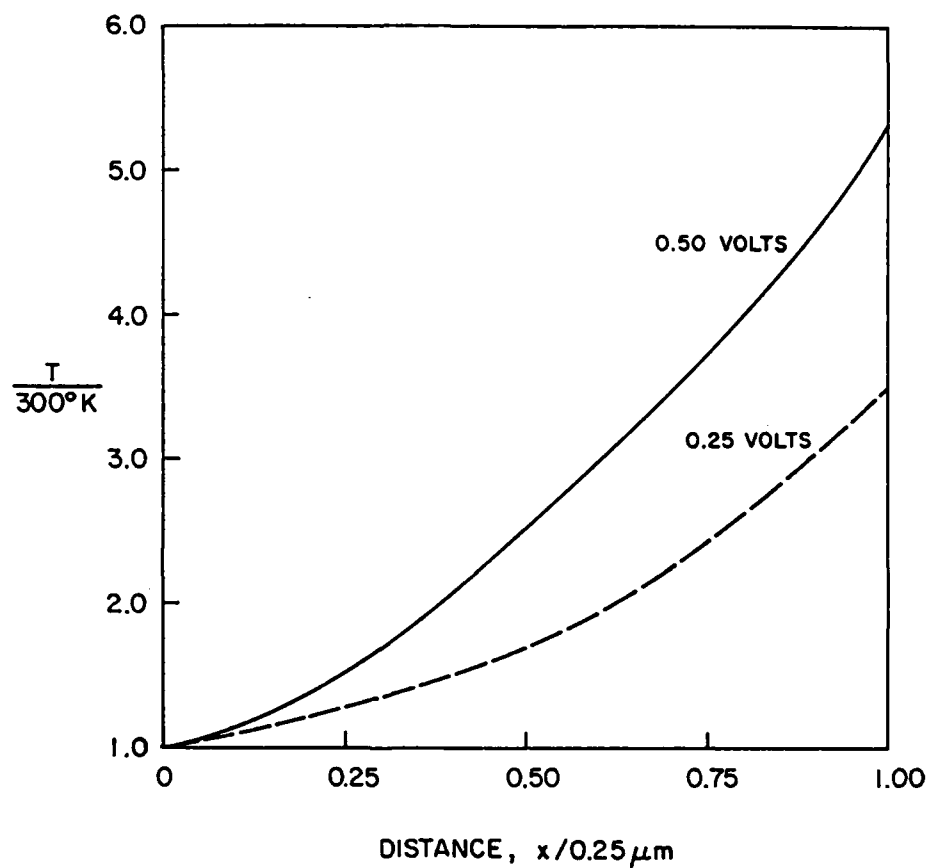


FIGURE 57. AS IN FIGURE 54, BUT FOR THE T-VALLEY ELECTRON TEMPERATURE.

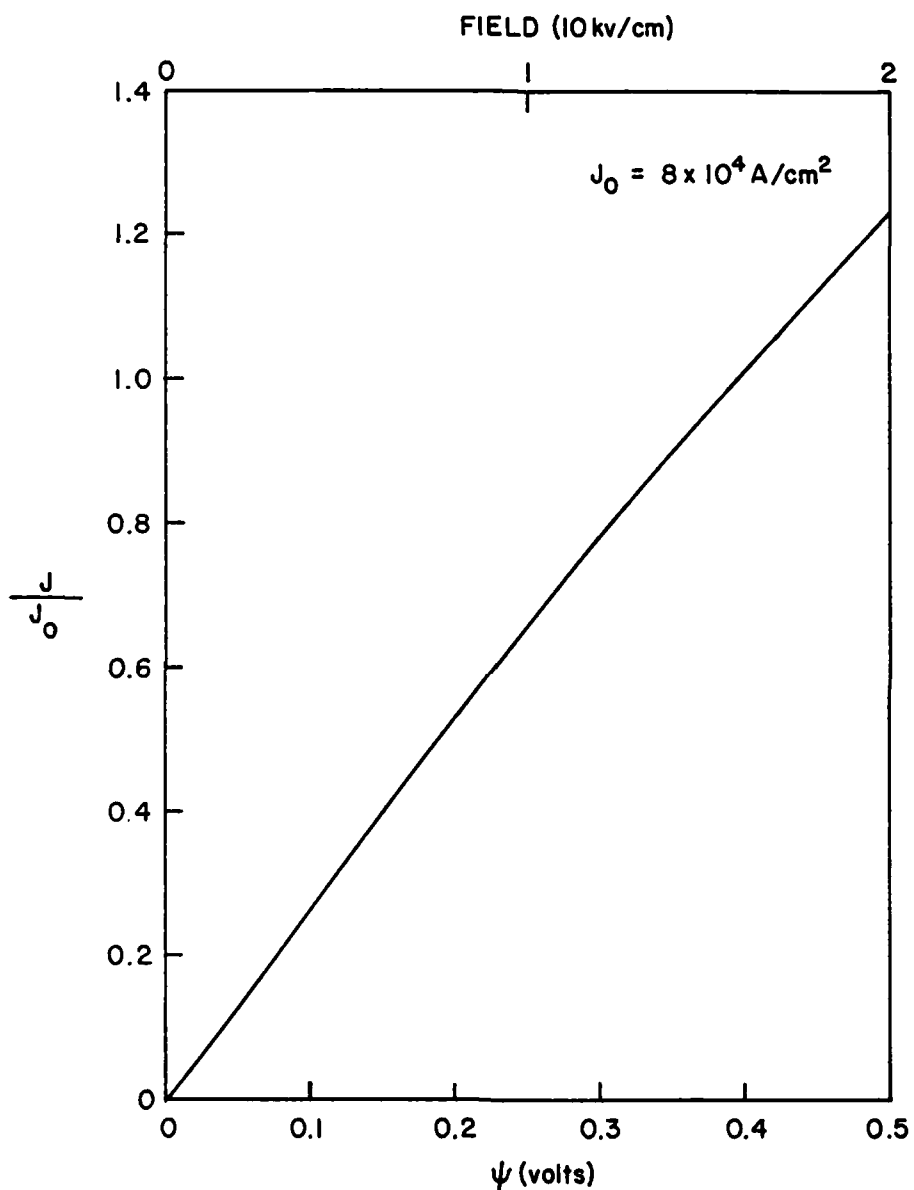


FIGURE 58. STEADY STATE CURRENT VERSUS VOLTAGE  
FOR A DONOR DENSITY OF  $5E + 15/\text{cm}^3$

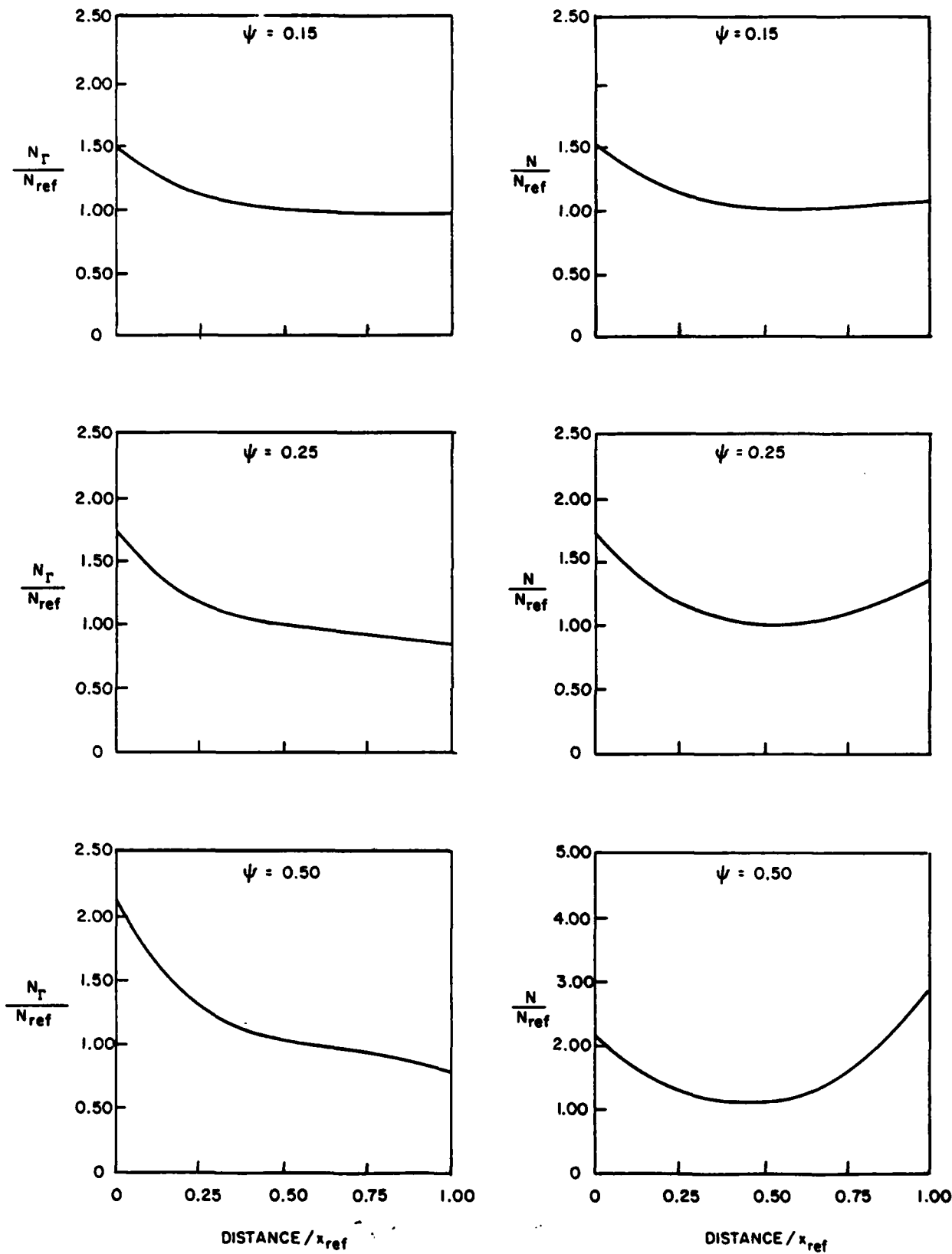


FIGURE 59. AS IN FIGURE 54, BUT FOR A DONOR DENSITY OF  $2 \times 10^{16}/\text{cm}^3$ .

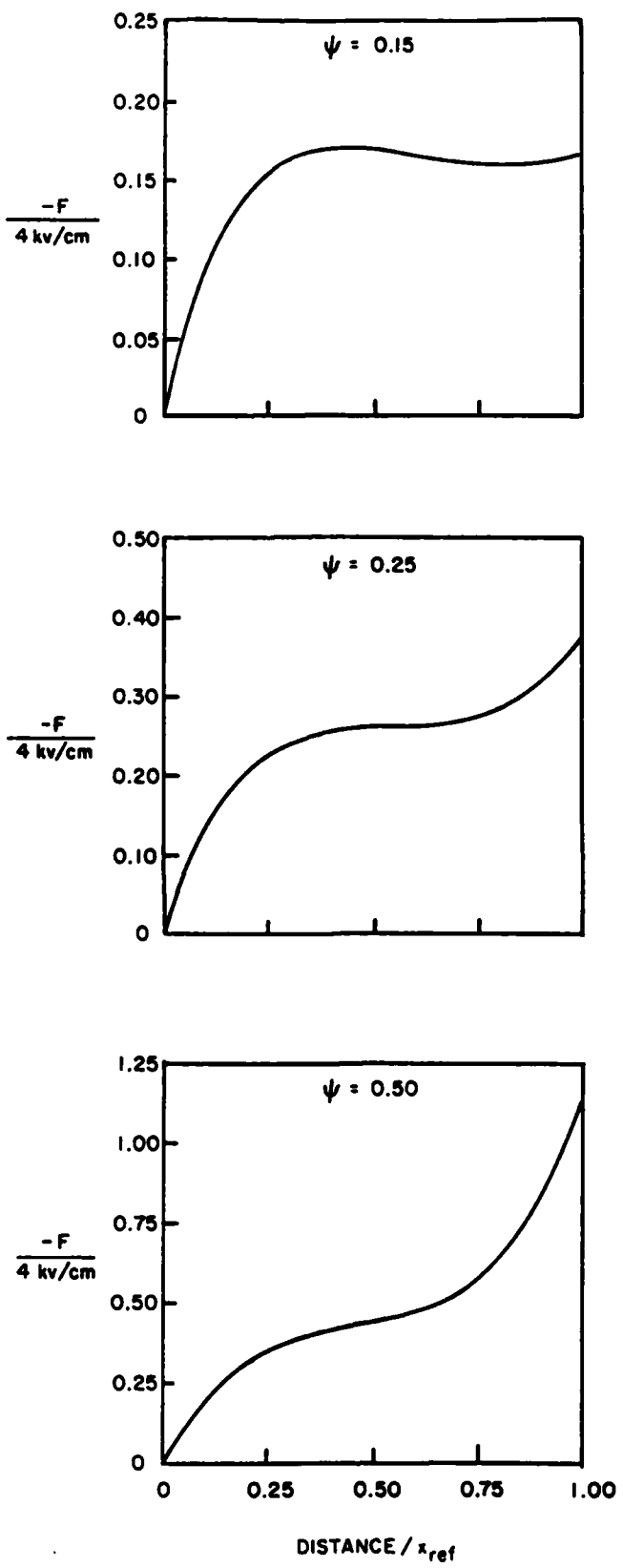


FIGURE 60. AS IN FIGURE 59, BUT FOR THE ELECTRIC FIELD VERSUS DISTANCE PROFILE.

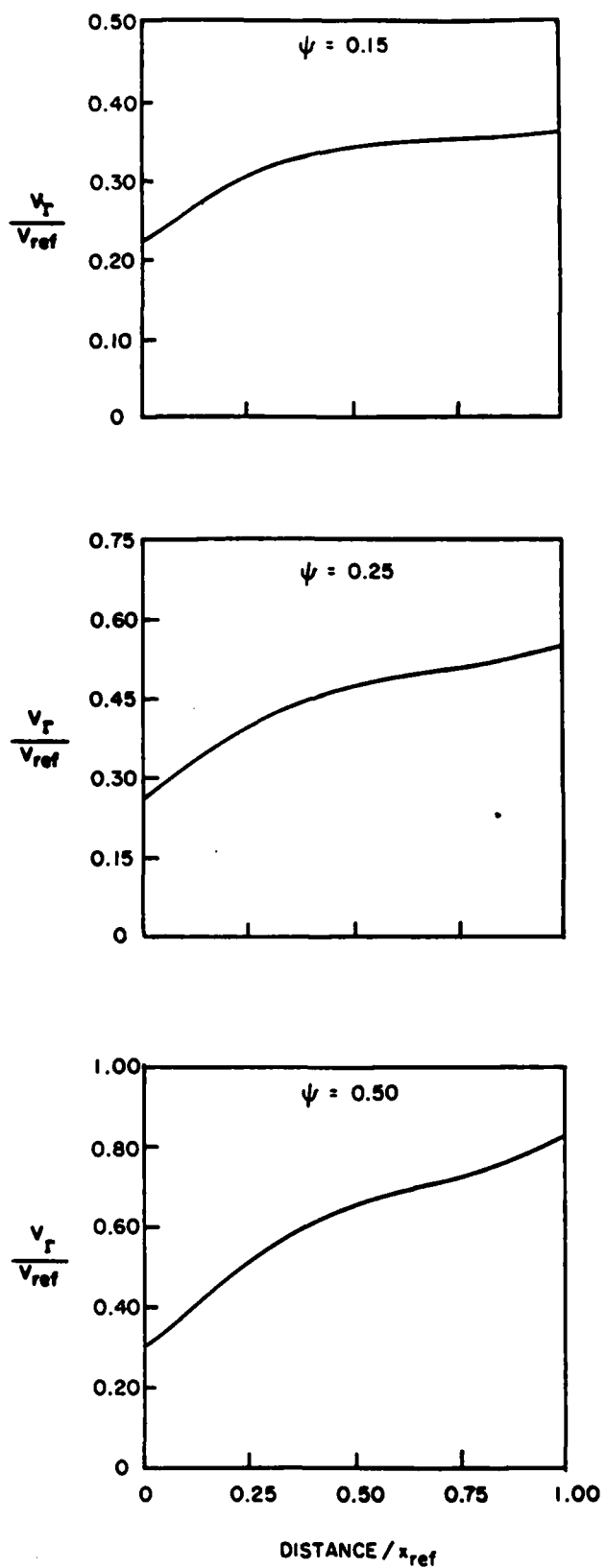


FIGURE 61. AS IN FIGURE 59, BUT FOR THE T-VALLEY CARRIER VELOCITY.

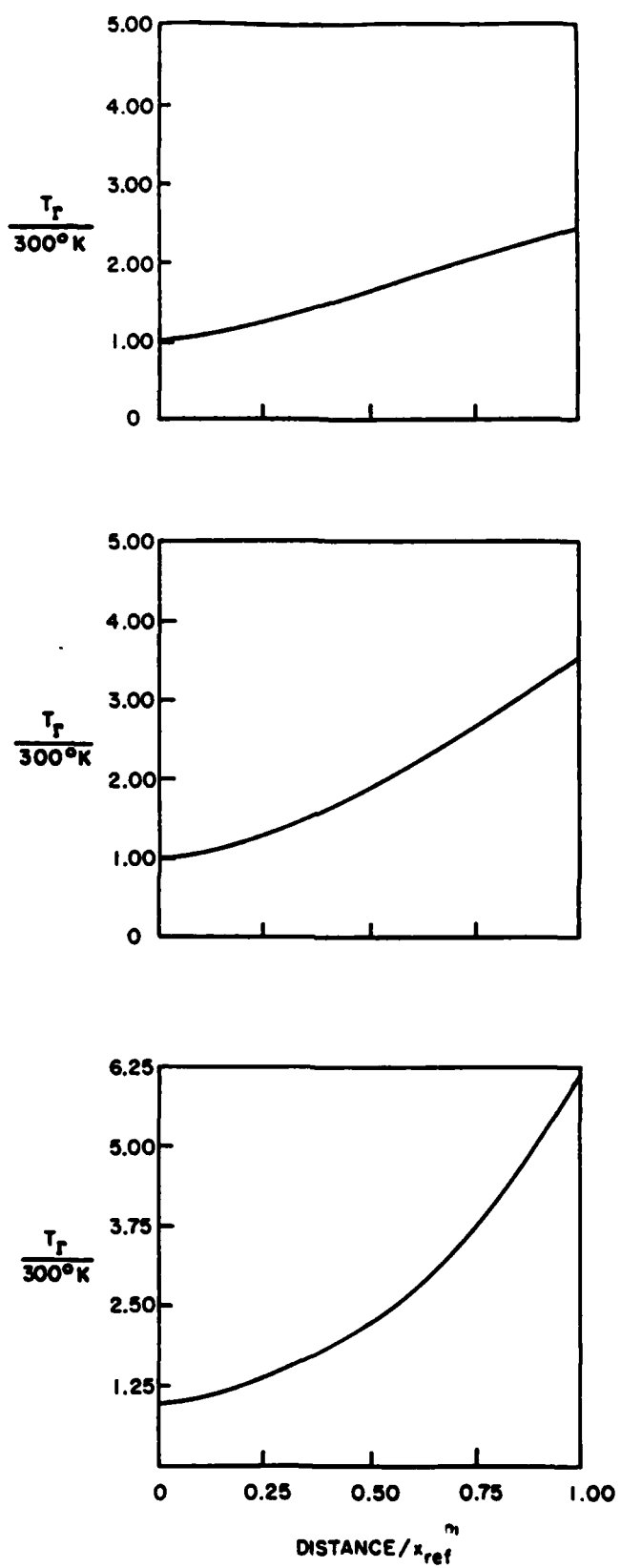


FIGURE 62. AS IN FIGURE 59, BUT FOR THE  $\Gamma$ -VALLEY ELECTRON TEMPERATURE.

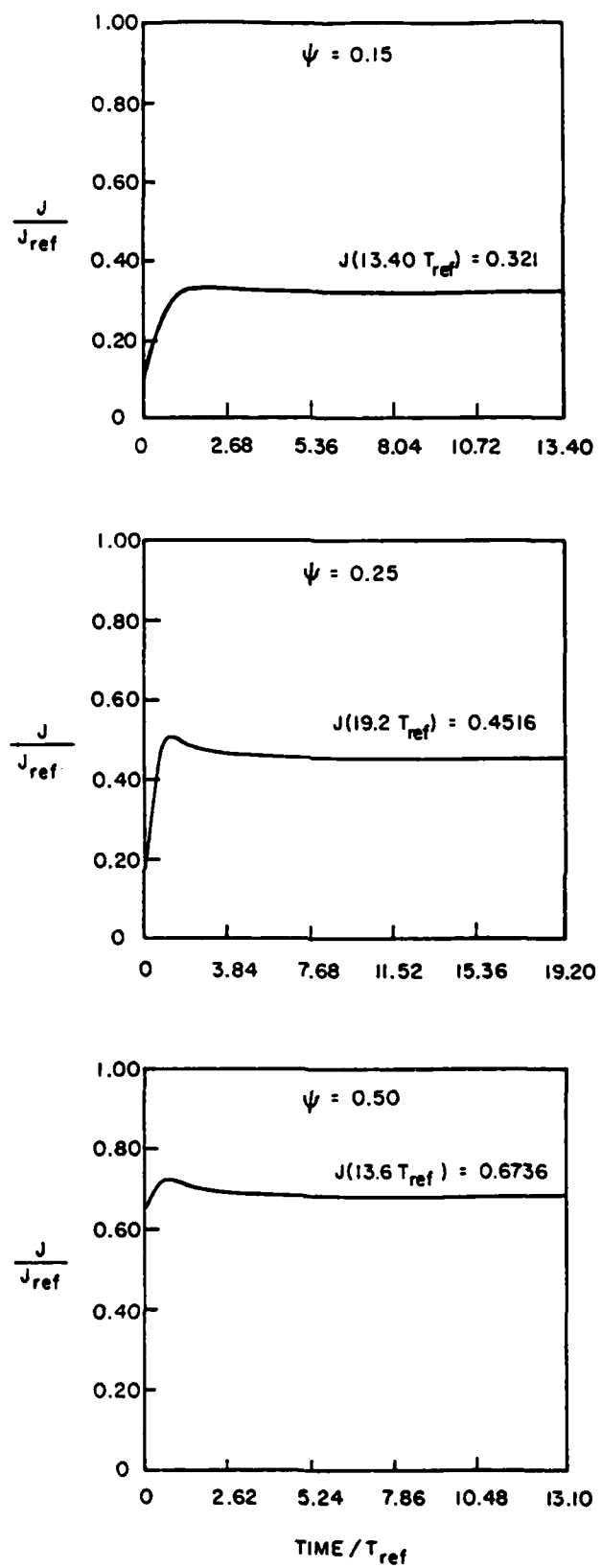


FIGURE 63. AS IN FIGURE 58, BUT FOR A DONOR DENSITY OF  $2 E+16/cm^3$ .

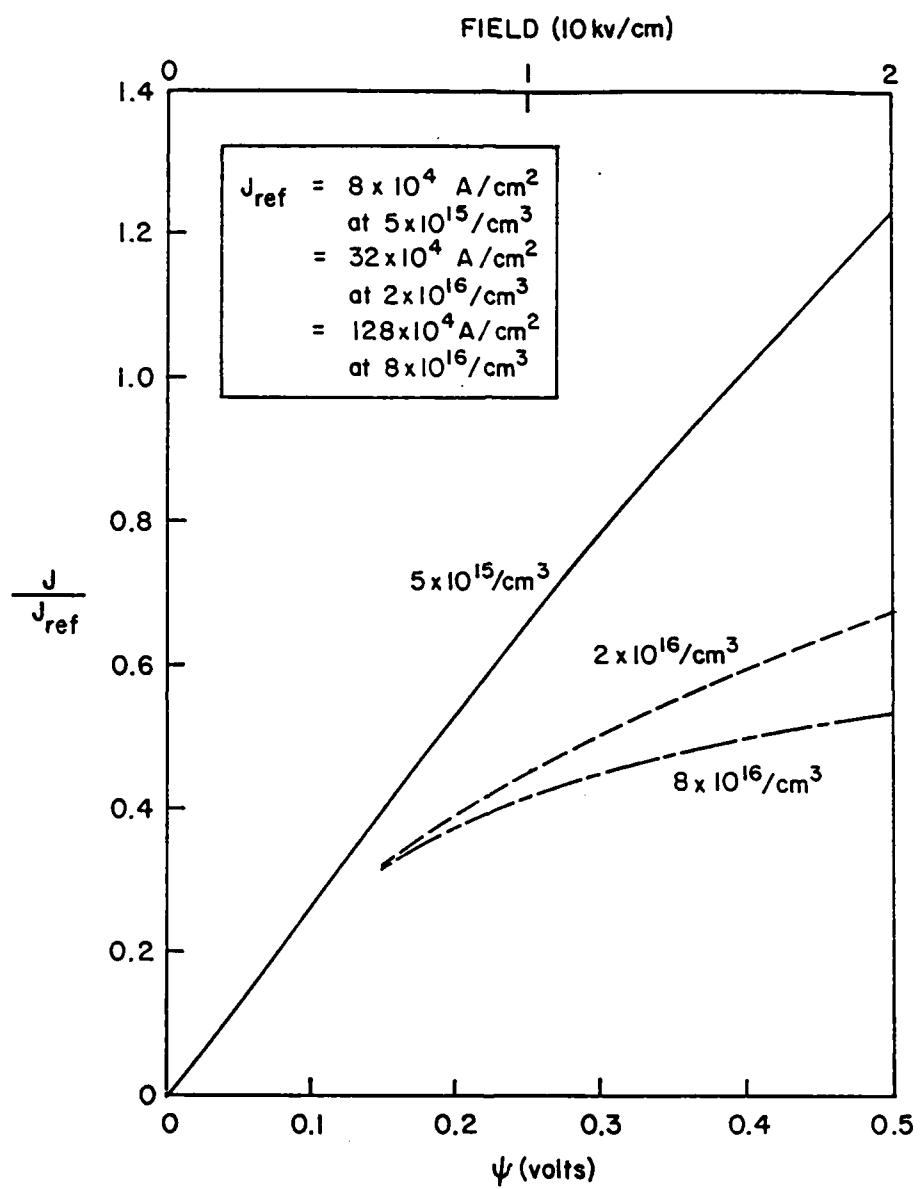


FIGURE 64. STEADY STATE CURRENT VOLTAGE RELATION VS.  
DONOR DENSITY ( $x_{ref} = 0.25\mu\text{m}$ )

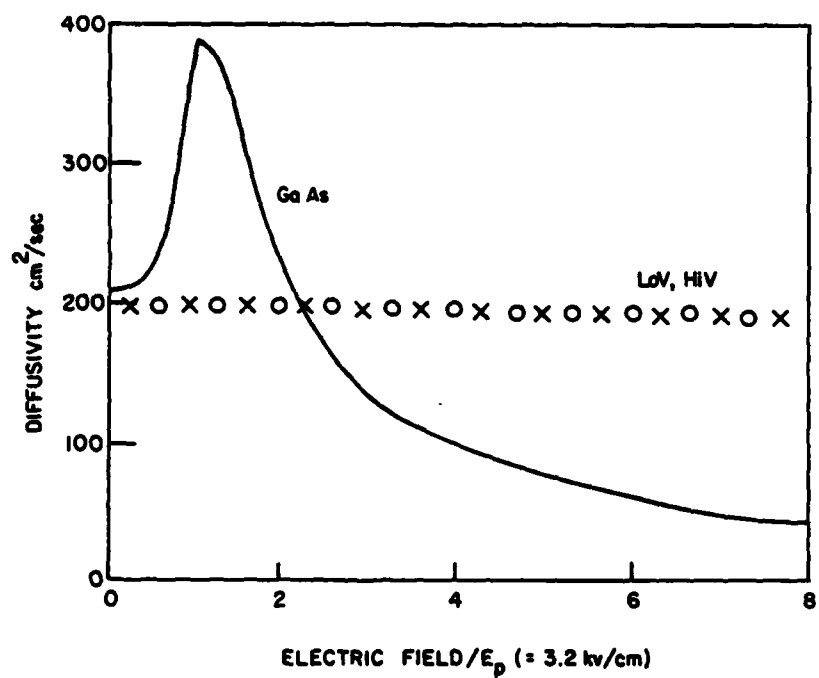
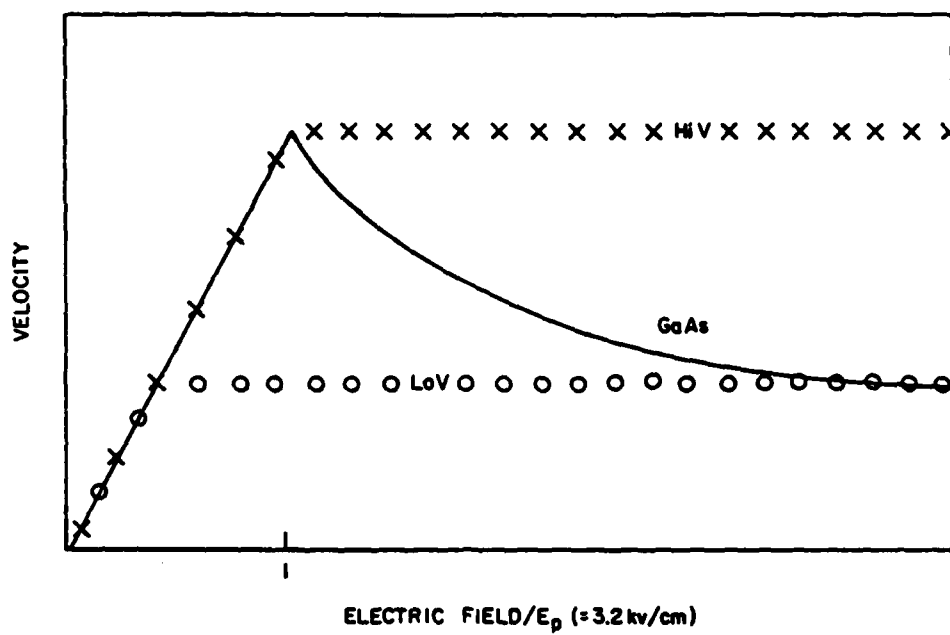


FIGURE 65. FIELD DEPENDENT VELOCITY RELATIONSHIPS USED TO DETERMINE THE RELEVANCE OF THE SATURATED DRIFT VELOCITY TO THE IDSS OF FETs.

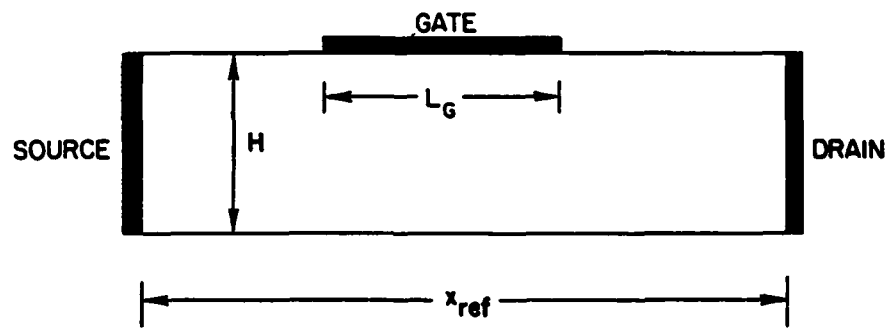


FIGURE 66. SKETCH OF THREE TERMINAL FET STRUCTURE USED IN CALCULATIONS.

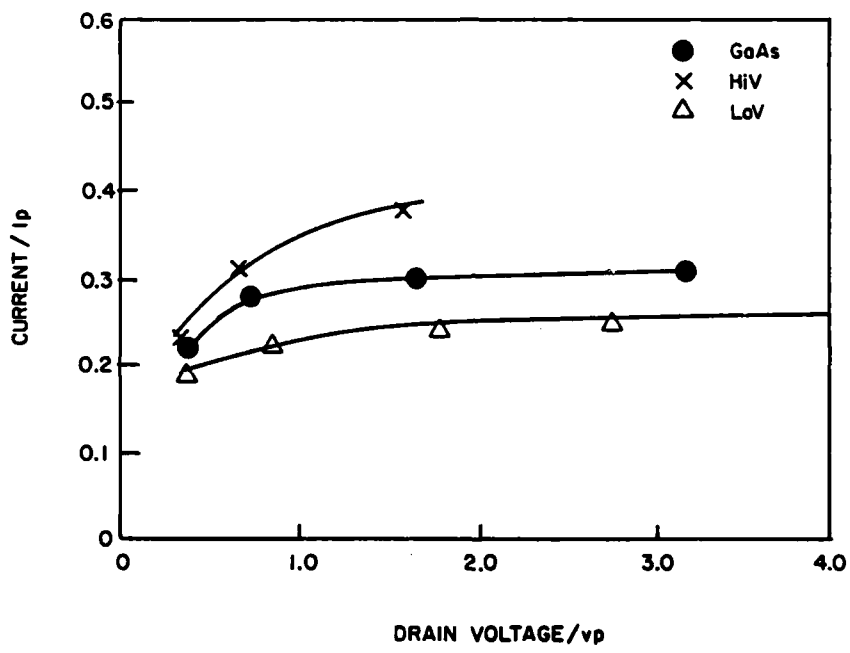


FIGURE 67. CURRENT-VOLTAGE RELATION FOR THE FIELD DEPENDENT VELOCITIES OF FIGURE 65.

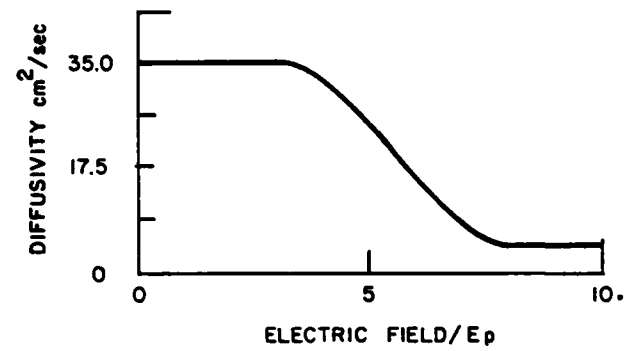
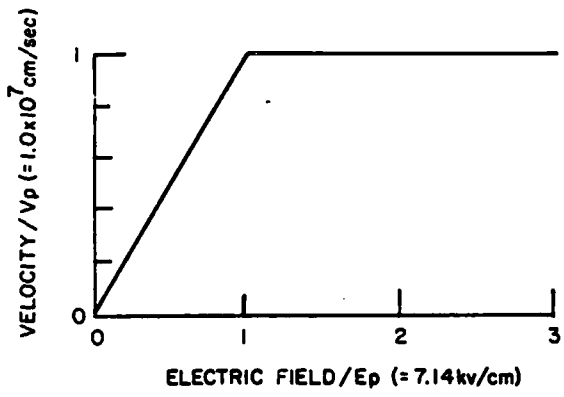


FIGURE 68. FIELD DEPENDENT VELOCITY AND DIFFUSIVITY FOR A SILICON UNIPOLAR FET CALCULATION.

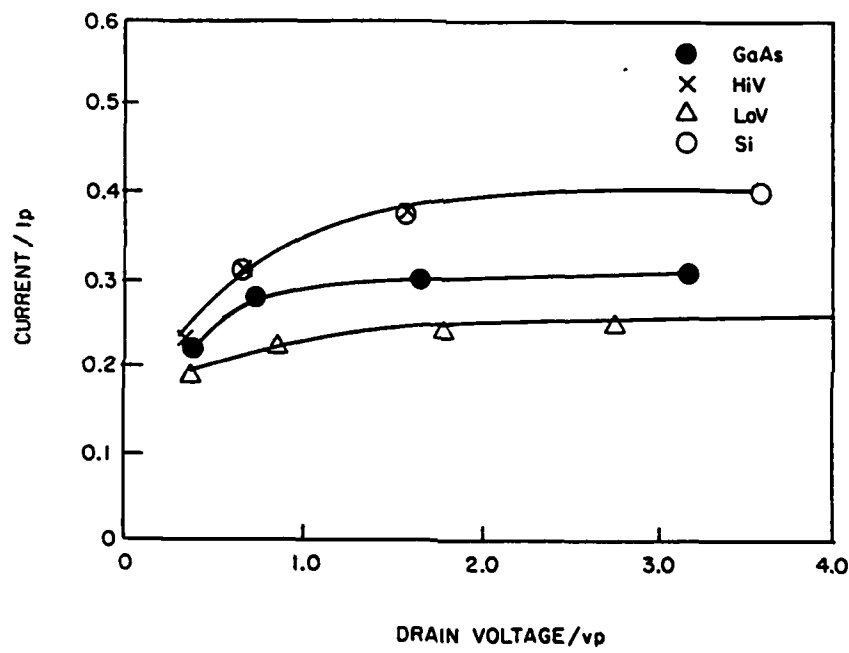


FIGURE 69. CURRENT-VOLTAGE RELATION FOR SILICON AND 'HiV'  
DRAWN ON THE SAME SCALE.

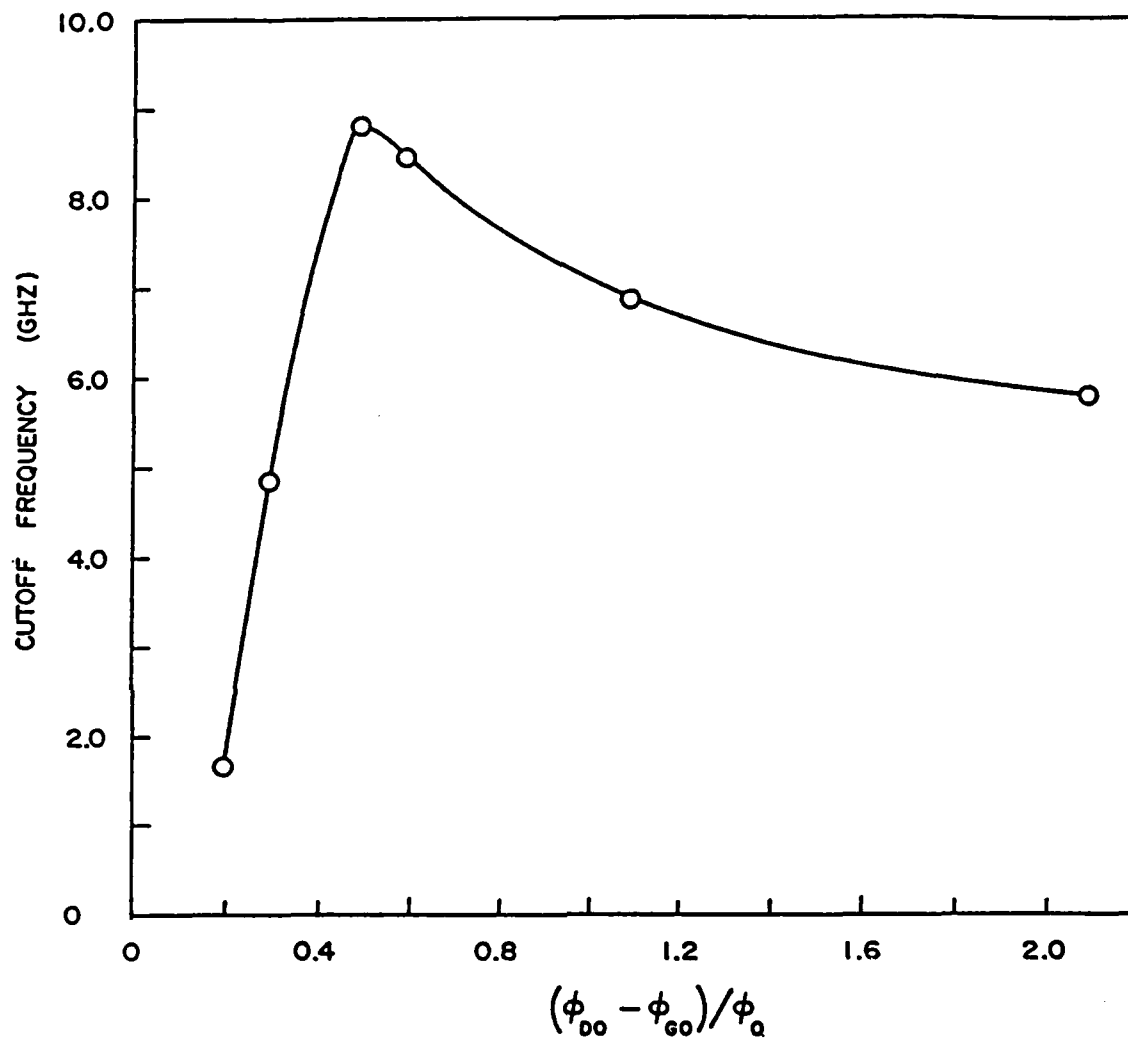
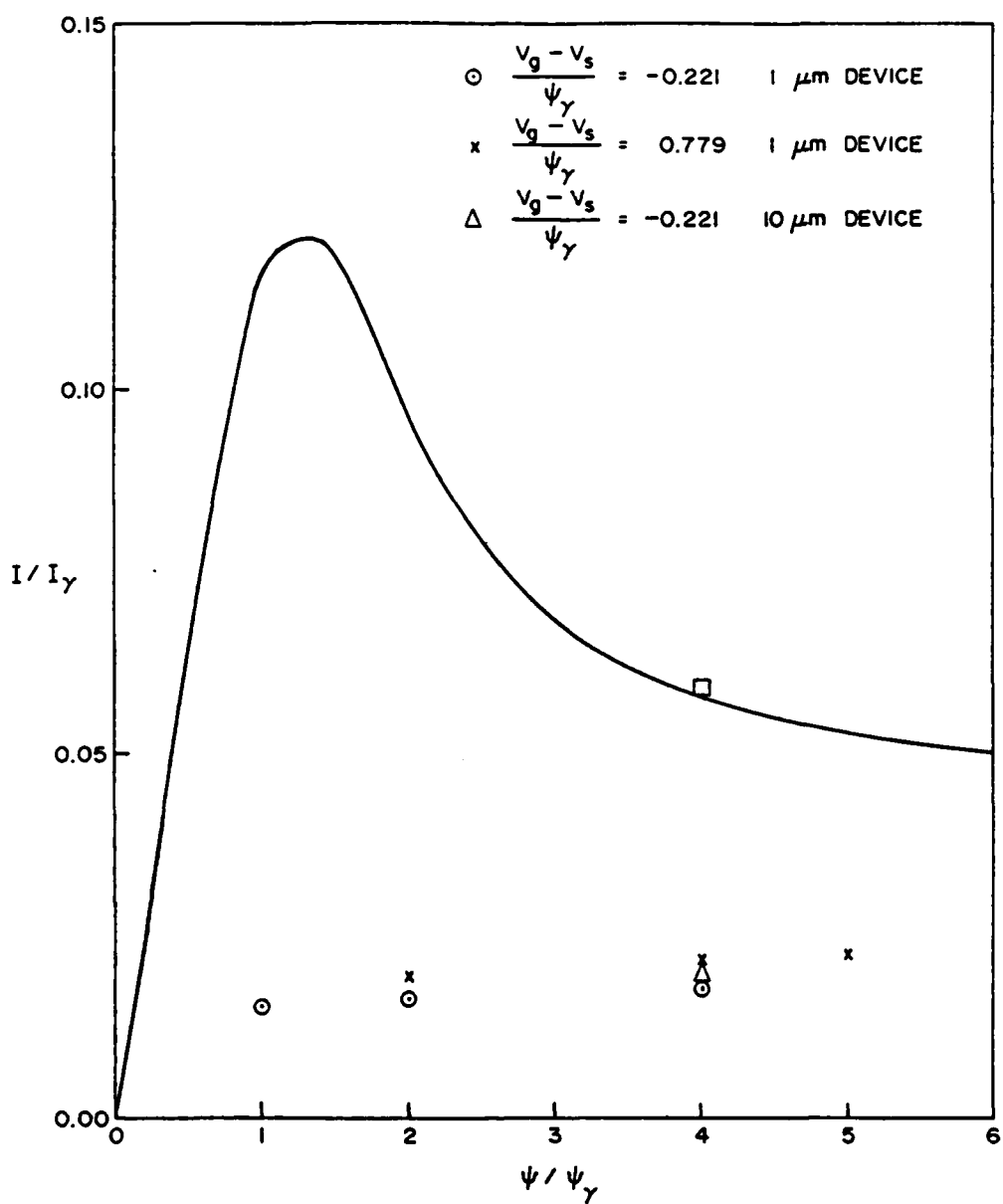


FIGURE 70. SMALL SIGNAL CUTOFF FREQUENCY IN GaAs FET WITH  $x_{ref} = 10.0$  MICRONS.



PLOT OF  $\frac{V_d - V_s}{\Psi_y}$  VS.  $\frac{I_d}{I_y}$

FIGURE 71. DRAIN CURRENT VERSUS DRAIN BIAS FOR SCALED AND UNSCALED GaAs FET.

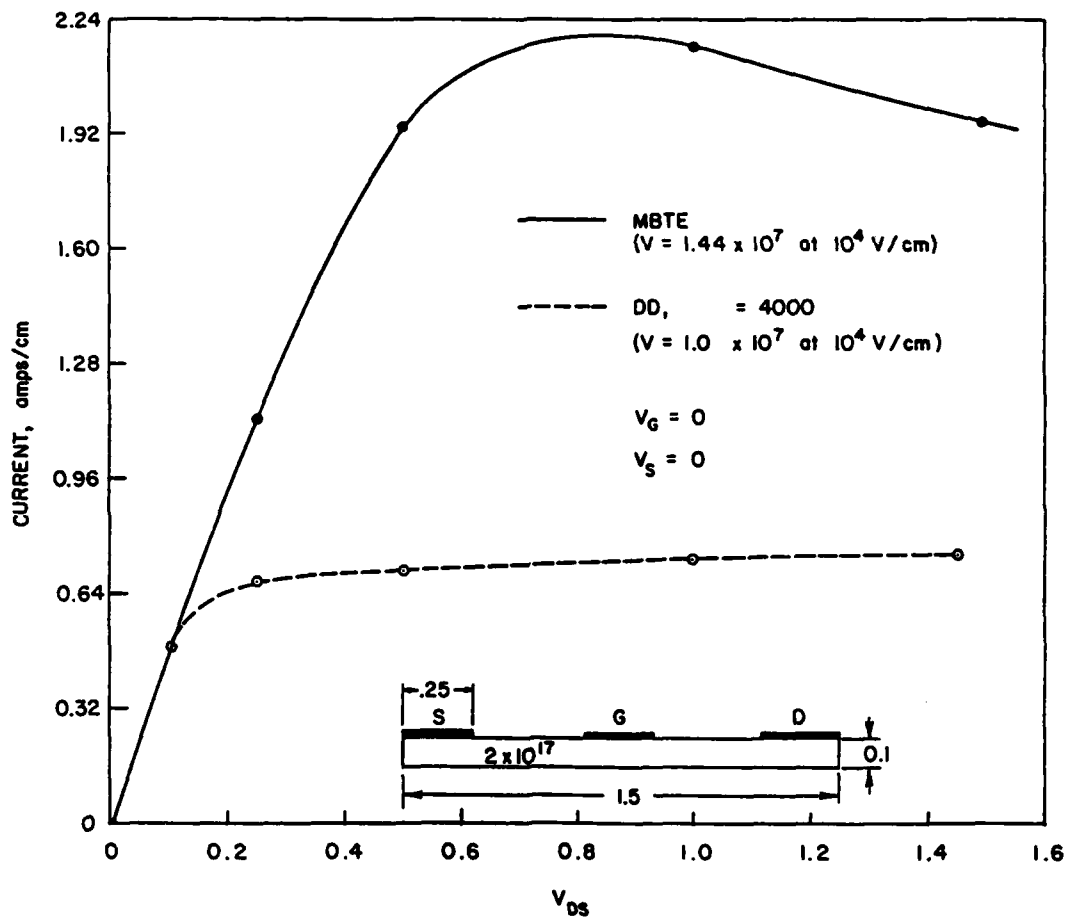


FIGURE 72. COMPARISON OF FET CHARACTERISTICS USING THE DDE AND MBTE FORMULATION. (STRUCTURE IS INDICATED WITH LENGTH IN MICRONS.)

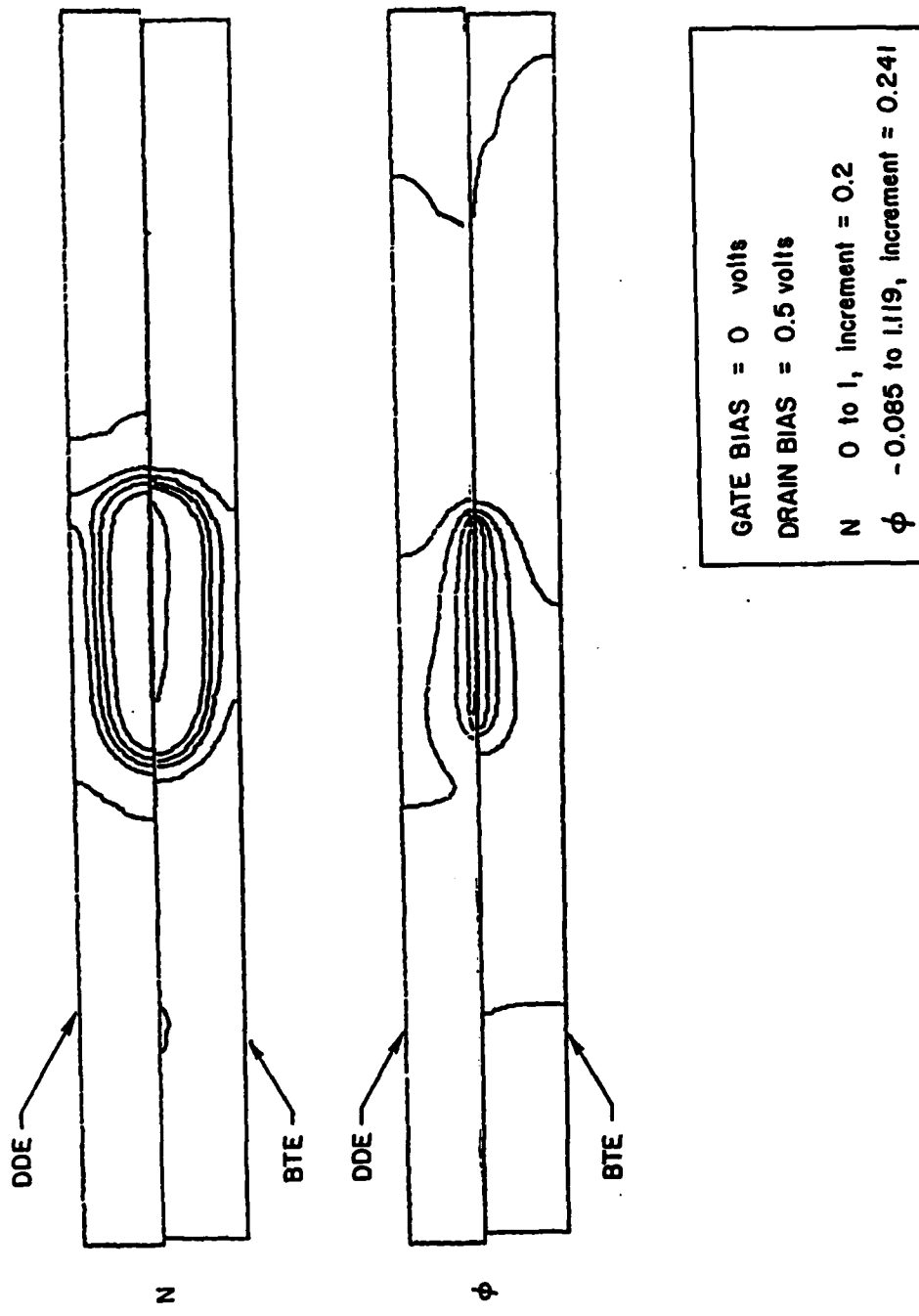


FIGURE 73. COMPARISON OF DOE AND MBTE CONTOURS FOR INDICATED BIAS.

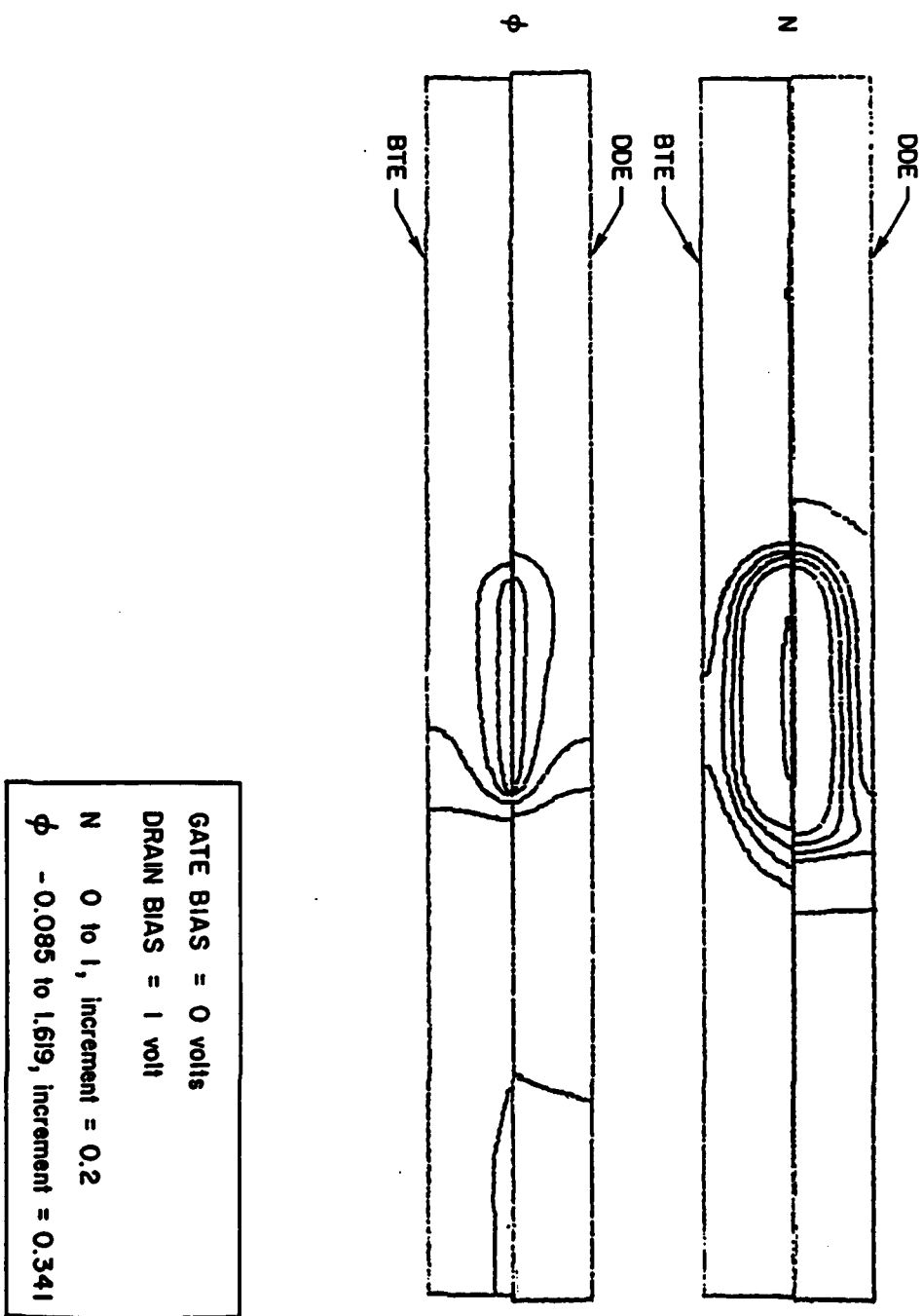


FIGURE 74. AS IN FIGURE 73.

TABLE I  
GALLIUM ARSENIDE  
PARAMETERS AND BOUNDARY CONDITIONS USED IN CALCULATION

PARAMETERS	$\Gamma$	L	COMMON
NUMBER OF EQUIVALENT VALLEYS	1	4	
EFFECTIVE MASS ( $m_e$ ) $\Gamma$ -L SEPARATION (ev)	0.067	0.222	0.33
POLAR OPTICAL SCATTERING			
STATIC DIEL. CONST.		12.90	
HIGH FREQ. DIEL. CONST.		10.92	
LO PHONON (ev)		0.0354	
$\Gamma$ -L SCATTERING			
COUPL. CONS. (ev/cm)		0.800 $\times 10^9$	
PHONON ENERGY (ev)		0.0278	
L-L SCATTERING			
COUPL. CONST. (ev/cm)		2.0 $\times 10^9$	
PHONON ENERGY (ev)		0.0354	
ACOUSTIC SCATTERING			
DEFORM. POT. (ev)	7.0	9.2	
NONPOLAR SCATTERING (L)			
COUPLING CONSTANT (ev/cm)		0.300 $\times 10^9$	
PHONON ENERGY (ev)		0.0343	

TABLE I. SCATTERING PARAMETERS USED IN THE GALLIUM ARSENIDE CALCULATION.

TABLE 2  
INDIUM PHOSPHIDE  
PARAMETERS AND BOUNDARY CONDITIONS USED IN CALCULATION

PARAMETERS	$\Gamma$	L	COMMON
NUMBER OF EQUIVALENT VALLEYS	1	4	
EFFECTIVE MASS ( $m_e$ )	0.080	0.300	
$\Gamma$ -L SEPARATION (ev)			0.52
POLAR OPTICAL SCATTERING			
STATIC DIEL. CONST.		12.35	
HIGH FREQ. DIEL. CONST.		9.52	
LO PHONON (ev)		0.0432	
$\Gamma$ -L SCATTERING			
COUPL. CONS. (ev/cm)		0.700 $\times 10^9$	
PHONON ENERGY (ev)		0.0278	
L-L SCATTERING			
COUPL. CONST. (ev/cm)		5.0 $\times 10^9$	
PHONON ENERGY (ev)		0.0432	
ACOUSTIC SCATTERING			
DEFORM. POT. (ev)	7.0	12.3	
NONPOLAR SCATTERING (L)			
COUPLING CONSTANT (ev/cm)		0.670 $\times 10^9$	
PHONON ENERGY (ev)		0.0343	

TABLE 2. SCATTERING PARAMETERS USED IN THE INDIUM PHOSPHIDE CALCULATION.

TABLE 3

$$n_1^* = n_1 / n_{ref}, \quad v_1^* = v_1 / v_{ref}$$

$$n^* = n / n_{ref}, \quad v_2^* = v_2 / v_{ref}$$

$$f_1 = \Gamma_1 / \Gamma_{ref}, \quad f_2 = \Gamma_2 / \Gamma_{ref}$$

$$x^* = x / x_{ref} \quad t^* = t / t_{ref}$$

$$\Gamma_{ref} = 1/t_{ref}$$

TABLE 3. DIMENSIONLESS VARIABLES CONNECTED WITH EQUATIONS (27) AND (28).

TABLE 4

$$\phi^* = \phi / \phi_{ref}$$

$$m_1^* = m_1 / m_{ref} , m_2^* = m_2 / m_{ref}$$

$$R_1 = k_B / m_1 , R_2 = k_B / m_2$$

$$R_{ref} = k_B / m_{ref}$$

$$R_1^* = R_1 / R_{ref} = \frac{1}{m_1^*} , R_2^* = R_2 / R_{ref} = \frac{1}{m_2^*}$$

$$f_3 = \Gamma_3 / \Gamma_{ref} , f_4 = \Gamma_4 / \Gamma_{ref}$$

$$\mu_1^* = \hat{\mu}_1 / \hat{\mu}_{ref} , \mu_2^* = \hat{\mu}_2 / \hat{\mu}_{ref}$$

$$P_f = e\phi_{ref} / m_{ref} V_{ref}^2$$

$$M = V_{ref} / V_a$$

$$V_a = \left( \frac{5}{3} R_{ref} T_{ref} \right)^{1/2}$$

$$\gamma = 5/3$$

$$Re = x_{ref} V_{ref} n_{ref} m_{ref} / \hat{\mu}_{ref}$$

TABLE 4. DIMENSIONLESS PARAMETERS ASSOCIATED WITH THE MOMENTUM BALANCE EQUATIONS 31 AND 32.

TABLE 5

$f_5 = \Gamma_5 / \Gamma_{ref}$	$f_6 = \Gamma_6 / \Gamma_{ref}$
$f_7 = \Gamma_7 / \Gamma_{ref}$	$f_8 = \Gamma_8 / \Gamma_{ref}$
$\kappa_1^* = \kappa_1 / \kappa_{ref}$	$\kappa_2^* = \kappa_2 / \kappa_{ref}$
$C_{V_1} = \frac{3}{2} R_1$	$C_{V_2} = \frac{3}{2} R_2$
$C_{V_1}^* = C_{V_1} / C_{Vref}$	$C_{V_2}^* = C_{V_2} / C_{Vref}$
$P_r = C_{Vref} \mu_{ref} / \kappa_{ref}$	$C_{Vref} = \frac{3}{2} R_{ref}$

TABLE 5. DIMENSIONLESS PARAMETERS ASSOCIATED WITH THE ENERGY BALANCE EQUATIONS 33 AND 34.

TABLE 6

$$S_n = \frac{x_{ref}^2 \epsilon n_{ref}}{\phi_{ref} \epsilon}$$

$$n_o^* = n_o / n_{ref}$$

TABLE 6. DIMENSIONLESS PARAMETERS ASSOCIATED WITH POISSON'S EQUATION 35.

TABLE 7

## CONSTANT SCATTERING AND POTENTIAL SCALING

 $\phi_{ref} = 1.0, \text{ GaAs}$ 

SCATTERING SCALING PARAMETER $\lambda$	0.5	1.0	2.0	4.0
REFERENCE LENGTH (microns)	2.0	1.0	0.5	0.25
$\kappa_{ref}$ (joules / $^{\circ}\text{K} \cdot \text{cm} \cdot \text{sec}$ )	$4.0 \times 10^{-6}$	$2.0 \times 10^{-6}$	$1.0 \times 10^{-6}$	$0.5 \times 10^{-6}$
$\mu_{ref}$ ( $\text{gm} / \text{cm} \cdot \text{sec}$ )	$11.48 \times 10^{-11}$	$5.74 \times 10^{-11}$	$2.87 \times 10^{-11}$	$1.44 \times 10^{-11}$
$n_{ref}$ ( $\text{cm}^{-3}$ )	$1.25 \times 10^{15}$	$5 \times 10^{15}$	$2 \times 10^{16}$	$8 \times 10^{16}$
$\mu_c$ (CATHODE MOBILITY) $\text{cm}^2 / \text{v} \cdot \text{sec}$	31,270	15,635	7,817.5	3,909

TABLE 7. REFERENCE QUANTITIES FOR CONSTANT SCATTERING AND POTENTIAL SCALING (BEGINNING WITH GaAs).

TABLE 8

$$Cn \equiv \frac{\mu_r \psi_r}{x_r v_r}$$

$$Sn \equiv \frac{e x_r^2 N_r}{\epsilon_r \psi_r}$$

$$Re \equiv \frac{x_r v_r}{D_r}$$

TABLE 8. DIMENSIONLESS PARAMETERS ASSOCIATED WITH THE CONTINUITY EQUATIONS 52 AND 53.

DISTRIBUTION LIST

Director, Advance Research Projects Agency 1400 Wilson Boulevard Arlington, VA 22209 Attn: Program Management	2
Scientific Officer Leader Electronics Division Office of Naval Research 800 North Quincy Street Arlington, VA 22217 Attn: Dr. Larry Cooper	3
Defense Contract Administration Services Management Area 96 Murphy Road Hartford, CT 06114	1
Director, Naval Research Laboratory Attn: Code 2627 Washington, DC 20375	6
Defense Technical Information Center Building 5, Cameron Station Alexandria, VA 22314	12
TACTEC Battelle Memorial Institute 505 King Avenue Columbus, OH 43201	1

**END**

**FILMED**

**3-85**

**DTIC**